EUROPEAN COMMISSION

European Research Area

RESEAL II

A large-scale in situ demonstration test for repository sealing in an argillaceous host rock – Phase II

FINAL REPORT

EUR 24161 EN

SEVENTH FRAMEWORK PROGRAMME

Interested in European research?

Research*eu is our monthly magazine keeping you in touch with main developments (results, programmes, events, etc.). It is available in English, French, German and Spanish. A free sample copy or free subscription can be obtained from:

European Commission
Directorate-General for Research
Communication Unit
B-1049 Brussels
Fax (32-2) 29-58220
E-mail: research-eu@ec.europa.eu
Internet: http://ec.europa.eu/research/research-eu

EUROPEAN COMMISSION

Directorate-General for Research
Directorate J – Energy (Euratom
Unit 2 - Fission

Contact: Christophe Davies

European Commission
Office CDMA 1/61
B-1049 Brussels

Tel. (32-2) 296 16 70
Fax (32-2) 295 49 91
E-mail: christophe.davies@ec.europa.eu

EUROPEAN COMMISSION

nuclear science and technology

RESEAL II

A large-scale in situ demonstration test for repository sealing in an argillaceous host rock – Phase II

Authors
M. Van Geet, W. Bastiaens, G. Volckaert, E. Weetjens,
X. Sillen, N. Maes (SCK•CEN, BE)
Ch. Imbert, P. Billaud, G. Touzé, M. Filippi (CEA, FR)
F. Plas (ANDRA, FR)
M.V. Villar, M. García-Gutiérrez, M. Mingarro (CIEMAT, ES)
A. Gens, B. Vallejan (UPC, ES)

Contract No: FIKW-CT-2000-00010

Final report

Work performed as part of the European Atomic Energy Community's R&T specific programme Nuclear Energy 1998-2002, key action Nuclear Fission Safety (Fifth Framework Programme)

2009

Directorate-General for Research
Nuclear Fission Safety

EUR 24161 EN

EUROPE DIRECT is a service to help you find answers to your questions about the European Union

Freephone number (*):
00 800 6 7 8 9 10 11

(*) Certain mobile telephone operators do not allow access to 00 800 numbers or these calls may be billed

A great deal of additional information on the European Union is available on the Internet.
It can be accessed through the Europa server (http://europa.eu).

Cataloguing data can be found at the end of this publication.

Luxembourg: Office for Official Publications of the European Communities, 2009

ISBN 978-92-79-13626-9
doi 10.2777/54857

Acknowledgement

The project was financially supported by the EC through the contract FIKW-CT-2000-00010 and matching funding was provided by ONDRAF/NIRAS and ANDRA. As coordinator the SCK•CEN thanks all the researchers and organizations involved in this project. Special thanks go to Christophe Davies, Bernard Dereeper and Johan Bel. We also acknowledge the important effort of the technicians involved in this project, especially those involved in the in-situ shaft sealing experiment in the HADES underground research laboratory, namely Frank Vandervoort, Tom Maes, Kris Moerkens, Christian Lefevre, Bert Vreys, Johan Peters and Louis Van Ravestyn.

Abstract

For plastic clays, it is believed that the breakthrough pressure corresponds with the minimum total stress (Volckaert *et al.,* 1995b; Ortiz *et al.,* 1997; Rodwell *et al.,*1999). The total stresses measured in the seal vary between 7 and 11 bar. Consequently, the measured breakthrough pressures are somewhat higher, but as mentioned before these measured breakthrough pressures should be considered as maximum values. Moreover, the shut in pressure observed in the first breakthrough test might be realistic and with a value of 8.3 bar lies within the range of total stresses measured inside the seal.

The radionuclide migration tests are still ongoing. Preliminary results of the migration in the EDZ seem to indicate that no preferential pathways for radionuclide migration exist.

A large amount of **numerical modelling** work has been performed as part of the RESEAL II project. The analyses have played an important role in assisting in the rational interpretation of the various tests performed in the project:

- Swelling pressure oedometer tests in the laboratory (hydromechanical analyses)
- Hydration stage of the shaft sealing test (hydromechanical analyses)

On the one hand, an advanced hydromechanical formulation has been used to perform coupled hydromechanical analyses that incorporate the possibility of considering simultaneously two overlapping structural levels. In this way the individual behaviour of the powder and pellets of the sealing mixture and their interactions can be considered explicitly. A double structure extension of the classical BBM model designed to account for expansive clay behaviour is used as mechanical constitutive law. The characteristic form of swelling pressure development observed in the laboratory tests has been successfully reproduced. It consists of an initial increase, followed by a reduction due to the collapse of the macrostructure and finally a stage of further swelling pressure increase. The satisfactory simulation extends to the two values of dry density tested with minimal changes of material parameters. The formulation provides additional information on the evolution of the microstructure and macrostructure throughout the test, helping to understand better the interplay between the different components of the sealing material. The information obtained appears consistent with microstructural observations of various types.

On the other hand a single porosity coupled hydromechanical formulation has been adopted with two possibilities for the analysis: a fully coupled computation and a chaining calculation in which hydraulic and mechanical problems are solved sequentially. The BBM constitutive model for unsaturated soils is adopted to represent the mechanical behaviour of the materials. It is interesting to note that, with an adequate use of the single porosity model and the BBM constitutive law, these analyses also reproduce satisfactorily the swelling pressure development, at least for the samples compacted at 1600 kg/m^3. It appears that the small swelling pressure associated with the less compacted samples can not be easily reproduced with the current state of the model. No significant differences are observed when comparing the coupled analyses with the chaining calculations.

The analysis of the shaft sealing test has provided a sterner challenge. This is to be expected because of the unavoidable uncertainties and heterogeneities associated with the performance of a large in situ test in field conditions. The analysis performed by UPC uses the same formulation

than for the simulation of the laboratory tests, a double structure constitutive model for the sealing material and the BBM constitutive law for the host rock. The simulation does provide a satisfactory overall reproduction of the process of hydration and swelling pressure development throughout the shaft seal. The prediction of water pressures, stresses and displacements in the host rock are also in qualitative agreement with observations. There are, however, a number of significant differences when performing individual detailed comparisons. Some of them are unavoidable; for instance an axisymmetric model can not account for different rates of hydration and stress development along different directions.

The simulation of the shaft sealing test by CEA uses the single porosity formulation and the BBM constitutive law for host rock and seal material. Again, the calculations reproduce qualitatively the evolution of hydraulic parameters in response to the hydration processes. Detailed comparisons, however, show also significant differences between observations and computed results. Variations of the hydraulic conditions of the simulations, examined by a set of sensitivity analyses, do not change radically the type of results obtained. Comparison with mechanical parameters is less comprehensive due to the short calculation times brought about by numerical convergence problems.

Considering the modelling of the shaft sealing test from a general perspective, it is apparent that the basic phenomena concerning the evolution of hydraulic and mechanical variables, both in the seal material and the host rock, are by and large adequately reproduced. There are no observations that radically contradict the modelling results. This implies that the formulations employed contain appropriate descriptions of the basic phenomena occurring in the seal and in the host rock as well as their interactions. Thus, closer quantitative agreement between computed results and observation is largely a matter of parameter variation and more detailed characterization of the field test. The double porosity model is capable to offer more thorough information about the evolution of the sealing material albeit at a higher complexity cost.

With respect to **performance assessment** (PA), it should be noted that several independent simulations have illustrated that high performance seals are not strictly necessary within diffusion dominated clayey rocks. However, all waste management agencies considering clayey host rocks include currently bentonite seals in their concept. It has been tried to translate the functional or qualitative requirements of seals for clayey host rocks into technical requirements. The contribution of RESEAL to demonstrate or understand these requirements is described.

- The feasibility of emplacing a borehole and shaft seal has been demonstrated
- however, hydration took much longer than foreseen
- The final hydraulic conductivity was as originally foreseen
- The bentonite seals did not reveal any preferential gas migration pathways and after gas breakthrough the original hydraulic conductivity was recovered
- No preferential pathways towards radionuclide migration were evidenced
- The large amount of laboratory experiments have underbuilt our knowledge in the behaviour of the sealing materials and hydro-mechanical modelling is strongly improved

The major open questions that remain are to extend the obtained results to larger scale access shafts, to extend the obtained results towards indurated clays and their typical EDZ behaviour and to get better insight in natural hydration and the effect of gas migration on the long term.

Table of Contents

1 Introduction

An essential item in the concept of geological disposal of high-level waste underground repositories is the backfilling and sealing of shafts and galleries. This is needed to avoid preferential pathways for water, gas and radionuclides migration. The demonstration of feasibility of the sealing on a representative scale is therefore essential. For about 20 years the applicability of highly compacted bentonite for this purpose has been investigated. The low permeability and high sorption capacity of the bentonite make it a very effective barrier.

Several large-scale sealing or backfilling experiments have been performed in crystalline rocks (Fairhurst *et al.,* 1993; ENRESA, 2000, 2006; Johannesson *et al.,* 2007; Martino *et al.,* 2007). In clay, only relatively small-scale backfilling and sealing experiments have been performed in the nineties in the framework of the development of Thermo-Hydro-Mechanical models (Volckaert *et al.,* 1996). They were essentially related to the study of the near field and its associated temperature effects. More recently, larger scale experiments in clay environments were installed (Volckaert *et al.,* 2000; Mayor *et al.,* 2005). One of the first of these experiments was the RESEAL project, which aimed to seal a shaft in plastic Boom Clay in Mol, Belgium (Volckaert *et al.,* 2000).

The RESEAL project started with a first phase in 1996 within the 4th framework program of the European Commission (Volckaert *et al.,* 2000). The project was co-financed by ONDRAF/NIRAS, ANDRA and ENRESA. The main objectives of this first phase were to:

- Define a procedure for the production and installation of a shaft seal, aiming to install a bentonite seal in a 2m diameter vertical shaft within the Boom Clay in the HADES URL in Mol, Belgium
- Obtain basic parameters on the hydro-mechanical behaviour of the sealing materials
- Install and hydrate a borehole sealing experiment, aiming at sealing a 25 cm diameter horizontal borehole in Boom Clay in the HADES URL in Mol, Belgium
- Design, instrument and install the shaft sealing experiment
- Perform first exploratory model simulations of the hydro-mechanical behaviour of the borehole and shaft seal tests.

The RESEAL project was continued by a second phase within the 5th framework program of the European Commission, which started in 2001. This phase was co-financed by ONDRAF/NIRAS and ANDRA. The main objectives were to:

- Increase the knowledge of the basic parameters on the hydro-mechanical behaviour of the sealing material used in the shaft seal
- Evaluate the performance of the borehole seal with respect to water, gas and radionuclide migration
- Evaluate the hydro-mechanical behaviour of the shaft seal and the surrounding host rock
- Evaluate the performance of the shaft seal with respect to water, gas and radionuclide migration
- To increase the capability of simulating the hydro-mechanical behaviour of the sealing material using numerical models.

Due to the slow hydration of the shaft seal, the RESEAL II project was only finished in 2007. The project was executed by SCK·CEN (co-ordinator), CEA, ANDRA, CIEMAT and UPC.

This report is fully stand-alone, however, for some details we refer to Volckaert *et al.* (2000). Within this report we will first describe the results of laboratory tests that aimed at gaining more insight into the hydro-mechanical behaviour of the FoCa pellet/powder mixture as used in the shaft sealing experiment. In the second chapter we shortly repeat the design, installation and hydration of the borehole seal as described in Volckaert *et al.* (2000) and include the information on the performance testing of this borehole seal. The third chapter illustrates the design and installation of the shaft seal experiment and will focus on the hydro-mechanical evolution during hydration and the performance of the seal after saturation. The fourth chapter describes the different hydro-mechanical codes used and the results of their application on laboratory tests and the borehole and shaft seal experiments. Finally, chapter five gives an overview of the literature data on the seal requirements and gives the conclusion of this project with respect to performance assessment.

2 Material characterization through laboratory experiments

The laboratory experiments aimed to have a good characterisation of the bentonite materials used in the in-situ experiments. In the borehole sealing experiment, two clays, FoCa and Serrata clay, were used. In the large scale shaft sealing experiment, only FoCa clay has been used. As a consequence, the major focus of the laboratory tests is on the FoCa clay.
The laboratory programme had two objectives. The first objective is to provide the necessary data on the sealing materials required for the hydro mechanical and transport modelling. The second objective is to investigate the pellet/powder mixture behaviour and to compare the properties of this heterogeneous material with these of the homogeneous powder material compacted at the same void ratio.
To this end, this chapter is divided into four parts. The first part describes both, the material and the preparation techniques used. The second part describes the hydro-mechanical parameters, with the main focus on FoCa clay and where possible comparing the behaviour of homogeneously compacted powder and the heterogeneous pellet/powder mixture. The third part is restricted to the migration parameters as determined on pellet/powder mixtures. Finally, a discussion and conclusions are gathered in the last part and put in perspective of the original objectives.

2.1 Material

2.1.1 Introduction

In the frame of the BACCHUS-2 project (Volckaert *et al*., 1996) an industrial scale technique to produce a granular material composed of bentonite powder mixed with high-density bentonite pellets was developed. This material can be easily applied to backfill irregularly shaped volumes and is rather cheap to produce. This material has been therefore selected for the sealing of the experimental shaft in the HADES URF within the RESEAL project. Nevertheless for the horizontal borehole sealing test of the RESEAL experiment, precompacted blocks of sealing material were used to avoid the technical problem of the use of mixtures in a horizontal configuration.

Two different materials have been studied in the framework of this project: a French bentonite, the FoCa clay and a Spanish bentonite, the Serrata clay. FoCa and Serrata clays are studied in laboratory and tested in the borehole sealing test. Concerning the shaft sealing in situ test, it is not technically and financially possible to test both materials. Therefore, only the FoCa clay was selected.

The basic information of the materials used is described here. Moreover, the pellet and mixture production of the material used within the shaft seal experiment is shortly described here. More information can be found in Volckaert *et al.* (2000).

2.1.2 FoCa clay

The FoCa clay (Fourges-Cahaignes clay) is a sedimentary clay from the Paris Basin, extracted in the Vexin region (Fourges-Cahaignes, France) and supplied by the SFBD Company (Société Française des Bentonites et Dérivés). The major component (i.e. 80% of the clay fraction) is an interstratified clay of 50% calcium beidellite and 50% kaolinite. It contains also kaolinite, quartz, goethite, hematite, calcite and gypsum (Coulon, 1987; Lajudie *et al*., 1994). The industrial process preparation consists of drying, grinding and sieving (max. grain size: 2 mm).

The cation exchange capacity (CEC), measured by the sorption of cobaltihexammine and Cu-ethylenediamine, is 71 meq/100g. The major exchangeable cations are Ca (73.1 meq/100g), Mg (6.5 meq/100g), Na (3.6 meq/100g) and K (0.8 meq/100g). The global CEC is lower than the sum of the major cations CEC due to secondary mineral phases (calcite, gypsum). These phases are dissolved and measured with the exchangeable cations, increasing the measured CEC value of each major cation.

The liquid limit of FoCa is 112%, the plastic limit is 50%, and the specific weight is 2.675. The hygroscopic water content, for a relative humidity around 60% and a temperature of 20°C, is comprised between 10 and 12%.

2.1.3 Serrata clay

The Serrata clay is a bentonite coming from the Cortijo de Archidona deposit (Almería, Spain), selected by ENRESA as suitable material for the backfilling and sealing of HLW repositories. The same clay is used for the FEBEX Project in the in-situ (Grimsel, Switzerland) and the mock-up (Madrid, Spain) tests (ENRESA 1998, ENRESA 2000). The processing at the factory has consisted in disaggregation and gently grinding, drying at 60 °C and sieving (max. grain size: 5 mm). It has a montmorillonite content higher than 90 %. The predominant phylosilicate is in fact a smectite/illite mixed layer, with 10-15 % of illite layers. Besides, it contains variable quantities of quartz, plagioclase, K-feldspar, calcite and opal-cristobalite-trydimite (Opal-CT).

The cation exchange capacity (CEC) is of 113±6 meq/100g, and the major exchangeable cations are: Ca (35-42 meq/100g), Mg (31-32 meq/100g), Na (24-27 meq/100g) and K (2-3 meq/100g).

The liquid limit of the bentonite is 103 ± 4 %, the plastic limit is 53±3 % and the specific weight is 2.70. The equilibrium gravimetric water content of the clay at CIEMAT laboratory conditions (R.H. 50±10 %, which corresponds to a suction of around 130 MPa) is about 13.7±1.3 %.

2.1.4 Pellets production

Sahut-Conreur Company in Raismes (France) manufactured the pellets. This company has a large experience in the compaction process, applied to powders and especially to different types of clays. The pellets are made from clay powder using a continuous compaction process. A compactor/granulator, such as that used for the pelletizing of coal powder or ore powders resulting from flotation processes, is applied. Its principle is shown in **Figure 2-1**.

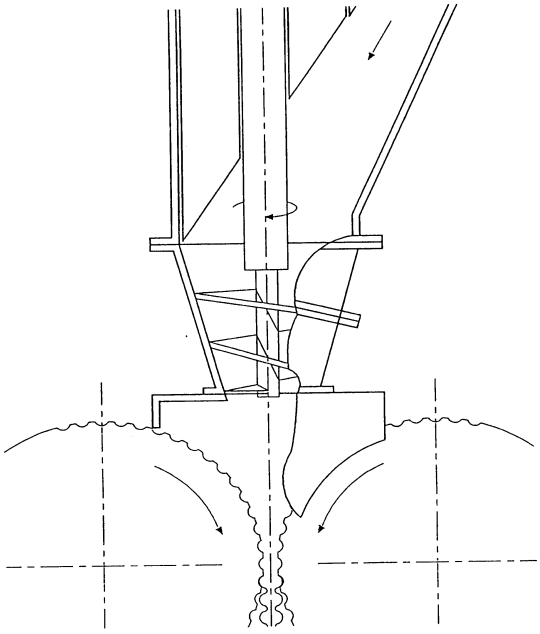

Figure 2-1: Principle of the compacter/granulator used to make pellets.

The powder falls in a conical screw of Archimedes which precompacts the powder and presses it between two moulding cylinders turning in opposite direction. The precompacted powder is pressed with a high force and dragged between the cylinders. More details about the fabrication process of the pellets can be found in Volckaert *et al.* (1996).

Different shapes and sizes of pellets have been tried, in order to obtain a high dry density. The best result has been obtained with pellets of approximately 25 mm x 25 mm x 15 mm of size (called B25/15 pellets). Several fabrication sequences consisting of pellets of FoCa clay and Serrata clay of different water contents have been made. Samples of each production have been characterised.

2.1.5 Production of the pellets used in the shaft seal experiment

For the large scale sealing test, SFBD (France) has delivered a special batch of FoCa clay (about 20 tons) with the following characteristics: granulometry 0-2mm and water content of 7 ±1.5%. Half of this batch was transformed into pellets by the company Sahut-Conreur at Raismes (France).

At the end of 1998, a pilot fabrication of pellets has been manufactured to verify the characteristics of the pellets made with the batch of FoCa clay.

The FoCa clay delivered by SFBD had a very low water content of about 4%, and the specifications were not respected. The production had to be stopped after only a few tens of kilos. Normally, natural clay has a tendency to fill in and to plug all the alveoli of the two compacting wheels but the pellets exhibited small cracks. The water content was too low and the pellets were not resistant. Therefore the natural clay has been humidified by spraying a controlled quantity of water on the clay and by mixing the clay at the same time in a mixing machine. The water content increased up to 8% water content, (+3% water content according to the Sahut-Conreur procedure). In fact, the new water content is between 7 and 8%. A new production has been performed with better results than the first one. To control this production, measurements have been performed on 3 pellets of natural FoCa (w=3.9%) and 6 pellets of humidified FoCa (w=6.7%). The results confirm that water content of about 7% to 8% is an optimal value to obtain high density pellets with FoCa clay.

2.1.6 The pellet/powder mixture

To obtain a granular backfill material with a high density, the pellets are mixed with powder of the same clay. The mixture's density can be increased by compaction applying vibro-compaction techniques as used in road construction. To demonstrate the applicability of this mixture on an industrial scale, it has been applied for the sealing of the experimental shaft in the HADES URF using a compaction technique for its installation on the non-instrumented part of the seal (see section on shaft seal).

The pellet/powder mixture has been optimised to obtain the best balance between saturation time, swelling pressure, hydraulic conductivity and ability to be compacted.
The previous results show that the mixture constituted of 65% pellets and 35% of powder gives the best dry density. But laboratory tests on oedometric cell showed that for a 65/35 mixture the

hydration time is very long. Moreover during the compaction process a more important segregation between the pellets and the powder with a 65/35 mixture than with the 50/50 mixture was observed. Therefore, a proportion of 50% pellets and 50% powder was selected for the shaft sealing test.

2.2 Hydro-mechanical parameters

2.2.1 Introduction

Here, we describe the hydro-mechanical parameters of mainly the FoCa clay as measured in laboratory setups. These parameters are important as they are necessary input for the hydro-mechanical modelling and as they provide us with a better insight into the behaviour of the clay as used in the in-situ experiments. It is tried to combine all available information gathered during RESEAL I and RESEAL II. The parameters described are the hydraulic conductivity, the retention curves, the swelling pressure evolution during infiltration tests, the final swelling pressure and the homogenisation of the pellet/powder mixture.

2.2.2 Hydraulic conductivity

As formulated by IAEA (IAEA, 1990), the major functional requirement of a seal is to have the same hydraulic conductivity as the host rock. Thus, the hydraulic conductivity is a very important parameter for seals and as such the change with function of dry density has been evaluated. **Figure 2-2** compares the hydraulic conductivity of the pellet/powder samples (measured within the RESEAL project) and of compacted powder of FoCa clay (Plas, 1988; Lassabatère, 1997). The majority of tests used distilled water as testing fluid, although for some data points synthetic Boom Clay water (0.015M $NaHCO_3$) has been used. As the ionic strength of Boom Clay water is low, no major effect of using this water is observed. However, a large scatter in the data is clearly observed. Plas (1988) (in Lassabatère, 1997) reported values for uniaxially and isotropically compacted powder that were measured consolidating saturated samples instead of establishing an hydraulic gradient. Tests performed on compacted powder by one institute (using one specific batch or even sub-batch) result in a clear trend with limited scatter. Moreover, these trends are parallel when using the same technique (permeameter tests). Only when another technique is used (oedometer tests), a deviating trend is observed. The values obtained in uniaxially compacted samples report lower values than the mixtures. It is believed that the experimental technique and the natural variation between batches or sub-batches causes the large scatter in data. The hydraulic conductivity of compacted powder samples and of the pellet/powder mixtures are in the same range. The data of the pellet/powder mixtures are generated by different laboratories and on different batches and as such cover the whole range of values.

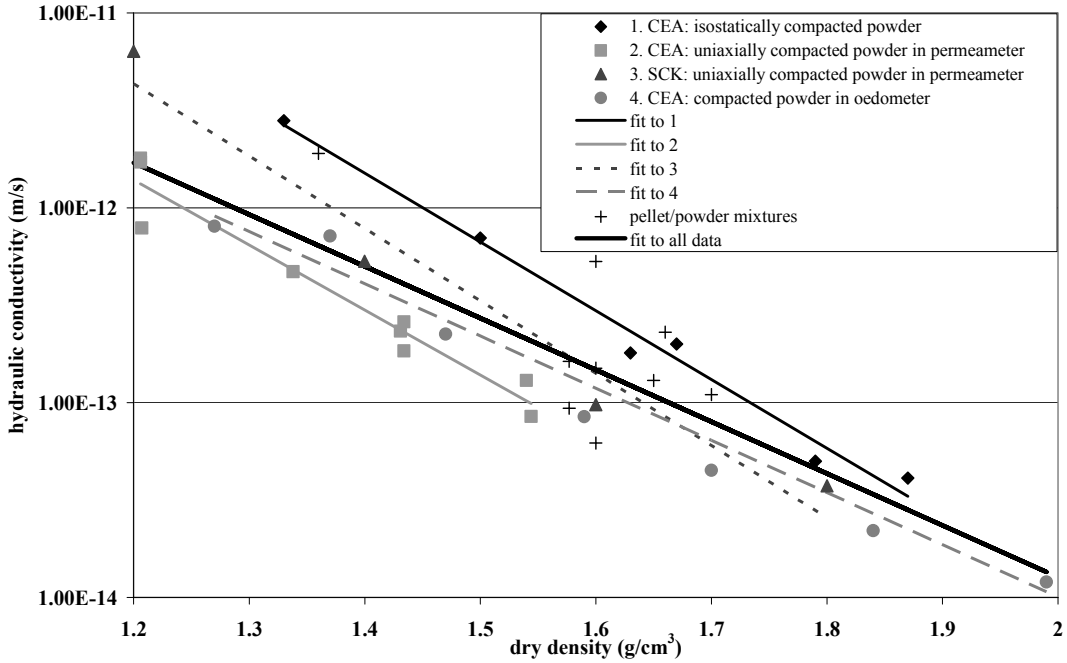

Figure 2-2: Comparison between the hydraulic conductivity of pellet/powder mixture and the compacted powder samples of FoCa clay.

The relationship between hydraulic conductivity (K, m/s) and dry density (ρ_d, g/cm³) has been established including all available data and results in:

$$\log K = -2.66\,\rho_d - 8.576 \qquad \text{Equation 1}$$

It should be noted that for dry densities lower than 1.2 g/cm^3, the hydraulic conductivity measured strongly deviates from the trends given here (not shown in figure).

For Serrata clay the relationship between hydraulic conductivity (K, m/s) and dry density (ρ_d, g/cm^3), for dry densities higher than 1.45 g/cm^3, lies below all data points given in **Figure 2-2** and can be expressed as:

$$\log K = -3.0\,\rho_d - 8.6 \qquad \text{Equation 2}$$

This equation has been obtained from tests in which distilled water was used as permeant and the clay was directly compacted in the permeability cell. The variation of the experimental values with respect to this fitting is around 40 %, but is believed to be caused by experimental uncertainties (take into account that the permeability values are in the order of 10^{-13} m/s).

2.2.3 Retention curves

The retention curve or soil water characteristic curve (SWCC) expresses the relation between degree of saturation and suction. It is an important law that has a strong influence on unsaturated flow. The curve also provides useful information about the pore structure of the material. As such the retention curve provides necessary data as input for the hydro-mechanical modelling of soils and clays. These retention curves have been determined on FoCa clay samples by different

laboratories in non-constrained samples, *i.e.* in samples whose volume could freely change during the determinations. However, only data are available on compacted FoCa powder or pellets, separately, and not on pellet/powder mixtures. **Figure 2-3** combines the data of different analyses (on compacted clay and pellets). Small differences between pellets and compacted clay might be observed, although no persuasive conclusion can be drawn taking into account all available data. As there might be differences between micro- and macro porosity in the pellet/powder mixture (see chapter 4 and Vallejan, 2008), available experimental data and literature data were used to fit water content (w) versus suction (s). Based on the available data, the following expressions are proposed:

$$w=-4.559 \ln(s) + 32.85 \qquad \textbf{Equation 3}$$

for powder compacted to high densities (and thus mainly containing microporosity) and

$$w=-4.353 \ln(s) + 31.82 \qquad \textbf{Equation 4}$$

for powder compacted to lower densities (and thus also containing an important fraction of macroporosity).

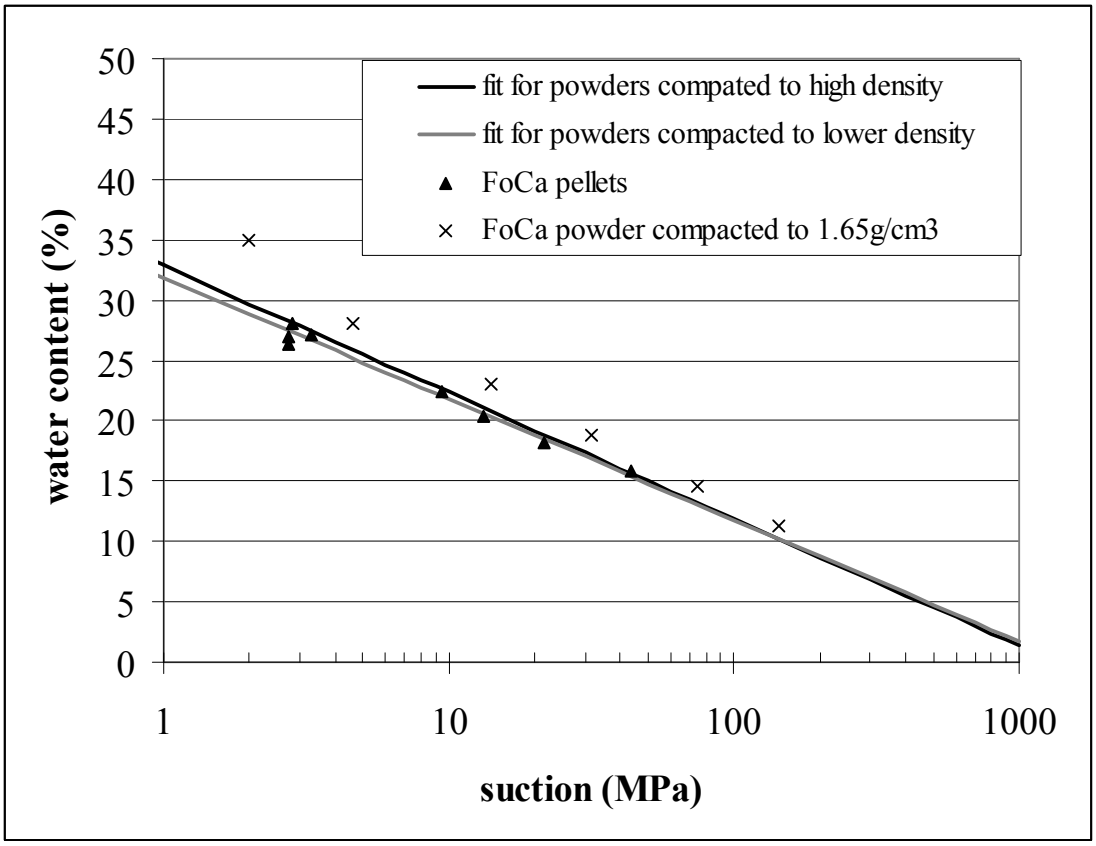

Figure 2-3: Comparison of the retention curves (water content) of pellets and compacted samples of FoCa clay and fitting expressions proposed (free volume determinations).

2.2.4 Infiltration tests

Infiltration tests have been performed by different laboratories in oedometric conditions with simultaneous measurement of swelling pressure, water intake and axial deformation. When mixtures are tested, it always concerns a 50/50 weight percent pellet/powder mixture. The experimental setups and the methodology followed are similar:

- constant volume
- column shaped samples
- saturation through bottom surface under low injection pressure (0.01 MPa)
- air evacuation through top surface
- initial water content between 4 and 5 % for the pellets and 5 and 12 % for the powder

The major differences between the tests are the height and diameter of the specimens, the water intake measurement method and the density of the mixture. The detailed descriptions can be found in Volckaert *et al.* (2000), Villar *et al.* (2005) and Imbert and Villar (2006).

Under these conditions, the kinetics of swelling pressure development goes along a well defined pattern in which the following phases can be distinguished:

- quick increase of pressure up to a peak
- progressive decrease of swelling pressure down to a minimum value that remains for a certain time
- new increase of swelling pressure at a decreasing rate, and
- eventual achievement of a stable pressure value.

The variations among the tests are due to the effect of initial height and dry density. The initial peak is less sharp for the samples of high initial dry density and increased height. Besides, the relation between the initial peak and the final swelling pressure depends on the dry density of the sample (**Figure 2-4**): for the lower dry densities, the peak value is similar or higher than the final value, whereas for dry density 1.6 g/cm^3, the final swelling pressure value is clearly higher than the peak one. Besides, the time needed to reach the initial peak pressure depends on dry density and height of the sample, increasing with both.

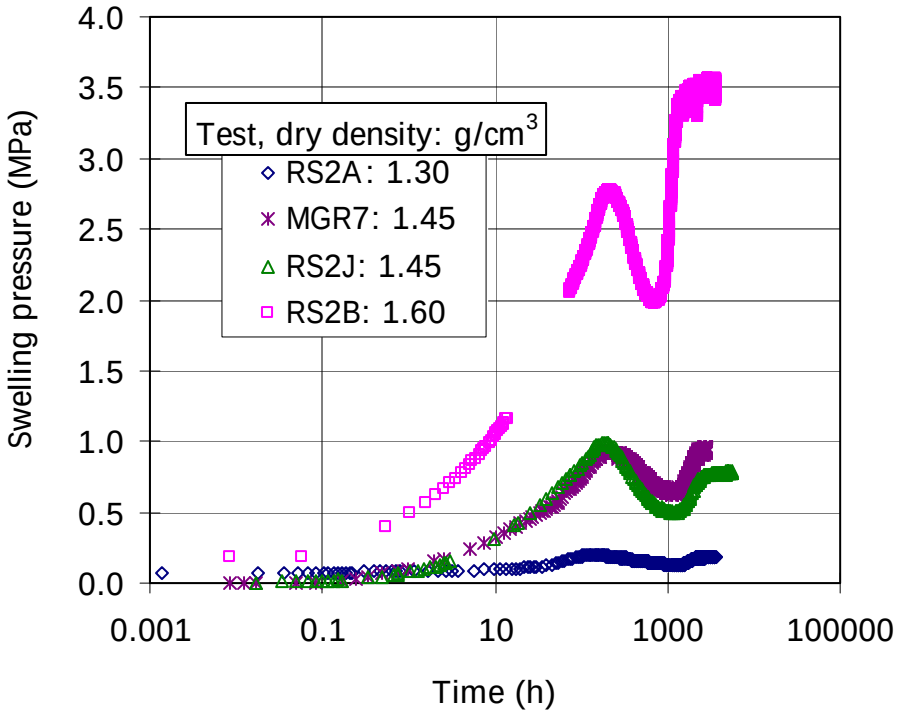

Figure 2-4: Evolution of swelling pressure in infiltration tests with 5 cm high samples of 50/50 pellet/powder mixtures of FoCa clay.

The swelling pressure curves obtained have been normalised with respect to the time to reach the peak pressure and to the maximum swelling pressure value (Imbert *et al*. 2004), in order to have a dimensionless representation. The curves thus obtained for the tests of dry density 1.60 g/cm^3 are plotted in **Figure 2-5**. In this way the kinetics of the tests become identical, irrespective of the height of the sample. Hence, there is not a scale effect on the results obtained, and samples 5- or 12-cm high seem to be equally representative.

On the other hand, the relation between the time to reach the final swelling pressure and the time to reach the peak pressure depends on dry density, being higher for the lower densities. For this reason, the dimensionless curves for dry densities 1.30 and 1.45 g/cm^3 are plotted separately in **Figure 2-6**. The comparison between **Figure 2-5** and **Figure 2-6** shows the influence of the initial dry density on the kinetics of swelling pressure evolution, and the existence of two distinct behaviours for low and high densities. Since the dry density of the pellets is always the same, the different dry densities of the mixture are caused by differences in powder density. The low dry densities of the powder result in higher initial permeability along the powder paths, which become preferential hydration channels, giving place to faster initial hydration and development of swelling pressure.

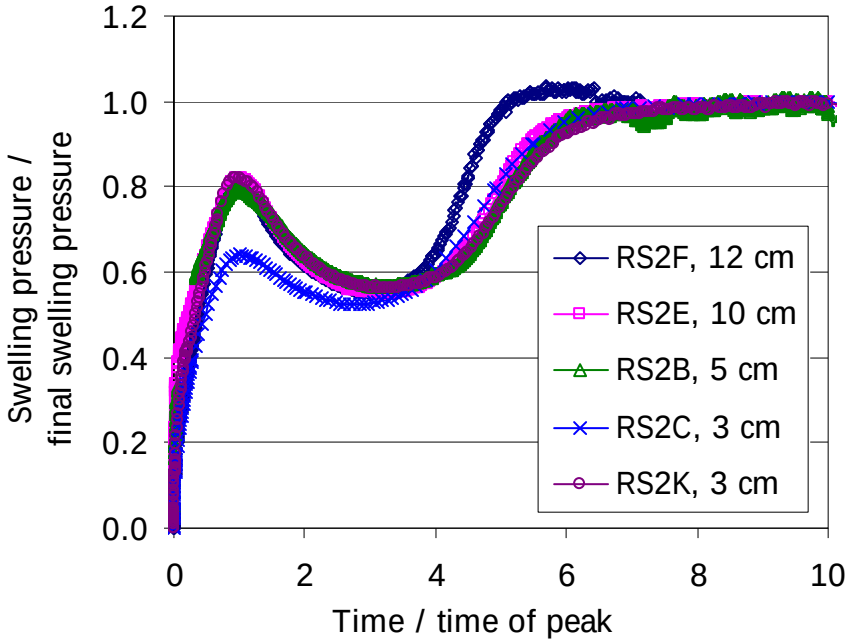

Figure 2-5: Dimensionless evolution of swelling pressure in the infiltration tests performed with mixtures (50/50) of FoCa clay compacted at ρ_d 1.60 g/cm^3 (the height of the specimens is indicated in the legend).

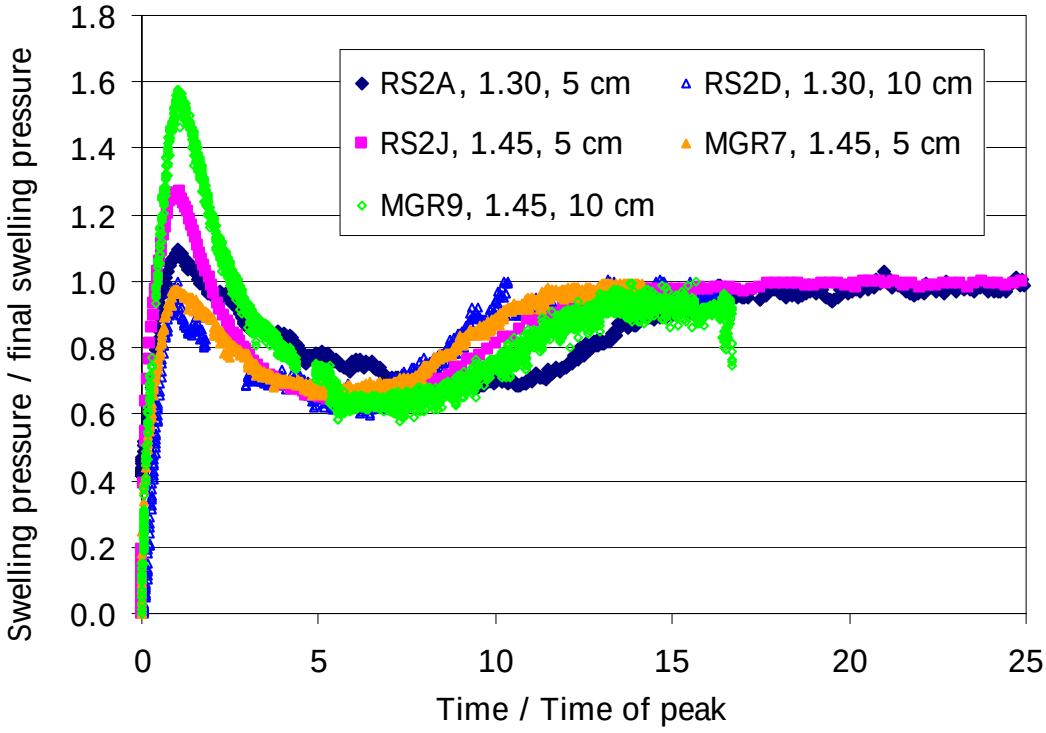

Figure 2-6: Dimensionless evolution of swelling pressure in the infiltration tests performed with mixtures (50/50) of FoCa clay compacted at low dry densities (indicated in g/cm^3 in the legend, where the height of the specimens is also shown).

It must be pointed out that the same pattern has been observed in the tests performed on different batches of FoCa powder. In fact, if the results obtained for compacted powder and for pellets/powder mixtures in samples of the same dry density and height are compared (**Figure 2-7**), not only the swelling evolution pattern, but also the actual swelling pressure values are similar.

Concerning the water intake, the comparison of tests on mixture and on compacted powder points to a faster initial intake of the mixture, although the same trend is found for both materials in the remainder of the tests (**Figure 2-8**). However, this does not translate into a quicker development of swelling pressure in the mixture, on the contrary, the kinetics of swelling pressure development is slightly quicker for compacted samples than for mixtures.
Summing up the observations concerning the swelling pressure evolution pattern, it can be concluded that the increase/decrease/increase pattern has been found irrespective of:

- the size of the sample, either height or diameter, as analogous results have been found by laboratories using different experimental setups: EGC (Pasquiou 1999, 2001), SCK·CEN (Volckaert *et al*. 2000);
- the injection pressure, that simply hastens the process;
- or the initial fabric (compacted powder or mixtures).

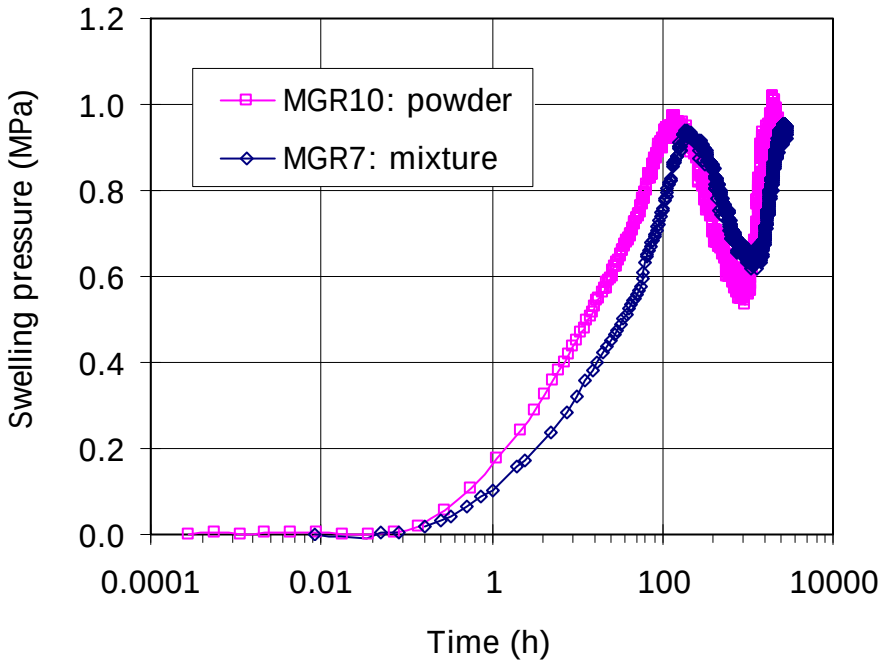

Figure 2-7: Evolution of swelling pressure in 5 cm high FoCa samples compacted at ρ_d 1.45 g/cm^3.

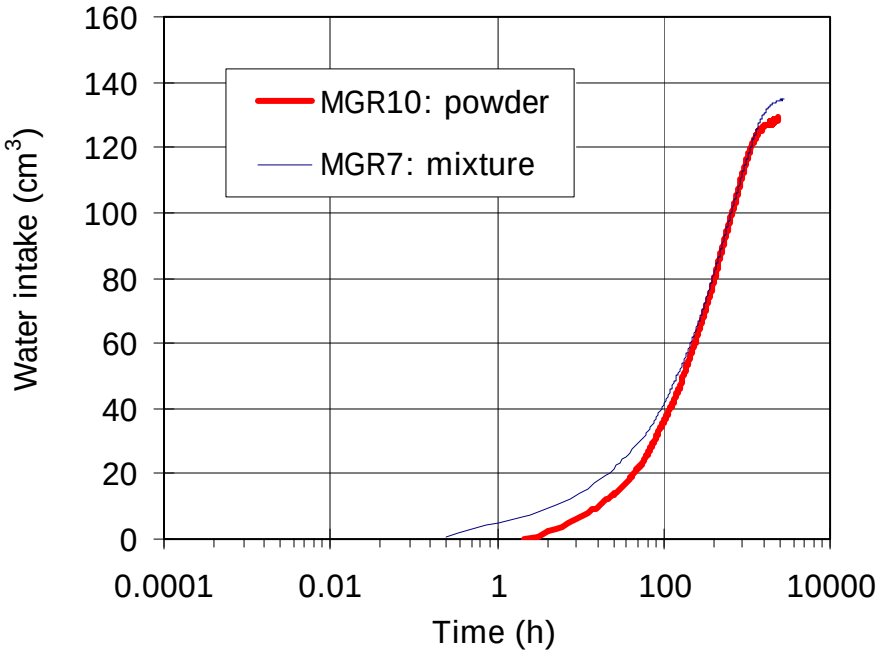

Figure 2-8: Evolution of water intake in 5 cm high FoCa samples compacted at ρ_d 1.45 g/cm^3.

It seems that the initial water content may also have an influence on the swelling pressure development kinetics. In the infiltration tests performed by CIEMAT during the first phase of the project, the decrease of swelling pressure after the initial peak was not observed (**Figure 2-9**). These tests were performed with a 50/50 FoCa bentonite pellet/powder mixture following the same procedures and in the same equipment than the tests shown above. The only difference between the first and the second phase tests was the initial water content of the pellets and powder, that was higher in the earlier tests, as the material came from a different manufacturing batch. This could be the reason for the absence of the increase/decrease/increase pattern of swelling pressure development. However, an intermediate period of softer pressure increase is actually detected. This could indicate that the collapse of the macrostructure on saturation is more important when hydration starts from high suctions, whereas it is compensated by an overall swelling of the microstructure when the initial suction is lower.

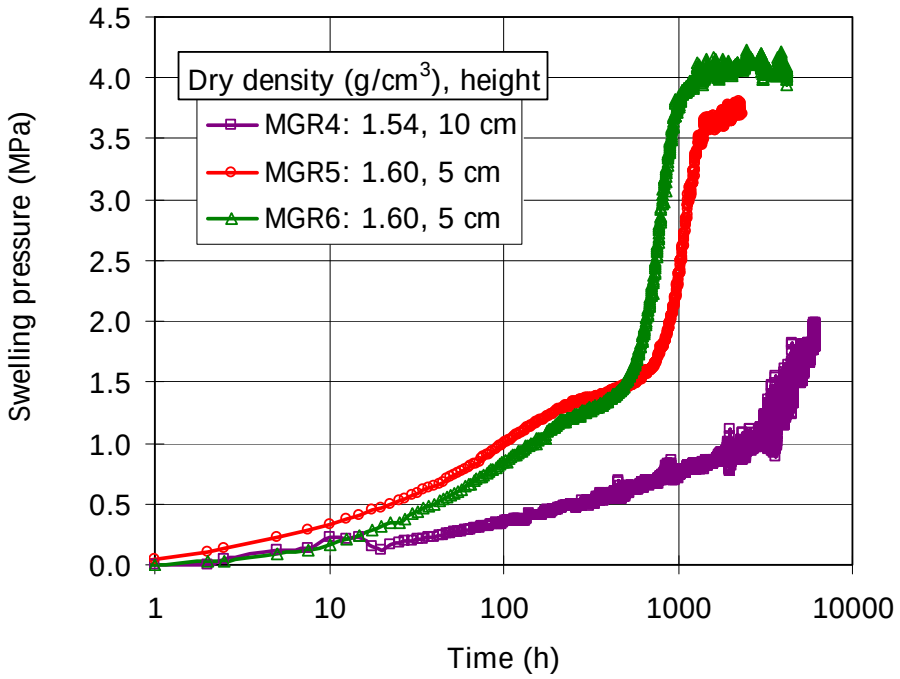

Figure 2-9: Evolution of swelling pressure in infiltration tests performed in 50/50 FoCa pellet/powder mixtures during RESEAL I (the initial water content is higher than in the tests shown above).

2.2.5 Final swelling pressure

During RESEAL I and RESEAL II many laboratory tests have been performed allowing to check the final swelling pressure of the FoCa clay as function of the dry density. The majority of the tests have been performed with deionised, deaerated water (only for four tests synthetic Boom Clay water has been used). The reason for setting up so many tests was to evaluate

- the effects of possible differences between different batches of clay
- the difference between compacted powder and pellet/powder mixtures.

Figure 2-10 summarises all available data. The major conclusion is that an important scatter on the data is present and as such predicting a precise final swelling pressure in function of dry density is not possible. On the other hand it is illustrated that there is a clear relation between final dry density and final swelling pressure. Moreover, the large amount of tests and data have demonstrated that:

- similar observations can be obtained by three different, independent laboratories using slightly different setups,
- different batches of FoCa clay have no major effect on the studied relation,
- the initial fabric (compacted powder or mixture of pellets and powder) has no major effect on the studied relation,
- scale effects might have an effect on the studied relation (tests in big oedometers tend to result in slightly higher swelling pressures than those obtained in small samples).

Taking into account all data, the followig fit between final swelling pressure (P_s, MPa) and final dry density (ρ_d, g/cm^3) is drawn:

$$P_s = 0.0061\ \rho_d^{13.272} \qquad \text{Equation 5}$$

The 95% percent confidence interval, taking into account all data, results in a lower and upper boundary at, respectively:

$$P_s = 0.0041\ \rho_d^{12.76} \qquad \text{Equation 6}$$

$$Ps = 0.0082\ \rho_d^{13.79} \qquad \text{Equation 7}$$

It can be noted that this fit corresponds with the fit of data available from tests on pellet/powder mixtures measured in big oedometers (Villar *et al*., 2005).

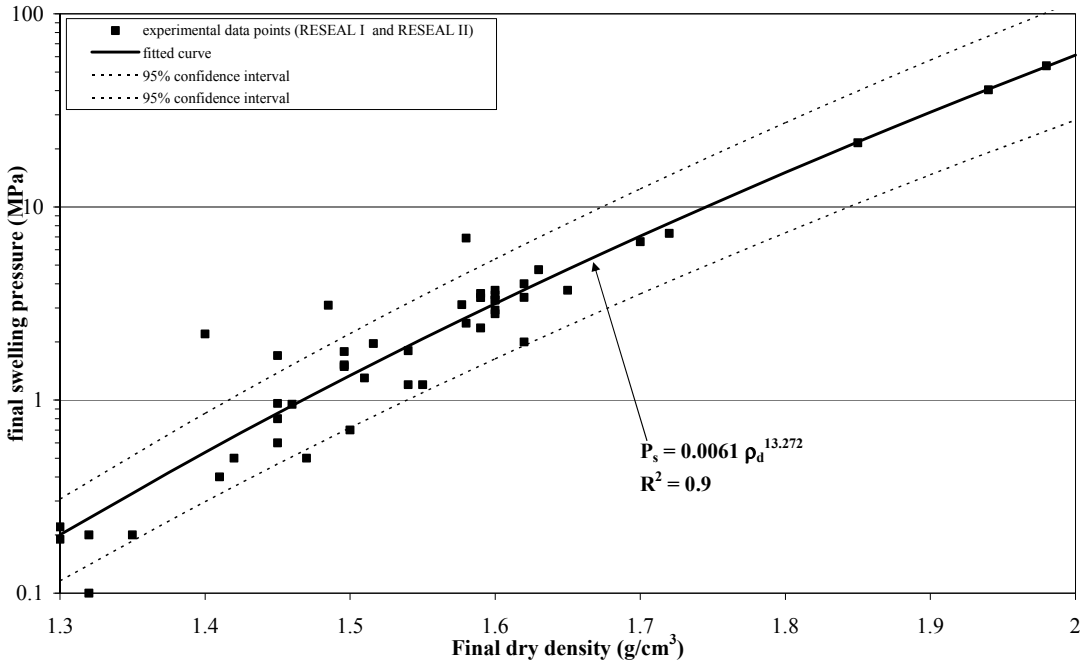

Figure 2-10: Swelling pressure of FoCa bentonite as determined in samples of different sizes and densities of compacted powder and pellets/powder mixtures.

For Serrata clay, the swelling pressure (P_s, MPa) of compacted samples can be related to the dry density (ρ_d, g/cm^3) through the following equation (Villar, 2002):

$$\ln P_s = 6.77\ \rho_d - 9.07 \qquad \text{Equation 8}$$

2.2.6 Homogenisation of the pellet/powder mixture

Dual-gamma ray attenuation and microfocus computer tomography have been used to characterise the evolution of the FoCa pellet/powder mixture during hydration. To this end, infiltration tests on specially designed setups have been performed. The method of dual gamma ray attenuation allows the simultaneous measurement of liquid and solid phase concentration in a given location. The microfocus computer tomography technique allows reconstructing a three dimensional view of the sample in terms of density variations, which is very useful in order to follow the homogenisation of the mixture. Details on the techniques and methodology can be found in Villar *et al.* (2005) and Van Geet *et al.* (2005a).

For the dual gamma ray attenuation, tests have been performed on 50/50 pellet/powder mixtures of dry density 1.30 and 1.60 g/cm^3. Here, only the results of the test at 1.30 g/cm^3 are shown. The sample was manually manufactured by alternating powder and pellet layers up to a height of 11.3 cm. Hydration took place by the bottom surface under the pressure of a 1-m water column. The periodic counting of photons allowed the determination of water content and density along the sample at different times. The results are plotted in terms of water content, dry density and degree of saturation in **Figure 2-11**, **Figure 2-12** and **Figure 2-13**. It can be observed that at the beginning of hydration, a sharp water front is developed. This front softens quickly, as the water content increase affects the whole sample, although less intensely in the areas farther from the water source. This means that there is no sharp limit between dry and wet areas. The sample reaches a homogeneous saturation after 221 days.

The dry density presents initially disparate values due to the natural heterogeneity of the mixture, which is accentuated by the small diameter of the cell. Nonetheless, hydration induces an equilibration of these values, reducing the higher densities and increasing the lower. The dismantling of the test after 491 days of hydration has allowed the visual inspection of this homogeneity.

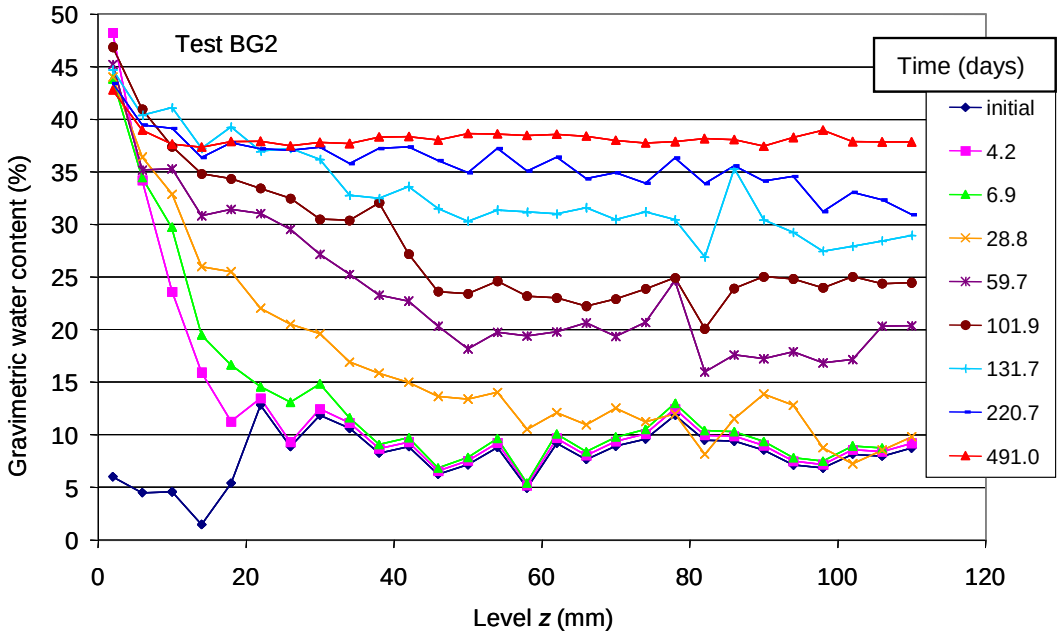

Figure 2-11: Evolution of water content at different levels of a sample of ρ_d 1.30 g/cm^3 during infiltration.

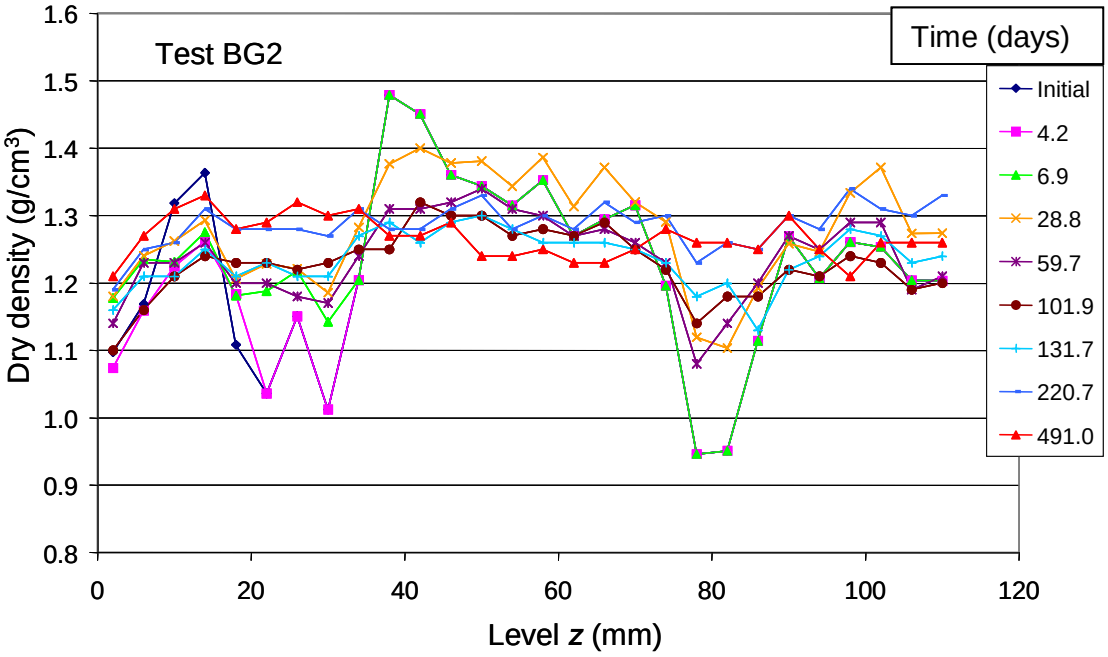

Figure 2-12: Evolution of dry density at different levels of a sample of ρ_d 1.30 g/cm^3 during infiltration.

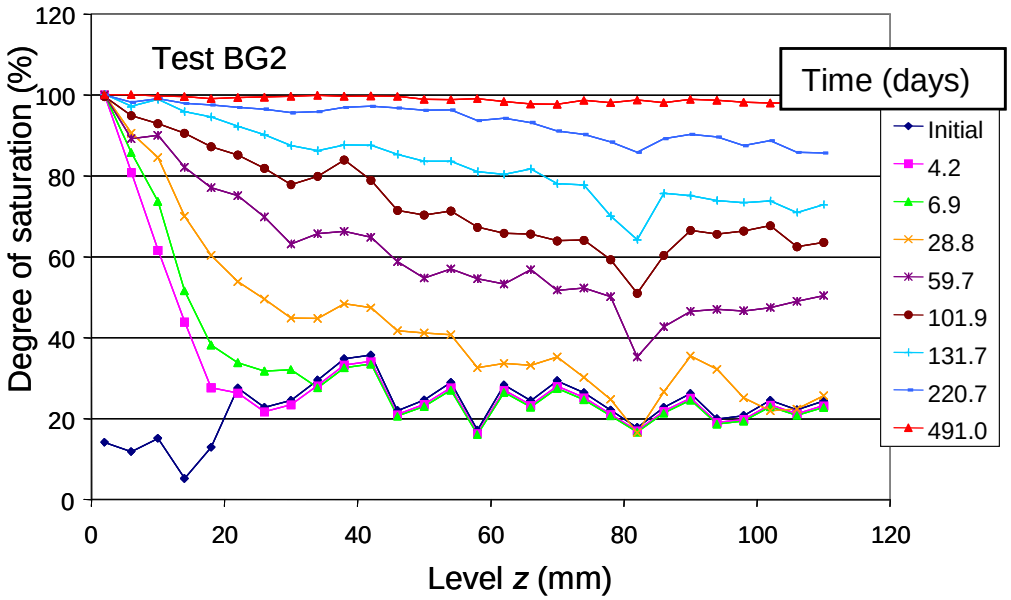

Figure 2-13: Evolution of degree of saturation at different levels of a sample of ρ_d 1.30 g/cm^3 during infiltration.

For the evaluation with microfocus computer tomography a 7-cm high cell was filled with a mixture of 50/50 pellet/powder mixture and compacted to a dry density of 1.36 g/cm^3. Boom clay pore water was injected through the bottom surface. **Figure 2-14** illustrates the changes observed during hydration by the visualisation of one vertical slice through the centre of the cell. After two weeks of hydration at very low pressures (implying especially suction) a distinction between the pellets and the powder could still be made. However, the bottom pellet had a more diffuse border compared with the surrounding powder and all pellets have a decreased density as a consequence of swelling. The mean bulk density of the powder at the bottom has increased from about 1.0 g/cm^3 to 1.6 g/cm^3. The results of the second hydration phase, one month at a very low pressure, show that the pellets can still be distinguished. Now the mean density of the

pellets has not changed, but the mean density of the powder at the bottom of the sample has increased from 1.6 to 1.7 g/cm^3 and the powder at the top of the sample has increased in density from 1.3 to 1.4 g/cm^3.

After these two phases of hydration at low pressures, an injection of water at about 0.5 MPa was performed. After one month of this injection, a homogenisation of the powder/pellet mixture was revealed. The whole sample now has a mean density of 1.8 g/cm^3. In the corners of the sample, lower values are found around 1.63 g/cm^3. The rest of the sample shows variations between 1.7 and 1.9 g/cm^3. However, homogenisation is not yet complete, as at the bottom of the sample, some fractures within the mixture can be delineated (Van Geet *et al*., 2005a). The fourth hydration has not really changed the observations. After the permeability test under an injection pressure of 0.6 MPa (5th hydration), full homogenisation is observed. The whole sample now has an average bulk density of 1.9 g/cm^3. Regions can be found with densities between 1.8 and 1.9 g/cm^3. The bottom corners of the sample are still somewhat lower in density (1.7 g/cm^3).

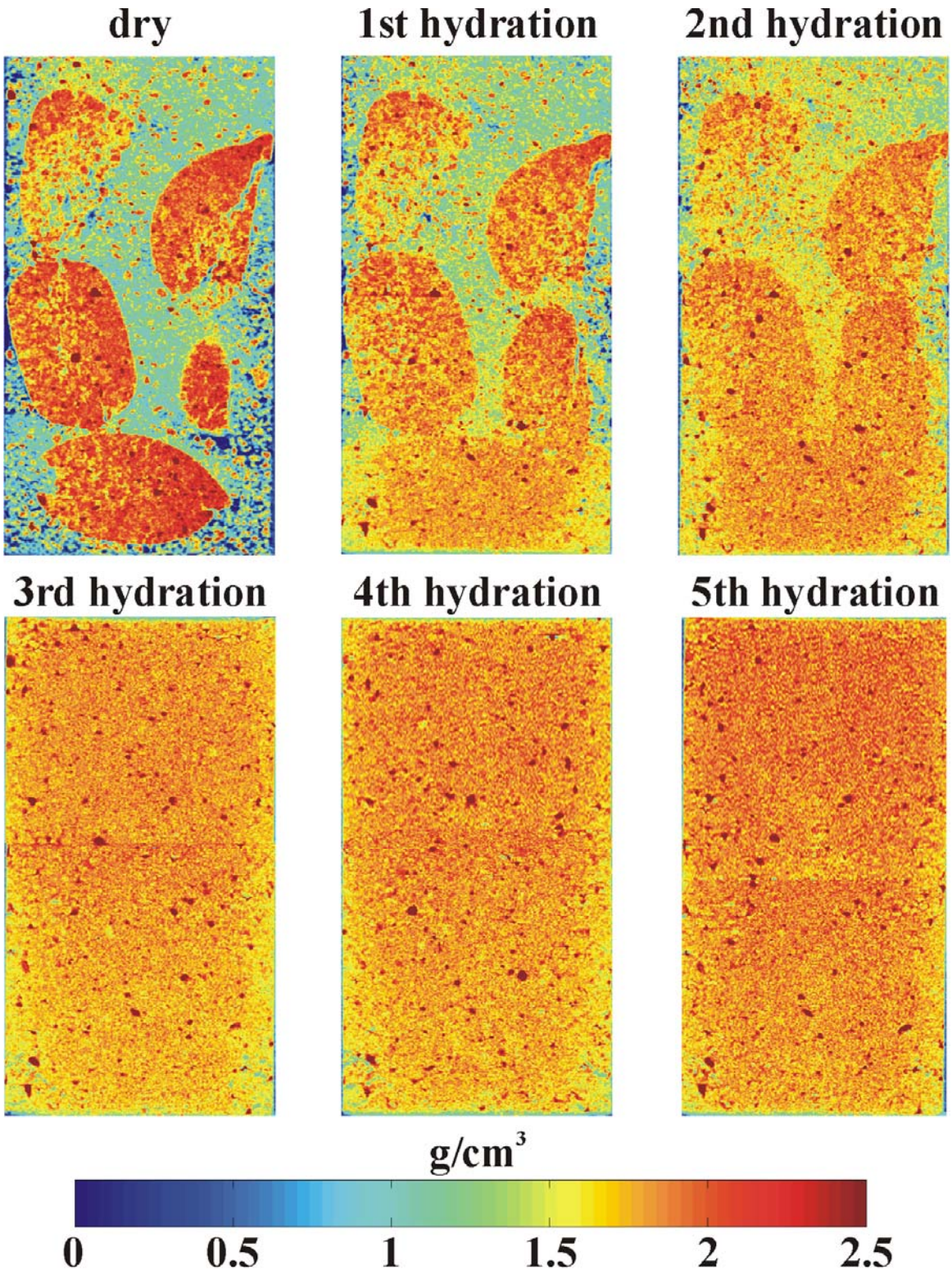

Figure 2-14: Recomputed vertical slices through the centre of the cell at every stage of hydration. By means of the correlation worked out, the attenuation coefficients are transformed into densities (Van Geet *et al.*, 2005a), made visible as colours. Width of the images is 38 mm.

2.3 Migration parameters

2.3.1 Introduction

The migration of radionuclides in clays is controlled by diffusion, what makes it necessary to determine the diffusion coefficients of the radionuclides as well as their accessible porosity. The behaviour of the neutral and conservative tritium and of the conservative anionic species iodide has been analysed in pellet/powder mixtures and in compacted powder.

2.3.2 Experimental setups used

Two laboratories (CIEMAT and SCK•CEN) have used two different setups to determine the migration parameters. CIEMAT used through-diffusion experiments with constant concentration gradient for the determination of the effective diffusion coefficients (Villar *et al.,* 2005). The compacted and saturated clay plugs are placed between two reservoirs: the inlet reservoir, where the tracer is added, and the outlet reservoir, where the measurements are carried out. The water in both reservoirs is continuously stirred, by means of a peristaltic pump, to obtain a homogeneous solution. **Figure 2-15** shows a schematic representation of the through-diffusion setup.

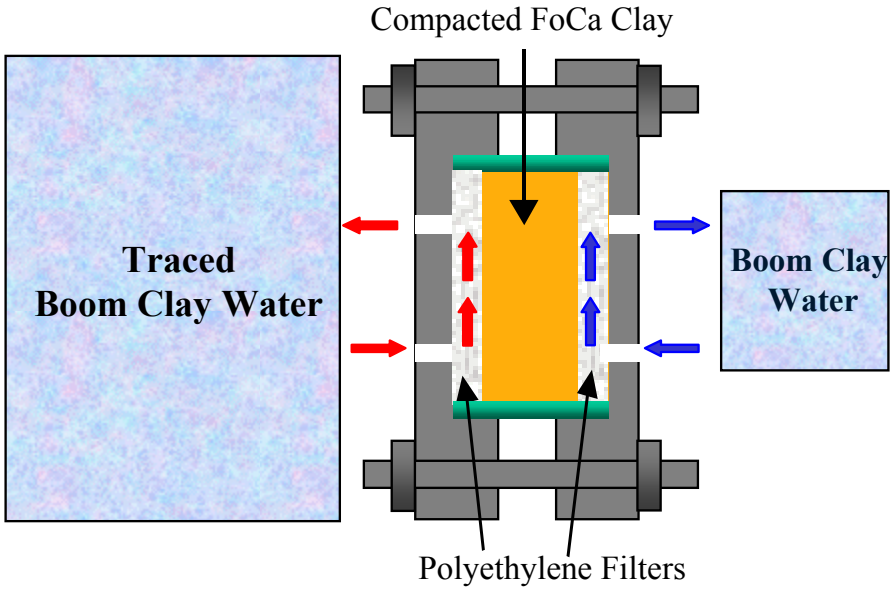

Figure 2-15: Schematic representation of the through diffusion test.

The diffusion process is initially characterised by a transient period, which develops gradually with time, until the tracer flux through the sample becomes constant and reaches the steady state. The curve of the cumulative solute recovery in the outlet reservoir versus time, at the steady state, is a straight line. The slope of this straight line provides the effective diffusion coefficient, and from the intercept of this straight line with the time axis the accessible porosity can be calculated (time-lag method).

SCK•CEN used a pulse injection type of percolation experiments (Villar *et al.,* 2005). **Figure 2-16** gives a schematic view of the setup. A cocktail of tritiated water and iodide was injected in the percolation cells containing saturated FoCa pellet/powder mixtures. The cocktail was injected by means of a HPLC injection valve equipped with a 20 µl injection loop. These experiments are set up in a thermostatic laboratory at 25°C, the pressure of the feed water is continuously monitored and is about 1 MPa. The water that percolates out of the clay core (approximately 0.2 ml/day) is sampled at regular time intervals and its activity is measured.
In order to derive migration parameters from the experiments, an analytical solution of the transport equation incorporated in a Fortran code is used. This fitting program allows fitting the total percolated quantity or the concentration, resulting in the migration parameters that best fit with experimental data (Aertsens *et al*., 1999 and Aertsens *et al*., 2005).

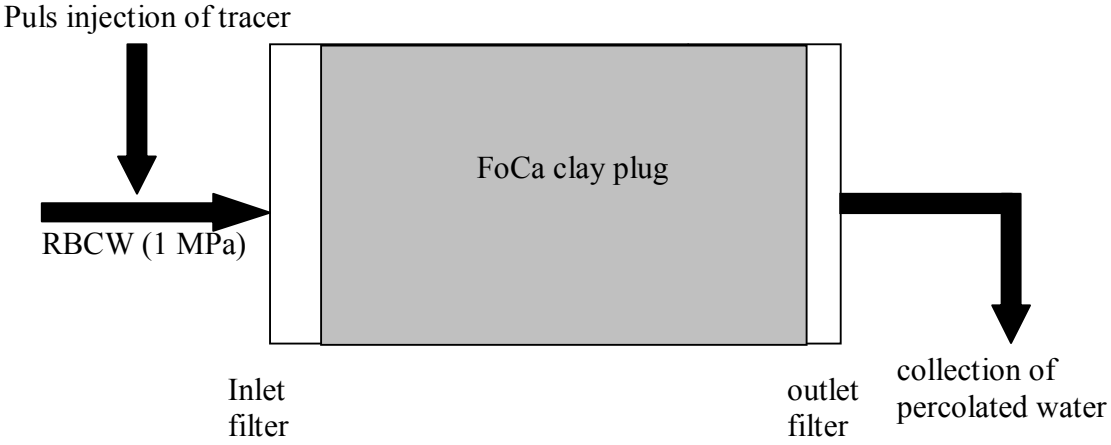

Figure 2-16: Schematic representation of the pulse injection type of percolation experiment.

2.3.3 Results

Figure 2-17 shows an example of the experimental results in through-diffusion experiments with pellet/powder clay mixtures for HTO and **Figure 2-18** for iodide. The figures present the cumulative amount of tracer (time integral of the flux) that passed to the outlet reservoir. The linear fit in the steady state region, from which the effective diffusion coefficient and the time lag can be obtained, is shown. The figures clearly show that for iodine it takes longer than for HTO to reach the steady state regime.
HTO experiments were carried out with the clay compacted at 1.33, 1.37, 1.43 and 1.46 g/cm^3, whereas iodide experiments were carried out at 1.34, 1.43 and 1.49 g/cm^3. The effective diffusion coefficient for HTO varied between $5.0 \cdot 10^{-11}$ and $2.0 \cdot 10^{-11}$ m^2/s decreasing when the dry density increased. This behaviour is associated with changes in the porous structure of the clay plugs and the decrease in the total porosity. In fact, an increase in the density produces higher tortuosity and, for this reason, lower tracer mobility (Sato *et al*. 1993). The effective diffusion coefficient for iodide varied between $3.0 \cdot 10^{-12}$ and $5.8 \cdot 10^{-13}$ m^2/s from lower (1.34 g/cm^3) to higher dry densities (1.49 g/cm^3).

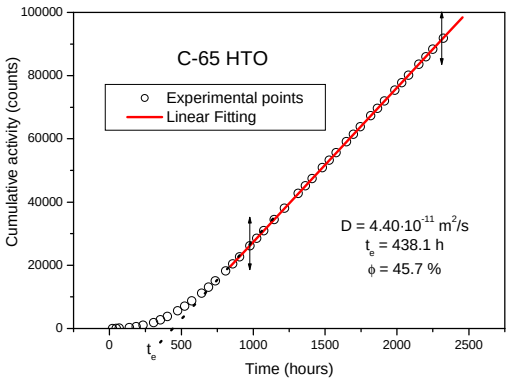

Figure 2-17: Experimental results of FoCa plug ρ_d 1.37 g/cm^3: cumulative HTO recovery and linear fit in the steady-state region

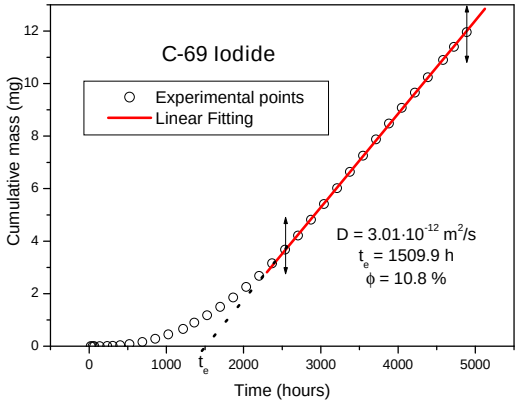

Figure 2-18: Experimental results of FoCa plug ρ_d 1.34 g/cm^3: cumulative iodide recovery and linear fit in the steady-state region

In order to know if the behaviour of the pellet/powder mixture differs significantly from the behaviour of the powder alone, it was necessary to perform tests with plugs made out of powder compacted at similar dry densities. Four additional diffusion experiments with HTO in clay samples of compacted powder were carried out.

Figure 2-19 shows a summary of the effective diffusion coefficients obtained at different dry densities in both powder and pellet/powder mixtures for HTO and iodide. It can be observed that when the HTO data in the powder (circles) are compared with those of the pellet/powder mixture (squares), no significant differences are appreciated and the deviations fall within the experimental error. This result indicated that, within the experimental time (three months for the hydration plus three months for the diffusion experiments), a complete homogenisation of the pellet/powder mixture is reached.

The effective diffusion coefficients for iodide were at least one order of magnitude lower than those for HTO for similar dry densities.

As can be seen in **Figure 2-19** the effective diffusion coefficients show an exponential decrease when the clay density increases. The decrease is significantly more pronounced in the case of iodide. The experimental values can be adjusted using exponential functions of the form $D_e = A \cdot e^{-B\rho}$, where A and B are constants and ρ is the bentonite dry density.

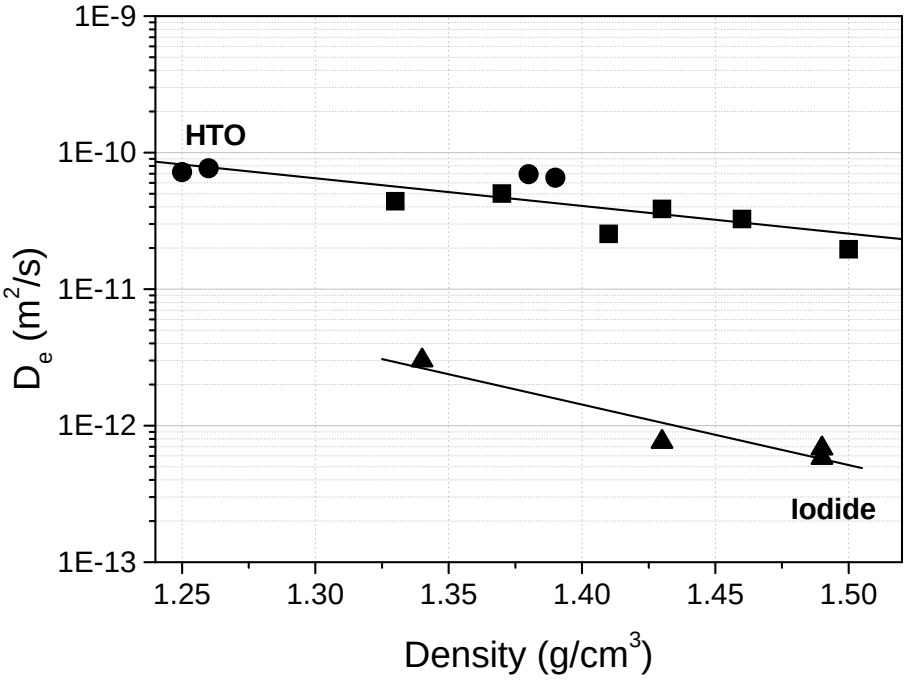

Figure 2-19: Summary of the effective diffusion coefficients obtained for HTO and iodide as a function of the dry densities of the pellets/powder mixture. The circles correspond to results obtained in compacted powder. The continuous lines correspond to the linear fits obtained.

The $^{125}I^-$ and HTO concentration profiles (activity corrected for decay and back-calculated to the time of injection) obtained from the percolating water through the FoCa plugs of the pulse injection type of percolation experiment are followed for more than 700 days and are given in **Figure 2-20**. The reproducibility of the three FoCa plugs is remarkable. The three cells behave exactly the same. An example of the modelling results is shown in **Figure 2-21**.

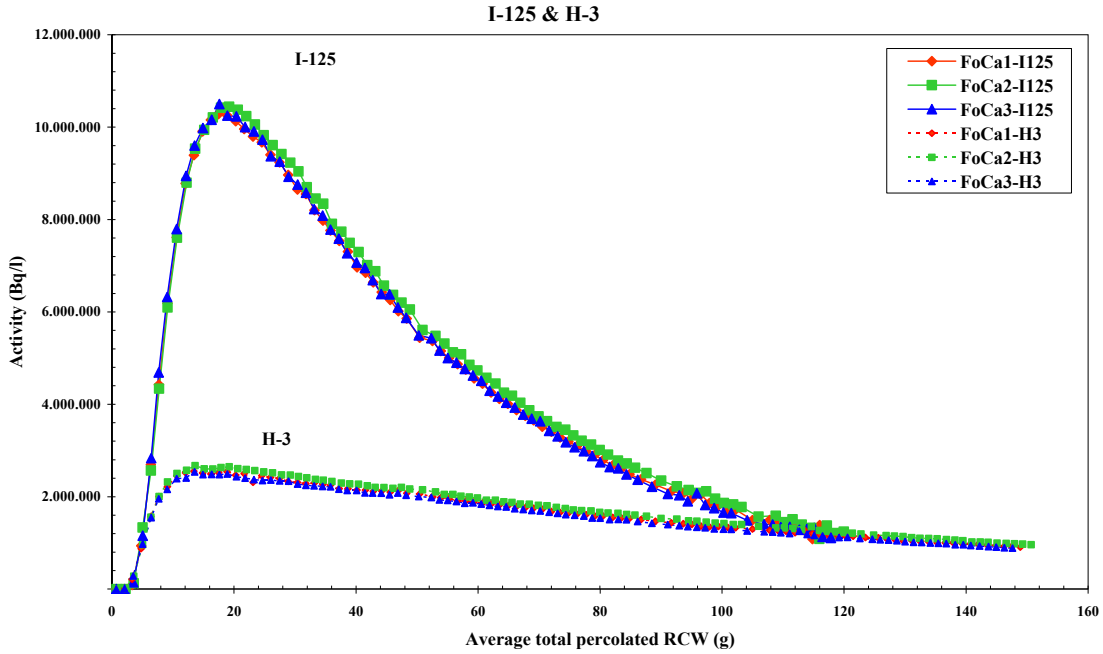

Figure 2-20: $^{125}I^-$ and HTO breakthrough curves for the percolation migration tests on FoCa plugs with a dry density of 1.6 g/cm³ (activity back-calculated to $t_{injection}$).

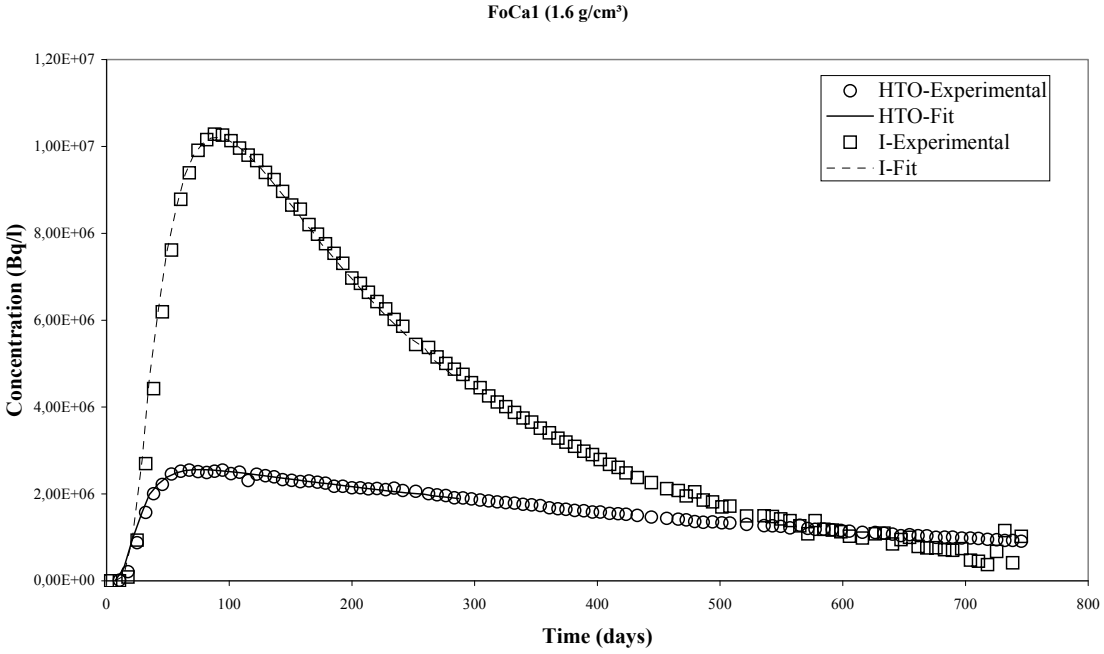

Figure 2-21: Modelled breakthrough curves for $^{125}I^-$ and HTO for FoCa1 plug (activity back-calculated to $t_{injection}$).

The fitting programme (D2fit-V2), fits three parameters: D_{app}, V_{app}, and Q_{tot}. From the fitted V_{app} and the experimentally measured $V_{Darcy,}$ the product ηR (porosity times retardation, but R=1 for conservative tracers) is obtained: $\eta R = V_{Darcy}/V_{app}$. And specifically, the correlation between Q and V_{app} is given.
As a control, the fitted Q_{tot} should be comparable with Q_{inj}.

Strictly spoken, the D_{app} fitted from the curve is the apparent dispersion coefficient (D^{i}_{app}), which is the sum of the apparent diffusion coefficient plus a hydrodynamic dispersion term:

$$D^{i}_{app} = D_{app} + \alpha V_{app} \qquad \textbf{Equation 9}$$

Alpha is the dispersion length (expressed in m). However considering a dispersion length of $1 \cdot 10^{-3}$ m (which is approximately the dispersion length for Boom Clay, having a similar dry density, Maes *et al*. 1999, Aertsens *et al*. 1999), with the low V_{app} observed in the experiments, this convective term is two orders of magnitude lower than the apparent dispersion coefficient and therefore neglected.

The D_{app} is a robust parameter, but due to the high correlation between Q_{tot} and V_{app} for HTO, the values for ηR are less reliable. The values for ηR for HTO (considering HTO as a conservative tracer, R=1) result in very high porosities, which are higher than the calculated total porosity of 0.40.

Also the long tailing for HTO is very puzzling. This tailing points to a process that somehow slows down the migration, hence a retardation. As a result, the product ηR fitted from the experiment becomes higher than expected. Currently we do not know if this tailing is due to experimental artefacts, or due to a real retardation effect.

As a possible retardation mechanism, we think of isotopic exchange. If one considers that isotopic exchange is a kinetic controlled process, and if the migration of HTO is fast compared to the kinetics of exchange, no isotopic exchange takes place. However, if the migration of HTO becomes slow enough, exchange might occur. This remains a hypothesis, and we have currently no means to prove or disapprove it.

2.3.4 Discussion

Ranges of diffusion coefficients for iodide and HTO in compacted bentonites covering two orders of magnitude for comparable dry densities are reported in the literature (Yu & Neretnieks 1997, García-Gutiérrez *et al*. 2001, Kozaki *et al*. 2001, Bradbury & Baeyens 2003, Ochs *et al*. 2001). This wide range reflects the different materials used, the different ionic strengths of the background waters, the different techniques (through-diffusion, in-diffusion...), the different interpretation methods (corrections for filter plates, etc.). On average, the values obtained by SCK•CEN by the pulse-injection technique for iodide are at the high end of this range.

When comparing to parameters obtained by SCK•CEN for Boom Clay (similar tests performed on clay cores of dry density 1.7 g/cm³ sampled over the entire thickness of the Boom Formation, Aertsens *et al*. 2005) the values obtained by SCK·CEN for the FoCa mixtures are similar:

D_{app} (HTO in BC)	=	$2.3\ 10^{-10}$ m²/s
η (HTO in BC)	=	0.37
D_{app} (I in BC)	=	$1.4\ 10^{-10}$ m²/s
η (I in BC)	=	0.16

However, when comparing to the values obtained by CIEMAT for FoCa mixtures of lower dry densities using the through-diffusion setup, the values seem not consistent (**Table 2-1**).

In order to compare the values, one needs to convert the D_{app} to D_{eff} according to the following relationship:

$$\eta R D_{app} = D_{eff} \qquad \textbf{Equation 10}$$

For both tracers R = 1. The problem is that, from the through-diffusion tests, the D_{eff} can be obtained as a robust parameter, but the porosities obtained by the "time-lag" method are not so robust. And as mentioned above, for the pulse-injection tests, the D_{app} is a robust parameter, but

due to the high correlation between Q and V_{app}, the porosity values should be evaluated very carefully.
As can be seen, the diffusion parameter values obtained by the through-diffusion tests are systematically lower and this for lower dry densities. As a result, the values obtained by the pulse-injection technique for the higher dry densities do not fit in the exponential relationship between the D_{eff} and dry density as observed by CIEMAT. A possible explanation for this discrepancy could be the differences in the experimental methodologies employed and their sensitivity for the determination of parameters.

Table 2-1: Comparison of the obtained diffusion parameters for iodide and HTO on FoCa clay plugs compacted at different dry densities by different methodologies. Values in italics are calculated parameters based on the measured parameters.

	HTO			**Iodide**		
SCK•CEN	D_{app}	η	D_{eff}	D_{app}	η	D_{eff}
1: 1.6 g/cm^3	$1.97 \cdot 10^{-10}$	0.50	*$0.99 \cdot 10^{-10}$*	$1.17 \cdot 10^{-10}$	0.17	*$1.99 \cdot 10^{-11}$*
2: 1.6 g/cm^3	$1.93 \cdot 10^{-10}$	0.54	*$1.04 \cdot 10^{-10}$*	$1.15 \cdot 10^{-10}$	0.18	*$2.07 \cdot 10^{-11}$*
3: 1.6 g/cm^3	$2.01 \cdot 10^{-10}$	0.54	*$1.09 \cdot 10^{-10}$*	$1.20 \cdot 10^{-10}$	0.17	*$2.04 \cdot 10^{-11}$*
CIEMAT	D_{app}	η	D_{eff}	D_{app}	η	D_{eff}
1.34-1.49 g/cm^3	*$0.5\text{-}1.0 \cdot 10^{-10}$*	0.28-0.46	$2.0\text{-}5.0 \cdot 10^{-11}$	*$2.2\text{-}2.8 \cdot 10^{-11}$*	0.02-0.11	$0.6\text{-}3.0 \cdot 10^{-12}$

2.4 Discussion and conclusions

It can be concluded that a large amount of experimental data on mainly the FoCa clay is available. These laboratory experiments have allowed optimising the compaction processes for the pellets production. The knowledge resulted in the use of 50/50 pellet/powder mixture in order to make a compromise between hydration time, swelling pressure, hydraulic conductivity and ability for compaction in a large scale test. Moreover, the huge amount of data resulted in the extraction of necessary parameters for hydro-mechanical modelling. However, as illustrated also here, several parameters show a large scatter. This scatter is most probably related to differences in experimental setup, experimental errors and natural variation of the material. It is clear that this scatter is not covered within the models and that only a best fit to the data is used for abstraction of the parameters. Also for the transport modelling, extraction of diffusion parameters has been established. A large scatter of experimental data points is observed and again this might be related to differences in the experimental methodologies employed. Further on, these laboratory tests have strongly increased our knowledge in the mechanism taking place, especially concerning the swelling pressure evolution during hydration. The better understanding of processes taking place is demonstrated by the good fit of experimental data and updated hydromechanical models (as will be shown in chapter 5). Finally, the homogenisation of the pellet/powder mixture is clearly illustrated with new non-destructive techniques as well as with the destructive analyses after several of the aforementioned laboratory tests.

3 The borehole seal experiment

The borehole sealing test aimed at sealing a borehole in the plastic Boom Clay by means of pre-compacted blocks of bentonite. The pre-compaction allows obtaining the required dry density of bentonite and as such the required permeability through the seal. The pre-compaction technique has been discussed in detail by Volckaert *et al*. (2000). The experimental setup used, allowed testing two bentonite materials, namely the FoCa clay and the Serrata clay. The setup was focused on characterising the hydration behaviour of the bentonite blocks, the bentonite – host rock interaction and the radionuclide migration through the seal (Van Geet *et al.,* 2007a).

3.1 Experimental setup

The experimental setup consists in a 250-mm diameter and 2.6 m long piezometer installed about 15 m deep into the clay in the HADES URL (Figure 3-1). This one is divided in two parts, the first part is dedicated to the sealing experiment (~2 m long), the second part to the gas generation experiment (~0.6 m long). The gas generation experiment is not included in the objective of the RESEAL project, but has been performed in the frame of the EC PROGRESS project (Rodwell *et al*., 2000).

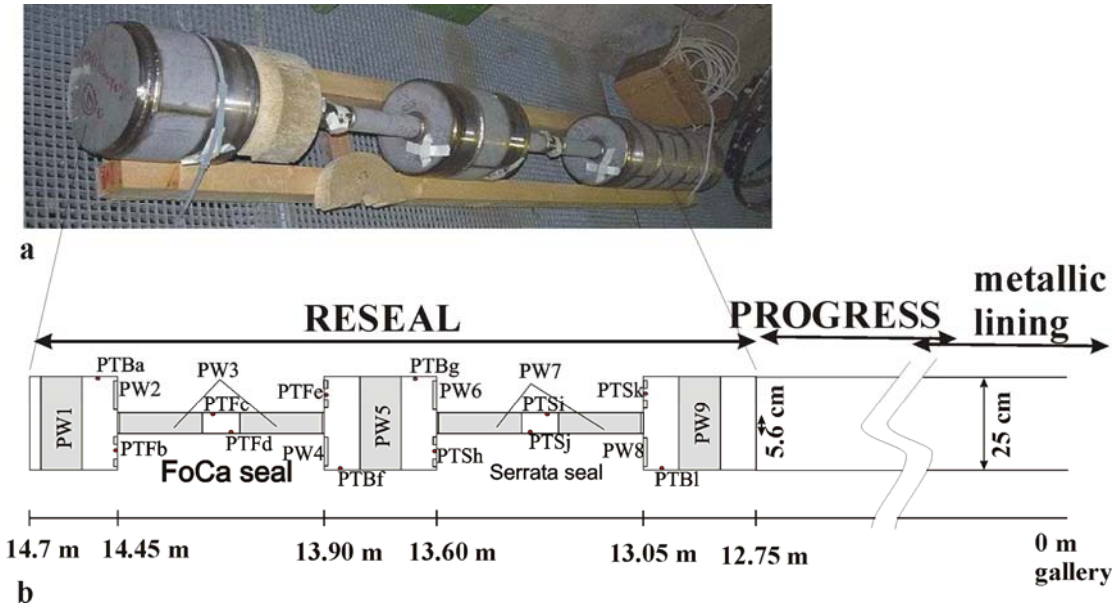

Figure 3-1: Photograph (a) and schematic view (b) of the piezometer used in the RESEAL borehole experiment (PW= pore water pressure sensor; PTB= total pressure sensor in contact with Boom Clay; PTF=total pressure sensor in contact with FoCa clay; PTS=total pressure sensor in contact with Serrata clay).

The RESEAL borehole sealing setup includes two testing compartments of 55 cm long with a central tube of about 56 mm diameter equipped with filters and total pressure sensors. The compartments are respectively filled with pre-compacted blocks of Serrata clay and FoCa clay installed around the central tube. The total pressure measurements are performed with miniature pressure sensors embedded in the setup. Behind each filter, there is a chamber and each chamber is connected to the main gallery with two microtubes. One tube is connected to a pressure sensor installed in the gallery and the other tube is foreseen for water or gas injections.

The lateral faces of the compartments consist of circular filters in which total pressure sensors are included. The different positions of the total pressure sensors give the opportunity to monitor the radial and the longitudinal stress in the seals. Close to the seal compartments, filters and total pressure sensors are installed. These water pressure and total stress measurement points are in contact with the host rock formation after convergence of the clay around the piezometer.

Figure 3-1 gives an overview of filter and sensor positions and names. The total stress sensors are identified by PT, followed by B for the sensors in contact with the Boom Clay, F for the sensors in contact with the FoCa clay and S for the sensors in contact with the Serrata clay and finally, a last letter identifies the sensor. A number from 1 to 9 preceded by PW identifies the filters.

3.2 Performance of instrumentation

The borehole seal is equipped with two types of instruments. Pore water pressure measurements through filter screens and total stress sensors through KULITE sensors (Van Geet and Volckaert, 2007). The filter screens are also widely used in Boom Clay environment. In contact with Boom Clay and in the borehole seal experiment these pore water pressure measurements through filter screens give reliable results, even about 10 years after installation.
12 total pressure sensors are installed, all of the KULITE type, are installed in the borehole seal experiment. However, the interpretation on (long-term) performance is less straightforward. In the first years all of them gave reliable results. Currently (9 years after installation), some of the total stress sensors give values below the pore water pressure in the surroundings. It is believed that this is caused by a bad connection between the sensor membrane and the surrounding clay. On the contrary some other total pressure sensors give pressures above 4.5 MPa, which is also rather unrealistic. Consequently, only 6 out of 12 (50%) give reliable results (Van Geet and Volckaert, 2007).

3.3 Experimental programme and results

During the several years that the RESEAL project was running, many tests have been performed on the borehole sealing experiment. Table 3-1: gives an overview of the chronological evolution of the borehole sealing experiments.

Table 3-1: Chronological overview of the experiments performed on the borehole seal

02 December 1997	Start of drilling
03 December 1997	End of drilling and installation of the sealing
04 December 1997	Start data acquisition for total pressure measurement
08 January 1998	Start data acquisition for water pressure measurement
15 April 1998	Start of the artificial hydration through filters 3 and 7
16 September 1998	End of artificial hydration
15-25 February 1999	Permeability test of the FoCa seal
17-26 March 1999	Permeability test of the Serrata seal
07 April – 25 September 1999	Gas breakthrough experiment
06 June 2002	125I tracer injection in filter 3
29 January 2004	End of the migration test

The experiments performed in 1999 are reported in Volckaert *et al*. (2000). For completeness, however, they will be shortly summarised here as well. The tests performed from 2000 on will be described in more detail.

3.3.1 Installation

The two seals made of half cylindrical elements were fixed together around the central hydration tube of each compartment with fine metallic wires. Table 3-2 gives the main characteristics of the seals before the installation. The dry density of the blocks of FoCa clay was 1.88 g/cm^3, while for the Serrata clay it was 1.76 g/cm^3. These dry densities were chosen to obtain a total

pressure of 4.4 MPa at full saturation (based on first laboratory experiments of both materials as described in Volckaert *et al*. (2000)), which corresponds to the lithostatic stress at the depth of the HADES laboratory. Taking into account all data of final swelling pressure, new curves are obatined (see Chapter 2). Taking into account the best fit of these data a swelling pressure of 3.12 MPa (95% confidence interval results in 1.65 to 5.35 MPa) should be obtained, which would correspond with a total pressure of about 4.7 MPa. This swelling pressure and a reduced dry density of 1.6 g/cm^3 and 1.5 g/cm^3, for FoCa and Serrata clay, respectively, should be obtained if the seal exactly fills the sealing compartments of 55 cm length and 25 cm diameter.

Table 3-2: Main characteristics of the seals before installation

	FoCa seal	**Serrata seal**
Length of the seal	51.8 cm	52.1 cm
Initial volume of the seal	22 956 cm^3	23 111 cm^3
Weight	48 085 g	45 666 g
Density	2.09 g/cm^3	1.97 g/cm^3
Grain density	2.68 g/cm^3	2.70 g/cm^3
Initial gravimetric water content	11.16%	12.42%
Porosity	0.30	0.35
Initial dry density of the seal	1.88 g/cm^3	1.76 g/cm^3

A horizontal borehole of 275 mm diameter and 14.7 m depth was drilled in the Test Drift part of the HADES URF towards the east. The setup of 2.6 m long was introduced at the end of the borehole and the rest of the borehole was lined with a metallic tube. The difference between the diameter of the setup and the borehole was foreseen to guarantee an easy installation of the equipment. The installation was done on December 3rd ,1997. Immediately after the installation, the total pressure sensors were connected to the data acquisition system to be able to follow up the convergence of the borehole around the setup.

3.3.2 Hydration

Figure 3-2 and Figure 3-3 show the water pressure and total stress evolution during hydration in the FoCa and Serrata seals, respectively, together with the pressure evolutions at the Boom Clay interface near each seal. Three months after the installation of the piezometer, convergence of the Boom Clay around the piezometer was observed. Once convergence has taken place, a substantial water exchange between host rock and seal starts. The convergence gradually progresses from the rear end of the piezometer towards the gallery, related to the larger disturbance caused by the borehole drilling close to the gallery. This causes the pressure increase to be faster in the FoCa seal, compared to the Serrata seal. The pressure increase is quite fast. For both sealing compartments, the radial stress evolution shows a small time lag compared to the longitudinal stress evolution.

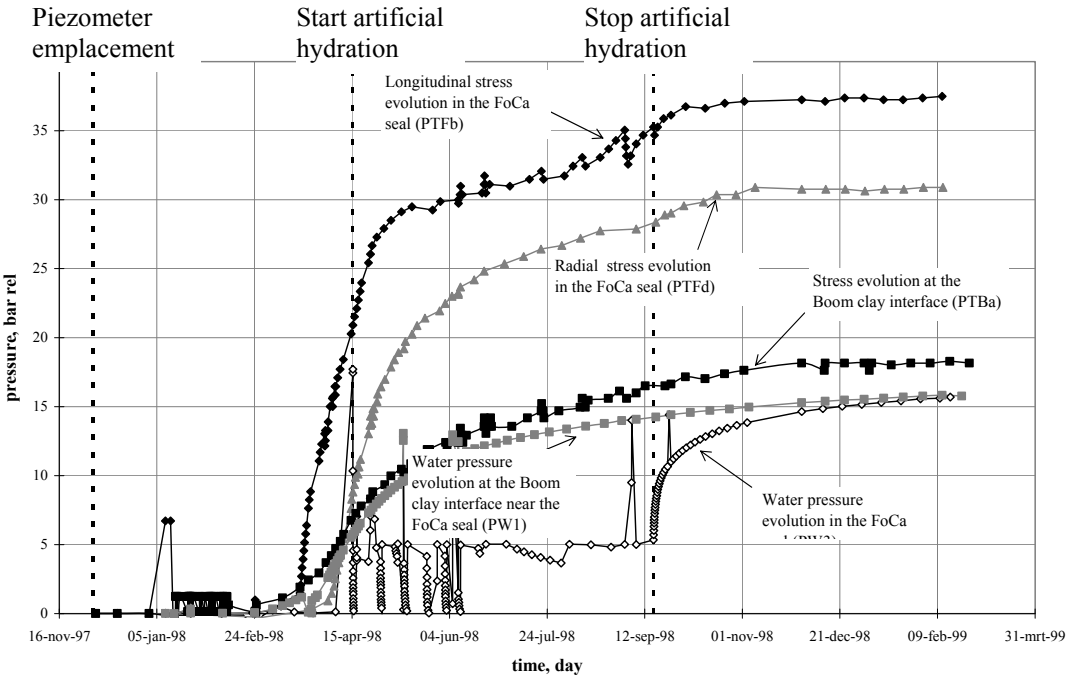

Figure 3-2: Water pressure and total stress evolutions in the FoCa seal and at the Boom Clay interface near the seal

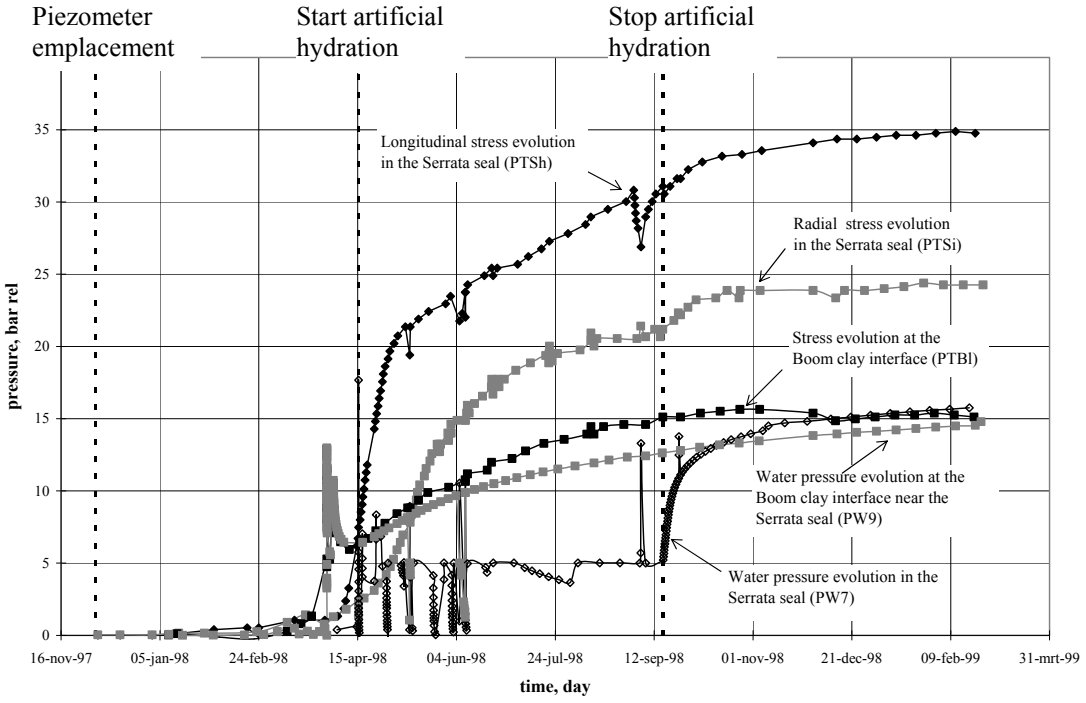

Figure 3-3: Water pressure and total stress evolutions in the Serrata seal and at the Boom Clay interface near the seal

On April 15th 1998, the artificial hydration through the central filters started. Water was injected at 0.5 MPa. The water injection was stopped on September 16th 1998. 0.5 litres and 0.7 litres of water were injected in the FoCa and Serrata seal, respectively. After the artificial water injection, pore water pressure slowly continues to increase up to the in-situ pore water pressure of 1.5 MPa is observed.

Over the length of the piezometer, a pore water pressure decrease is noticed from the rear end of the piezometer towards the gallery, caused by the natural drainage towards the gallery (Figure 3-5). However, an anomaly in this trend was found in both seals, but with the largest discrepancy at the Serrata clay seal. A chemical analysis of pore water sampled from this Serrata Clay showed a factor 10 increase in salinity compared to the salinity of the Boom Clay pore water. This pore water pressure anomaly might be caused by osmosis.

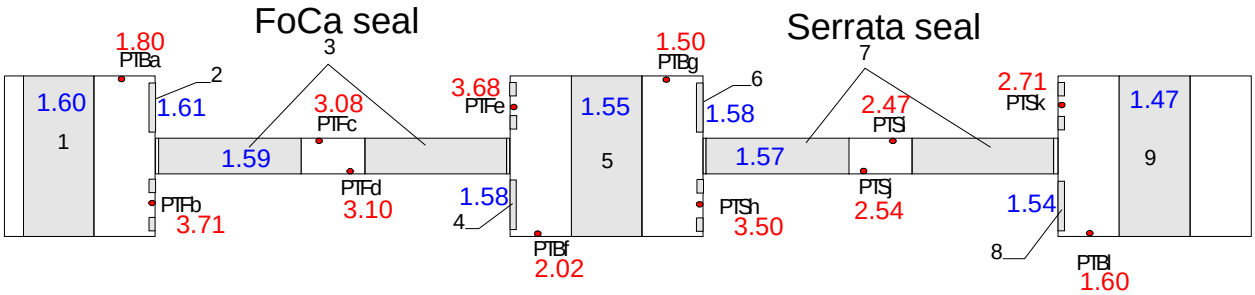

Figure 3-4: Pressure measured (MPa rel) in November 2005 (nearly 8 years after installation) at the different measurement points of the piezometer (PTB: total stress in Boom Clay; PTf: Total stress in FoCa seal; PTS: total pressure in Serrata seal; 1-9: filters, water pressure measurement points).

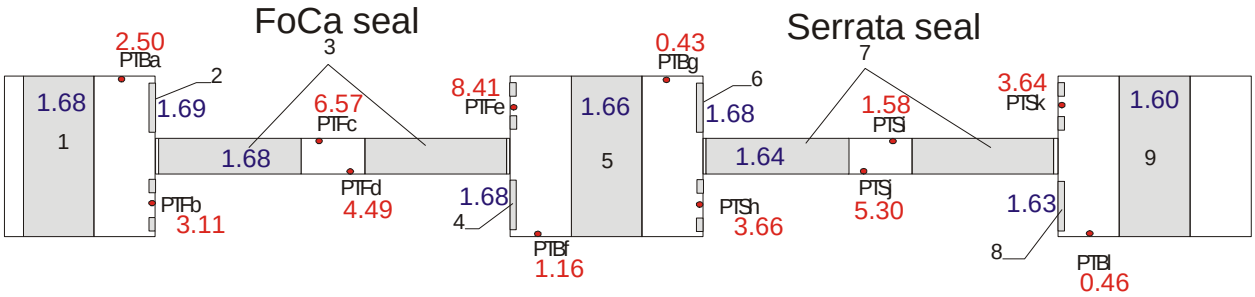

Figure 3-5: Pressure measured (MPa rel) in November 2005 (nearly 8 years after installation) at the different measurement points of the piezometer (PTB: total stress in Boom Clay; PTf: Total stress in FoCa seal; PTS: total pressure in Serrata seal; 1-9: filters, water pressure measurement points).

Based on the total pressure and pore water pressure analyses, the swelling pressures of the seals have been calculated. For the FoCa seal, a homogeneous swelling pressure is observed. The longitudinal swelling pressure is 2.10 MPa and the radial swelling pressure is 1.5 MPa. For the Serrata seal the swelling pressure was heterogeneous. The longitudinal swelling pressure ranged between 1.2 and 1.9 MPa and the radial swelling pressure ranged between 0.9 and 1.0 MPa. From the swelling pressures measured in the seal and the calibrations of the final swelling pressure versus dry density in laboratory experiments (Chapter 2), it is possible to calculate the reduced dry density of the seals due to the increase of the seal volume during hydration. As mentioned above (Chapter 2) a large scatter in these data of final swelling pressure versus dry density is observed. Considering the best fit of all available data, a reduced dry density of 1.51 g/cm^3 and 1.36 g/cm^3 are obtained for the FoCa and Serrata seal, respectively. The 95%

confidence interval of the data on FoCa clay gives reduced dry densities between 1.46 and 1.59 g/cm^3. From these data, the main characteristics of the seals after saturation are calculated (Table 3-3). After saturation and assuming a cilindrical shape of the seal, a diameter of 26.32 cm and 26.85 cm are obtained for the FoCa and Serrata seals, respectively. Even taking into account the large scatter on final swelling pressure of FoCa clay, the 95% confidence interval of data indicates that the diameter of the seal exceeds the foreseen diameter of 25 cm (25.73 to 26.79 cm).

Table 3-3: Main characteristics of the seals after saturation

	FoCa seal	**Serrata seal**
Length of the seal	55 cm	55 cm
Diameter of the filter 3 and 7	5.6 cm	5.6 cm
Reduced dry density	1.51 g/cm^3	1.36 g/cm^3
Final volume of the seal	28 647 cm^3	29 792 cm^3
External diameter of the seal	26.32 cm	26.85 cm
Water content at saturation versus wet weight	28.6%	35.6%

3.3.3 Permeability test

Permeability measurements have been performed in February and March 1999, after saturation on respectively the FoCa seal and the Serrata seal. The pressure on the filters 3 and 7 has been reduced to the atmospheric pressure to create a water pressure gradient through the seals, i.e. between the host rock and the central filter of both seals. From the following equation (Put *et al*., 1994; Bastiaens and Mertens, 2005; Bastiaens *et al*., 2005) the hydraulic conductivity can be calculated:

$$K = \frac{Q}{F \cdot \Delta P} \qquad \text{Equation 3-1}$$

with **K**: permeability (m/s)
Q: flow (m^3/s)
ΔP: pressure difference between the water pressure in the host rock and the water pressure in the filters
F: filter form factor for circular filter

$$F = \frac{2 \cdot \pi \cdot (l - D)}{\ln \frac{l}{D}} \qquad \text{Equation 3-2}$$

with **l**: filter length (44 cm in this case)
D: filter diameter (5.6 cm in this case)

This estimation was done with a pressure difference (ΔP) of 1.54 MPa for the FoCa seal and 1.49 MPa for the Serrata seal. We obtained a hydraulic conductivity of 4.3 10^{-13} m/s for the FoCa seal and 5.5 10^{-13} m/s for the Serrata seal.

The obtained values of the hydraulic conductivity are in good agreement with the laboratory values at the corresponding dry density, taking into account the reduced dry density of the seals. The theoretical hydraulic conductivity would be 2.56 10^{-13} m/s and 2.09 10^{-13} m/s for FoCa and Serrata clay of respectively 1.51 and 1.36 g/cm^3 dry density (see Chapter 2).

3.3.4 Gas breakthrough test

To test the gas sealing ability a gas injection was carried out. Gas was injected in the host clay formation from the filter PW1 (Figure 3-1) close to the FoCa seal compartment at the end of the borehole. Figure 3-6 shows the evolution of the pressures in and around the FoCa seal during the injection.

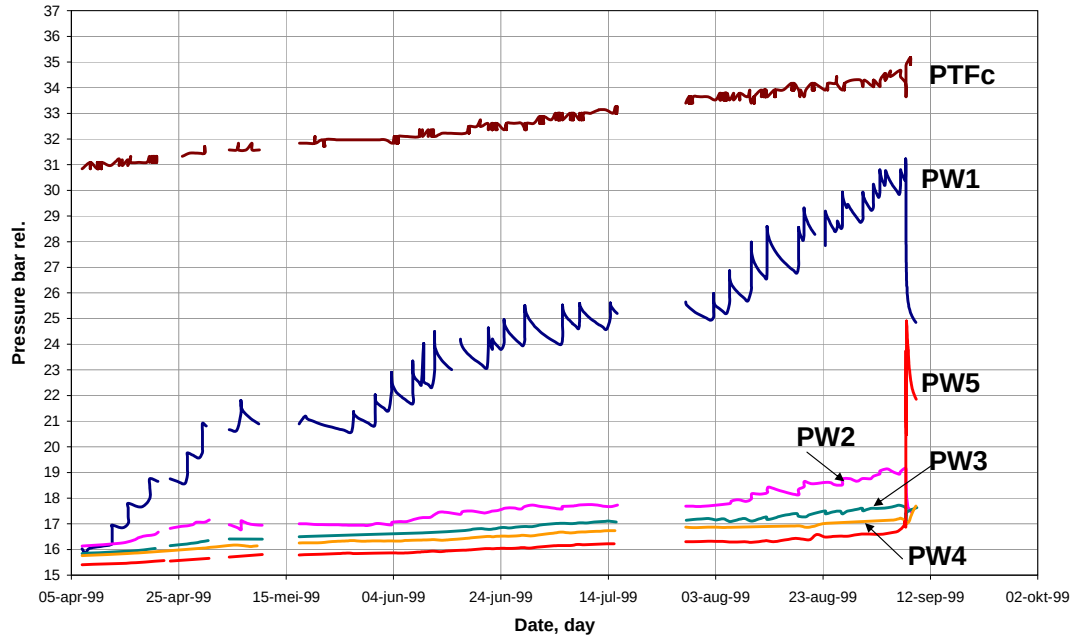

Figure 3-6: Evolution of the pressures in and around the FoCa seal during the gas injection

The gas pressure was increased step by step. The gas breakthrough occurred at a pressure level of about 3.1 MPa (recorded on PW1), i.e. a pressure equal to the radial total stress measured in the FoCa seal (PTFc) before the start of the gas injection. The breakthrough has been detected on the filter PW5 in contact with the Boom Clay located between the two seals. The breakthrough was confirmed by a sudden increase of the gas flow rate detected on the injection system. The pressure sensors connected to the filters in the FoCa seal, i.e. PW2, PW3 and PW4 show a very weak reaction to the breakthrough.

From this observation, it seems clear that the gas did not flow through the FoCa seal towards the nearest filter. However, gas flowed along the interface between the FoCa seal and the host rock or through the borehole EDZ of the host rock.

3.3.5 Radionuclide migration test

In order to test the efficiency of the sealing of a borehole and its surrounding EDZ by means of pre-compacted bentonite blocks, a radionuclide migration test has been setup. This should allow

gaining insight in the possibility of transferring laboratory observations towards in-situ conditions with regard to the bentonite behaviour. This migration test was limited to the FoCa seal. On June 6th 2002, 3.5 ml of solution with 3.28 10^8 Bq of ^{125}I labelled NaI was introduced. The half life of ^{125}I is 60.14 days.

PW3 (Figure 3-7) was used as injection filter of the ^{125}I labelled NaI solution. It should be noted that due to the limited space in the central tube of the piezometer, one single water conduit with a T branch is used to be connected to both parts of PW3. Pore water sampling during the migration test is performed through filters PW1 and PW5. To avoid any migration of the ^{125}I labelled water into filters PW2 and PW4, a gas cushion, at a pressure a little bit higher than the in-situ pore water pressure, is applied at those filters to prevent water inflow.

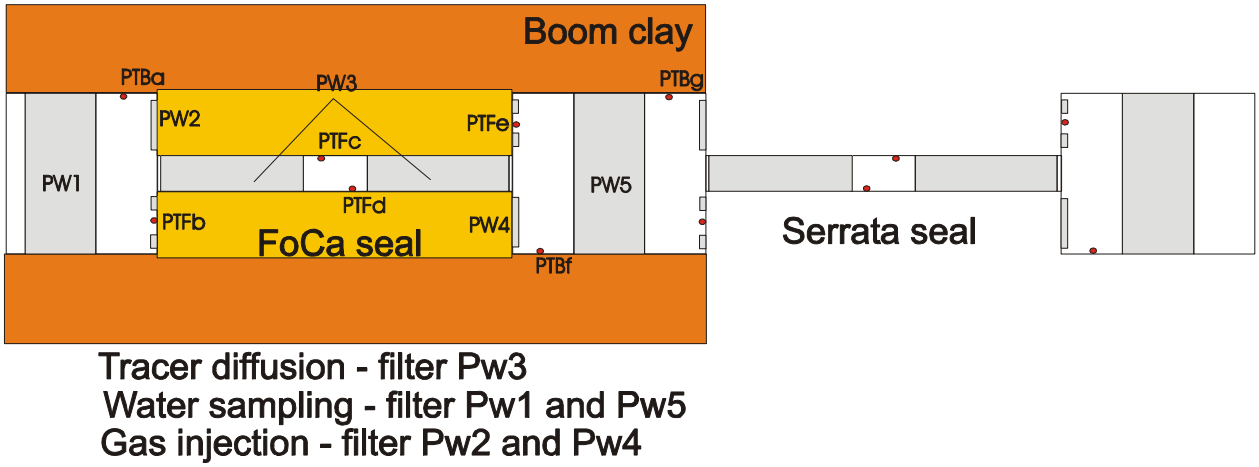

Figure 3-7: Schematic representation of the filters used for the radionuclide migration test in the FoCa seal.

To perform the migration experiment, a loop of stainless steel tubing of 3.5 ml is filled with Boom Clay pore water containing ^{125}I labelled NaI solution (3.28 10^8 Bq). One end of this loop is connected to the inlet water conduits of both parts of PW3 (connected with a T-branch). The other end of the loop is connected to the exit of a circulation pump. The inlet of the circulation pump is connected to the outlet of the water conduits of both parts of PW3 (connected with a T-branch). Consequently, a closed system is created. The pump is then used to circulate the water through the filter and the circulation system at a pressure only slightly higher than the in-situ pressure at the filter. This creates a homogenisation of the tracer and the clay water present in the circulation system. Due to the contact of the filter with the FoCa clay, diffusion of the tracer is enforced with only a small pressure difference. This kind of test is called a diffusive tracer injection.

The sampling from filters PW1 and PW5 was performed periodically with intervals of one month by collecting water during a period of 11 to 14 days. The dead volume of the water conduits is about 500 ml. A first volume of 500 ml is sampled to rinse the tubing, while a second volume of 500 ml is taken as sample. The first sampling was started on July 29, 2002 and only this first sampling was done in a fractionated way in order to optimise the sampling frequency. Sampling was regularly performed over a period of 600 days in both the PW1 and PW5 filters.

Figure 3-8 illustrates the evolution of the^{125}I concentration for filters PW1 and PW5. It is clear that activity is only measured in the filter nearest to the gallery. In the filter furthest from the gallery, no activity has been measured. This might be caused by an imperfect injection with the

used experimental setup. Using the same water conduits for both parts of the injection filter PW3, it is reasonable to accept that the labelled water only reached the part of the filter closest to the gallery, where the pressure is lowest. Probably due to the longer distance towards sampling filter PW1, activity is not measured there.

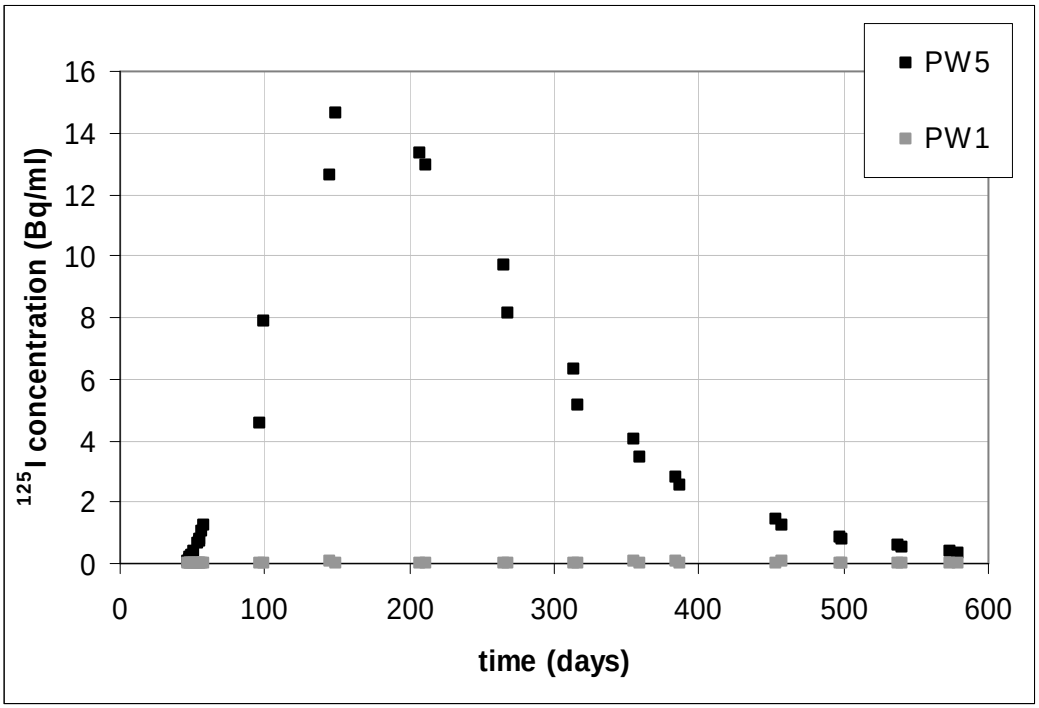

Figure 3-8: ^{125}I activity measured in the two filters (PW1 and PW5, see figure 1) close to the FoCa seal.

During the test, pore water pressures of all filters were monitored (Figure 3-9). The pressure in filters PW2 and PW4 remains very stable due to the gas cushion. The pressure in the sampling filters PW1 and PW5 shows the expected behaviour: a pressure drop during the sampling and, after sampling, a rather fast pressure recovery up to nearly the undisturbed in-situ pore water pressure. It should be noted that the pressure in the injection filter PW3 shows an unexpected behaviour. It was assumed that the pressure would remain rather constant in this filter during the circulation of the pump. However, careful examination of Figure 3-9 reveals that the sampling at filters PW1 and PW5 systematically induces a limited pressure drop in injection filter PW3. Moreover, since the second sampling, a continuous pressure decrease is noticed in PW3, even between samplings. This is caused by a small leak in the circulation system. The latter could not be fixed during the migration experiment.

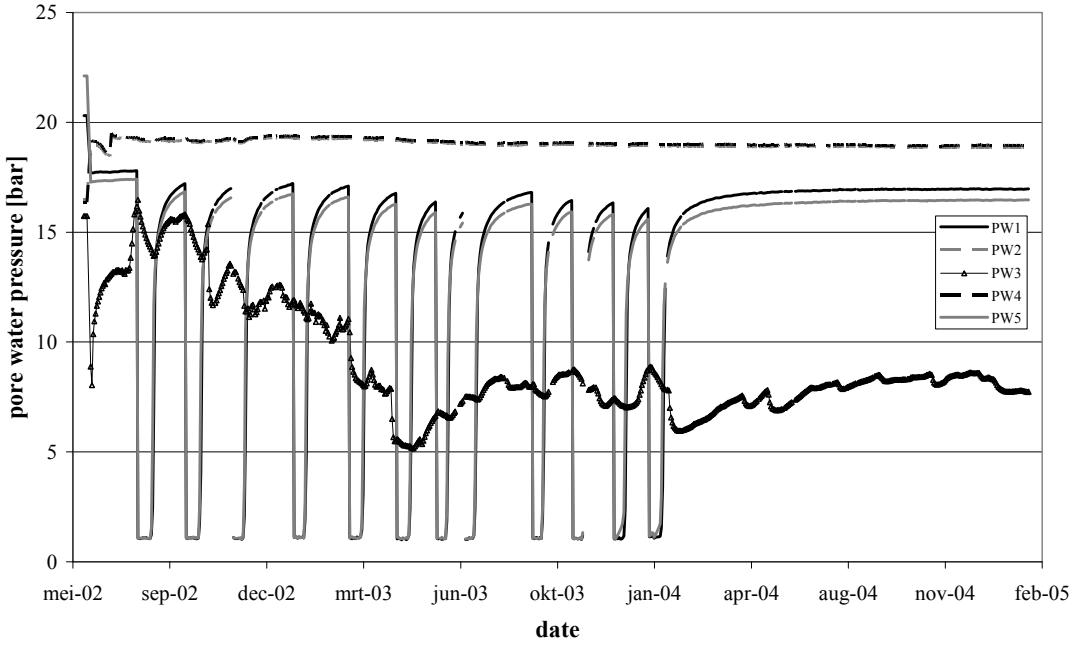

Figure 3-9: Pressures measured in filters PW1 to PW5 during the migration experiment.

3.4 Modelling

3.4.1 Hydration

Hydration of the pre-compacted bentonite blocks occurred quite fast (about five months to reach full saturation). The artificially injected volume of water corresponds with about 7% of the total water volume needed for full saturation of the seals. The largest fraction of hydration (more than 90%) thus occurred by natural hydration from the host rock, where a higher pore water pressure was present and where the contact surface was larger, compared to the injection filter. After saturation, the final diameter of the seals exceeded the 25cm diameter of the piezometer, foreseen to be filled by the seals. This resulted in a lower swelling pressure of the seals than aimed for. This is probably related to the quite important disturbance of the host rock by drilling the borehole, causing a slow convergence and reconsolidation.

The hydration of the borehole sealing test, including data obtained after the end of the hydration test, has been modelled by UPC with CODE-BRIGHT (Olivella, 1995). The data used come from laboratory data and from the in-situ permeability tests performed in 1999 on the two fully saturated bentonite seals. A low value for the initial stress inside the Serrata and the FoCa seals has also been considered because of the low reconsolidation of the host clay around the piezometer. Details on the model, equations and parameters used can be found in Volckaert *et al*. (2000).

A comparison of the results obtained during the modelling and the experiment are shown in Figure 3-10 for the Serrata seal. To avoid numerical convergence problems, the simulation has been carried out considering an initial isotropic stress state equal to 0.5 MPa. Saturation is observed close to the time at which PW6 begins to respond. Pore pressure at time of circuit closure appears to be slightly lower than the measured one. A delay between measurements and

simulation results exist between April 15th and September 16th 1998. One explanation of the slow response of PW6 may be related to the fact that it was initially not saturated because it was connected to the inner chamber filled with air. The sudden increase of pore water registered at August 9th , 1998 at that sensor could be an indicator of the same fact, because it could express the saturation of the filter. The final calculated swelling pressure remains higher than the measured one. It is, however, difficult to compare the computed and registered stresses since they do not start from the same initial state.
The computed volume of water injected from the central tube is compared with the measured ones. The predicted water intake is nearly zero, while measured water intake is about 0.7 litres.

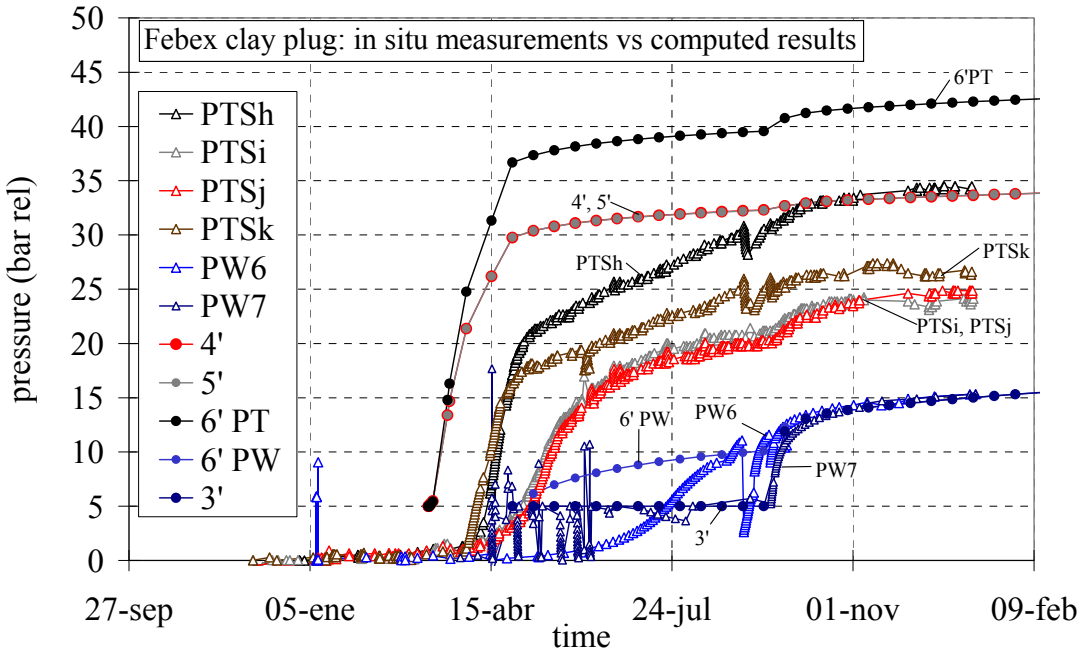

Figure 3-10: Comparison between the numerical and the experimental results of the hydration phase in 1998 of the Serrata clay (see Figure 1 for location of sensors). Simulations3' to 6' correspond with sensors as follows: 4'=PTSj; 5'=PTSi; 6'PT=PTSh and PTSk; 6'PW=PW6; 3'=PW7.

Results of the final modelling of the FoCa seal are compared with in situ measurements in Figure 3-11. Saturation is observed on April 15th, 1998. After this date, computed values of water pressure are higher than the readings at PW2. This fact could be explained in the same way as in case of water pressure sensor PW6, due to the desaturation of the filter. In the case of PW2, the sudden increase in the rate of pore water pressure increase is more evident, and the date of saturation of the filter may be estimated on August 19th, 1998. On the date of circuit closure, computed water pressure is slighlty above the measurement. Results in total pressure show a good agreement. The computed volume of water injected from the central tube is nearly zero litres, while the measured one is about 0.5 litres of water. As in the Serrata seal, the discrepancy is large. From a general point of view, it seems that the consideration of the average porosity of the brick/joint system leads to overestimating the hydraulic conductivity existing during the whole process. Inflow of water into the bricks governed by the porosity of the blocks appears then to be a factor to be taken into account in the simulation.

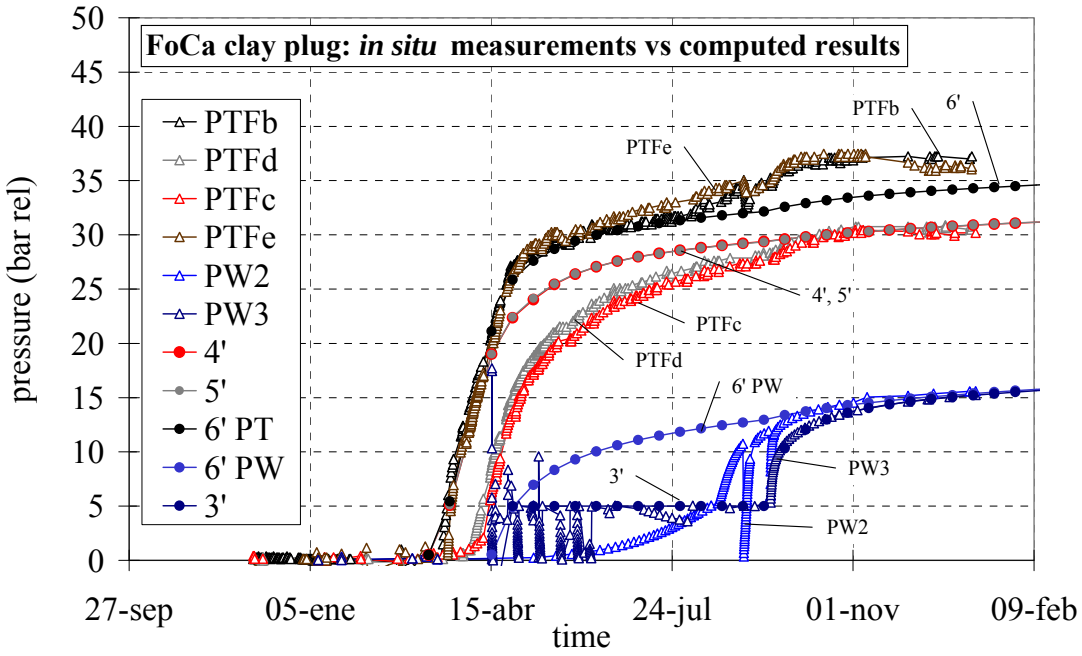

Figure 3-11: Comparison between the numerical and the experimental results of the hydration phase in 1998 of the FoCa clay (see Figure 1 for location of sensors). Simulations3' to 6' correspond with sensors as follows: 4'=PTFc; 5'=PTFd; 6'PT=PTFe and PTFb; 6'PW=PW2; 3'=PW3.

The final modelling of the borehole sealing experiment incorporates parameters of laboratory tests performed during the project and in situ permeability tests. The latter indicate a lower average dry density inside the seals due to the presence of joints. The prediction is quite good in terms of stresses by considering the real initial stress state. The rate of hydration is slightly overestimated when the average dry density is considered, indicating that the density of the bricks plays a role in the hydration kinetics. As a general remark, this exercise provides a useful estimation of most of the parameters involved in the hydro-mechanical response of an engineered barrier.

3.4.2 Radionuclide migration

Through radionuclide transport modelling, it was investigated whether the experimental data could be reproduced with reasonable parameter values. A first model considering only diffusive transport through the FoCa and Boom Clay could not be fitted to the observations. The modelling results shown in Figure 3-12 do not match the observations with respect to plume arrival time or long-term plume dissipation. Interestingly, the model results indicate that significant concentration differences might exist between the edge of PW5 which is closer to PW3, the mid-point of PW5 and the distant edge of PW5.

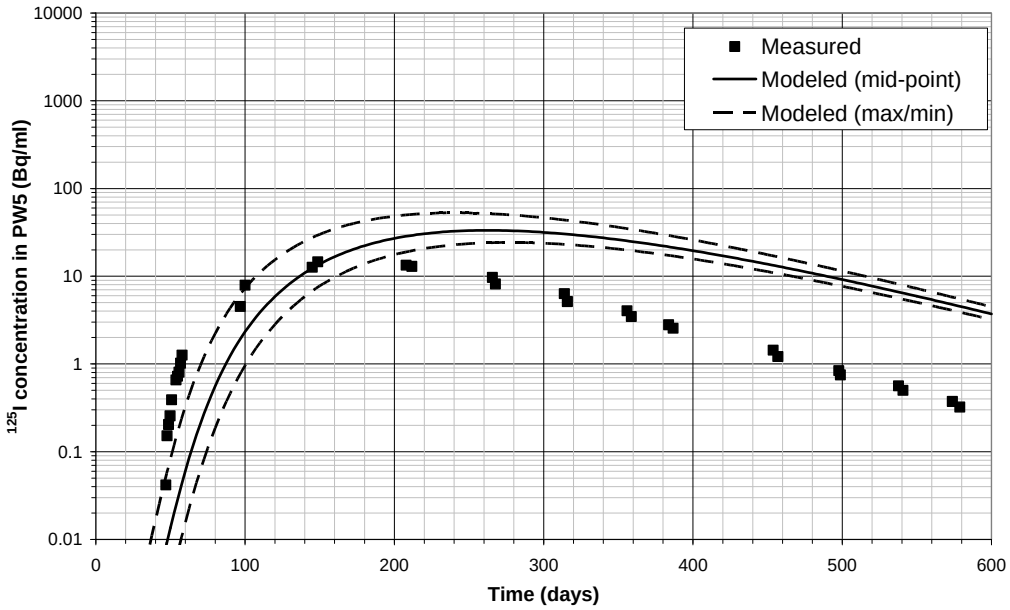

Figure 3-12: Comparison of observed ^{125}I concentrations from filter PW5 with predictions from a diffusive transport model.

As expected the advective transport of the tracer is not negligible, because of the substantial hydraulic pressure drop that is induced every time a sampling from PW5 occurs. As such, a coupled flow and transport simulation was performed to model this migration experiment. The hydraulic part of the simulation was calibrated to the measured outflow. The experimental data of the outflow as result of the sampling procedure could be modelled very well using a hydraulic conductivity K of 4.5 10^{-12} m/s. This value of K is equivalent to the horizontal conductivity K_h of the Boom Clay (De Cannière *et al*., 1994; Wemaere *et al*., 2002), which is about a factor 2 larger than the vertical conductivity (K_v=2.1 10^{-12} m/s). As such, it is clear that the smallest resistance, and thus the largest K of the formation determines the flow rate.

Introducing the hydraulic parameters and the measured PW3 and PW5 pressures in the coupled flow and transport model, we obtained the radionuclide breakthrough curve for the PW5 sample filter (Figure 3-13). However, the diffusion accessible porosity of the FoCa clay and the pore diffusion coefficient of the FoCa clay, experimentally determined by SCK•CEN or CIEMAT in laboratory experiments (see Chapter 2 and Villar *et al*., 2005), do not allow to fit the experimental data.
In general, the porosity determines mainly the time of the peak and its amplitude; varying the diffusion coefficient results in a shift in the concentration axis, and the slope of the tailing is determined by the RN's halflife. As the transport parameters of Boom Clay are well characterised, the parameter values for FoCa clay were varied in order to optimise the fit with the experimental data. The transport parameter values given in Table 3-4 allow obtaining the radionuclide breakthrough curve for the PW5, shown in Figure 3-13.

Table 3-4: Transport parameter values for advection-diffusion model (results shown in Figure 3-13)

Diffusion accessible porosity of Boom Clay	η_a	0.12	-
Pore diffusion coefficient of Boom Clay	D_p	2 10^{-10}	m^2/s
Diffusion accessible porosity of FoCa seal	η_a	0.06	-
Pore diffusion coefficient of FoCa seal	D_p	2 10^{-10}	m^2/s

The simulation results shown in Figure 3-13 exhibit even larger differences between concentrations at different locations within PW5, especially during sampling operations. However, it is clear from a comparison between Figure 3-13 and Figure 3-12 that the general trend of the measured concentrations is better reproduced when advection is taken into account.

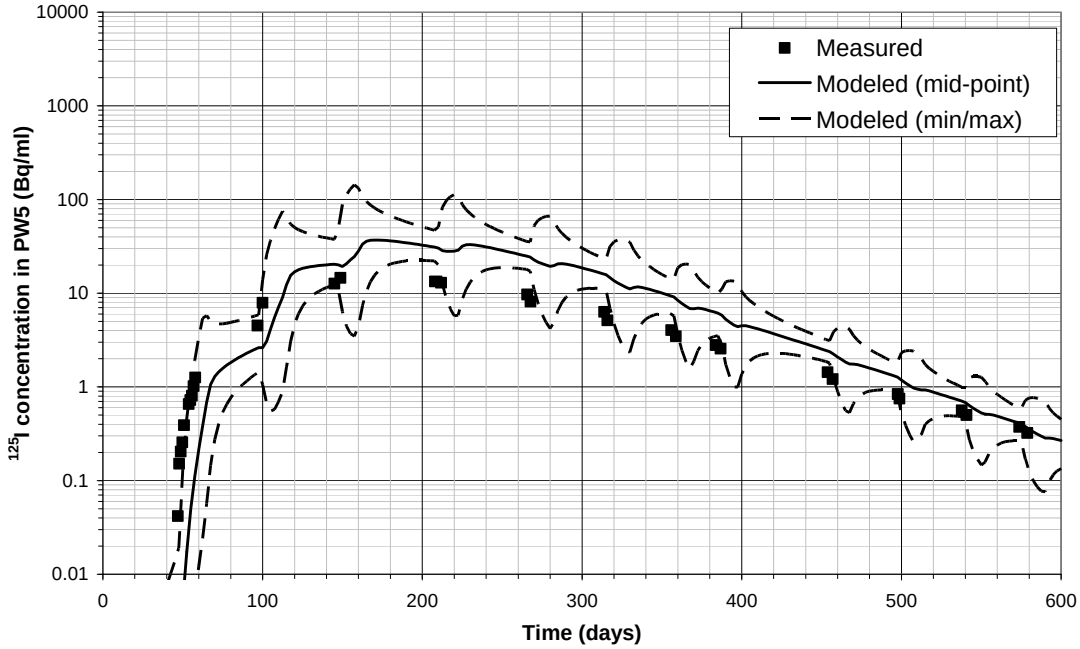

Figure 3-13: Comparison of observed ^{125}I concentrations from filter PW5 with predictions from a flow and advection-diffusion transport model.

Due to the large concentration gradient along the contact surface between PW5 and the Boom Clay, the concentration at the mid-point of PW5 might be a poor estimate of the concentration in the sampled fluid. Hence, the average concentrations at the times of sampling have been calculated by dividing the total convective flux of ^{125}I through the PW5 filter by the corresponding water outflow. These computed average concentrations are compared to the observations in Figure 3-14. Both the plume arrival and its long-term dissipation are satisfactorily captured by the model. However, the peak concentration is over-estimated by about a factor two.

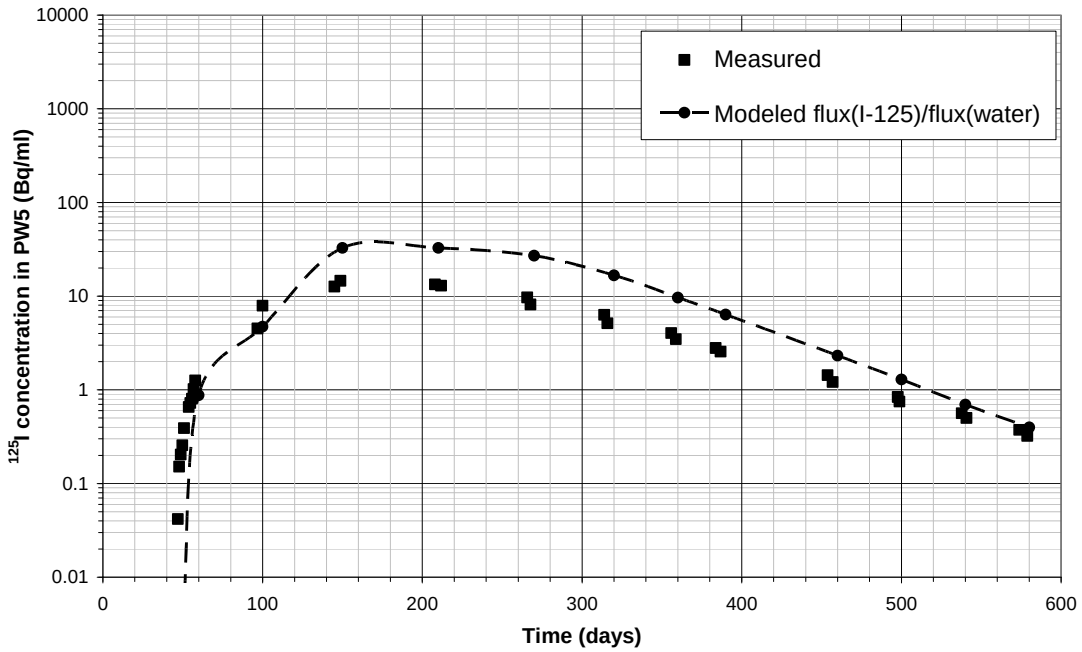

Figure 3-14: Comparison of observed ^{125}I concentrations from filter PW5 with flux-based estimates of the average concentrations from the flow and transport model.

A better description of the system, including measured pressure evolutions in PW1 and taking into account the hydraulic role of the second segment of PW3 in the model could possibly lead to better modelling results. It is also worth noting that at this point a best estimate of the radionuclide transport parameters have been used in the advection-diffusion model. As the Boom Clay parameters are very well known, these parameters were fixed and not adapted. However, for the FoCa clay a large spread of data was observed in the laboratory experiments (Villar *et al*., 2005). Therefore, the radionuclide transport parameters of FoCa clay were adapted within reasonable limits. In any case, **Figure 3-14** already seems to indicate that the observed concentrations can be reproduced adequately without resorting to preferential pathways such as fractures or poorly sealed interfaces.

3.5 Conclusions

On a small scale, the sealing of a borehole can provide valuable information on the feasibility and effectiveness of a sealing technique. It has been demonstrated that sealing a borehole in the plastic Boom Clay by means of pre-compacted blocks of bentonite is technically feasible. The pre-compaction technique allows obtaining a specific dry density in order to obtain the required physical characteristics of the seal. The emplacement of the seals did not provoke any problems. The hydration of the seals occurred reasonably fast and hydration occurred mainly from the host rock. However, it should be noted that other large scale experiments with pre-compacted bentonite blocks illustrated very slow hydration (Villar *et al*., 2005a). Probably, due to the limited thickness of the seals and the lower average dry densities in the discussed borehole sealing experiment, no problems for the hydration were observed. The obtained swelling pressures are lower than originally foreseen, but this is actually related to the disturbance of the host rock and not due to a changed behaviour of the seal in in-situ conditions compared to laboratory conditions. The hydraulic conductivity measured in-situ fits very well the predicted

values based on laboratory measurements. The gas breakthrough experiment clearly showed that no preferential gas flow through the seal does occur. With the used setup, it is not possible to distinguish whether gas flow occurred through the EDZ of the host rock or through the host rock – seal interface. Concerning the radionuclide migration through the seal, the comparison of observed concentrations with modelling results does not yield evidences of the presence of preferential pathways within or around the seal. This does not mean that poorly sealed interfaces and fractures do not exist, but if such features are present, these do not seem to play a significant role in the tracer transport process. This observation is further emphasized by the fact that the sampling procedure makes advection quite significant in the transport experiment.

Finally, concerning sealing boreholes in a plastic clay we generally conclude that:

- pre-compacted bentonite blocks can be used and the sealing is technically feasible
- the required physical parameters (dry density at saturation and swelling pressures) can be obtained by choosing the right initial dry density
- the efficiency of the seal towards water and gas migration can be fairly well predicted
- no evidences of the presence of preferential pathways could be detected from tracer test results.

4 The shaft seal experiment

The shaft seal experiment was installed within the experimental shaft of the HADES Underground Research Facility (see **Figure 4-1**). To this end, the bottom part of the shaft was filled with grout and the concrete liner was removed at the location of the seal. The sealed section is about 2.2 m in diameter and about 2.2 m in height and consists of a mixture of 50% of powder and 50% of highly compacted pellets of FoCa clay. The seal is kept in place with a top concrete lid of about 1 m thick. A large amount of sensors measuring amongst others pore water pressure, total stress, displacement and relative humidity allow following the hydro-mechanical evolution of the seal and the surrounding host rock. Several filters inside the sealed section enabled artificial hydration to reduce the time needed to attain saturation.

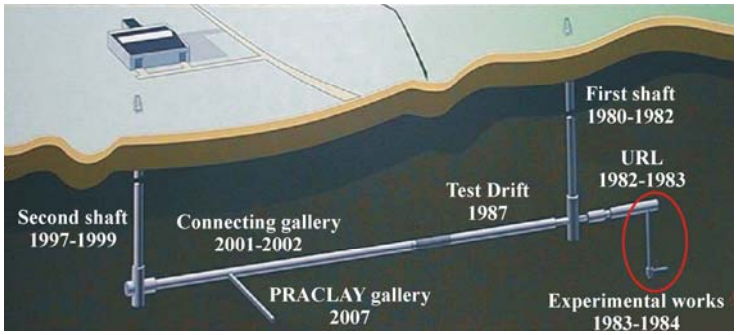

Figure 4-1: Construction history of HADES. The shaft seal experiment is located in the experimental shaft.

4.1 Design and installation

Appendix A1 details the design of the shaft seal and the location and naming of the sensors inside the seal and the surrounding host rock. **Figure 4-2** gives an overview of the design.

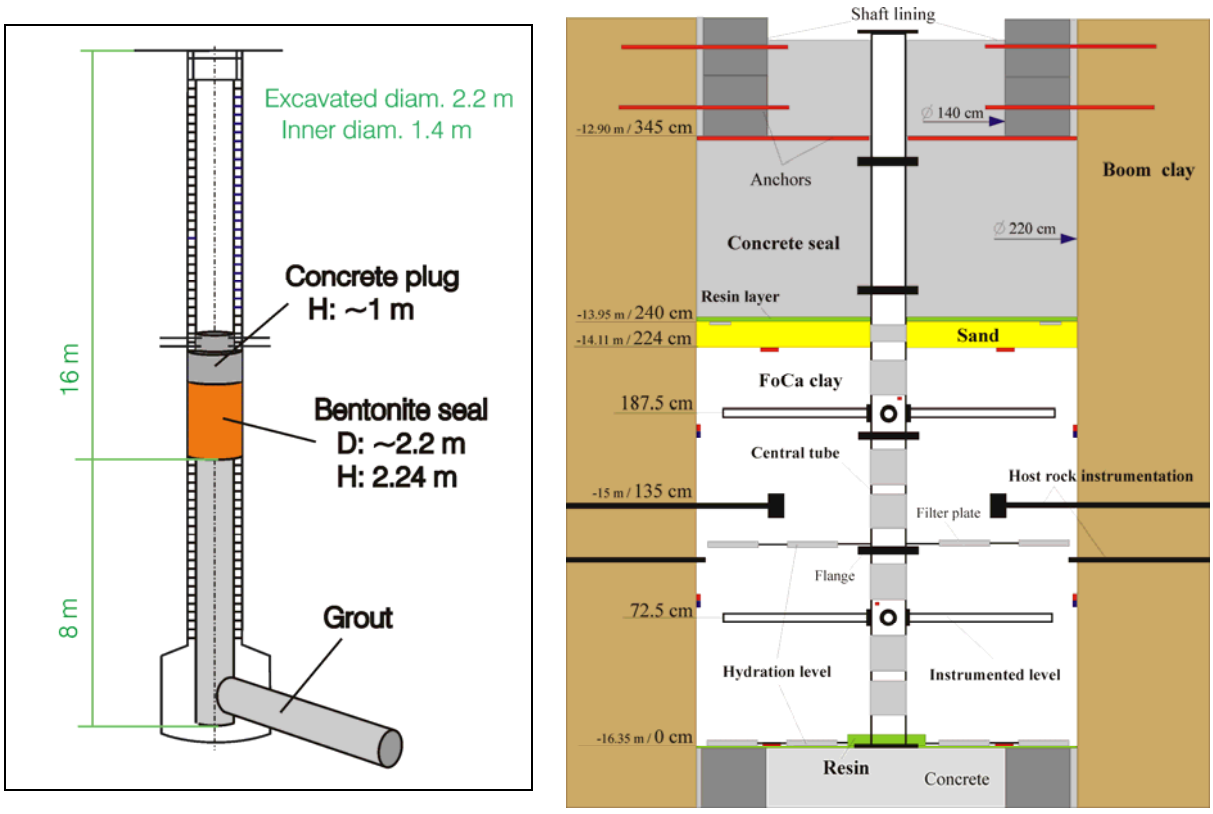

Figure 4-2: Schematic overview of the location of the seal inside the experimental shaft (left) and of the seal design, including the instruments (right).

4.1.1 Seal

The shaft seal experiment was built inside the experimental shaft of the HADES URF. The experimental shaft has an internal diameter of 1.4 m and the shaft lining consists of concrete blocks of 30 cm thick. Between the lining and the Boom clay, a grout layer of about 10 cm had been applied during the building of the shaft.

Five main phases can be distinguished in the preparation and installation of the shaft sealing test, they are detailed below. **Table 4-1** gives the installation schedule.

Table 4-1: Schedule of the preparation and installation of the shaft seal.

16-19 Feb 1998	Phase 1: backfilling of the bottom of the shaft with grout
23 Mar 1999 ➔ 2 Apr 1999	Phase 2: shaft preparation and anchorage of the lining
23 Aug 1999 ➔ 3 Sep 1999	Phase 3: removal of the shaft lining
6-14 Sep 1999	Phase 4: installation of the seal
15-17 Sep 1999	Phase 5: closing of the seal

1. The bottom of the shaft, including the experimental gallery, was backfilled with grout up to the location selected for the seal. The bottom of the seal is located about 16.35 m below the main gallery.
2. For safety reasons, the two lining rings above the seal location were anchored in the Boom clay (**Figure 4-3**). Radial boreholes of 1 m depth were drilled through each block before removing the lining at the location of the future seal and a steel bar was installed in each of them. The steel bar ends in the shaft were fixed to one another and the upper ring of anchors has been bound on three points to upper blocks with metallic plates.
3. The shaft lining (i.e. the concrete blocks and the grout layer) was removed over a height of 3.45 m (**Figure 4-4**, **Figure 4-5**). The lining was replaced by a temporary metallic lining of 2 m diameter (see **Figure 4-6**). The aim was not to limit the convergence of the host formation but to protect the workers from falling clay blocks. After removal of the lining, fissures in the Boom clay were observed and during the installation of the seal a lot of clay blocks fell off the shaft wall. Van Geet *et al.* (2005b) describe these observations.
4. After removal of the lining, the seal and the seal instruments were installed. First, a resin layer was placed at the bottom of the seal to render the seal water and gas tight towards the underlying grout. Next, the shaft was filled with the FoCa clay mixture of 50% powder and 50% pellets over a height of 2.24 m (**Figure 4-7**). The material and mixture is described in Chapter 2. The first 60 cm of the seal were compacted with a vibro-compactor[1] (**Figure 4-8**), i.e. the compaction was stopped just below the first instrumented level. From this level on, the sealing material was installed without further compaction in order to avoid damage to the instruments. In the compacted section, a density of 1.54 g/cm³ was obtained compared to the uncompacted density of 1.38 g/cm³. The initial water content of the mixture is about 6%. Table II summarizes the main characteristics of the seal after installation. Due to the uncertainties on the diameter caused by the falling of blocks during the operation, the seal diameter and the subsequent calculated values for the density are an approximation.
5. A layer of 15 cm of sand was placed on top of the mixture, it acts as a big filter allowing an axial water injection from the top of the seal. A resin layer was placed on top of the sand layer to render the seal water and gas tight. On top of the resin layer a reinforced-anchored concrete plug of about 1 m height was installed to block the seal axially.

[1] The vibro-compactor was designed by CEA/DCC, [Volckaert *et al.,* 2000] describes the development of the compactor and the compacting method.

Figure 4-3: Anchorage of the two rings of blocks of the shaft lining above the future location of the seal.

Figure 4-4: Removal of the shaft lining at the level where the seal will be installed.

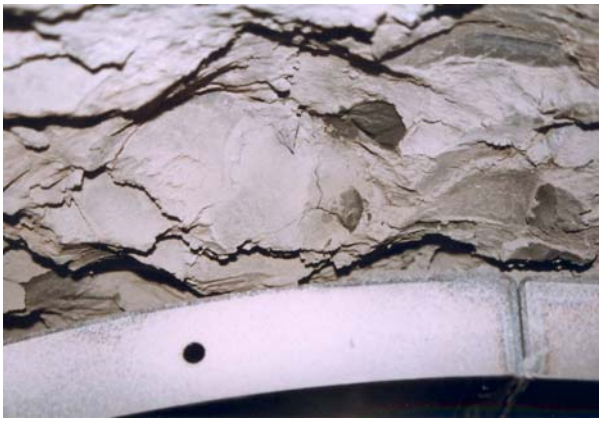

Figure 4-5: View of the Boom clay wall after removal of the lining.

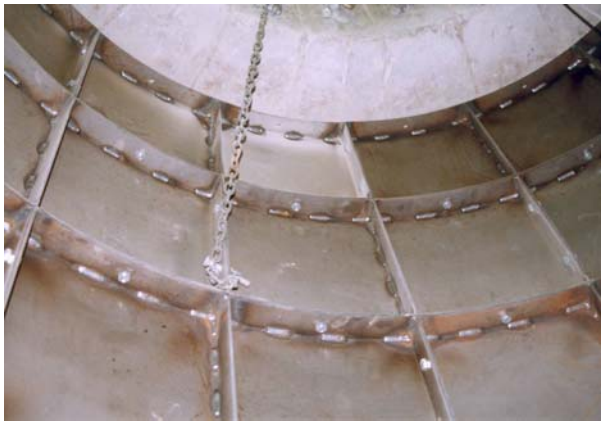

Figure 4-6: Temporary metallic lining to protect the workers for falling clay blocks.

Figure 4-7: Installation of the seal: dumping the FoCa mixture in the shaft (left) and a top view of the shaft during installation (right).

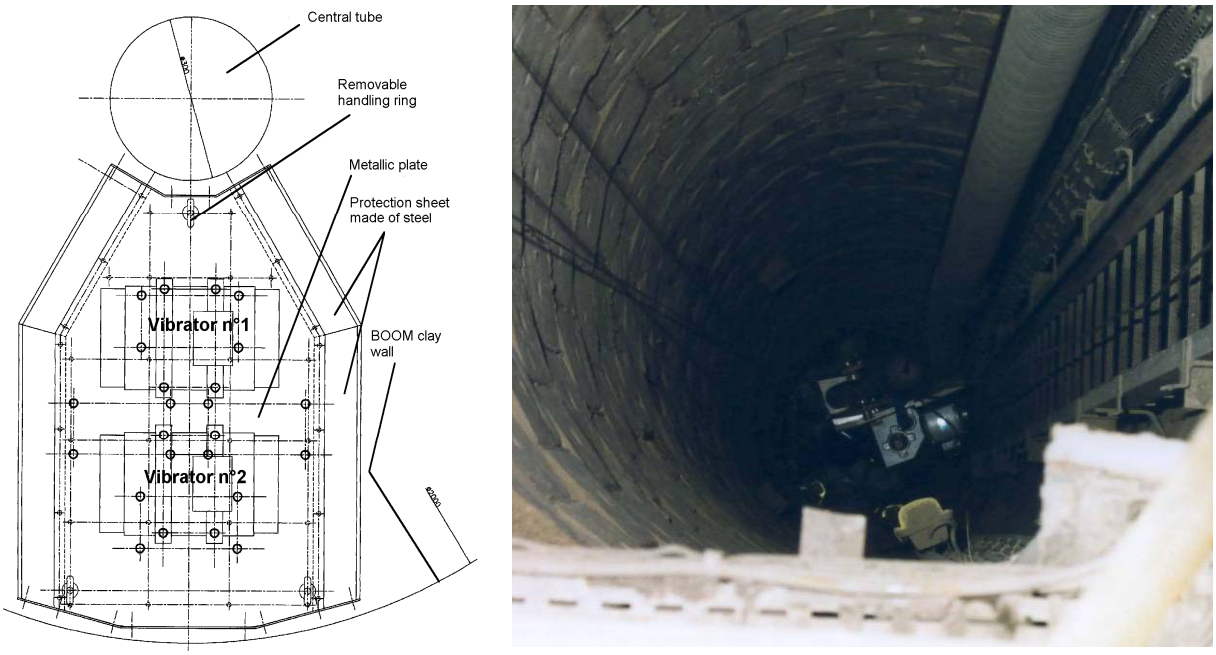

Figure 4-8: Top view of the vibro-compactor designed for the shaft sealing test (left) and a picture of the compactor in the shaft (right).

Table 4-2: Main characteristics of the seal after installation.

Height of the seal	2.24 m
Diameter	2.10-2.20 m
Compaction on the first 60 cm (bottom of the seal)	
Weight of mixture	3472 kg
Volume (corrected for volume of instruments)	~2.25 m³
Density	~1.54 g/cm³
Water content	6%
Dry density	~1.45 g/cm³
Manual filling on 164 cm	
Weight of mixture	8348 kg
Volume (corrected for volume of instruments)	~6.16 m³
Density of the mixture without compaction	~1.38 g/cm³
Water content	6%
Dry density	~1.30 g/cm³

4.1.2 Seal instruments

During the installation of the seal, a lot of sensors were installed in the seal to be able to monitor and test the HM-behaviour of the seal. **Table 4-3** gives an overview of the location, number and type of sensors selected to monitor the seal. Regarding their installation, two categories can be distinguished:

- One part of the sensors inside the seal was mounted on a steel structure which was placed in the centre of the shaft.
- Another part of the sensors is embedded in the seal itself (or at the seal/host-rock interface); all cables and micro-tubes are routed through the central tube.

Table 4-3: General overview of the location, number and type of sensors selected to monitor the seal.

Location	*Code*	*Type of measure*	*Nb**	*Type of sensor*
Central tube	PW	Water pressure	7	Druck transmitter PTX 1400
	PT	Total stress	2x3	KULITE ETM-203-375M
	TC	Temperature	2	Thermocouples Type T
Boom Clay/FoCa seal interface (including some sensors on the three radial host rock piezometers that are actually located just inside the seal)	PW	Water pressure	2x3	Vibrating wire piezometer
			1x2	KULITE sensor HKM-375M (adapted)
			1x3x1	Druck transmitter PTX 1400
	PT	Total stress	2x3	Vibrating wire oil filled pressure cell
			1x2	KULITE sensor HKM-375M (adapted)
			1x3x2	KULITE HKM-155C-375M
	RH	Relative humidity	1x2	ROTRONIC sensor
	TH	Temperature	1x2	ROTRONIC sensor (same as RH)
Instrumented levels	PW	Water pressure	2x3x2	KULITE ETM-203-375M
	PT	Total stress	2x3x4	KULITE ETM-203-375M
	RH	Relative humidity	2x3x1	VAISALA HMP 233 (cf. CIEMAT)
	TH	Temperature	2x3x1	VAISALA (same as RH)
	TC	Temperature	2x3x5	Thermocouples Type T
	DX	Displacement	2x1x2	MTS Temposonics II
Hydration levels	PW	Water pressure	2x6	Druck transmitter PTX 1400
Upper and lower seal section	PT	Total stress	2x4	Vibrating wire oil filled pressure cell

* *q* x *X* or *2* x *Y* x *Z*
q: number of levels
X: number of sensor per level (instrumented or hydration level)
Y: number of rod per instrumented level
Z: number of sensor per instrumented rod

The steel structure in the shaft consists of a central tube and two instrumented levels as shown on **Figure 4-2**. The 0.22 m diameter central tube was installed in five sections: three sections inside the seal and the last 2 (non-instrumented) sections at the level of the concrete on the top of the seal. **Figure 4-9** shows the lower section of the central tube before assembly. The central tube is equipped with sensors to measure pore water pressure (7), total stress (6) and temperature (2).

The instrumented levels are situated at 72.5 cm and 187.5 cm from the bottom of the seal. Each level consists of 1 displacement transducer and 3 instrumented rods installed in a same plane with 90° angle between each other (**Figure 4-10**). The rods and the displacement sensors are connected to the central tube. Both levels are equipped with the same sensors at the same position on the rods. Each rod is equipped with sensors to measure pore water pressure (2), total stress (4), relative humidity (1) and temperature (5).

Most of the sensors embedded in the seal itself (or at the seal/host-rock interface) are located in the so-called hydration levels. These are located at the bottom and at mid-height of the seal and

they both contain 6 porous filter discs to measure pore pressure (**Figure 4-11**). The sand layer on top of the seal is also considered as a hydration level. At the level of the instrumented levels and hydration levels, instruments are also embedded near the interface. Furthermore, some sensors were embedded at the top and the bottom of the seal.

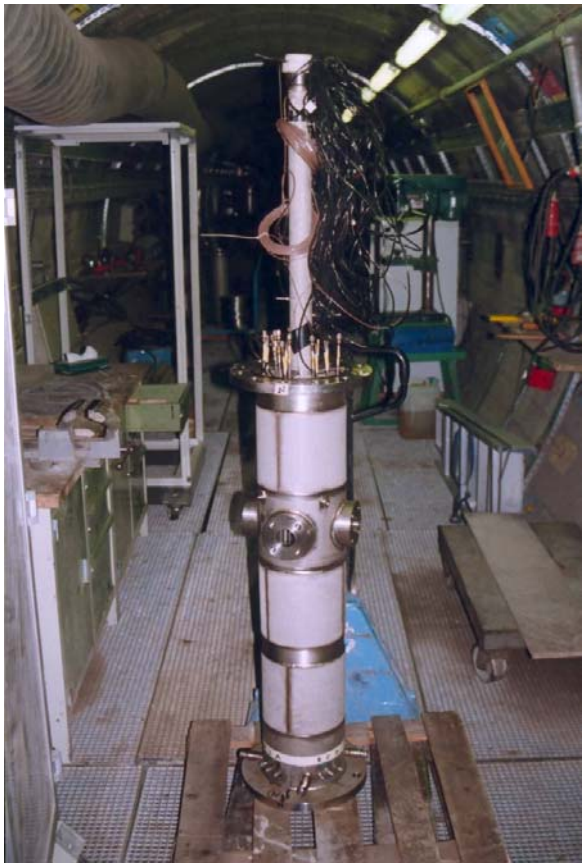

Figure 4-9: Lower section of the central tube.

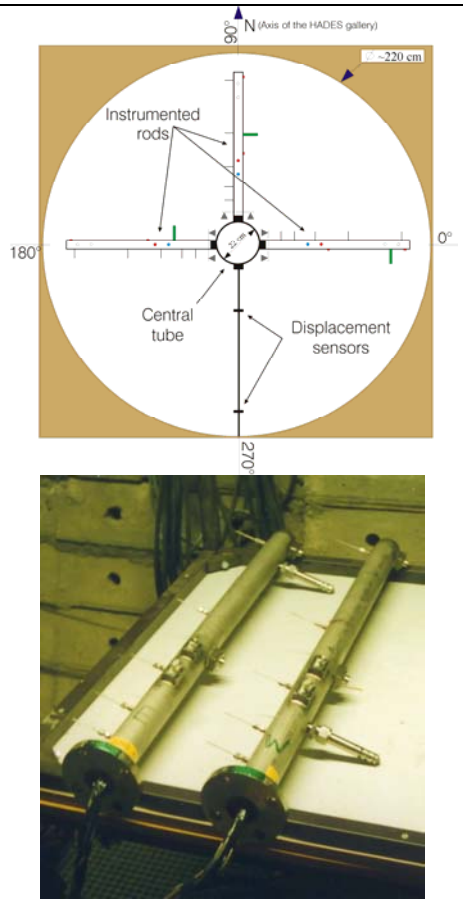

Figure 4-10: Top view of an instrumented level (top) and instrumented rods before assembly (bottom).

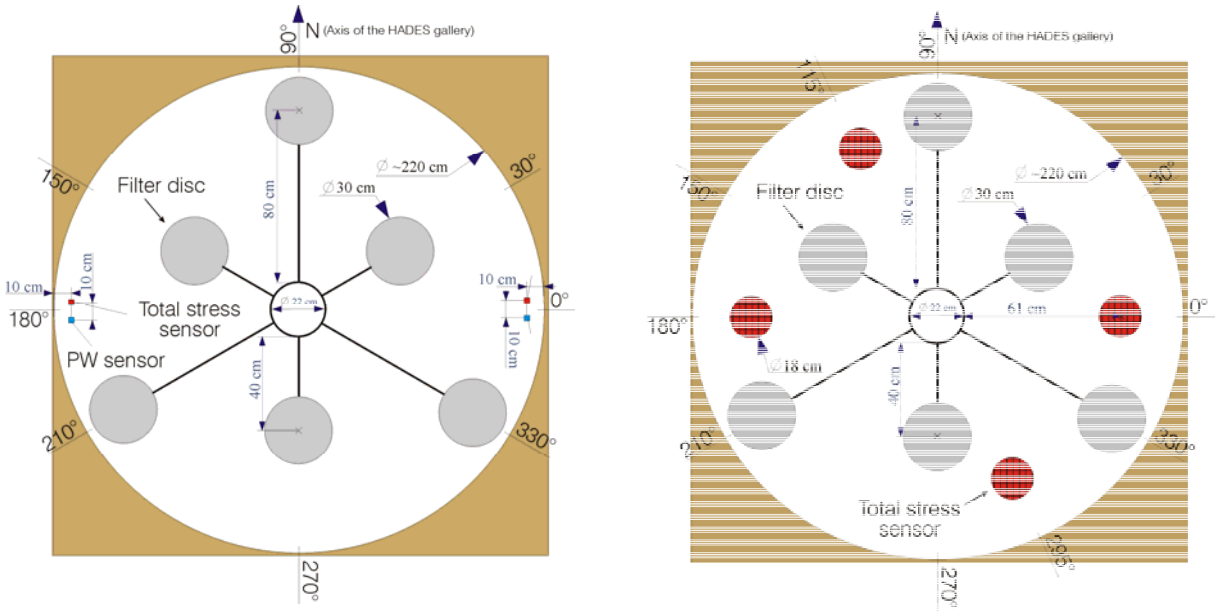

Figure 4-11: Lay-out of the two main hydration levels: middle level (left) and bottom level (right).

4.1.3 Host rock instruments

Prior to the installation of the seal, the host rock had been instrumented to measure pore water pressure, total stress and displacements (radial to the shaft). **Figure 4-12** shows an overview of the host-rock instruments, **Table 4-4** gives a general overview of the location, number and type of sensors selected to monitor the host rock. The installation was performed in the period April-July 1998, about one year before the installation of the seal, allowing the host rock instruments to reach an equilibrium state before the installation of the seal itself.

At the level of the future seal, three small piezometers of about 1 m length were installed radially from the experimental shaft at 1.35 m from the bottom of the seal. The radial piezometers measure pore pressure (x5) and total stress (x10). **Figure 4-13** shows the drilling works prior to the installation and **Figure 4-14** shows the installed piezometer.

Displacement sensors were placed 30 cm below each piezometer. Cores were taken to this end during the drillings for the radial piezometers. The displacement sensors (magnets) were sandwiched between clay cores as illustrated in **Figure 4-15**. The metallic rod was inserted in a central hole throughout the whole clay core. The whole set-up was then replaced in the borehole. An installed displacement sensor is visible on **Figure 4-14**, just below the piezometer. In order to have a fixed reference point, the front end of the metallic rod was fixed to its corresponding piezometer.

Finally, a vertical piezometer of about 20 m length was installed from the main gallery, parallel to the experimental shaft, measuring pore pressure (x8) and total stress (x16). The vertical piezometer was placed parallel to the shaft at about 1 m from the shaft lining. The distance of 1 m was based upon modelling (Volckaert *et al.,* 2000).

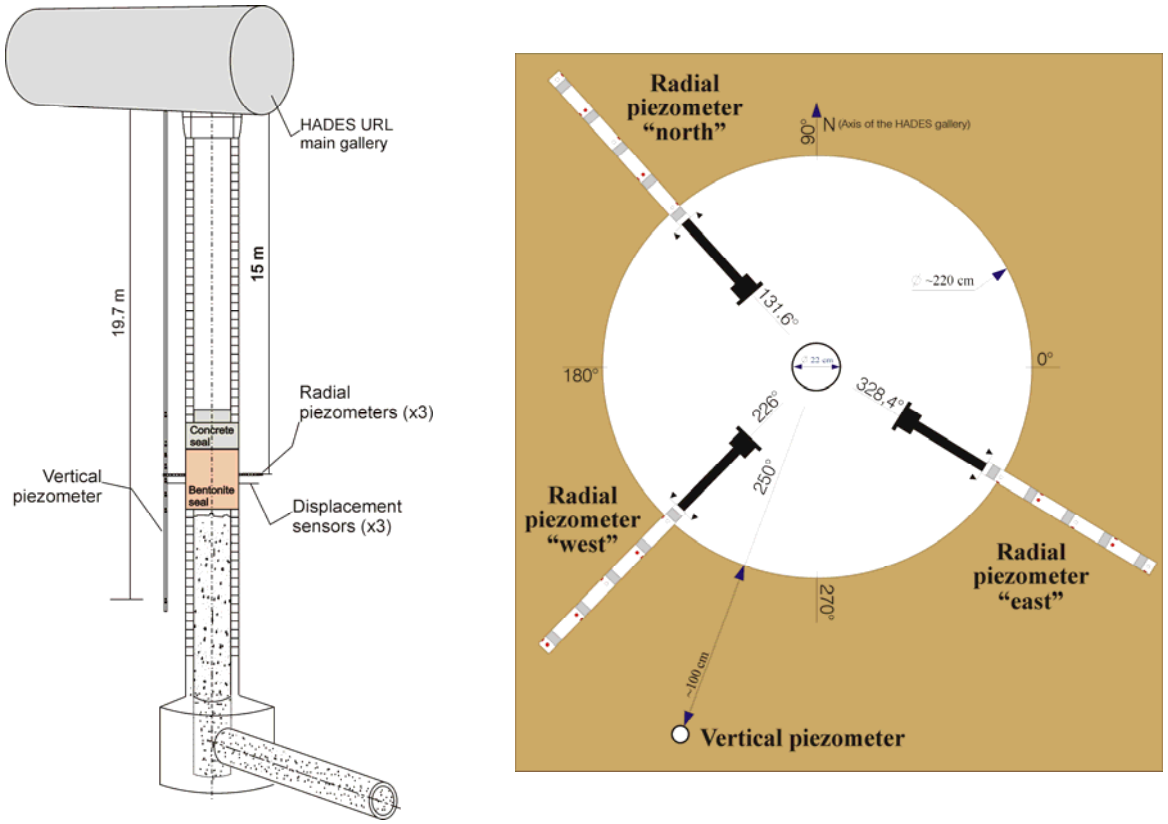

Figure 4-12: Host rock instruments: overview (left) and top view (right).

Table 4-4: General overview of the location, number and type of sensors selected to monitor the host rock.

Location	*Code*	*Type of measure*	*Nb**	*Type of sensor*
Vertical piezometer	PW	Water pressure	8	Druck transmitter PTX 1400
	PT	Total stress	16	KULITE HKM-155C-375M
Horizontal piezometers	PW	Water pressure	1x3x4	Druck transmitter PTX 1400
	PT	Total stress	1x3x8	KULITE HKM-155C-375M
Horizontal rods	DX	Displacement	1x3x2	MTS Temposonics II

* *q* x *Y* x *Z*
q: number of levels
Y: number of rod per instrumented level
Z: number of sensor per instrumented rod

Figure 4-13: Drilling through the concrete lining of the shaft for the installation of a radial piezometer.

Figure 4-14: View of one of the radial piezometers, after removal of the lining of the shaft.

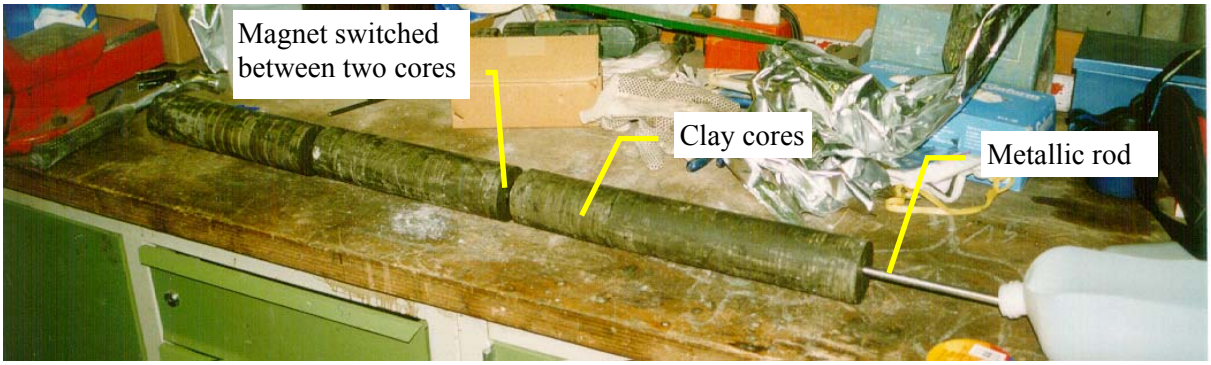

Figure 4-15: Picture of the installation of the displacement sensors. The metallic rod is inserted into the centre of the clay cores and two magnets are sandwiched between the clay cores.

4.2 Description of the instruments

This section gives some information about the type and performance of the seal and host rock instruments. Appendix A1 details the position of the sensors, appendix A5 contains the technical drawings of the in-house designed instruments and structural components inside the seal and in the surrounding host rock.

4.2.1 Nomenclature

In naming the sensors, the following methodology was applied (**Table 4-5**):

Sensor code: AA-B(B)-CCx-D(D)-EE

Table 4-5: Nomenclature of the RESEAL instruments.

AA	Measurement type	temperature (TC of TH), pore water pressure (PW), total stress (PT), relative humidity (RH) or displacement (DX)
B(B)	Location (medium)	seal (S), host rock (H) or interface seal/host rock (SH)
CC	Location (type)	piezometer (PZ), instrumented level (IL), hydration level (HL)
x	Level inside the seal	bottom (b), middle (m) or top (t)
D(D)	Direction	north (N) i.e. direction of the axis of main gallery, west (W), east (E), south (S) and 'vertical' (V) i.e. parallel to the axis of the shaft
EE	Sensor number	1, 2, …

Table 4-6 gives a summary of the type and the quantity of all measurement points.

Table 4-6: Summary of the type and the quantity of all measurement points.

Type of sensor	*Seal*	*Host rock*	*Total*
Water pressure	42	20	62
Total stress	52	40	92
Temperature	40	/	40
Air relative humidity	8	/	8
Displacement	4	6	10
Total	*146*	*66*	*212*

4.2.2 Temperature sensors

Three types of temperature sensors were used inside the seal:

1. Each of the three rods of the two instrumented levels contains 5 thermocouples type T. Two additional sensors of this type were placed on the heater installed inside the central tube. These thermocouples were delivered by Thermocoax.
2. Each of the three rods of the two instrumented levels contains a RH sensor manufactured by VAISALA and adapted by CIEMAT to resist the high water pressures during the experiment. These sensors are also equipped with a Pt 100 IEC 751 1/3 class B temperature sensor.
3. At the top instrumented level, two Rotronic RH sensors were installed. These sensors are also equipped with a Pt 100 1/3 DIN temperature sensor.

4.2.3 Pore water pressure sensors

Four types of pore pressure sensors were used in the seal and the host rock:

1. Filter screens
   Filter screens are widely used throughout the Boom Clay characterisation around the HADES URF and also within RESEAL. The overall lay-out is always the same and consists of a permeable filter screen, a small volume chamber and two water tubes that run up to the main gallery (see **Figure 4-16**) where one of them is connected to a pore water pressure sensor (Druck transmitter PTX 1400). The most widely used filter screen is stainless steel type 304, from Krebsöge (SIKA R5 = mean pore size of 5 µm).
   In RESEAL, disc-shaped filter screens were placed in the hydration levels (**Figure 4-17**). Cylindrical filter screens were used in the host rock piezometers (**Figure 4-17**) and on the central tube (**Figure 4-9**).

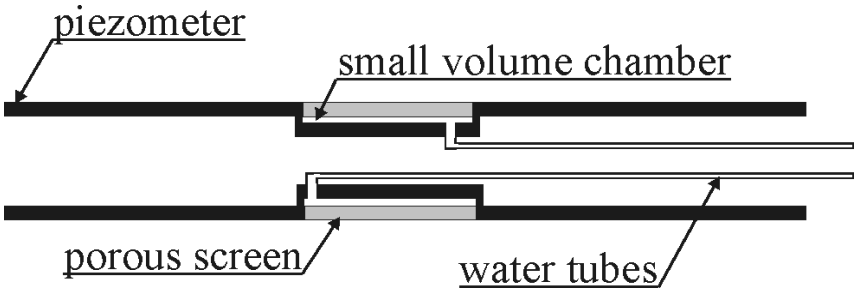

Figure 4-16: Schematic cross-section through a piezometer containing a filter.

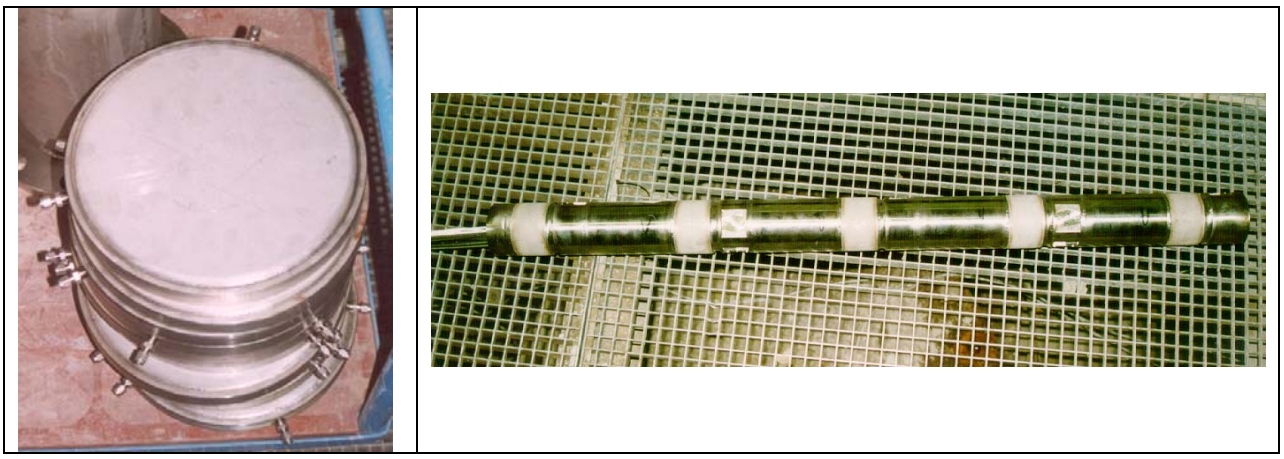

Figure 4-17: Piezometric filters: stack of disc-shaped filters with two connections visible on each disc (left) and one of the radial host rock piezometers (right).

2. Vibrating wire piezometer
   Each of the two instrumented levels was equipped with 3 vibrating wire pore pressure sensors manufactured by Soil Instruments Limited. Water enters the sensors through a porous ceramic with a pore diameter of approximately 1 µm. The sensors were installed at the interface between the host rock and the seal (**Figure 4-18**); their pressure range is 50 bar.

3. KULITE transmitter ETM-203-375M

This type of sensor is actually a total pressure sensor (see later on). However, the sensor is inserted in a stainless steel body that is topped with a permeable filter plate with a pore size of 5 µm (**Figure 4-19**). The big advantage compared to the filter screens described above is the fact that very small devices can be installed. Each of the three rods of the two instrumented levels contains sensors of this type. The sensors are rated up to 55 bar sg.

4. KULITE transducer HKM-375M

These sensors are similar than the one described above, however they were somewhat adapted by CEA. The sensors have been installed near the interface FoCa seal/Boom Clay, at the level of the middle hydration level; they are rated up to 35 bar abs.

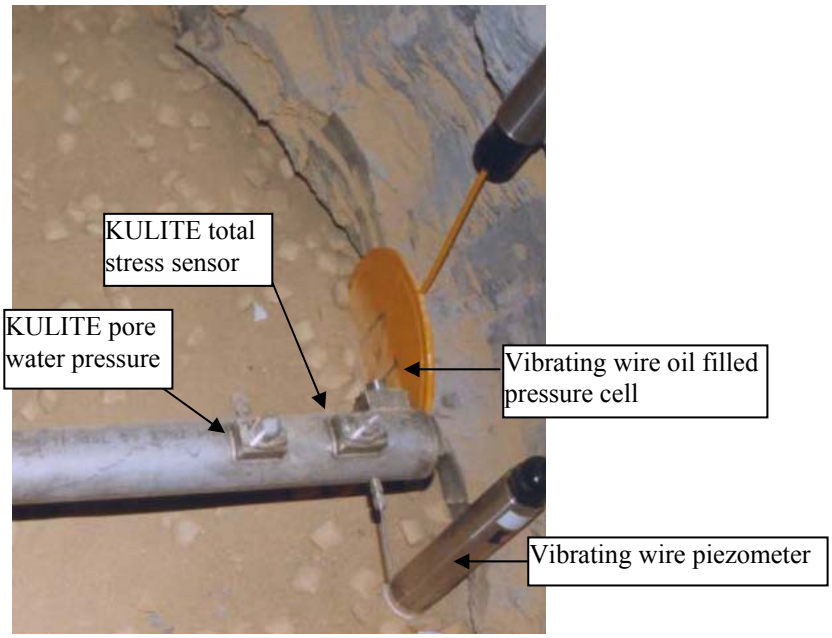

Figure 4-18: Detail picture of the instruments used in the shaft seal of the RESEAL experiment with miniature KULITE total stress sensors and vibrating wire oil-filled pressure cell.

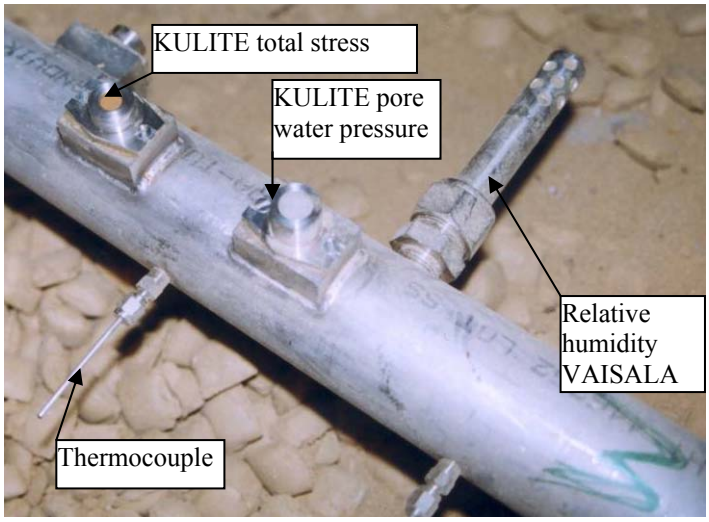

Figure 4-19: Detail picture of the instruments used in the shaft seal of the RESEAL experiment, illustrating KULITE miniature total stress sensor with a clay pellet on the membrane, KULITE miniature pore water pressure with a filter screen on top of the membrane, a relative humidity sensor and a thermocouple.

4.2.4 Total stress sensors

Several types of total stress sensors were used in the seal and the host rock:

1. KULITE sensors

Kulite pressure transducers are miniature piezoresistive sensors. Within the RESEAL project, these sensors were specially designed in order to have an open chamber in contact with the membrane. This chamber was then filled with a compacted bentonite pastille (**Figure 4-19**), in order to ensure a good contact with the surrounding material. The whole was then placed inside the in-situ set-up. Three types were used within RESEAL:

- KULITE HKM-155C-375M transducers were used on the vertical (16 sensors) and radial (3 times 8 sensors) piezometers. The sensors are rated up to 55 bar sg.
- KULITE ETM-203-375M transmitters were used on the rods of the instrumented levels (4 on each rod, see **Figure 4-18**) and the central tube (6 sensors). The sensors are rated up to 55 bar sg.
- Two KULITE HKM-375M sensors were adapted for the in-situ test by CEA, they have been installed at the interface FoCa seal/Boom Clay, at the level of the middle hydration level; they are rated up to 70 bar abs. This device consists of a miniature stress sensor connected to a reservoir of elastomere containing an incompressible fluid (**Figure 4-20**). It has a diameter of 17 mm and a length of 100 mm. This sensor has the advantage to measure the integrated pressure from two sides.

2. Vibrating wire oil-filled pressure cell

The cell consists of a circular or rectangular flat jack formed from two sheets of steel welded around the periphery. The narrow gap between plates is filled with hydraulic oil and is connected to a vibrating wire transducer. Both at the bottom and the top of the seal, 4 of these circular sensors were installed. Furthermore, at each of the two instrumented levels, 3 of these sensors were installed at the interface between the host rock and the seal (one sensor in front of each instrumented rod, see **Figure 4-18**).

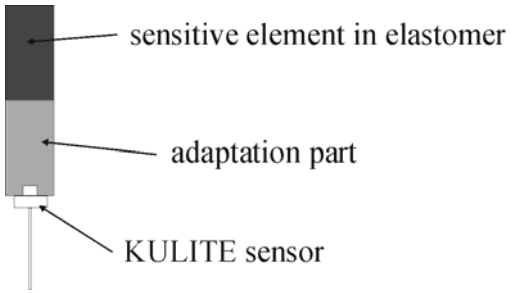

Figure 4-20: Schematic view of the adaptation performed by CEA to some of the KULITE sensors used inside the shaft seal of the RESEAL project.

4.2.5 Relative humidity sensors

Within the RESEAL shaft seal, two methods have been used:

1. Installation of relative humidity sensors

Two commercially available relative humidity sensors are used:

- A VAISALA HMP-233 sensor was installed on each of the three rods of the two instrumented levels (**Figure 4-19**).
- Two ROTRONIC Hygromer I-2000 sensors (**Figure 4-21**) were installed in the top instrumented level. The porous cylinder of one of the humidity sensors has been encapsulated inside a compacted clay cap. This adaptation, simulating a pellet, will allow monitoring the hydration of a pellet in the mixture. The other sensor without clay cap will allow measuring the relative humidity in the powder of the mixture.

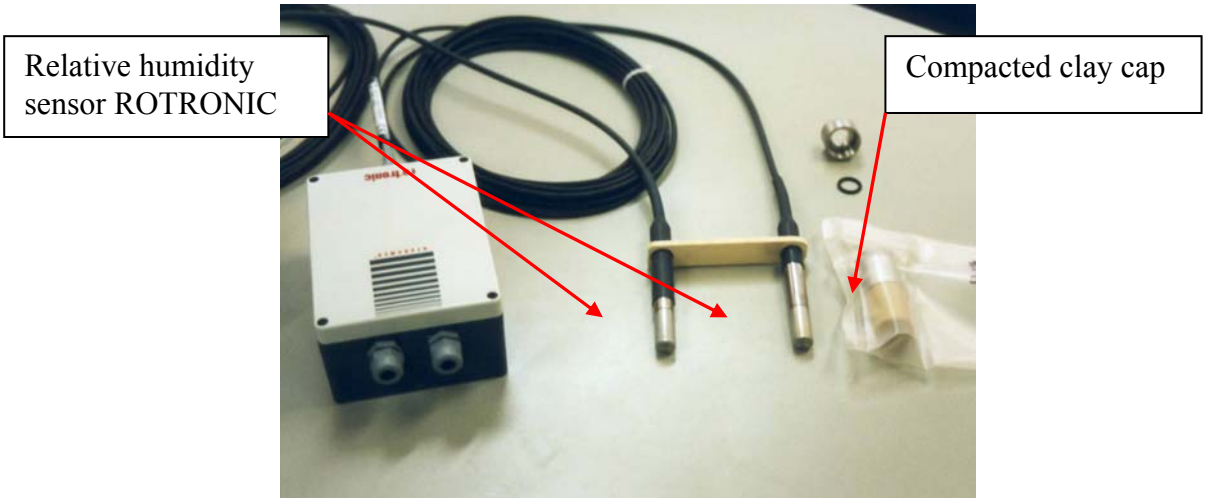

Figure 4-21: Relative humidity sensors adapted by CEA/SESD for the in situ test. The porous cylinder of one of the humidity sensors has been encapsulated inside a compacted clay cap simulating a pellet.

2. Indirect measurement of saturation by means of a thermal pulse.
A heating element is entered inside the central tube and emits a known quantity of heat. The thermal dissipation through the bentonite is measured with temperature sensors (thermocouples) along an axis perpendicular to the heat source. Comparing these measurements with the dry state allows measuring the variation of thermal conductivity of the bentonite, which depends on the saturation.

4.2.6 Displacement sensors

Displacement sensors of the magnetostrictive principle have been installed in the host rock and the seal itself to measure radial deformations. The instrument used is the same in both cases, namely Temposonics TMX-M100 multiple transducer interface with multi magnets. The resolution of the system is ~1 mm.

Around the shaft seal of RESEAL, 3 times 2 displacement sensors were installed in the host rock (**Figure 4-15**). It should be mentioned that the electronics at the end of the metallic rod were not watertight and therefore were inserted in an in-house made stainless steel chamber. Another 2 set-ups, each containing 2 sensors, were installed in the seal itself; one in each instrumented level.

The vertical movement of the top of the shaft seal is monitored by two redundant set-ups (**Figure 4-22**).

- A potentiometer manufactured by GLÖTZL with its fixed point on the shaft lining, just above the top of the seal.
- A wire extensometer (manual read-out) with its fixed point in the top of the main gallery.

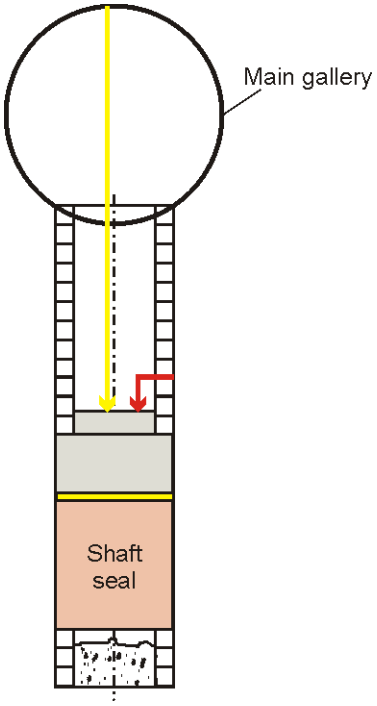

Figure 4-22: Position of the fixed points of the displacement sensors on the top of the shaft seal: GLÖTZL potentiometer (red) and wire-extensometer (yellow).

4.2.7 Performance of the instruments

Based on Van Geet and Volckaert (2008), the performance of the used instrumentation is described here.

Temperature sensors
The thermocouples performed very well. Only one (out of 32) failed during the experiment. Both thermistors of the ROTRONIC RH sensors are still working properly. Three (out of six) thermistors of the VAISALA RH sensors failed.

Pore pressure sensors
Pore pressure measurements in Boom Clay with the in-house designed filter screens are thought to be very reliable over long periods of time. This is confirmed in the shaft seal experiment: all filters in the host rock give reliable results. However, almost 50% of the filter screens inside the seal are giving bad or doubtful measurements. The problem does not lay with the sensors as such but rather with the filter screens and/or tubings: clogging of the filter screens and/or tubings and leaks or wrongly connected tubings might be an issue. This topic is further dealt with in section 4.3.3.

The vibrating wire piezometers are performing reasonably. Four (out of 6) are giving good results, the other two indicate the same trends but have a higher noise level. Both KULITE sensors adapted by CEA are giving reliable results. Of the remaining 12 KULITE cells, about 50 % is still measuring atmospheric pressure and one was broken during installation. It is

impossible to say whether the sensors measuring atmospheric pressure are defective or whether no pore pressure build-up has occurred at the location of these sensors. Furthermore, some sensors have only started to measure higher than atmospheric pressure since the start of 2007. A possible cause might be the use of filter plates on top of the sensors with a mean pore size of 5µm in contact with bentonite powder. The latter might enter and obstruct the pores, thus jeopardizing or delaying good pore water pressure measurements. The use of filters with a smaller mean pore size might again increase the reliability of these sensors.

Total stress sensors
46 total pressure sensors are installed within the shaft seal. 14 of them are vibrating wire oil filled pressure cells and all of them give reliable results. Two of them are KULITE sensors adapted by CEA and both of them give reliable results. The remaining 30 total stress sensors are of the KULITE type. Three of them broke during installation and four of them seem to give unreliable results. Consequently, about 80% of the KULITE sensors inside the seal is working properly.

The KULITE total stress sensors in the host rock perform less well. Roughly 30 % give reliable results at this moment. Many of the defective sensors gave quite good results at the start of the experiment but broke down after several years. It is also remarkable that on one particular host rock piezometer (radial east) eight (out of 10) sensors are giving reliable results.

RH sensors
In total 8 RH sensors have been installed in the shaft seal experiment of RESEAL. Seven of them give reliable results until failure at 100 %. The sensors used in the shaft seal experiment are very accurate within the range 0-95 % relative humidity (+/- 1.5 % RH). However, above 95 % RH, actually the region of interest, the error increases to +/- 2.5 % RH) and the results are thus less reliable. So actually, they mainly give information on the local full saturation of the bentonite, rather than detailed information on the evolution of the relative humidity/suction. Moreover, once 100 % of RH is reached, the sensor is broken.

The indirect method to measure RH using a thermal pulse was not fully applied in the shaft seal. The disadvantage of the technique is that a calibration is needed (and only an in-situ calibration is correct). This means that the in-situ values for dry and saturated bentonite need to be determined. Only once these data are available, this means at full saturation, a recalculation of the intermediate values is possible. Moreover, no continuous analyses can be performed and the technique is once again less sensitive for more saturated media, so that in the region of interest (90 – 100 % RH) the technique is less reliable. Some more info about the performed tests is given in section 4.3.2. This technique was applied in the BACCHUS 2 experiment (Volckaert *et al.,* 1996).

Displacement sensors
Three times two sensors were installed in boreholes around the seal experiment:

- Borehole "east": both sensors are performing well.
- Borehole "north": one sensor is performing well, the noise level of the other one increased about two years after installation but overall trends are still reliable.
- Borehole "west": both sensors failed about 2.5-3 years after installation.

Two times two sensors were installed inside the shaft seal:

- Middle instrumented level: both sensors are performing well.
- Bottom instrumented level: both sensors failed about 2.5-3 years after installation.

Both the manual and automatic displacement sensors measuring the vertical movement of the top of the seal are performing well.

4.3 Hydration

4.3.1 Hydration system and hydration strategy

The artificial hydration of the seal started on 3rd of May 2000, about 7 months after the installation of the seal. Appendix A2 contains the detailed logbook of the actions performed on the shaft seal. Water was injected through the filters on the vertical central tube in the seal and through the filters of the hydration levels. Synthetic Clay Water (SCW) was used mimicking the composition of undisturbed Boom Clay pore water (De Craen *et al.,* 2004). Its composition is given in **Table 4-7**.

Table 4-7: Salt contents for 1 litre of Synthetic Clay water (SCW).

$MgCl_2.6H_2O$	22 mg
KCl	25 mg
Na_2SO_4	0.3 mg (10 ml of 3 mg dissolved in 100 ml)
NaCl	10 mg
$NaHCO_3$	1170 mg
H_3BO_3	43 mg
NaF	11 mg
$CaCO_3$	1000 mg (calcium saturated by an excess of solid)

The two hydration levels are on the middle and at the bottom of the seal, and are composed of six metallic filter discs of 30 cm in diameter. The central tube (Ø 22 cm) has six injection filters distributed on the height of the seal and a seventh one inside the sand layer which was installed on the top of the seal to act as a large axial injection filter. The sand layer is equipped with two metallic filter discs of 10 cm in diameter. **Figure 4-23** shows the locations of the injection filters.

Table 4-8 gives an overview of the hydration history. During the course of the experiment, injection pressure was changed several times and hydration was stopped and restarted several times. Moreover, after some weeks of artificial hydration, a leak was detected at the top of the seal. For this reason the continuous injection in the sand layer was stopped. During the following years, some water was injected in the sand layer from time to time to ensure its saturation.

In total, about 1.95 m³ of water was artificially injected. **Figure 4-24** shows the evolution of the volume of injected water and the injection pressure[2] applied.

[2] These are the pressures as measured at the pump. To know the injection pressure at the level of the seal, the pressure corresponding to the water column between the pump and the injection filter should be added. This additional pressure is comprised between 1.6 and 1.8 bar.

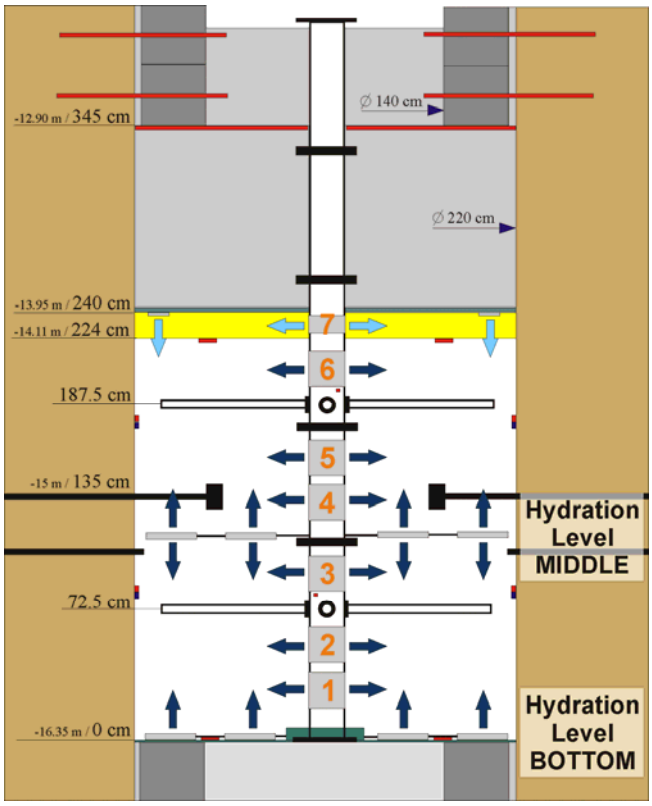

Figure 4-23: Hydration scheme. Artificial hydration was performed through metallic filters on the central tube and two hydration levels (middle and bottom) Due to a leak, injection through the dedicated sand layer was ended shortly after the start of artificial hydration.

Table 4-8: History of the artificial hydration.

Date	Action
3 May '00	Start of artificial hydration. P_{abs} = atmospheric pressure + water column.
27 May '00	Hydration of sand layer was stopped.
23 January '01	Change hydration pressure. P_{abs} = 1.48 bar + water column.
26 February '01	Change hydration pressure. P_{abs} = 1.97 bar + water column.
15 May '02	Change hydration pressure. P_{abs} = 2.97 bar + water column.
17 May '02	Change hydration pressure. P_{abs} = 1.97 bar + water column.
29 May '02	Change hydration pressure. P_{abs} = 2.47 bar + water column.
6 February '03	Change hydration pressure. P_{abs} = 2.68 bar + water column.
13 November '03	Stop hydration through filters V1, HLB1 en HLB5.
20 November '03	Stop hydration through filters V5, HLB4, HLM1, HLM2, HLM5 and HLM6.
26 November '03	All hydration filters closed except: HLB2, HLM1, HLM2, HLM5 and HLM6.
2 December '03	Hydration system stopped.
24 December '03	Restart of the hydration on all filters in the seal.
26 January '04	Hydration stopped.
10 May '04	Restart of hydration on filters V2, V3, V4, V6, HLM3 and HLM4.
9 July '04	Hydration stopped.
5 August '04	Restart of hydration on filters V2, V3, V4, V6, HLM3 and HLM4.
2 June '05	Change hydration pressure. P_{abs} = 3.08 bar + water column.
28 October '05	Stop hydration through V3, V4, HLM3 and HLM4 (only V2 and V6 remain).
5 April '06	Hydration stopped.

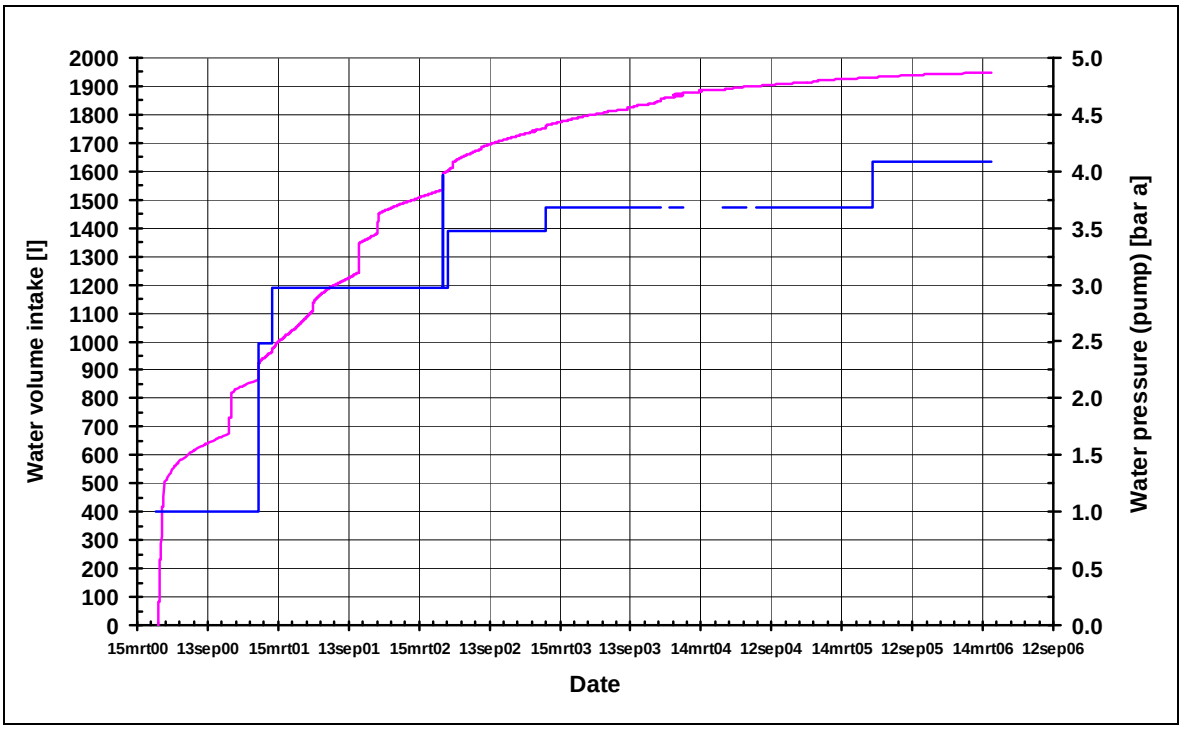

Figure 4-24: Volume of the artificial hydration (pink) and water pressure at the pump (blue).

4.3.2 Saturation

Figure 4-25 shows the RH measurements inside the seal at the instrumented levels. Sensor RH-S-ILt-W was defective from the start of the test. Measurements are only available starting from August 2001; there was a problem with the sensor cabling from the start of the experiment that was solved at that time.

Figure 4-26 and **Figure 4-27** show the RH measurements at the interface between the seal and the host rock for respectively the ROTRONIC sensor without and with clay cap (corresponding to RH in powder and pellet). **Figure 4-28** shows the measurement of RH on 18th April 2007.

Based upon the RH-measurements, we conclude that:

- The first months of the saturation process is rather fast but afterwards it slows down, after reaching about 70-90% of relative humidity.
- Full saturation is reached earlier at the interface than in the seal itself.
- Inside the seal, saturation is heterogeneous.
- The Rotronic sensor with clay cap (representative for pellet saturation) measures somewhat faster saturation than that without clay cap (representative for powder saturation).
- In the seal, it takes a long time to get the last 5-10% of saturation. It should be noted that the accuracy of RH-sensors in this range is much less than at lower RH values.
- Artificial hydration (temporarily) speeds up the saturation process, cf. ROTRONIC sensors at the seal/host rock interface in May 2000 (**Figure 4-26** and **Figure 4-27**). Despite artificial hydration, it remains difficult to achieve the last percentages of full saturation (see next bullet).
- Increasing the hydration pressure can enhance saturation, cf. VAISALA sensors on 15th May 2002 (especially sensor RH-S-ILb-E). However, the effect of increasing hydration

pressure is limited at higher saturation degree. It seems that it is very difficult to achieve the last percentages of full saturation.

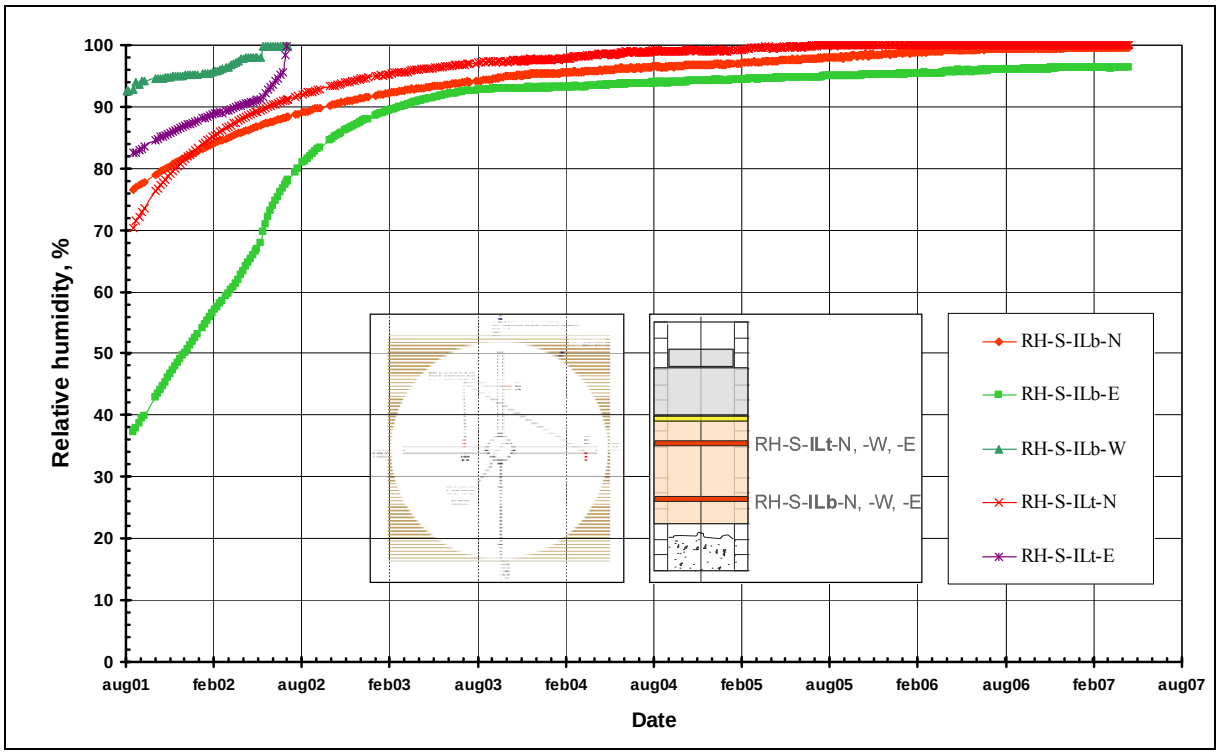

Figure 4-25: RH measurements in the seal at the instrumented levels (VAISALA sensors).

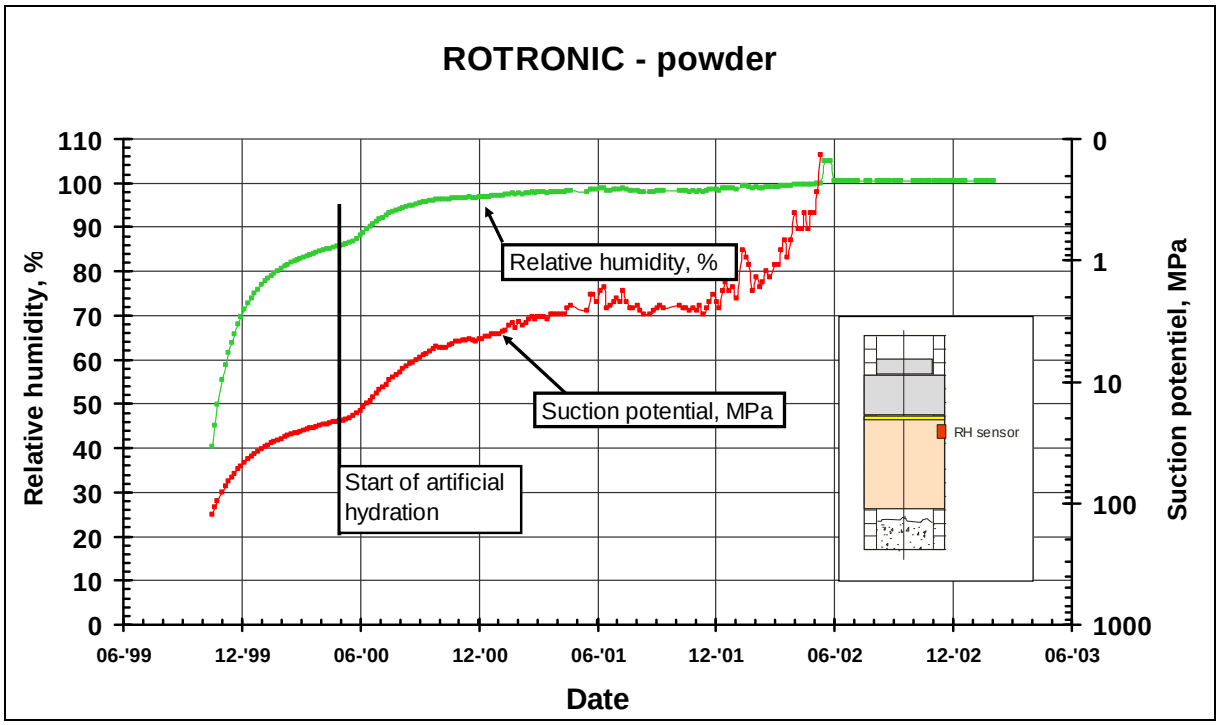

Figure 4-26: RH measurements at the seal - host rock interface (ROTRONIC sensor without clay cap).

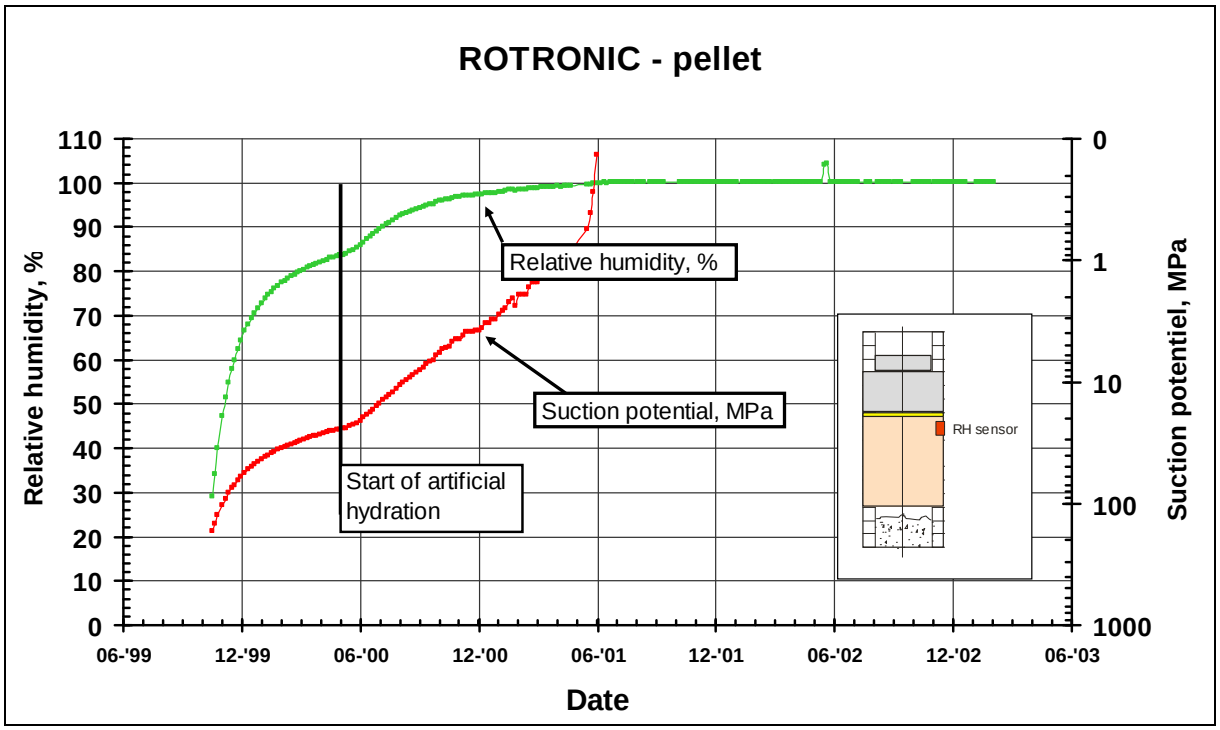

Figure 4-27: RH measurements at the seal - host rock interface (ROTRONIC sensor with clay cap).

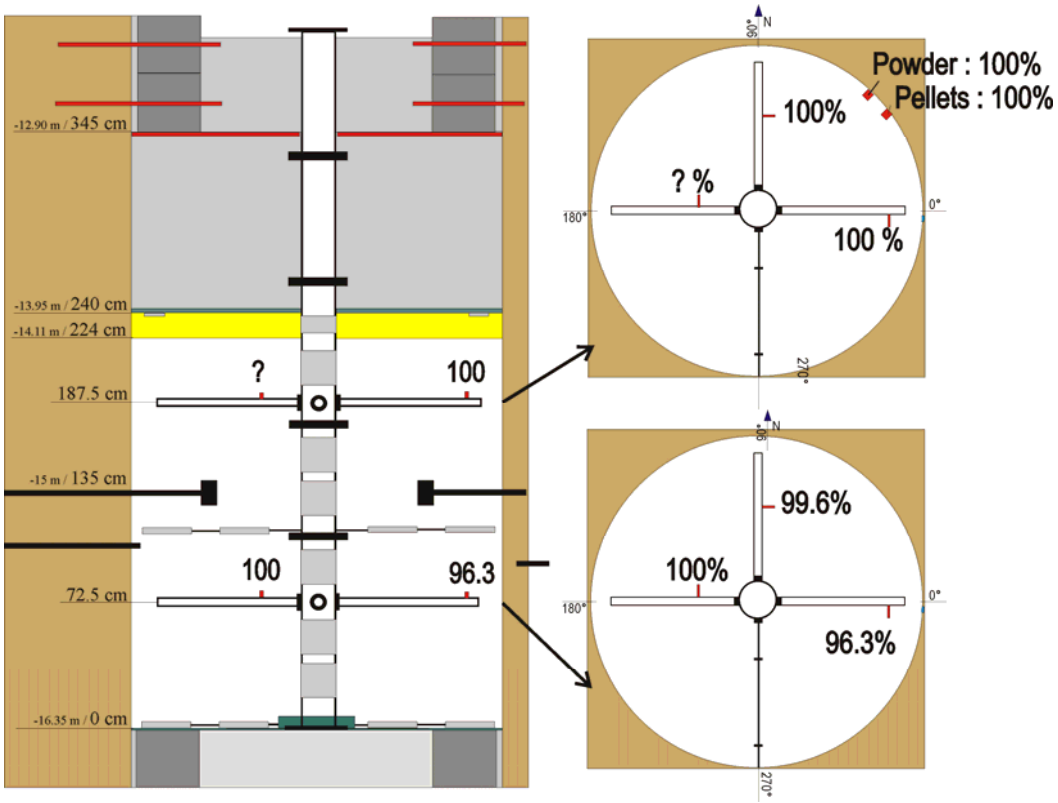

Figure 4-28: Overview of RH-measurements on 18th April '07.

As mentioned in the section about sensor performance, the indirect method to measure RH using a thermal pulse was not fully applied in the shaft seal. Some measurements were made at the start of the experiment but the measurements were stopped after some 1.5 years. Indeed, the measurement and interpretation are quite laborious, the accuracy is not higher than that of the

other measurements and full conclusions can only be drawn once full saturation is reached. **Figure 4-29** shows the results of the 5 test campaigns performed. The measurements show an increase of the thermal conductivity; this corresponds to an increase of saturation but, as explained, it is impossible to quantify the degree of saturation on the basis of these results alone.

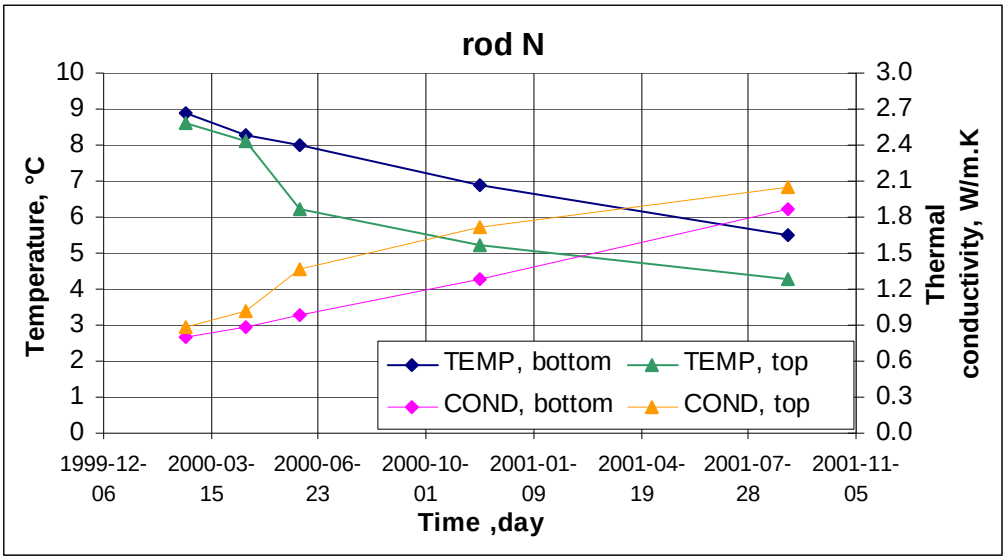

Figure 4-29: Result of thermal pulses.

4.3.3 Some remarks about the performance of the hydration system

During the course of the experiment, several observations indicated that the hydration system did not always perform as designed. To illustrate this, **Figure 4-30** and **Figure 4-31** show the pressures at the injection filters (period October 2003 – March 2004), respectively for the central tube and the bottom hydration level. Up to November 2003, all of these filters were connected to the hydration system. Nevertheless, different types of behaviour can be observed:

1. Filters which are clearly connected to the hydration system resulting in a "saw tooth" behaviour. Every time the trigger pressure of the hydration pump is reached, the pump increases the pressure to a certain value after which the pressure slowly dissipates until the trigger level is reached again. Example: PW-S-HLb-NEint-6, brown curve on **Figure 4-31**.
2. Filters which do not show the "saw tooth" behaviour of the first type but which measure a pressure higher than the hydration pressure. Example: PW-S-HLb-SEext-5, purple curve on **Figure 4-31**.
3. Filters which do not show the "saw tooth" behaviour and are at a pressure lower than the hydration pressure. Example: PW-S-HLb-NWint-1, green curve on **Figure 4-31**.

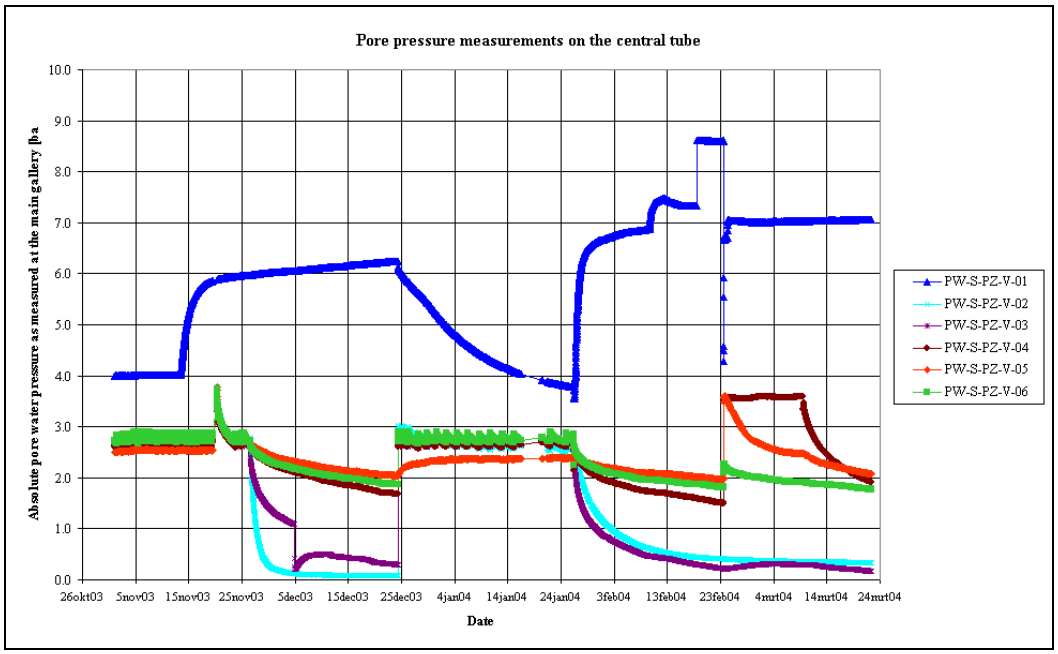

Figure 4-30: Pore pressure measurements at the central tube (October 2003 – March 2004).

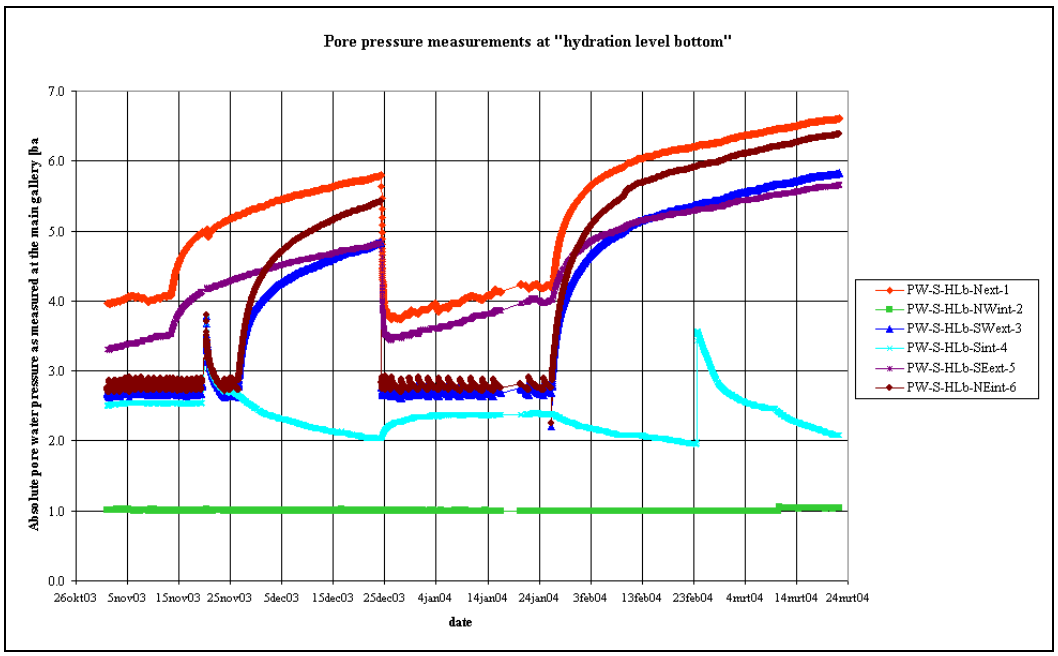

Figure 4-31: Pore pressure measurements at "hydration level bottom" (October 2003 – March 2004). Note that due to an error in the sensor cabling, the measurements labelled as HLb-Sint-4 are in reality the readings of sensor PZ-V-05 (cf. Figure 4-30).

Several manipulations were performed to better understand the behaviour of the different types of filters. Possible causes of these problems are:

- The filters and/or tubes are clogged by fine bentonite particles. The mean pore size of the filters is 5 µm. Experience tells that this is a good value for piezometers in Boom Clay. Less experience is available in bentonites and a smaller pore size could give better results.
- During the installation of the experiment some of the twin tubes were interchanged, an experimentally detected example is the following. At the end of the experiment it was

determined that sensors PW-S-HLb-Sint-4 and PW-S-PZ-V-05 (cf. **Figure 4-30** and **Figure 4-31**) were in fact connected to the two twin tubes of the same filter (V05 on the central hydration tube). In return, the two twin tubes of filter Sint-4 in the bottom hydration level were both connected to the hydration system. The possibility exists that other errors remain undetected and that some sensor results do not correspond to the intended location. However, the twin tubes of the majority of the filter screens inside the seal are connected correctly. Moreover, the filter screens in the host rock all seem to be connected correctly. **Table 4-9** gives an overview of the status of 18 hydration filters inside the seal during the experiment.

Table 4-9: Connection/performance of hydration filters.

Filter	OK !	OK ?	NOT OK
PW-S-PZ-V01		**X**	
PW-S-PZ-V02	**X**		
PW-S-PZ-V03	**X**		
PW-S-PZ-V04	**X**		
PW-S-PZ-V05			**X**
PW-S-PZ-V06	**X**		
PW-S-Hlb-N		**X**	
PW-S-Hlb-NW		**X**	
PW-S-Hlb-SW	**X**		
PW-S-Hlb-S		**X**	**X**
PW-S-Hlb-SE		**X**	
PW-S-Hlb-NE	**X**		
PW-S-Hlm-N	**X**		
PW-S-Hlm-NW		**X**	
PW-S-Hlm-SW	**X**		
PW-S-Hlm-S	**X**		
PW-S-Hlm-SE	**X**		
PW-S-Hlm-NE	**X**		

As a result of the limitations in the performance of the hydration system, the artificial hydration did not occur as homogeneously as planned. This could explain inhomogeneous behaviour observed throughout the seal. It also shows that great care is needed when installing and interpreting complex experiments.

During the performance of hydraulic conductivity testing at the bottom hydration level, another observation was made that needs to be taken into account when interpreting the seal behaviour. During these tests in November 2005 – January 2006, water was injected at several filters at ~14 bar; the "in-situ" pressure at the bottom hydration level was ~9.5 bar at that time. The test on filter PW-S-Hlb-SW was performed without any problems; during this test water flowed out of the filter at a rate of about 20 ml/day. After some initial problems, the test on filter PW-S-Hlb-N also yielded similar flow rates. However, when filter PW-S-Hlb-NE was connected to the system and was put at 14 bar, about 450 ml was injected during 2 minutes. This probably indicates a leak towards the grout below the seal and/or the central tube. A fracture in the resin layer between the seal and the grout below is indeed possible. As a consequence, it is well possible that some of the 1950 l of water artificially injected for the hydration of the seal did instead flow outside the seal. On the other hand, water from outside the seal could have entered the seal through similar leaks in the resin layer.

4.3.4 Conclusions on hydration

The seal saturation occurred both by natural and artificial hydration. About 1950 L was injected artificially. This corresponds to ~55% of the calculated volume needed to saturate the entire seal. This percentage should be interpreted as a maximum: it is possible that some leaks are present at the bottom (and top) of the seal, making it possible that some of the injected water did not take part in the hydration.

We can conclude that artificial hydration speeds up the hydration process and that higher injection pressures lead to faster hydration. However, it remains very difficult to achieve the last percentages of full saturation (it takes longer to increase from 90 to 100 % RH than to increase from initial conditions to 70-80 % RH). Consequently, artificial hydration parameters only have a minor influence on the total time needed for full saturation.

4.4 Hydro-Mechanical measurements

Appendix A4 contains the plots of all hydromechanical measurements performed within the shaft seal experiment.

4.4.1 Seal: total stress

The vibrating wire total stress sensors seem to give the most reliable measurements. **Figure 4-32** and **Figure 4-33** show the evolution of total stresses at the seal/host rock interface, respectively at the bottom and top instrumented level. Total stresses are systematically higher at the bottom level than at the top level. Within each level, the measured values are close to each other. The values on 18th April 2007 are between 10.7 and 11.1 bar (relative) at the bottom level and between 7.1 and 8.1 bar (relative) at the top level. Effects playing a role in this observation could be the higher density in the lower part of the seal at the start of the experiment and/or the distance to the top of the seal and the concrete top plug (at zero total stress). Except perhaps in the first months, stress increase is more or less linear since the start of the experiment and the increase is still on-going.

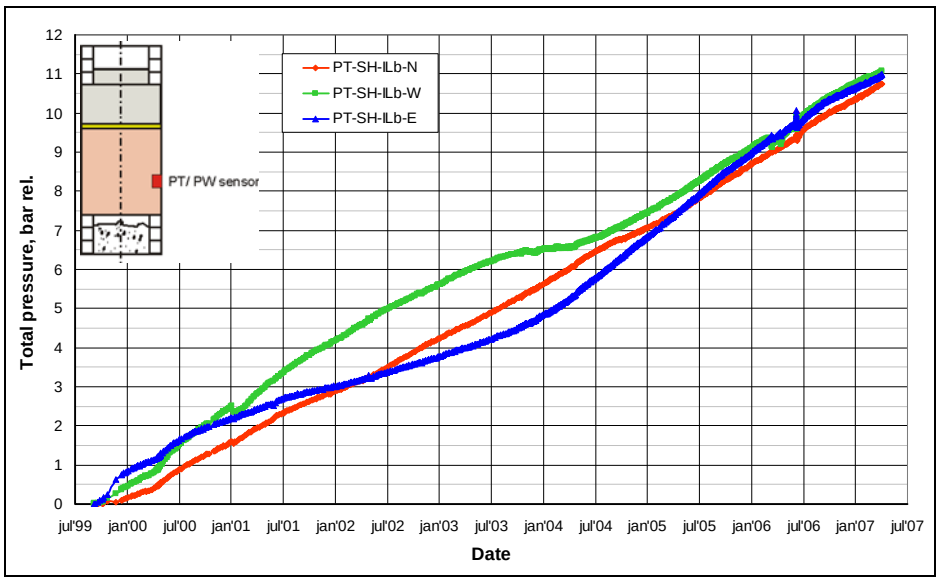

Figure 4-32: Total stress at the seal/host rock interface (at instrumentation level bottom).

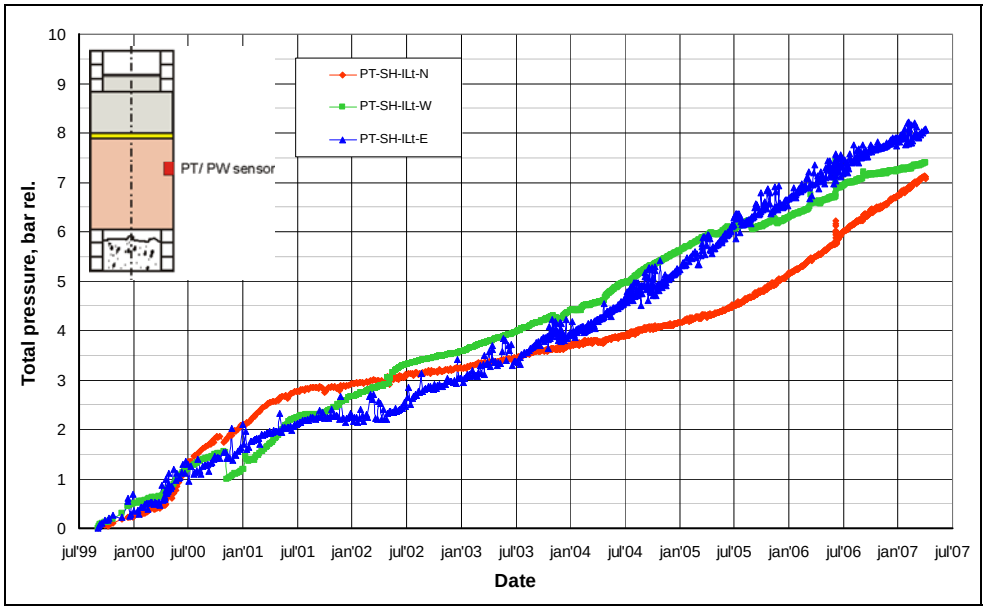

Figure 4-33: Total stress at the seal/host rock interface (at instrumentation level top).

The vibrating wire total stress sensors inside the seal give similar results. At the top of the seal (just below the sand layer) stresses between 6.1 and 7.3 bar (relative) are measured on 18th April 2007. At the bottom of the seal (on top of the resin layer) stresses between 9.3 and 13.6 bar (relative) are measured[3]. **Figure 4-34** shows the results of the sensors just below the sand layer.

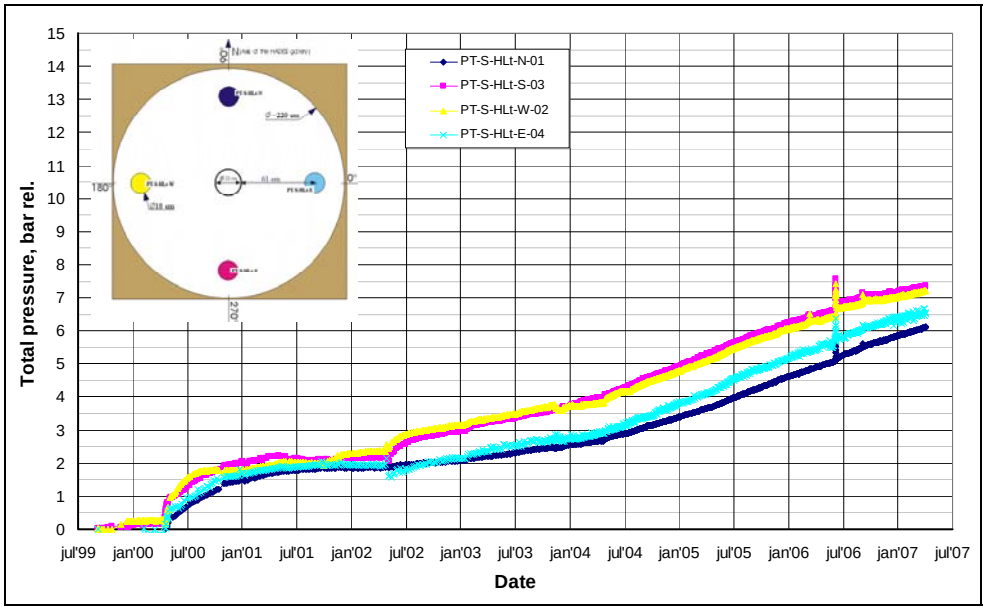

Figure 4-34: Total stress at the top of the seal (at hydration level top).

The total stress measurements sensors on the rods of the two instrumented levels show a less gradual evolution. They show several sudden increases or decreases and trend changes. Whilst the vibrating wire sensors give an integrated result for a certain part in the seal (due to their

[3] One particular sensor at this level measures a value of 6.1 bar (relative) but is most probably defective since November 2005.

relatively big dimensions), the KULITE cells in the instrumented levels seem to be more influenced by local effects. There is a bigger dispersion on the results of these sensors. An influence of the orientation of the sensor is noticeable, in particular at the lower instrumented level where circumferential stresses are systematically higher than vertical stresses. The opposite seems to be true at the top instrumented level, although the phenomenon is less pronounced.

These observations are illustrated on **Figure 4-35** (results for the northern rod of the lower instrumented level) and **Figure 4-36** (results for the northern rod of the top instrumented level). Sensors 1 and 3 measure circumferential stresses, sensors 2 and 4 measure vertical stresses.

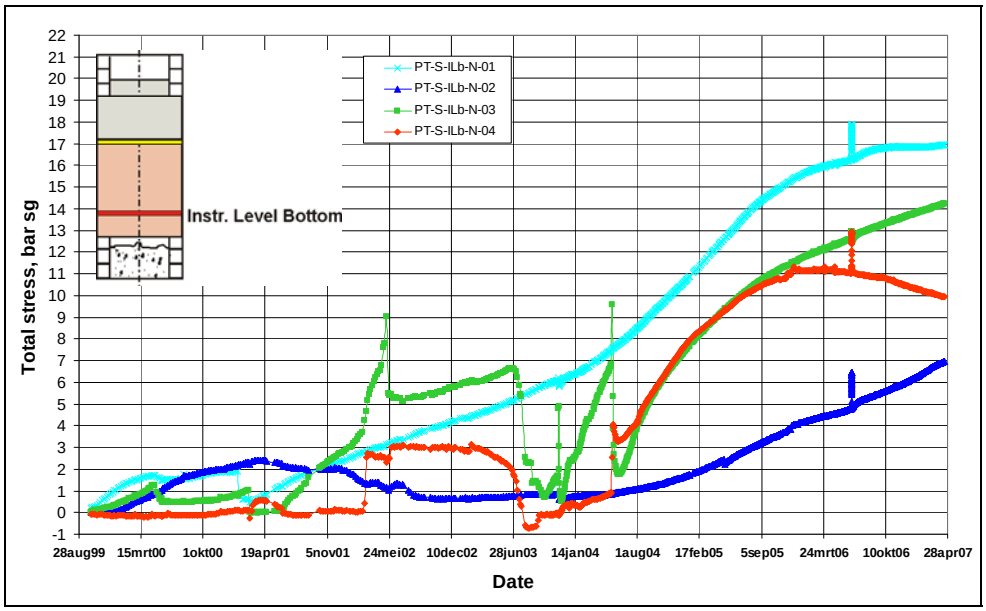

Figure 4-35: Total stress in the seal (at the northern rod of instrumented level bottom).

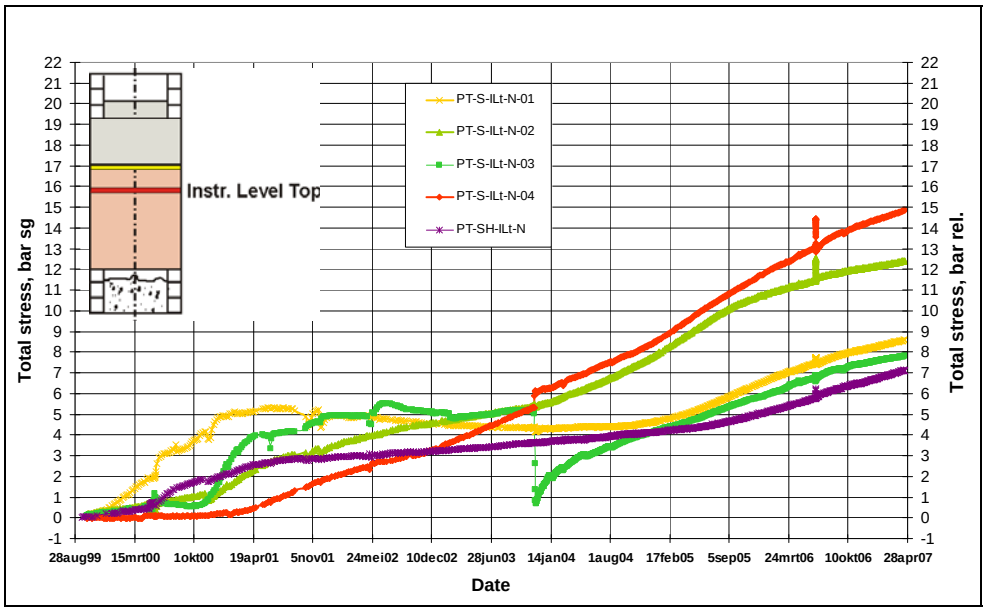

Figure 4-36: Total stress in the seal (at the northern rod of instrumented level top); one curve (purple) shows the total stress at PT-SH-ILt-N, at the seal/host rock interface near this rod.

4.4.2 Seal: pore pressure & effective stress

The vibrating wire pore pressure sensors at the seal/host rock interface measured no pore pressure at all during the first years of the experiment. However, between mid 2004 and mid 2005 they all started to increase. The increase is still ongoing. On 18th April 2007, the values were between 1.2 and 2.8 bar (sealed gauge) at the top instrumented level and between 4.0 and 5.2 bar (sealed gauge) at the lower instrumented level. **Figure 4-37** shows the results at the top instrumented level. When combining these results with the total stress results at the same locations, effective stress can be estimated. Since the rise of pore pressure, effective stresses remain more or less constant or even decrease a bit. Effective stresses appear to be somewhat lower at the bottom level than at the top level.

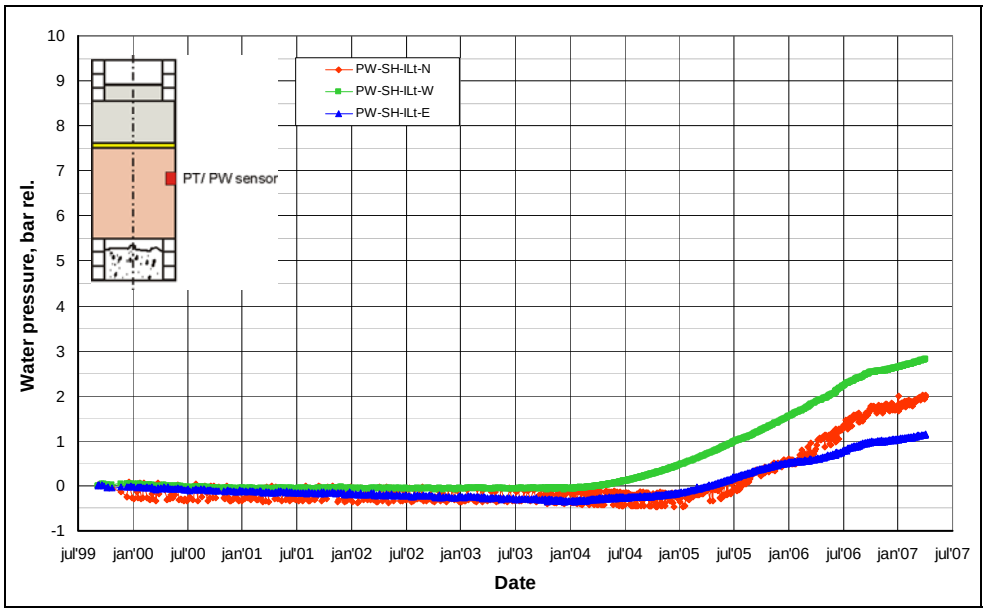

Figure 4-37: Pore pressure at the seal/host rock interface (at instrumentation level top).

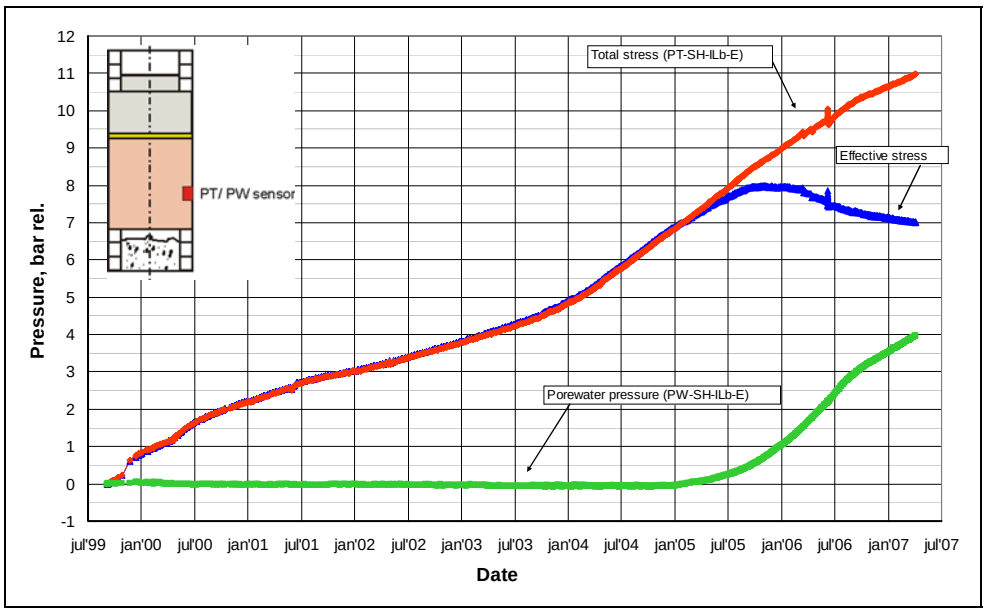

Figure 4-38: Total stress, pore pressure and effective stress at the seal/host rock interface (at the eastside of instrumented level bottom).

The evolution of pore pressure, total and effective stress near the interface is confirmed by measurements by other sensor types, i.e. the adapted KULITE sensors installed at the middle hydration level (**Figure 4-39**).

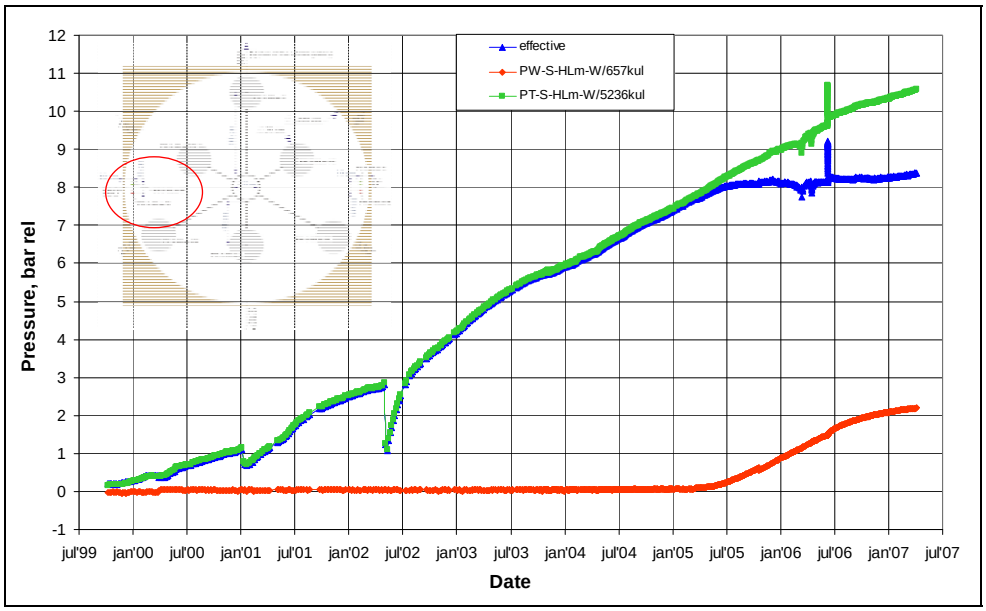

Figure 4-39: Total stress, pore pressure and effective stress near the seal/host rock interface (at the west side of hydration level middle).

The more chaotic evolution of total stress measurements at the instrumented rods is also present in the pore pressure measurements at those locations. This is illustrated in **Figure 4-40**. Some of the KULITE sensors measure pore pressures since several years, some of them only for specific periods of time, some only recently and some others not (yet). Again, the variety of the measurements is the result of the fact that these sensors give very local information. A remarkable observation is that all sensors at the top level are measuring (at least) some pore pressure at the start of 2007 and none of the sensors at the bottom level. Some sensors at the bottom level seem to start increasing at this moment (mid 2007).

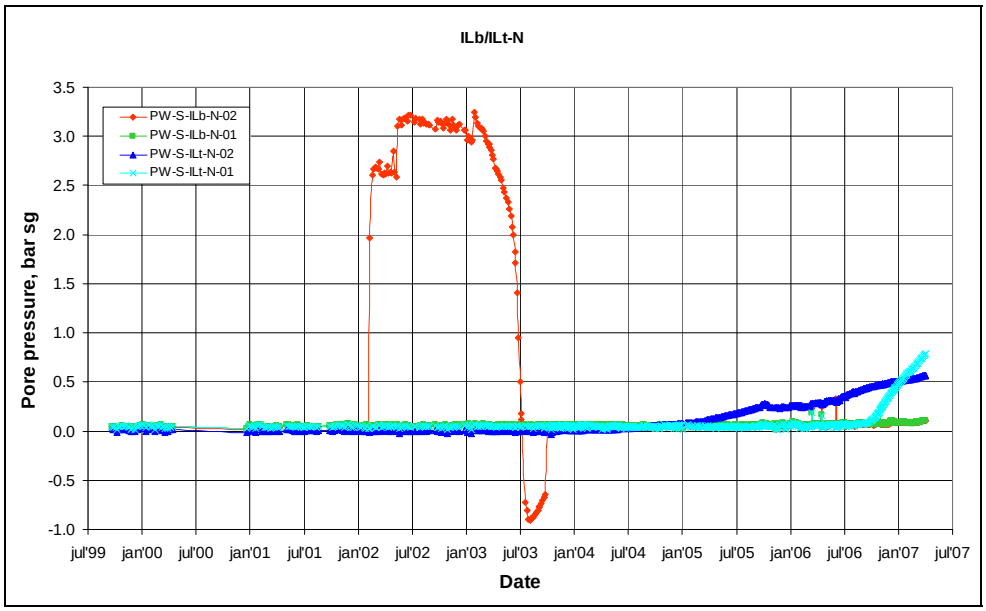

Figure 4-40: Pore pressure in the seal (at the northern rod of instrumented level bottom).

Finally, the filter screens used for the artificial hydration were also used to measure pore pressure whenever the artificial hydration was stopped. At the bottom hydration level 11 bar (absolute) was measured on 18th April 2007. Pore pressures at the other locations (middle hydration level and central tube) vary substantially but are generally speaking lower than 4 bar (absolute).

4.4.3 Seal: displacements

The displacements inside the seal are illustrated on **Figure 4-41**, showing the results at the top instrumented level:

- Near the centre of the seal (at about 1/3 between the shaft centre and the interface), a small inwards movement is observed in the first half year. This trend is than reversed and during the next ~2 years an outward movement was observed. At that moment the trend changed again and a (slower) inward movement was observed. At 18th April 2007 the sensor has almost returned to its initial position.
- Near the interface (at about 2/3 between the shaft centre and the interface), the initial behaviour is inversed: a small outward movement is observed in the first half year and this trend is than reversed. However, no further trend inversions occurred at this measuring point. At 18th April 2007 the sensor seems to have reached an equilibrium (or is slowly changing his trend) and is located some 3 cm inward in comparison to its initial position.

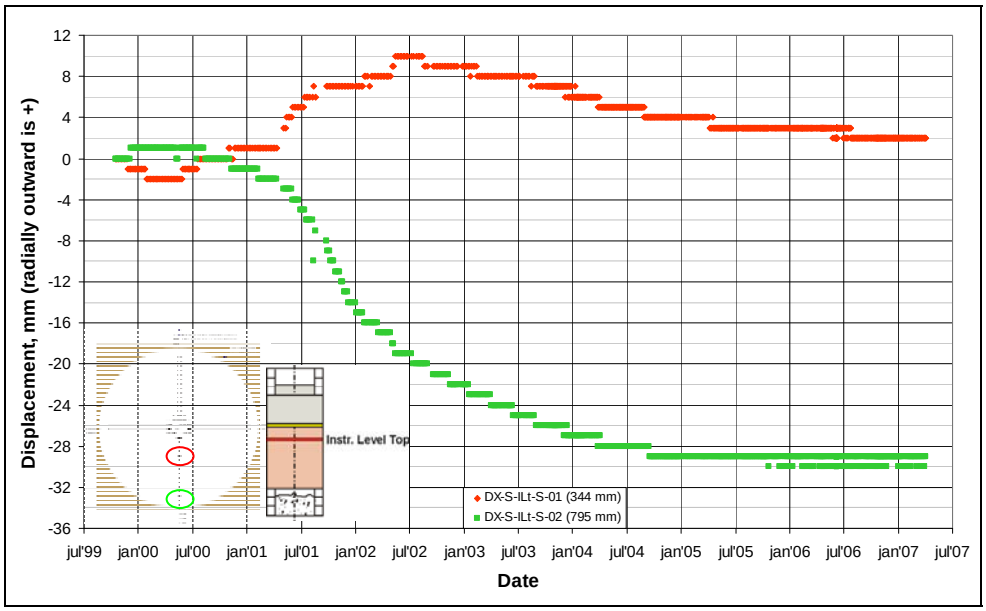

Figure 4-41: Displacements in the seal (at instrumented level top).

Displacements of the top of the seal are shown in **Figure 4-42**. The most representative measurement is the one with the top of the main gallery as a reference point (yellow curve). Indeed, the reference point of the red curve is pushed upward by the movement of the seal, resulting in an underestimation by a factor 3-4 of the seal movement.

The initial and current volumes of the bentonite seal can be calculated:

V_0: pi x 1.1^2 x 2.24 - 0.105 = 8.41 m^3

V_1: pi x $(1.1-0.03)^2$ x (2.24+0.012) - 0.105= 8.00 m^3

The measurements indicate that the seal volume has decreased with about 5%. This also means that the resulting dry density of the seal has increased ~5%, from 1.34 g/cm^3 up to 1.41 g/cm^3.

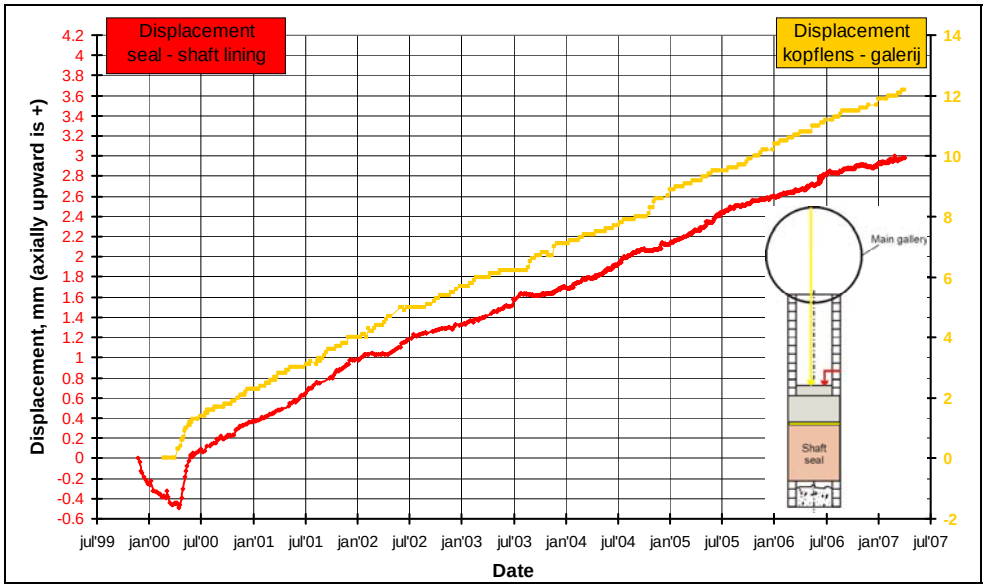

Figure 4-42: Displacements of the top of the seal. Two different reference points were used: inside the experimental shaft (red) and at the top of the main gallery (yellow).

4.4.4 Conclusions of seal measurements

For analysis of total/effective stress and pore pressure, the measurements of the vibrating wire sensors at the interface are the most appropriate. **Table 4-10** summarises the measurement values of these sensors on 18th April 2007. Effective stress ranges from 4.5 to 7 bar. Values are somewhat higher for the "east" sensors than for the other two orientations, mainly due to lower pore pressures at these locations[4]. This slight in-homogeneity is also visible in the pore pressures measurements in the host rock (cf. radial piezometers, section 4.4.6), as illustrated on **Figure 4-43**. It is difficult to define a cause for this asymmetry but it might well be caused by installation related issues and it can be temporary. Indeed, total stresses and pore pressures in the seal, the host rock and at the interface are still in transition and equilibrium is not yet reached.

The expected swelling pressure in the seal can be calculated based on the dry density, as expressed by Equation 5 in Chapter 2:

$$P_s = 0.0061\ \rho_d^{\ 13.272} \qquad \textbf{Equation 2-5}$$

An average dry density of 1.41 g/cm³ was determined above, resulting in a calculated swelling pressure of 5.8 bar. The measured values are somewhat higher but one should note that due to the nature of the formula (cf. exponential) small variations on the value of the dry density have a big impact on the result. Furthermore, calculation of the dry density copes with several uncertainties, e.g. exact excavation profile of the shaft seal.

On average, effective stress (and certainly total stress) measurements are higher in the bottom level than in the top level. This is in line with the higher initial dry density at the bottom part of the shaft seal. Furthermore, the distance to the top of the seal can also play a role (cf. atmospheric pressure).

Table 4-10: Measurements of the vibrating wire sensors at the interface on 18th April 2007. Total stress and pore pressure are measured, effective stress is calculated.

	Total stress [bar]	Pore pressure [bar]	Effective stress [bar]
ILtop EAST	8	1	7
ILtop WEST	7.5	3	4.5
ILtop NORTH	7	2	5
ILbottom EAST	11	4	7
ILbottom WEST	11	5	6
ILbottom NORTH	10.5	5	5.5

[4] One should note that contradictory to these observations, the so-called CEA-sensors in the middle hydration levels indicate higher pore pressures at the east-side than at the west-side of the seal. However, these sensors are located 10 cm inside the seal and not at the actual interface which might explain the difference in behaviour.

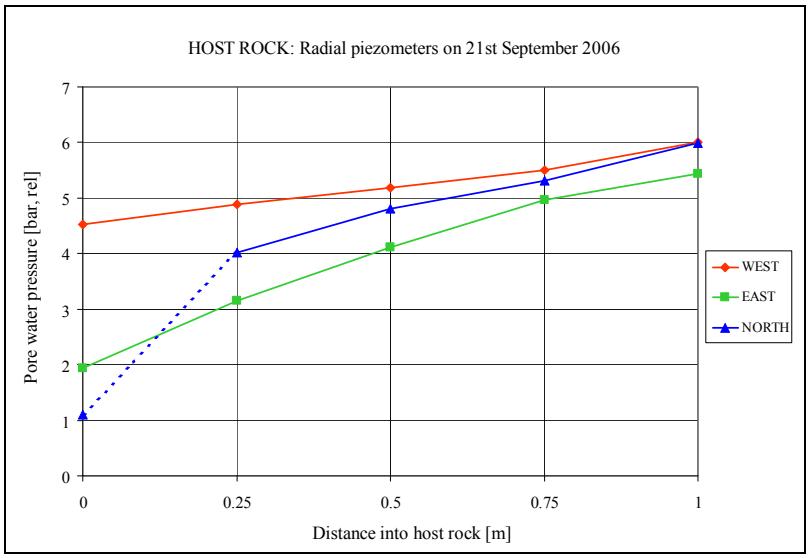

Figure 4-43: Pore pressure profiles measured by the radial piezometers in the host rock. The measurement filter at 0 m on piezometer "north" is less reliable. A slight asymmetry is visible.

Conclusions of the displacement measurements are combined with those of the displacement measurements in the host rock (see section 4.4.7).

4.4.5 Host rock: total stress

Total stress measurements in Boom Clay have always proven to be difficult. Also in the RESEAL experiment, the evolution of the measurements is chaotic and several sensors seem to have failed. Most sensors work fine before the installation of the seal but become defective afterwards. The best results were obtained by the sensors on the eastward radial piezometer (**Figure 4-44** and **Figure 4-45**).

During the first months total stress increases and a sort of equilibrium is reached. Generally speaking, higher stresses are measured as the distance to the shaft increases. A sharp drop is observed when the shaft lining is removed. Some time after installation of the seal, stresses start to increase again. At this moment, the increase seems to be on-going although at a slower rate, the values in April 2007 are roughly between 8 and 13 bar (relative). Sudden jumps and trend changes are observed but an overall increasing trend is visible. Some of these artefacts are induced by experimental manipulations, mostly involving the porous filter screens on the piezometer, e.g.:

- Stress peak in August 1998 is caused by an imposed pressure increase on some of the filter screens of the piezometer.
- The drop of PT7 on the eastern piezometer in June 2005 followed the removal of gases at the adjacent filter screens.

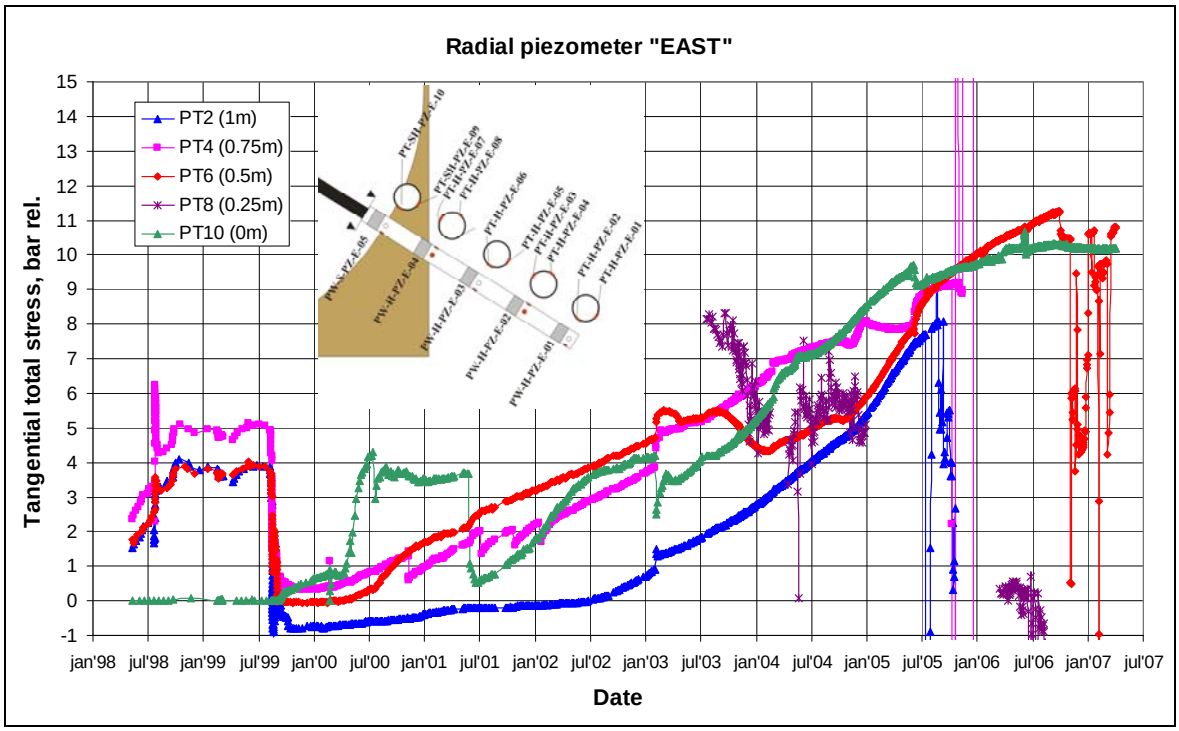

Figure 4-44: Tangential total stress in the host rock on the eastern radial piezometer.

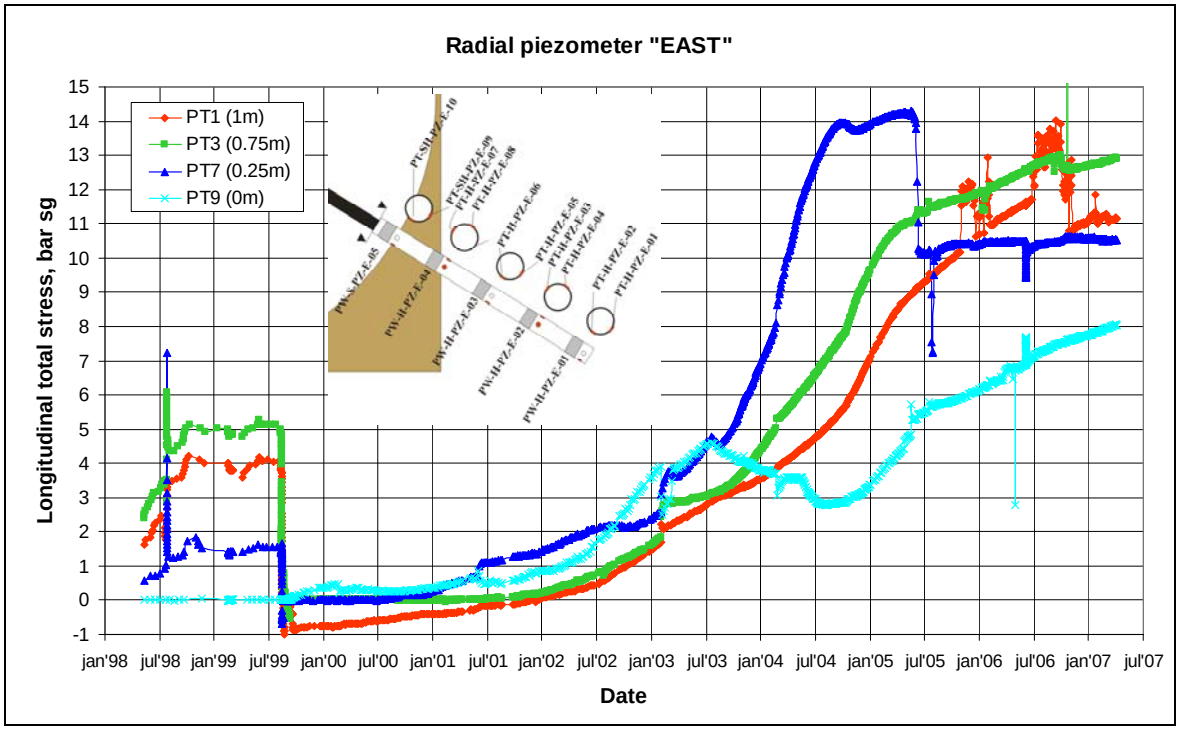

Figure 4-45: Longitudinal total stress in the host rock on the eastern radial piezometer.

4.4.6 Host rock: pore pressure & effective stress

Figure 4-46 shows the pore pressures measured by the western radial piezometer. Before the removal of the shaft lining, the behaviour is quite similar to that of total stress. Indeed, effective stress remains very limited during this period. Pore pressure increases with increasing distance to the shaft. Filter 5 is measuring atmospheric pressure in this period since it is not located inside

the clay but inside the future shaft seal. When the lining is removed, a sharp pore pressure drop is noticed, even down into suction, **Figure 4-47** shows this phenomenon in detail for the northern radial piezometer. During several days, the sensors measure -1 bar (relative) but almost certainly the actual suction is even stronger; -1 bar is the low range of the sensors. After several days/weeks, a sharp increase is observed indicating that a connection is established between the filter screen and the atmosphere. In other words, fractures have been developed due to the decompression of the host rock around the shaft where the lining has been removed.

During the following few years, the sensors seem to remain in contact with the atmosphere. In the course of 2002, most of them start to increase again. The sharp increase in February 2003 is caused by a flushing of the piezometer tubes to remove all gases. At this moment, the graphs also show a jump of 1.45 bar. This is in fact an artefact: because the pore pressure sensors are located in the main gallery (about 14.5 m above the actual filters), the pressure of the water column in the tubes (1.45 bar) should be added. Of course, when the tubes are empty (connected to the atmosphere) the water column should not be added. When the lining was removed (and the filters went into suction), the water column was no longer added. This was started again mid-February 2003; note that this moment is chosen somewhat arbitrary, once most filters were showing a pressure increase.

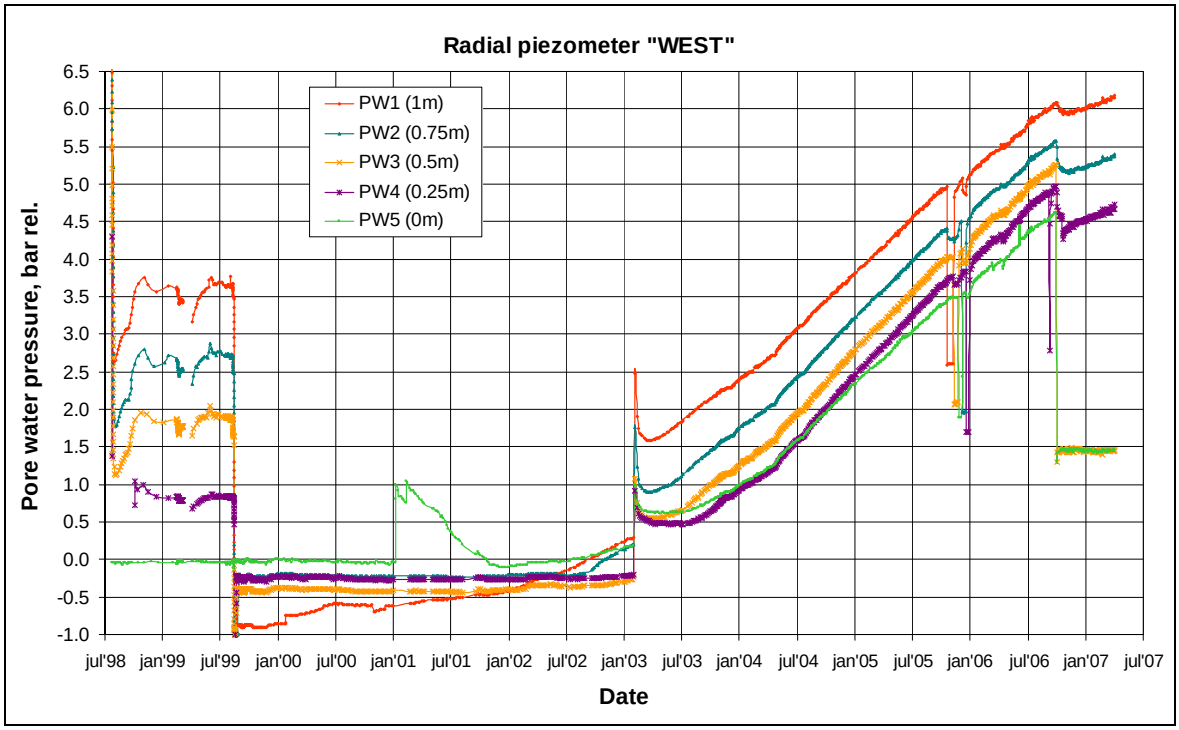

Figure 4-46: Pore pressure in the host rock at the western radial piezometer.

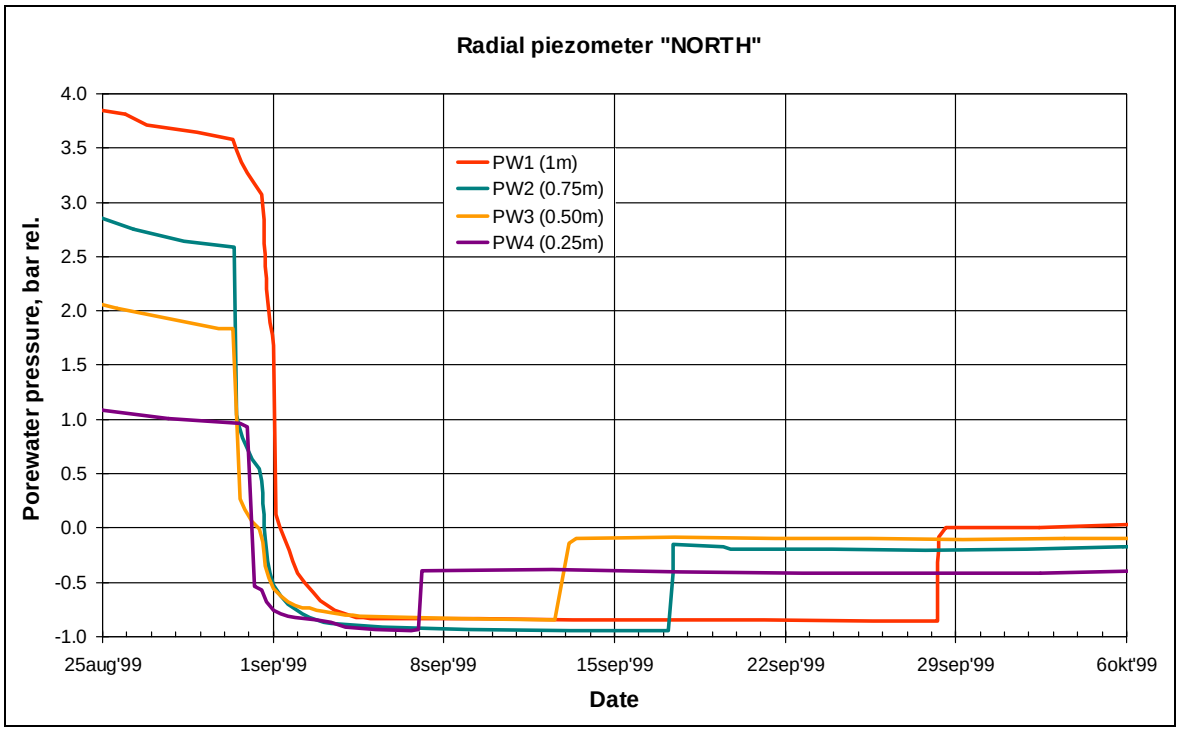

Figure 4-47: Detail of the pore pressure reaction at the northern radial piezometer on the removal of the shaft lining.

Figure 4-48 shows the results of the vertical piezometer that was installed at about 1 m distance from the shaft seal. The three deepest filters, situated below the level of the seal, measure the highest pore pressures. The filters above (PW-V8) and at the level of the top and bottom of the seal (respectively PW-V7 and PW-V4) measure the lowest pressures. When the shaft lining is removed, filters 4 through 7 show the same behaviour as the filters of the radial piezometers.

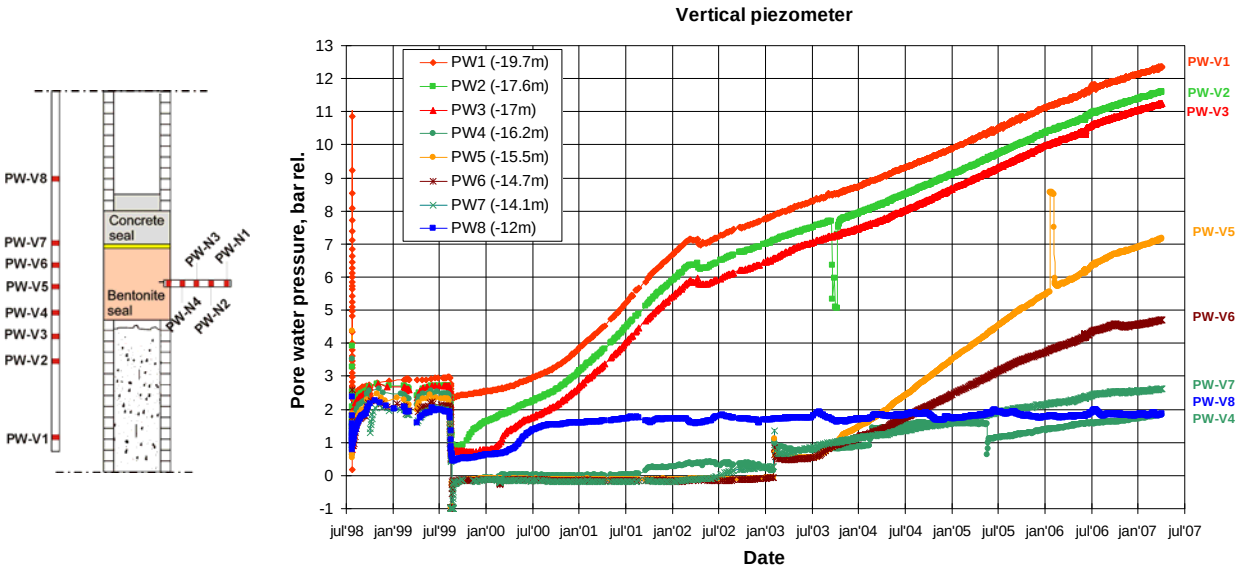

Figure 4-48: Pore pressure in the host rock at the vertical piezometer: filter locations (left) and measurements (right).

4.4.7 Host rock: displacements

The displacement sensors were installed about 16 months before the removal of the shaft lining. **Table 4-11** shows the displacements after installation and at the moment the lining is removed. The sensors closest to the seal (inside the northwards drilling) measure an inward convergence of the host rock of some 5-15 mm during the first 0.5 year. The other sensors remain more or less stable up until the lining is removed. Again the sensors closest to the seal show the biggest inward movement (2-5 mm).

Table 4-11: Displacements inside the host rock.

Sensor	Distance to the seal	Inward movement after installation	Inward movement after removal of the lining
DX-H-N01	104 mm	~13 mm	~5 mm
DX-H-N02	142 mm	~7 mm	~2 mm
DX-H-E01	350 mm	/	~1 mm
DX-H-E02	511 mm	/	~1 mm
DX-H-W01	547.5 mm	/	/
DX-H-W02	749 mm	/	/

After the initial inward movement, the shaft seal pushes outward during the first 6-12 months after the installation of the seal. Afterwards, the tendency of the host rock to move inwards becomes more important than the tendency of the seal to swell outward. This phase lasts about 4 years. Finally, the trend inverses again: the tendency of the seal to swell outward becomes more important than the tendency of the host rock to move inwards. During this last phase, only information of the eastward borehole is available (sensors at 350 and 511 mm inside the host rock). The observations are comparable with the displacements inside the seal near the interface (cf. **Figure 4-41**), however the last phase of inward movement is not present at the interface.

Figure 4-49 shows the radial displacements 350 and 511 mm inside the host rock.

An important remark about the displacement measurements inside the host rock concerns the reference point of these measurements. After installation of the sensors in the host rock, the rods were fixed to the shaft lining, providing a fixed reference point. After the lining was removed, each of the rods was fixed to the corresponding radial piezometer above. However, it can not be excluded that these piezometers undergo (small) radial displacements. As a consequence, the reference point of the displacement measurements in the host rock is no longer fixed.

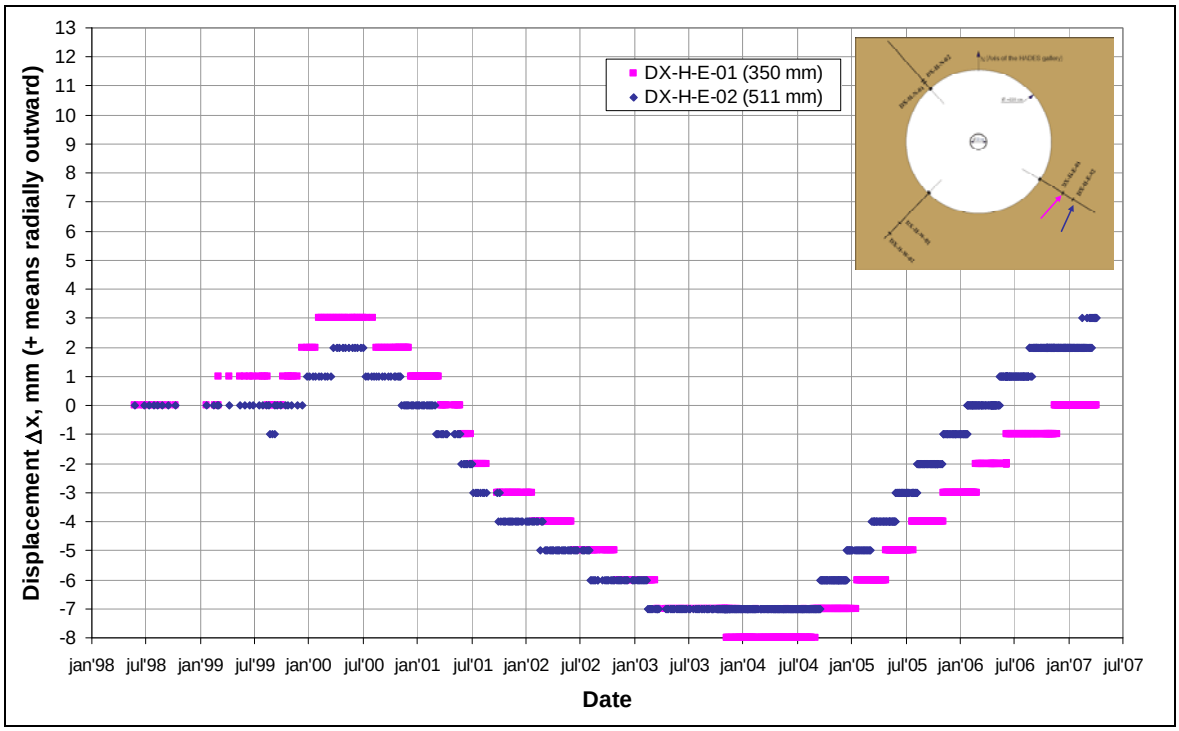

Figure 4-49: Displacements in the host rock at the eastside of the seal (at hydration level middle).

4.4.8 Conclusions of host rock measurements

Measurement of total stresses in the host rock proved to be more complicated than in the seal itself. This is in line with previous experience at the HADES URF. The sensors seem to be very sensitive for local and/or temporary phenomena. Furthermore, installation-related issues play an important role. Consequently, the measured total and effective stresses in the host rock should be interpreted rather qualitatively than quantitatively.

The removal of the concrete lining of the shaft has a strong effect on the EDZ. Fractures were formed around the shaft, causing many blocks to fall from the shaft wall during installation of the seal. It is impossible to distinguish between re-activation of existing fractures (caused during excavation) and newly developed fractures caused by removal of the lining. The fractures in connection with atmospheric pressure occur up to at least 1 m into the host rock, but are limited (in height) to a cylindrical zone around the part of the shaft where the lining was removed.

A slight asymmetry is observed in the measurements of the radial piezometers, this was discussed in section 4.4.4 (cf. **Figure 4-43**).

The observed trends and trend changes of the displacement measurements can be related to certain events. This is illustrated in **Figure 4-50**.

- Several observations can be linked to the start of artificial hydration (on 3rd May 2000):
  - The top of the seal starts to move upwards (**Figure 4-42**: sudden positive increase, which occurs in May 2000).
  - The sensors in the host rock start to move inward; a major suction of pore water from the host rock towards the seal exists in this period.
  - Also those sensors in the seal close to the interface start to move inward.

    - The sensors close to the centre of the shaft seal start to move outward; the artificial hydration causes a fast swelling in the central part of the seal.
- The displacement observed close to the centre of the seal changes from outward to inward around July 2002; this means that the central part of the seal equilibrates with the rest of the seal and the host rock. This is also the moment at which the first two VAISALA sensors and the ROTRONIC sensor representative for the bentonite powder indicate full (local) saturation of the seal.
- In the time period 2002-2004 (roughly) the radial piezometers in the host rock indicate a re-pressurization of the EDZ. At this time, the movement in the host rock inverts: the sensors now move outward. One should note that the sensors in the seal do not show the same behaviour at that moment. However, one should keep in mind that the measurement inside the seal, closest to the interface with the host rock is still located at least 30 cm from that interface (it might be even more because of the irregularities of the shaft wall). Consequently, quite a large volume (almost 50% of the total seal volume) of bentonite between this measuring point and the host rock is still present and this can cause the, at first sight, contradictory movement of seal and host rock in this period. On the other hand, displacements in the seal seem to slow down or even come to a stop after this period; this corresponds to the moment that pore pressures inside the seal start to increase (before, no pore pressure was measured).

Displacements are still ongoing although at a reduced rate, indicating that the interaction between the bentonite and the host rock is not at full equilibrium.

For the interpretation of the displacement measurements, it is important to keep in mind that the reference point of the host rock displacement sensors was not 100% fixed. Contrary to this, the reference point for the sensors inside the seal were fixed, hence the most reliable estimation of the absolute value of the displacements must be based on the seal sensors.

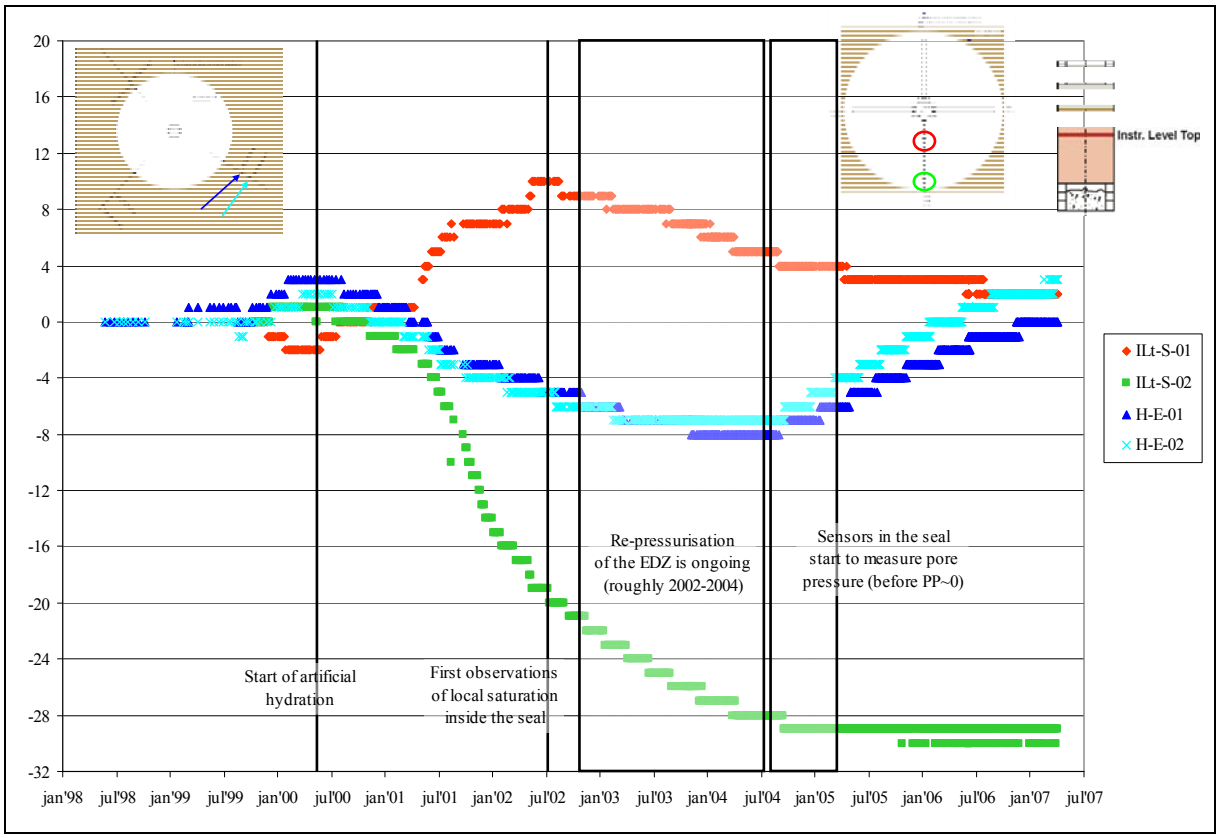

Figure 4-50: Illustration of the subsequent stages of the displacement measurements, relations with events and other observations in the seal and the host rock are illustrated schematically.

4.5 Testing the seal performance

4.5.1 Hydraulic conductivity

During the course of the seal experiment, hydraulic conductivity was measured inside the seal as well as in the surrounding host rock. Constant head tests in steady-state flow regime were carried out. Hydraulic conductivity is calculated as follows:

$$k = \frac{Q}{F \cdot \Delta h}$$ **Equation 4-1**

where **Q** is the steady state flow rate [m³/s], **Δh** is the applied pressure difference [m] and **F** is a factor depending on the filter geometry [-]. Appendix A4 describes the experimental procedure and its theoretical background.

Table 4-12 gives the results of the tests.

Table 4-12: Hydraulic conductivities measured in and around the RESEAL experiment. A positive head corresponds to an injection test; a negative head corresponds to an extraction test. Tests during which experimental problems occurred are highlighted in grey.

Filter location	Filter ID	Date	Head [m]	k [10^{-12} m/s]
SEAL - Vertical piezo	*V01*	*2-2004*	*5.0*	*11.2*
SEAL - Vertical piezo	*V01*	*2-2004*	*16.0*	*2.1*
SEAL - Vertical piezo	*V04*	*3-2004*	*23.5*	*13.5*
SEAL - HLM	Sint-4	3-2004	15.8	3.5
SEAL – HLM	Sint-4	4-2004	23.6	2.2
SEAL – HLM	SWext-3	4-2004	23.7	1.7
SEAL- HLB	*Next-1*	*11-2005*	*-43.5*	*0.4*
SEAL- HLB	*Next-1*	*11-2005*	*45.0*	*6.5*
SEAL- HLB	*Next-1*	*12-2005*	*45.0*	*24.0*
SEAL - HLB	SWext-3	12-2005	43.4	5.6
SEAL – HLM	SWext-3	1-2006	28.1	1.1
SEAL – HLM	Sint-4	1-2006	46.2	8.1
SEAL – HLM	SWext-3	5-2006	31.2	1.1
Host Rock (1m)	Radial west-1	11-2005	-23.8	3.1
Host Rock (0.5m)	Radial west-3	12-2005	-19.6	3.1
Interface (0m)	Radial west-5	12-2005	-16.3	2.7
Host Rock (0.75m)	Radial west-2	12-2005	-25.9	3.3
Host Rock (0.25m)	Radial west-4	1-2006	-21.6	3.2
Host Rock (0.5m)	Radial north-3	1-2006	-18.0	3.0
Host Rock (0.75m)	Radial east-2	2-2006	-21.9	2.8
Host Rock (1m)	Vertical-5	2-2006	29.8	5.4

Hydraulic conductivities between 2.5 and 3.5 10^{-12} m/s were measured in the radial piezometers in the host rock. These values are consistent with literature values (e.g. Bastiaens *et al.,* 2006). On one particular piezometer (radial West), all filters were tested. To check these measurements, some filters on the other two radial piezometers were tested as well. Within the first meter from the seal, no significant influence of the distance is observed (**Figure 4-51**). The value determined on the vertical piezometer, at 1 m from the seal, is higher because of the different orientation of the filter. On the radial piezometer the axis of the cylindrical filters is parallel to the bedding. Therefore the results are a combination of the horizontal and vertical hydraulic conductivity. On the vertical piezometer the result is mainly influenced by the horizontal conductivity. Since $k_H \sim 2.k_V$, the obtained results are plausible.

Prior to the installation of the seal, hydraulic conductivity tests have been carried out on clay cores recovered during drilling of the boreholes for the radial piezometers. **Table 4-13** gives the hydraulic conductivity measured from clay cores around the shaft at about 15 m from the HADES gallery. The conductivity was measured along the axis of the cores, meaning parallel to the bedding (cf. k_H). The results are in line with the in-situ measurements described in the previous paragraph and are within the range of hydraulic conductivity measured in-situ or on samples from other locations. Hydraulic conductivity seems to be homogeneous around the shaft.

Table 4-13: Hydraulic conductivity of the Boom clay measured on cores taken around the small shaft at about 15-m far from the HADES gallery (The direction N-S is the orientation of the main gallery)

Location and orientation around the shaft	k (m/s)
Near the shaft lining: - Orientation north - Orientation south east	 $4.50.10^{-12}$ $5.14.10^{-12}$
About 1 m far from the lining - Orientation north - Orientation south east	 $5.05.10^{-12}$ $5.07.10^{-12}$

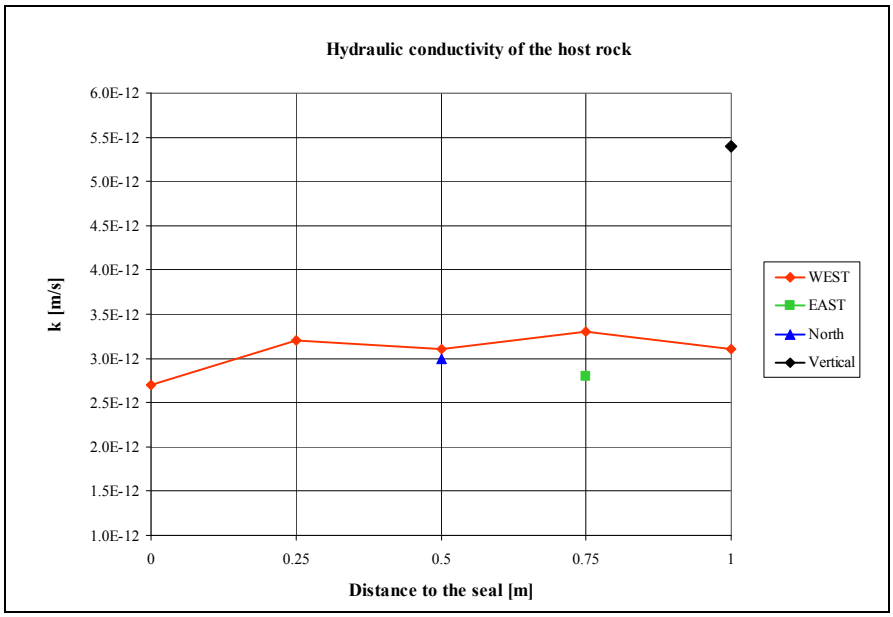

Figure 4-51: Hydraulic conductivity of the host rock and at the interface.

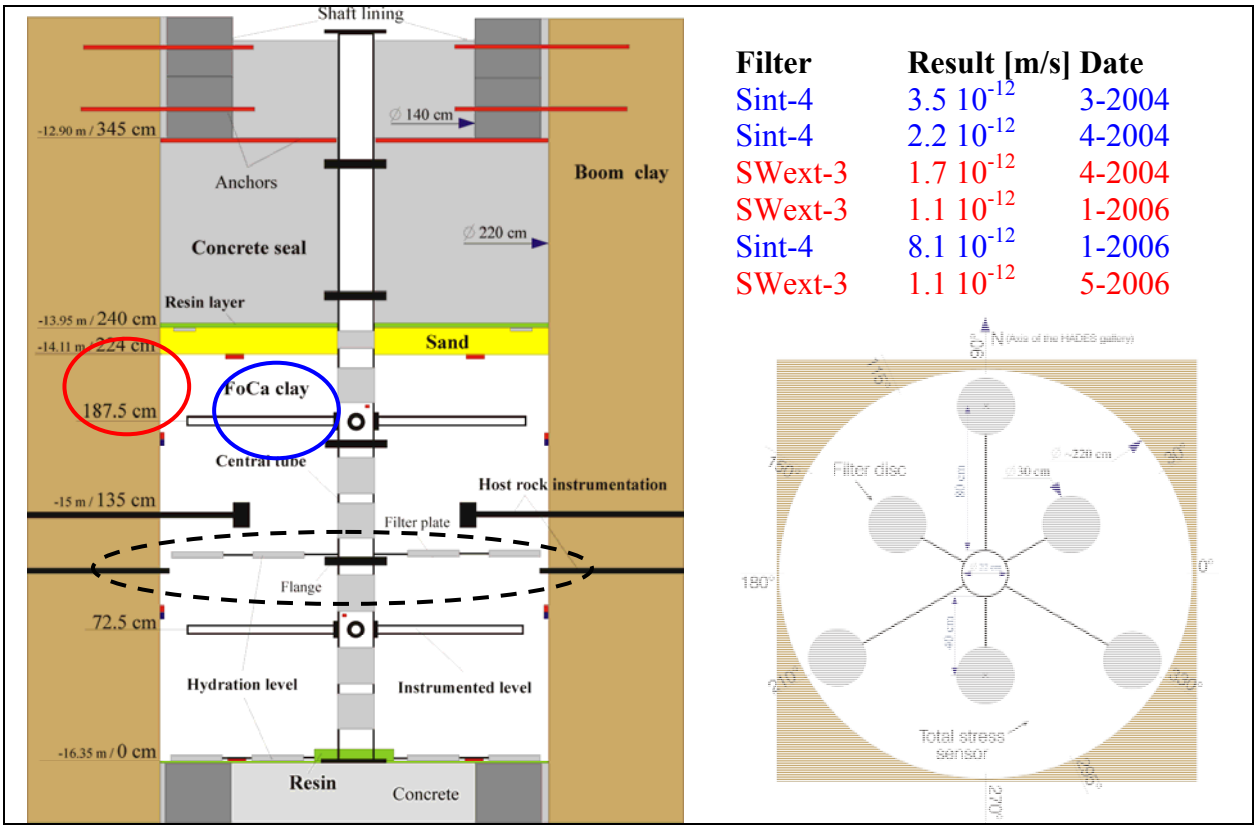

Filter	Result [m/s]	Date
Sint-4	$3.5\ 10^{-12}$	3-2004
Sint-4	$2.2\ 10^{-12}$	4-2004
SWext-3	$1.7\ 10^{-12}$	4-2004
SWext-3	$1.1\ 10^{-12}$	1-2006
Sint-4	$8.1\ 10^{-12}$	1-2006
SWext-3	$1.1\ 10^{-12}$	5-2006

Figure 4-52: Hydraulic conductivities in the seal measured at the middle hydration level.

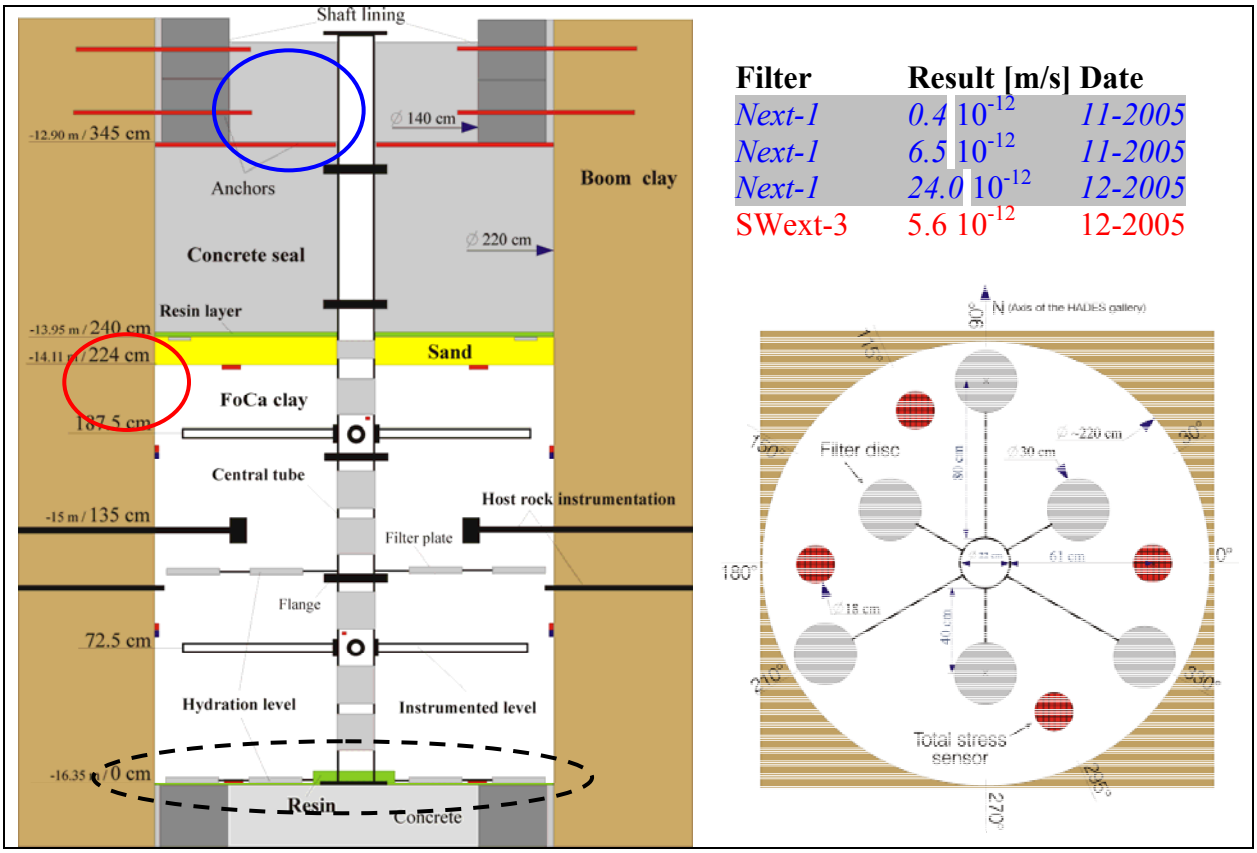

Filter	Result [m/s]	Date
Next-1	*0.4* 10^{-12}	*11-2005*
Next-1	*6.5* 10^{-12}	*11-2005*
Next-1	*24.0* 10^{-12}	*12-2005*
SWext-3	$5.6\ 10^{-12}$	12-2005

Figure 4-53: Hydraulic conductivities in the seal measured at the bottom hydration level.

	Filter	Result [m/s]	Date

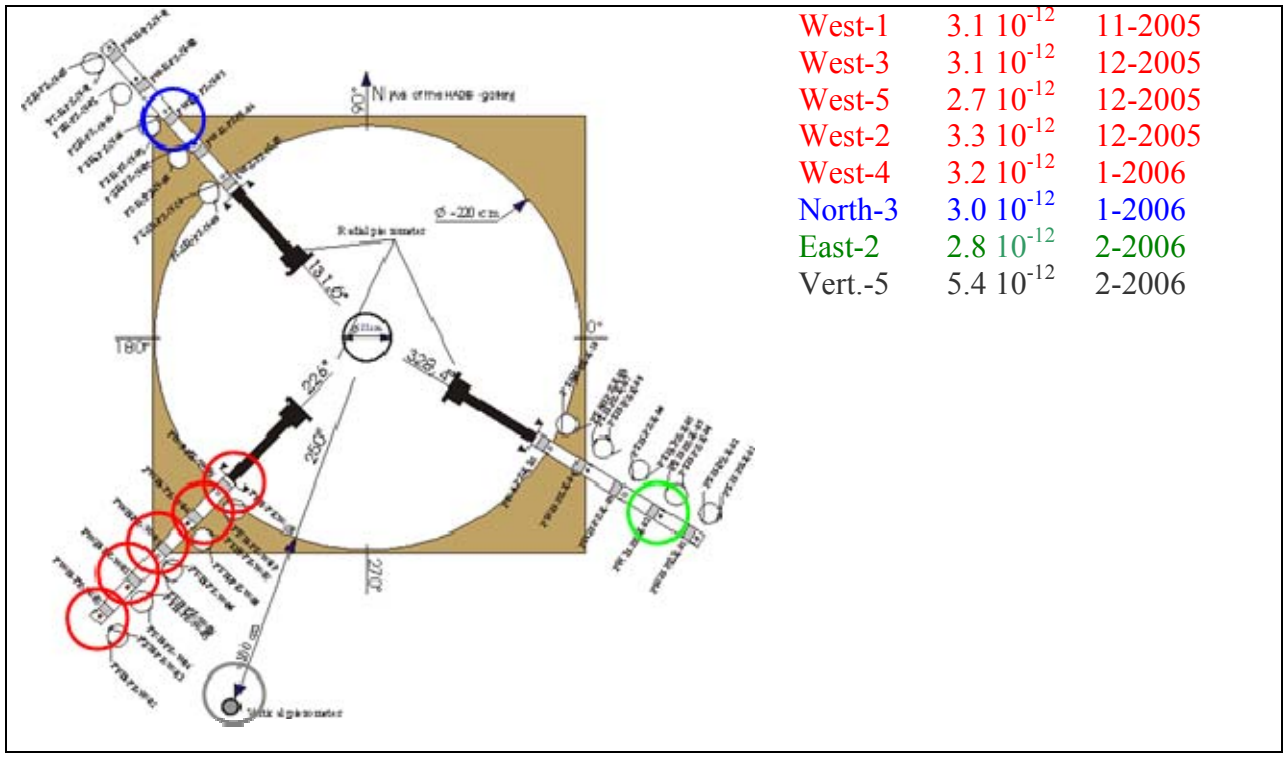

Figure 4-54: Hydraulic conductivities in the host rock measured at the radial and vertical piezometer.

During hydraulic conductivity tests on some of the filters inside the seal experimental problems were encountered, e.g. on filters V01 and V04 of the central tube of the seal and filter "Next" in the bottom hydration level. Possible causes of these problems are:

- The filters and/or tubes are clogged by fine bentonite particles. The mean pore size of the filters is 5 µm. Experience tells that this value is perfect for piezometers in Boom Clay. Less experience is available in bentonites and a smaller pore size could give better results.
- Filter spacing on the central tube is sometimes small, down to 5 cm. During some of the conductivity tests, a strong reaction of neighbouring filters was observed. This could indicate a hydraulic shortcut along the piezometer tube and would lead to erroneous test results.
- It is possible that cracks are present in the resin layer at the bottom of the seal. This way, water injected through the filter can flow in the concrete plug below the seal instead of in the seal itself, again giving erroneous results.
- Some of the twin tubes were interchanged, some errors were detected experimentally during the experiment (see section 4.3.3, p.23-24). The possibility exists that other errors remain undetected and the injection is performed at other locations than intended.

However, most of the results obtained on filters in the hydration levels are reliable, only those on filter Next of the bottom hydration level are doubtful. All reliable results are in the order of 10^{-12} m/s. These values are higher than measured in the RESEAL borehole sealing test (5.5 10^{-13} m/s). One of the possible causes is the real dry density of the bentonite. In the borehole sealing test, precompacted blocks were used and the set-up allowed a good control of the initial dry density (1.51 g/cm³ was calculated). In the case of the shaft seal experiment it was more difficult to control the real dry density:

- The shaft sidewalls were irregular due to fall-outs of clay blocks.
- It was not possible to compact the entire seal due to the presence of instruments.

- Some vertical uplift of the seal was observed, indicating an increase of total seal volume and thus a reduction of actual dry density.

According to the laboratory experiments, the measured values of hydraulic conductivity (~10^{-12} m/s) correspond to a dry density between 1.0 and 1.3 g/cm³; according to equation 1 (Chapter 2) this corresponds to a swelling pressure between 0.2 and 2 bar. Compared to the observed measurements and the calculations based on the seal volume (resulting in a dry density of 1.41 g/cm³), these values are low. However, a lot of scatter is present in the experimental results used to determine the correlation between hydraulic conductivity and dry density so only the order of magnitude can be determined. Moreover, the previously determined dry density of 1.41 g/cm³ is still plausible.

4.5.2 Conclusions about hydraulic conductivity measurements

Hydraulic conductivity measurements of the host rock yield values in line with values reported in literature. This is true for laboratory measurements made on cores taken prior to the installation of the shaft seal as well as for the in-situ measurements made using the radial piezometers during the shaft seal experiment. The results reflect the known anisotropy of hydraulic conductivity on Boom Clay (k_H~2.k_V).

Hydraulic conductivities measured inside the seal are of the expected order of magnitude. One should be careful in deducing the dry density (and swelling pressure) from these results; an important amount of scatter on the experimental results used to determine these relations can induce significant errors.

4.5.3 Gas breakthrough experiment

The aim of this test was to induce a gas breakthrough close to or at the seal-host rock interface (or the adjacent EDZ). The most logical choice at first sight would have been to perform the gas injection at one of the "No. 5-filters" on the radial piezometers (filters just inside the seal). However, for these filters breakthrough could occur along the piezometer itself instead of along the seal/host rock interface (Volckaert *et al.,* 1995). Therefore, gas was injected at filter PW-S-HLm-SW, a disc shaped filter close to the seal/host rock interface (5-10 cm). The breakthrough experiment was performed using N_2.

The gas injection system designed and used in the framework of EC project MEGAS was adapted and reused (Volckaert *et al.,* 1995). The gas is injected in the filter by a pressurised mercury reservoir; **Figure 4-55** shows an overview of the setup. The system includes a pressure transducer to measure the injection pressure and a magnetic displacement transducer to measure the gas flow rate.

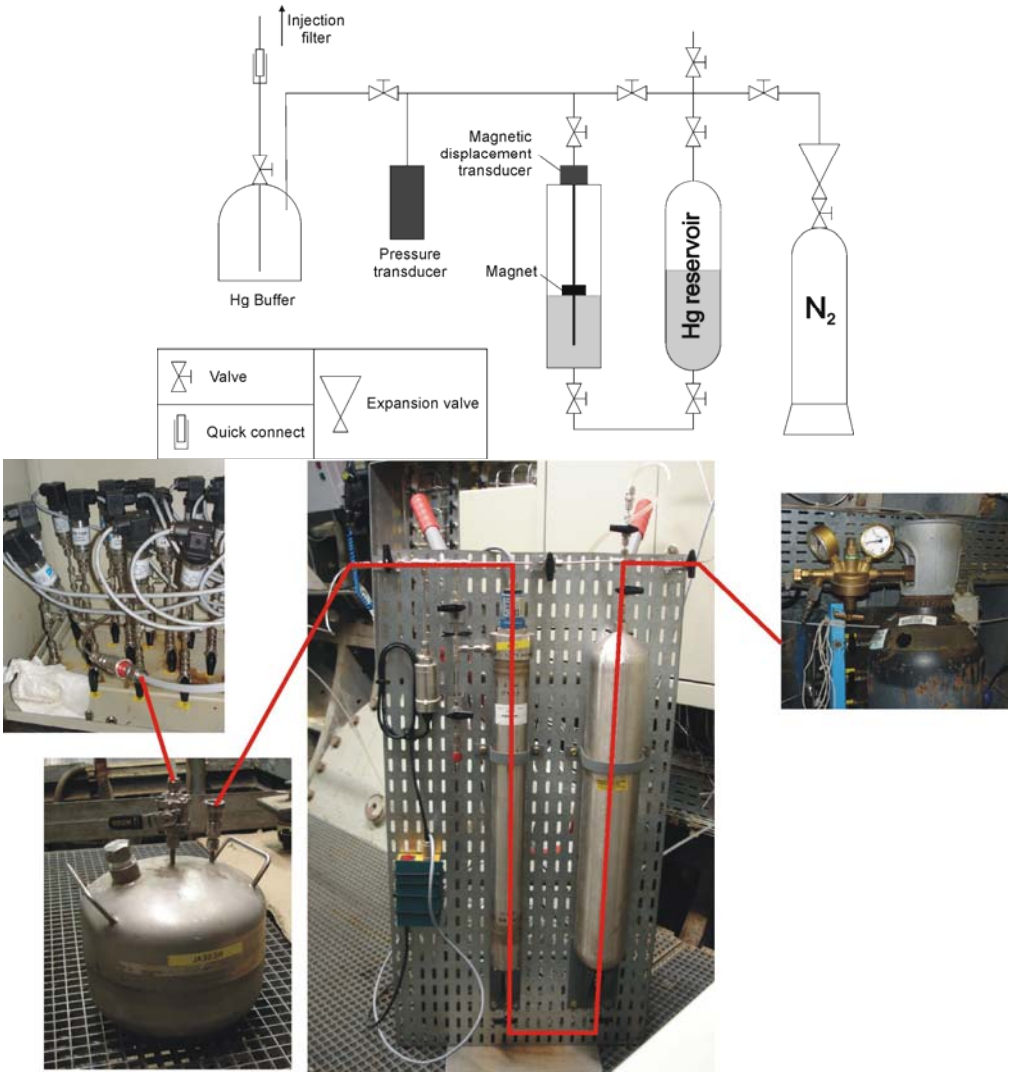

Figure 4-55: Gas injections system used in the gas breakthrough experiment.

The procedure was the following:

- Hydraulic conductivity is measured at the injection filter.
- All water is removed from the injection filter. This is done through the twin tube system which connects each pore pressure filter with the main gallery. N_2 is used to flush the tubes and filter. A pressurised gas reservoir (at 4 bar abs) is connected to the filter.
- The gas pressure is increased step by step with 1 bar increments until breakthrough. Gas pressure and flow rate is monitored. Enough time for equilibration is needed between the subsequent steps, but on the other hand the total test period is to be limited as well. There are at least 2 days between subsequent steps. **Table 4-14** gives an overview of the pressure steps. The volume of injected gas is shown for each step. The given volumes are the gas volumes at 1 bar, calculated assuming ideal gas behaviour.
- The filter is kept at ~1.1 bar abs during 4 weeks.
- A second breakthrough is initiated (cf. **Table 4-14**).
- Hydraulic conductivity is measured two weeks after second breakthrough.

Table 4-14: Overview of the pressure increase steps of the gas breakthrough test.

Date	Pressure set at	Gas volume injected [eq. l @ 1 bar]	Gas flow rate [ml/day]
20-2-2006 13:20	4.0 bar abs	0.07	38
22-2-2006 9:30	6.0 bar abs	0.23	45
27-2-2006 13:30	7.0 bar abs	0.17	25
6-3-2006 9:20	8.0 bar abs	0.17	75
8-3-2006 15:40	9.0 bar abs	0.23	49
13-3-2006 9:00	10.0 bar abs	0.08	35
15-3-2006 16:00	11.0 bar abs	0.20	42
20-3-2006 9:20	12.0 bar abs	0.57	253
22-3-2006 15:30	13.1 bar abs	1.23	262
27-3-2006 8:20	14.3 bar abs	1.90	1297
28-3-2006 20:00	Breakthrough at 13.3 bar abs	6.78	~80000
1 month pause			
28-4-2006 9h	10.2 bar abs	Not measured	
28-4-2006 14h	14.0 bar abs	Not measured	
29-4-2006 0h	Breakthrough at 12.8 bar abs	Not measured	

Even at low gas pressures, a small quantity of gas is injected. This probably corresponds to gas dissolving in the pore water and some gas entering the seal by diffusion (Volckaert *et al.,* 1995). Starting from injection pressures of ~12 bar, the observed gas flow rate increases. Breakthrough occurs at 13.3 bar; after the gas pressure was set at a higher value (14.3 bar) and had somewhat dissipated. This indicates that the breakthrough itself is not only governed by the gas pressure as such but also depends on time-related phenomena. This implies that the obtained breakthrough value of 13.3 bar is to be considered as a maximum. Indeed, potentially breakthrough could have happened during one of the previous steps at lower gas pressure, would the time period have been somewhat longer. This remark is also made by Hildenbrand *et al.* (2002) when using a stepwise pressure increase. After breakthrough, the pressure at the injection system stabilises at a pressure of about 8.3 bar. In classic hydraulic well fracturing, this is called the shut-in pressure and is assumed to be equal to the local value of σ_3 (Kehle, 1964).

Figure 4-56 shows the evolution of the gas pressure applied and the response of pore water pressure measured throughout the seal. It is clear that during the last steps, most pore pressure filters are influenced. At the moment of the breakthrough itself, most filters show a rise in pressure. Some filters however (all in the top instrumented level) show a pressure drop. The drop at the injection filter is about 5 bar, the magnitude of the increases (or drops) at the responding filters is about 0.5 bar. The same observations are made by the total stress sensors (**Figure 4-57**): most show an increase, some a decrease. The magnitude of the response of most total stress sensors is about 0.2 bar. The sensors on the western rod of the bottom instrumented level show a decrease of total pressure of about 1 bar.

It is concluded that no direct connection was established between the injection filter and one of the other instruments; the western rod of the bottom instrumented level shows the strongest reaction. These sensors are close to the injection point.

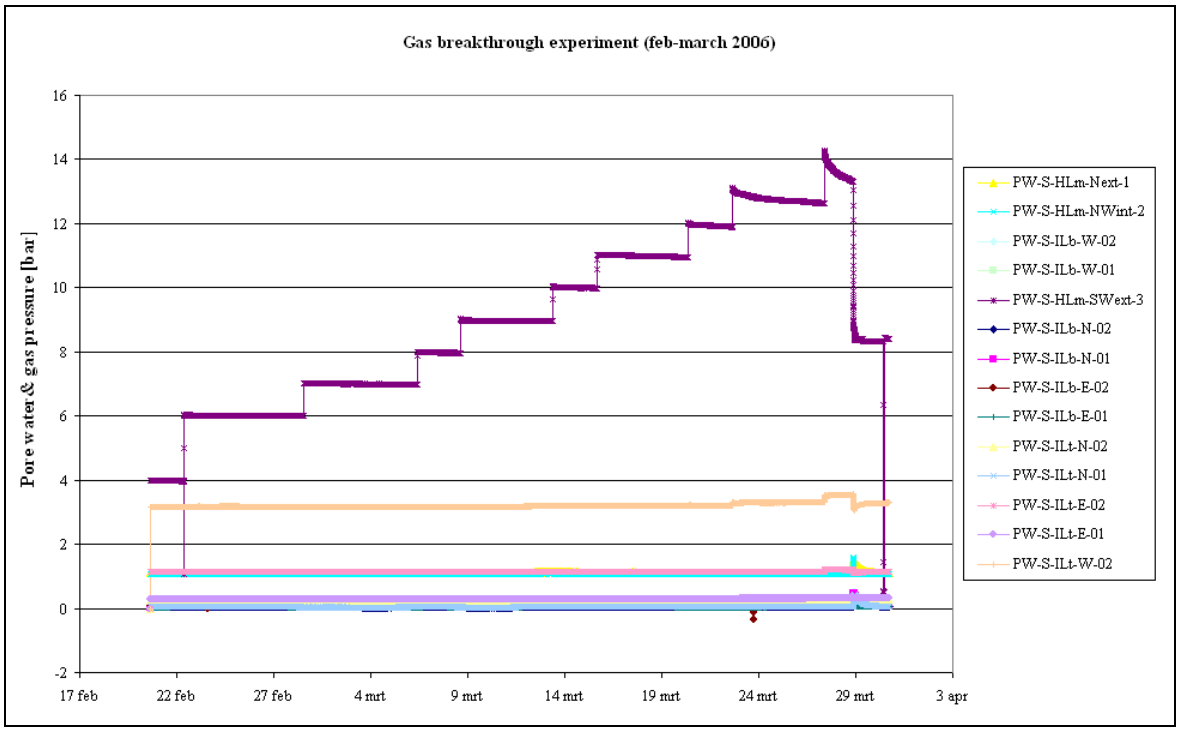

Figure 4-56: Overview of gas pressure during the first breakthrough experiment and the response of pore water pressure at surrounding filters.

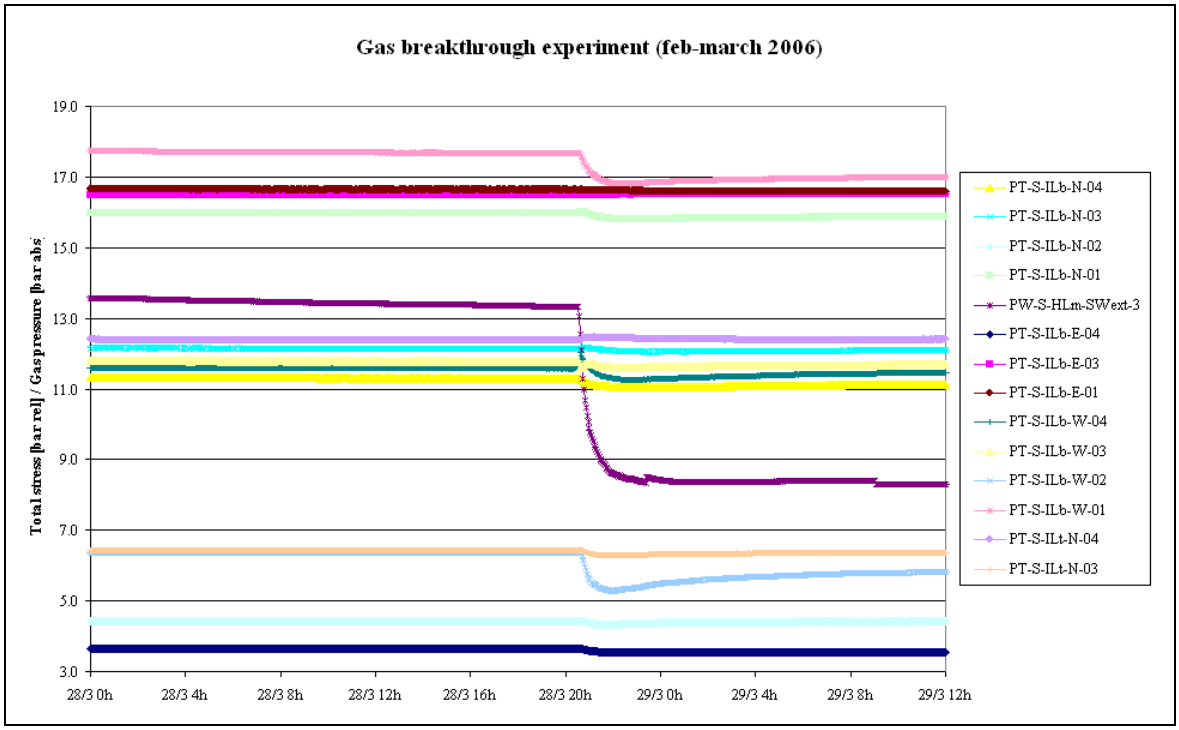

Figure 4-57: First gas breakthrough: pressure at the injection filter and response of total stress sensors in the seal.

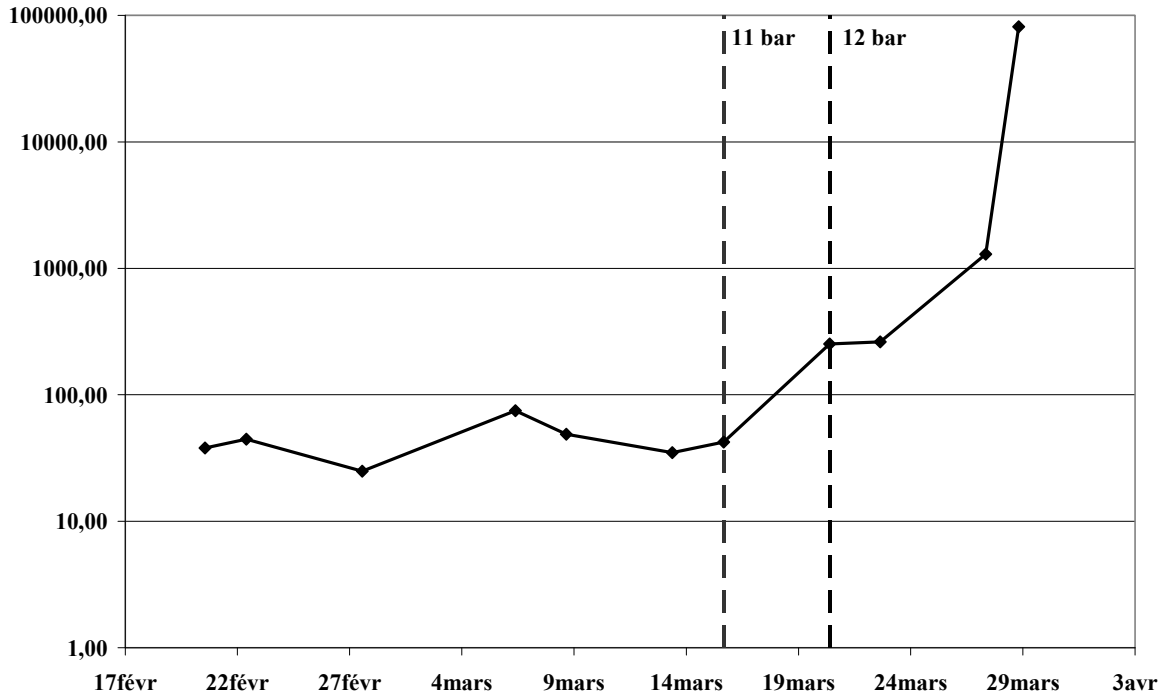

Figure 4-58: Measured flow rates (recalculated at volume at 1 bar pressure) during the first gas breakthrough test. Increasing the pressure to 12 bar significantly increases the gas flow rate.

In **Figure 4-58** the gas flow rates, recalculated at 1 bar pressure, during the first gas breakthrough test are shown. It can be seen that increasing the pressure from 11 to 12 bar significantly increases the gas flow rate.

Comparable observations were made during the second breakthrough, established 1 month after the first one. This time breakthrough occurred at 12.8 bar. Again, breakthrough occurred some hours after the gas pressure was increased to the highest level (14.0 bar in this case). The response of pore water pressure (**Figure 4-59**) and total stress (**Figure 4-60**) sensors is more pronounced during the second breakthrough. Again the western rod of the bottom instrumented level shows the most pronounced reaction. Indeed, pore pressures at this rod increase sharply. However, a real connection between the injection filter and any other filters is not observed as the difference in pressure remains at least 1 bar (**Figure 4-59**). Moreover, the pressure changes are recovering very fast (matter of days), which is not in line with earlier in-situ observations (Volckaert *et al.,* 1995). Probably, a local non saturated part of the seal was filled with gas or gas escaped along a leak somewhere in the instrumentation in the neighbourhood. Notice, that the pore water pressure sensors 1 and 2 on the western rod of instrumented level bottom recorded zero bars absolute pressure before the experiment, but clearly react to the gas breakthrough. This time, the gas injection system stabilises at a pressure of 4.3 bar after breakthrough, but this shut-in pressure is thought not to be representative as a leak somewhere in the system might exist. Gas flow rates during this second gas breakthrough test are not available.

The hydraulic conductivity determined at the injection filter HLM-SWext-3 was the same one month before the start of the breakthrough experiment and 2 weeks after the second breakthrough: a value of 1.1 10^{-12} m/s was measured.

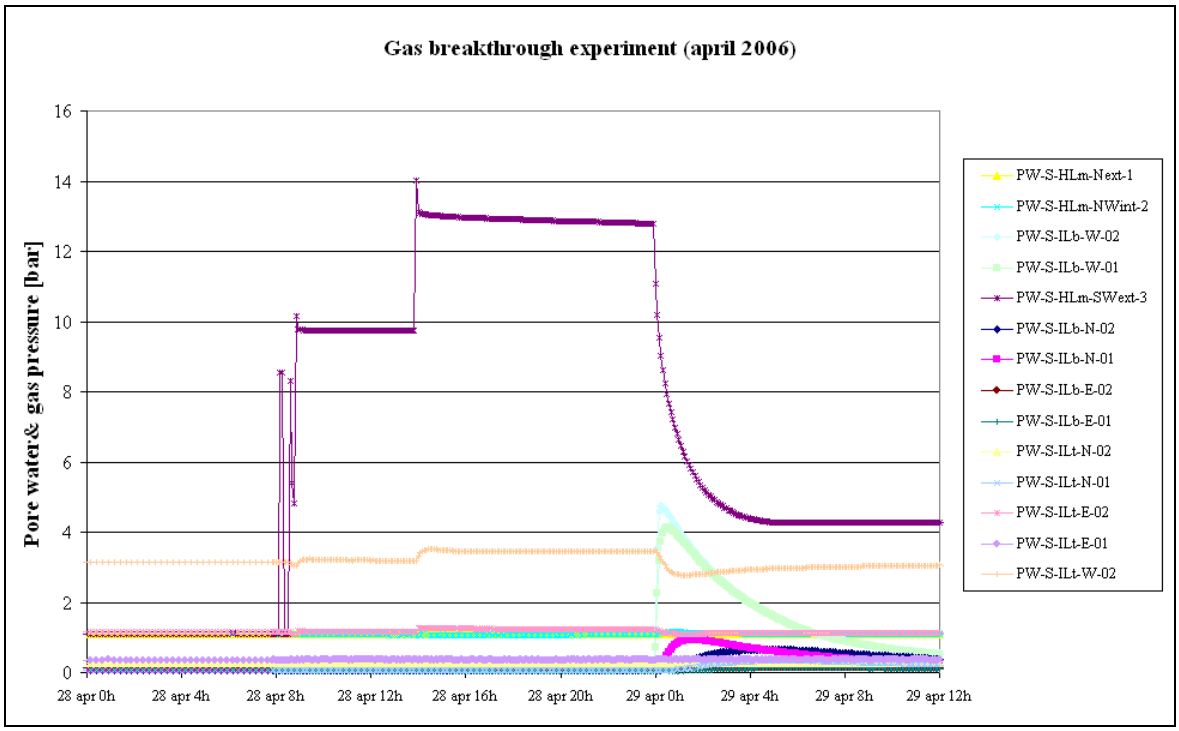

Figure 4-59: Overview of gas pressure during the second breakthrough experiment and the response of pore water pressure at surrounding filters.

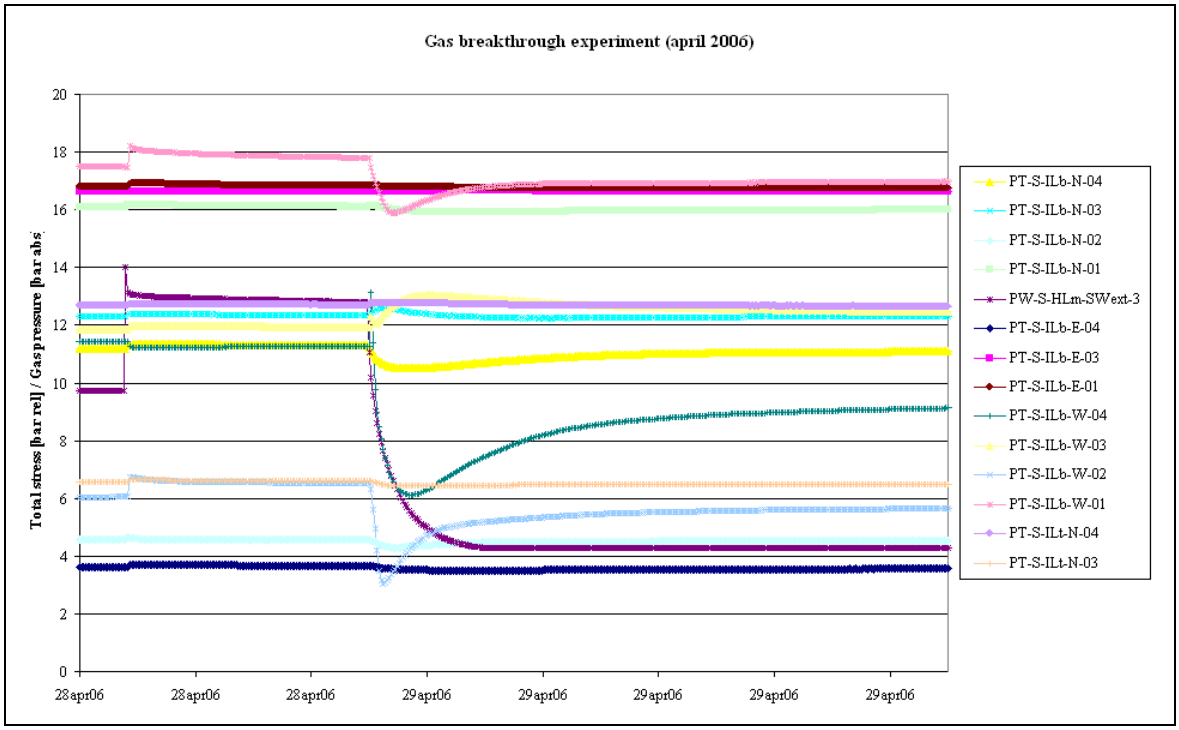

Figure 4-60: Second gas breakthrough: pressure at the injection filter and response of total stress sensors in the seal.

4.5.4 Conclusions about the gas breakthrough experiment

Two gas breakthrough tests were performed in the seal, using the same injection filter twice. An interesting feature of the set-up is the fact that one of the cylindrical filters was used to apply the gas pressure build-up. These filters are "floating" in the bentonite seal, meaning that no preferential pathways exist a priory. In borehole experiments, such a path way is often present (cf. interface between instrument and host rock).

It is observed that breakthrough pressures were twice almost the same: 13.3 bar vs. 12.8 bar. Moreover breakthrough in both cases occurred only a while after the highest pressure was applied. This indicates that the recorded values are at the high end. It can not be excluded that breakthrough would have occurred at lower pressures if that pressure would have been applied over a longer period of time. In both cases the most pronounced reactions were observed on the western rod of the bottom instrumentation level. No clear connection between filters was established in the both tests. The observations made in the second test seem to indicate that a local unsaturated zone existed or more likely that gas could escape through a leak in the instrumentation.

For plastic clays, it is believed that the breakthrough pressure corresponds with the minimum total stress (Volckaert *et al.,* 1995; Ortiz *et al.,* 1997; Rodwell *et al.,*1999). The total stresses measured in the seal vary between 7 and 11 bar. Consequently, the measured breakthrough pressures are somewhat higher, but as mentioned before these measured breakthrough pressures should be considered as maximum values. Moreover, the shut in pressure observed in the first breakthrough test might be realistic and with a value of 8.3 bar lies within the range of total stresses measured inside the seal.

4.5.5 Hydraulic shock

In this test the effect of a large hydraulic shock on the seal is tested. An elevated water pressure was suddenly applied at the filters of the bottom hydration level on 22nd June 2006. The response on the rest of the seal (and surrounding host rock) was monitored. The pump and accumulator of the hydration system were used to perform the test. The set-up is limited to an injection pressure of ~22 bar. Just before the test, pore pressure measured at HLb was about 10 bar.

At the start of the test, the hydration system was set at 10 bar. Next, the pressure regulator was set at 15 bar but the pressure measured at the filter only increased very slowly. Some 30 minutes later only 12.5 bar was reached and the test was stopped. It is unclear why higher pressures could not be obtained. Potential causes were already mentioned in section 4.3.3: clogging of tubes/filters and the possible interchange of filters.

Although the desired pressure was not reached, sensors throughout the seal registered the hydraulic shock. Pore water pressure sensors in the top and bottom instrumented levels show a response (0.5-1 bar increase). Moreover, most of the total stress sensors throughout the seal show a clear increase up to 2 bar which almost corresponds to the applied increase (~2.5 bar) at the bottom hydration level; **Figure 4-61** shows an example.

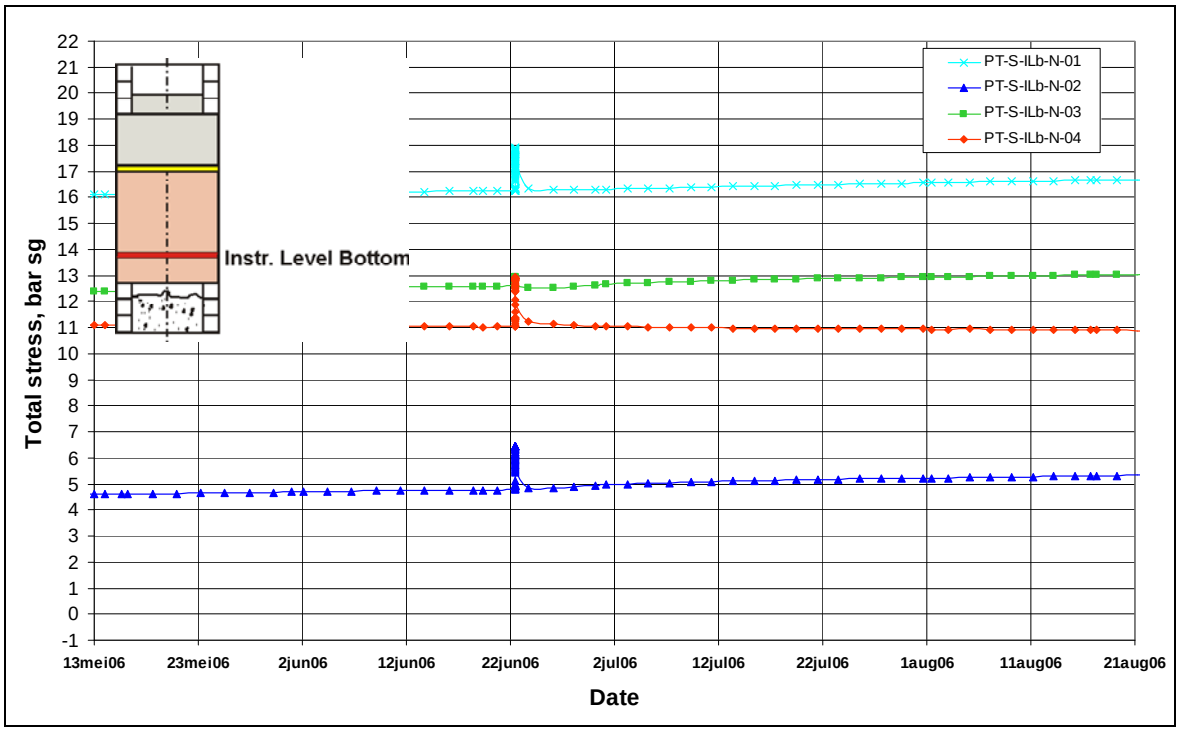

Figure 4-61: Response of total stress at the northern rod of the bottom instrumented level.

On 21st September 2006 some tests were made on the circulation pumps for the migration experiment. During these tests, water pressure was increased 1-2 bar at the filters on the central tube in the seal. This can be considered as a second – much smaller and shorter - hydraulic pulse test. Indeed, some pore water pressure sensors in the top and bottom instrumented levels show a response. However, very few total pressure sensors are affected.

4.5.6 Conclusions about the hydraulic shock test

Due to technical limitations of the set-up, the pressure levels of the hydraulic shock test were rather low. Consequently, the test is not fully representative for the situation which was intended to be simulated. However, the influence of increasing the pore pressure at the bottom hydration level was noticed throughout the entire seal. Total pressure sensors showed an increase of ~50-100 % of the applied pressure increase. Pore pressure sensors also showed a response, but to a lesser extent (~25-50% of the applied increase).Sensors in the host rock did not respond.

Similar observations were made during the second (unintended) hydraulic shock.

Apart from the strong HM coupling in the seal, no additional conclusions can be formulated.

4.5.7 RN migration

Radionuclide migration in the surrounding EDZ

After saturation of the seal, the radionuclide migration within the EDZ surrounding the shaft seal was tested. The data will be compared with well known data of radionuclide migration within undisturbed Boom Clay. This should allow investigating whether relicts of fractures, created during excavation of the shaft and (re-)created during removal of the concrete lining (see section 4.1.1) have an effect on the overall radionuclide migration.

Set-up

The radial piezometers at the centre of the seal height and extending up to 1m into the surrounding host rock are used for these tests (**Figure 4-62**). Three of such piezometers are available at different directions around the seal. As each piezometer contains five filters at different depths within the host rock, three different injection filters were chosen in order to test the effect of distance towards the host rock – seal interface. The two neighbouring filters of each injection filter were used as sampling filters. **Figure 4-62** schematically illustrates the injection and sampling filters in the host rock surrounding the shaft seal.

The tracer used is ^{125}I, as also used within the borehole seal experiment. On October 13th, 2006, $2.3 \cdot 10^{8}$ Bq of ^{125}I labelled NaI was introduced in the filters on the north and west oriented piezometers. About half of the activity, $9.9 \cdot 10^{7}$ Bq, of 125I labelled NaI was introduced in the filter on the east oriented piezometer. The half life of ^{125}I is 60.14 days. For each piezometer a different injection system was installed. These injection systems are similar to the one used in the borehole seal experiment. A loop of stainless steel tubing of 3.5 ml is filled with Boom Clay pore water containing ^{125}I labelled NaI solution. One end of this loop is connected to the inlet water conduits of the injection filter. The other end of the loop is connected to the exit of a circulation pump. The inlet of the circulation pump is connected to the outlet of the water conduits of the injection filters. Consequently, a closed system is created for each injection filter. The pump is then used to circulate the water through the filter and the circulation system at a pressure only slightly higher than the in-situ pressure at the filter. This creates a homogenization of the tracer and the clay water present in the circulation system. Due to contact of the filter with the Boom Clay, diffusion of the tracer is enforced with only a small pressure difference. This kind of test is called a diffusion tracer injection.

Based on the experience of the borehole seal, we adapted the sampling scheme during these radionuclide migration tests. As we know that fractures seal rather fast within Boom Clay (Bernier *et al.,* 2007), it is known that possible relicts of these fractures and their effect on radionuclide migration will be rather small. In order to detect any possible effect, the sampling filters were kept open continuously in order to create a hydraulic gradient between the injection and sampling filter. This hydraulic gradient is the only way to slightly increase a possible remaining effect of the former fractures (e.g. increased porosity) and to be able to detect it.

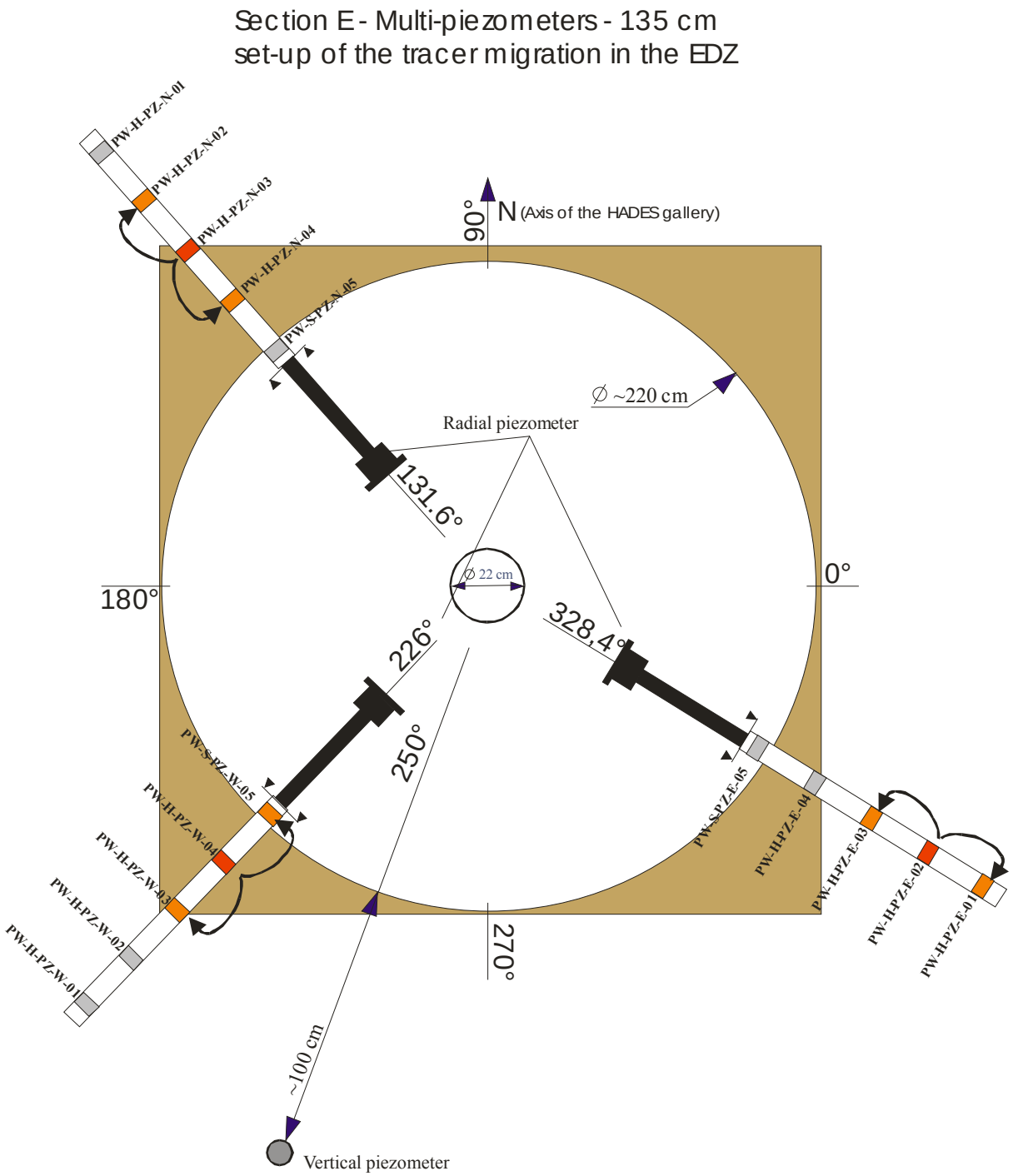

Figure 4-62: Schematic illustration of the tracer migration test in the Boom Clay around the shaft seal experiment. Filters in red correspond with injection filters, while filters in orange correspond with sampling filters.

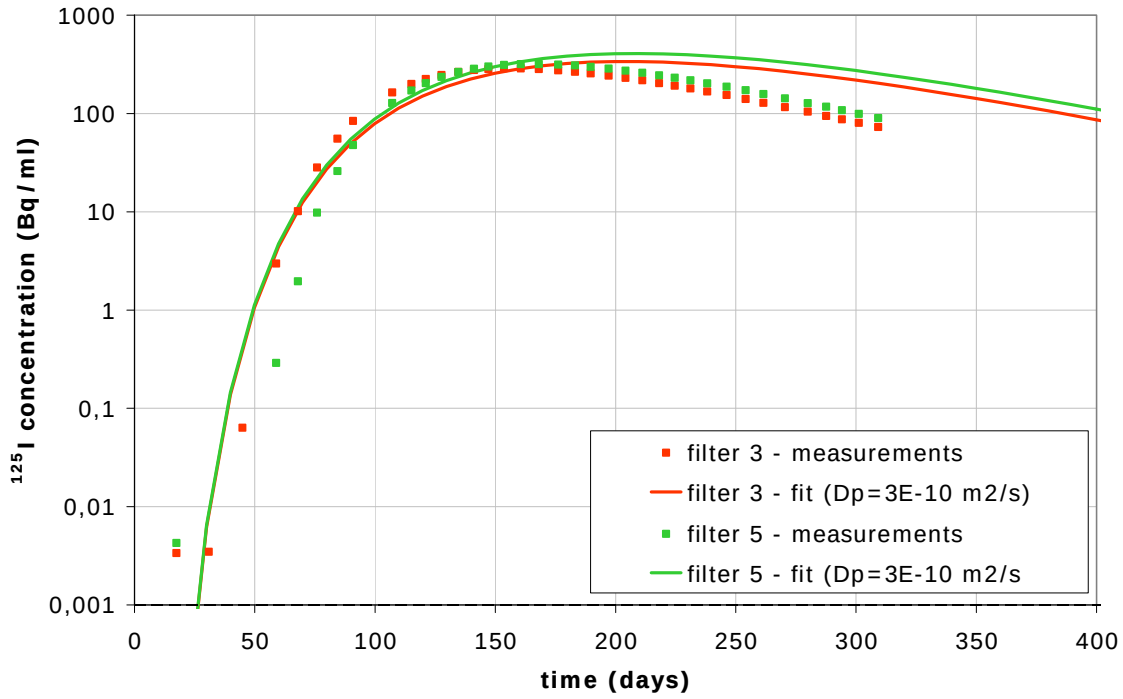

Figure 4-63: Comparison of observed 125I concentrations from sampling filters in the host rock on the piezometer oriented to the west with a fit from an advective-diffusive transport model.

The migration tests in the host rock are still running, so here we only give some preliminary conclusions. As a matter of example, we illustrate the radionuclide migration measurements in the two sampling filters of the piezometer oriented to the west (**Figure 4-63**). Incorporating the advective flux due to sampling and incorporating the typical porosity and diffusion parameters of undisturbed Boom Clay for 125 I, a reasonable fit with the experimental data can be obtained. However, it is already clear that the tailing will be overestimated with this model. Currently, it is checked which parameters need to be varied to approach the measurements and whether we can underpin this with physical phenomena that might play.

Radionuclide migration in the seal

Once the radionuclide migration in the host rock around the shaft seal is finished, a similar radionuclide migration test will be performed within the shaft seal itself. The idea is to test the migration parameters of a saturated bentonite pellet/powder mixture and to test any possible heterogeneities within the seal (e.g. the central versus the outer part of the seal and the compacted versus the uncompacted part of the seal).

This radionuclide migration test still needs to be started, but here we describe already the experimental set-up. The migration test will again be performed with ^{125}I. In order to test the possible heterogeneities within the seal, three different injection filters are chosen. **Figure 4-64** illustrates the injection and sampling filters for this radionuclide migration test. One filter is located near the interface Boom Clay – seal. A second injection filter is located on the central tube. These two filters are more or less located at the same level within the seal height, within the uncompacted part, and thus should allow investigating possible differences between the outer and central part of the seal. A third injection filter is located at the bottom of the seal on the

central tube. The latter filter is chosen to compare the radionuclide migration in the uncompacted and compacted part of the shaft seal experiment. The injection systems will be identical to the one described above for the migration test within the surrounding host rock. The sampling is also similar to the one described above for the migration test within the surrounding host rock, however, only one sampling filter for each injection filter is chosen. As a continuous sampling will be performed on each sampling filter, again a hydraulic gradient will be created between the injection and sampling filter. This gradient is applied in order to highlight any possible differences in migration parameters as again only small differences are suspected.

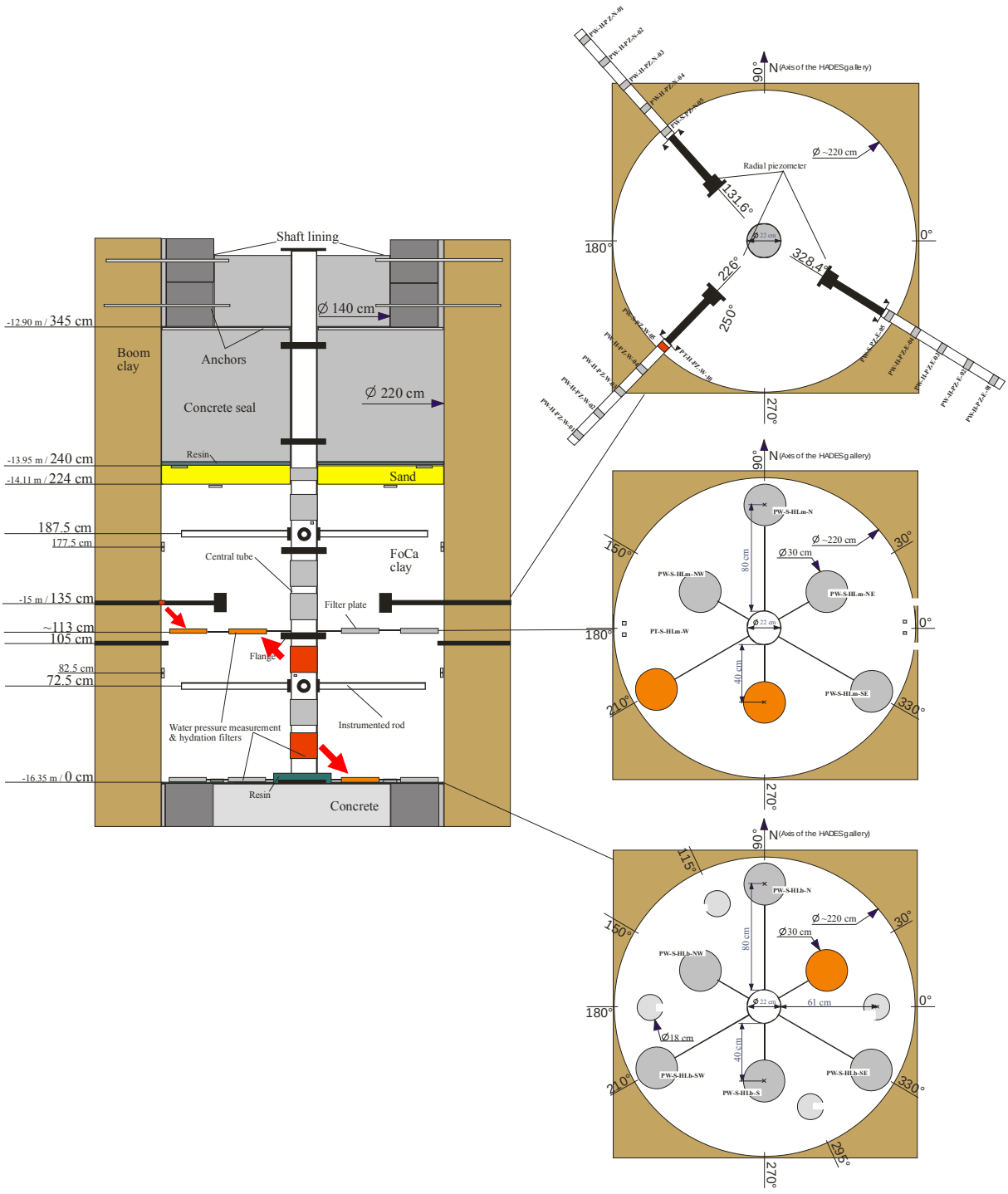

Figure 4-64: Schematic illustration of the tracer migration test in the FoCa Clay of the shaft seal experiment. Filters in red correspond with injection filters, while filters in orange correspond with sampling filters.

4.6 Conclusions

The RESEAL shaft seal experiment put into evidence the feasibility to design and construct a bentonite shaft seal. It also showed that the period needed to get full saturation of the seal can be important. Furthermore, artificial hydration seems to have only a limited influence on the duration of this process, at least in the current configuration. About 55% of the water volume required for full saturation was injected through the hydration system but a large uncertainty exists on the amount of water that actually contributed to the saturation of the seal (cf. possible leaks). One should note that the diameter of the test (~2.2 m) is relatively small compared to the access shafts necessary for an actual geological disposal site. Consequently, even larger saturation times could be anticipated in this case.

At full saturation (18th April 2007), effective stress ranges from 4.5 to 7 bar. Values are somewhat higher for the "east" sensors than for the other two orientations, mainly due to lower pore pressures at these locations. This slight in-homogeneity is also visible in the pore pressures measurements in the host rock. It is difficult to define a cause for this asymmetry but it might well be caused by installation related issues and it can be temporary. Indeed, total stresses and pore pressures in the seal, the host rock and at the interface are still in transition and equilibrium is not yet reached.

An average dry density of 1.41 g/cm³ was determined for the shaft seal, resulting in a calculated swelling pressure of 5.8 bar. The measured values of swelling pressure are somewhat higher but one should note that due to the nature of the formula (cf. exponential) small variations on the value of the dry density have a big impact on the result. Furthermore, calculation of the dry density copes with several uncertainties, e.g. exact excavation profile of the shaft seal.

On average, effective stress (and certainly total stress) measurements are higher in the bottom level than in the top level. This is in line with the higher initial dry density at the bottom part of the shaft seal. Furthermore, the distance to the top of the seal can also play a role (cf. atmospheric pressure).

Measurement of total stresses in the host rock proved to be more complicated than in the seal itself. This is in line with previous experience at the HADES URF. The sensors seem to be very sensitive for local and/or temporary phenomena. Furthermore, installation-related issues play an important role. Consequently, the measured total and effective stresses in the host rock should be interpreted rather qualitatively than quantitatively.

The removal of the concrete lining of the shaft has a strong effect on the EDZ. Fractures were formed around the shaft, causing many blocks to fall from the shaft wall during installation of the seal. It is impossible to distinguish between re-activation of existing fractures (caused during excavation) and newly developed fractures caused by removal of the lining. The fractures in connection with atmospheric pressure occur up to at least 1 m into the host rock, but are limited (in height) to a cylindrical zone around the part of the shaft where the lining was removed.

The observed trends and trend changes of the displacement measurements can be related to certain events. Several observations can be linked to the start of artificial hydration (on 3rd May 2000). When the first relative humidity sensors inside the seal indicate (local) saturation, the displacement observed close to the centre of the seal changes from outward to inward. When pore water pressure starts to increase again in the host rock, the movement of the host rock inverts, the sensors now move outward. When pore water pressure inside the seal starts to

increase, displacements inside the seal seem to slow down or even stop. Displacements are still ongoing although at a reduced rate, indicating that the interaction between the bentonite and the host rock is not yet at full equilibrium.

Hydraulic conductivity measurements of the host rock yield values in line with values reported in literature. This is true for laboratory measurements made on cores taken prior to the installation of the shaft seal as well as for the in-situ measurements made using the radial piezometers during the shaft seal experiment. The results reflect the known anisotropy of hydraulic conductivity on Boom Clay ($k_H \sim 2.k_V$).

Hydraulic conductivities measured inside the seal are of the expected order of magnitude. One should be careful in deducing the dry density (and swelling pressure) from these results; an important amount of scatter on the experimental results used to determine these relations can induce significant errors.

Two gas breakthrough tests were performed in the seal, using twice the same injection filter, which floats inside the bentonite seal.
It is observed that breakthrough pressures were twice almost the same: 13.3 bar vs. 12.8 bar. Moreover breakthrough in both cases occurred only a while after the highest pressure was applied. This indicates that the recorded values are at the high end. It cannot be excluded that breakthrough would have occurred at lower pressures if that pressure would have been applied over a longer period of time. In both cases the most pronounced reactions were observed on the western rod of the bottom instrumentation level. No clear connection between filters was established in the both tests. The observations made in the second test seem to indicate that a local unsaturated zone existed or more likely that gas could escape through a leak in the instrumentation.

For plastic clays, it is believed that the breakthrough pressure corresponds with the minimum total stress (Volckaert *et al.,* 1995; Ortiz *et al.,* 1997; Rodwell *et al.,*1999). The total stresses measured in the seal vary between 7 and 11 bar. Consequently, the measured breakthrough pressures are somewhat higher, but as mentioned before these measured breakthrough pressures should be considered as maximum values. Moreover, the shut in pressure observed in the first breakthrough test might be realistic and with a value of 8.3 bar lies within the range of total stresses measured inside the seal.

Due to technical limitations of the set-up, the pressure levels of the hydraulic shock test were rather low. Consequently, the test is not fully representative for the situation which was intended to be simulated. However, the influence of increasing the pore pressure at the bottom hydration level was noticed throughout the entire seal. Total pressure sensors showed an increase of ~50-100 % of the applied pressure increase. Pore pressure sensors also showed a response, but to a lesser extent (~25-50% of the applied increase).Sensors in the host rock did not respond.
Apart from the strong HM coupling in the seal, no additional conclusions can be formulated.

The radionuclide migration tests are still ongoing. Preliminary results of the migration in the EDZ seem to indicate that no preferential pathways for radionuclide migration exist.

5 Hydromechanical modelling of laboratory tests and the shaft seal test

During RESEAL II the hydromechanical models were updated and extended in order to better simulate the experimental observations. To this extent the newly available laboratory tests were used to calibrate the models, which were then applied to model the large scale in-situ shaft seal test. This chapter is structured as follows:

- Brief description of the theoretical formulations used in the coupled hydromechanical analyses
- Coupled hydromechanical modelling of laboratory infiltration tests
- Coupled hydromechanical modelling of the in situ shaft sealing test

5.1 Theoretical formulations

5.1.1 UPC formulation

5.1.1.1 Balance equations

To be able to reproduce numerically the hydromechanical interactions occurring on the pellets/powder mixture during wetting, a theoretical formulation and a constitutive model capable of taking into account the expansion and shrinkage of clay aggregates has been used by UPC.

The formulation involves the simultaneous solution of a set of equations, *i.e.* the mass balance equations, the momentum balance equation (mechanical equilibrium) for deformable porous medium and, in non-isothermal problems, the internal energy balance for the total porous medium.

To establish the mass balance equations, it is considered that the porous medium is composed by three species (mineral, water, and air), and is distributed in three phases (solid, liquid and gas). This is called the compositional approach and consists of balancing the species rather than the phases. Phase equations are obtained by adding the equations of balance of all species contained in each phase.

Solid mass balance

The balance of the mineral (solid phase) can be expressed using the material derivative as:

$$\frac{D\phi}{Dt} = \frac{(1-\phi)}{\rho_s}\frac{D\rho_s}{Dt} + (1-\phi)\left(\dot{E}_v\right) \qquad \textbf{Equation 5-1}$$

where $\dot{E}_v = \nabla \bullet \dot{\mathbf{u}}$ is the increment of the total volumetric strain referred to the whole medium.

When coping with double porosity media, the concept of two overlapping porous media can be used (Sánchez 2004) .The media is divided into two overlapping but distinct continuum. In the case of clays, the first one represents the macrostructure composed by the clay aggregates and the larger pores, while the second one represents the microstructure. These two sub-domains have the following characteristics:

- The fluid flow within each sub-domain is independent of the flow in the other sub-domain and any coupling between them is controlled by a leakage term. Hence, fluid pressure, and any other variable such as saturation, porosity or permeability, are considered separately.
- Specific mechanical models for each medium are considered.
- Two different porosity values should be defined, hence the term *double porosity model:*

$$\phi_1 = \frac{Vv_1}{V}$$ **Equation 5-2**

$$\phi_2 = \frac{Vv_2}{V}$$ **Equation 5-3**

$$\phi = \phi_1 + \phi_2$$ **Equation 5-4**

With two different global porosities, ϕ_1 and ϕ_2 respectively, and with ϕ as the global porosity, the evolution of porosity can be expressed as (Sánchez 2004):

$$\frac{D\phi}{Dt} = \frac{D\phi_1}{Dt} + \frac{D\phi_2}{Dt} = \frac{(1-\phi)}{\rho_s}\frac{D\rho_s}{Dt} + (1-\phi_1-\phi_2)\left(\dot{E}_{v1} + \dot{E}_{v2}\right)$$ **Equation 5-5**

In the previous equation, it is assumed that the total volumetric deformation can be expressed as the sum of the volumetric deformations of each medium.

Water mass balance

The water mass balance equation for the case of two overlapping flow domains is:

$$\frac{\partial}{\partial t}\left(S_{lj}\phi_j\right) + \nabla \bullet \left(\mathbf{j}_{lj}\right) + (-1)^{j+1}\Gamma^w = f_j^w$$ **Equation 5-6**

where S_{lj} is the liquid saturation of medium *j*, $\mathbf{j}_{lj}$ is the total mass fluxes of water in the liquid phase ; f_j^w is the external mass supply of water per unit volume of medium *j*, and Γ^w is the term related to the water mass exchange between the two media.

A quasi steady model was assumed for the process of liquid transfer between both media. The amount of transferred mass is proportional to the differences between the two media pressures (or potentials):

$$\Gamma^w = \gamma(\Psi_1 - \Psi_2)$$ **Equation 5-7**

where γ is the leakage parameter and Ψ_j (j=1,2) represents the total water potential for medium *j*.

5.1.1.2 Mechanical constitutive law

The mechanical constitutive model, called BExM ((Alonso *et al.* 1999; Gens and Alonso 1992; Sánchez *et al.* 2001)) distinguishes two structural levels: the microstructural level at which swelling of active minerals takes place and the macrostructural level responsible for major structural rearrangement.

The behaviour of the macrostructure is defined by means of the well known BBM (Alonso *et al.* 1987; Alonso *et al.* 1990). The BBM describes many significant features of low activity clayey soils as the existence of plastic deformations induced by stress and suction, the changes in soil stiffness induced by suction, the collapse of soil upon wetting or the coupling between deformations induced by suction and stresses (Josa *et al.* 1992).
With the inclusion of the microstructural behaviour the scope of the model is increased to the range of soils with expansive behaviour; some of the aspects that can be represented are (Gens and Alonso 1992):

- the dependence of swelling on moisture content, dry density and applied pressure;
- the strong dependency of swelling on void ratio;
- the irreversibility and stress path dependency of swelling strains;
- and the dependency of swelling pressures on testing method

Using the BExM, and the collected and interpreted information from laboratory experiments for the cited material, the behaviour of the mixture has been reproduced.

5.1.1.3 Numerical implementation

The interactions have been followed in detail thanks to the possibility of using the model inside a FE code designed for coupled THM problems in double porosity media (Olivella *et al.* 1994; Sánchez *et al.* 2004): CODE_BRIGHT. Details of the numerical implementation are given in Olivella *et al.* (1996) and Sanchez *et al* (2005). CODE-BRIGHT has been applied on many occasions to study the behaviour of engineered barriers for nuclear waste in deep disposals. This type of problem involves all the phenomena that the code considers (Gens *et al.* 1998; Olivella 2002).

Moreover, in recent years the code was extended, and geotechnical problems in which two overlapping porous media play an important role (as is the case of the highly expansive clays considered in this project) can be analyzed thanks to the modifications made by Sanchez *et al.* (2004).

5.1.2 CEA formulation

5.1.2.1 Balance equations

The CEA model objective is the description of the hydraulic flow and a mechanical behaviour of a saturated or unsaturated expansive porous media. Typically the porous media taken into account is natural or remoulded clay; when the media is not free to expand a swelling pressure occurs.

Three phases must be considered: water, solid and air. The first hypothesis is that the air doesn't move and its pressure is constant, equal to the atmospheric pressure; so the conservation laws are developed for only two phases: water (liquid) and solid. The temperature is constant; no explicit energy conservation equation is required. Then the four remaining conservation laws for describing the behaviour of the porous media are the following:

Water mass conservation equation:

$$\frac{\partial}{\partial t}\left(\rho_w \omega S\right) + div\left(\rho_w \omega S \overrightarrow{\mathcal{V}}_w\right) = 0$$

Equation 5-8

Solid mass conservation equation

$$\frac{\partial}{\partial t}\left(\rho_s (1-\omega) S\right) + div\left(\rho_s (1-\omega) S \overrightarrow{\mathcal{V}}_s\right) = 0$$

Equation 5-9

The water momentum conservation come from generalized Darcy's law:

$$\overrightarrow{\mathcal{W}}_w = K_w \overrightarrow{grad}\, h_w$$

Equation 5-10

The porous media momentum conservation equation is an equilibrium equation:

$$div(\overline{\overline{\sigma}}) + \overrightarrow{f} = 0$$

Equation 5-11

The combining of the first three equations results in one hydraulic conservation equation known as Richards' equation (Huyakorn and Pinder, 1983). Here it is written as a function of the water head pressure.

$$C(h_w)\frac{\partial h_w}{\partial t} - div\left(K_w(h_w)\overrightarrow{grad}\, h_w\right) = T(h_w, p)$$
$$C(h_w) = \left(-\frac{\partial S}{\partial s}\omega + \omega S \beta_w + (1-\omega)\beta_s\right)\rho_w g$$
$$T(h_w, p) = -\left(S - 1 + \left(1 + (S-1)\omega\right)\frac{1-\omega_0}{(1-\omega)^2}\right)\frac{\partial \omega}{\partial t}$$

Equation 5-12

Two constitutive laws are associated with the hydraulic conservation equation: retention law and formulation of permeability considered for saturated or unsaturated medium.

Retention law relates the water saturation to the suction; the Van Genuchten formulation is used for all materials and hysteresis is neglected:

$$S_e = \left(1 + \left(\frac{s}{s_{ref}}\right)^{\frac{1}{1-\lambda}}\right)^{-\lambda} \qquad S_e = \frac{S - S_r}{1 - S_r}$$

Equation 5-13

The water permeability is composed of intrinsic and relative permeabilities; it depends on the water saturation:

$$K_w(S_e) = \frac{\rho_w g}{\mu_w} . k_{rw} k_w$$

Equation 5-14

Two permeability laws are used. The first one is the Kozeny expression, applied to the FoCa clay:

$$k_{rw}k_w = k_i.S_e{}^A k_0.\left(\frac{\omega}{\omega_k}\right)^3\left(\frac{1-\omega_k}{1-\omega}\right)^2$$

Equation 5-15

The second expression is the Van Genuchten law, applied to the Boom Clay.

$$k_{rw}k_w = k_i.S_e{}^A\left(1-\left(1-S_e{}^{\frac{1}{\lambda}}\right)^{\lambda}\right)^B$$

Equation 5-16

The water density is given by:

$$\rho_w = \rho_{w0}exp\left(\beta_w\left(u_w - u_{w0}\right)\right)$$

Equation 5-17

5.1.2.2 Mechanical constitutive law

The porous media momentum conservation equation is a mechanical conservation law of the whole porous media, its associated law describes the behaviour of the media, here the BBM constitutive law is used. Hereafter the law characteristics and the mechanical parameters are introduced very summarily. For more explanation on BBM model see Alonso *et al.* (1990).

The BBM model define, in three-dimensional space (p, q, s), a yield surface limited by the following expression:

Loading-Collapse curves	$p_0 = p_c\left(\frac{p_0^*}{p_c}\right)^{\frac{\lambda(0)-\kappa(s)}{\lambda(s)-\kappa(s)}}$
Suction Increase surfaces	$s = s_0$
minimum suction surfaces	$s = 0$
ellipse at constant suction	$q^2 - M^2(p+k.s)(p_0-p) = 0$
Critical State Lines	$q = M.(p+k.s)$
cohesion with suction line	$p = k.s$

Equation 5-18

The two relations between specific volume and net mean stress in elastic and elasto-plastic increments are the following. Then the corresponding parameter definitions are also given.

$$dv = -\kappa(s)\frac{dp}{p} \qquad dv = -\lambda(s)\frac{dp}{p}$$

Equation 5-19

$$\begin{array}{llll} & if \quad s > 1MPa & \kappa(s) = \kappa_0.(1-\alpha_k.\ln(s)) & else \quad \kappa(s) = \kappa_0 \\ if \quad 0 < s & \lambda(s) = \lambda(0).((1-r).\exp(-\beta.s)+r) & else & \lambda(s) = \lambda(0) \end{array}$$

In the same way, the two relations between specific volume and suction in elastic and elasto-plastic increments are the following. Here the expression for one parameter is given; the second parameter, λ_S, has a constant value.

$$dv = -\kappa_s(s,p)\frac{ds}{s+p_{at}} \qquad dv = -\lambda_s\frac{ds}{s+p_{at}}$$

Equation 5-20

$$if \quad 0 < s \quad \kappa_s(s,p) = \kappa_s^0.\left(1-\beta_{ks}.\ln\left(\frac{p}{p_{ref}}\right)\right).\exp(-\gamma.s) \quad else \quad \kappa_s = 0$$

5.1.2.3 Numerical implementation

Due to the dependence of permeability K_W and saturation S to water pressure head h_W (see the hydraulic constitutive laws) the Richards' equation is a highly non linear partial differential equation used in saturated and unsaturated zones.

The hydraulic local equation (Richard's equation) is solved by numerical methods (Bernard-Michel and Genty, 2006): spatial discretization is based on Mixed Hybrid Finite Elements Method (Dabbene, 1998), time discretization is an Euler implicit scheme and the nonlinearities are solved by a fixed point method based on Picard scheme. As the Richards' equation is written in *h*-based formulation, the numerical mass conservation is assured by source term addition (Celia *et al.* 1990). This numerical hydraulic model is named H model, the main variable is the water head pressure *h*, defined in the center of the mesh elements.

The mechanical momentum conservation equation and related BBM constitutive law constitute the mechanical model (M model). These local equations are solved numerically with the help of FEM formulation (Leboulch and Millard, 1997). The main variable is the displacement, defined at the mesh nodes.

The two models H and M are implemented in CAST3M software program (Verpeaux *et al.*, 1988). At each time step the two models are solved sequentially in a Picard iteration: H model calculates with known porosity a new suction, and M model calculates with known suction a new porosity. This describes a hydro-mechanical coupling formulation. In the case of H model does not use the porosity coming from M model, a hydro-mechanical chaining formulation results.

Elementary validations have been realized for the two H, M models:

- experimental and analytical validation for H model (Bernard-Michel and Genty, 2006);
- code comparison for the BBM constitutive law in M model (Filippi, 2007).

5.2 Modelling the laboratory experiments

Infiltration tests (see chapter 2), performed by CEA and CIEMAT in the frame of RESEAL II, have been selected for coupled hydromechanical modelling. It was felt that before applying the theoretical formulations to the hydration of the shaft seal, it was necessary first to prove them in the modelling of laboratory tests. In this way the models could be calibrated in a more controlled environment and the effect of individual parameters more readily assessed. It would not be satisfactory to simulate the hydration process in the large scale experiment with a model that was not able to reproduce the basic behaviour of the material as observed in the infiltration laboratory tests. A fundamental feature of that behaviour is the progressive homogenization of the mixture as hydration progresses.

The tests were performed under oedometric conditions (i.e. uniaxial deformation with zero lateral strain) with simultaneous measurement of swelling pressure, water intake and axial deformation. When mixtures were tested, they were composed of a 50/50 weight percent pellet/powder proportion, both made up of FoCa clay. The experimental setups and the methodology followed are similar:

- constant volume
- column shaped samples
- saturation through bottom surface under low injection pressure (0.01 MPa)
- air evacuation through top surface
- initial water content between 4 and 12 %
- dry density between 1.30 and 1.60 (g/cm^3)

The major differences between the tests are the height and diameter of the specimens, the water intake measurement method and the density of the mixture. The detailed descriptions of the equipment and methods can be found in Villar *et al.* (2005). The main characteristics of the tests performed are summarised in Table 5-1.

Table 5-1: Characteristics of infiltration tests.

Reference	Diameter (cm)	Height (cm)	Dry density (g/cm^3)	Initial *w* pellets (%)	Initial *w* powder [1] (%)
RS2A	12	5	1.30	4	12
RS2D	12	10	1.30	5	12
RS2G	12	12	1.30		
RS2J	12	5	1.45	4	5
MGR7	10	5	1.45	5	12
MGR8	10	10	1.45	5	12
MGR9	10	10	1.45	5	6
RS2C	12	3	1.60	5	12
RS2K	12	3	1.60		
RS2B	12	5	1.60	4	12
RS2E	12	10	1.60	4	5

Reference	Diameter (cm)	Height (cm)	Dry density (g/cm^3)	Initial *w* pellets (%)	Initial *w* powder [1] (%)
RS2F	12	12	1.60	4	5
MGR10	10	5	1.45		12
MGR11	10	5	1.60		12

Tests starting with RS have been performed by CEA whereas the tests starting with MGR have been performed in the CIEMAT laboratory. Exceptionally, tests MGR10 and MGR11 were performed on FoCa clay powder only.

UPC has modelled the following tests: MGR7, MGR 9, RS2B, RS2E, RS2F and RS2J (densities 1.45 and 1.60 g/cm^3) whereas CEA analysed the following tests: RS2B, RS2C, RS2E and RS2F (density 1.60 g/cm^3).

5.2.1 Analysis performed by UPC

5.2.1.1 Features of analysis

Table 5-2 lists the initial characteristics of the tests that have been modelled numerically by UPC (Gens *et al.,* 2009). These characteristics have been taken from Villar *et al.* (2005). The initial height of the samples was measured at the end of compaction.

Table 5-2: Initial characteristics of the swelling pressure tests modelled by UPC

Test label	Height (mm)	ϕ (mm)	Dry density g/cm3	Dry density pellets g/cm^3	Initial w% Pellets	Dry density powder g/cm^3	Initial w% powder	Initial w% sample	Void ratio
				CIEMAT					
MGR7	50	100	1.45	1.894	4.6	1.175	12.00	8.30	0.841
MGR9	100	100	1.45	1.894	5.0	1.182	5.80	5.25	0.838
				CEA					
RS2B	50	120	1.60	1.894	4.31	1.385	11.83	8.07	0.672
RS2E	100	120	1.60	1.894	4.49	1.390	5.07	4.78	0.670
RS2F	120	120	1.60	1.894	4.49	1.390	5.07	4.78	0.670
RS2J	50	120	1.45	1.894	4.00	1.175	5.00	4.78	0.840

Data available on the initial conditions of the samples were used to estimate the initial values of the variables used by the double structure constitutive model. The variables needed for the numerical simulations are the micro and macropore volumes, and the micro and macrostructural suctions. They need to be estimated on the basis of the available information, since micro and macrostructural porosity can only be quantified through destructive MIP tests, and no kind of suction control was used during the tests.

The double structure formulation defines two different porosity values. These are the microstructural ϕ_m and the correspondent value for the macrostructure, ϕ_M.

The known macroscopic details of each sample are the volumes, the solid masses and the water masses of all three: sample, powder and pellets. From this information the total porosity can be easily calculated. However, the microstructural and macrostructural porosities can not be similarly calculated; neither in the powder nor in the pellets. It is necessary to resort to MIP results to be able to make estimations.

Data on the microstructural pore volumes of the pellets was obtained from the tests performed by CEA and CIEMAT. For the powder, the same type of data has been estimated from MIP tests found in the literature. In Valleján (2008), the complete estimation of the initial values for both variables can be found.

In Figure 5-1 a plot with the values of total, micro and macro porosities and void ratios for the powder compacted at different densities is shown. (Dashed lines correspond to porosity and continuous lines to void ratio. Diamonds correspond to total values, squares to micropores and triangles to macropores).

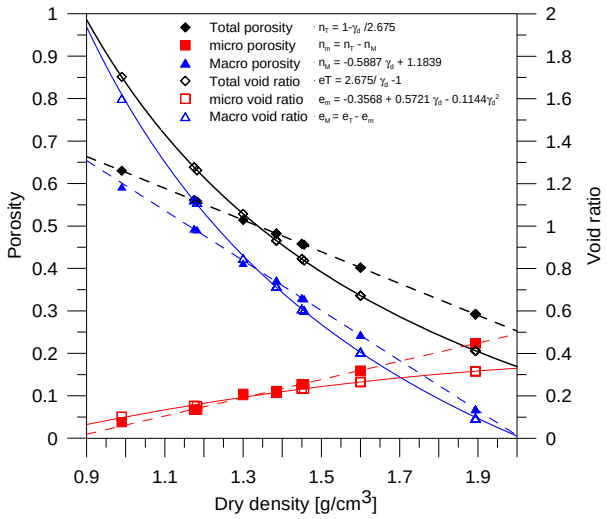

Figure 5-1: Relation between micro, macro and total porosities vs dry density

Microstructure and macrostructure initial saturation degree

The flux of water in the double porosity THM formulation is described by means of Darcy's law; the movement of water is a consequence of the total water potential acting on the soil. In the case of double-porosity media it is possible to have a non equilibrium between the potentials of the micro and macrostructure.

For the simulations of the infiltration tests it was assumed that the water potentials associated to each pore level were initially non-equilibrated, i.e. micro and macro suctions were considered to be different.

The assumption was made to account for the differences in water content existing between powder and pellets at the moment of sample preparation. In fact a limited internal movement of water from powder to pellets before hydration can be inferred on the μCT tomography images (see Figure 5-2).

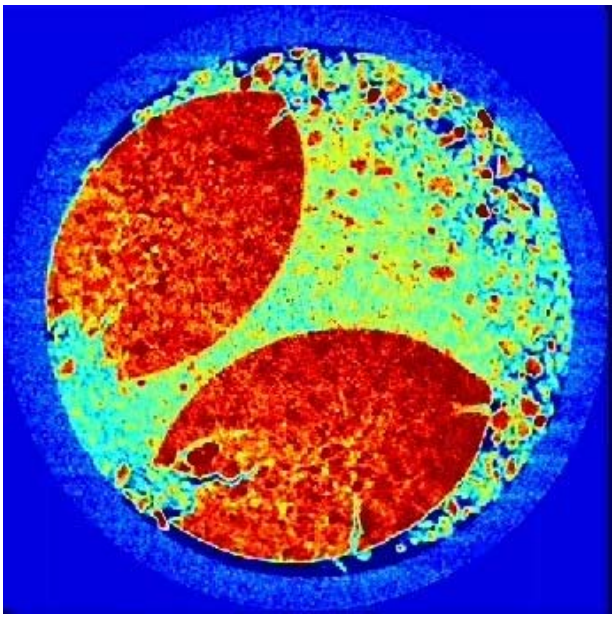

Figure 5-2: Image obtained before hydration on a sample studied by means of μC tomography. (van Geet *et al*, 2005a)

Knowing the saturation degree, the initial suction in each structure is assigned in accordance to the retention curve adopted. However there is not a simple way to figure out how much water is present on micro and macrostructures.

The initial amount of water in the samples was very low as shown in Table 5-2. The pellets had a water content of 5%, the powder of FoCa7 clay used in two of the samples had a water content of 12%, and the powder of FoCa RESEAL had a water content of ~5%.

For the samples studied, due to the low value of water content in powder and pellets, it is to be expected that most of this water is strongly attached to the mineral surface, i.e. it should be microstructural water. In samples with a water content of 12% in the powder it is probable that a slight amount of water may exist in the macrostructure.

The assumption made to overcome the problem of estimating the amount of water in the micro and macrostructure of pellets and powder was to consider a percentage of the water volume for each structure.

Three percentages were considered. For the pellets 70% of the water volume was considered microstructural water, a value similar to the proportion of micropores. For the powder two values were considered, one for each density. For samples with the powder compacted to 1.36 gr/cm^3, 50 % of the water volume was considered to be on the microstructure. Finally, for the low density samples with the powder compacted to 1.18 gr/cm^3, 25 % of the water volume was considered to be microstructural water.

This is a coarse estimation of the proportion of water in each structure, but as it will be seen from the results, there is a good correspondence between the measured water intake and the numerical estimations. It is also believed that the important fact to take into account is the very dry initial state of the sample and the fact that the inclusion of water at the beginning of the tests is mainly

done by the microstructure. This is achieved by adopting a high value for the leakage parameter Γ.
Once it was decided to use the previous percentages of micro and macro water on powder and pellets, calculations of the saturation degrees of the macro and microstructure were performed. The estimation of the initial suction values for each structure was made by means of the retention curves. The values obtained for each sample will be presented together with the simulation results.

Hydromechanical parameters

The values for the parameters used by the different equations are shown hereafter. They were estimated on the basis of the tests made during the project and from values found in the literature.

The parameters needed for the hydraulic constitutive equations correspond to the retention curve, the intrinsic and the relative permeability models.

The parameters for the retention curve of the microstructure were assessed by fitting the experimental values obtained with high density samples. On the other hand, the parameters for the macrostructure were obtained by fitting the results of tests made on samples with low values of dry density. Both fits were constrained to follow closely the values obtained under isochoric conditions, as well as avoiding large suction values at low degrees of saturation. The curves can be seen in Figure 5-3 and Figure 5-4.

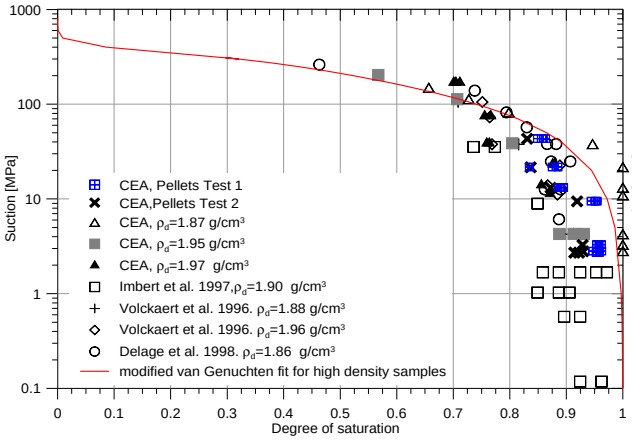

Figure 5-3: Retention curve for micro dominated samples

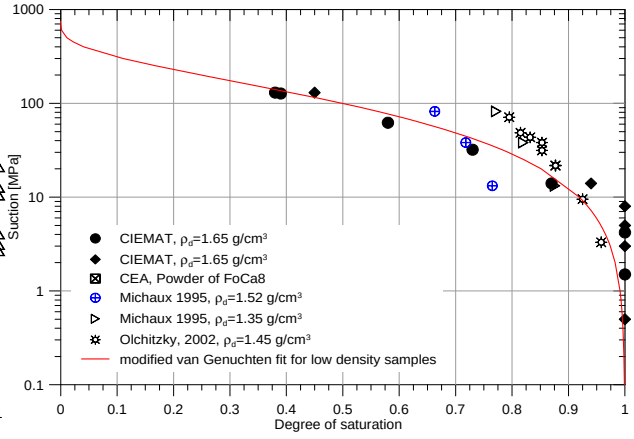

Figure 5-4: Retention curve for macro dominated samples

For the intrinsic permeability, the values of the parameters were assessed using both the results of tests performed on mixtures of powder and pellets, and the back analysis of the numerical results. The adopted curves are shown in Figure 5-5.

For the relative permeability, a low value of the exponential is used for the macrostructure, while a higher value is adopted for the microstructure, to account for the fact that water in micro pores has a lower mobility. Both values were assessed by back analysis of the infiltration tests.

In Table 5-3 the parameters for each hydraulic constitutive model are summarized.

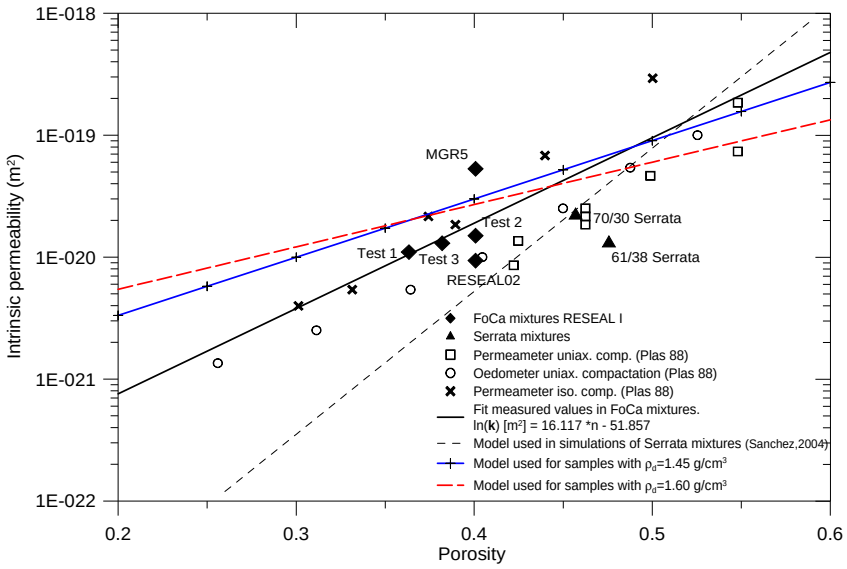

Figure 5-5: Model used for the variation of intrinsic permeability with porosity for two different sample densities

Table 5-3: ***Hydraulic parameters used in simulations***

Constitutive law	Analytic expression	Parameter	Macro	Micro
Retention curve	van Genuchten's expression $S_e = \left(1+(s/P_0)^{\frac{1}{1-\lambda_0}}\right)^{-\lambda_0}\left(1-\frac{s}{P_d}\right)^{\lambda_d}$ with $S_e = \frac{S_l - S_{rl}}{S_{ls} - S_{rl}}$	*Po (MPa)* λ_0 *Pd (MPa)* λ_d S_{ls} S_{rl}	15 0.064 750 3.899 1.00 0.0	378.95 0.899 800 2.243 1.00 0.00
Intrinsic permeability	Kozeny's expression High density samples γ_d=1.60 g/cm^3 $k_j = k_0 \exp^{b(\phi_j - \phi_0)}$	K_0 (m^2) ϕ_0 b	3.0x 10^{-20} 0.40 8.00	2.8 x 10^{-20} 0.40 8.00
	Low density samples γ_d=1.45 g/cm^3 $k_j = k_0 \exp^{b(\phi_j - \phi_0)}$	K_0 (m^2) ϕ_0 b	3.0x 10^{-20} 0.40 11.00	2.8 x 10^{-20} 0.40 11.00
Relative liquid conductivity	Power law $K_{rl} = AS_e^{\ B}$	*A* *B* S_{ls} S_{rl}	1 3.0 1.00 0.00	1.0 3.0 1.00 0.00
Leakage parameter	$\Gamma^w = \gamma(\Psi_1 - \Psi_2)$	γ *(kg/s/m^{3}MPa)*		5.00x10-5

With respect to the mechanical constitutive model, the adoption of the parameters was made taking into account the information available on tests performed on similar materials. For the approximation of the elastic parameters of the BBM, the tests of Figure 5-6 were used; they were performed on samples of compacted FoCa clay.

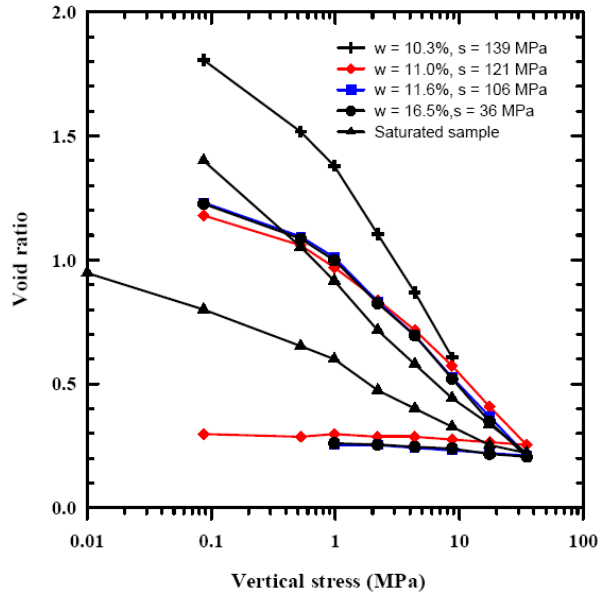

Figure 5-6: Oedometer curves of compacted FoCa clay at distinct water contents. From Volckaert *et al.* 2000

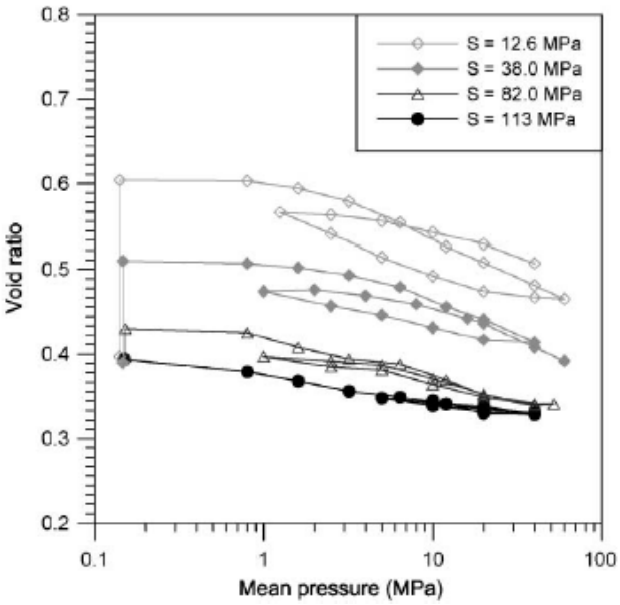

Figure 5-7: Evolution of void ratio during loading-unloading cycles with controlled suction. From Volckaert *et al.* 2000

The elastic compressibility coefficient (κ) shown by the samples is between 0.09 for saturated conditions, and 0.015 for a suction of 110 MPa .

These tests were also helpful for the estimation of the plastic parameters. The stiffness against changes in the net mean stress for virgin states at saturation (λ_0) presented a value of 0.196, as well as a value of 0.22 for higher suctions.

The approximate shape of the loading-collapse curve was obtained by means of the tests presented in Figure 5-7 and by back analysis of the results.

For the microstructural behaviour, the tests presented in Figure 5-8 were used. They were performed on samples compacted at a high dry density (γ_d=1.85 g/cm^3). These tests show an almost elastic response when submitted to several suction and load reversals. The slope of the void ratio variation with suction is between 0.032 and 0.044.

For the influence of the microstructural deformations on the macrostructure, only one mechanism activates in all the tests, the microstructural swelling MS (s_s=60 MPa). Negative values of the interaction function are adopted when the ratio p/p_0 equals one to induce hardening on the macrostructure.

The final values adopted for the mechanical constitutive models are summarized in Table 5-4. Due to the different initial conditions at compaction in some of the samples, the model parameters change slightly for some tests. In the following sections more insight is given into those differences. Given a certain dry density, the tests depart with approximately the same amount of micro and macroporosity. An isotropic behaviour is assumed since no information on the lateral stress was obtained during the infiltration tests. The effectiveness of the plastic parameters cannot be estimated since only one wetting cycle was performed.

The tests' simulations have been performed using a 1-D boundary value problem, with elements of 0.05cm high (size) as well as restricted displacements on both ends. Hydration is simulated prescribing a constant pressure of 0.01 MPa on one side.

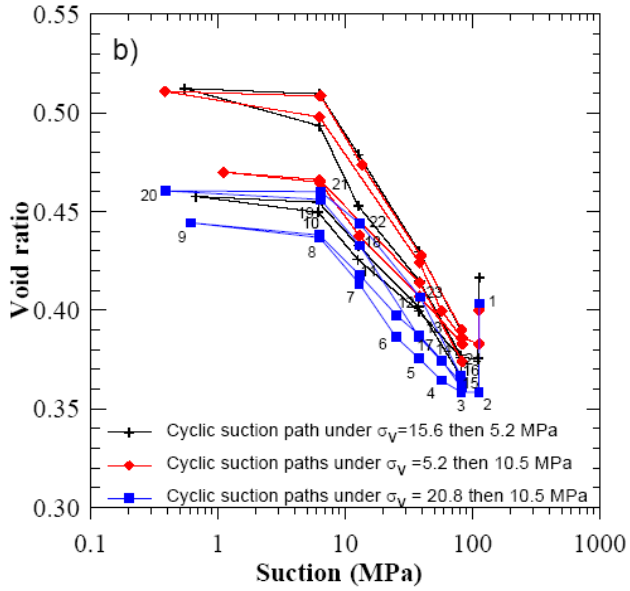

Figure 5-8: Void ratio suction relationship for three specimens following cyclic suction paths under constant vertical stress.

Table 5-4: Mechanical parameters used in simulations

Constitutive law	Analytic expression	Parameter	Low density samples	High density samples
BBM Elastic part	$d\varepsilon_v^e = -\frac{\kappa}{1+e_M}\frac{dp}{p} - \frac{\kappa_s}{1+e_M}\frac{ds}{s+p_{atm}}$	κ κ_s	0.1 0.003	0.1 0.003 0.300
Yield locus	with $p_0 = p_c\left(\frac{p_0^*}{p_c}\right)^{\frac{\lambda(0)-\kappa}{\lambda(s)-\kappa}}$ and $\lambda(s) = \lambda(0)\,(r + (1\text{-}r)e^{-\beta s})$	p^*_0 (MPa) p_c (MPa) r $\lambda(0)$ β (MPa^{-1})	0.14 0.005 0.65 0.23 0.025	0.14 0.005 0.72 0.20 0.035
BExM Microstructural behaviour	$K_m = \frac{1+\overline{e_m}}{\kappa_m}\hat{p}$	κ_m	0.045	
Interaction functions Microstructural swelling	$f_s = f_{s0} + f_{si}\left(1-\frac{p}{p_0}\right)^{ns}$	f_{s0} f_{si} n_s	−2.0 1 2	

5.2.1.2 Results and discussion

Tests with dry density = 1.45 g/cm^3

Among the tests performed by CIEMAT at γ_d= 1.45 g/cm^3, the ones labelled MGR7 and MGR9 are analyzed. CEA performed one test at the same density labelled RS2J. Tests MGR7 and RS2J were 5 cm in height, and test MGR9 was 10 cm in height. The influence of the size of the sample is examined.

Figure 5-9 shows the measurements of swelling pressure of the three tests. It can be seen how, at the beginning, the three samples show a similar behaviour, a quick increase in swelling pressure to approx 1 MPa and followed by its reduction. Once pressure recovers the differences between the tests are more evident. For instance, tests RS2J and MGR9 present a final swelling pressure lower than the peak. Test MGR7, on the other hand, shows a higher value of swelling pressure on the trough and a final pressure equal to the peak (an increase in injection pressure from 0.1 MPa to 0.6 MPa in this test caused a sudden final increase to 1.16 MPa). Besides the height, the differences between the tests were the diameter (10 cm for MGR7 and 12 cm for RS2J and MGR9) and the water content of the powder (w_{powder}=12% in MGR7 and w_{powder}=5 % in RS2J and MGR9). The latter aspect was dominant.

In Gens *et al*. (2009) each aspect of these tests is analysed in detail. Comparisons between the laboratory results and the simulations are also made. Here, only the modelling results of test MGR7 are given as a matter of example.

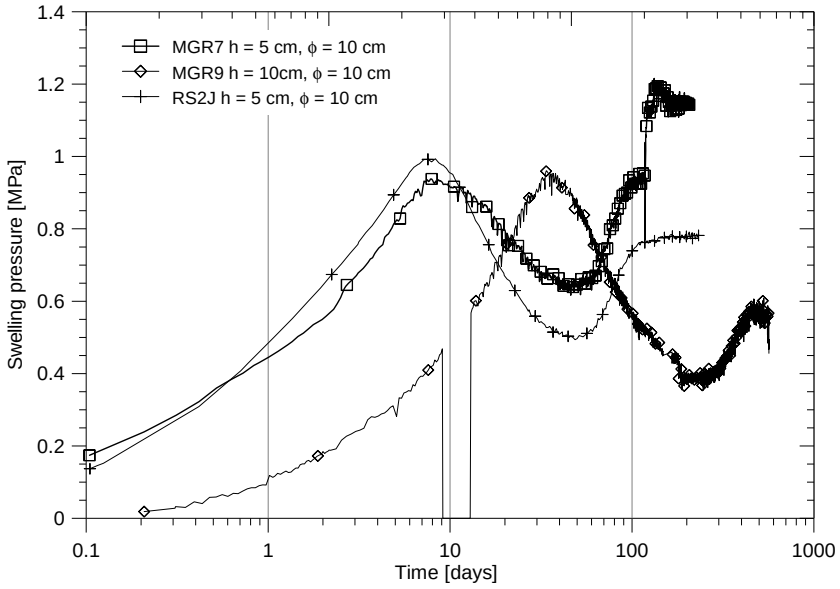

Figure 5-9: Results obtained for infiltration tests with γ_d=1.45g/cm^3

Test MGR7

The infiltration test MGR7 was performed with a 50/50 mixture of RESEAL II pellets (with an initial water content of w=5%, S_l = 0.298) and FoCa7 powder (w=12%, S_l = 0.251). Globally the water content of the sample was 8.3% (S_l = 0.263). The test lasted 217 days. At the end of the hydration the pellets were not apparent, although a detailed inspection allowed distinguishing areas of different coloration due to the fact that FoCa pellets and FoCa7 powder, have somewhat different colours.

To start with the numerical simulations, the initial conditions were calculated and values were obtained for the micro and macro porosities. The initial suctions are summarized in Table 5-5 and were obtained using the retention curve adopted for each structure (see Figure 5-3 and Figure 5-4).

Table 5-5: Numerical initial conditions for test MGR7

n_T	n_M	n_m	e_M	e_m	s_{Macro}	s_{micro}
0.458	0.331	0.127	0.610	0.235	212 MPa	285 MPa

A first thing to notice from the perspective of the mechanical constitutive modelling is that, in these low density samples a large proportion of the porosity is macrostructural (72% in this case). Another thing to notice is that the micro suction is higher than macrostructural suction. This means that, during the first moments, the microstructure will take water from the macrostructure, causing some shrinkage of the latter. The movement of water from zones of higher potential to zones of lower potential was appreciated on the sample studied by means of µCT tomography (van Geet *et al*, 2005a).

The model simulates a macrostructural contraction caused by the increase in suction, which can be appreciated in Figure 5-10. In this graph the macrostructural liquid pressure[5] is plotted against the macro specific volume (v_M=1+e_M) in three elements, located at the bottom (close to the hydration boundary), middle and top of the sample. It can be seen how at the beginning and during a short period of time, the elements that are not in contact with the hydration front increase their suction, suffering a contraction. This contraction is considered elastic.

[5] liquid pressure is plotted with a change of sign in order to be able to use a logarithmic scale

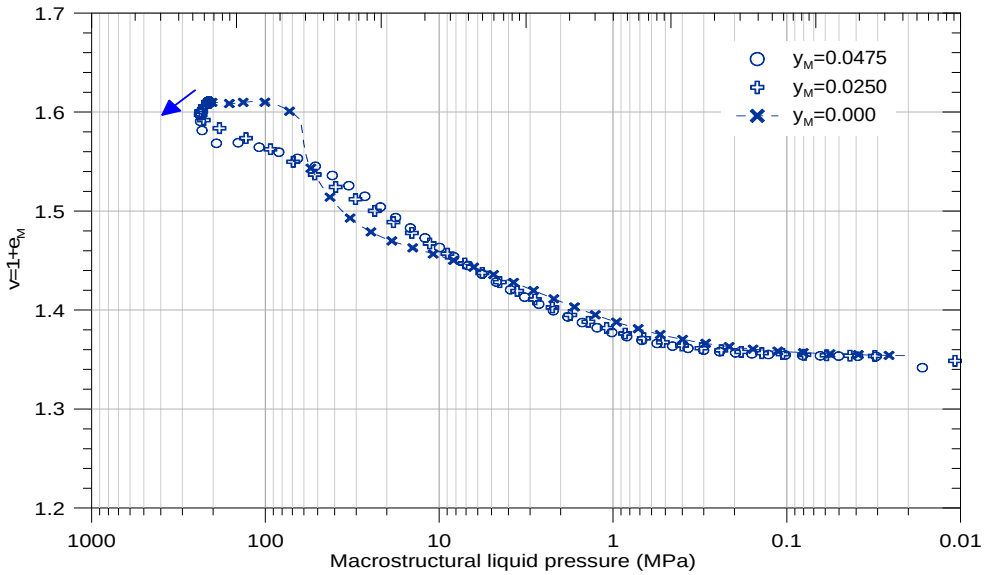

Figure 5-10: Macrostructure liquid pressure vs specific volume. Test MGR7

Figure 5-11 shows the evolution in time of micro and macro liquid pressures. The values presented correspond to the same three elements as before located at the bottom, middle and top of the sample. Symbols are for macrostructural values and lines for microstructural values.
It can be seen how at the beginning of the tests micro and macro suctions are different, and how equilibrium is reached due to the water mass exchange. The element close to the hydration boundary (y_m=0.00) shows, for a longer period, the differences in the liquid pressure. Farther elements soon reach equilibrium and, doing so, microstructure hydrates and macrostructure dries.

Figure 5-12 shows the vertical net stress versus the macrostructural liquid pressures, together with the initial "LC" yield line[6]. It can be seen that, when water starts entering the sample, suction reduces in elements close to the hydration boundary and swelling pressure starts to develop. The stresses approach the LC line and "touch" it at high values of suction.

The drop or collapse presented by the tests is a typical behaviour found in swelling pressure tests of clays compacted dry of optimum (Alonso *et al*., 1987), and which have developed large pores during compaction. When an expansive soil is submitted to wetting at zero volume change, a sharp increase in swelling pressure is developed. In this case it will be mainly due to the pellets expansion, as can be seen in Figure 5-13b. Since the macrostructure has an open structure (measured by a ratio p/p_0 that equals one) the confining pressure reduces as wetting continues, in order to maintain an overall zero volume change.

[6] for simplicity the LC line evolution is not drawn

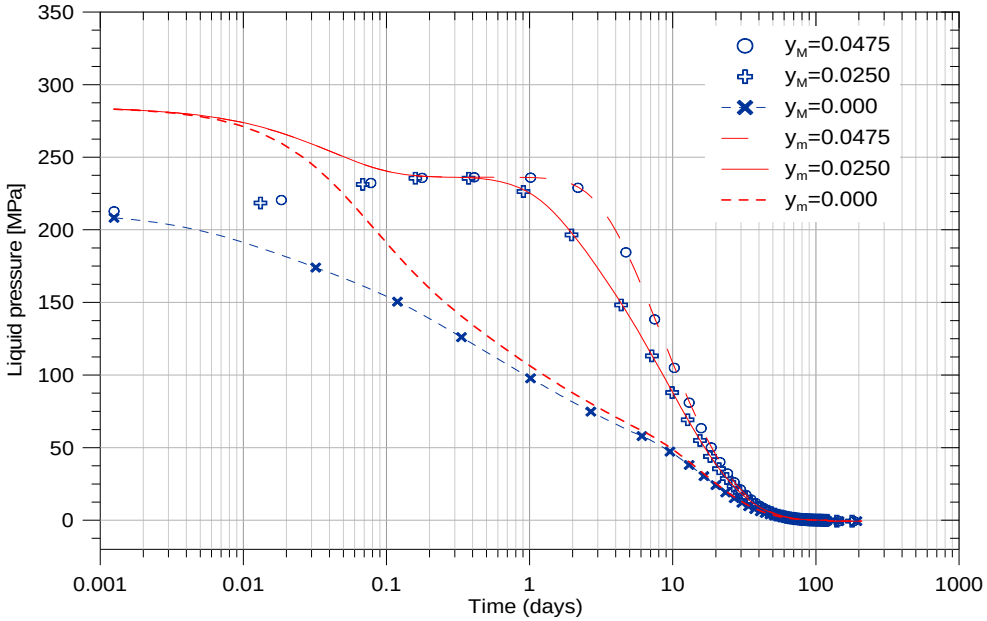

Figure 5-11: Micro and macro liquid pressure evolution in different elements. Test MGR7

Figure 5-13 helps to illustrate all the processes that the model considers as hydration proceeds. Figure 5-13a contains the swelling pressure evolution in time. Figure 5-13b shows the evolution of the specific volumes and Figure 5-13c presents the evolution of the saturated preconsolidation pressure p_0*, which is the hardening parameter of the model.

Figure 5-13b shows (with symbols) that the macrostructure of the element in contact with water (y=0.0) increases its void ratio slightly at the beginning of the test, but then starts to collapse after touching first the *MS* yield line (approx at t~5 days) and later the *LC* yield line (approx at t~7 days).

When this first element reaches the liquid pressure equilibrium between structures (in Figure 5-11) it shows the same volumetric deformations than the rest of the elements (in Figure 5-13b).

The swelling pressure continues to rise after the collapse of the first element (an inflexion point can be appreciated at Figure 5-13a. It is not until the rest of the elements touch the *MS* and the *LC* yield lines and start to collapse, that the swelling pressure drops (t~14 days).

As shown in Figure 5-13b, the microstructure starts to swell as soon as the water enters. The high value of the parameter Γ allows the water to enter easily on the microstructure.

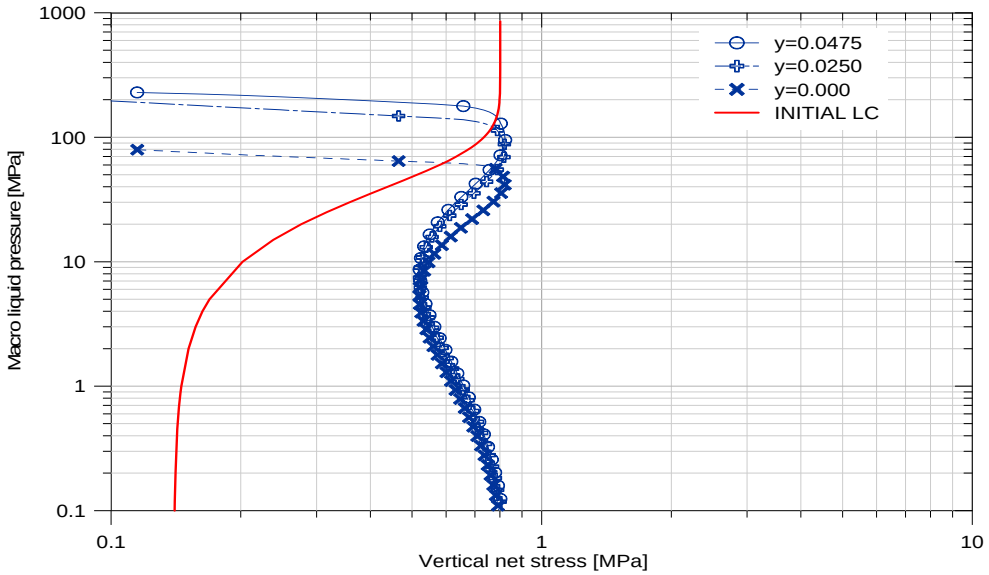

Figure 5-12: Vertical net stress versus macrostructural liquid pressure. Test MGR7

While the macrostructure collapses, the microstructure keeps swelling. This fact counteracts the collapse of the macro. At around 35 days the swelling pressure stops decreasing, micro has been able to stop the collapse and at approximately 50 days, the microstructure reverses the tendency and swelling pressure rises again to its final value of 1.17 MPa.

At the end, in the case of the simulations of test MGR7, the macrostructural void ratio has changed from e_{M0}= 0.61 to e_{Mf}~0.35, and the microstructural void ratio has changed from e_{m0}= 0.24 to e_{Mf}~ 0.49. On the presentation of test MGR9 it will be shown how the porosity evolution follows qualitatively the porosity evolution of mixtures as shown by MIP tests performed after saturation.

Figure 5-13c shows the moment at which the saturated preconsolidation pressure starts to increase its value in each element. After the first element reduces the suction to the established value of 60 MPa, the MS mechanism is activated. The first part of the plastic strains causing hardening, are induced by the activation of this mechanism. Soon the same element touches the *LC* yield line, and both mechanisms are active. Shortly after this, the rest of the elements, touch first the *LC* yield line, then the *MS* line, and the effects are reflected on the evolution of the swelling pressure.

At this point, it is interesting to compare the numerical simulations with the measurements made in laboratory. With respect to the swelling pressure evolution, the correspondence with the measurements can be seen in Figure 5-14 and Figure 5-15. The parameters of the macrostructural stiffness for virgin states $\lambda_{(s)}$, were slightly changed to better reproduce the lower peak pressure and the higher final pressures of this test, when compared to the others. The values used were β=0.034, λ_0=0.185 and r=0.675. Since the sample was compacted with high water content on the powder, those changes of stiffness are possible.

The model is able to capture the kinetics of the swelling pressure evolution registered by the test. The good correspondence of the evolution of the swelling pressure in time has been achieved in great part due to the good simulation of the water intake.

In Figure 5-16 the water intake obtained in the simulation is compared with the water actually measured. As can be observed the evolution is very similar. If the water intake is not well captured, similar shapes of the swelling pressure evolutions can be achieved, but not the time and rate of swelling pressure recovery.

Towards 120 days an increase on injection pressure was made on the test. The simulation considers this increase although the water intake was not further measured in the laboratory.

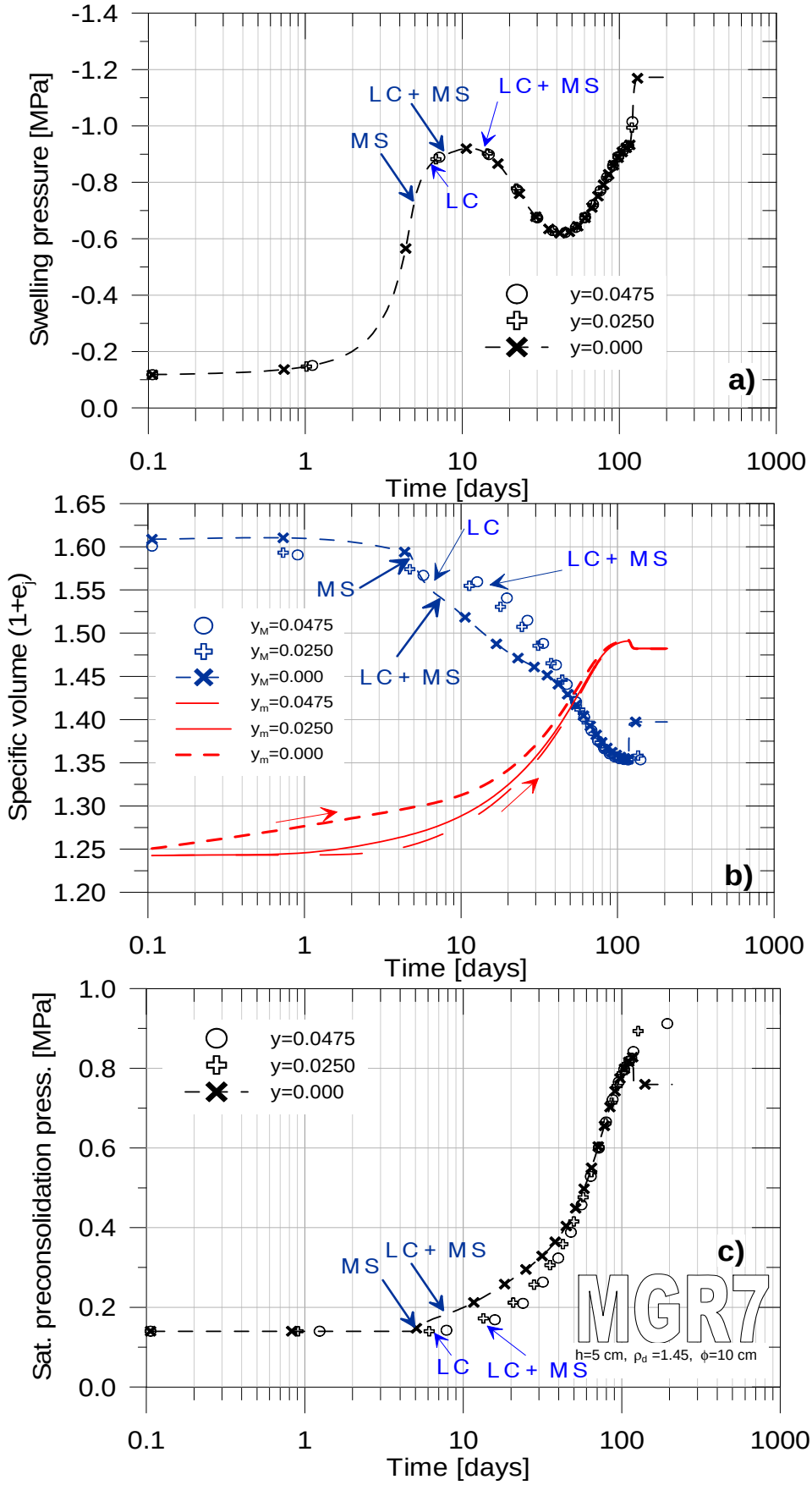

Figure 5-13: Simulation results for test MGR7. a) Evolution in time of the swelling pressure, b) evolution of the specific volume and c) evolution of the saturated preconsolidation net stress.

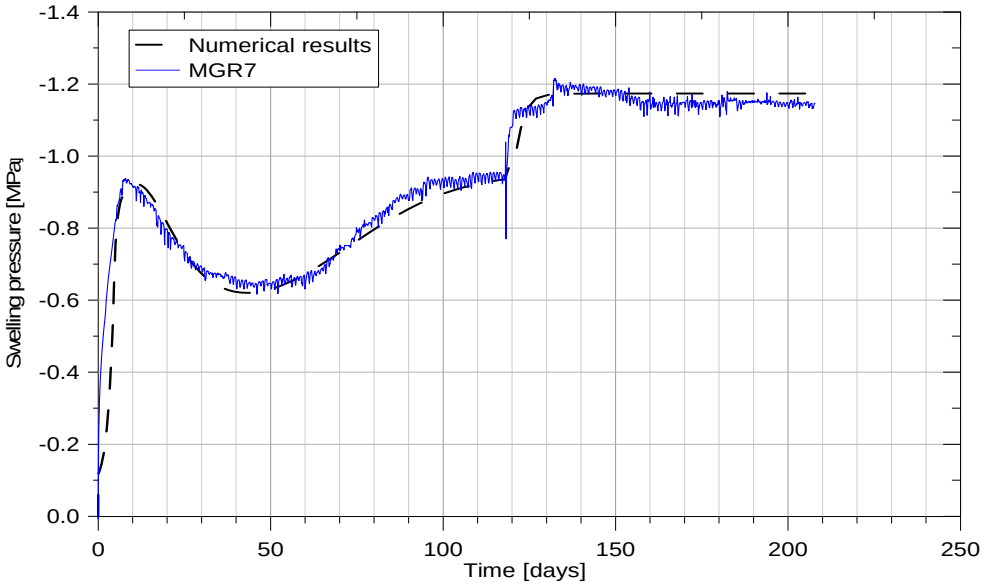

Figure 5-14: Swelling pressure evolution. Comparison between test and computations for test MGR7. Linear time scale

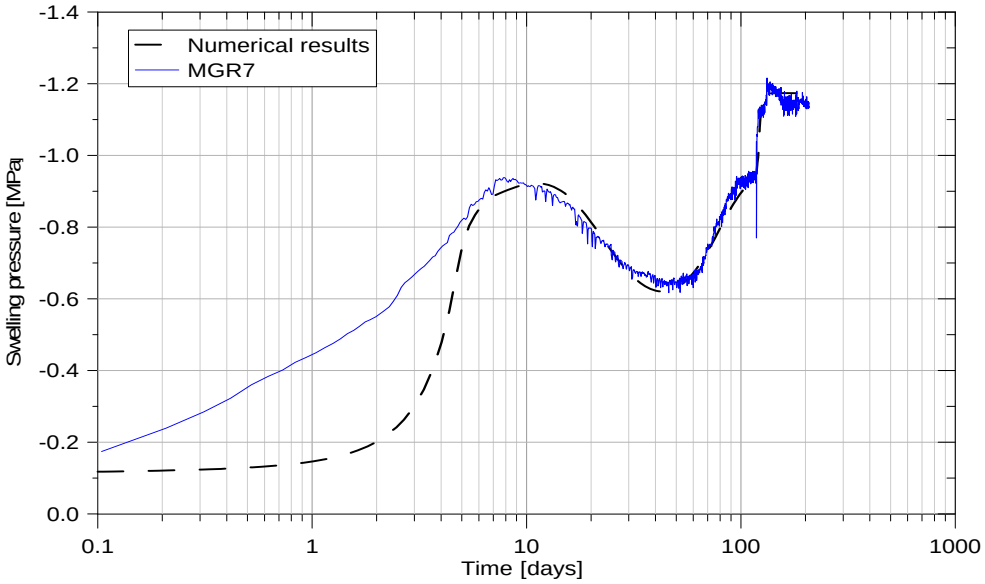

Figure 5-15: Swelling pressure evolution. Comparison between test computations for test MGR7. Logarithmic time scale.

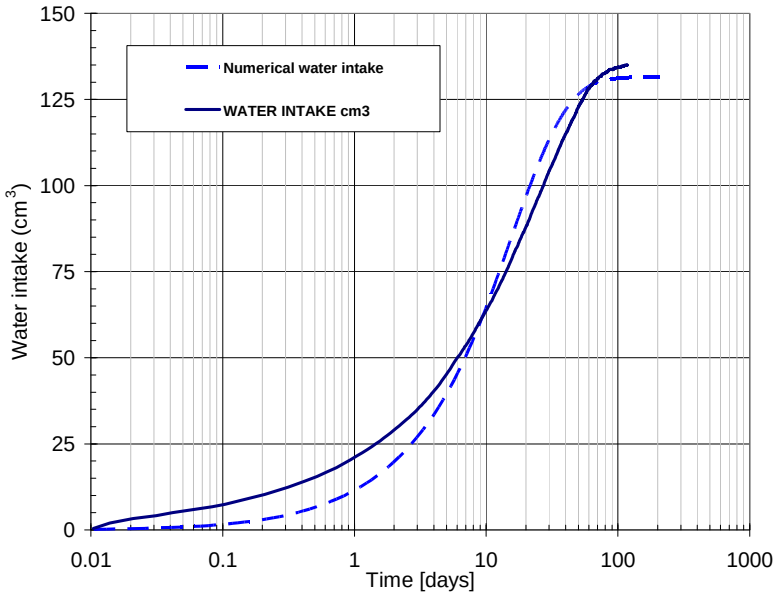

Figure 5-16: Water intake evolution. Comparison between test and computations. Test MGR7.

Remarks on Tests with Dry Density = 1.45 g/cm^3

The modelling of the infiltration tests performed on the mixtures of pellets/powder compacted at a low density of 1.45 kg/m^3 was performed successfully (see also Gens *et al*. (2009) for modelling details on test MGR9 and RS2J). Both the large collapse of the macro and the recovering of the swelling pressure have been simulated by means of a double porosity constitutive model, that explicitly takes into account the effects of each structure in a simplified manner.

The proportion of micro and macroporosity for tests compacted at a dry density of 1.45 g/cm^3 was considered to be 28% of micropores and 72% of macropores, in accordance with the MIP results on FoCa clay pellets and others clays compacted at similar densities.

For the initial saturation degree of each structure it was decided to consider that, concerning the pellets, 70% of the water was inside the micropores. For the powder it was considered that 25% of the water was allocated on the micropores.

The samples are largely dominated by the characteristics of the macrostructure, as has been seen in the results of the numerical simulations presented.

All the samples developed a sharp increase on the swelling pressure shortly after the start of the hydration. The test MGR9 took almost 10 days due to its larger size.

After this first increase, the stress path of the element in contact with the water entrance, "touches" either the MS yield line or the LC yield line, depending on the hydration rate. Due to the small proportion of micropores, the moment at which the MS plastic mechanism starts to act is known but its effects are not easily appreciated. This is due to the small influence defined by means of the interaction functions.

Then the collapse is dominated by the openness of the macrostructure. The simulations show that hydration after touching the MS and the LC yield lines causes a reduction in the swelling pressure, due to the collapse of the macrostructure (reflected as a reduction of its void ratio).
The effects of the microstructure are evident in the recovering of the swelling pressures. It is at this point when differences between tests are evident. The slope of the drop on the swelling pressures, the minimum value achieved and the maximum value reached after recovering differ from one test to the other. Differences are seen mainly at the end of the tests, when saturation is reached (see Figure 5-9).

For instance, test MGR7 had a higher water content at compaction. As mentioned, compacting on the wet side of optimum causes the development of small pores. The possibility of having a larger proportion of micropores in sample MGR7 was considered as a possible cause of the higher final swelling pressure of this test. Simulations were made considering a larger proportion of micropores. However, good results were not achieved.

In the simulations presented, the irrecoverable deformations caused by the microstructure on the macro have been considered small. The model controls those effects by means of two interaction functions. The existence of an elastic domain, in which the microstructural swelling does not cause plastic deformations on the macrostructure, was also considered.

For test MGR7, this domain was reduced and the influence of the microstructural swelling on the macrostructure was increased. The target was to produce a larger hardening on the macrostructure, attaining larger swelling pressures at the end. However, the influence of the interaction functions was required to be different in each test, causing more hardening in test MGR7 and less in test MGR9. Good results again were not achieved.

The opposite possibility of considering a higher proportion of macropores in tests RS2J and MGR9 was also studied. The interaction functions were also changed to consider the reverse effect, a softening of the macrostructure caused by the expansion of the microstructure. This was done by considering positive values of the interaction functions at $p/p_0 = 1$. Again good results were not achieved.

Due to the good results obtained when considering different values of the stiffness against virgin states, $\lambda_{(s)}$, it was decided to change only this parameter from one test to another. This change is plausible since the initial water content at compaction changed from test to test.

Tests with dry density = 1.60 g/cm3

The infiltration tests at a dry density of 1.60 g/cm^3 were performed by CEA. They are labelled RS2B, RS2E and RS2F.

The differences between those tests were the height (from 3 to 12 cm) and in two of the tests the initial water content of the powder.

Figure 5-17 shows the swelling pressures obtained in laboratory. It can be seen how, with exception of test RS2C, they exhibit a similar behaviour. A very small reduction of the swelling pressures with sample height can be noted.

As expected, swelling pressures are considerably higher than those obtained with the low density samples discussed in the previous section. Peak pressures are around 2.6 MPa (instead of 1

MPa), final pressures are around 3.2 MPa. Final values achieved are higher than peak values. The drop of the swelling pressures after the peak is similar in samples B, E and F.

The parameters applied in the simulations of these tests are shown in Table 5-4. The percentage of pores considered to be micropores is 40%. The proportion of water considered to be on the microstructure at the beginning of the tests is 70% for the pellets and 50% for the powder.

As in previous section, some samples were compacted with a high water content in the powder, the effects are discussed in Gens *et al*. (2009) where each test is analyzed in detail and simulation results compared with test results. Here, only test RS2B is described in detail as a matter of example.

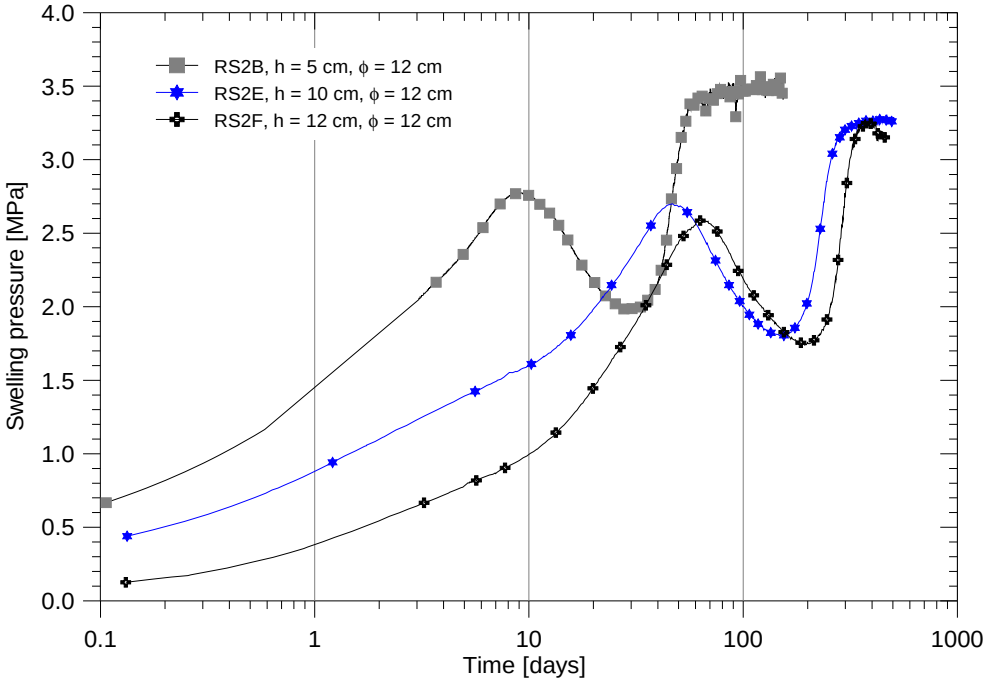

Figure 5-17: Results obtained for oedometer tests with γ_d=1.60 g/cm^3

Test RS2B

Infiltration test RS2B was performed with a 50/50 mixture of RESEAL II pellets (w=4.3%, S_l=0.28) and FoCa7 powder (w=11.8%, S_l = 0.34), the sample water content was w=8% (S_l=0.32%).

The height of the sample was 5 cm and its diameter 12 cm. The test lasted 150 days, 50 days less than test MGR7 and 78 less than test RS2J, all with the same height. The shorter duration of this test might have been a consequence of the sample preparation. This fact could not be checked since no tests were performed to the sample at the end of hydration to determine the final water content or the final apparent density.

To be able to simulate the fast development of hydration, the spring parameter of the boundary condition was increased in order to prescribe the injection liquid pressure more immediately available than in previous cases (see Olivella, 2002).

The values obtained for the micro and macro porosities and the initial suctions are summarized in Table 5-6. With the hypothesis made about porosity and water partition between structures, the suction value obtained for the microstructure is just a little higher than the value obtained for the macro.

Table 5-6: Numerical initial conditions for test RS2B

n_T	n_M	n_m	e_M	e_m	s_{Macro}	s_{micro}
0.402	0.159	0.243	0.407	0.265	206.6MPa	237.2 MPa

In the previous section, it was shown that the two tests compacted with high water content in the powder showed a lower final swelling pressure than samples compacted with dry powder. Test RS2B on the other hand, shows a slightly higher swelling pressure than the rest of the tests with the same dry density but with lower water content in the powder.

Two actions were made to be able to simulate the results of this test with the parameters shown in Table 5-4 but departing from a lower suction than in the rest of the tests. The first was to assume that suction between all the samples did not differ excessively at low degrees of saturation. To achieve this, the retention curves used and presented in Figure 5-3 and Figure 5-4 are very flat between 10 and 30% of the saturation degree. The second action was to increase the preconsolidation pressure parameter from 0.375 to 0.45. In the following Figures, the results obtained on the simulations of this test are shown.

Figure 5-18 shows the variation of the specific volumes (micro and macro) as liquid pressures increases. The macrostructure of the first element swells at the beginning of the test. Afterwards, the stress path touches the *MS* yield line and its void radio reduces drastically. The rest of the elements are first compressed due to the expansion of the microstructure. When their suctions reduce, they swell a little and then start collapsing.

Figure 5-19 presents the evolution in time of the liquid pressure. If compared with the results obtained with test MGR7 (Figure 5-20), major differences are observed for the element in contact with hydration; it hydrates faster. The rest of the elements show a very similar evolution.

Figure 5-18 presents the evolution in time of the liquid pressure. If compared with the results obtained with test MGR7 (Figure 5-10), major differences are observed again for the element in contact with hydration; it hydrates faster. The rest of the elements show a very similar evolution.

In Figure 5-20, the vertical net stress versus suction is presented. The increase of the vertical net stress as liquid pressures raises can be seen, the stresses reach values of 3 MPa. The position of the *LC* yield curve in this test defines a larger elastic domain.

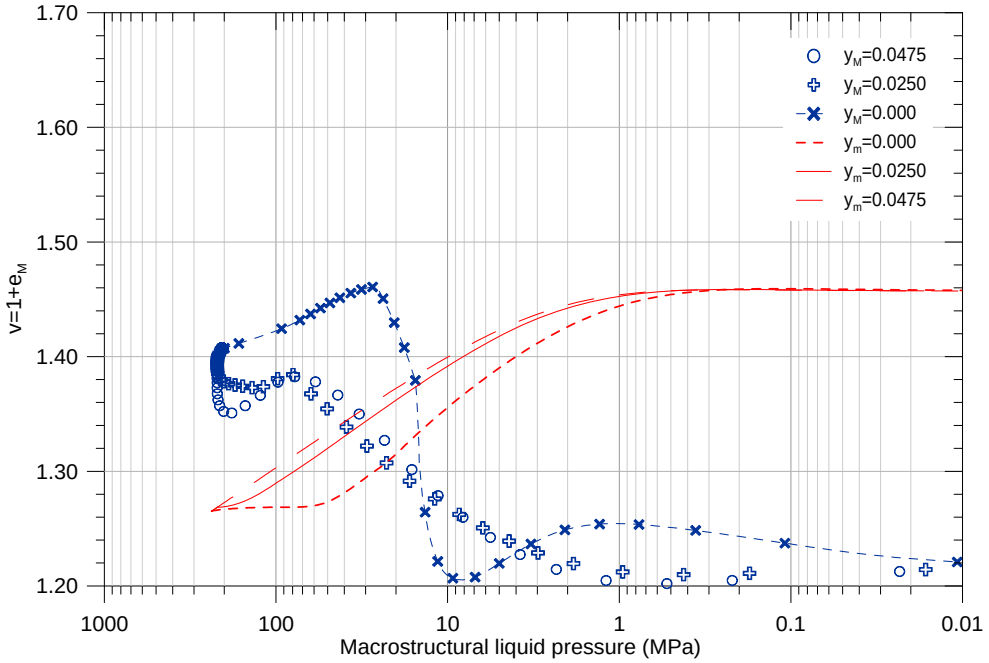

Figure 5-18: Macrostructural liquid pressure versus specific volume. Test RS2B.

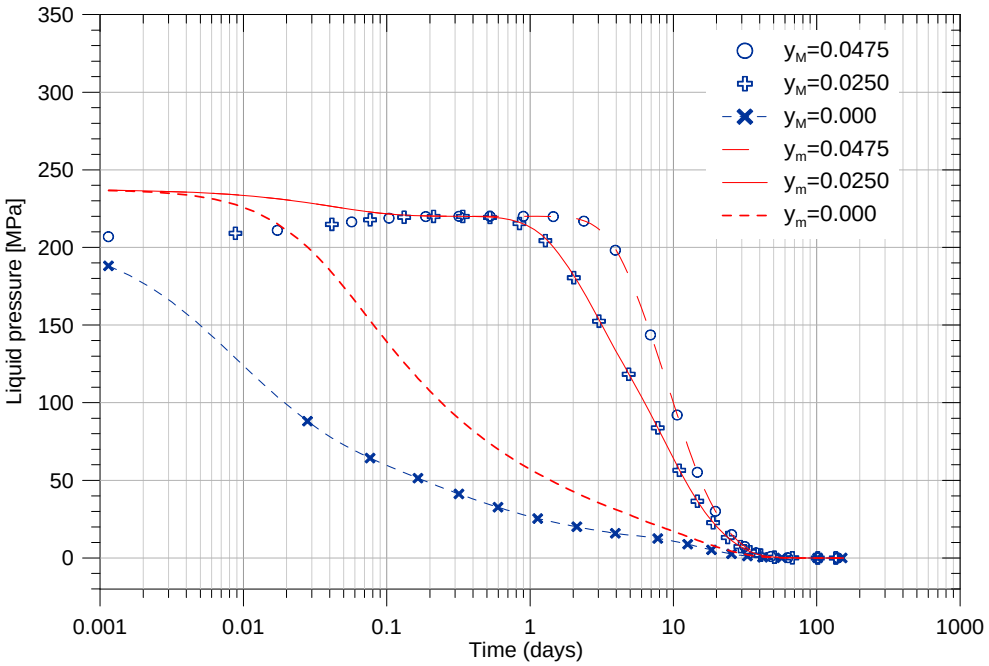

Figure 5-19: Time evolution of liquid pressures. Test RS2B.

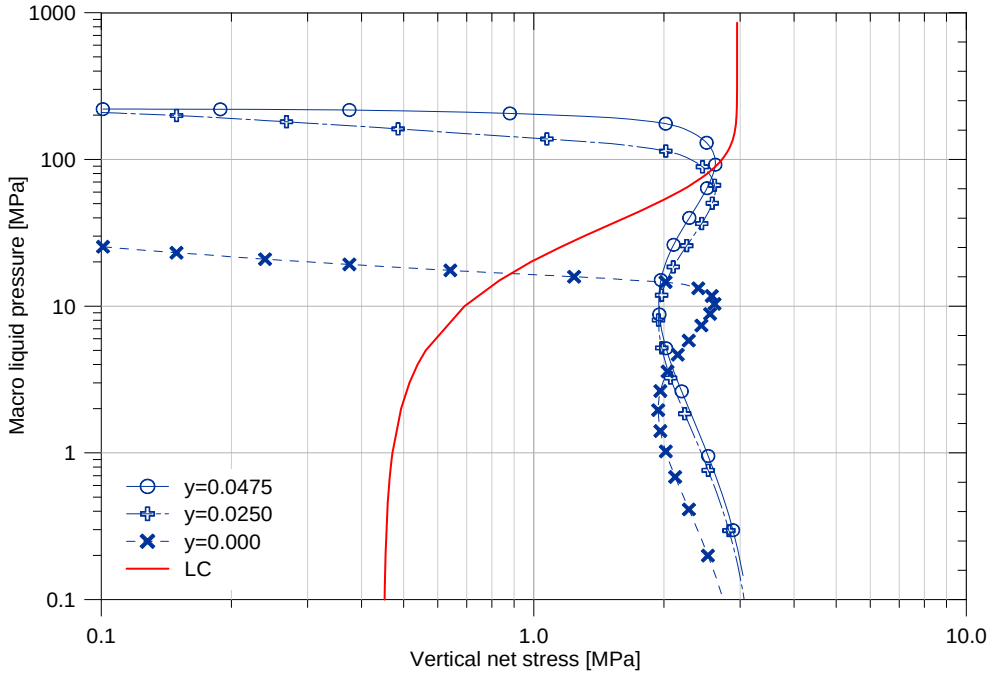

Figure 5-20: ***Vertical net stress versus Macrostructural liquid pressure. Test RS2B.***

The evolution of the swelling pressures, the specific volume and the saturated preconsolidation pressure are shown in Figure 5-21a, b and c. The influence of the fast hydration can be seen from the quick arrival of the stresses (t~3 days) to the *MS* and *LC* yield lines. It can also be noted in the evolution of the specific volumes and on the hardening parameter. The time at which the microstructure is completely saturated and only the *LC* mechanism keeps acting on the macrostructure can also be observed. At around 25 days, the microstructural swelling counteracts the collapse and the swelling pressure rises again, the final value achieved is ~3.4 MPa.

At the end of simulations of test RS2B, the macrostructural void ratio changed from e_{M0}=0.407 to e_{Mf}=0.21, the microstructural void ratio changed from a value of e_{m0}=0.265 to e_{mf}=0.457.

The evolution of the hardening parameter is shown in Figure 5-21c. The effects of the microstructural deformations on the macrostructure are more evident than in previous tests. This is due to the fact that there is a higher influence of the microstructural deformation for this density as a result of closer packing.

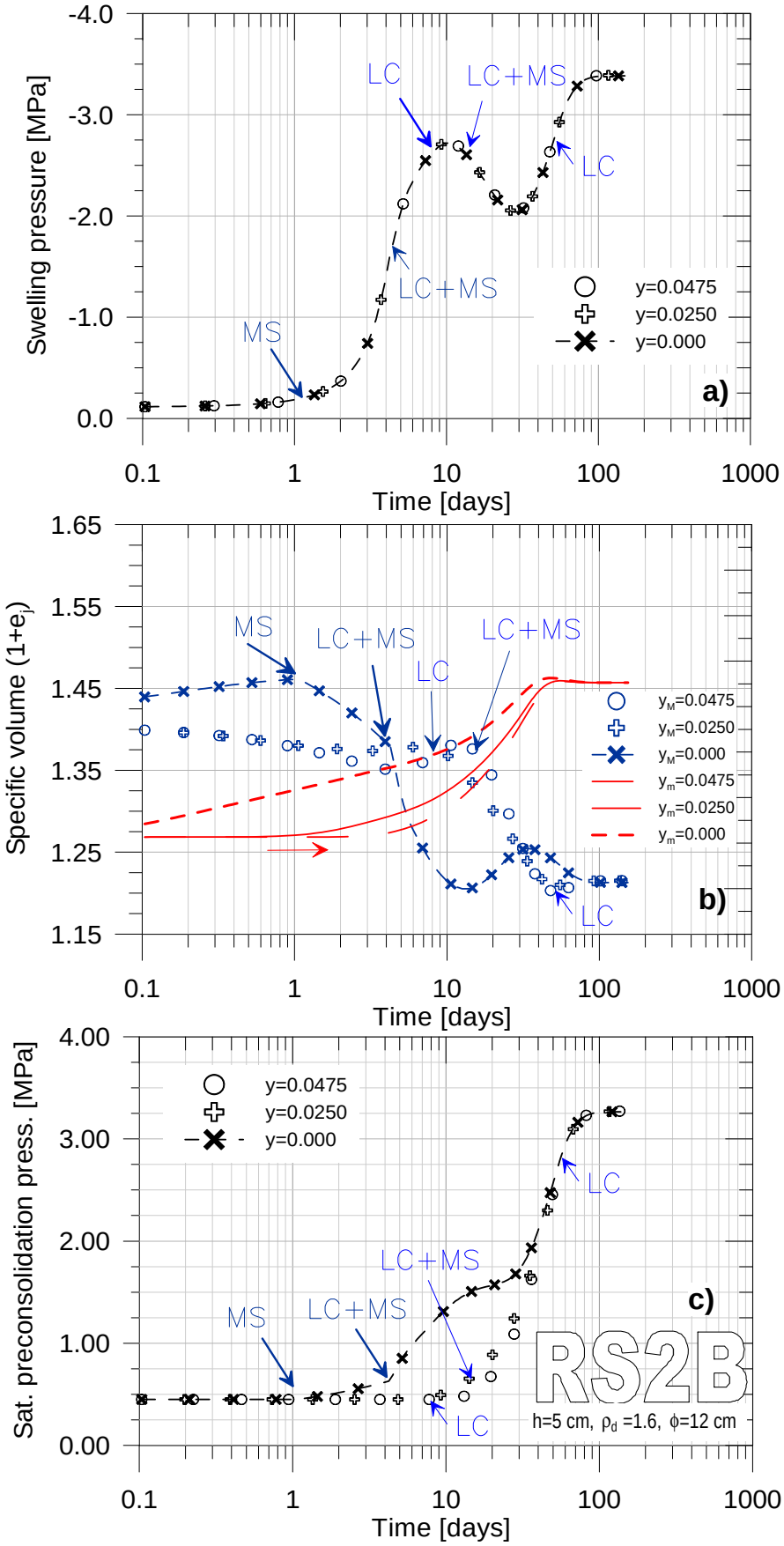

Figure 5-21: Simulation results for test RS2B. a) Evolution in time of the swelling pressure, b) evolution of the specific volumes and c) evolution of the saturated preconsolidation net stress.

The comparisons between simulations and test results are shown in Figure 5-22 and Figure 5-23. With the modification of the preconsolidation pressure from a value of 0.375 to 0.45 the model is able to capture the kinetics of the swelling pressure evolution as registered by the test using the parameters shown in Table 5-4.

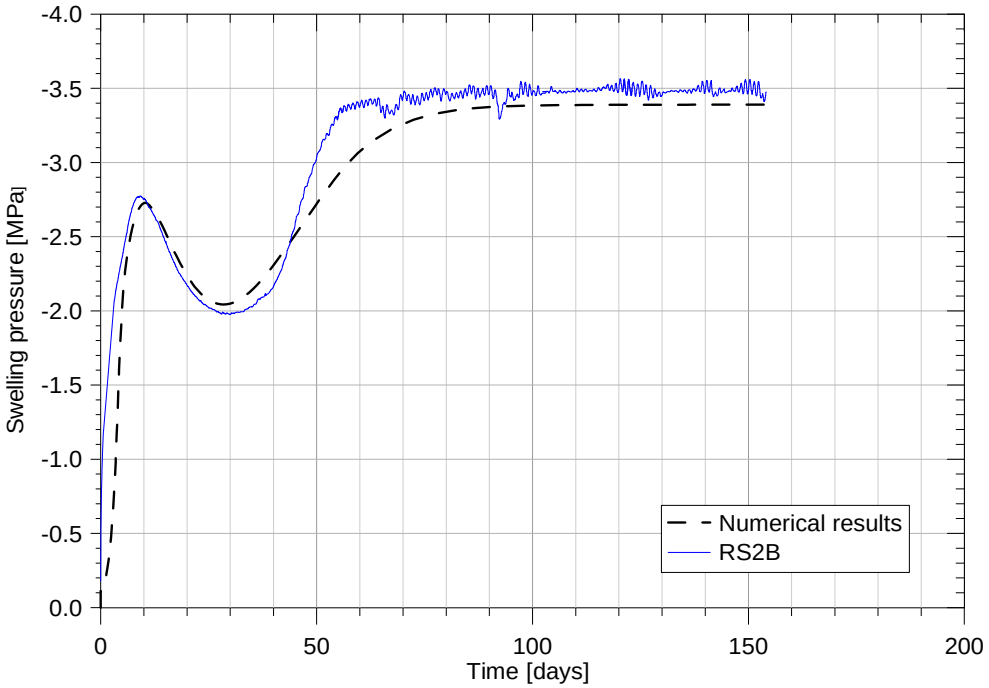

Figure 5-22: Swelling pressure evolution. Comparison between test and computations for test RS2B. Linear time scale.

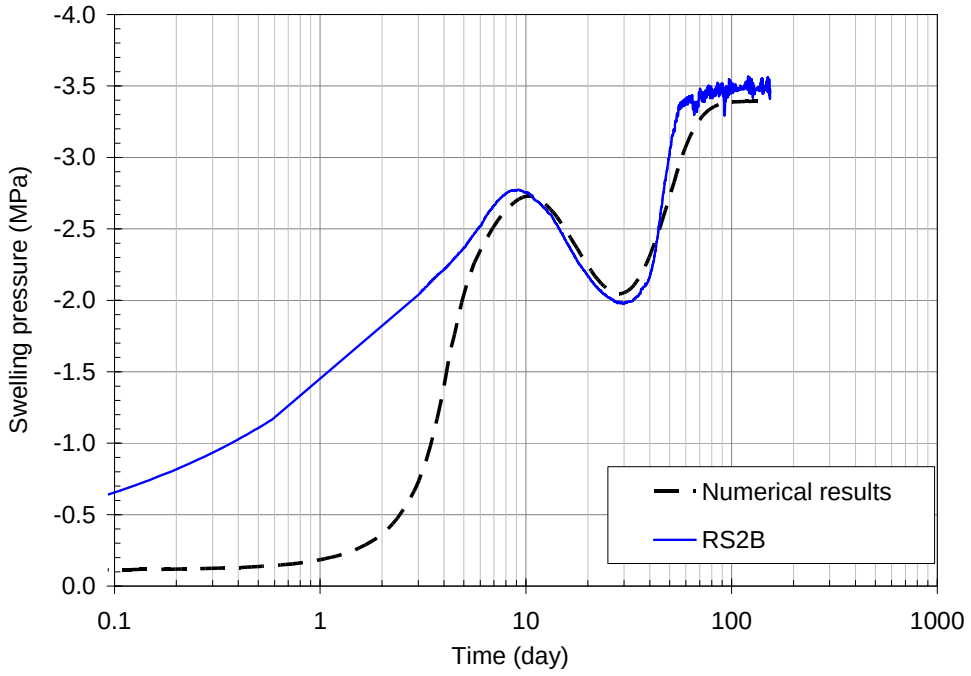

Figure 5-23: Swelling pressure evolution. Comparison between test and computations for test RS2B. Logarithmic time scale.

With respect to the water intake, unfortunately the volumes measured in the lab were overestimated due to a problem with the water lines, especially at the end of the test. In Figure 5-24 the water intake obtained in the simulation is compared with the water actually measured.

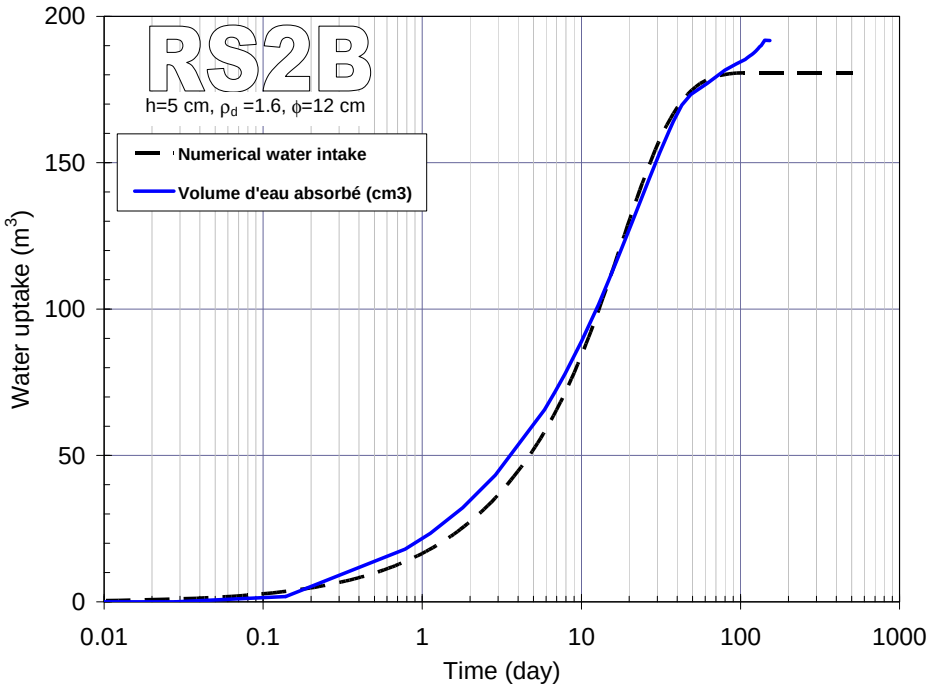

Figure 5-24: Water intake evolution. Comparison between test and computations. Test RS2B.

Remarks on tests with Dry Density = 1.60 g/cm^3

The results obtained concerning the prediction of the swelling pressures, evolution of the water intake and evolution of the porosities are in satisfactory agreement with tests results.

In the numerical analysis an effort was made to maintain the parameters unchanged from test to test to evaluate the effectiveness of the constitutive model. Whereas for the lower dry densities the peak value is similar or higher than the final value, for dry density 1.6 g/cm^3, the final swelling pressure is clearly higher than the peak value. With respect to the time for hydration, the initial peak is reached later if the initial dry density is higher, the height of the sample also delays the peak.

This characteristic evolution of the swelling pressure is not exclusive of the mixtures of powder and pellets. The same type of behaviour is observed in isochoric oedometer tests on compacted clay (Pusch 1982). Such behaviour corresponds to any material with a marked double structure.

The results obtained under the frame of RESEAL II with a sample of compacted powder also demonstrate this fact. Figure 5-25 shows the results of two swelling pressure tests performed on compacted powder of FoCa7 clay by CIEMAT at a nominal dry density of 1.45 g/cm^3 (MGR10) and 1.60 g/cm^3 (MGR11). Samples were 5 cm height and its initial water content was w=12%. In both tests, the swelling pressure development has followed the same pattern as for the mixtures, with the characteristic intermediate phase of swelling pressure reduction. The test with low dry density follows a pattern almost identical to test MGR7. The high density sample results also resemble those of test RS2B.

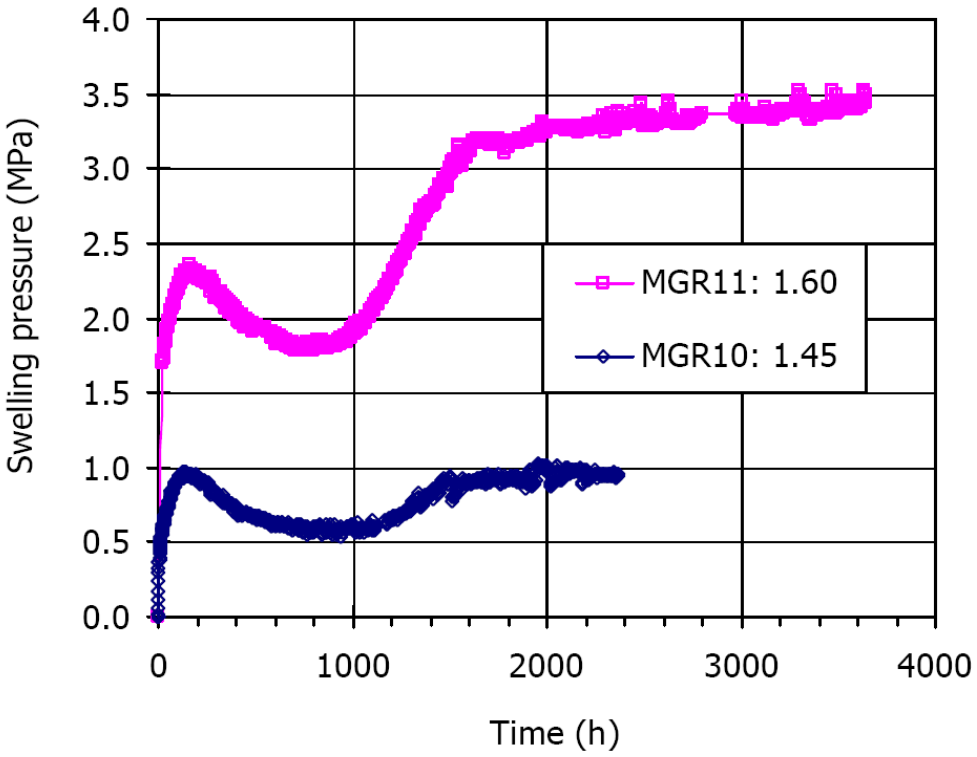

Figure 5-25: Evolution of swelling pressure in infiltration tests with FoCa7 powder compacted at different dry densities (in g/cm3). From Villar *et al.* 2005.

5.2.2 Analysis performed by CEA

5.2.2.1 Features of analysis

The experimental data of clay sample wetting have been obtained from CEA/LECBA (Imbert *et al*., 2004). The samples are composed of FoCa clay pellets and powder at equal dry mass. The samples with the same dry density, 1600 kg/m^3 are selected. The lower density (e.g. 1300 kg/m^3 for RS2A sample) causes a very low swelling pressure that can not be reproduced with this modelling. Four tests are simulated: RS2B, RS2C, RS2E, RS2F as described in Gens *et al*. (2009). However, here only the results of test RS2B are given as a matter of example. The characteristics are given in Table 5-7. All the samples have the same diameter: 12 cm.

The water is injected at the sample bottom. The water injection mode is through one meter of water in a burette.

As the clay sample is contained in a rigid cell, during the wetting phase a swelling pressure develops in the sample. A residual displacement is in fact observed at the top of the cell, but this displacement is neglected in the model.

The aim of the model validation is to reproduce the water volume injection at the bottom of the sample and the swelling pressure in the sample.

Table 5-7: Sample wetting test, physical characteristics used in CEA modelling

Characteristics	RS2B sample	RS2C sample	RS2E sample	RS2F sample
sample height [cm]	5.0	3.0	10.0	10.0
initial solid grain density [kg/m^3]	2675.0	2675.0	2675.0	2675.0
initial pellets dry density [kg/m^3]	1894.0	1894.0	1894.0	1894.0
pellets water content [-]	0.0431	0.0459	0.0449	0.0449
powder water content [-]	0.1183	0.1175	0.0507	0.0507
pellets dry mass [g]	452.39	271.43	904.78	1085.73
powder dry mass [g]	452.39	271.43	904.78	1085.73
initial characteristics of the sample				
mean dry density [kg/m^3]	1600.0	1600.0	1600.0	1600.0
mean porosity [kg/m^3]	0.402	0.402	0.402	0.402
mean water content [-]	0.0807	0.0817	0.0478	0.0478
mean suction [Pa]	$3.60\,10^8$	$3.48\,10^8$	$1.50\,10^9$	$1.50\,10^9$

Two series of calculations have been performed. The first one is a chaining hydro-mechanical calculation; the second one is a coupling hydro-mechanical calculation.

Initial conditions. A homogenized material with mean characteristics coming from the elementary clay pellets and powder properties is defined. So the initial suction and a corresponding water pressure head for a mean material is calculated, see Table 5-7. The initial stress is at atmospheric pressure.

Boundary conditions. At the bottom of the sample, the water pressure head is equal to the pressure induced by the burette or the pump, on all other boundaries there is no water flux. On all boundaries, the normal displacement to the surface is zero.

The sample is cylindrical, the initial and boundary conditions have symmetry of revolution, and therefore the problem to solve is an axisymmetric one. Consequently, a 3D CAST3M model with axisymmetric conditions is used.

The retention and permeability curves parameters are given in Table 5-8 (CEA sample FoCa clay), they come from Reseal I data report (Volckaert *et al*., 2000). The mechanical behaviour is based on the BBM elasto-plastic parameters given in the same table.

The time and space discretization is relatively fine: 2 mm height for the cell mesh, and time step is in the interval from 42 s to 1 day.

Table 5-8: Hydromechanical parameters used in CEA modelling

Parameters	CEA sample FoCa clay	Shaft test FoCa clay	Shaft test Boom clay
Van Genuchten retention curve			
λ [-]	0.27	0.27	0.60
s_{ref} [MPa]	17.00	17.00	20.00
S_r [-]	0.00	0.01	0.01
Kozeny permeability			
k_i [m^2]	$6\,10^{-21}$	$6\,10^{-21}$	-
A [-]	3.00	3.00	-
ω_k [-]	0.405/0.382	0.405/0.382	-
Van Genuchten permeability			
k_i [m^2]	-	-	$4.5\,10^{-21}$
A [-]	-	-	0.50
λ [-]	-	-	0.60
B [-]	-	-	2.00
BBM parameters : elastic coefficient			
shear modulus G [Pa]	$150\,10^6$	$150\,10^6$	$150\,10^6$
Poisson coef. ν [-]	0.4955	0.4955	0.333
BBM parameters : elastic function $v = f(\ln(-p))$			
κ_0 [-]	0.002	0.12	0.0265
α_k [-]	$3\,10^{-9}$	$3\,10^{-9}$	0.00
BBM parameters : elastoplastic function $v = f(\ln(-p))$			
$\lambda(0)$ [-]	0.16	0.17	0.26
r [-]	0.75	0.17	0.564
β [$Pa-1$]	$5\,10^{-8}$	$5\,10^{-8}$	$5.44\,10^{-5}$
BBM parameters : elastic function $v = f(\ln(s))$			
κ_s^0 [-]	0.10	0.07	$3.22\,10^{-3}$
β_{ks} [-]	0.12	0.00	0.00
γ [-]	$1.4\,10^{-8}$	0.16	0.00
p_{ref} [$Pa-1$]	10^4	10^4	–
BBM parameters : elastoplastic function $v = f(\ln(s))$			
λ_s [-]	0.70	0.70	$3.22\,10^{-2}$
BBM parameters : yield surfaces definition			
initial p_0^* [Pa]	$1.2\,10^6$	$4\,10^5$	$6\,10^6$
initial s_0 [Pa]	10^7	10^7	10^7
reference p_c [Pa]	10^5	10^5	10^5
slope k [-]	0.10	0.10	$7.32\,10^{-3}$
slope M [-]	1.50	1.50	1.00
water, grain solid compressibilities			
β_w [$10^{-10}Pa^{-1}$]	4.50	4.50	4.50
β_s [$10^{-11}Pa^{-1}$]	1.80	1.80	1.80
ρ_{w0} [$10^2kg/m^{-3}$]	9.98	9.98	9.98
u_{w0} [10^5Pa]	1.01	1.01	1.01
viscosity μ_w [$10^{-3}kg/(m.s)$]	0.89	0.89	0.89

5.2.2.2 Results and discussion

First the RS2B case is analysed with the hydro-mechanical chaining process and the parameters given in Table 5-8. Those parameters have been chosen to ensure a good agreement with the

RS2B experimental results so a relatively good result is obtained for the evolution of swelling pressure.

The calculated swelling pressure results from the BBM constitutive law. Three time phases can be observed, first an increase of the pressure until the first peak, then a reduction and finally a second increase of the pressure (Figure 5-26).

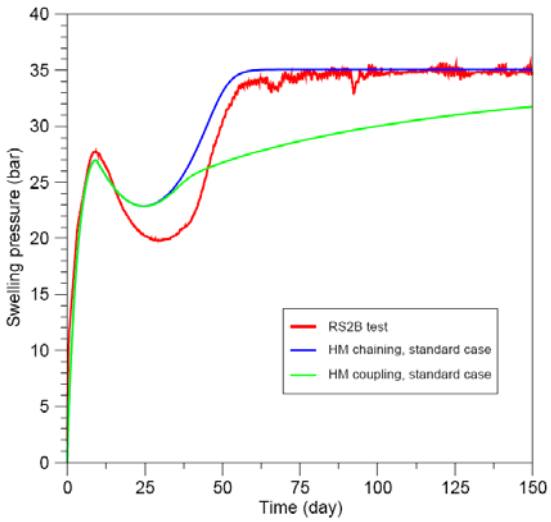

Figure 5-26: Sample wetting simulation, RS2B swelling pressure.

At the beginning the increase of the pressure is caused by the wetting of sample bottom which induces an elastic increase of the porosity in this region quantified by compressibility coefficient κ_s in s-v graph. Then a compression is induced in the sample, first elastic then elasto-plastic, quantified respectively by compressibility coefficients κ, λ in p-v graph. The net mean stress p, that drives the behaviour of the material, increases from the bottom to the top of the sample, and with it, the clay plastification. At peak, the entire sample is in plastic state.

Then the pressure decreases in an elastic process until a minimum, corresponding to the decreasing value of the net mean stress p at the top of the sample. The medium is not yet completely saturated at this minimum, and a new swelling pressure increase is obtained with the upward water flow, then it stops when sample saturation is complete. At this stage the stress is uniform along the sample and the porosity keeps an asymmetrical form: higher value at the bottom, lower at the top.

Concerning the injected volume in the sample (Figure 5-27), no water flux at the sample top is considered. It is the reason why a discrepancy between experimental and calculated results can be noted. The calculation reaches the constant value corresponding to the entire saturation of the sample, the experimental data increases due to water evaporation at the sample top and a leakage noticed by the experimenters in the tube coming from the burette. Moreover, the slope of the injected volume gives us the permeability coefficient of the clay, the data given in the Table 5-8 seems to be the correct one.

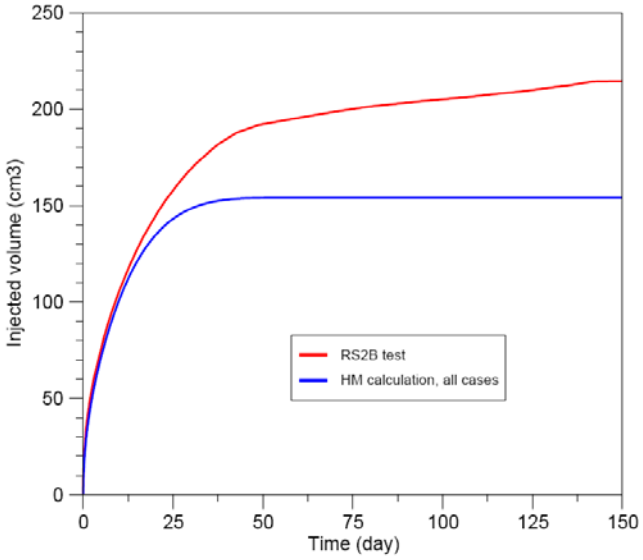

Figure 5-27: Sample wetting simulation, RS2B injected water volume.

Afterwards the hydro-mechanical coupling model has been applied to the RS2B test with the same hydro-mechanical parameters. The swelling pressure result gives the same value than the preceding model until the minimum value, and then the last slope is much gentler. The similar results between the hydro-mechanical chaining and coupling models can be explained by the fact that the porosity variation is relatively small during the wetting process in a global constant volume (Figure 5-28).

To control the results convergence, the RS2B test is calculated in chaining mode with smaller and higher time steps: 21 seconds to half an hour for lower time steps and 340 seconds to 4 days for higher time steps. No changes in the results are observed.

In the same way, the RS2B test is calculated in chaining mode with two different meshes: 1 mm and 5 mm for the element mean height. Again no changes in the results are observed.

Then the hydro-mechanical parameters optimized for RS2B test is applied to three others tests calculation in chaining and coupling processes. RS2C, RS2E and RS2F test calculations give relatively good results with these calculation conditions. The results are improved with a few parameter modifications; these modifications are applied only in the hydro-mechanical chaining (Gens *et al*., 2009).

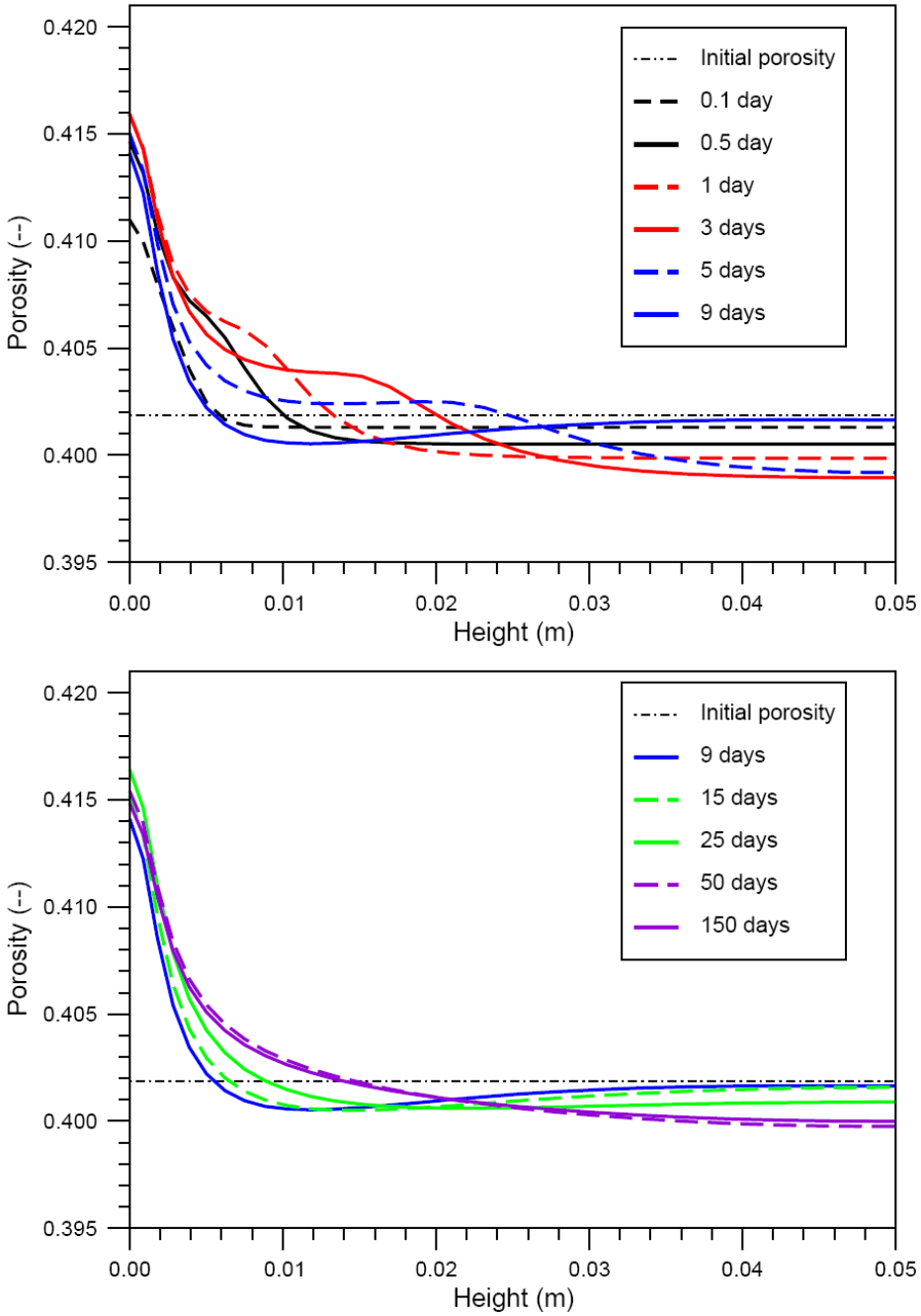

Figure 5-28: Sample wetting simulation, RS2B porosity.

It can be observed that relatively good modelling results are obtained with FoCa clay wetting calculation in a confined volume, FoCa clay is composed of pellets and powder. The hydro-mechanical chaining modelling is therefore adequate to reproduce the experimental results.

5.3 Modelling the shaft sealing test

The experimental set up is described in chapter 4. Here, the hydromechanical modelling results of UPC and CEA are given.

5.3.1 Analysis performed by UPC

5.3.1.1 Features of the model

In order to perform the hydromechanical numerical analysis of the shaft sealing test, the finite element code CODE-BRIGHT has been used. A double porosity media was considered for the clay seal and a single porosity medium was adopted for the rock. For the hydromechanical response of the seal, the BExM constitutive model was used using the parameters assessed from the infiltration tests.

The space discretization used on the simulation of the shaft sealing test is an axisymmetric representation of the shaft and the host rock. It represents a slide of 50 m with the axis placed at the centre of the central hydration tube. Consequently, the far boundary of the host rock is located at a distance of 50m (45 times the radius of the clay plug).

A structured mesh of 2748 elements was used. A piezometric water level equal to 220 m of water column was considered in the far boundary. This value is the average value calculated with the code PORFLOW at seal test level (Ortiz *et al*. 1996; Volckaert and Bernier 1996). On the shaft boundary, an atmospheric pressure (P_l=0.10 MPa) was considered. The influence of the main gallery on the piezometric water levels was not taken into account in the simulations, see Figure 5-29. The geometry of the mesh and the initial boundary conditions are depicted in Figure 5-30.

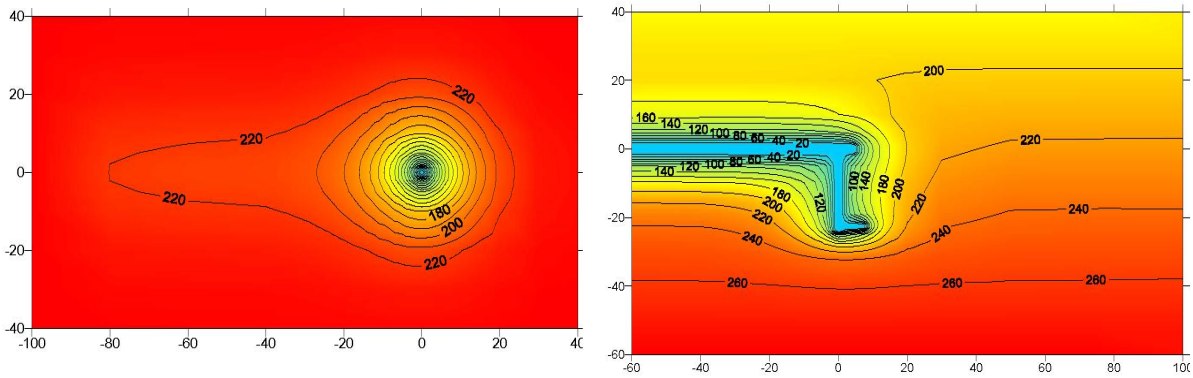

Figure 5-29: Pore water pressure profiles around the shaft and the HADES gallery calculated with the code PORFLOW. From (Volckaert *et al.* 1996c).

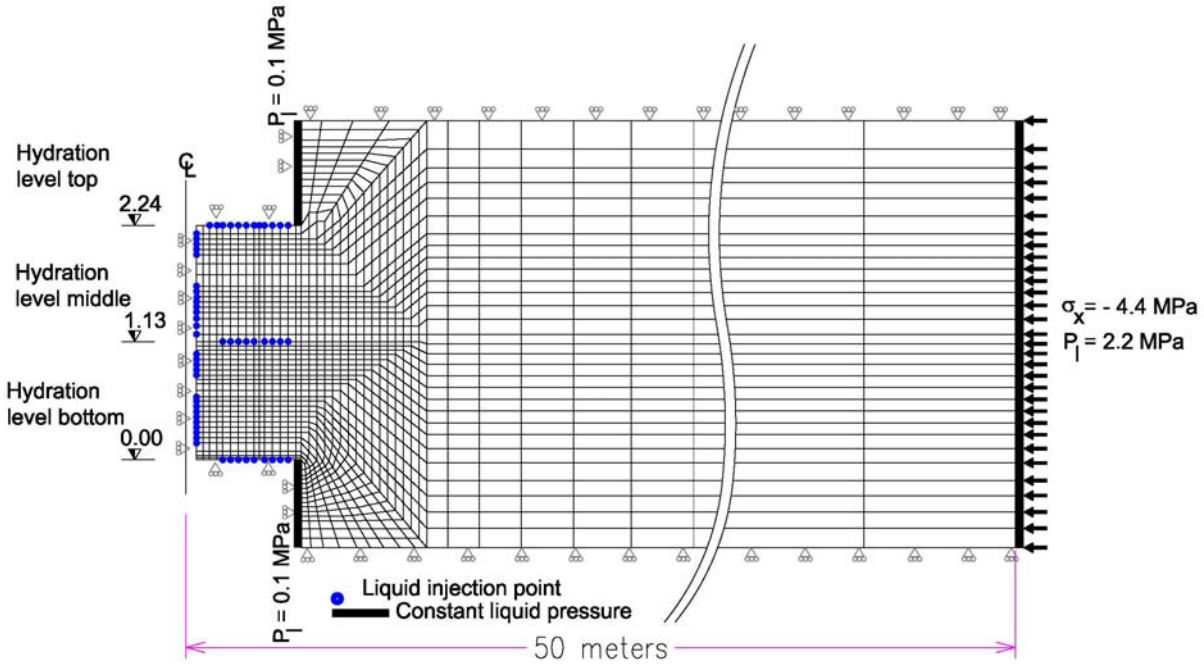

Figure 5-30: Spatial discretisation and boundary conditions considered

Rock initial conditions

With respect to the initial state of stresses, the corresponding lithostatic value (4.4 MPa) has been prescribed for the host formation. On the far boundary this value is fixed.

The removal of the shaft's lining was simulated in order to calculate the initial stresses close to the excavated zone in the host rock. The lining removal was considered to reduce the stresses of the excavated face to a low value. A feature of CODE-BRIGHT allows to turn-off certain zones in a mesh and thus the clay seal materials were turned off. A "zero stress" value was taken for the contact between seal and rock, allowing the program to calculate the new stress field. After equilibration of stresses and water pressures, an isotropic stress of 0.11 MPa was assigned to the fill mixture. Resulting initial stresses can be seen in Figure 5-31.

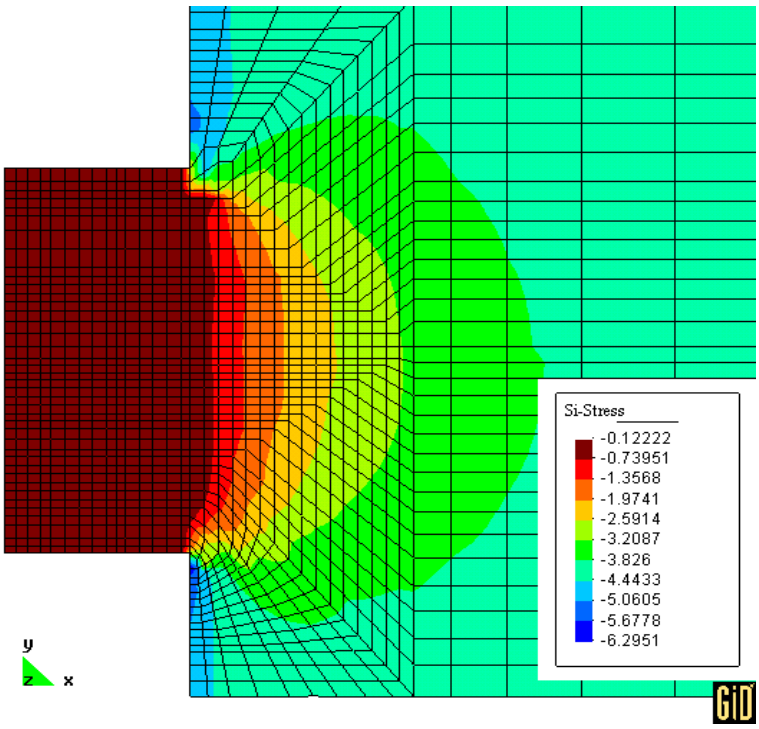

Figure 5-31: Initial state of stresses

The seal was divided into 2 different materials in order to distinguish between the first 60 cm that correspond to a compacted material (γ_d=1.543 g/cm^3), and the zone where no compaction was performed to avoid damage of the sensors (γ_d= 1.387 g/cm^3). In Figure 5-32, a view of the materials considered is shown.

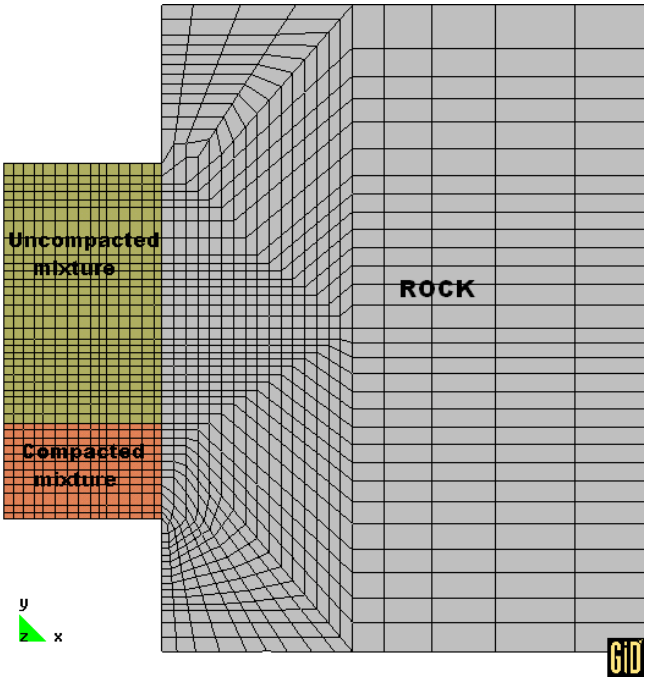

Figure 5-32: Materials considered

Seal initial conditions

Concerning the initial variables of the double porosity Expansive Model, it was necessary to calculate them for the two densities installed. Table 5-9 presents the detailed characteristics for each density:

Table 5-9: Initial characteristics of the pellets/powder mixture installed on the shaft

Height (cm)	Dry density g/cm^3	Dry density pellets g/cm^3	Initial w% pellets	Dry density powder g/cm^3	Initial w% powder	Initial w% sample	Void ratio
COMPACTED ZONE							
60	1.543	1.894	4.49	1.302	7.51	6.00	0.734
UNCOMPACTED ZONE							
164	1.387	1.894	4.49	1.093	7.51	6.00	0.929

To approximate the percentage of micropores present on the mixture, the methodology followed for the infiltration tests was used. Since the pellets were of the same type than those used in the infiltration tests, a micropore volume of 76.5% was considered. For the powder, the percentage of micropores was calculated using the formula given in Figure 5-1 with the values of dry densities presented in Table 5-9.

To estimate the amount of water present on each level of structure, it was considered that the pellets contained 70% of its water in the micropores, in the same way as for the infiltration tests. Concerning the powder, the amount of water on the micropores was considered to be 50% for the compacted zone, and 25% for the uncompacted zone. With these proportions the degrees of saturation in the compacted zone were S_{lmacro}=0.141 and S_{lmicro}=0.367. In the no-compacted zone, the correspondent values were S_{lmacro}=0.132 and S_{lmicro}=0.301.

The values of micro and macroporosities obtained for each zone and the suctions associated with the saturation degrees were obtained using the retention curves of Table 5-3 and are presented in Table 5-10.

Table 5-10: Numerical initial conditions for the compacted and uncompacted zones on the Shaft Sealing Test simulations

	n_T	n_M	n_m	e_M	e_m	s_{Macro}	s_{micro}
Compacted seal	0.423	0.278	0.145	0.482	0.252	272.1 MPa	278.5 MPa
Uncompacted seal	0.482	0.366	0.116	0.706	0.223	279.7 MPa	308.3 MPa

Hydromechanical parameters

The hydromechanical parameters obtained from the analysis of the low density infiltration test RS2J (1.45 g/cm^3) were used for the no-compacted material zone, and those obtained for test RS2E (1.60 g/cm^3) were used for the high density zone. Those parameters are presented in Table 5-4.

The constitutive relationships do not consider a double structure material for the host rock. The parameters needed for the hydraulic constitutive equations correspond to the retention curve, the intrinsic permeability and the relative permeability for the whole material.

Different data sets have been considered for the retention curve. The final adopted curve follows the results obtained by Rhattas (1995), see Figure 5-33. In the simulations this curve allows the rock to dry at low values of suction, in accordance with the in-situ water pressure measurements (shown later in Figure 5-38).

The graph plots show the retention curves found in literature that have been used in other simulations for the Boom Clay. The adopted curve is similar to that used in the BACCHUS 2 project. The results of two tests performed on Boom Clay during RESEAL I are also shown on the same graph. In those tests, small samples (2.5 cm height) of well preserved clay cores from the HADES underground laboratory were submitted to different stress-suction paths under oedometric conditions (Volckaert *et al*. 2000).

Concerning the relative hydraulic conductivity, k_{rl}, and due to lack of data, a closed form of van Genuchten's expression was used to represent its variation with the degree of saturation. The final value adopted for λ was assessed by back-analysis of the results, see Figure 5-34

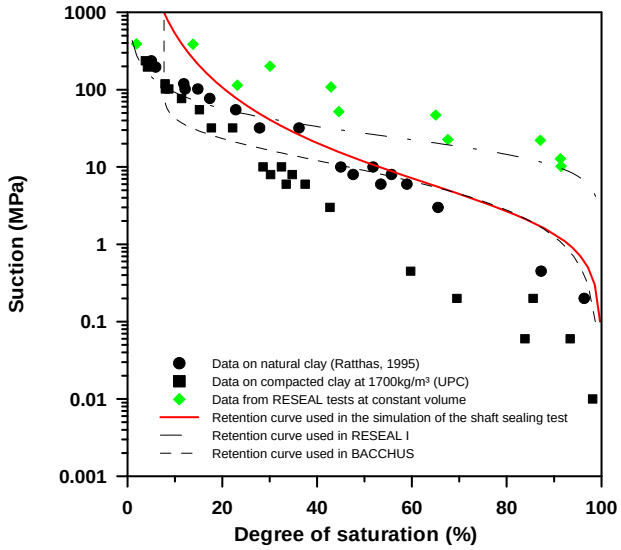

Figure 5-33: Soil-water retention curve. Fit for the Boom Clay.

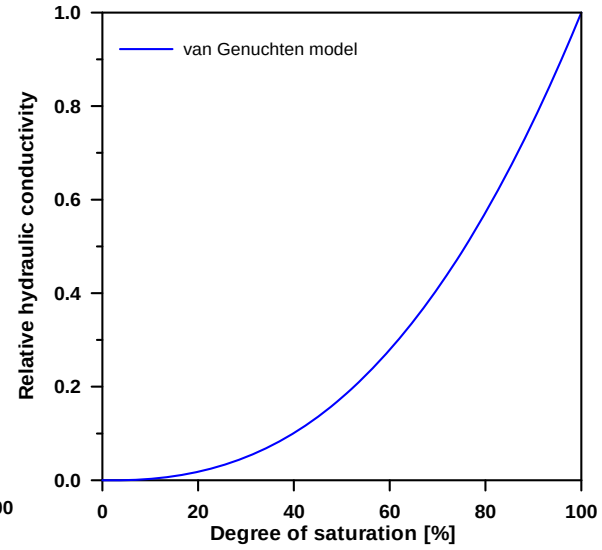

Figure 5-34: Variation of the relative liquid permeability with saturation for the Boom Clay.

In recent years, the determination of the hydraulic conductivity of the Boom Clay and its anisotropy has been a major research topic. It has been measured in core samples (centimeter scale), by means of in situ tests (injection or slug tests) in boreholes (meter scale), or by using the small lateral shaft of the HADES URF as a large scale permeameter (decameter scale). All the investigations yield coherent values of hydraulic conductivity in the order of 10^{-12} m/s for the most argillaceous part of the formation. The ratio between the horizontal and vertical conductivities, as determined in the laboratory from permeameter cell measurements, is about 2 for the Putte and Terhagen Members. In the simulations a back analyzed isotropic value of saturated conductivity of 6.4×10^{-13} m/s has been adopted as the value that gives the best agreement with observations.

In Table 5-11 the hydraulic parameters adopted for the host rock are summarized.

Table 5-11: Hydraulic parameters used for the host rock in the shaft sealing simulations

Constitutive law	Analytic expression	Parameter	Value
Retention curve			
	$S_e = \left(1 - \left(\frac{s}{P_0}\right)^{\frac{1}{1-\lambda_0}}\right)^{-\lambda_0}$ with	$P_o(MPa)$	2.5
		λ_0	0.3
		S_{ls}	1.0
		S_{rl}	0.0
	$S_e = \frac{S_l - S_{rl}}{S_{ls} - S_{rl}}$		
Intrinsic permeability, Constant value			
	$k = k_0\left(\frac{\phi^3}{(1-\phi)^2}\right)$	k_0 (m^2)	5.0x10^{-19}
		ϕ	0.37
Relative permeability, van Genuchten model			
	$K_{rl} = \sqrt{S_e}(1-(1-S_e^{1/\lambda})^{\lambda})^2$	λ	1.20
		S_{ls}	1.00
		S_{rl}	0.00

The BBM was used to describe the unsaturated behaviour of the host rock. The parameters presented by Vaunat and Gens (2005) and Volckaert and Bernier (1996) were adopted. Most of those parameter values were assessed during BACCHUS 2 from suction-controlled tests on different specimens. In some of these suction-controlled oedometer tests, a compacted mixture of Boom Clay powder and pellets was tested (γ_d=1.5 g/cm^3). In others the material was powder of Boom Clay compacted at γ_d =1.7 g/cm^3, which is the in-situ value (Volckaert and Bernier 1996). Poisson's ratio was estimated from in situ measurements.

In Table 5-12, the parameters adopted for the elastic and plastic parts of the BBM are shown. The adopted saturated preconsolidation pressure (p_0^* = 6 MPa) was larger than that suggested by Horseman *et al*. (1985) for the actual depth of the experiment.

5.3.1.2 Results and discussion

Seal hydration results

Confidence in the simulation of the mechanical problem requires a correct assessment of the hydration phase. In order to evaluate the model performance, the simulation results are compared with the available measurements of water intake, relative humidity and liquid pressure. Those measurements were obtained at different points inside the seal, offering in this way a global view of the state of hydration of the shaft.

The first comparisons correspond to the water intake. As explained before, the shaft was artificially hydrated by means of the infiltration filters installed on it. The total water intake of the in situ test was registered by SCK•CEN. In the simulations, hydration is imposed by prescribing the liquid pressure at the corresponding boundary nodes. Figure 5-35 shows the

liquid pressures contour fields just after the simulated hydration begins. The nodes where the liquid pressure is prescribed can be observed at the location of the filters. The amount of water injected is calculated by integrating in time the fluxes on the injection nodes.

Table 5-12: Mechanical parameters for the Boom Clay used in simulations of the shaft sealing test

Constitutive law	Analytic expression	Parameter	Values
BBM Elastic part	$d\varepsilon_v^e = -\frac{\kappa}{1+e_M}\frac{dp}{p} - \frac{\kappa_s}{1+e_M}\frac{ds}{s+p_{atm}}$	κ κ_s	0.0265 0.00322
Deviatoric part	Shear modulus G is computed from bulk modulus K_t considering that Poisson's coefficient ν is constant.	ν	0.4
Yield locus	$q^2 - M^2(p_0 - p)(p + p_s) = 0$	M	1.00
	with $p_0 = p_c\left(\frac{p^*_0}{p_c}\right)^{\frac{\lambda_{(0)}-\kappa}{\lambda_{(s)}-\kappa}}$	p^*_0 (MPa) p_c (MPa) r $\lambda(0)$	16.00 0.06 0.564 0.26
	and $\lambda(s) = \lambda(0)\,(r + (1-r)e^{-\beta s})$	β (MPa^{-1})	0.0544
	and $p_s = -k_s\, s$	k_s	0.00732

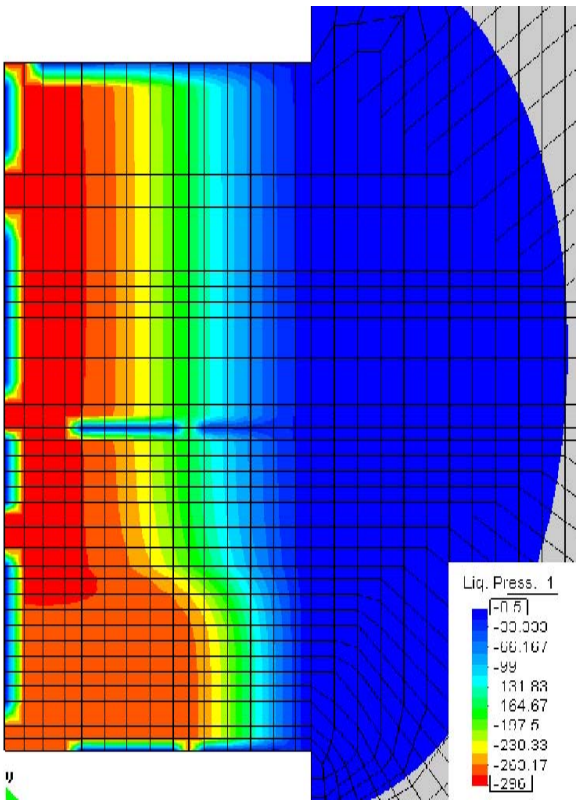

Figure 5-35: Contour fields of liquid pressure at the beginning of artificial hydration

In Figure 5-36 the numerical (dotted line) and the measured (continuous line) volumes of injected water are compared. Symbols represent the pressures applied on the filters and refer to the right hand axis. Simulations span from September 1999 to May 2006.

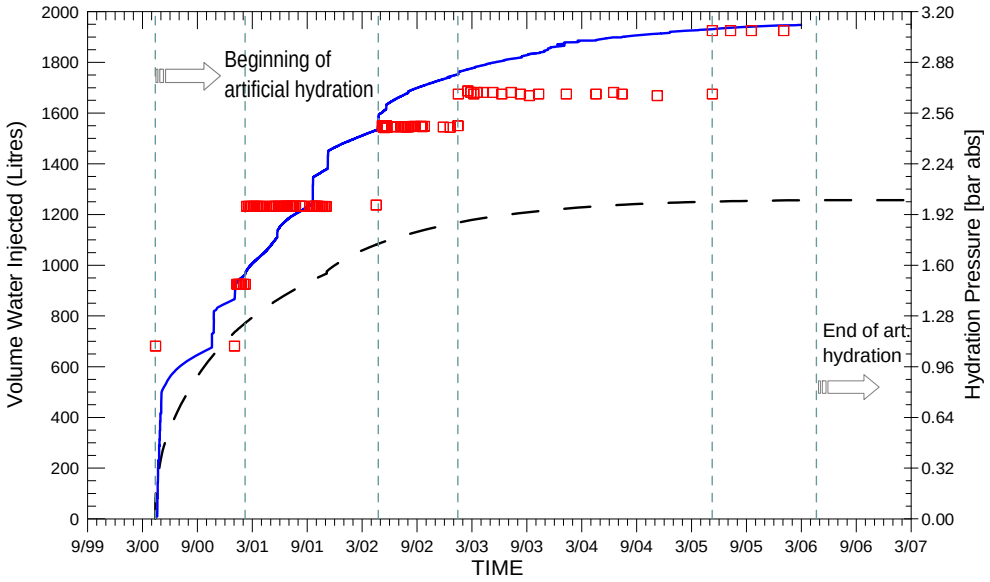

Figure 5-36: Water volume injected. Observations and computed results

The steps that can be appreciated in the measured water volume are a consequence of several increments on the hydration pressure, that where applied in an attempt to accelerate hydration.

These pressure increments were considered on the simulations, without causing steps on the computed water intake. Differences can be noted, especially after the first year. The computed water intake is about half the measured volume.

In 2006 a series of hydraulic tests were made in the shaft and filters were checked. It was noted that some of the injection filters in the middle and top hydration levels were not injecting water at least since May 2005 and that, from February 2004, some of the water injected at the bottom level might have filtered to the concrete plug due to a break in the resin. This might explain part of the differences between measured and registered injected volume. Yet, before drawing conclusions about the effectiveness of the numerical simulations of the water intake, other results have to be considered.

The next plots show the evolution recorded by the relative humidity sensors. Eight of such sensors were installed, one on each instrumented rod (six in total) and two at the interface with the rock (on the instrumented level top, ILT). The type of sensor used on the rods was a humidity/temperature measuring probe model HMP 233, manufactured by Vaisala. For the contact with the rock a ROTRONIC sensor type was used.

At the beginning, due to the dry state of the clay mixture, the seal took water from the host rock to equilibrate the potentials on both media. As a result, the suction on the seal in the boundary with the rock decreased. On the other hand, the rock probably de-saturated.

The two RH sensors located near the host rock (sensors RH-SH-ILT) illustrate the water entrance from the rock during those first days, see Figure 5-37. One of the sensors was located inside a compacted clay cap that simulated a pellet; the other sensor was in the powder, in order to compare the hydration of pellets and powder.
Artificial hydration started in May 2000, just after a 226 day period of natural hydration, as indicated in the graph. The dates at which hydration pressure was increased are shown in Table 4-8. They are indicated on the plots with vertical dashed lines.

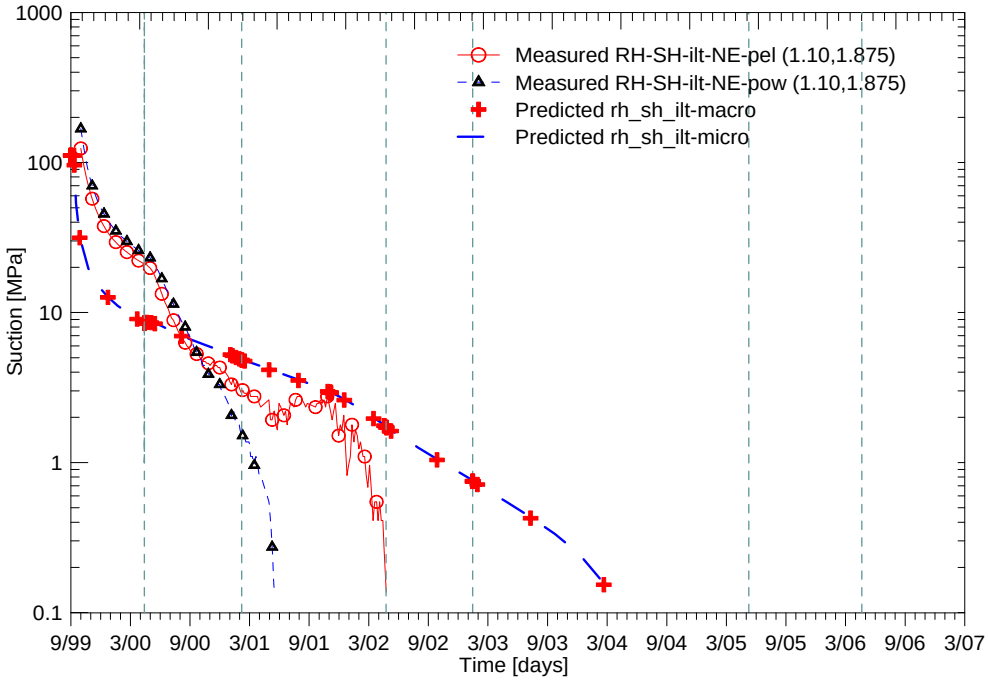

Figure 5-37: Evolution in the suction of two sensors located near the host rock; RH-SH-ilt.

As it can be seen, before May 2000, the measured suction decreased from ~168 MPa to ~ 23 MPa, due to the entrance of water from the rock. The sensor located inside the compacted clay cap hydrated faster, indicating that it had a larger amount of micropores than the one located on the powder. By February 2002 both were already saturated.

Numerical results along the first days show a fast suction reduction. Later, the hydration rate decreases due to the unsaturated state reached by the rock under low suction values, which reduces the amount of water entering from the Boom Clay (see the adopted retention curve for the host in Figure 5-33). As a consequence, complete saturation is numerically achieved by March 2004, two years later than the measurements.

Previous comparisons show a slow numerical hydration at the interface with the rock. However, simulated results agree with the water pressure measurements made at the same top level at other locations. Data obtained from pore water pressure sensors do not report complete re-saturation until March 2004 (see West sensor in Figure 5-38), in line with model predictions.

On the same instrumented level top (h=1.875) the relative humidity sensors of the rods gave information on the suction evolution inside the seal. Measurements of sensors RH-S-ILT are shown in Figure 5-39. The diagram in the plot shows their location. Sensor RH-ILT-W failed right from the beginning, and no useful information could be retrieved.

Measurements could not be recorded until August 2001, but it still can be seen that suction reduction is only weakly influenced by the rock water entrance before applying artificial hydration.

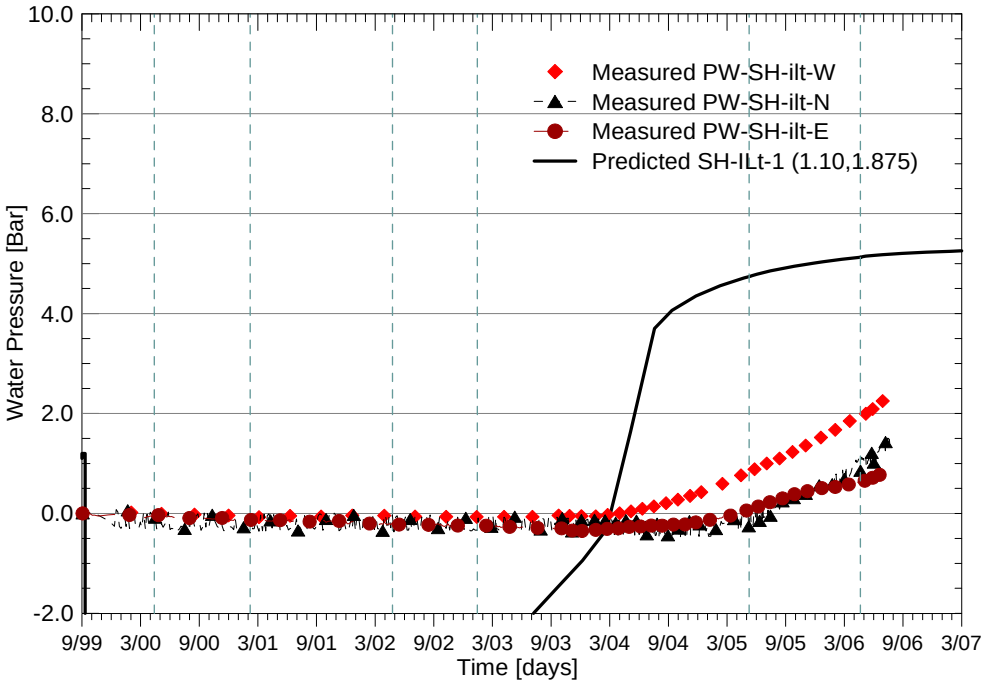

Figure 5-38:Evolution of water pressures on sensors PW-SH-ilt West, East and North.

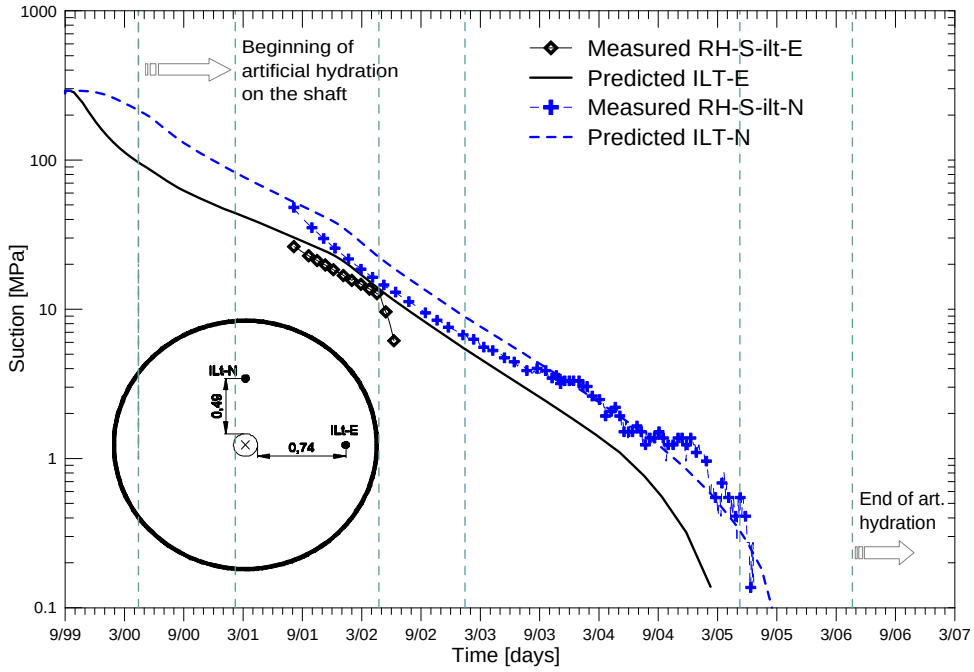

Figure 5-39: Evolution in time of suction on the instrumented level top

Sensor RH-S-ILT-E was closer to the rock interface and hydrated a little faster than RH-S-ILT-N, which was located in the middle of the seal. On May 2002 its suction dropped and no more measurements were obtained (this happened at the instant when a hydration pressure increment was applied). Up to this moment numerical results fitted measurements.

The measurements on the North direction showed complete suction reduction in June 2005, after the last hydration pressure increment. Equal results occurred in the liquid pressure sensors of the seal/rock interface shown in Figure 5-38. Numerical results for sensor RH-S-ILT-N agree very well with those measurements.

The pore water pressure measurements obtained from the instrumented rods (PW-ILT-01 and 02) confirm that close to the rock saturation is achieved in May 2005 in the East section. However the North section does not seem to be saturated. The measurements are shown in Figure 5-40 and Figure 5-41.

Sensor PW-ILT-E-01, which is close to the rock (r=0.805), shows a certain influence of the hydration pressure increments, and reports positive water pressures on May 2005, almost at the same time as the pore water sensors of the seal/rock interface shown on Figure 5-38. The North sensor was not indicating saturation by August 2006. Simulations on the other hand showed complete saturation by August 2005.

For the point ILT-02 which is closer to the central tube (r=0.37), the influence of the pressure increments on the measurements is evident and no clear conclusions can be drawn about the moment at which complete saturation is achieved; only the North sensor seems to record positive pressures after the last pressure increment on May 2005. Simulation results, on the other hand, showed positive water pressures from February 2006.

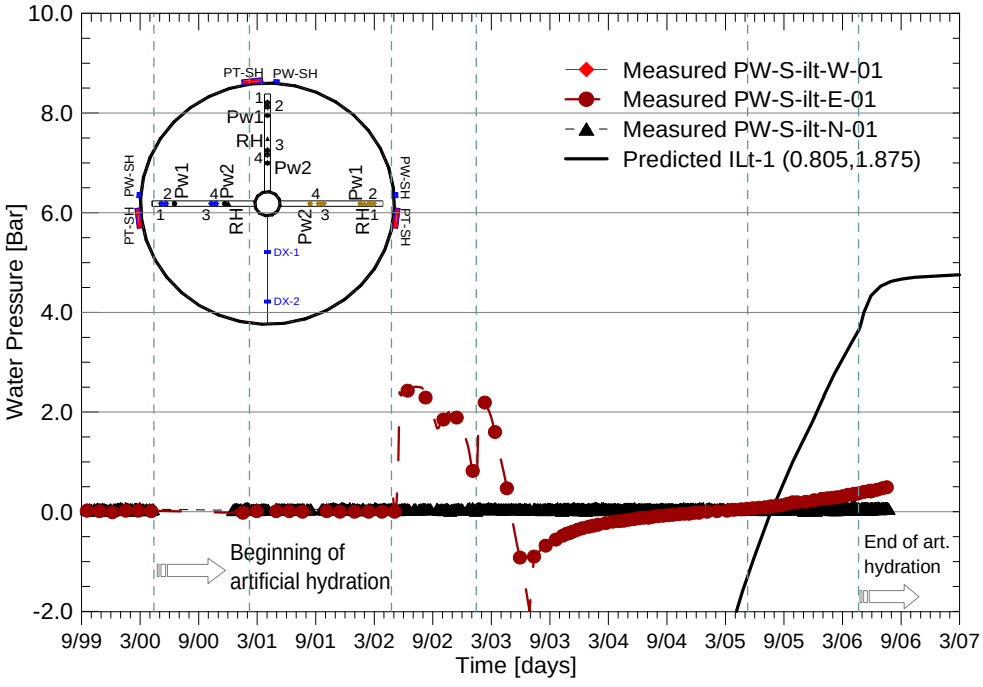

Figure 5-40: Evolution of pore water pressures on the ILT-01 (r=0.80 m)

From all the available information of the Instrumented Level Top, different hydration patterns have been detected, depending mainly on the direction measured. For instance, the West section only had one pore water sensor functioning on the seal/rock interface, and indicated that the zone was saturated in July 2004, one year earlier than in the other directions. The East section, on the other hand, indicated positive water pressures close to the rock in June 2005 and at r=0.805 in

August 2005. Finally, the North direction measurements indicated positive water pressure at the seal/rock zone in July 2005, a zero suction in July 2005 at r=0.49, and positive water pressures at r=0.37 in March 2005. This section is the one offering more information.

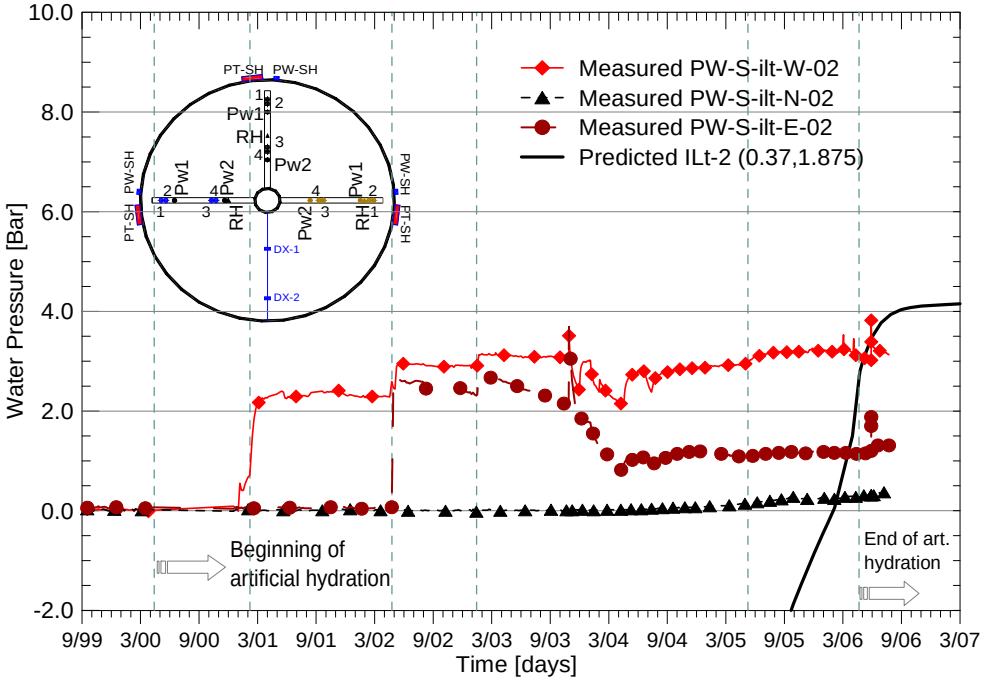

Figure 5-41: Evolution of pore water pressures on the ILT-02 (r=0.37 m)

For this instrumented level top, there are no more measured values inside the seal. However, due to the presence of the hydration filters on the central tube it is expected that a more hydrated state has been reached closer to the centre tube, and that the middle part of the seal (r=0.5 m) is the zone where hydration takes longer.

To analyze the hydration state of the seal between the ILT and ILB, there are some water pressure sensors on the hydration mid-level (h= 1.13 m), see Figure 5-42. Again, data correspond to a zone close to the rock. It can be detected the moment at which water pressures begin to rise, indicating saturation between October 2004 and May 2005. The model predicts that this happens earlier, in March 2004. Simulations in this case do notice the last pressure increment and the moment at which hydration stops.

For the Instrumented Level Bottom, the liquid pressure measurements available from the seal/rock interface are shown in Figure 5-43. Between December 2004 and May 2005, those sensors start showing positive values. The sensor in West direction shows some erratic behaviour but a certain trend can be seen. The simulations, on the other hand, predict that saturation is reached earlier, in March 2004.

In Figure 5-44 the suction measurements from the bottom rod are presented. As can be seen they differ widely depending on direction. This rod is still on the non compacted material (h=65 cm), but very close to the compacted one. The influence of the zone of lower permeability can be noted on the measurements.

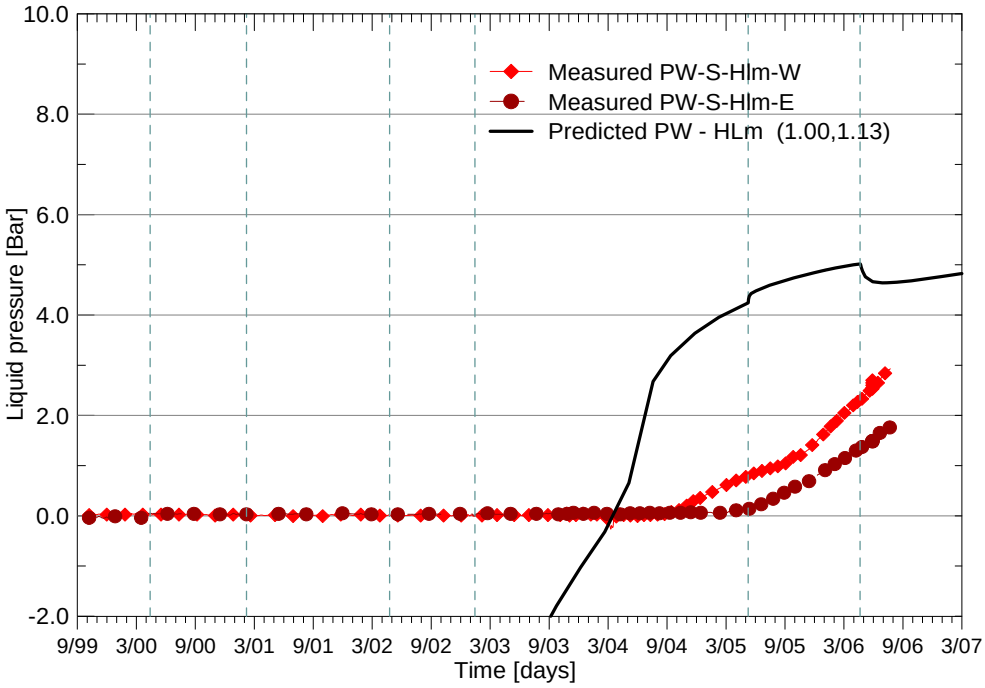

Figure 5-42: Evolution of pore water pressures on the hydration level middle (h= 1.13, r=1.00 m)

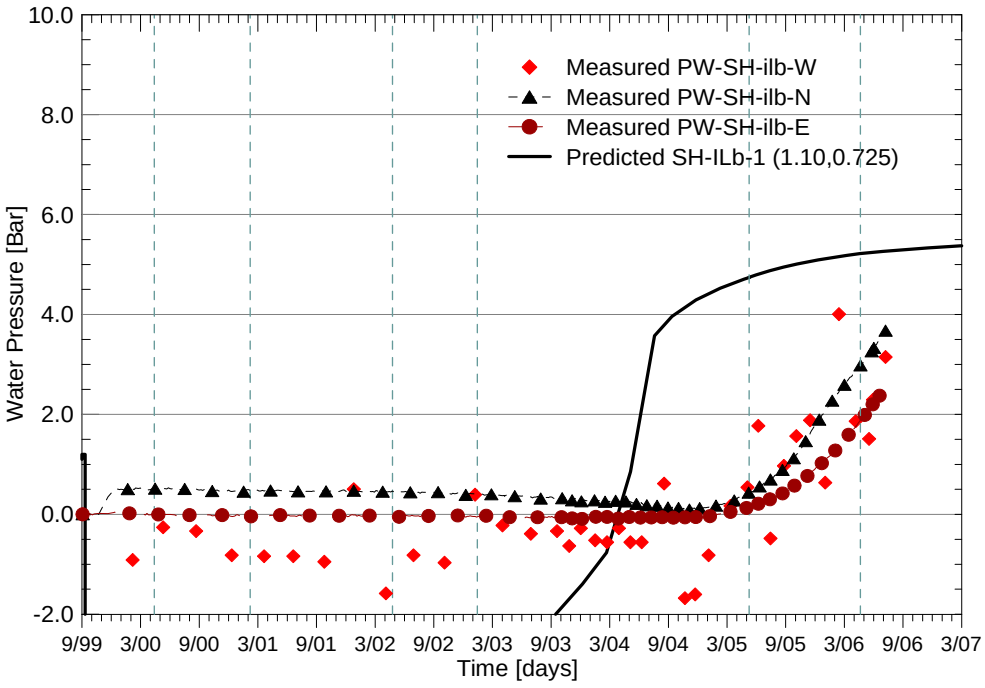

Figure 5-43: Water pressure evolution at r = 1.10m. Instrumented level bottom

Sensor RH-S-ILB-W which was closer to the central tube shows the faster hydration. In contrast, the measurements for the point closer to the rock, RH-S-ILB-E, develop a slow hydration evolution, and the point is not completely saturated by July 2006. Measurements for the East and North directions show a slowdown on the hydration rate after August 2003.

Measurements are counter-intuitive especially for point ILB-E, because, as observed in the water pressures measured on the seal/rock interface (Figure 5-43), the East direction has become saturated by May 2005.

Simulations on the other hand only agree in part with measurements of point RH-S-ILB-N in the middle of the seal. For the West and North points, in the middle and close to the central tube, numerical results have almost the same development, slower than for Instrumented Level Top, and not completely saturated by the end of the simulations in March 2007.

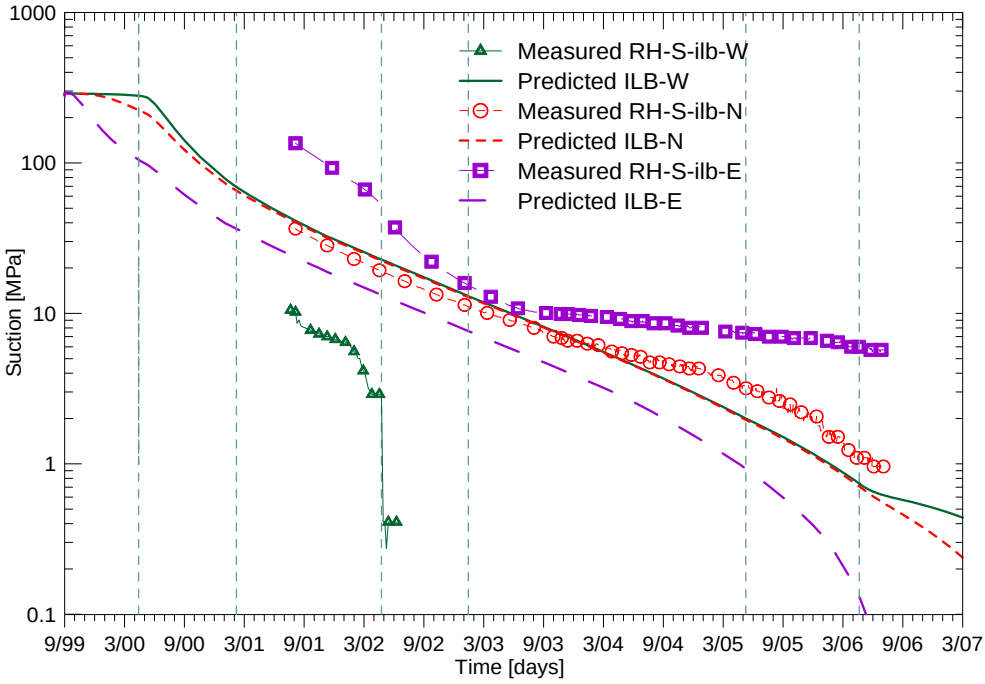

Figure 5-44: Evolution in time of suction on instrumented level bottom

The water pressure measurements in the Instrumented Level Bottom are shown in Figure 5-45 and Figure 5-46. Measurements do not record any change, with the exception of some reaction after the water pressure increments. Not even the West sensor at r=0.37 which was close to sensor RH-ILB-W, and showed an important suction reduction before failing. Data seem to indicate that the seal, in the ILB is not completely saturated by August 2006.

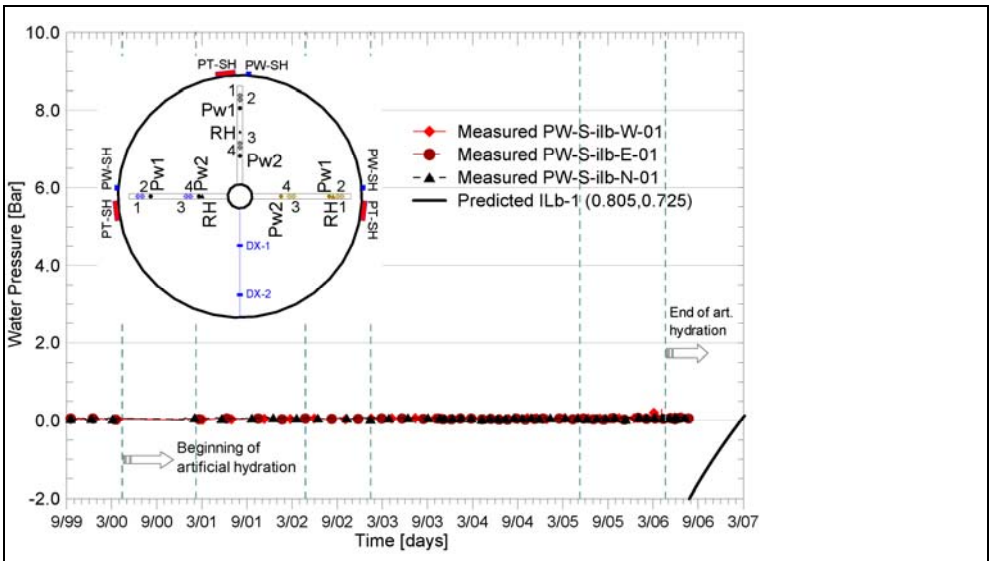

Figure 5-45: Water pressure evolution at r = 0.805 m. Instrumented Level Botom

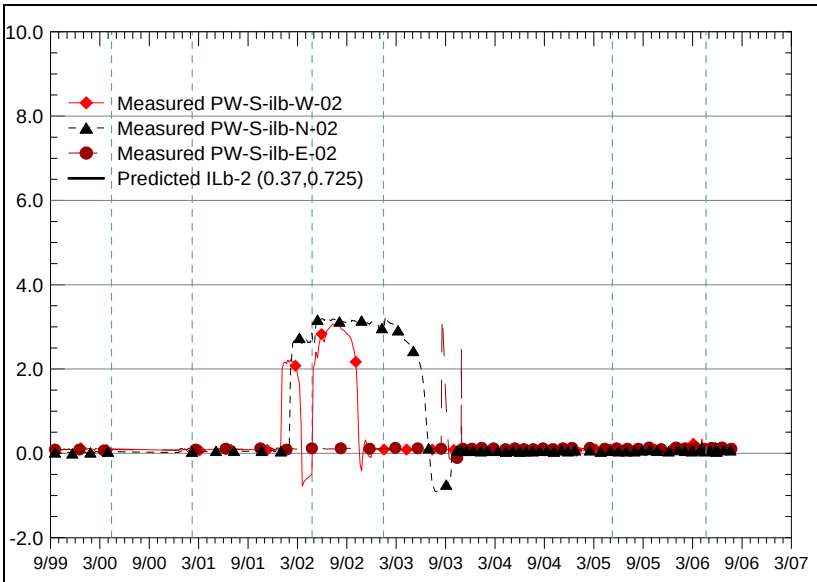

Figure 5-46: Water pressure evolution at r = 0.37 m. Instrumented Level Bottom

The simulations, do show that complete saturation is reached in the zone close to the rock at r=0.805m at the end of the simulations. On the zone close to the central tube, no saturation is achieved during the simulated period (this is why the predicted line is not visible in Figure 5-46 as positive pressures are not achieved). On the ILT numerical saturation was achieved in September 2005 and in February 2006 respectively. Evidently, in the simulations, the lower permeability of the compacted zone delays saturation in the inner part of the seal.

It was mentioned that some of the injection water in the bottom might have filtered through the resin seal into the concrete plug. The possibility that this leak might have affected the hydration of the ILB was checked numerically. A simulation was made on which the number of nodes injecting water from the bottom of the seal was reduced to 50% from February 2003 until the end of the simulation. This date was chosen because it is the moment at which the ILB suction measurements exhibit a change in the hydration rate.

In Figure 5-47 and Figure 5-48 the recalculated water pressure and the evolution of suction on the ILB are presented. They last longer than in the previous case, and as long as the North sensor's measurements. The analysis indicates that, a leak of water to the concrete might have contributed to the slow hydration of the compacted zone. However, simulated suctions for sensor ILB-E are still quite far away from the measurements.

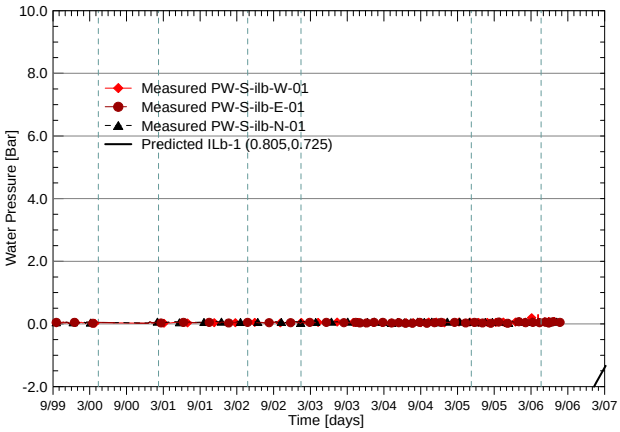

Figure 5-47: Water pressure evolution at r=0.805m considering the leaks to the concrete

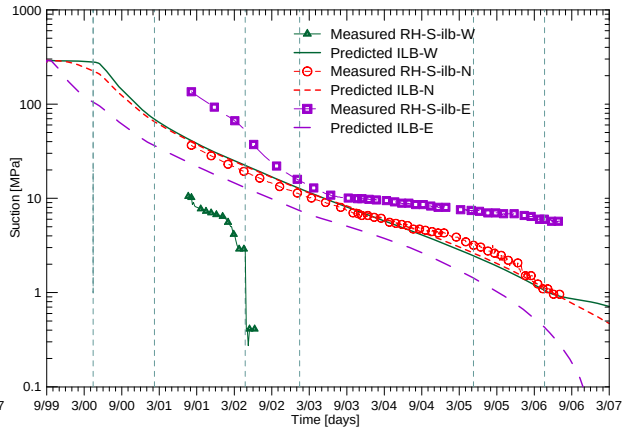

Figure 5-48: . Evolution of suction on ILB considering the leaks to the concrete

With the data available it is difficult to draw a conclusion about the hydrated state of the bottom of the seal by August 2006. It can only be said that it should be almost saturated at least from the rock to the middle part of the seal, since RH measurements report a suction of 1 MPa, a value for which the saturation degree is around 98%.

Seal mechanical results

In this section, the results of the evolution of the stresses inside the seal are presented. It is of special interest to see whether the mixture can finally achieve the desired swelling pressure, and whether the double porosity constitutive model can predict the behaviour of the seal, using the parameters calibrated with the infiltration tests.

To begin with, the evolution of the vertical and circumferential effective stress is shown for the Instrumented Level Top at different distances from the central tube. They are presented from Figure 5-49 to Figure 5-52. Graphical information on the location of the sensors is presented in each plot. Results are presented for total stresses (continuous line) and when numerical saturation is achieved, effective stresses are plotted using a dashed line.

The Instrumented Level Top is in the non compacted zone. The approximate dry density on this zone was γ_d =1.387 g/cm^3. The final values of swelling pressures in infiltration tests with γ_d =1.45 g/cm^3 were between 0.6 and 1 MPa, depending on the initial water content of the powder.

As can be seen, the measurements show differences between different directions in points located at the same radial distance. These differences are a consequence of the inherent variablity of an in situ test.

The evolutions of stresses in points close to the rock (ILT-01 and ILT-02) show a small increase on the stresses before the beginning of the artificial hydration. Afterwards some of them reach a peak, then they show a small decrease and finally most of them keep increasing its swelling pressure at an approximately constant rate. By August 2006 the circumferential stresses lie between 6 and 8 bars. The vertical values range from 7 to 12 bars. Total saturation in this zone was achieved approximately on May 2005, water pressures slowly rise afterwards and the effect on total stresses is not noticeable.

The sensors located in the centre of the seal (ILT-03 and ILT-04) begin rising at the start of artificial hydration. All directions show a different behaviour until the end of 2003 when they keep increasing at a constant rate.

The simulations, on the other hand, show an increase of the stresses when the water from the rock starts to enter, they reach a peak one year later (~ 7.0 bar) and a small trough can be appreciated two years later. Finally, the swelling pressure rises again at a constant rate. This type of behaviour that was consistent with the swelling pressure tests is shown by only one of the sensors, the ILT-01-North (see Figure 5-52).

At the end of the simulations, the total stress predicted by the model for the Instrumented Level Top is approximately 10 bar, a value in agreement with the measurements of vertical stress.

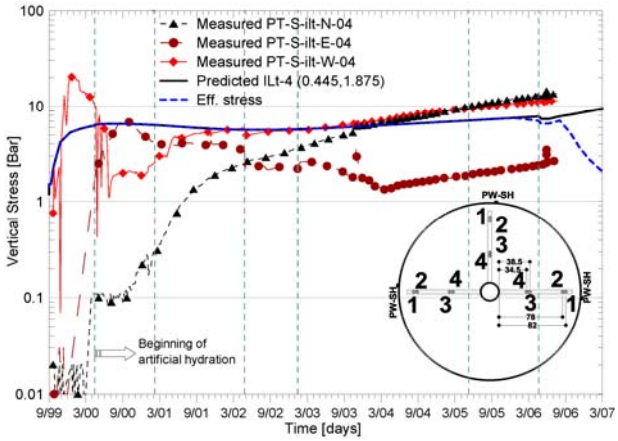

Figure 5-49: ***Vertical stress increment at r = 0.445 m. Instrumented level top.***

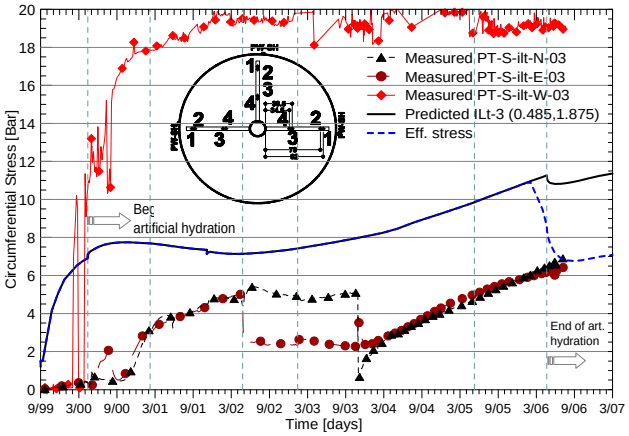

Figure 5-50: Circumferential stress increment at r = 0.485 m. Instrumented level top.

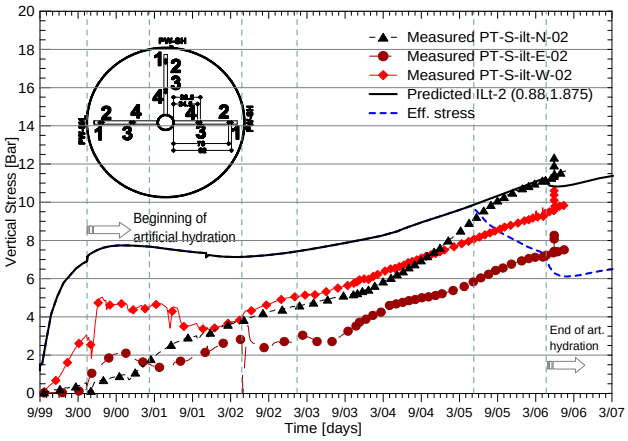

Figure 5-51: Vertical stress increment at r = 0.88 m. Instrumented level top.

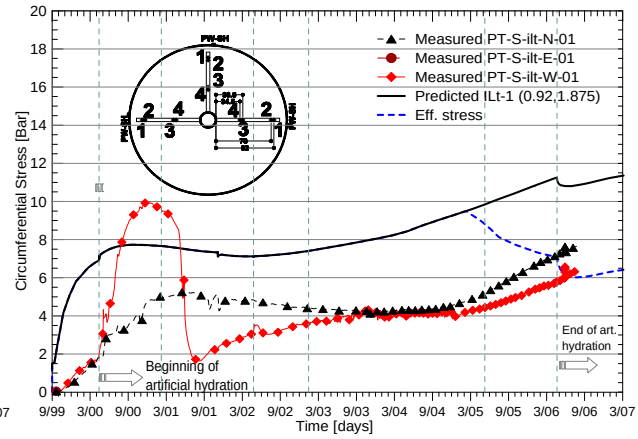

Figure 5-52: Circumferential stress increment at r = 0.92 m. Instrumented level top.

The sensors located on the interface with the rock at the same Instrumented Level Top, give information on the evolution of the radial stress; the measurements are shown in Figure 5-53. Other vertical stress measurements are available from the sensors located in the Hydration Level Top, they were in contact with the sand layer and the values measured are shown in Figure 5-54. As it can be observed, both plots show the same evolution in all directions, with a constant and gradual increase of stress values after the beginning of the artificial hydration. The values reached by August 2006 are between 5 - 8 bar, values a little lower than the ones reported by the sensors of the instrumented rods. Simulations show a different behaviour during the first years, and at the end indicate a larger stress value of 10 bar.

At this point it is interesting to show the displacements measured in the concrete plug placed over the seal. In Figure 5-55 the values measured on the top of the seal, at the centre and with respect to the concrete lining, are plotted. These displacements of the concrete plug might have contributed to the lower value of stresses at the hydration level top.

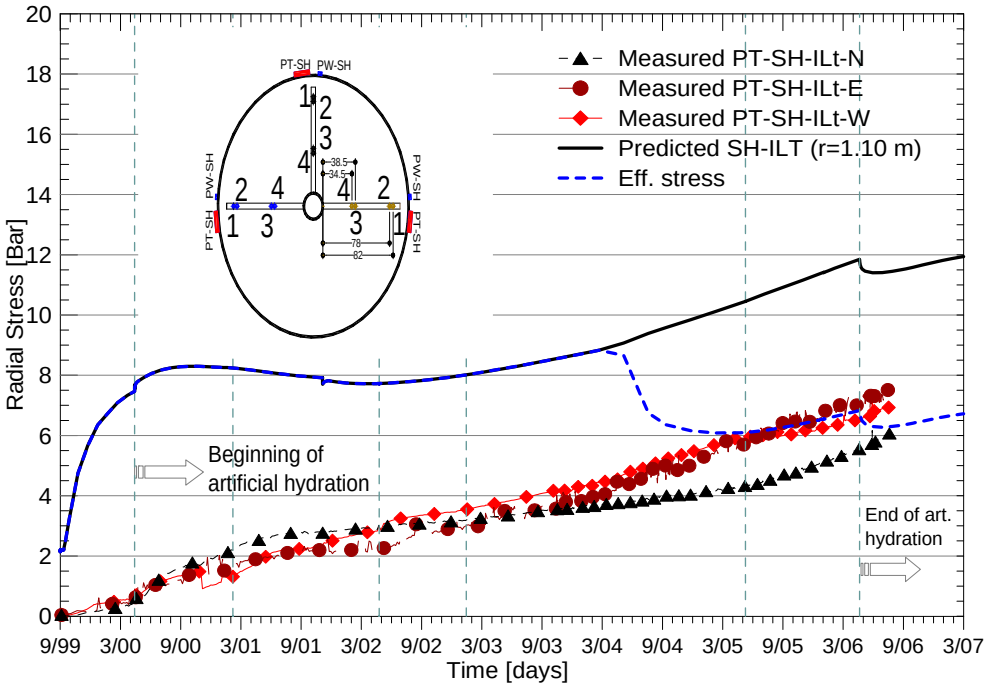

Figure 5-53: Radial stress increment at r = 1.10 m. Instrumented level top

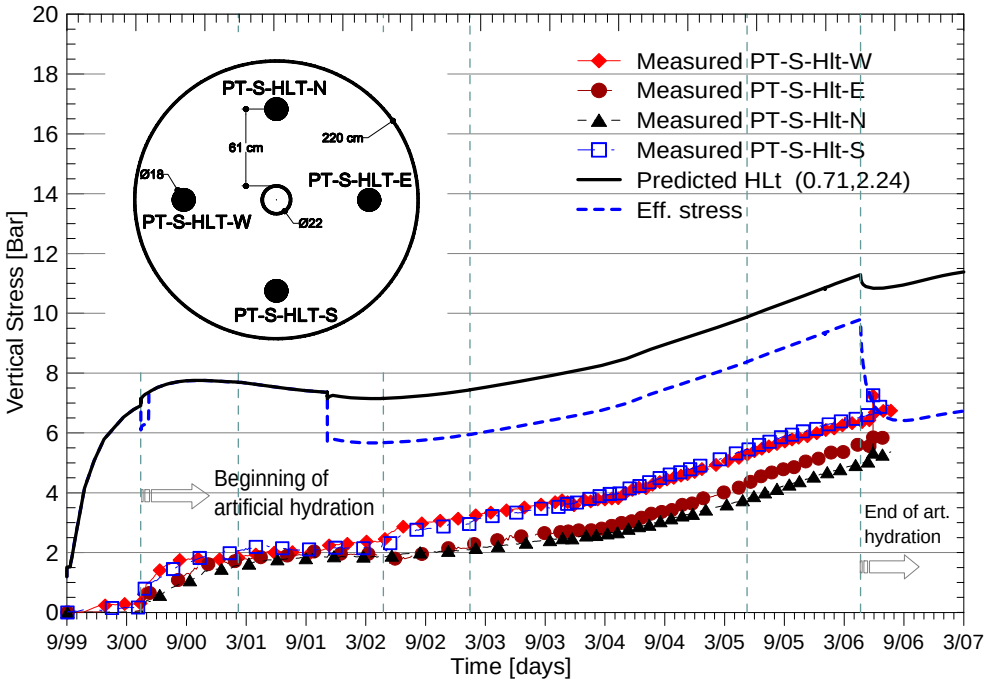

Figure 5-54: Vertical stress increment at r = 0.71 m. Hydration level top

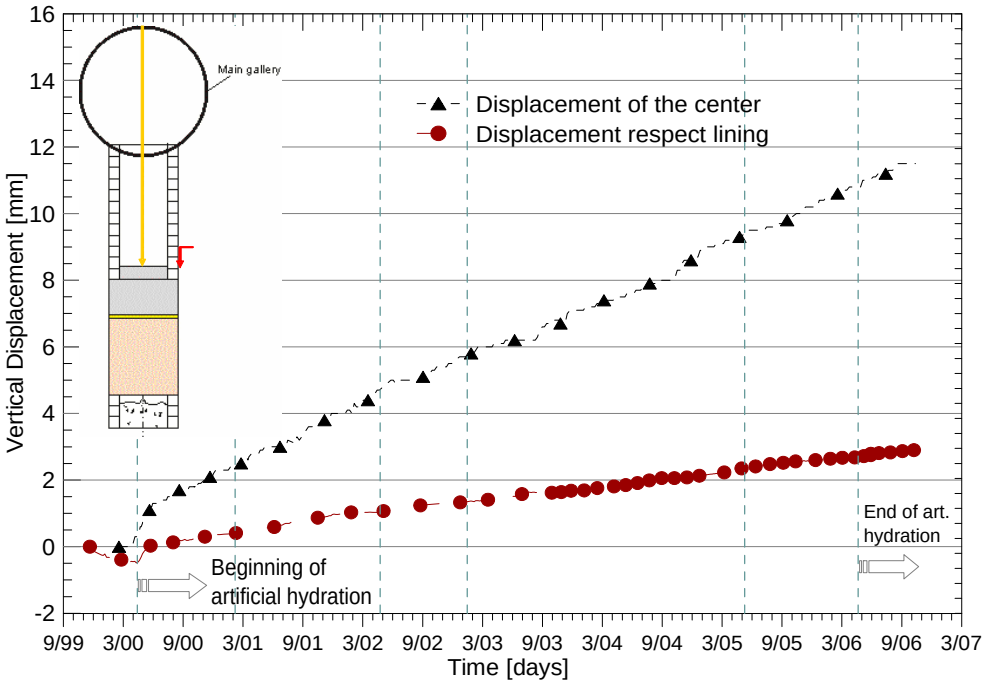

Figure 5-55: Displacements measured on the top of the seal

The measurements from sensors on the Hydration Level Middle are shown in Figure 5-56. They were made with a special sensor equipped with a black rubber cap filled with de-aired silicone oil in an effort to measure mean stresses. The measurements show the same pattern of development as the previous ones, a constant stress build up was registered, final value registered was 10 bars in August 2006. Simulations, on the other hand, agree with the final value but differ in the stress build-up.

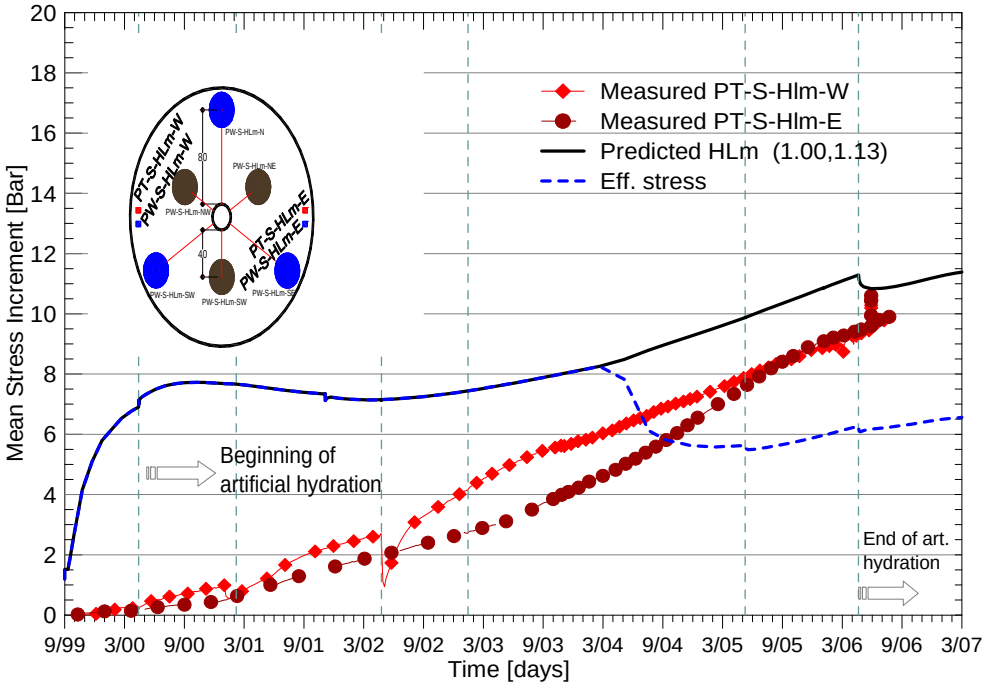

Figure 5-56: Mean stress increment at r = 1.10 m. Instrumented level middle

For the Instrumented Level Bottom, the measurements show a greater dispersion between the different directions, see from Figure 5-57 to Figure 5-60, especially for the sensors located in the middle of the seal (PT-S-ILB-04).

The vertical stress measured at the middle of the rods (r=0.445 m) does not seem to notice artificial hydration until the second increment on the hydration pressure in May 2002. Approximately in September 03, the stress evolution show an important jump that reaches a maximum value of approximately 10 bars in the West and North section. Circumferential stresses at the same distance show an approximately gradual stress build-up until the same date when they show a drop and a final sharp increase to values between 12 and 17 bars.

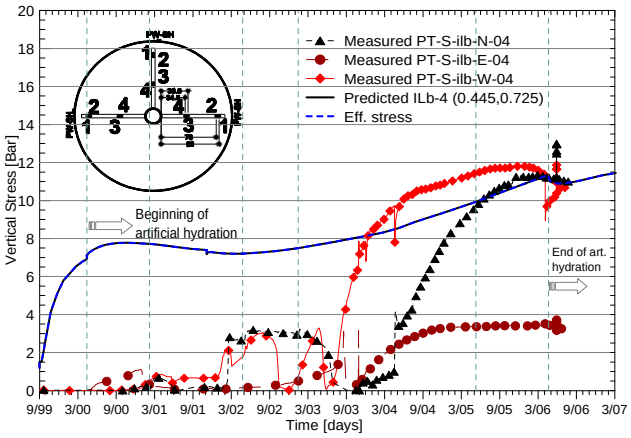

Figure 5-57: Vertical stress increment at r = 0.445 m. Instrumented level bottom.

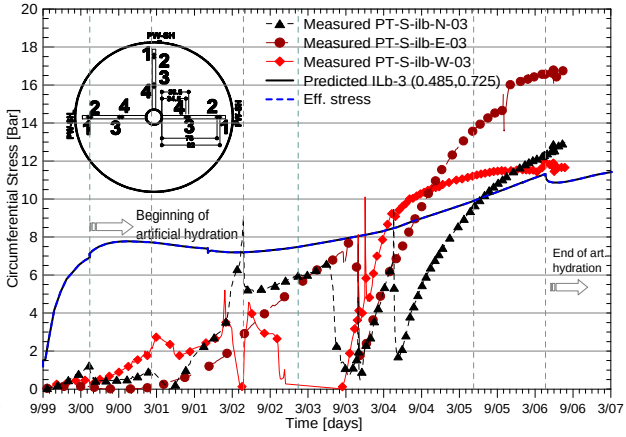

Figure 5-58: Circumferential stress increment at r = 0.485 m. Instrumented level bottom.

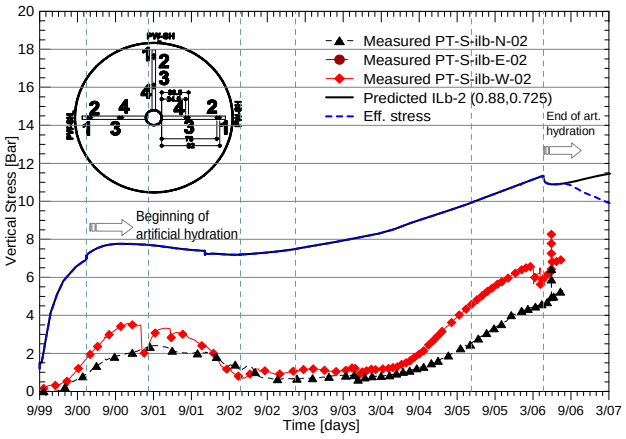

Figure 5-59: Vertical stress increment at r = 0.88 m. Instrumented level bottom.

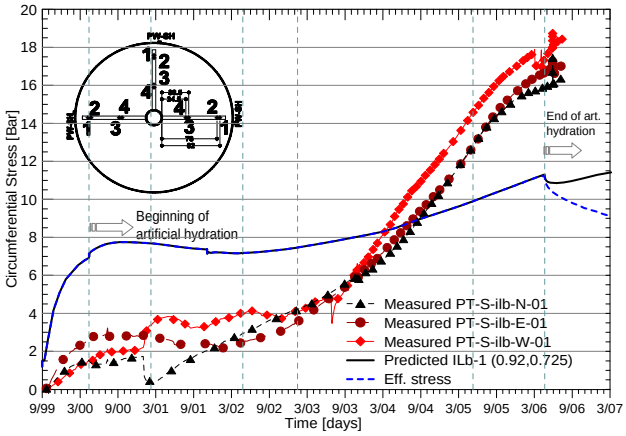

Figure 5-60: Circumferential stress increment at r = 0.92 m. Instrumented level bottom.

The sensors closer to the rock show a more homogeneous development between the different directions. However, the evolution is different between the vertical and the circumferential stresses. Vertical stress measurements (Figure 5-58) report a peak in 2001 of approximately 3.5 bar, afterwards a collapse that reaches the minimum in 2003 and then a recovery of the stresses that by August 2006 has reached a value of about 5-7 bar. On the other hand, the circumferential stress reaches a peak at approximately 2.0 bar in September 2000, and then it continues increasing at a constant rate until August 2006. The values reached vary between 16 - 18 bars and appear to be stabilizing.

The sensors located on the interface with the rock at the same Instrumented Level Bottom, give information on the evolution of the radial stress; the measurements are shown in Figure 5-61. Other vertical stress measurements are available from the sensors located at the Hydration Level Bottom, see Figure 5-62. As it can be seen, both plots show the same evolution in all directions, with a constant and gradual increase on the stress values after the beginning of the artificial hydration. The values reached by the radial stresses in August 2006 are of the order of 10 bar, a value a little lower than those reported by the sensors of vertical stress located at the Hydration Level Bottom that reached 12 bar in the North direction.

Obviously an axisymmetric model cannot fit all the measurements simultaneously if they depend on direction. Moreover, in this in-situ test, the different sensors located on the rods show a marked heterogeneity. Still it is considered that the simulations predict reasonable well the overall behaviour of the hydration levels top, middle and bottom, as well as the data obtained from the rods of the Instrumented Level Top.

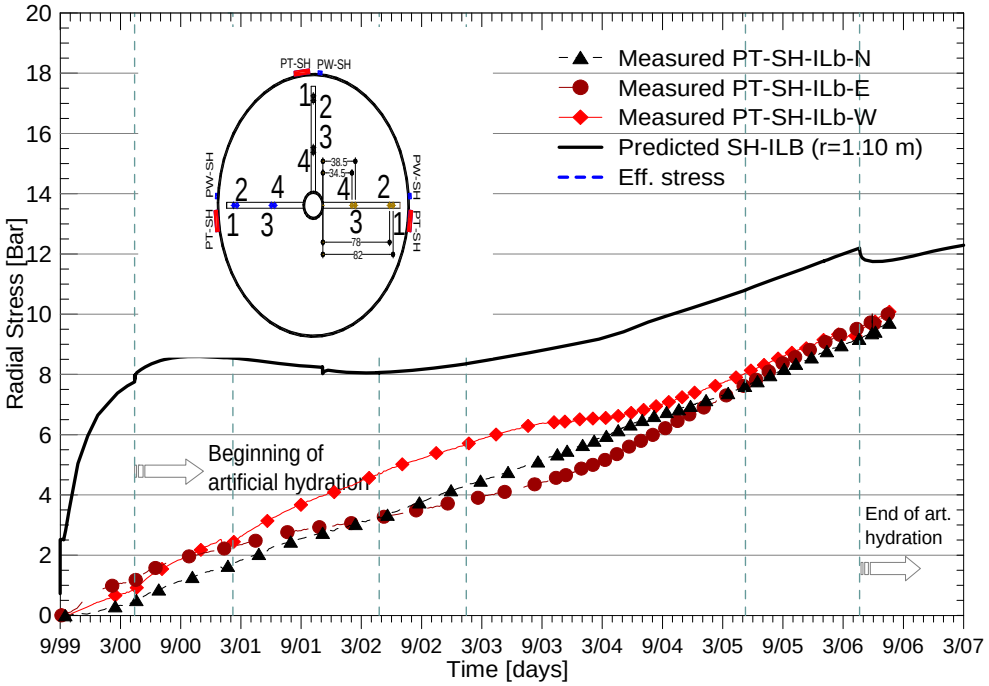

Figure 5-61: Radial stress increment at r = 1.10 m. Instrumented level bottom.

However measurements from the Instrumented Level Bottom are very different depending on orientation, and simulations only follow a similar stress build up to that measured in sensors PT-S-ILB-02, but predict a higher final swelling pressure. For the rest of sensors at the ILB measured stresses are higher and the model does not reproduce their behaviour satisfactorily.

Rock water pressures and stresses

The host rock instrumentation allowed the measurement of the changes caused on the rock by the seal installation and by its subsequent hydration. The host rock instrumentation was placed in six small boreholes drilled from the shaft, at the level of the test, in three radial directions. Three of them measured water pressure and total stresses, and the other three measured displacements.

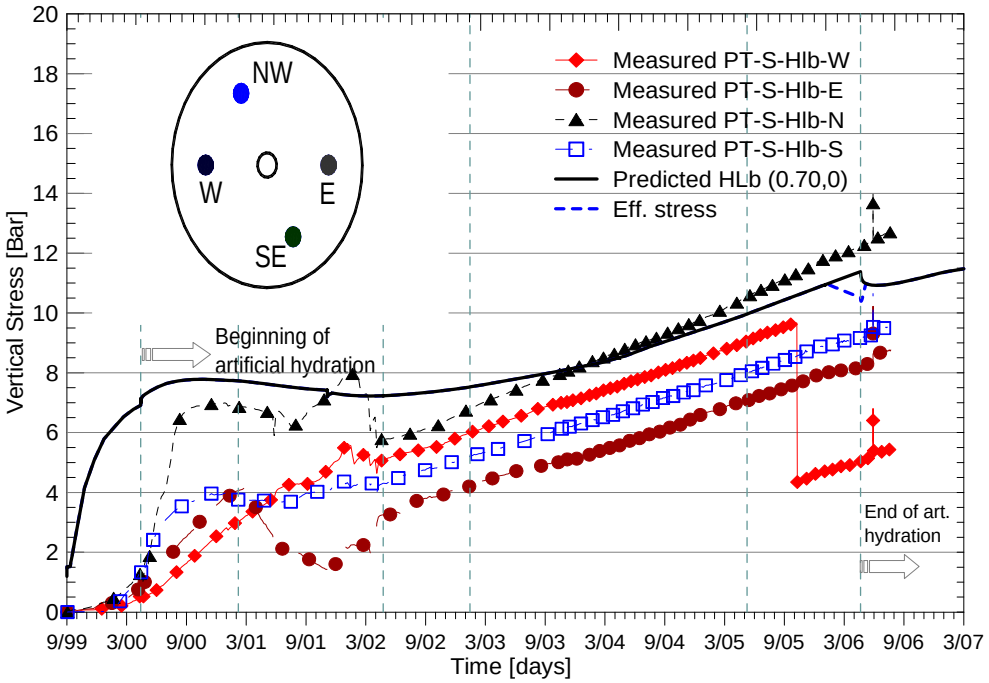

Figure 5-62: Vertical stress increment at r = 0.70 m. Hydration level bottom

In the following plots the measurements obtained from the boreholes are compared with the results obtained on the simulations. To begin with, the changes on water pressures are shown in Figure 5-63 to Figure 5-67; they correspond to the sensors located at different distances from the central tube, as shown in the diagrams contained in each graph.

As it can be seen, after the seal installation the water pressures show zero values for a long period of time. This is caused by the de-saturation of the rock caused by the installation of the seal. In February 2003, the air from the tubes connecting the host rock piezo-filters to the water pressure sensors in the main gallery was removed, and the measurements show a small increase in water pressure.

As a consequence, the moment of re-saturation of the rock is not known specially for the sensors place farther away. All the sensors on the West section report re-saturation around this date. The re-saturation in other directions is delayed more. For the point closest to the seal interface (r=1.10m), measurements are influenced by the subsequent increments of injection pressure and it is difficult to establish the moment at which North and East directions report positive water pressures.

The analysis, on the other hand, indicates resaturation eight months later. Except for the seal/rock interface where differences are not as large, numerical results report a slower hydration process. Liquid pressures after saturation show a rate of increase slower than the measurements. The rate of recovery of the simulated liquid pressures depends in part on the details of the boundary condition at the lining over and under the seal (see Figure 5-30) and on the rock liquid permeability.

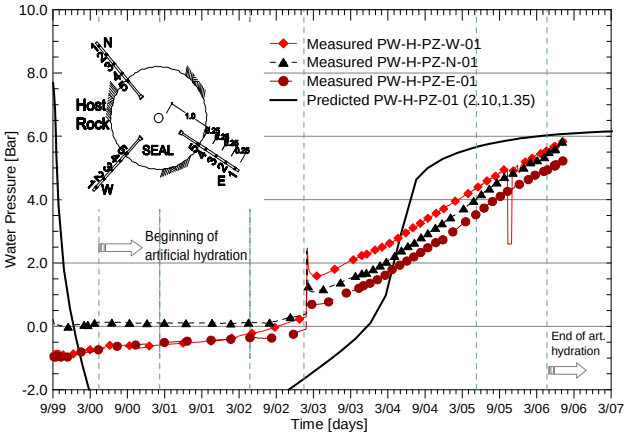

Figure 5-63: Rock water pressure at r = 2.10 m.

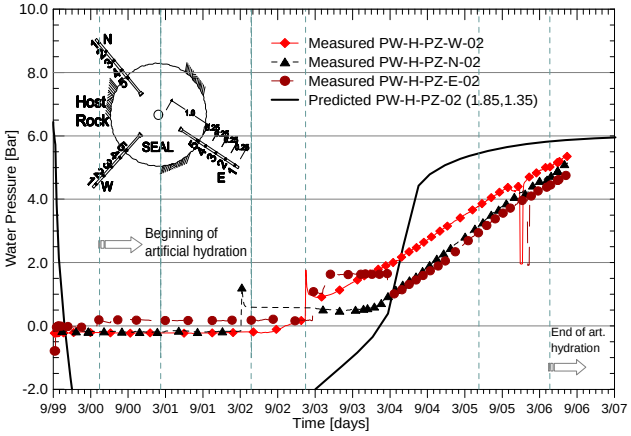

Figure 5-64: Rock water pressure at r = 1.85 m.

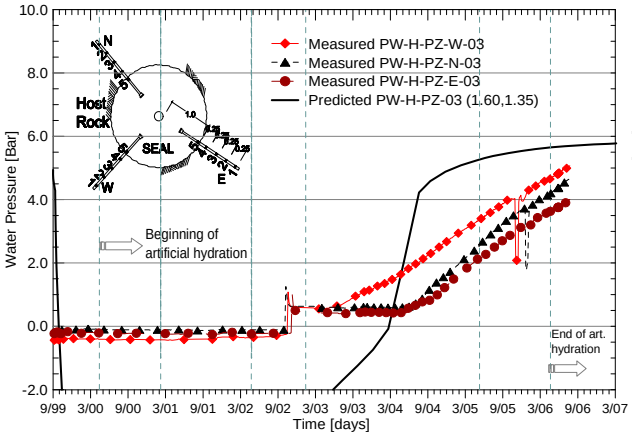

Figure 5-65: Rock water pressure at r = 1.60 m.

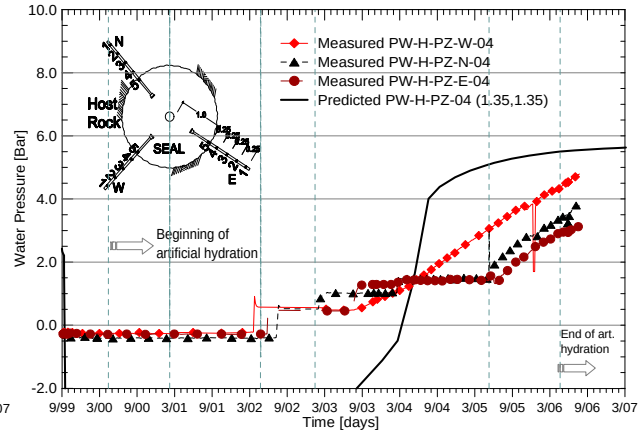

Figure 5-66: *Rock water pressure at r = 1.35 m*.

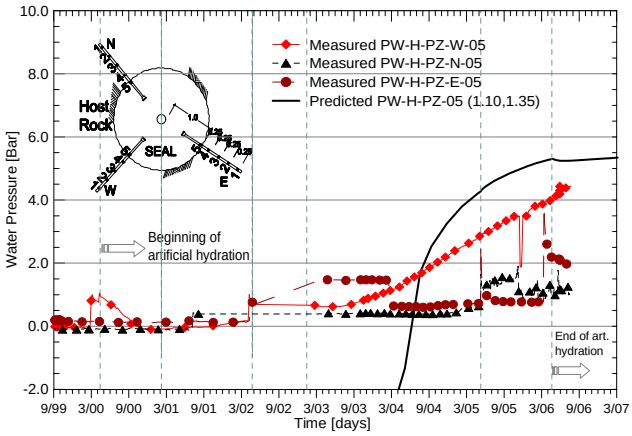

Figure 5-67: Rock water pressure at r = 1.10 m.

In Figure 5-68 and Figure 5-69 the data obtained from the displacement sensors installed in the rock are shown. Displacements at the beginning are positive, when artificial hydration starts, they become positive indicating a movement of the rock towards the seal. As soon as the Boom Clay is saturated (see Figure 5-65), it moves back towards its original position.

The movements predicted by the model, on the other hand, indicate a fast movement of the rock towards the shaft when it loses water due to the presence of the dry seal. Afterwards the rock returns gradually to its original position as hydration progresses.

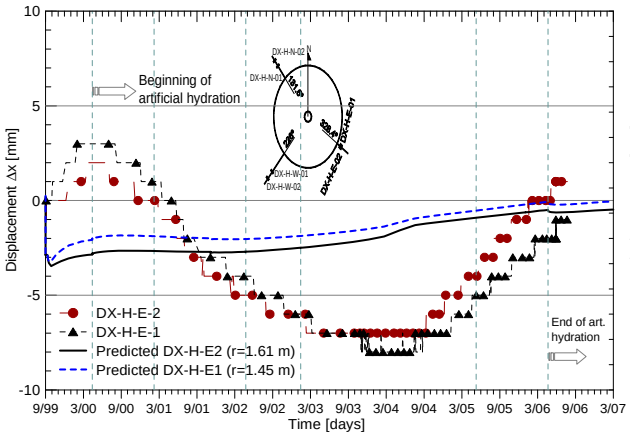

Figure 5-68: Displacements on the rock at the East drill (r = 1.45 and 1.65 m.)

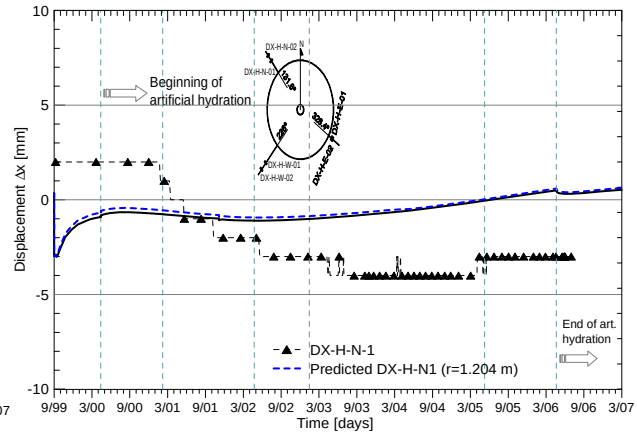

Figure 5-69: Displacements on the rock at the North drill (r = 1.20 and 1.24 m.)

The mechanical response of the rock to the installation of the seal is shown from Figure 5-70 to Figure 5-79. They correspond to the circumferential and vertical stress measurements performed with the multi-piezometers.

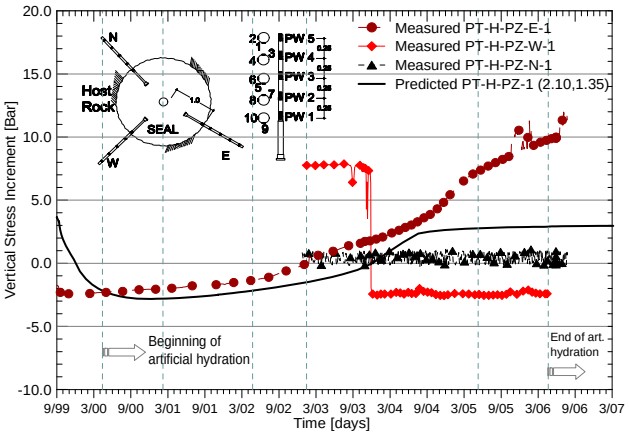

Figure 5-70: ***Rock vertical stress increment at r = 2.10 m.***

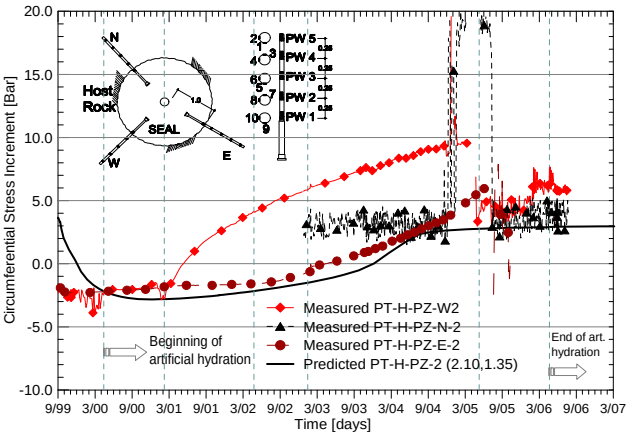

Figure 5-71: Rock circumferential stress increment at r = 2.10 m

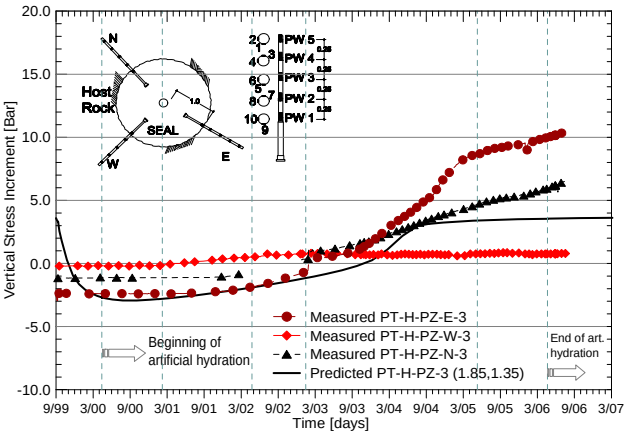

Figure 5-72: ***Rock vertical stress increment at r = 1.85 m.***

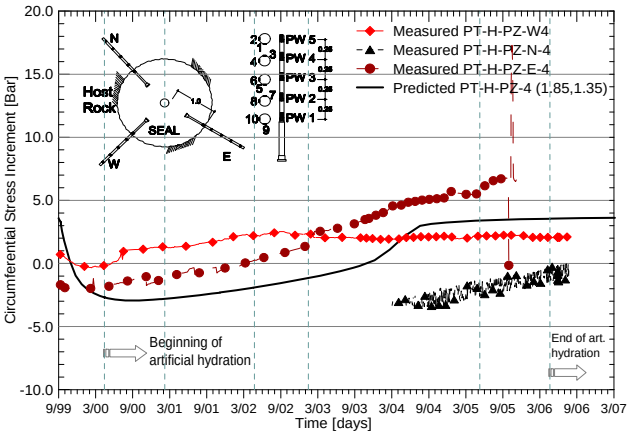

Figure 5-73: Rock circumferential stress increment at r = 1.85 m

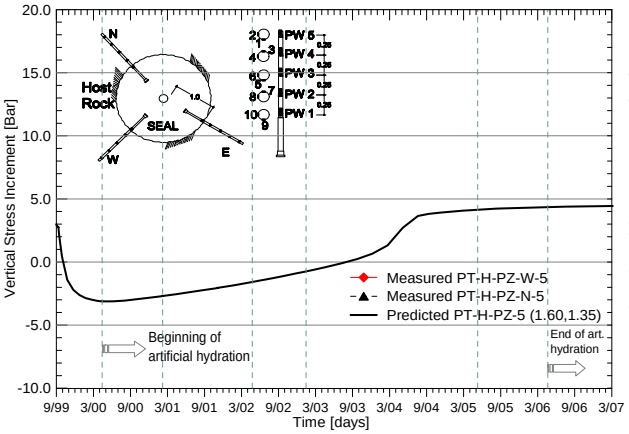

Figure 5-74: ***Rock vertical stress increment at r = 1.60 m.***

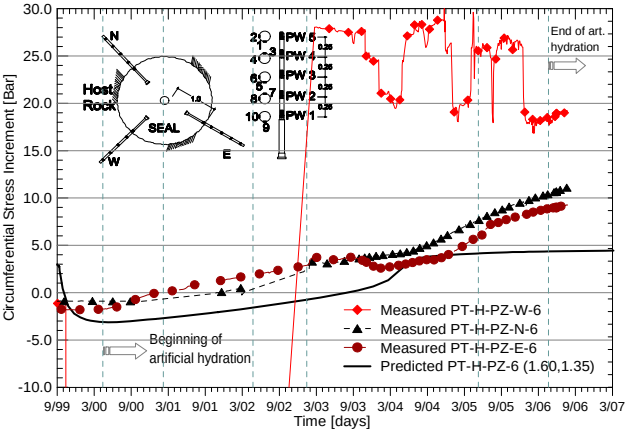

Figure 5-75: Rock circumferential stress increment at r = 1.60 m.

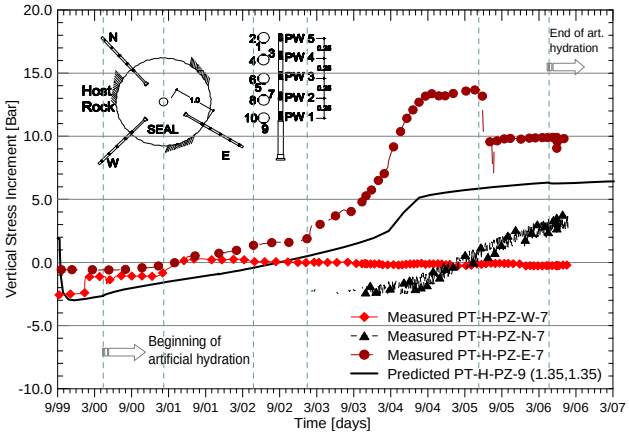

Figure 5-76: ***Rock vertical stress increment at r = 1.35 m.***

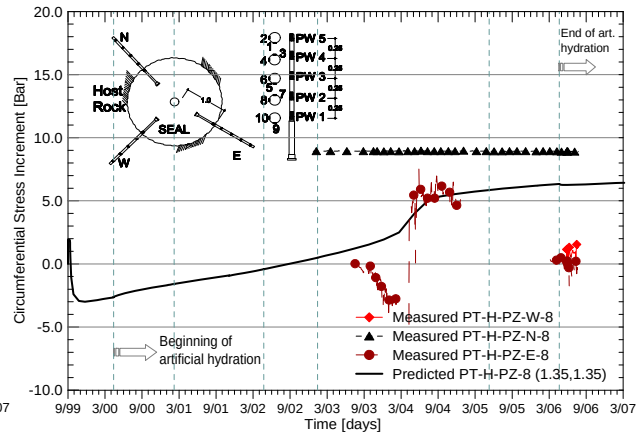

Figure 5-77: Rock circumferential stress increment at r = 1.35 m.

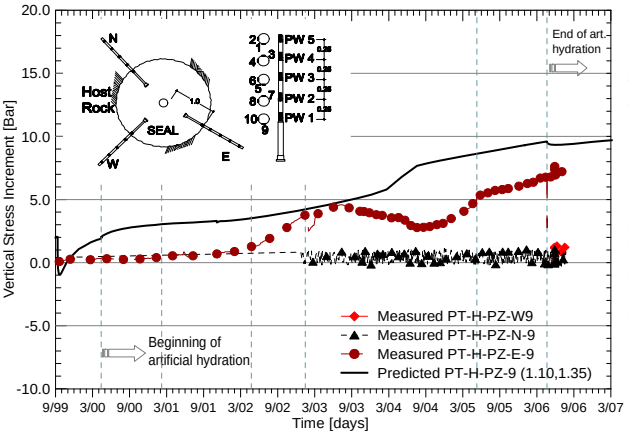

Figure 5-78: ***Rock vertical stress increment at r = 1.10 m.***

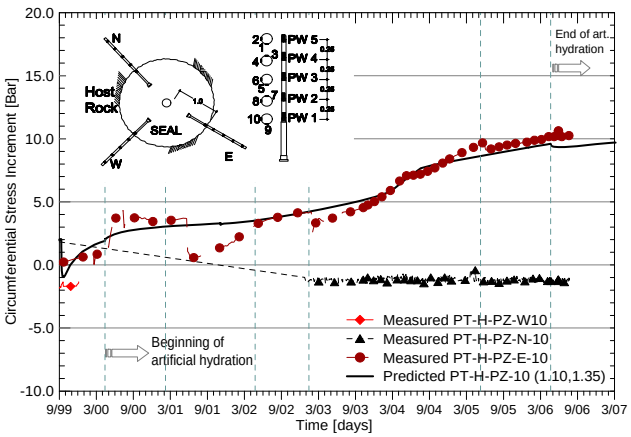

Figure 5-79: Rock circumferential stress increment at r = 1.10 m.

To be able to make better comparisons, the numerical results are shown for total stress increments. This is done to better include measurements that start from a zero value. In the plots, it can be observed that de-saturation of the rock is accompanied by shrinkage of the Boom Clay, which undergoes displacements towards the seal as shown by the displacement observations. Since the shrinkage is volumetric, the prediction for circumferential stress decreases during that stage.

When the seal starts to swell, the host clay interface moves back and the circumferential stress is partly recovered. During water pressure equilibration, after the complete hydration of the clay, the total circumferential stress increases at a constant rate.

Data measurements show a tendency qualitatively similar to the predicted path. Total stress sensors measurements indicate a rapid reduction in the total circumferential stress, followed by a slow increase starting approximately at the time of seal swelling. From a quantitative point of view, measurements appear to indicate that the stress changes are more moderate.

5.3.2 Analysis performed by CEA

5.3.2.1 Features of the model

Initial conditions

In the analysis of the shaft sealing test, like in the laboratory tests calculations, a homogenized FoCa clay material is considered for the lower and the upper zones, the characteristics of which are given by the experimenters in Table 5-13. The seal is unsaturated. The initial stress in the whole seal is assumed to be a spherical tensor equal to the atmospheric pressure.

Boom Clay composes the host rock; its physical characteristics are given in Table 5-14. In natural state, before the shaft sinking, the host rock is fully saturated, the water pressure is the hydrostatic pressure of the site: $2.2\ 10^6$ Pa. A natural stress tensor slightly anisotropic is considered:
$\sigma_{xx} = \sigma_{yy} = -4.22\ 10^6$ Pa, $\sigma_{zz} = -4.10\ 10^6$ Pa.

After the shaft sinking, an EDZ appear in the host rock around the shaft, but uniform properties of the entire host rock are used. For the seal hydration, the initial state in the host rock is calculated by a transient hydro-mechanical decompression.

Table 5-13: Shaft sealing test, physical characteristics

Characteristics	FoCa clay pellets/powder lower zone	FoCa clay pellets/powder upper zone	Boom clay
solid grain density $[kg/m^3]$	2675.0	2675.0	2650.0
dry density $[kg/m^3]$	1458.36	1282.27	-
water content [-]	0.06	0.06	-
porosity [-]	0.455	0.521	0.39
saturation [-]	0.193	0.148	1.
suction [-]	$1.64\,10^9$	$3.5\,10^9$	-

Hydraulic boundary conditions

Concerning the seal boundary conditions, in the first phase the water goes from the saturated host rock to the seal, a zero water flux is applied on the other boundaries. In the second phase ($t > 228.4$ day) a forced water injection is applied on the filters. Figure 5-81 represents the pump pressure, the water pressure at the filters is the sum of pump pressure and hydrostatic pressure (from the HADES gallery pump location to filter). A scheme of hydraulic boundary conditions is shown Figure 5-80 in axisymmetric mode. At the interface seal/host rock a continuity condition is assumed for water flux.

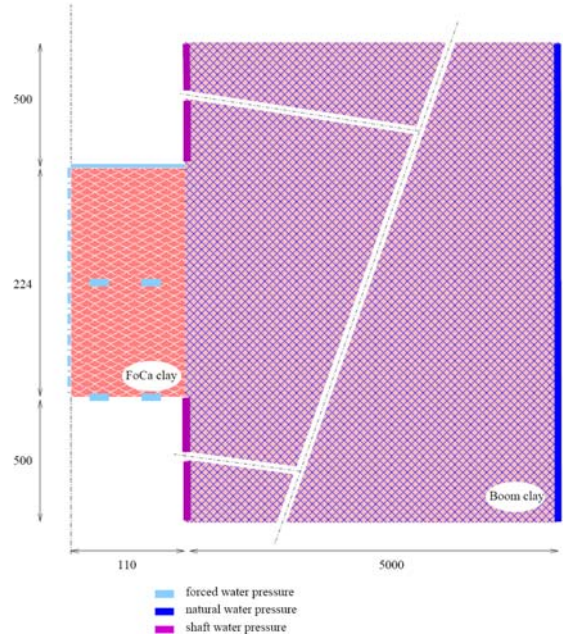

Figure 5-80: Shaft sealing simulation, hydraulic boundary conditions.

On the host rock boundary, on the parallel surface far from the shaft, the natural hydrostatic pressure is applied: 2.2 10^6 Pa. At the shaft boundary before the seal installation and according to experimenters' data a water pressure head corresponding to an air shaft relative humidity of 100 % is used; during the seal hydration, the experimenters propose a 60 % air relative humidity rate. Anywhere else, i.e. in the perpendicular surface of the shaft and far from the seal, a zero water flux is applied.

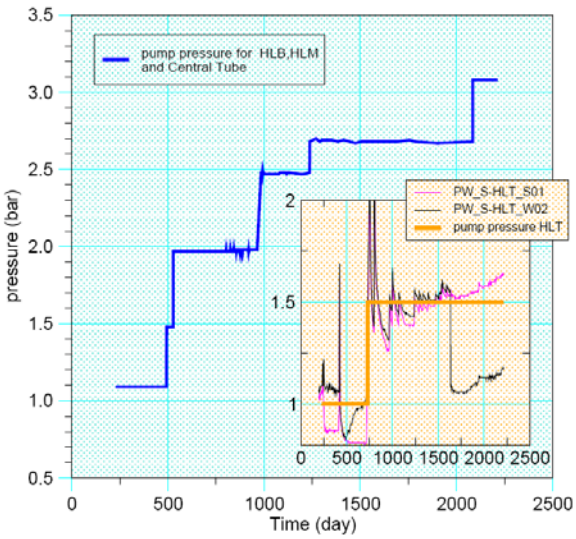

Figure 5-81: Shaft sealing simulation, pump water pressure.

Mechanical boundary conditions

At the seal boundary, a zero normal displacement is applied whereas at the interface seal/host rock a continuity condition is assumed for displacement.

On the host rock, in the parallel surface far from the shaft the natural stress is applied. At the shaft boundary, an atmospheric pressure is applied. Anywhere else, i.e. in the perpendicular surface of the shaft and far from the seal, a zero normal displacement is applied.

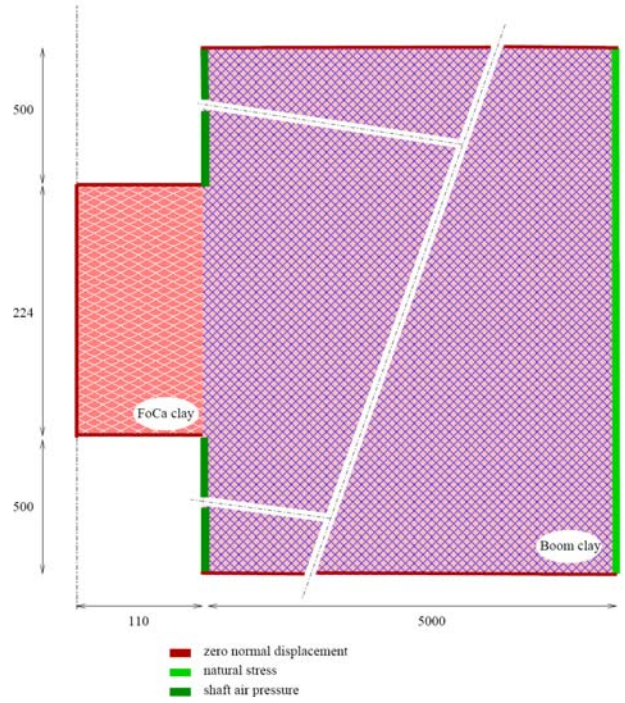

Figure 5-82: Shaft sealing simulation, mechanical boundary conditions.

Geometry and discretization

The geometry of the seal and host rock is axisymmetric. The water injection filters in the horizontal hydration level are not strictly placed in an axisymmetric mode around the central tube. Like in the laboratory test calculations, axisymmetric hydro-mechanical behaviour is assumed. The bottom and middle levels filters are represented by two rings, internal (near the axe) and external (near the host rock), at two levels; their total surface is the filters surface.

The seal dimensions are given by the experimenters, the host rock boundaries are far from the seal: horizontally 50 meters from the shaft and vertically 5 meters below and above the seal. The reference case mesh used in the calculations (Figure 5-83) is composed of 8924 nodes and 5906 elements.

The space discretization in the presented mesh is relatively coarse:

- in the seal, the mesh size is in the range from 2.7 cm to 5.8 cm ;
- in the host rock, near the seal the mesh size is in the range from 5 cm to 14 cm.

The standard time discretization is also relatively coarse: the time step increase from 1350 s to one day. The simulation period is 2300 days, for the reference case, the total time steps is 3336 and the CPU time is about 20 hours on AMD Opteron processor 252.

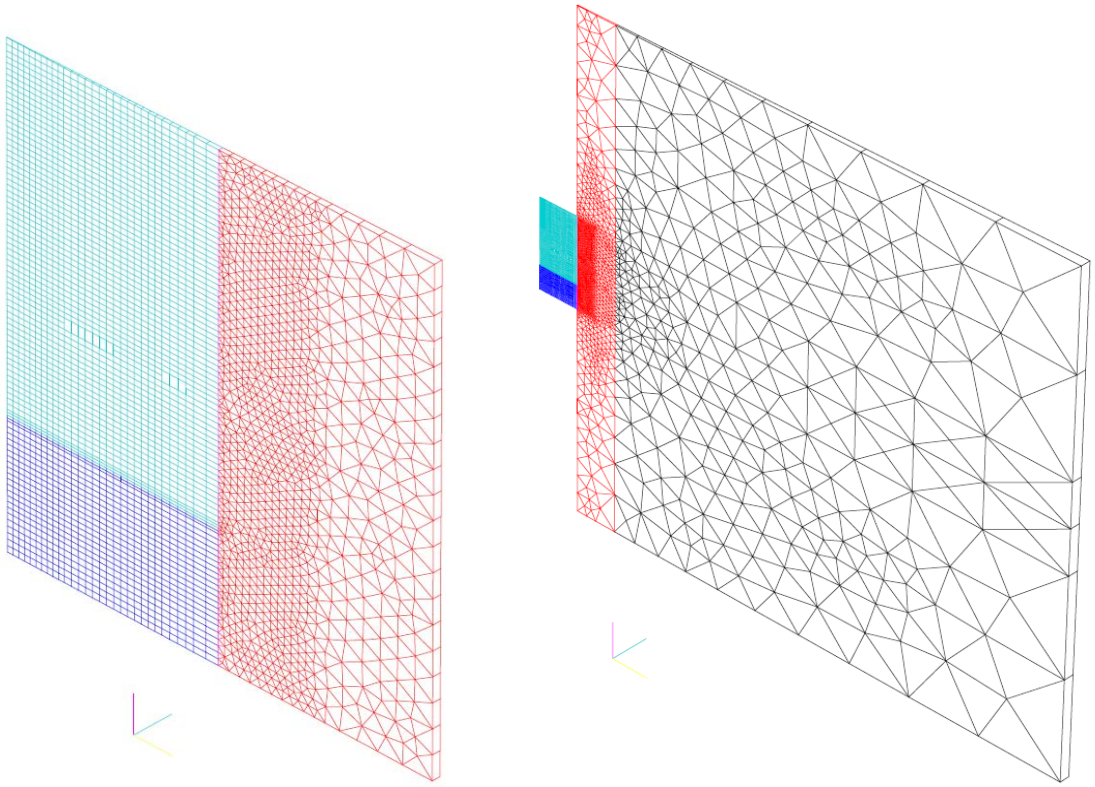

Figure 5-83: Shaft sealing simulation, mesh.

Physical characteristics

The retention and permeability curves parameters, the BBM elasto-plastic parameters are given in the Table 5-14 for FoCa and Boom Clay. They come from Reseal I data report (Volckaert *et al*., 2000).

Initial state in the host rock due to shaft sinking

The analysis of seal hydration requires the knowledge of the initial condition in the host rock; this initial state is calculated by a transient hydro-mechanical decompression.

The host rock is initially in a hydro-mechanical natural state. At the shaft boundary, water pressure and stress decreasing from natural conditions to atmospheric pressure are applied. The hydro-mechanical constitutive laws of the host rock are the usual ones: Van Genuchten retention and permeability curves, BBM behaviour; the parameter values are given in Table 5-14.

The hydro-mechanical coupling calculation is stopped when the pressure water is sufficiently low, about 5 bar at one meter of the shaft surface (according to experimental data). The resulting state of the host rock (Figure 5-84 and Figure 5-85) is certainly not completely realistic, but it represents a better approximation than a constant natural water pressure or stress.

Table 5-14: Hydromechanical parameters used in CEA modelling

Parameters	CEA sample FoCa clay	Shaft test FoCa clay	Shaft test Boom clay
Van Genuchten retention curve			
λ [-]	0.27	0.27	0.60
s_{ref} [MPa]	17.00	17.00	20.00
S_r [-]	0.00	0.01	0.01
Kozeny permeability			
k_i [m^2]	$6\,10^{-21}$	$6\,10^{-21}$	-
A [-]	3.00	3.00	-
ω_k [-]	0.405/0.382	0.405/0.382	-
Van Genuchten permeability			
k_i [m^2]	-	-	$4.5\,10^{-21}$
A [-]	-	-	0.50
λ [-]	-	-	0.60
B [-]	-	-	2.00
BBM parameters : elastic coefficient			
shear modulus G [Pa]	$150\,10^6$	$150\,10^6$	$150\,10^6$
Poisson coef. ν [-]	0.4955	0.4955	0.333
BBM parameters : elastic function $v = f(\ln(-p))$			
κ_0 [-]	0.002	0.12	0.0265
α_k [-]	$3\,10^{-9}$	$3\,10^{-9}$	0.00
BBM parameters : elastoplastic function $v = f(\ln(-p))$			
$\lambda(0)$ [-]	0.16	0.17	0.26
r [-]	0.75	0.17	0.564
β [$Pa{-}1$]	$5\,10^{-8}$	$5\,10^{-8}$	$5.44\,10^{-5}$
BBM parameters : elastic function $v = f(\ln(s))$			
κ_s^0 [-]	0.10	0.07	$3.22\,10^{-3}$
β_{ks} [-]	0.12	0.00	0.00
γ [-]	$1.4\,10^{-8}$	0.16	0.00
p_{ref} [$Pa{-}1$]	10^4	10^4	–
BBM parameters : elastoplastic function $v = f(\ln(s))$			
λ_s [-]	0.70	0.70	$3.22\,10^{-2}$
BBM parameters : yield surfaces definition			
initial p_0^* [Pa]	$1.2\,10^6$	$4\,10^5$	$6\,10^6$
initial s_0 [Pa]	10^7	10^7	10^7
reference p_c [Pa]	10^5	10^5	10^5
slope k [-]	0.10	0.10	$7.32\,10^{-3}$
slope M [-]	1.50	1.50	1.00
water, grain solid compressibilities			
β_w [$10^{-10}Pa^{-1}$]	4.50	4.50	4.50
β_s [$10^{-11}Pa^{-1}$]	1.80	1.80	1.80
ρ_{w0} [$10^2 kg/m^{-3}$]	9.98	9.98	9.98
u_{w0} [$10^5 Pa$]	1.01	1.01	1.01
viscosity μ_w [$10^{-3}kg/(m.s)$]	0.89	0.89	0.89

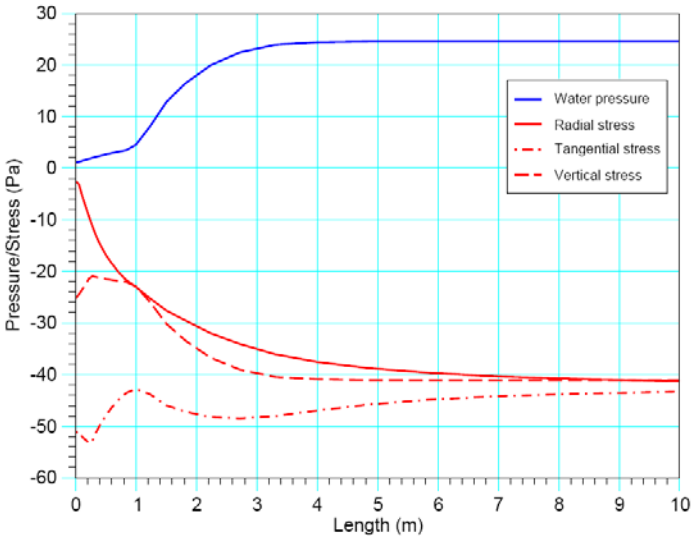

Figure 5-84: Simulation of initial condition in the host rock, water pressure, stress.

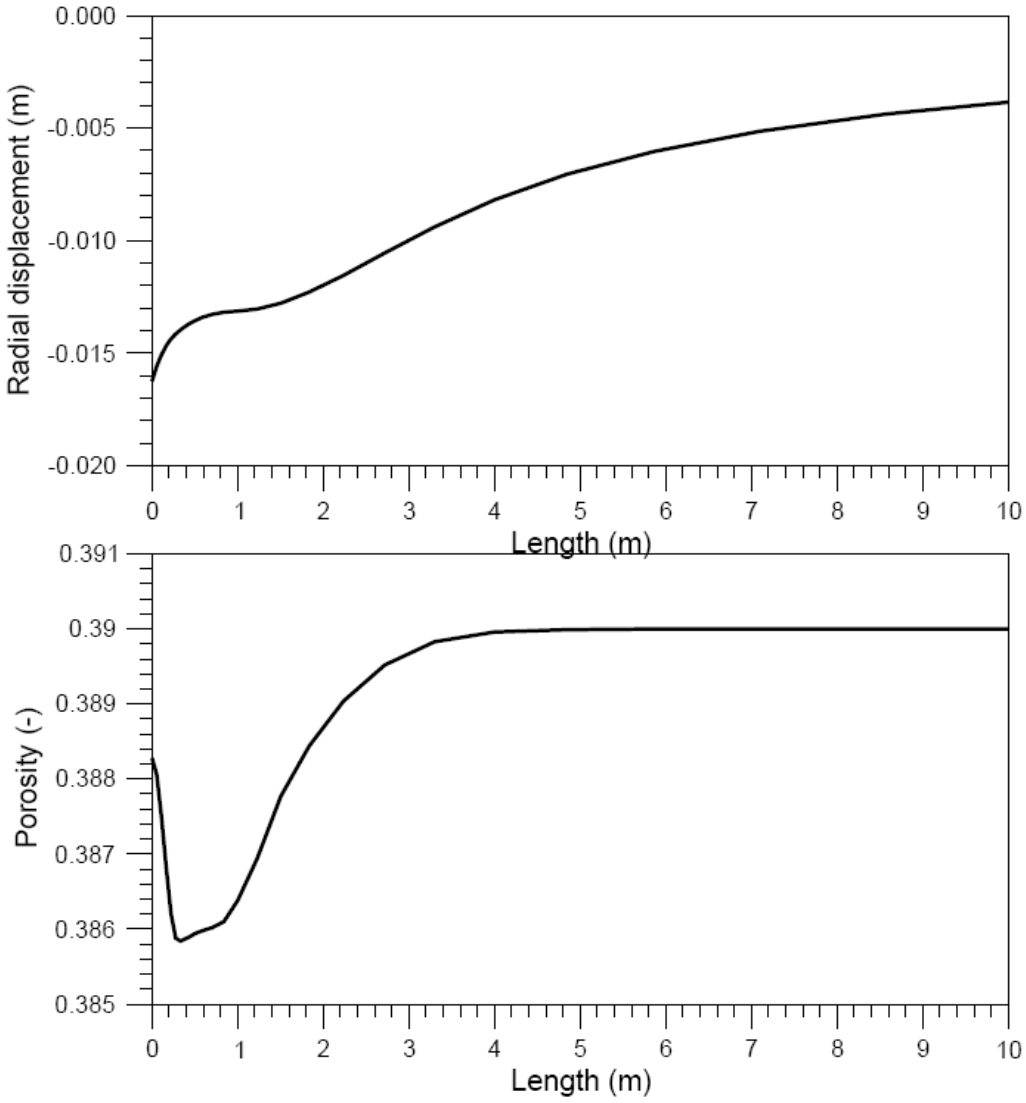

Figure 5-85: Simulation of initial condition in the host rock, displacement, porosity

5.3.2.2 Results and discussion

First a reference case is considered and then a sensitivity analysis on hydraulic parameters is performed. Finally, a few mechanical results are shown in the chaining mode of hydro-mechanical modelling.

Reference case

The reference case is defined by bentonite and host rock characteristics shown in Table 5-13 and Table 5-14, initial and boundary conditions are those outlined above and a specific choice in boundary condition on the shaft surface: 100 % air humidity rate; therefore the suction at this surface is zero.

The water injected in the seal (Figure 5-86) shows a calculation result similar to the test result at the end of simulation: 1.85 m^3 forced injected water at 2300 days ; however a steady state by the host rock appear more quickly in the calculation, around 750 days after the hydration start. At this time the calculated water flux through the filters and at the interface seal/host rock are nearly zero (Figure 5-87), the seal is saturated: the maximum water volume is reached at 4.2 m^3. The experimental injected water flux increases again slowly at 2300 day, an explication may be some water leakage (e.g. in the upper part of the seal from the sand filter to the shaft).

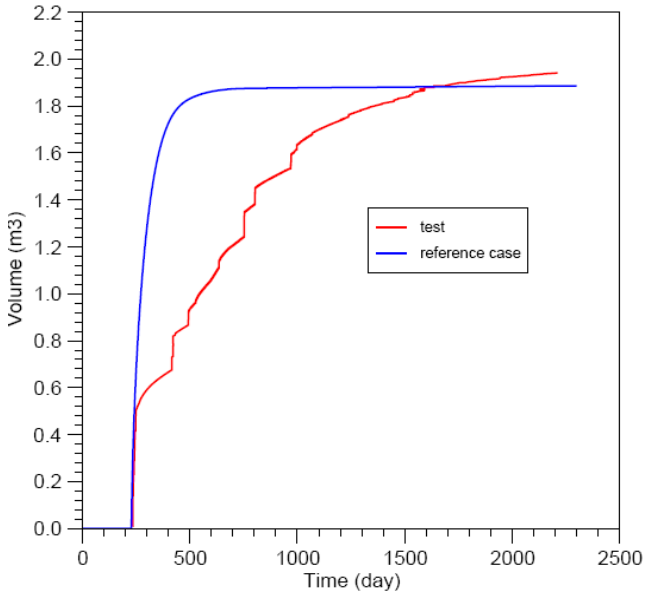

Figure 5-86: Water forced injection in the seal, reference case.

The qualitative calculation results in the seal and the near host rock are quite good before and after the water forced injection beginning at 228.4 day (Figure 5-88 and Figure 5-89). The lower part of the seal has a higher density and is hydrated more slowly.

The comparison of experimental and calculation pressure water results in the instrumented levels of the seal (Figure 5-90 and Figure 5-91) shows a calculated water pressure lower than the experimental one: under one absolute bar at the steady state. At the interface seal/host rock the calculated water pressure is higher (Figure 5-92): 2 bar at the top and 2.5 bar at the bottom of the seal.

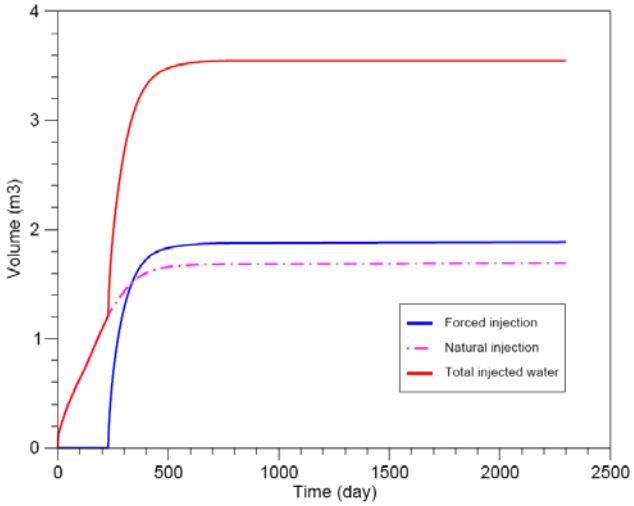

Figure 5-87: Water in the seal, reference case.

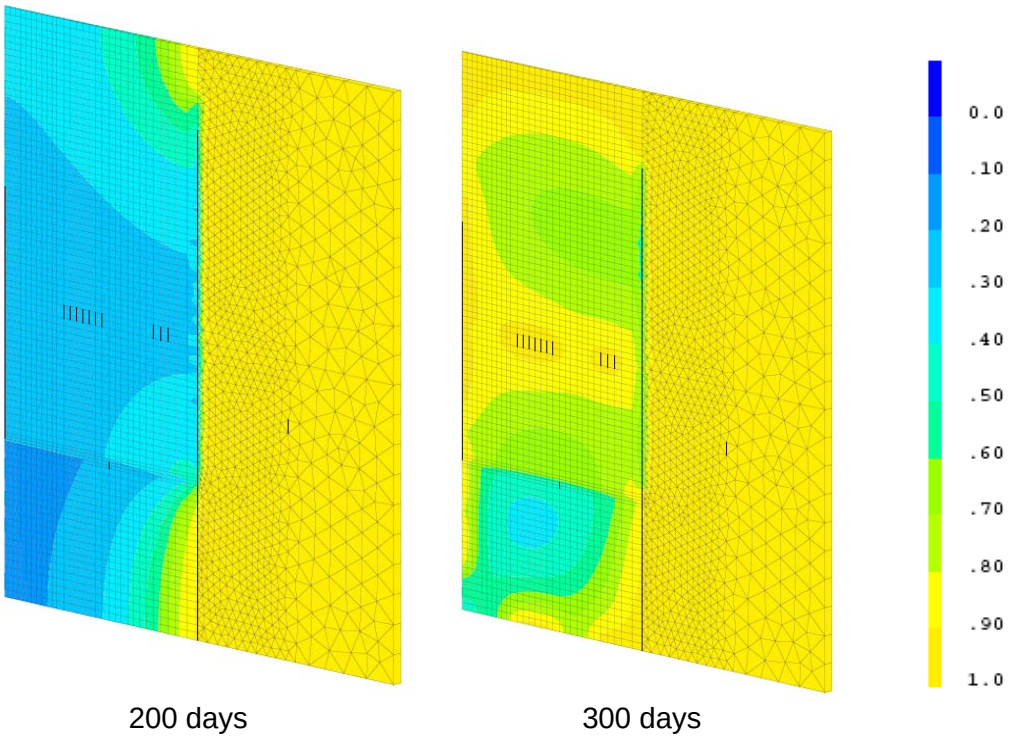

Figure 5-88: Seal, host rock saturation isovalues, reference case.

The differences between calculated and experimental suction in the seal (Figure 5-93 and Figure 5-94) confirm the quicker hydration obtained with the hydraulic model. The interfacial suction bentonite/host rock in Figure 5-95 shows on the contrary a delay in the hydration at this interface.

Initially, the host rock is entirely saturated. When in contact with the unsaturated seal, the host rock desaturates slightly, then the host rock saturation arises rapidly to generate, in front of the bentonite seal, a calculated steady state water pressure higher than experimental one at 2300 days (Figure 5-96 and Figure 5-97). In the upper or lower zone of the seal, the calculated water pressure in the host rock at steady state is much lower than experimental one: the experimental

water pressure increase regularly to 11 bar), the calculated pressure is constant at 6 bar (Figure 5-98).

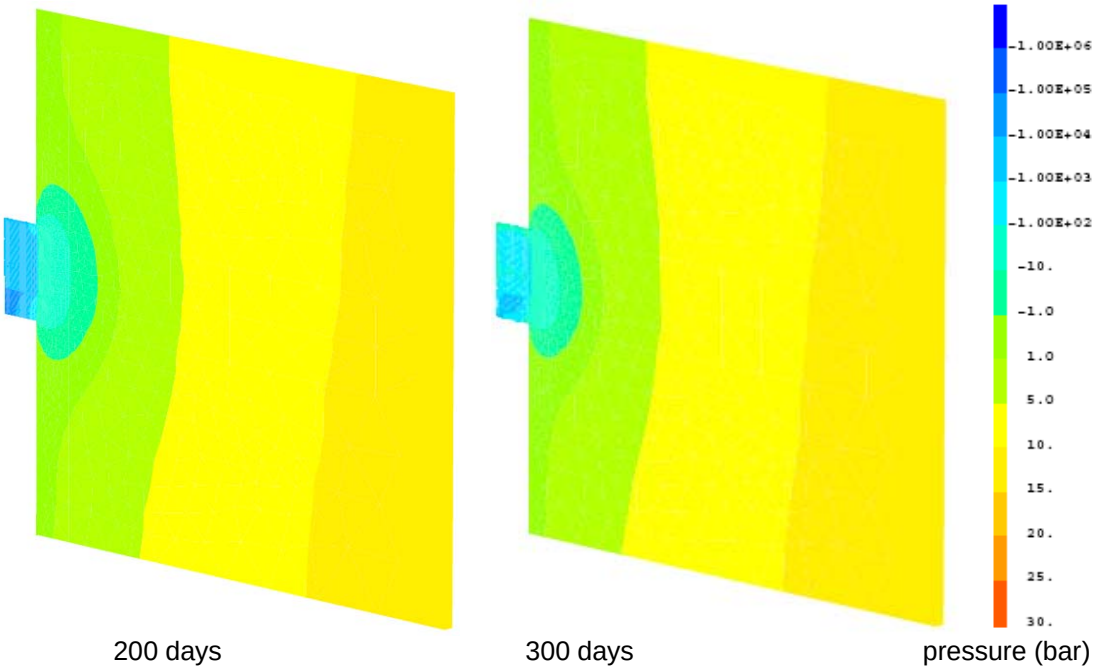

Figure 5-89: Seal, host rock water pressure isovalues, reference case.

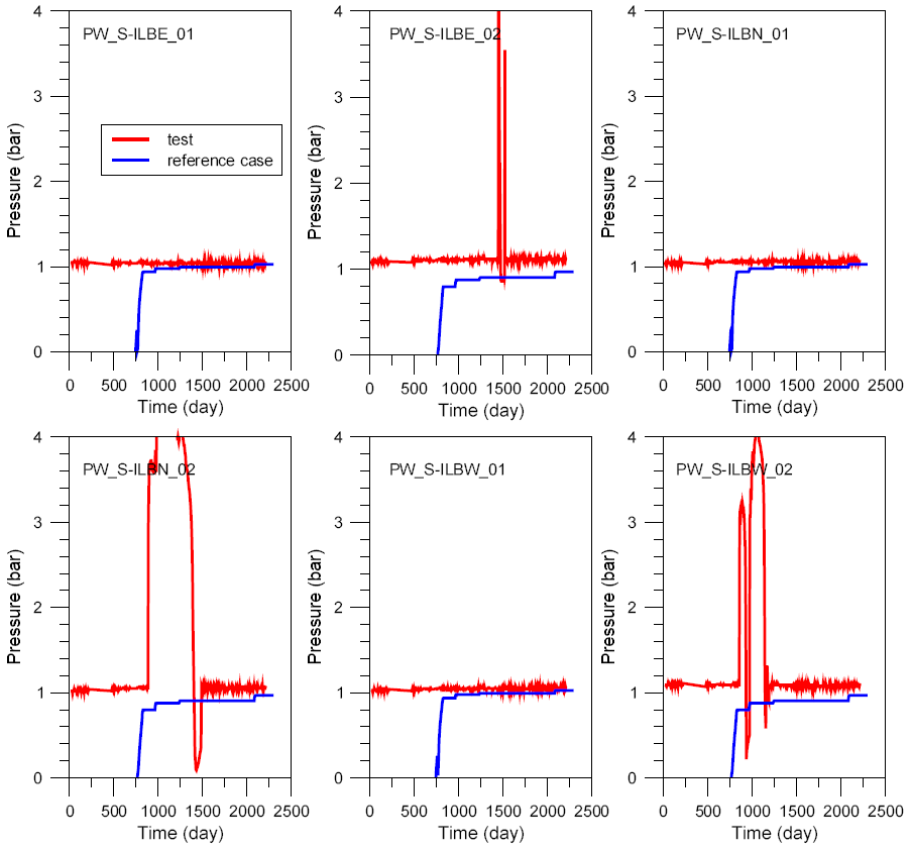

Figure 5-90: Seal water pressure at bottom instrumentation level, reference case.

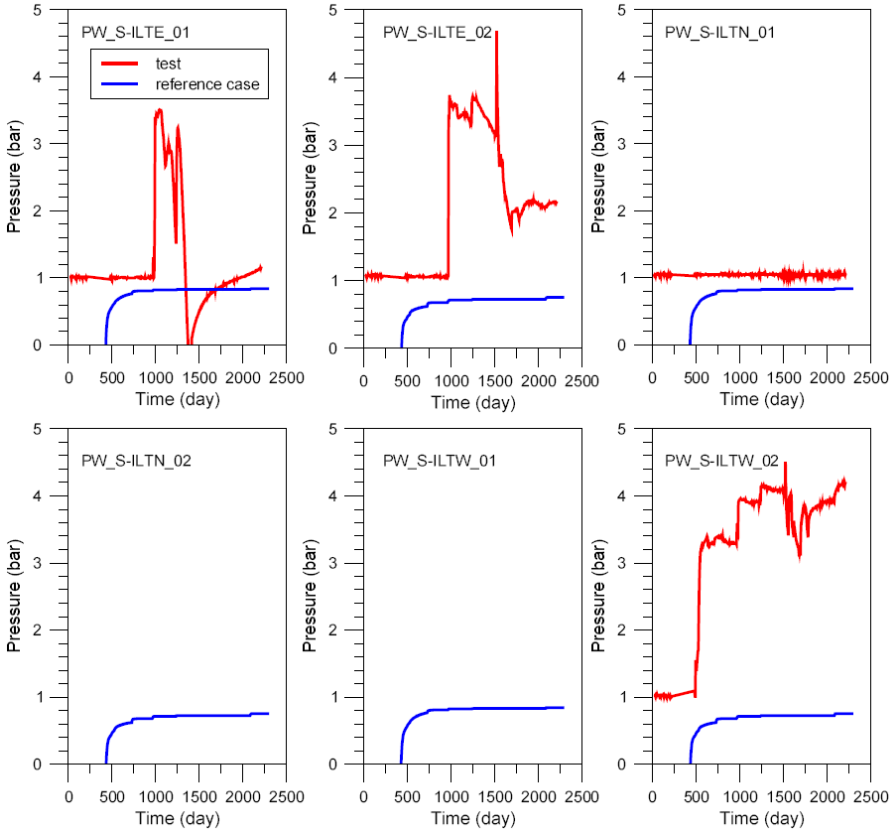

Figure 5-91: Seal water pressure at top instrumentation level, reference case.

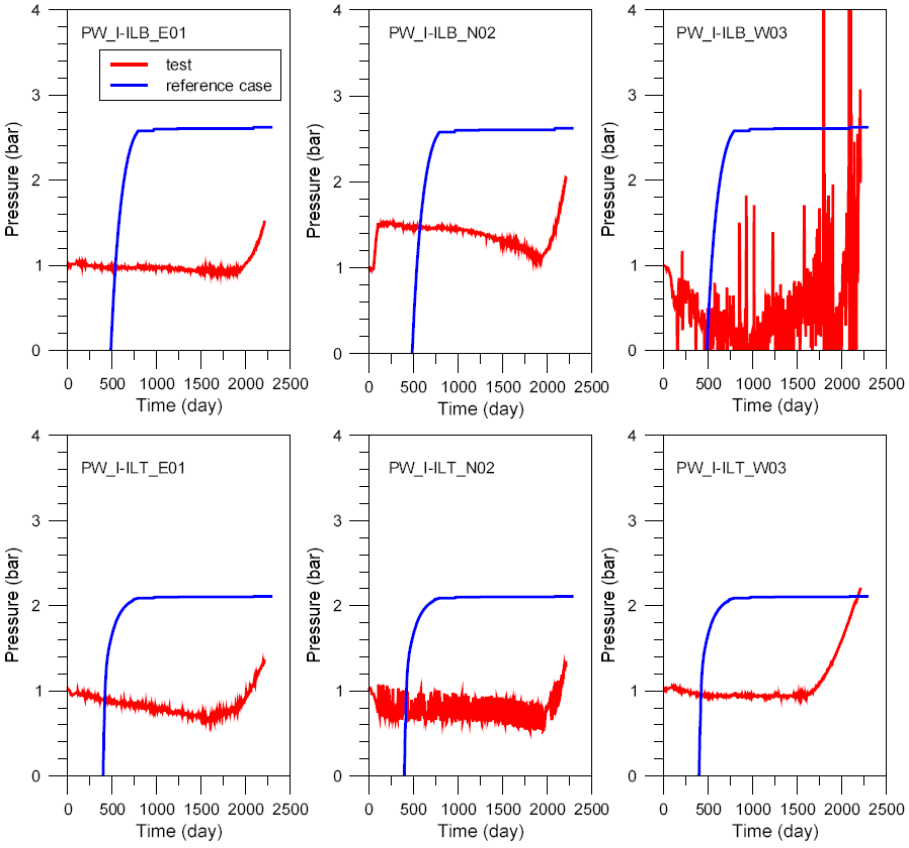

Figure 5-92: Interface water pressure, reference case.

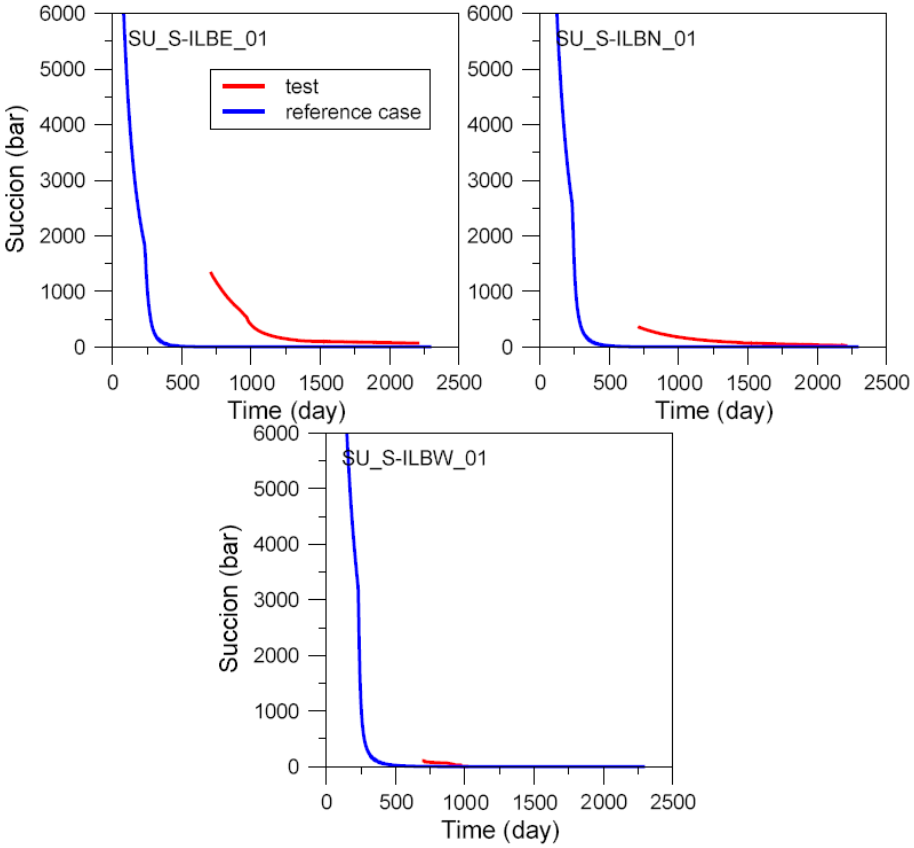

Figure 5-93: Seal suction at bottom instrumentation level, reference case.

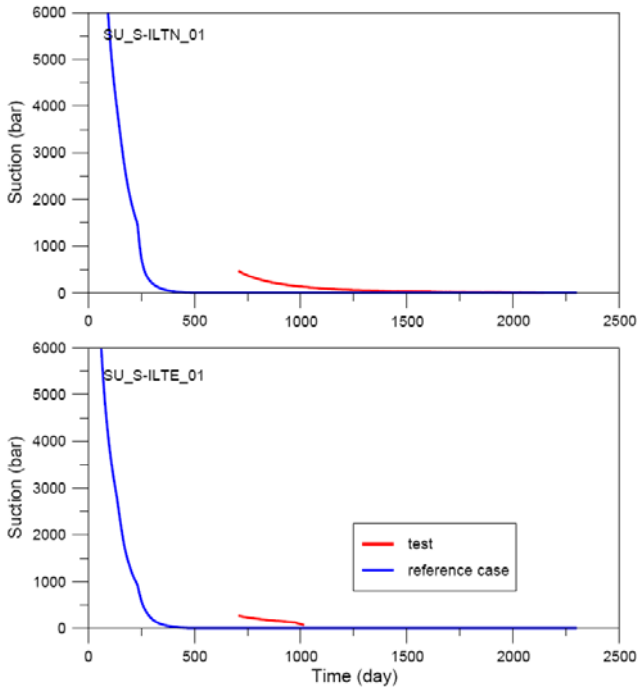

Figure 5-94: Seal suction at top instrumentation level, reference case.

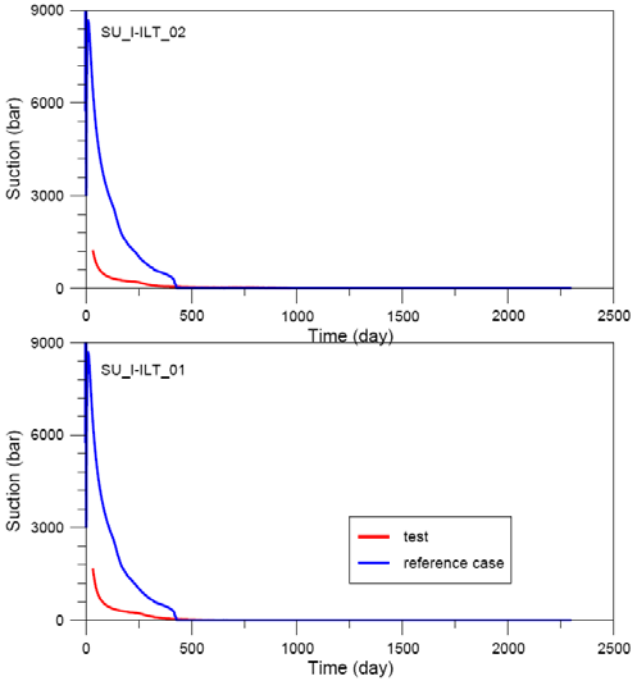

Figure 5-95: Interface suction at top instrumentation level, reference case.

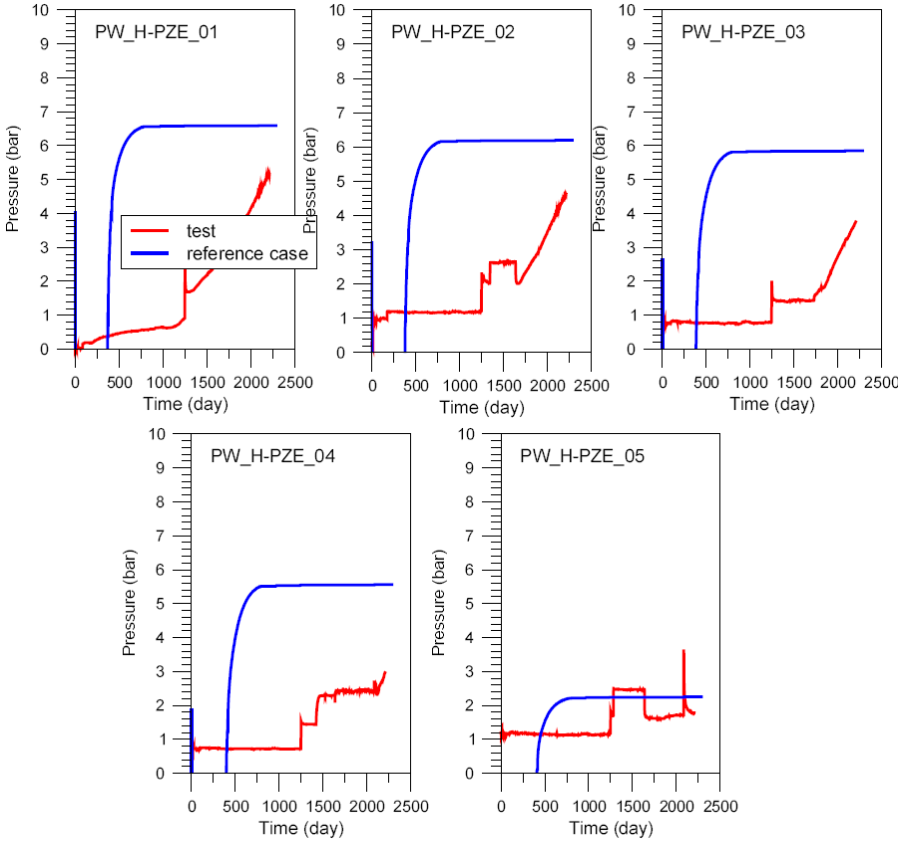

Figure 5-96: Host rock water pressure along east piezometer, reference case.

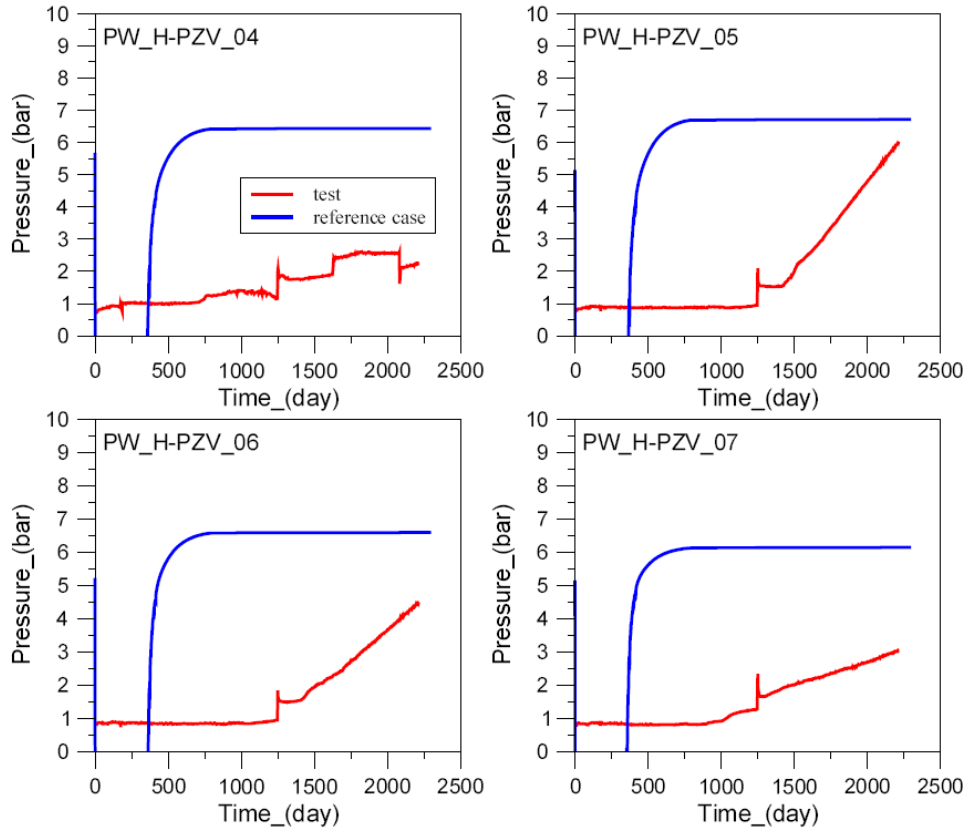

Figure 5-97: Host rock water pressure along vertical piezometer 2, reference case.

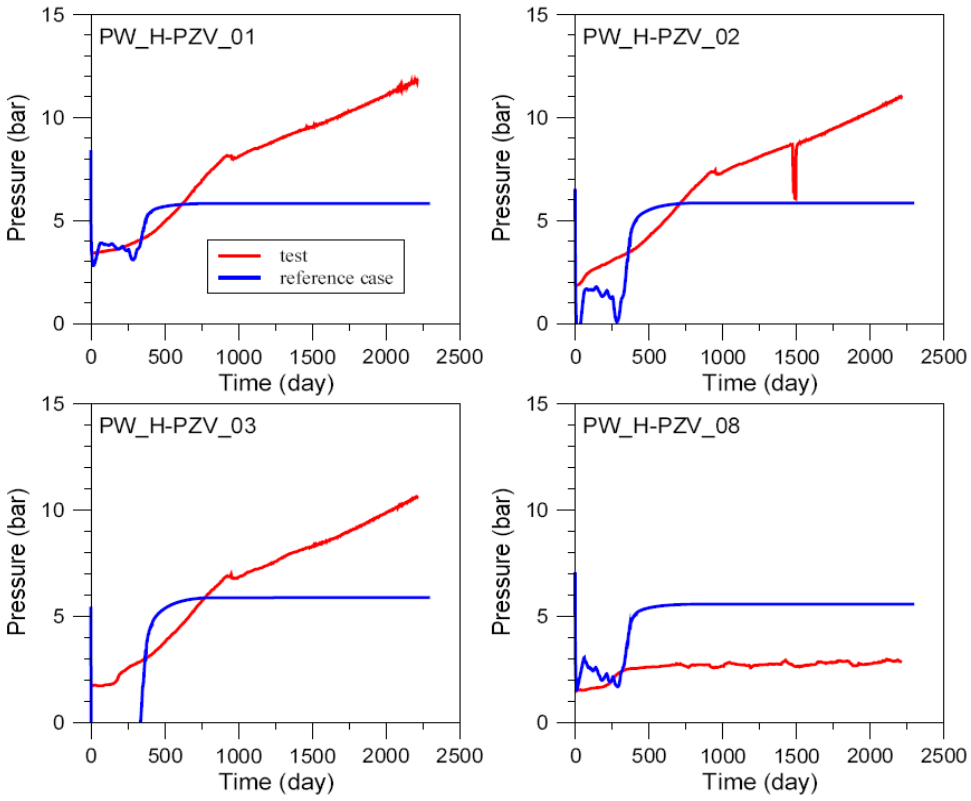

Figure 5-98: Host rock water pressure along vertical piezometer 1, reference case.

Calculated saturation is shown in the seal (Figure 5-99), and suction in the host rock at one meter from the shaft (Figure 5-100) on vertical sections. The saturation increase in the seal and the suction variation in near host rock are consistent with the preceding explanations: a non uniform hydration of the seal due to the different bentonite density, an increasing suction in the host rock at the transient beginning.

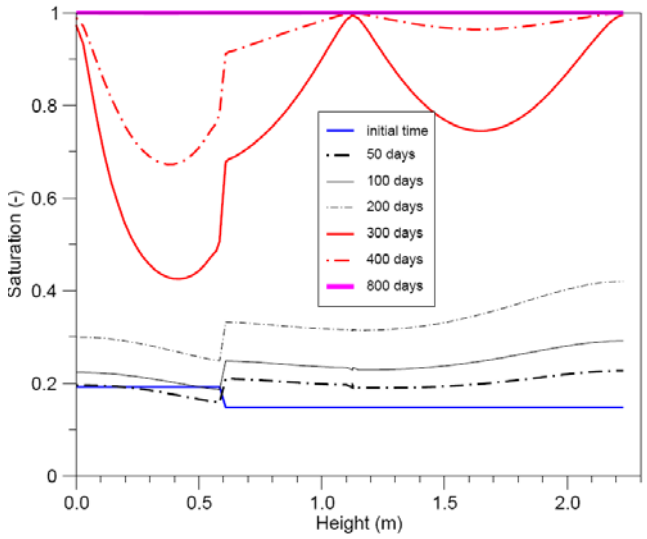

Figure 5-99: Saturation in the seal, reference case.

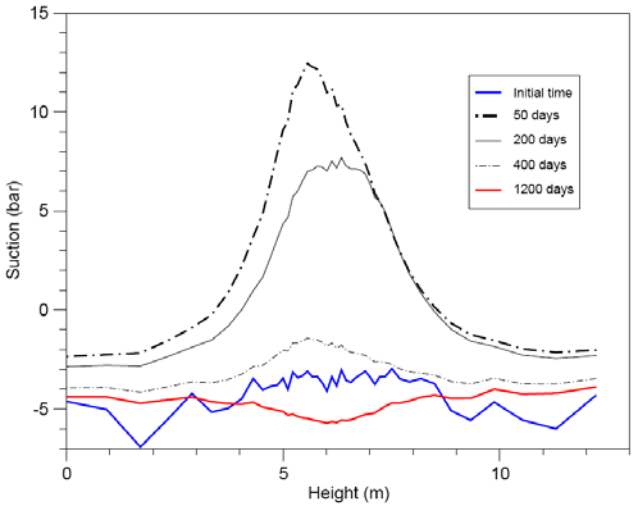

Figure 5-100: Suction in the near host rock, reference case.

The reference case water injection is near the experimental water injection. However the calculated transient process shows a discrepancy with the experimental results: the seal is saturated too early compared with observations. A steady state is reached in the entire seal and host rock while the experimental water forced injection is not finished at 2300 days; experimental water pressure increase in the seal and in the host rock.

Sensitivity analysis of hydraulic parameters

First a numerical trial is performed reducing the time step. Along the simulation, the new time step increases from 675 s to a half day, so the total time step is doubled: 7818, instead of 3336 in the reference case. The calculated results are the same than for the reference case.
A sensitivity analysis is carried out to investigate the predominant hydraulic parameters in the shaft sealing test. The following variables and parameters can be mentioned:

- air relative humidity in the shaft ;
- real filters surface for water forced injection : some injection filters are out of order, others are in uncertain state ;
- unsaturated EDZ ;
- EDZ host rock permeability : near the seal the EDZ permeability may be a little higher than bulk host rock permeability ;
- initial water content in the seal.

A sensitivity analysis has been conducted on the air relative humidity in the shaft. The suction is derived from the humidity rate by Kelvin's law, and applied as Dirichlet condition on the surface shaft. The results of two values of relative humidity are presented here: 100% (reference case), 99% (AHR99 case); and a zero water flux in the shaft surface is applied. The results in Figure 5-101, Figure 5-102 to Figure 5-105 show that best fitting calculation/experiment is given by the reference case: 100% air relative humidity. The zero water flux gives unrealistic results: too high water pressure; the 99 % air relative humidity does not give a satisfactory result in the host rock.
¡

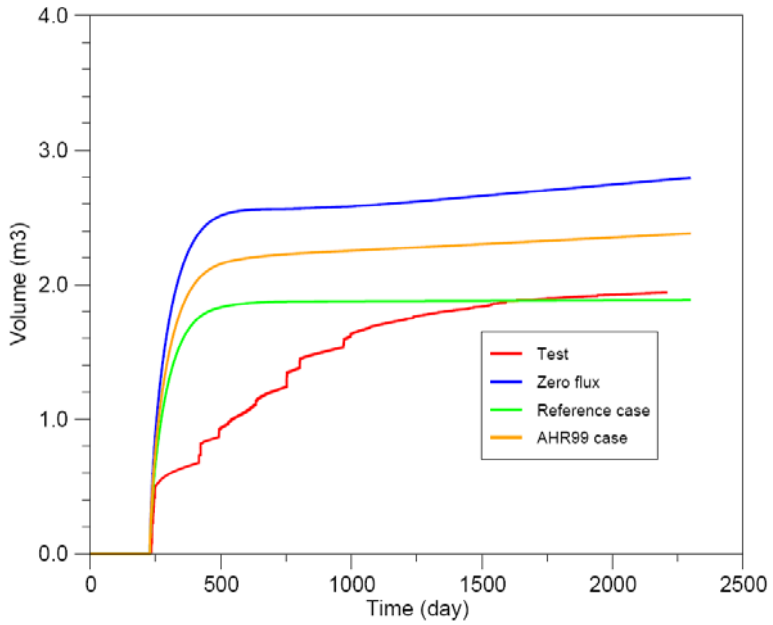

Figure 5-101: Water forced injection in the seal, air relative humidity variation.

The total injection surface is also tested. In the reference case all filters work, the bottom and middle filters surface are limited as follows: internal rings in bottom and middle level (CI case), middle rings (CM case), internal middle ring (CM1), internal bottom ring (CB1). The calculated results show some differences: the lower the injection surface, the lower is the injected water volume (Figure 5-106). There are some differences concerning water pressures (Figure 5-107).

The seal saturation process is a result of both filter water intake and host rock water inflow; in the reference case there is an approximate balance between the two water sources, it is not the case for the smaller filter surface CB1: twice as much water comes from the host rock (Figure 5-108).

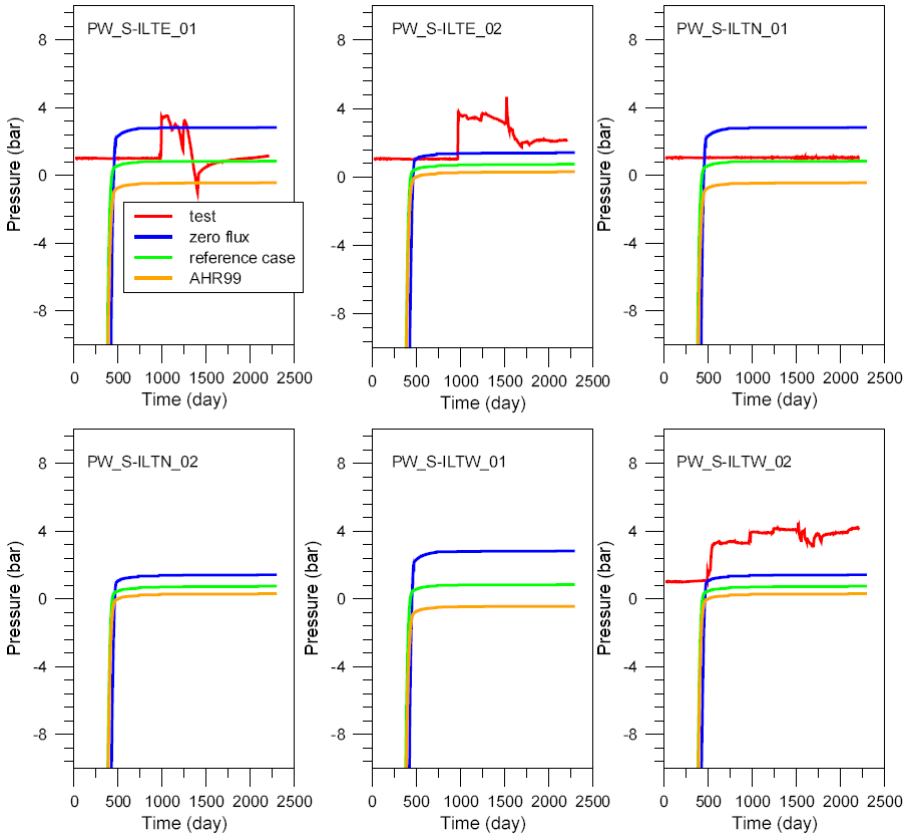

Figure 5-102: Seal water pressure at top level, air relative humidity variation.

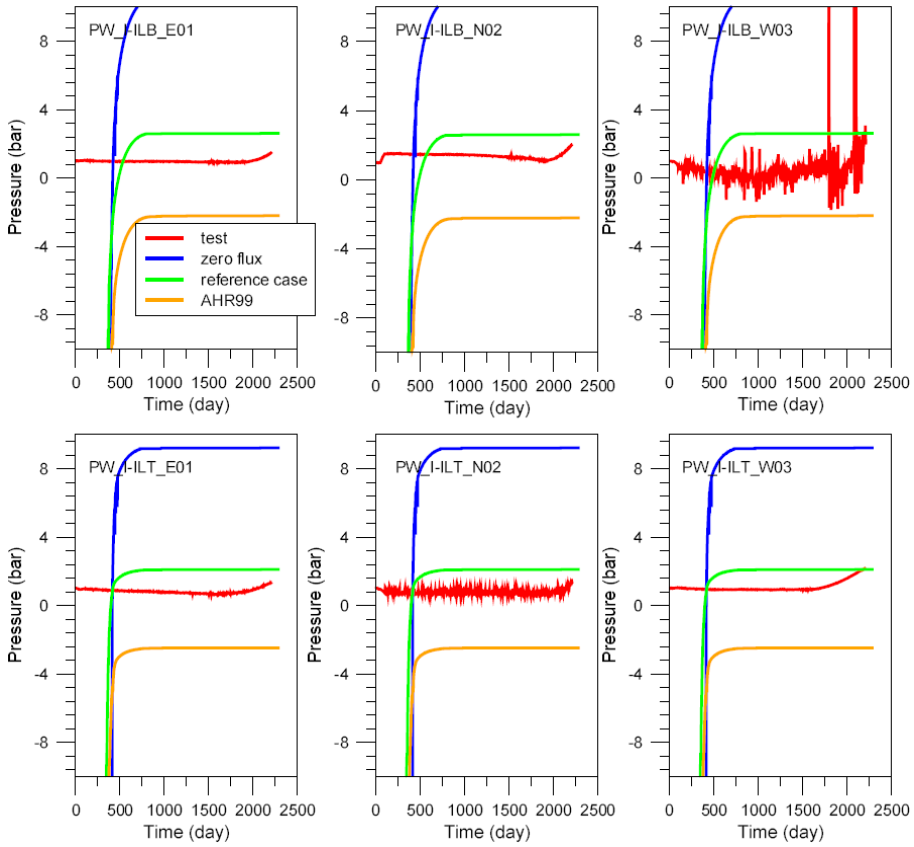

Figure 5-103: Interface water pressure, air relative humidity variation.

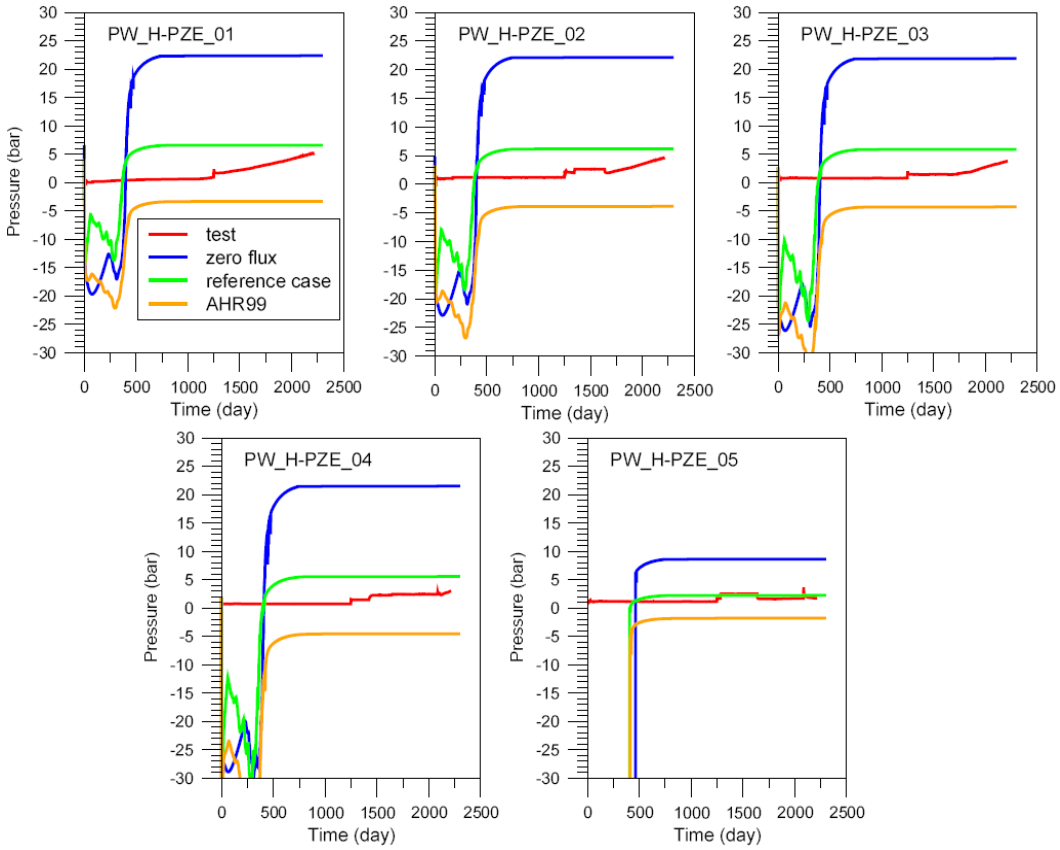

Figure 5-104: Host rock water pressure along east piezometer, air relative humidity variation.

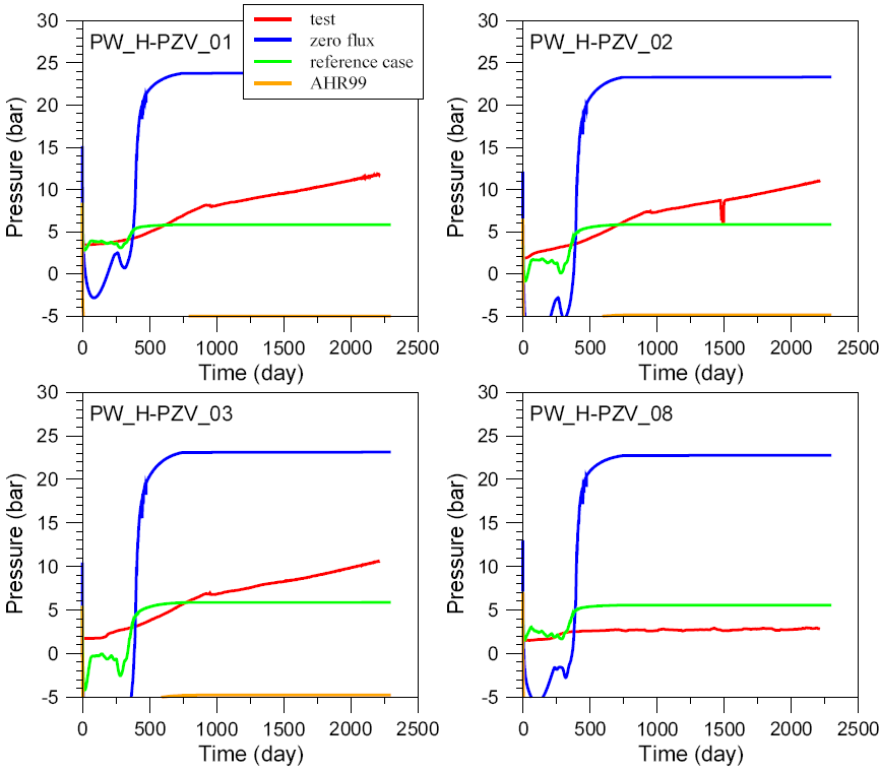

Figure 5-105: Host rock water pressure along vertical piezometer, air relative humidity variation.

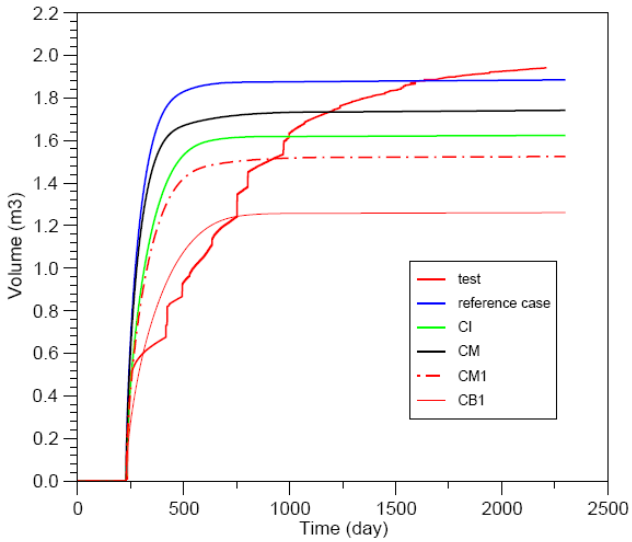

Figure 5-106: Water forced injection in the seal, water injection surface variation.

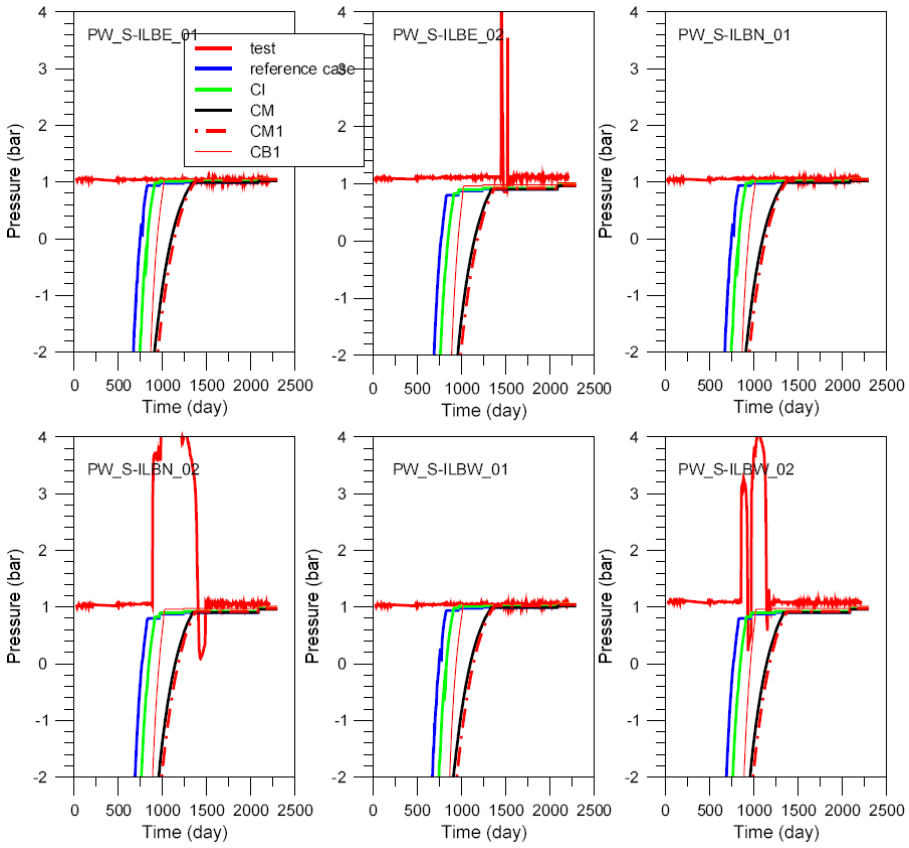

Figure 5-107: Seal water pressure at bottom level, water injection surface variation.

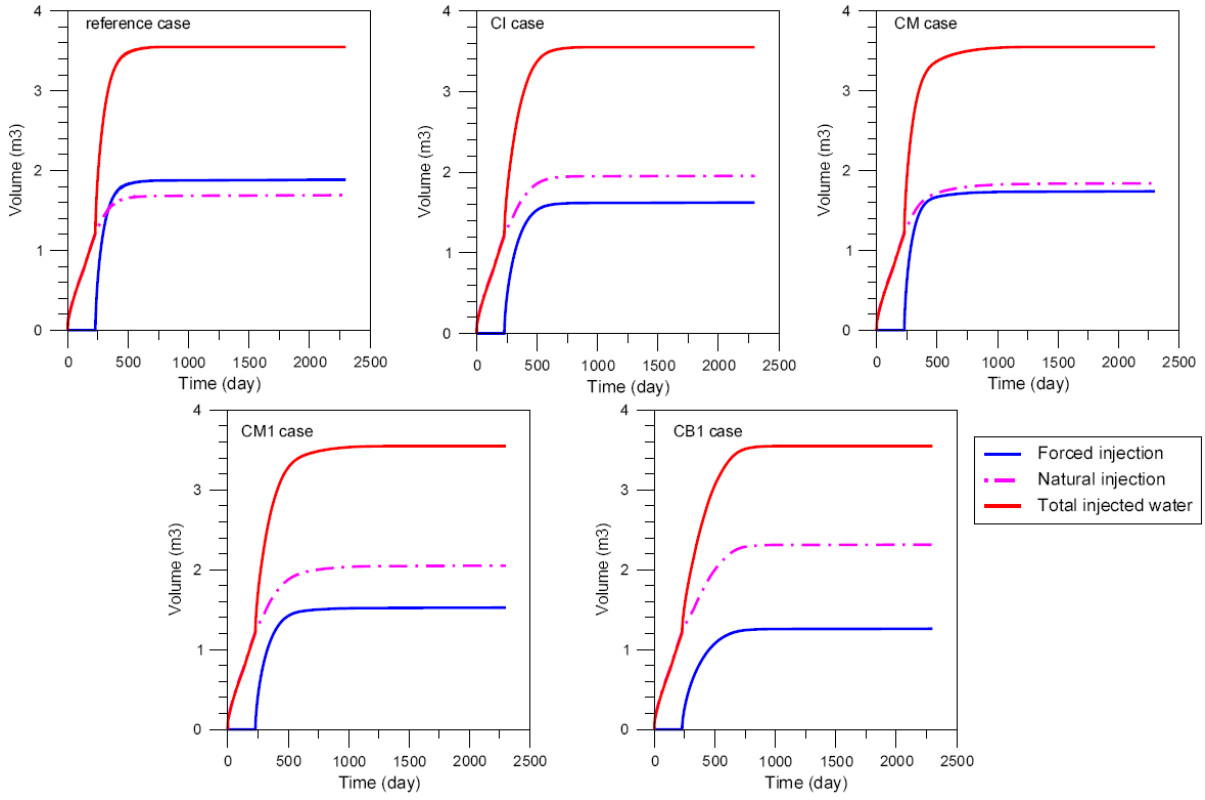

Figure 5-108: Water in the seal, water injection surface variation.

A different degree of saturation is applied in the host rock EDZ, a one meter deep zone near the shaft. The reference case is saturated, and three other degrees of saturation are tried: 0.99, 0.95 and 0.90. The forced injected water is higher in the lower EDZ saturation: the water volume injected in the seal, coming from the host rock is reduced less than twice as much (1.7 m^3 to 1.2 m^3) when the degree of saturation changes from 1 to 0.90. No change in seal water pressure is observed.

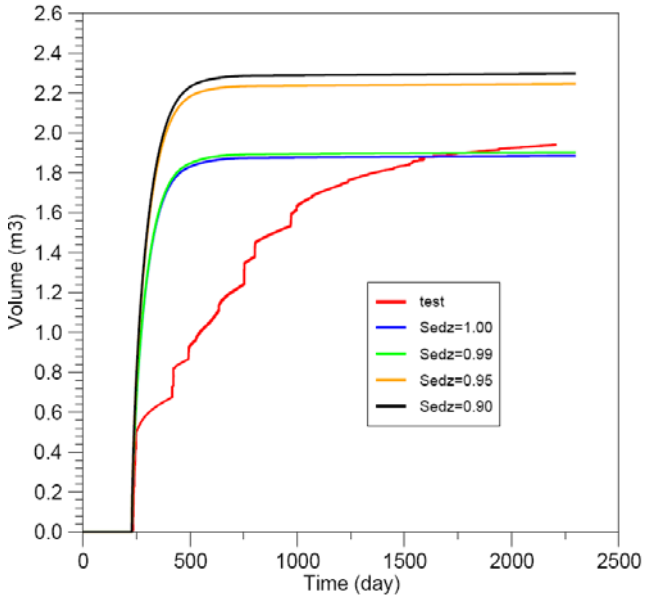

Figure 5-109: Water forced injection in the seal, EDZ saturation variation.

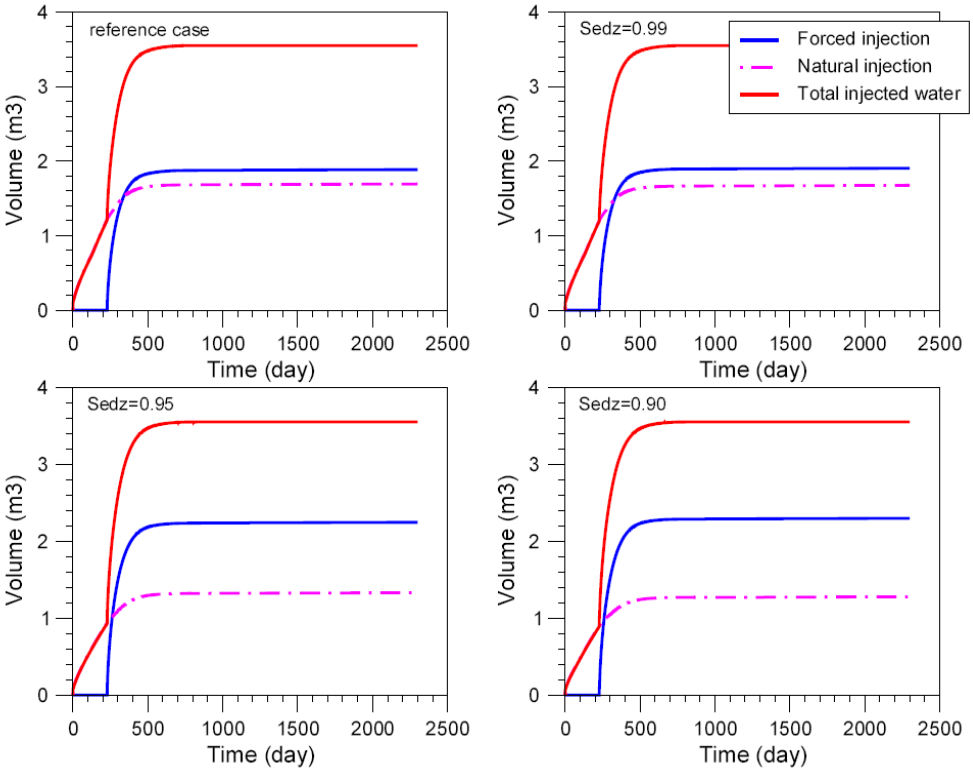

Figure 5-110: Water in the seal, EDZ saturation variation.

A EDZ permeability modification has also been applied. The reference case permeability coefficient is 4.5 10^{-19} m^2. For an increased value of $6x10^{-19}$ m^2 the forced injected water reduces to 0.5 m^3, the seal water pressure does not change much, the interface and host rock water pressures decrease respectively to 0.5 and 1.5 bar. For a reduced value of 10^{-20} m^2, no change is observed.

The initial seal water content in the reference case is W_i = 0.06, corresponding to a degree of saturation S_i = 0.19. Two modifications of initial water content had been tried:

- C1 : W_i = 0.05, corresponding saturation S_i = 0.16 ;
- C2 : W_i = 0.07, corresponding saturation S_i = 0.22.

C1 and C2 give respectively an increase, decrease of forced injected water in the seal of approximately 0.5 m^3, a small seal water pressure variation (0.2 bar) and no change in the host rock.

The sensitivity analysis shows the importance of host rock characteristics. First of all, the boundary conditions in the shaft should be considered, the better agreement between calculation and experiment results is obtained with 100 % air relative humidity. The kinematics of the forced injected water is unchanged with the variation of suggested parameters: the appearance of steady state is about the same in all cases.

Mechanical results

BBM model is the mechanical constitutive law; the associated parameters are given in Table 5-14. Due to mechanical convergence problems, the mechanical results are shown only until 400 days, at this date no significant displacements or stresses are observed in the seal or the host rock. The radial and axial displacements are very small, lower than 1.3 mm (Figure 5-111). The host rock moves slightly towards the shaft axis, and, in the same way, the seal. The comparison with radial displacement test results shows a too small computed displacement and if the calculated radial displacement slope is correct in the first 400 days near the central tube, it is not near the host rock. In the host rock, at the beginning the experimental displacement is always positive, it is not the case in calculated displacement. No significant changes appear with FoCa mechanical parameters modifications like in laboratory tests.

Possible explanations for the discrepancies from the calculation are:

- Boom Clay mechanical parameters not suitable, especially in the host rock near the shaft
- BBM constitutive law not suitable for the host rock EDZ.

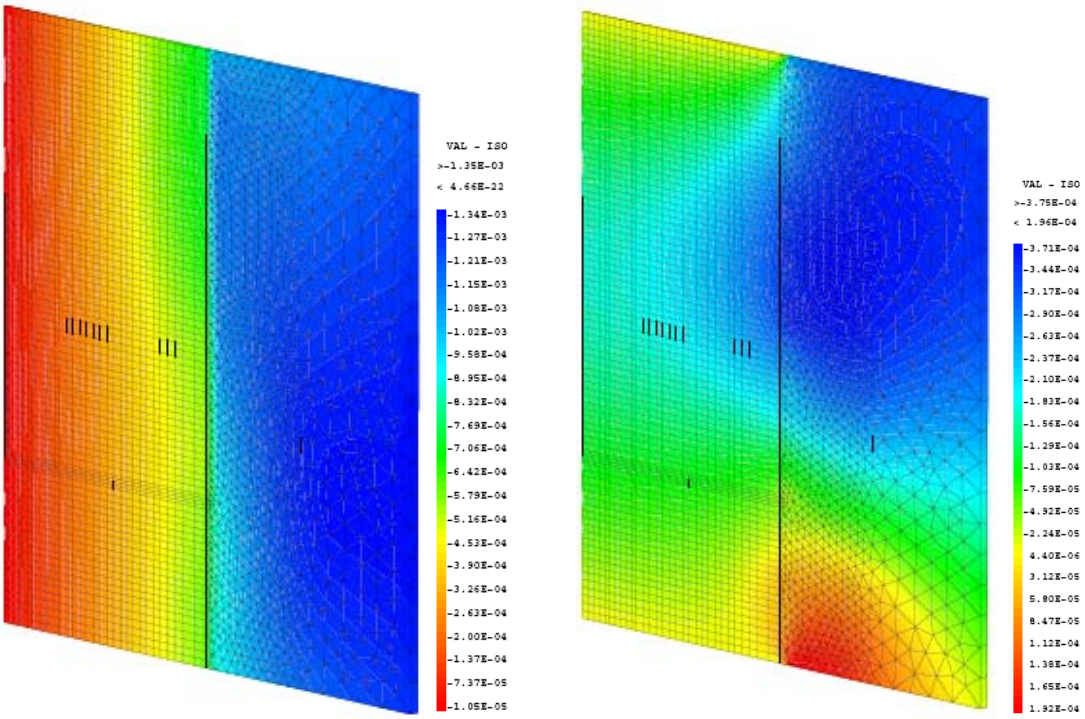

Figure 5-111: Displacements isovalues in seal and host rock at 400 days.

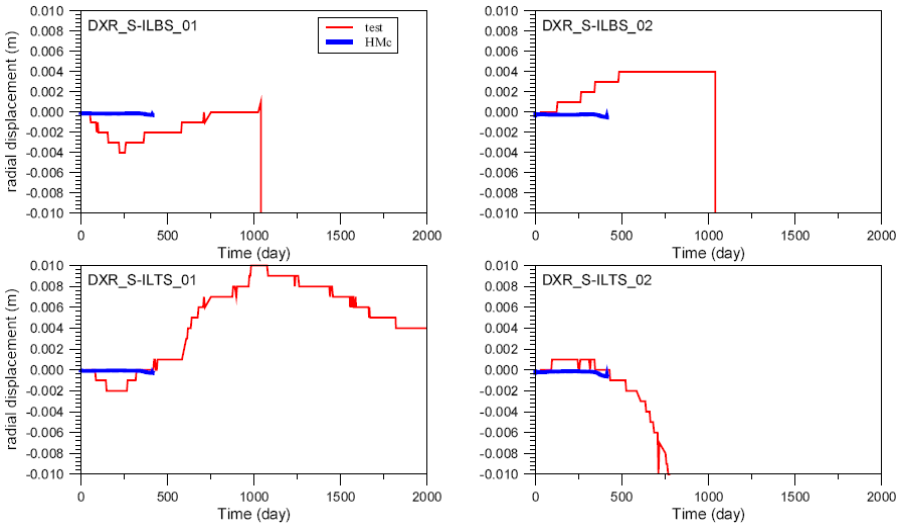

Figure 5-112: Radial displacement in the seal.

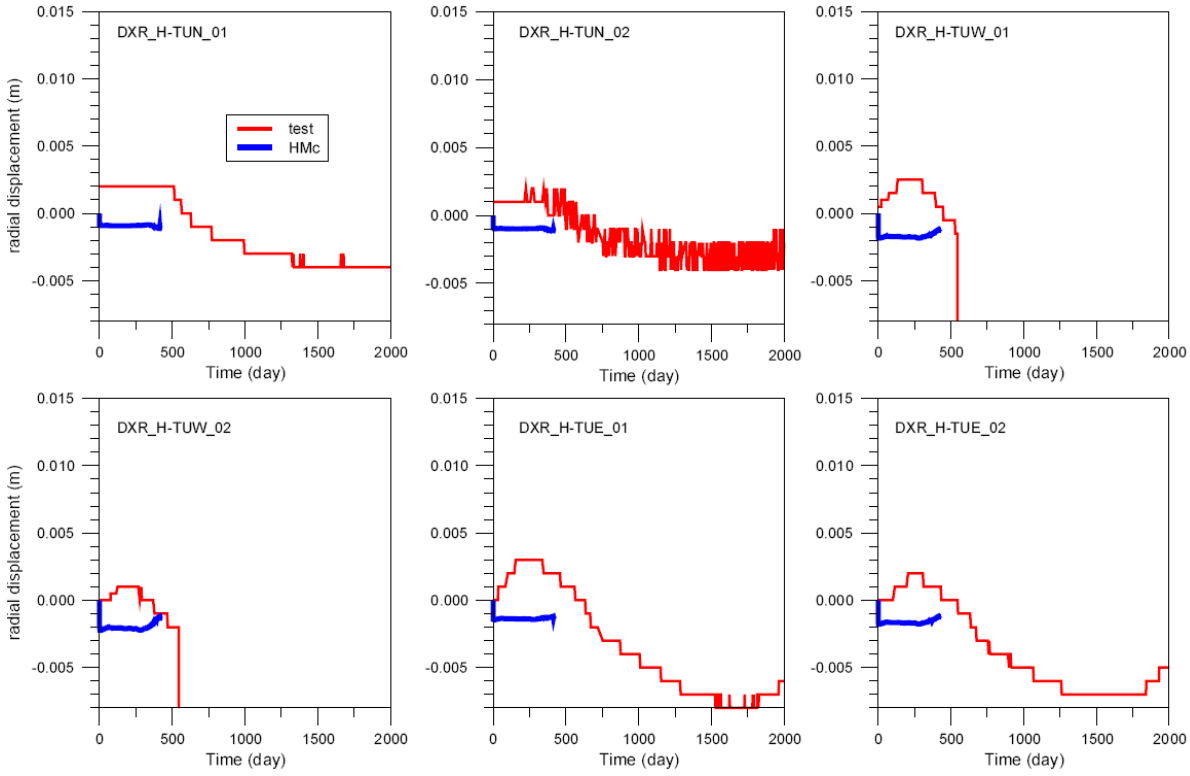

Figure 5-113: Radial displacement in the host rock.

5.4 Conclusions

A large amount of numerical modelling work has been performed as part of the RESEAL II project. The analyses have played an important role in assisting in the rational interpretation of the various tests performed in the project:

- Swelling pressure oedometer tests in the laboratory (hydromechanical analyses)
- Hydration stage of the shaft sealing test (hydromechanical analyses)

The numerical analyses have been performed by CEA and UPC.

An advanced hydromechanical formulation has been used by UPC to perform coupled hydromechanical analyses that incorporates the possibility of considering simultaneously two overlapping structural levels. In this way the individual behaviour of the powder and pellets of the sealing mixture and their interactions can be considered explicitly. A double structure extension of the classical BBM model designed to account for expansive clay behaviour is used as mechanical constitutive law. The characteristic form of swelling pressure development observed in the laboratory tests has been successfully reproduced. It consists of an initial increase, followed by a reduction due to the collapse of the macrostructure and finally a stage of further swelling pressure increase. The satisfactory simulation extends to the two values of dry density tested with minimal changes of material parameters. The formulation provides additional information on the evolution of the microstructure and macrostructure throughout the test, helping to understand better the interplay between the different components of the sealing material. The information obtained appears consistent with microstructural observations of various types.

CEA has adopted a single porosity coupled hydromechanical formulation with two possibilities for the analysis: a fully coupled computation and a chaining calculation in which hydraulic and mechanical problems are solved sequentially. The BBM constitutive model for unsaturated soils is adopted to represent the mechanical behaviour of the materials. It is interesting to note that, with an adequate use of the single porosity model and the BBM constitutive law, the CEA analyses also reproduce satisfactorily the swelling pressure development, at least for the samples compacted at 1600 kg/m^3. It appears that the small swelling pressure associated with the less compacted samples can not be easily reproduced with the current state of the model. No significant differences are observed when comparing the coupled analyses with the chaining calculations.

The analysis of the shaft sealing test has provided a sterner challenge. This is to be expected because of the unavoidable uncertainties and heterogeneities associated with the performance of a large in situ test in field conditions. The analysis performed by UPC uses the same formulation than for the simulation of the laboratory tests, a double structure constitutive model for the sealing material and the BBM constitutive law for the host rock. The simulation does provide a satisfactory overall reproduction of the process of hydration and swelling pressure development throughout the shaft seal. The prediction of water pressures, stresses and displacements in the host rock are also in qualitative agreement with observations. There are, however, a number of significant differences when performing individual detailed comparisons. Some of them are unavoidable; for instance an axisymmetric model can not account for different rates of hydration and stress development along different directions.

The simulation of the shaft sealing test by CEA uses the single porosity formulation and the BBM constitutive law for host rock and seal material. Again, the calculations reproduce qualitatively the evolution of hydraulic parameters in response to the hydration processes. Detailed comparisons, however, show also significant differences between observations and computed results. Variations of the hydraulic conditions of the simulations, examined by a set of sensitivity analyses, do not change radically the type of results obtained. Comparison with mechanical parameters is less comprehensive due to the short calculation times brought about by numerical convergence problems.

Considering the modelling of the shaft sealing test from a general perspective, it is apparent that the basic phenomena concerning the evolution of hydraulic and mechanical variables, both in the seal material and the host rock, are by and large adequately reproduced. There are no observations that radically contradict the modelling results. This implies that the formulations employed contain appropriate descriptions of the basic phenomena occurring in the seal and in the host rock as well as their interactions. Thus, closer quantitative agreement between computed results and observation is largely a matter of parameter variation and more detailed characterization of the field test. The double porosity model is capable to offer more thorough information about the evolution of the sealing material albeit at a higher complexity cost.

6 Integration of results in performance assessment

The IAEA glossary (IAEA, 2003) defines a seal as:

"an engineered barrier placed in passages within and leading to a repository to isolate the waste and to prevent seepage of water into or radionuclide migration from the repository area. Sealing is performed as part of repository closure."

The definition of a seal covers all the possible places in a repository where seals can be placed (see also ANDRA, 2005; NAGRA, 2002):

- at the end, or somewhere within the gallery
- in an access gallery
- in an access shaft

Moreover, different types of seals might be considered for the pre-closure and post-closure phase of a repository life-time (Bel and De Preter, 2005). The functional requirements of the seals in the pre-closure phase might easily be taken up by concrete, while for the seals of the post-closure phase, bentonite is mainly chosen as most important material.

It should be noted that this document is only referring to bentonite seals within a clayey host rock. This chapter is subdivided into four topics. Topic 1 gives an overview of the functional requirements attributed to a seal, based on a review of the international literature. Topic 2 then describes the possible requirements of a seal for a repository in a clay formation. This topic will take into account the functional requirements as imposed by performance assessment and/or safety assessment and as inspired from any other point of view. Moreover, it will be tried to translate these functional requirements into technical requirements. Topic 3 will then evaluate to which extent the RESEAL project has contributed to the better understanding of any of these technical requirements. Finally, topic 4 will conclude with some open questions remaining.

6.1 International overview of the functional requirements of a seal

In its technical Reports Series No 319 "Sealing of underground repositories for radioactive waste" (IAEA 1990) the IAEA formulates the seal performance objectives as follows:

"The overall objective of penetration sealing is to restore the viability of the formation affected by the penetration to assure long term isolation of waste radionuclides. An ideal goal of repository sealing activities is to leave ground water circulation within and in the vicinity of the disposal formation exactly as it was before site exploration and development. It follows logically that sealed shafts, tunnels and boreholes should have the same hydraulic conductivities as the geological materials through which they pass."

In this statement the IAEA presents an ideal case and one needs to consider to which extent this requirement is practical. In many host rocks, the goal of restoring the original hydraulic conditions may be completely impossible to reach. In particular, the excavation disturbed zone may retain a somewhat enhanced hydraulic conductivity regardless of the remedial techniques used. In this case the IAEA suggests the use of performance assessment models to evaluate the consequences of the increased hydraulic conductivity around shafts, tunnels and boreholes.

Taking the above considerations into account the IAEA summarizes the performance objectives as follows:

- "Hydraulic conductivities of the shaft and borehole seals should be sufficiently low to ensure that the effectiveness of the geological material as an isolation barrier is not compromised;
- Hydraulic conductivity of the system should not be influenced significantly by the condition of the bonding between the seal and the host rock at any such interfaces;
- Hydraulic conductivity of the disturbed zones must be compatible with the radiological protection objectives as defined by the regulatory authorities;
- Properties of the sealing materials should not change significantly with time or should change slowly and predictably in such a way that the performance will remain in compliance with the radiological protection objectives."

An international literature review of Volckaert and Bernier (1996b) illustrates that several countries with important developments on seals at that time, agree that the presence or absence of seals has little or no effect on the overall performance of the repository system. This is based on the different safety assessment calculations performed by these countries. However, all countries considered the installation of seals anyway as:

- a cautious and conservative approach is appropriate
- an element of robustness, because the seal will protect other components of the engineered barrier system
- it is consistent with the multiple functions (barrier) concept
- sealing will add to the confidence in the long-term isolation
- it will reduce public concern regarding long-term hazards.

The same literature review also indicated that mainly qualitative requirements are given to the seals by the different countries considered. The major objective of the repository sealing is the restoration of the capability of the geological barrier to assure long-term waste isolation. Some

authors add for the seal the objective of prevention of human intrusion and compartmentalization of the repository.

For the functional requirements of the seals all authors mention in the first place the hydraulic conductivity which should preferably be such to restore the initial hydraulic conditions. The ideal situation would be that the seals have a hydraulic conductivity not higher than the host rock. In practice a higher hydraulic conductivity can be acceptable when performance assessment calculations show that the dose or risk criteria for repository performance are still fulfilled. The sealing of the EDZ is considered as an essential functional requirement for the seals. Another important functional requirement given by most authors is that the seal has to withstand the maximum expected gas and water pressures at the repository depth. The seal has to be able to resist the stress induced by the convergence of the host rock. Several authors require a redundancy in the sealing system and thus require more than one seal.

For the sealing material most authors require a long lifetime, but do not give a minimal value and suggest that the seal lifetime should be derived from performance assessment calculations. From the indications given in this literature, the authors have derived that the minimum lifetime would be between a few thousand years up to about 100 000 years. Such lifetimes require a good chemical stability and compatibility with the host rock.

More recent literature, especially based on the Safety Case reports of Switzerland (NAGRA, 2002) and France (ANDRA, 2005) confirm the above described qualitative requirements of the seals. No major changes were attributed in recent years. In the Dossier 2005 (ANDRA, 2005) and the Safety Report (NAGRA, 2002) for example, it is mentioned that the seals should limit the circulation of water and should contribute to the compartmentalization of the repository. To this end, the seals should have a low hydraulic conductivity and a swelling capacity so that any cavities that remained after emplacement of the bentonite get filled as well. Indeed, such cavities might lead to preferential pathways. In both cases, the seals are specially designed in order to locally seal also the EDZ around the excavations. The reference concepts described in both documents, clearly illustrate the foreseen redundancy of the seals (**Figure** 6-1).

For the specific reference concept described in Dossier 2005 (ANDRA, 2005), some quantitative data are given, taking into account the hydro-mechanical and chemical changes that are expected to occur. The most important phenomenon that is considered is the possible chemical alteration of the concrete bulkheads. This might lead to a degradation of the concrete, which might create on the long-term some additional space for the seal. Due to the swelling capacity of the seal, this additional space would be filled again, but the overall hydraulic conductivity of the seal would increase as well. The fact that the concrete water might induce chemical alterations within the bentonite seal material, which possibly might lead to lower swelling capacities, is not explicitly discussed.

It should be mentioned that both documents do not discuss the required life time of the seals, neither do they state that the seal should withstand the expected gas pressure. Moreover, Dossier 2005 (ANDRA, 2005) even indicates that before full saturation of the seals, biphasic gas transport through the seals is possible, which will avoid (micro-) fracturation within the seals.

Further on, it must be noted that none of the reports reviewed give information on the timing at which all or some of the functional requirements of the seal should properly function. The approach consists firstly in designing seals as much as possible and reasonable. Then based on phenomenological analysis, qualitative safety analysis and/or FEPs (definition of expected

evolution and possible deviations), performance analysis and safety analysis verify that/how seals guarantee safety objectives (i.e. functions) with time.

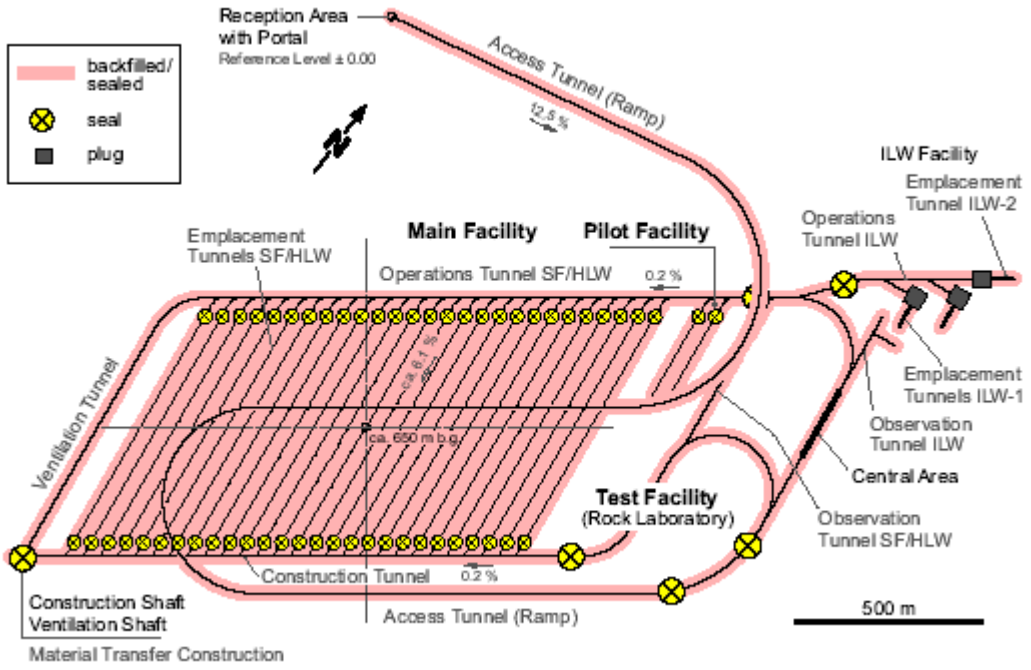

Figure 6-1: Status of the repository after final sealing and closure of the facility (NAGRA, 2002). Seals are considered to comprise highly compacted bentonite, along with a concrete bulkhead. Plugs at the entrances to ILW emplacement tunnels are composed of concrete.

6.2 Requirements of seal for a repository in a clay formation

For low permeable sedimentary rocks, the high level requirement of seals from post-closure safety assessment would be to ensure that transport through the near field remains controlled by diffusion. This requirement returns to the contribution of seals to high level safety functions such as: "to limit water flow within the repository" and "to limit radionuclide flow within the repository towards the access". Firstly, this requirement is supported by a hydraulic performance of seals. To access this high level performance, low level (sub) requirements/performances are added in terms of technology and/or in terms of phenomenological characteristics, such as swelling (hydro-mechanical characteristics) capacity of seal core or removing concrete lining. This leads to design seals as a whole system (i.e. component) with (sub) components, for example the bentonite core, the concrete walls, the concrete lining, the bentonite cut-off (Andra's design) and the EDZ. (**Figure 6-2**)

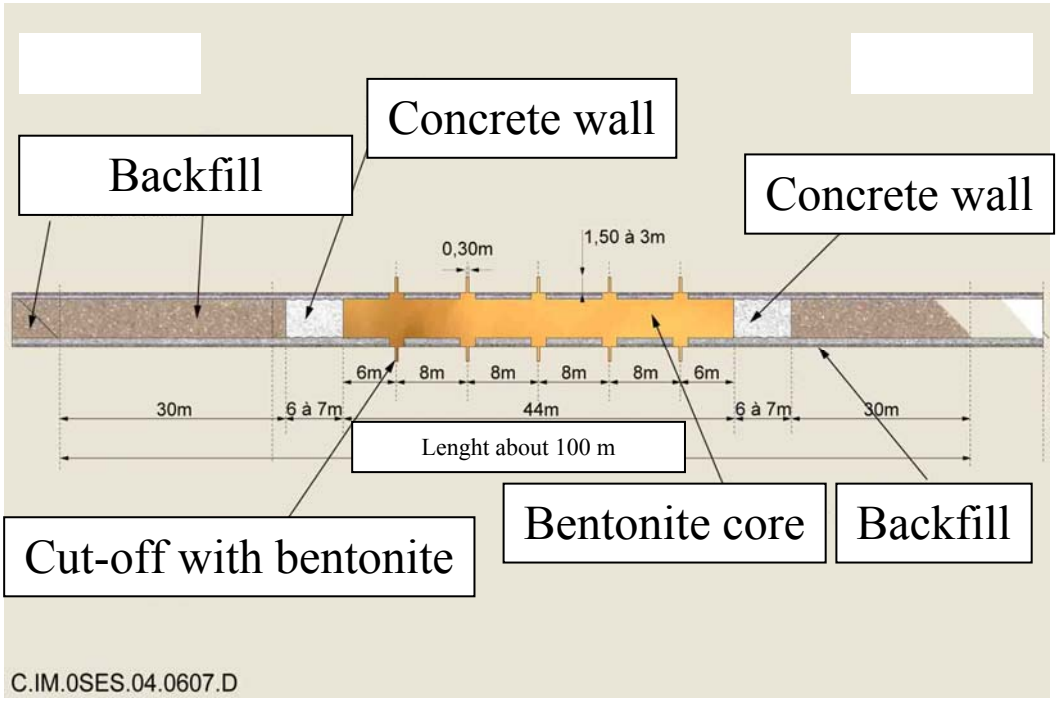

Figure 6-2: Schematic view of a gallery seal (ANDRA 2005)

6.2.1 Functional requirements from PA/SA on long term safety

Seal failure may generate degradation or modification of the performance characteristics of the safety functions, jeopardizing the hydraulic properties associated with the seals. In addition, a generalised seal failure may induce a potential short-circuit of the geological barrier. Different events may generate a seal failure, in all or some components of the seals such as:

- Insufficient swelling of the bentonite against the clay (combined with uncertainty on deferred behaviour of EDZ);
- Extent of alkaline disturbance from cementicious components (lining, wall) in the bentonite clay core and/or the cut-offs (Andra's concept for gallery seals), that may reduce the bentonite swelling capacities;
- Gas pressure and migration (such as irreversible damage of bentonite swelling and/or EDZ permeability)
- Backfill specifications inadequate in the light of expected long-term mechanical performance, that may lead to mechanical deformation of bentonite core and EDZ;
- unability to emplace the bentonite (ex. with no residual gaps);
- unability of emplacement technology of seal hydraulic cut-offs and/or bentonite core;

In order to assess the robustness of the repository system, "poor sealing" situations have been currently studied (Andra, 2005 and Nagra, 2002), with respect to various combinations of such defects in repository components (shafts, galleries). These situations also included any failure possibly associated with the development of a damaged zone around the repository structures, more significant than that considered in the normal (i.e. reference or expected) evolution scenario and possibly constituting a radionuclide transfer pathway and/or influencing the long-term evolution of the repository.

The undesired outcome is that diffusion in the near field may not be the dominant migration process, so that radionuclides release from the shaft outlet at the roof of the clay layer formation

exceeds that considered in the normal (i.e. reference or expected) evolution scenario during the post-closure period [in particular higher than radionuclide flow through the clay layer barrier]. As in the case of the normal evolution scenario, analysis approaches were geared towards two objectives:

- to understand the behaviour of the system in case of seal failure or non-closure. Performance indicators are used to verify the efficiency of the functions implemented: water flows and radionuclide flux through the repository, in particular through the access pathways;
- to evaluate the radiological impact (dose indicator) associated with the various situations.

The analysis of the seal failure scenarios has shown that the repository system is robust with respect to a failure of all seals, and to chemical disturbances relating to the seals. Indeed, given the studied seal failure situations, even considering degraded hydraulic parameters for EDZ, seal core and/or radionuclides release, the impact associated with the activity that migrates through the repository is negligible when compared to that which diffuses through the clay layer barrier (as in the normal evolution scenario). The peak doses associated with the repository transfer pathway remain, in all situations, significantly lower than the activity fraction that migrates through the clay layer barrier (by a factor of at least 10 to 100). More specifically, several points can be highlighted from a hydraulic point of view:

- In cases where a non-simultaneous failure of shaft and gallery seals is considered, the hydraulic disturbance of the repository remains limited because of the efficiency of the seals, which provide redundant cover for the failed seals. The water flows through the repository remain limited.
- In the event of simultaneous failures of shaft and gallery seals, the hydraulic disturbance is stronger, but remains limited due in particular to the low permeability of the clay layer and EDZ, which limit water ingress. (**Table 6-1**)
- In the case of degraded EDZ performance, EDZ constitutes a significant drainage. Radionuclides flows increase and water flow rates leaving the geological barrier are significantly higher than in the reference situation. Once EDZ presents severely degraded characteristics, the properties of the seal core and hydraulic cutoffs, as pessimistically represented (anchored only in the fractured zone), no longer provide any significant gains. Even in the most pessimistic configuration, the flows remain very small. (**Table 6-1**)

Table 6-1: Example of evolution of water outflow from the shafts in different "seal" situations (ANDRA, 2005)

Situation	Water outflow from the shafts (m^3/y) Spent fuel disposal (inventory scenario S2)
All the seals are efficient (SEN)	0,5
All the seals are defective	2,4
All seals of access drifts are defective	1,0
Abandoned shafts	1,4
All seals of zone drifts are defective	0,75
All seals are efficient + degraded EDZ	6,3
All seals are defective + degraded EDZ	7,5
All seal of access drifts + degraded EDZ	7,1

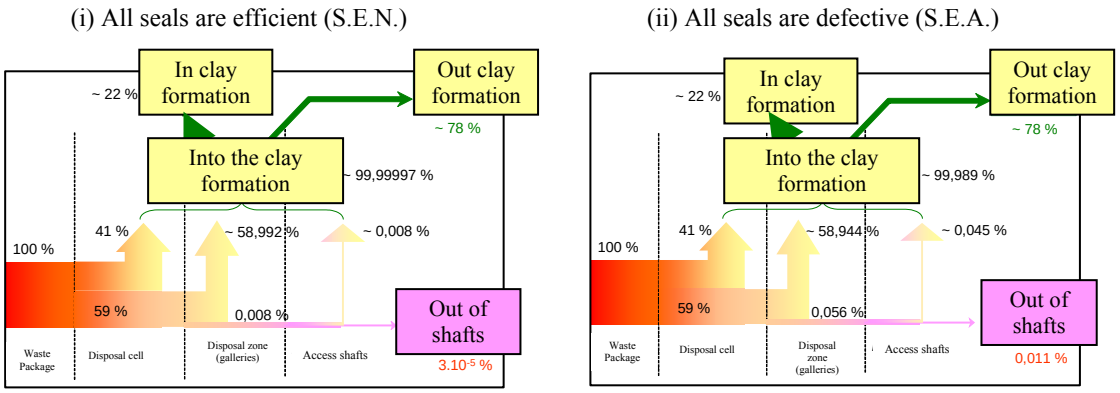

Figure 6-3: Example of Performance Assessment for seal: mass of I^{129} at one million years for Spent Fuel disposal (ANDRA, 2005)

For all situations studied, the dominant transfer pathway remains the clay layer barrier: the dose associated with this transfer pathway is similar to the one of the normal evolution scenario, considering the (very) low proportion of radionuclides (mainly long lived and highly soluble ones, like ^{129}I) that migrates through the repository (less than at least three orders of magnitude, in comparison with clay barrier pathway). Dose impact appears to be sensitive to EDZ properties. However, if EDZ degraded properties increase the dose due to the repository transfer pathways by one order of magnitude, no consequences are observed on the global impact (**Figure 6-3**).

The integration of conservative representations of radionuclide release from waste package and seal core geochemical parameters has also no influence: (i) due to the slowness of water flow through the repository, the clay layer barrier « traps » radionuclides that may be sensitive to bentonite geochemistry; and (ii) radionuclides that contribute to the impact are not sensitive to the geochemical properties of the seal cores.

In conclusion, it is worth noting that the seals are significant contributors to the safety functions but that the clay layer provides redundancy by limiting water inflow, even in case of failure of all seals. Due to the efficiency of these systems, impacts of « seal failure » altered evolution scenarios do not appear to be greater than those of normal evolution scenario. This indicates that seals are not essential to safety.

6.2.2 Resulting technical requirements

Some types of high density bentonite seals have been first designed for waste repositories within fractured crystalline rocks (Pusch, 1981; Pusch *et al.,* 1987; Lopez and Johnson, 1986), in which significant groundwater flow and advective transport could occur locally in the absence of seals. In analogy with the designs of waste repositories in crystalline rocks, similar types of seals, consisting of high swelling and low permeable bentonite, are also included in the current reference concepts for waste repositories in sedimentary rocks. The recent literature, also illustrated that all waste agencies do consider the emplacement of seals, even when not strictly necessary. As such, it will be attempted here to translate the qualitative functional requirements reported above into technical requirements.

As all current designs consider the emplacement of seals, a logic, but important requirement is that it is feasible to construct such a seal. On the one hand, this implies that the sealing material can be emplaced and that this operation does not threaten the safety of the workers. On the other hand, this feasibility implies that the bentonite material can be produced in a form easy to install and still guaranteeing the needed characteristics.

Based on the information given above, the major functional requirement of the seal is to limit the circulation of water in and around the repository. As such, a low hydraulic conductivity is demanded. As this hydraulic conductivity is inversely related to the dry density of the bentonite (see Chapter 2), compacted bentonite with a high dry density is needed for the seals.

Within the international review performed by Volckaert and Bernier (1996b), it was also stated that the seals should withstand the expected gas pressure at the repository depth. The most important gas production in waste repositories is related to the anaerobic corrosion of metals, giving rise to hydrogen production. The gas pressure build up depends on the corrosion rate and the capacity of the system to transport the produced gas - away from the Engineered Barrier System. At very low saturations, gas might be transported in a monophasic gas phase. With increased saturation, when continuous gas pathways are no longer present, but before full saturation of the high density bentonites, a substantial amount of gas can be evacuated through the bentonite seals by diffusion and biphasic flow, which would limit the gas pressure build up. However, once the high density bentonite is fully saturated the biphasic flow is getting very small, limiting the amount of gas that can be evacuated. This mostly results in a gas pressure build up, that might lead to gas transport through microfractures or even fractures. Consequently, there might exist some kind of contradiction between the functional requirement to have a low hydraulic conductivity and the functional requirement to withstand gas pressures when trying to convert the functional requirements into technical requirements. High density bentonites are needed to obtain a low hydraulic conductivity, similar to the hydraulic conductivity of the host rock. However, once these high density bentonites are saturated, they also form an important barrier for gas transport and might induce gas pressure build up. Depending on design, the gas pressure might be higher than the pressure the seals, or the host rock, can withstand, so that microfractures or fractures are created. However, it needs to be mentioned that this is strongly depending on the design considered. First of all, the amount of metal, the surface area of the metal exposed to water and the corrosion rate will strongly influence the gas production. Secondly, the hydration time of the seal will strongly influence the gas transport by diffusion and biphasic transport.

This hydration time is again strongly coupled with the seals chosen. For the high density bentonites, chosen for their low hydraulic conductivity, the hydration time is much longer than for low density bentonites. It needs to be repeated that in none of the documents reviewed, especially those considering seals in sedimentary host rocks, a clear indication is given on the timing at which all or some of the requirements of the seal should properly function. This might be related to the fact that current safety assessment calculations indicate that seals are not essential in this type of host rock. Consequently, it is very difficult to clearly indicate the technical requirement needed with regard to the coupled characteristics of hydraulic conductivity, gas tightness and hydration time.

Whenever gas pressure is too high, gas pathways will be formed and self sealing of the fractures should occur so that the seal can fully regain its function, especially concerning low hydraulic conductivity, - after the gas pressure has disappeared. In other words, the performance of the

seal with respect to gas pressure build up has to be on par with that of the host rock and both have to be sufficient to ensure lasting safety.

Likewise, once radionuclides are released from the waste, it is the objective of the seals to avoid preferential pathways for radionuclides. As such, the transport mechanism through the seals should be diffusion dominated. To this end, small pores and a low hydraulic conductivity would be beneficial. Moreover, a homogenisation of the mixture or blocks used is a prerequisite to avoid any preferential pathways.

On top of that, the seals will contribute to redundancy and as such will help in providing a robust system. Although not strictly needed for safety as illustrated by safety assessment calculations, they will reduce the public concern regarding long-term hazards and they might contribute to the operational safety. If in an unforeseen case the partly filled repository would flood, one might remove the water by pumping and continue the operational phase without too many special treatments and loss of time if bentonite seals were emplaced. The latter will first limit the water influx into the disposal galleries and consequently, will avoid contamination of the water in the rest of the repository.

The seals should be stable to any effects resulting from the thermal disturbance that can be expected at its location. Moreover, the seal also needs to be chemically stable concerning chemical disturbances expected in its surroundings. Currently worked out reference designs (ANDRA, 2005) consider the use of concrete bulkheads at both ends of the seals in order to keep the seal confined during hydration (so that swelling pressure can build up and low hydraulic conductivities can be obtained). Apart from this contact with concrete, the seals are mostly in contact with the host rock.

Finally, a good understanding of the different processes that are expected during the life time of a seal is important in order to enable the modelling of these phenomena. This is necessary, as modelling is essential to predict or scope the long-term behaviour of seals as is needed for a waste repository.

6.3 Lessons learned from RESEAL

As we have tried to translate the functional or qualitative requirements of seals into technical requirements, we will here evaluate the contribution of the RESEAL project to the demonstration or better understanding of these technical requirements. An attempt has been made to outline the conclusions of the RESEAL project with respect to different technical requirements described above into one table (**Table 6-2**)

Table 6-2: Overview of the use of the RESEAL project within the different requirements formulated above.

	requirement	RESEAL outcome
design	Feasible	✓
	Safely installable	✓
Confidence building	Same K as host rock	✓
	Hydration time, depends on functional requirement, which depends on the position of the seal	?
	fast: immediate fulfillment of function	☒
	slow: may smooth THM transient in host rock	✓
	No easy gas breakthrough and $K_{seal}<K_{host}$	✓
	Self sealing	✓
	No preferential migration of RN	✓
	Homogenisation of mixture	✓
	Stable (THMC) during required lifetime	Not tested
	Good process understanding allowing to model	Increased, but not sufficient
PA (sensu stricto)	Ensure diffusive transport within NF	Test running

In order to fully design a repository, it needs to be demonstrated that it is feasible to install seals and that this installation can be performed in a safe way. Both in-situ experiments, the borehole seal experiment and the shaft seal experiment, have demonstrated the feasibility of emplacement. Moreover, two types of sealing materials, namely pre-compacted blocks and pellet/powder mixture, have been used. Within the shaft seal, the additional compaction of the pellet/powder mixture, in order to obtain even higher dry densities, has been illustrated. Finally, the installation of both seal types in the in-situ experiments passed without any accidents or insurmountable problems. However, it needs to be mentioned that RESEAL only demonstrated the feasibility of sealing a shaft of 2.2m diameter. This is far from the expected diameter of an access gallery or shaft (in the order of 5 to 10m diameter). Moreover, the installation of a seal in a horizontal gallery has neither been demonstrated.

As the majority of requirements described above are no direct consequences of the results of performance assessment calculations, they can be grouped as requirements that underbuild the confidence in the system. The most important requirement is that the seal has a hydraulic conductivity equal to or lower than the hydraulic conductivity of the host rock. For both in-situ experiments, the borehole seal and the shaft seal, the target hydraulic conductivity, more or less equal to the one of the undisturbed host rock, was reached. Moreover, these in-situ measurements correspond with the values predicted on laboratory experiments.

The behaviour of the seal during gas pressure build up is related to the initial dry density and thus related to the hydraulic conductivity, swelling pressure and hydration time. Within the borehole seal experiment it has been demonstrated that the saturated seal was not a preferential pathway for gas migration. In contrast to that, when gas pressure was high enough, gas migrated along the interface bentonite – host rock or through the EDZ of the host rock. With the used

experimental set-up, no distinction could be made between these both processes. Within the shaft seal experiment, a gas pressure was built up inside the seal. The processes of gas migration are similar as the ones described for natural clay host rocks (Volckaert *et al.,* 1995; Ortiz *et al.,* 1997; Horseman *et al.,* 1996).

Also related to this low hydraulic conductivity, is the process of hydration. As mentioned before, no clear requirement on hydration time could be formulated. The requirement might depend on the position of the seal and might be strongly dependent on the reference design. Anyhow, the RESEAL project illustrated that for relatively thin rings of bentonite, like the ones used in the borehole seal experiment, the hydration goes rather fast. However, on a larger scale, as in the shaft seal experiment, hydration takes a very long time, even much longer than originally predicted. It should be reminded that similar observations were made in other large-scale experiments using high density bentonite (Mayor *et al.,* 2005; ENRESA, 2000, Fairhurst *et al.,* 1993). It should be noted that before full saturation of the seal, no major water transport across the seal is expected, because the suction of the bentonite remains high until nearly full saturation.

Within the shaft seal experiment, a gas pressure build-up was performed twice on the same filter. As the breakthrough occurred at nearly the same pressures and as the observation of gas breakthrough was not at the same positions, there does not seem to be a preferential gas pathway, even after a first gas breakthrough. After the experiments of gas breakthrough, it was analysed whether these gas pathways had an important impact on the hydraulic conductivity of the seal. In other words, it was analysed if the seals exhibit self sealing properties. Within the shaft seal experiment, the hydraulic conductivity of the seal in the neighbourhood of the formerly created gas pathway, recovered fast to its original undisturbed value.

During the ^{125}I migration test in the borehole seal, an important hydraulic gradient was created by the water sampling procedure. The measured concentrations at the observation filter can be reproduced by a model which takes advective transport due to this gradient into account in addition to molecular diffusion. Moreover, no evidence of a preferential migration of the tracer, e.g. along the original joints of the blocks, was observed within the used set-up.

In addition several non-destructive techniques and destructive analyses on laboratory samples have illustrated the homogenisation of the pellet/powder mixture, used in the shaft seal experiment. The migration experiments with ^{125}I within this shaft seal experiment are still ongoing, and no conclusions can be drawn yet.

The long-term stability of the bentonite material used towards mainly thermal and chemical disturbances was not demonstrated within the RESEAL project. However, as the bentonite is chemically not too different from the clayey host rock, no major chemical changes are expected. For the effect of alkaline fluids as a result of the contact with concrete we refer to other projects, dealing with this issue (ECOCLAY II, 2005). The thermal load on the seals is strongly dependent on the design of the repository, as further away from heat emitting wastes, the seals will only suffer a small temperature increase.

Next, we can state that the efforts made during the RESEAL project have strongly increased our knowledge in the processes occurring within hydrating seals. Most markedly, is the evolution of the swelling pressure during hydration, which is now well characterised and understood. The latter is clearly demonstrated by the good fit between the hydro-mechanical models and the experimental data of these laboratory tests. Moreover, the good correspondence between the

experimental data of the borehole seal experiment and the model simulations, illustrate that a small scale seal experiment can be fairly well predicted. However, for the large scale in-situ shaft seal experiment the general trends of the hydro-mechanical behaviour can be predicted, but are still far from a good fit with the experimental observations. Especially the very long hydration time is currently not reproduced by the models. On top of that, experimental data points of hydraulic conductivity, swelling pressure and migration parameters illustrate large uncertainties (variations around 1 order of magnitude). Up to now we are not able to attribute these variations to differences in experimental set-ups or to the lack of a very detailed understanding of all processes.

As mentioned before, the strict requirements from the safety assessment point of view are rather limited. The main requirement is probably to ensure a diffusive transport within the near field around a repository. Within the RESEAL project, a radionuclide migration test was performed in the excavation disturbed zone (EDZ) around the in-situ shaft seal experiment. During hydration, fractures were clearly demonstrated within the EDZ. However, once the seal was nearly saturated, the fractures sealed. The migration of ^{125}I through this EDZ did not demonstrate any major relicts of the fractures, that jeopardise the diffusive transport within the host rock and specifically through the EDZ. However, it needs to be mentioned that this observation cannot be exclusively attributed to the swelling of the seal. Former experiments (Bernier *et al.,* 2007) within the Boom Clay have clearly demonstrated the fast self sealing capacity of this host rock. Moreover, migration experiments through formerly fractured Boom Clay, also did not reveal any change of the migration parameters. As such we can only conclude that for a plastic clay host rock, like Boom Clay, diffusive transport within the near field is observed after saturation of the seal.

6.4 Open questions remaining

In the broad sense (laboratory test, borehole sealing test, shaft sealing test, modelling) RESEAL constitutes a significant step in the confidence of the performance of a shaft sealing in an argillaceous host rock. Furthermore, progress was made in technological emplacement, understanding and modelling of phenomenological processes (hydration and swelling of bentonite pellets, gas transfer in saturated bentonite pellets core, hydro-mechanical interaction between a bentonite core and a clay host rock). This allows continuing with confidence future research on some open questions remaining on both, the technological and phenomenological level:

- To extend to large scale (i.e. real) access shaft (larger diameter, heavier lining, and larger height and at larger depth...);
- To extend to indurated clays (OPALINUS Clay and Callovo-oxfordian Argilites), in particular taking into account the hydro-mechanical characteristics of EDZ in this type of clay rock (shape, extension, time scale of hydraulic self sealing…)
- To cover all phenomenological conditions expected in repository situations, in particular natural hydration of the bentonite pellets core, effect of gas migration on long term

Lastly, RESEAL only relates to seal emplacement of access shafts. If its results can be qualitatively extended to sealings of galleries, the emplacement of such sealings, the evaluation of their phenomenological behaviour (hydration, hydro-mechanical loading, hydro-mechanical interaction with clay rock, gas transfer…), and the evaluation of their hydraulic performance at large (including effects of thermal loading and gas loading) must also be carried out.

7 References

Aertsens, M., Put, M. and Dierckx, A., 1999. An analytical model for pulse injection experiments. In: Feyen, J. and Wiyo, K. (Eds.). Modelling of transport processes in soils at various scales in time and space. Int. Workshop of EurAgEng's Field of Interest Soil and Water. Wageningen Pers, Wageningen. 67 pp.

Aertsens, M., Dierckx, A., De Cannière, P., Janssen, K., Moors, H., Van Ravestyn, L., Van Gompel, M. and Put, M., 2005. Determination of the hydraulic conductivity, the product ηR of the porosity η and the retardation factor *R*, and the apparent diffusion coefficient *Dp* on Boom Clay cores from the Mol-1 drilling. SCK•CEN report, R-3503, 21 pp.

Alonso, E. E., Gens, a., and Hight, D. W. (1987). "Special problem soils. General Report." *Proc. 9th European Conf. on Soil Mechanics and Foundation Engineering. Dublin,* 1087-1146.

Alonso, E. E., Gens, A., and Josa, A. (1990). "A constitutive model for partially." *Géotechnique,* 40(3), 405-430.

Alonso, E. E., Vaunat, J., and Gens, A. (1999). "Modelling the mechanical behaviour of expansive clays." *Eng.Geol.,* 54 173-183.

ANDRA, 2005. Dossier 2005 Argile. Les recherches de l'ANDRA sur le stockage géologique des déchets radioactifs à haute activité et à vie longue.

Bastiaens, W. and Mertens, J., 2005. EDZ Around An Industrial Excavation in Boom Clay. Impact of the excavation disturbed or damaged zone (EDZ) on the performance of radioactive waste geological repositories. Proceedings of a European Commission CLUSTER conference, Luxembourg 3-5 November, 2003, EUR21028 pp. 248-254.

Bastiaens, W., Bernier, F. and Ling Li, X., 2005. SELFRAC: experiments and conclusions on fracturation and self-healing processes in clays. 2nd International meeting on Clays in Natural & Engineered Barriers for Radioactive Waste Confinement, March 14-18, 2005, Tours, France.

Bastiaens, W., Bernier, F., and Li, X.L.,2006. An Overview of Long-Term HM Measurements around HADES URF. Multiphysics coupling and long term behaviour in rock mechanics, Proc. Intern. Symp., Liège, 2006, May 9-12, 15-26.

Bel, J. and De Preter, P. The use of seals in a deep disposal system for high-level and long-lived waste in Belgium. A position paper, Febuary 2005. ONDRAF/NIRAS report

Bernard-Michel G., Genty A. (2006). "Modules d'écoulement et de transport en milieux poreux non saturés dans CAST3M– modèle de Richards ", rapport CEA/DM2S/SFME/MTMS/RT/06-011/A.

Bernier, F., Li, X.L., Bastiaens, W., Ortiz, L., Van Geet, M., Wouters, L., Frieg, B., Blümling, P., Desrues, J., Viggiani, C., Coll, C., Chanchole, S., De Greef, V., Hamza, R., Malinsky, L., Vervoort, A., Vanbrabant, Y., Debecker, B., Verstraelen, J., Govaerts, A., Wevers, M., Labiouse, V., Escoffier, S., Mathier, J.-F., Gastaldo, L., Bühler, Ch., 2007. Fractures and Self-healing Within the Excavation Disturbed Zone in Clays (SELFRAC). European Commission report, EUR22585, 62pp.

Bradbury, B. and Baeyens,B., 2003. A comparison of apparent diffusion coefficients measured in compacted Kunigel V 1 bentonite with those calculated from batch sorption measurements and De (HTO) data: a case study for Cs(I), Ni(II), Sm(III), Am(III), Zr(IV) and Np(V). PSI-Bericht 03-02, PSI, Villigen.

Celia M.A., Boulotas E.T., Zarba R.L. (1990). "A general mass-conservative numerical solution for the unsaturated flow equation". *Water. Resour. Res*. 26(7), 1483-1496.

Coulon, H., 1987. Propriétés physico-chimiques de sédiments argileux français : contribution au stockage de déchets radioactifs. PhD thesis. Université des sciences et techniques de Lille Flandres-Artois.

Dabbene F. (1998). "Mixed Hybrid Finite Elements for transport of pollutants by underground water"*, Proc. Of the 10th Int. Conf. On Finite Elements in Fluids*, Tucson, USA

De Cannière P., Put M.J. and Neerdael B., 1994. "Hydraulic characterization of the Boom Clay formation from the HADES underground laboratory in Mol: Evolution and assessment of the piezometric techniques", Hydraulic and hydrochemical characterisation of Argillaceous rocks, NEA int. workshop, Nottingham, UK, 7-9 June 1994, pp. 159-166.

De Craen, M., Wang, L., Van Geet, M., Moors, H., 2004. Geochemistry of Boom Clay pore water at the Mol site. Ref. SCK•CEN-BLG-990, SCK•CEN, Mol (Belgium), ISSN 1379-2407.

ECOCLAY II (2005) ECOCLAY II : Effects of Cement on Clay Barrier Performance - Phase II. Final Report, EC project n°FIKW-CT-2000-00028 ; Andra report n°CRPASCM04-0009, 381 p.

ENRESA 1998: FEBEX Bentonite: origin, properties and fabrication of blocks, Publicacion Tecnica 4/98, Madrid, Spain.

ENRESA, 2000. FEBEX project - Full-scale engineered barriers experiment for a deep geological repository for high level radioactive waste in crystalline host rock. FINAL REPORT. ENRESA Technical Report, PT 1/2000.

ENRESA, 2006. Full-scale Engineered Barriers Experiment. Updated Final Report 1994-2004. Publicación Técnica ENRESA 05-0/2006. 590 pp. Madrid.

Fairhurst, C., Gera, F., Gnirk, P., Gray, M., Stillborg, B., 1993. OECD/NEA International Stripa project, Overview volume I – Executive summary.

Filippi M. (2007). "Validation de l'implémentation de la loi de comportement mécanique BBM dans le code CAST3M". report CEA/DM2S/SFME/MTMS.

Garcia-Gutierrez, M., Missana, T., Mingarro, M., Samper, J., Dai, Z. and Molerino, J., 2001. Solute transport properties of compacted Ca-bentonite used in FEBEX project. Journal of Contaminant Hydrology, 47, pp. 127-137.

Gens, A., and Alonso, E. E. (1992). "A framework for the behaviour of unsaturated expansive clays." *Can.Geotech.J.,* 29 1013-1032.

Gens, A., García-Molina, A. J., Olivella, S., and Alonso, E. E. (1998). "Analysis of a full scale in situ test simulating repository conditions." *Int.J.Numer.Analyt.Methods Geomechanics,* 22 515-548.

Gens, A., Filippi, M., Vallejan, B., Van Geet, M., Volckaert, G. and Bastiaens, W., 2009. RESEAL II project – Final report on modelling (WP4). SCK•CEN report ER-80.

Hildenbrand, A., Schlömer, S. and Krooss, B.M., 2002. Gas breakthrough experiments on fine-grained sedimentary rocks. Geofluids, 2, pp. 3-23.

Horseman, S. T., Winter, M. G., and Entwistle, D. C. (1985). "Geotechnical characterisation of Boom clay in relation to the disposal of radioactive waste." British Geological Survey. Natural Environment,

Horseman, S.T., Higgo, J.J.W., Alexander, J. and Harrington, J.F., 1996. Water, Gas and Solute Movement through Argillaceous Media. NEA – Clay Club report CC-96/1. OECD, Paris, France.

Huyakorn P.S., Pinder G.F. (1983) "Computational Methods in Subsurface Flow". Ed. Academic Press

IAEA, 1990. Sealing of underground repositories for radioactive wastes. IAEA Technical Report Series No. 319, Vienna.

IAEA, 2003. Radioactive Waste Management Glossary, Edition 2003.

Imbert, C., Billaud, P., Touzé, G., 2004. Caractérisation hydro-mécanique du matériau argileux utilisé dans l'essai de scellement de puits à échelle un «RESEAL ». Projet européen « RESEAL phase II ». Rapport final. Rapport technique DPC/SCCME 04-694-A. Gif-sur-Yvette. 69pp.

Imbert C. and Villar, M.V., 2006. Hydro-mechanical response of a bentonite pellets/powder mixture upon infiltration. Applied Clay Science, 32, pp. 197-209.
Johannesson, L.E., Börgesson, L., Goudarzi, R., Sanden, T., Gunnarsson, D., Svemar, C., 2007. Prototype repository: A full scale experiment at Äspö HRL. Physics and Chemistry of the Earth, 32, pp. 58-76.
Josa, A., Balmaceda, A., Gens, A., and Alonso, E. E. (1992). "An elastoplastic model for partially saturated soils." Swansea: Pineridge Press, 815-826.
Kehle, R. O., 1964. The Determination of Tectonic Stresses Through Analysis of Hydraulic Well Fracturing. J. Geophys. Res. 69, 259-273.
Kozaki, T., Inada, K., Sato, S., Oaci, H., 2001. Diffusion mechanism of chloride ions in sodium montmorillonite. J. Contaminant Hydrology, 47, pp. 159-170.
Lajudie, A., Raynal, J., Petit, J.C., Toulhoat, P., 1994. Clay based materials for engineered barriers : a review. Materials Research Society Symposia Proceedings of Kyoto, pp. 221-230.
Lassabatère, T., 1997. Synthese des connaissances experimentales sur le comportement hydromecanique de l'argile FoCa pure sechee compactee. CEA-report, N.T. SESD/97.11, 42pp.
Leboulch D., Millard A. (1997). "Implémentation dans CASTEM2000 de deux modèles de comportement mécanique des argiles non saturées ", rapport CEA/DMT/97-076.
Lopez, R.S and Johnson, L.H., 1986. Vault sealing research and development for the Canadian Nuclear Fuel Waste Management Program. AECL report 9053.
Maes, N., Moors, H., Dierckx, A., De Cannière, P. and Put, M., 1999. The assessment of electromigration as a new technique to study diffusion of radionuclides in clayey soils. J. Contaminant Hydrology, 36, pp. 231-247.
Martino, J.B., Dixon, D.A., Kozak, E.T., Gascoyne, M., Vignal, B., Sugita, Y., Fujita, T., Masumoto, K., 2007. The tunnel sealing experiment: An international study of full-scale seals. Physics and Chemistry of the Earth, 32, pp. 93-107.
Mayor, J.C., Garcia-Siñeriz, J.L., Alonso, E., Alheid, H.J., Blümling, P., 2005. Engineered barrier emplacement experiment in Opalinus Clay for the disposal of radioactive waste in underground repositories. ENRESA Technical Report, PT 02/2005.
NAGRA, 2002. Safety Report. Demonstration of disposal feasibility for spent fuel, vitrified high-level waste and long-lived intermediate-level waste. Nagra report, NTB 02-05.
Ochs, M., Lothenbach, B., Wanner, H., Sato, H. and Yui, M., 2001. An integrated sorption-diffusion model for the calculation of consistent distribution and diffusion coefficients in compacted bentonite. J. Contaminant Hydrology, 47, pp. 283-296.
Olivella, S., 1995. Non isothermal multiphase flow of brine and gas through saline media. PhD Thesis, 197 pp., Technical University of Catalonia, Barcelona, Spain.
Olivella, S. (2002). *CODE-BRIGHT USER'S GUIDE,* Departamento de Ingeniería del Terreno UPC, Barcelona.
Olivella, S., Carrera, J., Gens, A., and Alonso, E. E. (1994). "Non isothermal multiphase flow of brine and gas trough saline media." *Transp.Porous Media,* 15 271-293.
Olivella, S., Gens, A., Carrera, J. & Alonso, E.E. 1996. "Numerical formulation for a simulator (CODE-BRIGHT) for the coupled analysis of saline media". *Engineering Computations*, 13(7): 87-112.
Ortiz, L., Put, M., Bruyn, D. D., Bernier, F., and Moerkens, K. (1996). "Large scale Measurement of the hydraulic conductivity of the Boom clay." NIRAS/ONDRAF SCK•CEN.
Ortiz, L; Volckaert, G., De Cannière, P., Put, M., Sen, M.A., Horseman, S., Harrington, J., Impey, M.D., Einchcomb, S., 1997. MEGAS: Modelling and Experiments on Gas migration in Repository Host Rocks, Final Report – Phase 2, European Commission Report EUR 17453 EN, Luxembourg.

Pasquiou, A., 1999. Pellets d'argile: élaboration et caractérisation Thermo-Hydro-Mécanique. Deuxième rapport d'avancement de thèse. Rapport ANDRA C RP AMAT 99.077. (In French).

Pasquiou, A. 2001. Pellets d'argiles gonflantes. Elaboration et caractérisation hydro-mécanique. PhD Thesis. Université des Sciences et Techniques de Lile, Lille.

Plas, F., 1988. Une méthode de mesure indirecte de la perméabilité des matériaux de type sol: la consolidation uniaxiale. Principe et application à l'argile de référence Fo-Ca. CEA-report, N.T. SESD/88.21.

Pusch, 1981. Borehole sealing with Highly Compacted Na Bentonite. SKB-KBS Technical Report 81-09, Swedish Nuclear Fuel Waste Management Co., Stockholm.

Pusch, R. (1982). "Mineral-water interactions and their influence on the physical behaviour of highly compacted Na bentonite." *Can.Geotech.J.,* 19 381-387.

Pusch, R., Börgesson, L. and Ramqvist, G., 1987. Final Report of the Borehole, Shaft, and Tunnel Sealing Test – Volume II: Shaft plugging. STRIPA project. SKB Technical Report 87-02.

Put M.J., De Cannière P., Moors H., Fonteyne A. and Van Gompel M., 1994. "Continuation of the migration experiments in the Boom Clay (Laboratory and in-situ)", Progress report for the period September 1, 1993 – February 28, 1994.Work performed for CEC under contract FI 2W/0039 (unpublished progress report).

Rhattas, M. (1995). "Transfert de masse dans les matériaux à faible porosité. Analyse théorique et résultats expérimentaux." PhD thesis, Université d'Orléans, Orléans, France.

Rodwell, W.R., Harris, A.W., Horseman, S.T., Lalieux, P., Müller, W., Ortiz Amaya, L. and Pruess, K., 1999. Gas migration and two-phase flow through engineered and geological barriers for a deep repository for radioactive waste. A joint EC/NEA Status Report. European Commission Report EUR 19122 EN, Luxembourg.

Rodwell, W.R. (Ed.), 2000. PROGRESS: Research into gas generation and migration in radioactive waste repository systems. Final Report. European Commission Nuclear Science and Technology report EUR 19133.

Sánchez, M. (2004). "Thermo-hydro-mechanical coupled analysis in low permeability media." PhD thesis, Universidad Politécnica de Cataluña, Barcelona, España.

Sánchez, M., Gens, A., Guimaraẽs, L., and Olivella, S. (2001). "Generalized plasticity model for THM simulations involving expansive clays." *6th Intl. Workshop on Key Issues on Waste Isolation Research,* 45-61.

Sánchez, M., Gens, A., Guimaraẽs, L. d. N., and Olivella, S. (2005). "A double structure generalized plasticity model." *Int. J. Numer. Analyt. Methods Geomechanics,* 29(8), 751-787.

Sato, H., Ashida, T., Kohara, Y. and Yui, M., 1993. Study on retardation mechanism on 3H, 99Tc, 137Cs, 237Np and 241Am in compacted sodium bentonite. Scientific Basis for Nuclear Waste Management XVI. Mater. Res. Soc. Symp. Proc., vol 294, pp. 403-408.

Valleján, B. (2008). "*Hydromechanical Modelling of Heterogeneous Mixtures for Repository Seals*." PhD thesis in preparation.Universidad Politécnica de Cataluña, Barcelona, España.

Van Geet, M., Volckaert, G. and Roels, S., 2005a. The use of microfocus X-ray computed tomography in characterising the hydration of a clay pellet/powder mixture. Applied Clay Science, 29, pp. 73-87.

Van Geet, M., Bastiaens, W., Volckaert, G., Vallejan, B., Gens, A., 2005b. Reconaissance study of EDZ around a large scale shaft sealing demonstration test (RESEAL). Impact of the excavation disturbed or damaged zone (EDZ) on the performance of radioactive waste geological repositories. In: Proceedings of a European CommissionCLUSTER Conference, Luxembourg, 3–5 November 2003, EUR 21028EN, pp. 134–142.

Van Geet, M. and Volckaert, G., 2008. PRACLAY plug test: Lessons learned from BACCHUS 2 and RESEAL to optimize the instrumentation. SCK•CEN report R-4723.

Van Geet, M., Volckaert, G., Bastiaens, W., Maes, N., Weetjens, E., Sillen, X., Vallejan, B. and Gens, A. (2007a). "Efficiency of a borehole seal by means of pre-compacted bentonite blocks". *Physics and Chemistry of the Earth*, 32, 123-134.

Vaunat, J., and Gens, A. (2005). "Analysis of the hydration of a bentonite seal in a deep radioactive waste repository." *Eng.Geol.,* 81 317-328.

Verpeaux P., Charras T., Millard A. (1988). "CASTEM 2000 une approche moderne du calcul des structures, calcul des structures et intelligence artificielle", Fouet, Ladeveze, Ohayon, Ed. Pluralis pp 261-271.

Villar, M.V. 2002. Thermo-hydro-mechanical characterization of a bentonite from Cabo de Gata. A study applied to the use of bentonite as sealing material in high level radioactive waste repositories. Publicacion technical ENRESA 01/2002. Madrid, 258 pp.

Villar, M.V., Imbert, C., Billaud, P., Touzé, G., Garcia-Gutierrez, M., Mingarro, M., Van Geet, M., Maes, N., Aertsens, M. and Volckaert, G., 2005. RESEAL II – A large scale in situ demonstration test for repository sealing in an argillaceous host rock – phase II: Final report on laboratory tests. SCK•CEN report ER-1, 88 p.

Villar, M.V.; García-Siñeriz, J.L.; Bárcena, I. & Lloret, A., 2005a. State of the bentonite barrier after five years operation of an in situ test simulating a high level radioactive waste repository. Engineering Geology, 80, pp. 175-198.

Volckaert, G., Bernier, F., Alonso, E., Gens, A., Samper, J., Villar, M.V., Martin, P.L., Cuevas, J., Campos, R., Thomas, H., Imbert, C. and Zingarelli, V. 1996c. Thermal-hydraulic-mechanical and geochemical behaviour of the clay barrier in radioactive waste, Final report, European Commission report EUR 16744.

Volckaert, G. and Bernier,F. 1996b. Functional requirements for the seal and the material for shaft sealing. SCK•CEN report R-3125.

Volckaert, G., Bernier, F. and Dardaine, M., 1996. BACCHUS 2 – Demonstration of the in situ application of an industrial clay based backfill material. European Commission Nuclear Science and Technology. Final Report EUR 16860.

Volckaert, G., Dereeper, B., Put, M., Ortiz, L., Gens, A., Vaunat, J., Villar, M.V., Martin, P.L., Imbert, C., Lassabate`re, T., Mouche, E., Cany, F., 2000. A large-scale in situ demonstration test for repository sealing in an argillaceous host rock RESEAL project – phase I. European Commission, Luxembourg, EUR 19612, 273pp.

Volckaert, G., Ortiz, L., De Cannière, P., Put, M., Horseman, S.T., Harrington, J.F.,Fioravante, V., Impey, M., MEGAS. (1995) MEGAS: Modelling and experiments on gas migration in repository host rocks, Final Report., European Commission Report EUR 16235, Luxembourg.

Wemaere, I., Marivoet, J., Labat, S., Beaufays, R. and Maes, T., 2002. Mol-1 borehole (April – May 1997): Core manipulations and determination of hydraulic conductivities in the laboratory. SCK•CEN report, R3950, 56pp.

Yu, J.-W. and Neretnieks, J., 1997. Diffusion and sorption properties of radionuclides in compacted bentonite. SKB Technical Report 97-12, SKB, Stockholm, Sweden.

Appendix 1 - Design & instrumentation of the shaft seal

Design & instrumentation of the shaft seal

1. Introduction

This document details the design of the shaft seal and the location and the identification of the measurement points inside the seal and in the surrounding host rock.

2. Identification of the sensors

Sensor code: AA-B(B)-CCx-D(D)-EE

AA	type of measure : temperature (TC of TH), pore water pressure (PW), total stress (PT), relative humidity (RH) and displacement (DX);
B(B)	location : seal (S), host rock (H) or interface seal/host rock (SH)
CC	location such as piezometer (PZ), instrumented level (IL), hydration level (HL) (see plan p.3)
x	level inside de seal : bottom (b), middle (m) or top (t) (see plan p.3)
D(D)	direction : north (*N)* i.e. direction of the axis of main gallery, west (*W)*, east (*E)*, south (*S)* and 'vertical' (V) i.e. parallel to the axis of the shaft.
EE	numbering of the sensors

3. Design and instrumentation

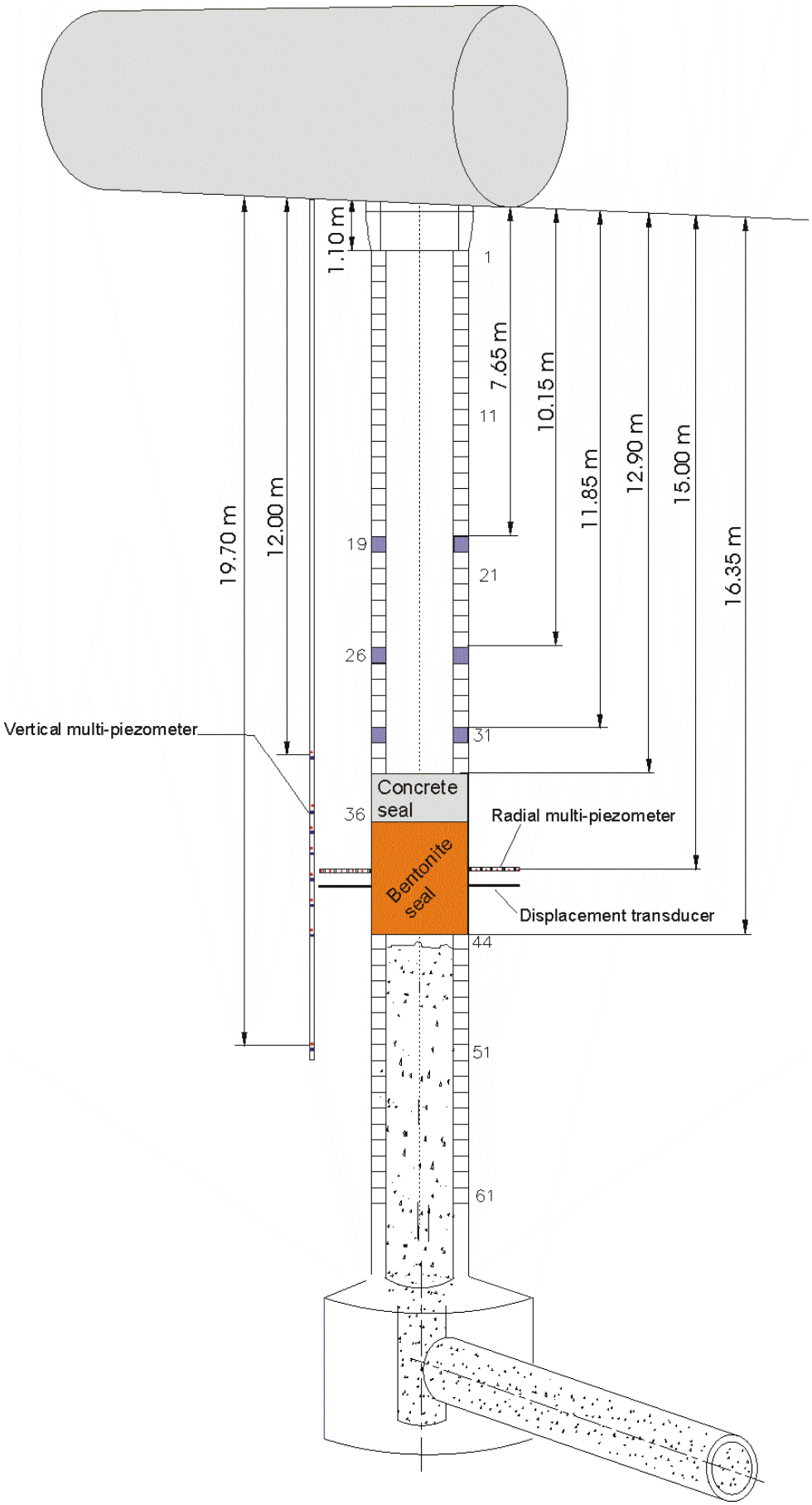

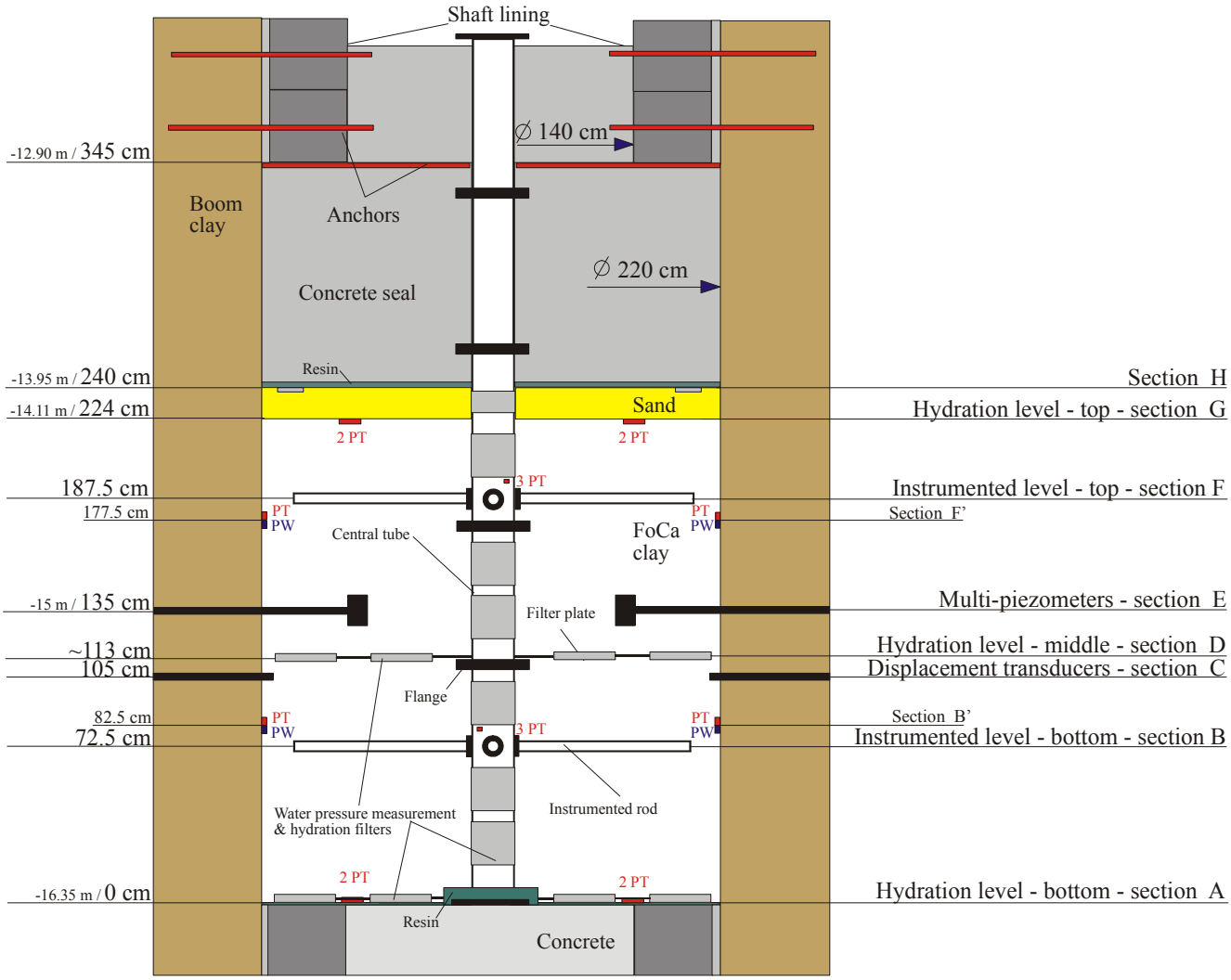

Section	h [cm] [7]	D [cm] [8]
A – Hydration Level – bottom	0	-16.35
B – Instrumented Level – bottom	72.5	
C – Displacement transducers	105	
D – Hydration level – middle	~113	
E – Multi-piezometers	135	-15.00
F – Instrumented level – top	187.5	
G – Hydration Level	224	-14.11
H	240	-13.95

[7] *h* distance from the bottom of the seal
[8] *D* distance from the main gallery (see plan p. 2)

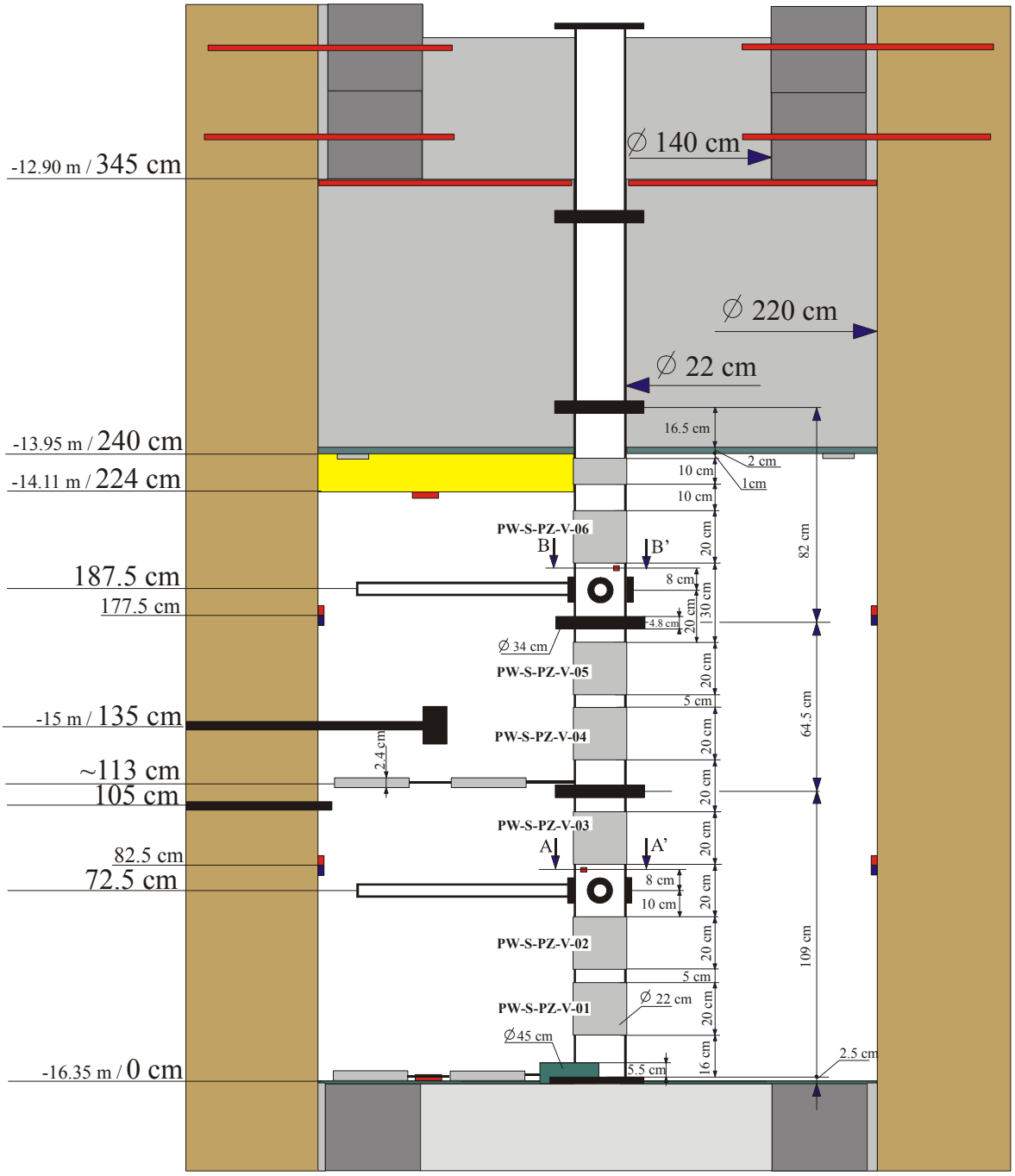

Section AA'

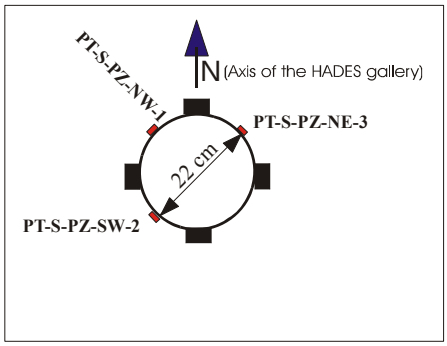

Section BB'

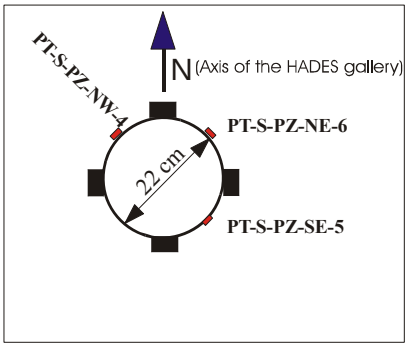

Location and identification of the sensors on the central tube

Total stress sensor				
Sensor code	Location			
PT-S-**PZ**	θ [9]	*h [cm]*	*r [cm]*[10]	*direction* [11]
-NW-01	135°	80.5	0	radial
-SW-02	225°	80.5	0	radial
-NE-03	45°	80.5	0	radial
PT-S-**PZ**	θ	*h [cm]*	*R [cm]*	*direction*
-NW-04	135°	195.5	0	radial
-SE-05	315°	195.5	0	radial
-NE-06	45°	195.5	0	radial

Water pressure			
Sensor code	Location		
PW-S-**PZ**	θ	*h [cm]*	*r [cm]*
-V-01	-	27.5	0
-V-02		52.5	0
-V-03		92.5	0
-V-04		132.5	0
-V-05		157.5	0
-V-06		207.5	0

[9] θ angle, following the mathematical convention (when viewing from the top of the seal)
[10] *r* radial distance from the central tube
[11] *direction* in case of stress measurements i.e. stress direction (radial, longitudinal or tangentiel stress)

SECTION A - **H**ydration **L**evel - **b**ottom - 0 cm

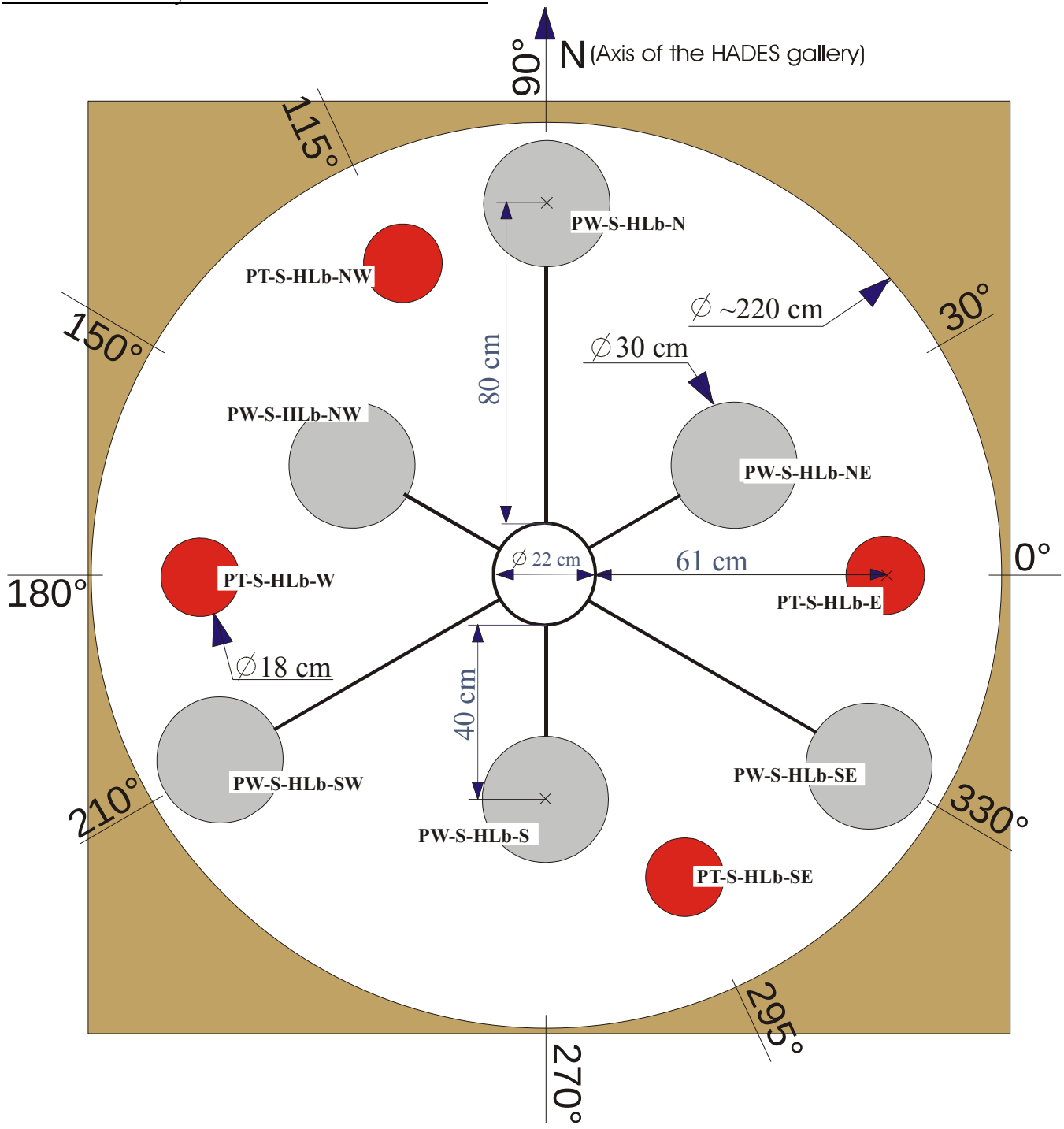

Location and identification of the sensors

Water pressure		
Sensor code	Location	
PW-S-**HLb**	θ	*r [cm]*
-N	90°	80
-NW	150°	40
-SW	210°	80
-S	270°	40
-SE	330°	80
-NE	30°	40

Total stress			
Sensor code	Location		
PT-S-**HLb**	θ	*r [cm]*	*direction*
-NW	115°	61	long.
-W	180°	61	long.
-SE	295°	61	long.
-E	0°	61	long.

SECTION B -**I**nstrumented **L**evel - **b**ottom -72.5 cm

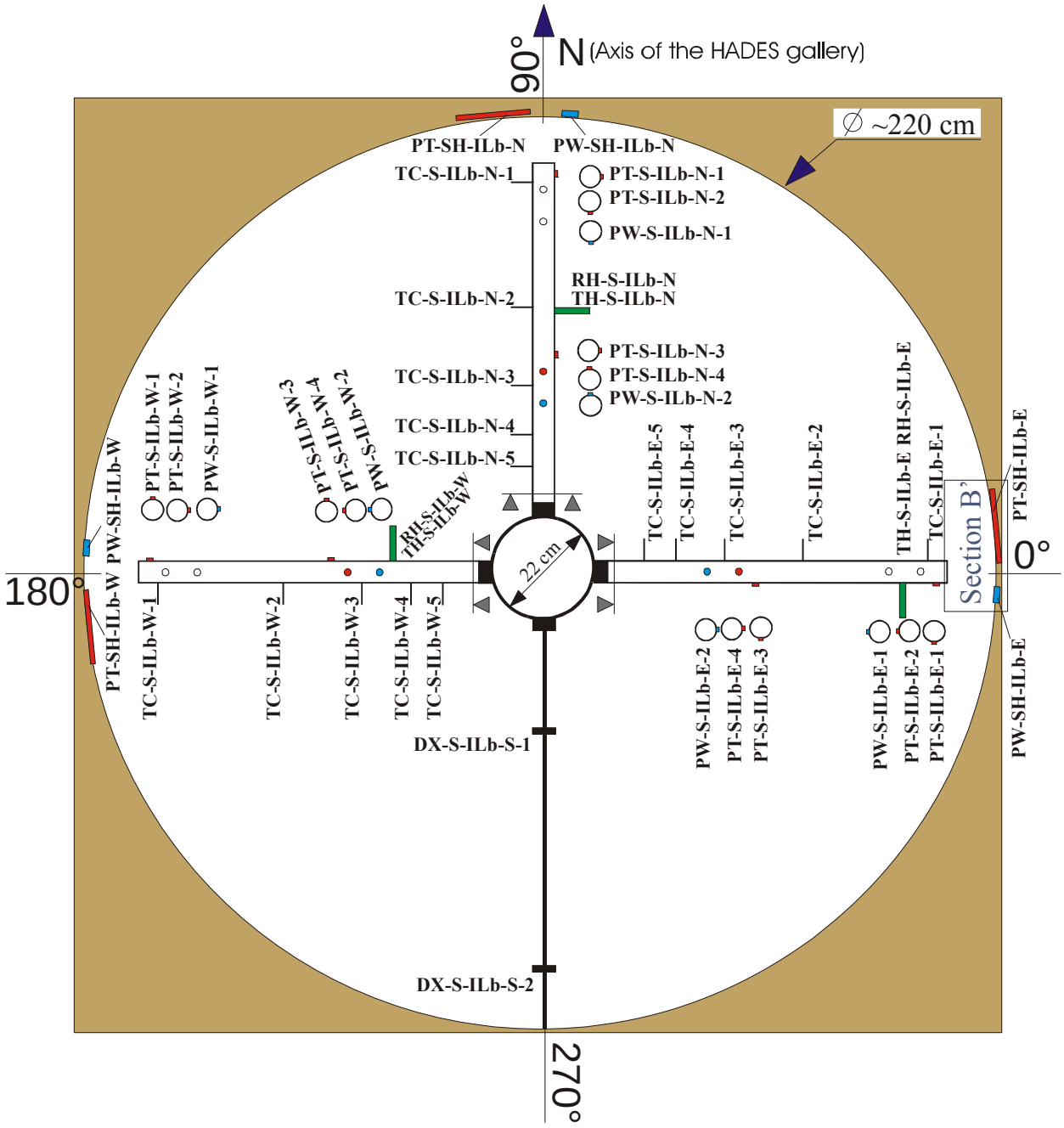

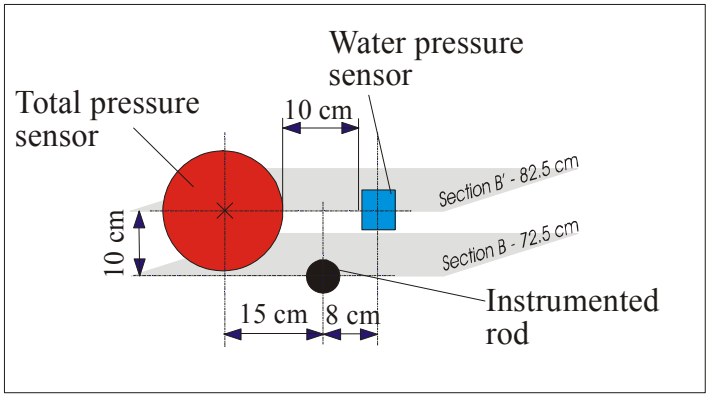

Details of the instrumented rods of section B

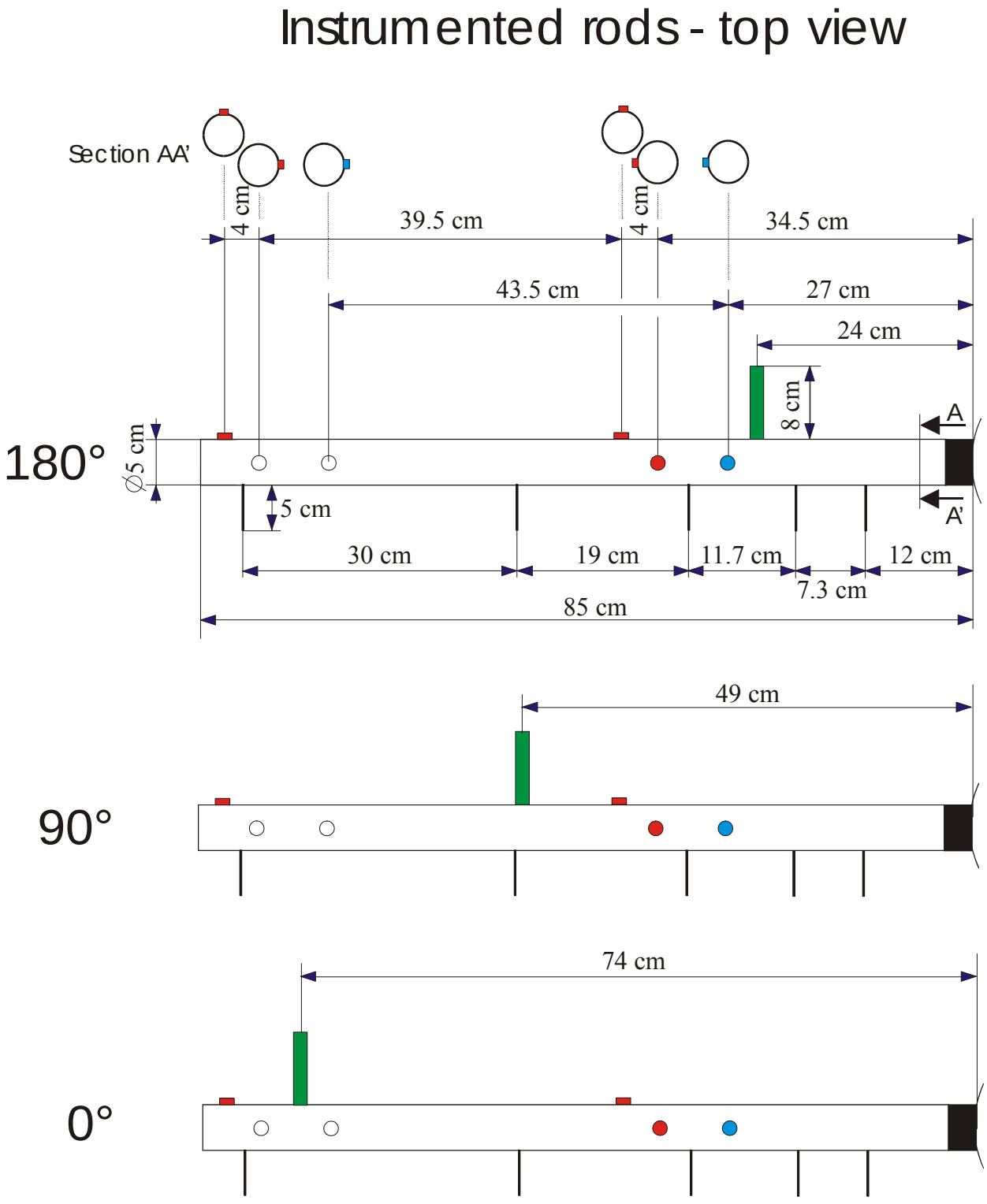

Location and identification of the sensors

- Section B

Water pressure		
Sensor code	Location	
PW-S-**ILb**	θ	*r [cm]*
-N-1	90°	70.5
-N-2	90°	27
-W-1	180°	70.5
-W-2	180°	27
-E-1	0°	70.5
-E-2	0°	27

Total stress			
Sensor code	Location		
PT-S-**ILb**	θ	*r [cm]*	*direction*
-N-1	90°	82	trans.
-N-2	90°	78	long.
-N-3	90°	38.5	trans.
-N-4	90°	34.5	long.
-W-1	180°	82	trans.
-W-2	180°	78	long.
-W-3	180°	38.5	trans.
-W-4	180°	34.5	long.
-E-1	0°	82	trans.
-E-2	0°	78	long.
-E-3	0°	38.5	trans.
-E-4	0°	34.5	long.

Temperature		
Sensor code	Location	
TC-S-**ILb**	θ	*r [cm]*
-N-1	90°	80
-N-2	90°	50
-N-3	90°	31
-N-4	90°	19.3
-N-5	90°	12
-W-1	180°	80
-W-2	180°	50
-W-3	180°	31
-W-4	180°	19.3
-W-5	180°	12
-E-1	0°	80
-E-2	0°	50
-E-3	0°	31
-E-4	0°	19.3

-E-5	0°	12
Relative humidity + temperature		
Sensor code	Location	
RH-S-**ILb** TH-S-**ILb**	θ	*r [cm]*
-N -W -E	90° 180° 0°	49 24 74

Displacement		
Sensor code	Location	
DX-S-**ILb**	θ	*r [cm]*
-S-1 -S-2	270° 270°	41.4 82.8

- section B' - 82.5 cm

Water pressure		
Sensor code	Location	
PW-SH-**ILb**	θ	*r [cm]*
-N -W -E	90° 180° 0°	100 100 100

Total stress			
Sensor code	Location		
PT-SH-**ILb**	θ	*r [cm]*	*direction*
-N -W -E	90° 180° 0°	100 100 100	radial radial radial

SECTION C -Displacement transducers - 105 cm

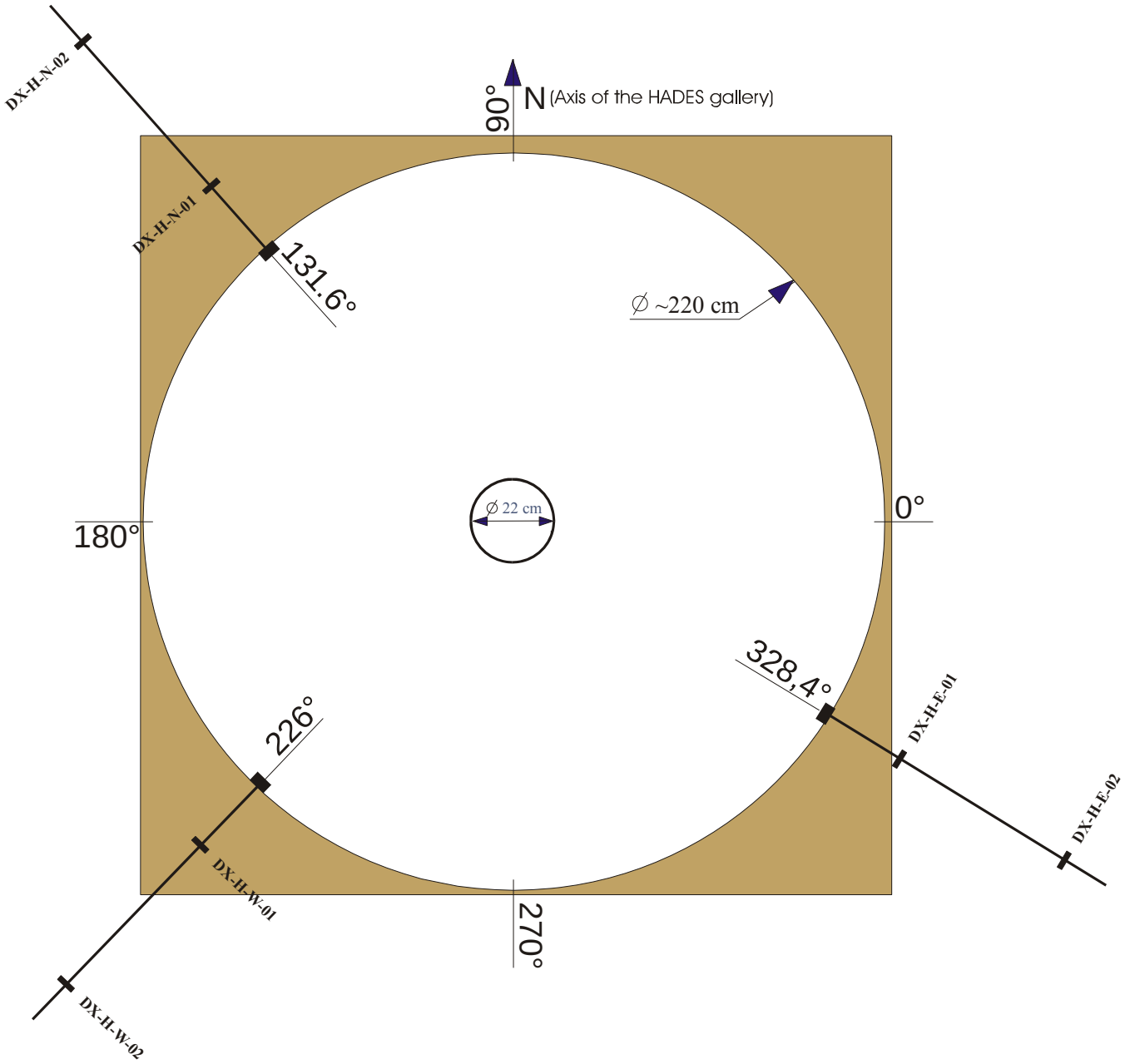

Location and identification of the sensors

Displacement		
Sensor code	Location	
DX-H-	θ	*r [cm]*
-N-1	131.6°	10.40
-N-2	131.6°	14.20
-W-1	226°	54.75
-W-2	226°	74.90
-E-1	328.4°	35.10
-E-2	328.4°	51.00

SECTION D - **H**ydration **L**evel - **m**iddle - 113 cm

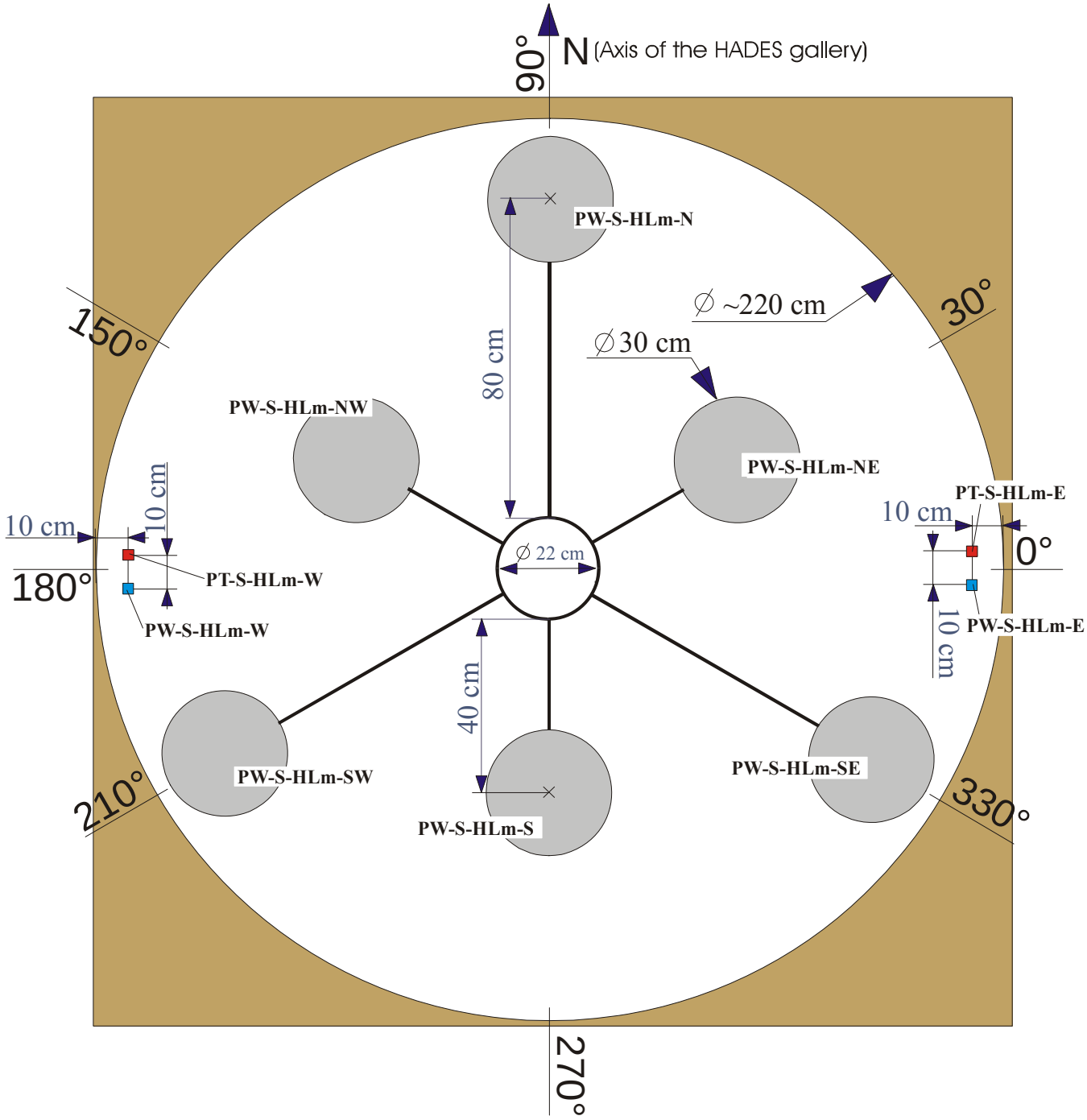

Location and identification of the sensors

Water pressure		
Sensor code	Location	
PW-S-**HLm**	θ	*r [cm]*
-N	90°	80
-NW	150°	40
-SW	210°	80
-S	270°	40
-SE	330°	80
-NE	30°	40
-E	0°	90
-W	180°	90

Total stress		
Sensor code	Location	
PT-S-**HLm**	θ	*r [cm]*
-E	0°	90
-W	180°	90

SECTION E- Multi-piezometers - 135 cm

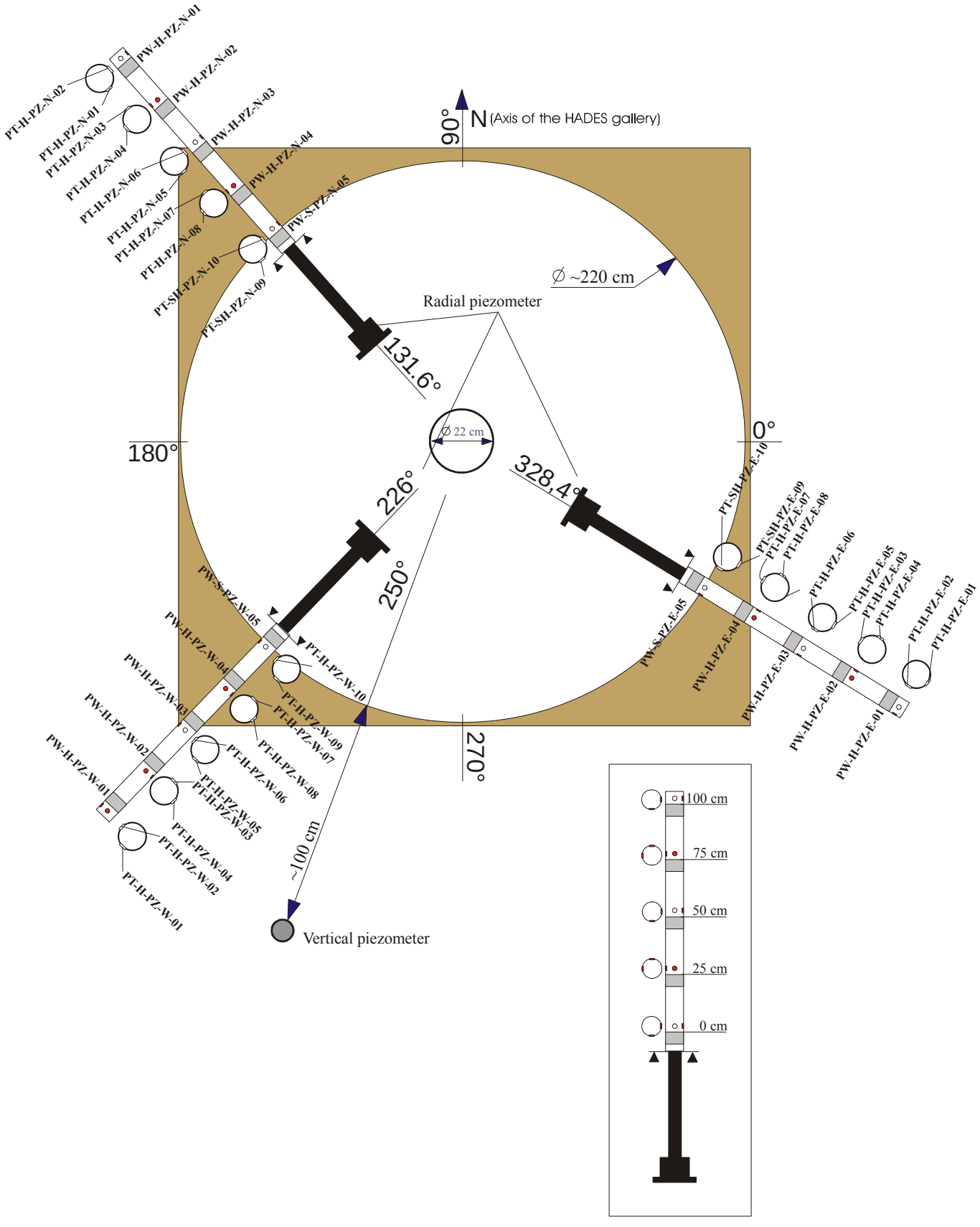

Location and identification of the sensors

Water pressure		
Sensor code	Location	
PW-H-PZ	θ	*R [cm]* [12]
-N-1	131.6°	100
-N-2		75
-N-3		50
-N-4		25
-W-1	226°	100
-W-2		75
-W-3		50
-W-4		25
-E-1	328.4°	100
-E-2		75
-E-3		50
-E-4		25
PW-S-PZ	θ	*R [cm]*
-N-5	131.6°	0
-W-5	226°	0
-E-5	328.4°	0

Total stress			
Sensor code	Location		
PT-H-PZ	θ	*R [cm]*	*orientation*
-N-1	131.6°	100	long.
-N-2		100	tang.
-N-3		75	long.
-N-4		75	tang.
-N-5		50	long.
-N-6		50	tang.
-N-7		25	long.
-N-8		25	tang.
-N-9		0	long.
-N-10		0	tang.
-W-1	226°	100	long.
-W-2		100	tang.
-W-3		75	long.
-W-4		75	tang.
-W-5		50	long.
-W-6		50	tang.
-W-7		25	long.
-W-8		25	tang.
-W-9		0	long.
-W-10		0	tang.
-E-1	328.4°	100	long.
-E-2		100	tang.

[12] *R* radial distance from the seal/host rock interface

-E-3 -E-4 -E-5 -E-6 -E-7 -E-8 -E-9 -E-10		25 25 0 0	long. tang. long. tang. long. tang. long. tang.

SECTION F -**I**nstrumented **L**evel - **t**op –187.5 cm

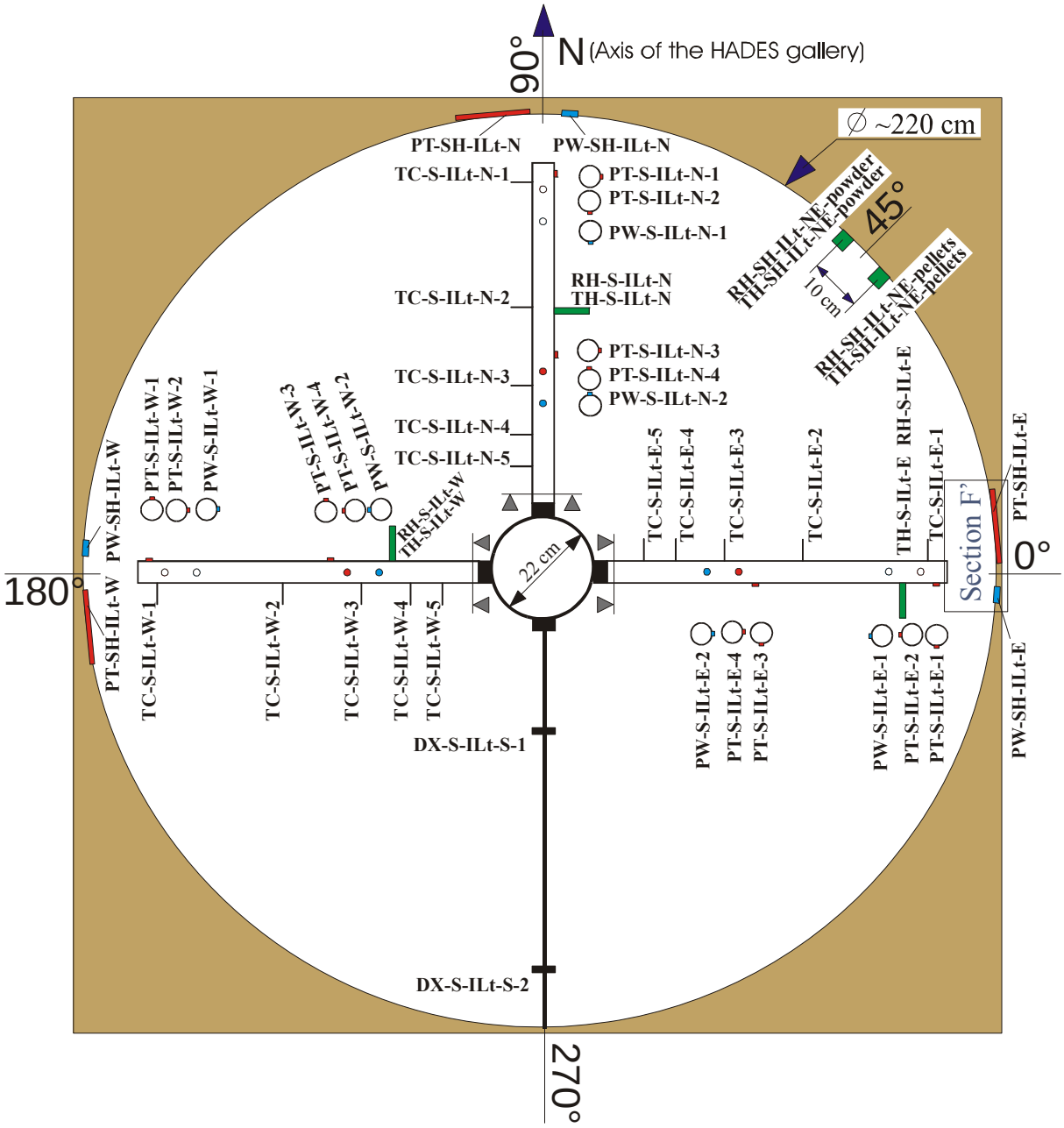

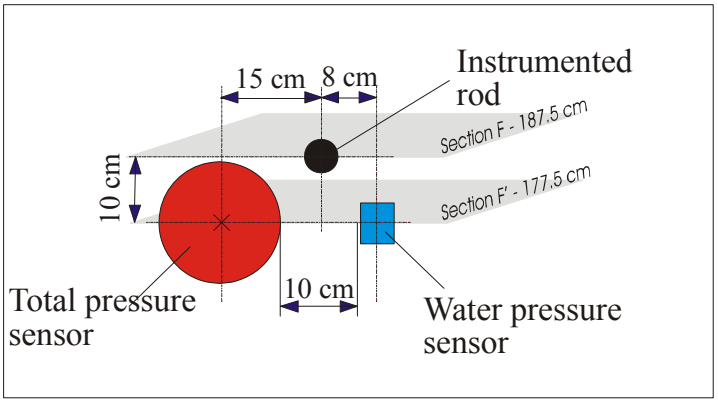

Details of the instrumented rods are the same as for section B (see above)

Location and identification of the sensors

Water pressure		
Sensor code	Location	
PW-S-**ILt**	θ	*r [cm]*
-N-1	90°	70.5
-N-2	90°	27
-W-1	180°	70.5
-W-2	180°	27
-E-1	0°	70.5
-E-2	0°	27

Total stress			
Sensor code	Location		
PT-S-**ILt**	θ	*r [cm]*	*direction*
-N-1	90°	82	trans.
-N-2	90°	78	long.
-N-3	90°	38.5	trans.
-N-4	90°	34.5	long.
-W-1	180°	82	trans.
-W-2	180°	78	long.
-W-3	180°	38.5	trans.
-W-4	180°	34.5	long.
-E-1	0°	82	trans.
-E-2	0°	78	long.
-E-3	0°	38.5	trans.
-E-4	0°	34.5	long.

Temperature		
Sensor code	Location	
TC-S-**ILt**	θ	*r [cm]*
-N-1	90°	80
-N-2	90°	50
-N-3	90°	31
-N-4	90°	19.3
-N-5	90°	12
-W-1	180°	80
-W-2	180°	50
-W-3	180°	31
-W-4	180°	19.3
-W-5	180°	12
-E-1	0°	80
-E-2	0°	50
-E-3	0°	31
-E-4	0°	19.3
-E-5	0°	12

Relative humidity + temperature		
Sensor code	Location	
RH-S-**ILt** TH-S-**ILt**	θ	*r [cm]*
-N	90°	49
-W	180°	24
-E	0°	74
-NE (powder)	45°	100
-NE (pellets)	45°	100

Displacement		
Sensor code	Location	
DX-S-**ILb**	θ	*r [cm]*
-S-1	270°	34.4
-S-2	270°	79.5

- section F' - 177.5 cm

Water pressure		
Sensor code	Location	
PW-SH-**ILt**	θ	*r [cm]*
-N	90°	100
-W	180°	100
-E	0°	100

SECTION G - **H**ydration **L**evel - **t**op - 224 cm

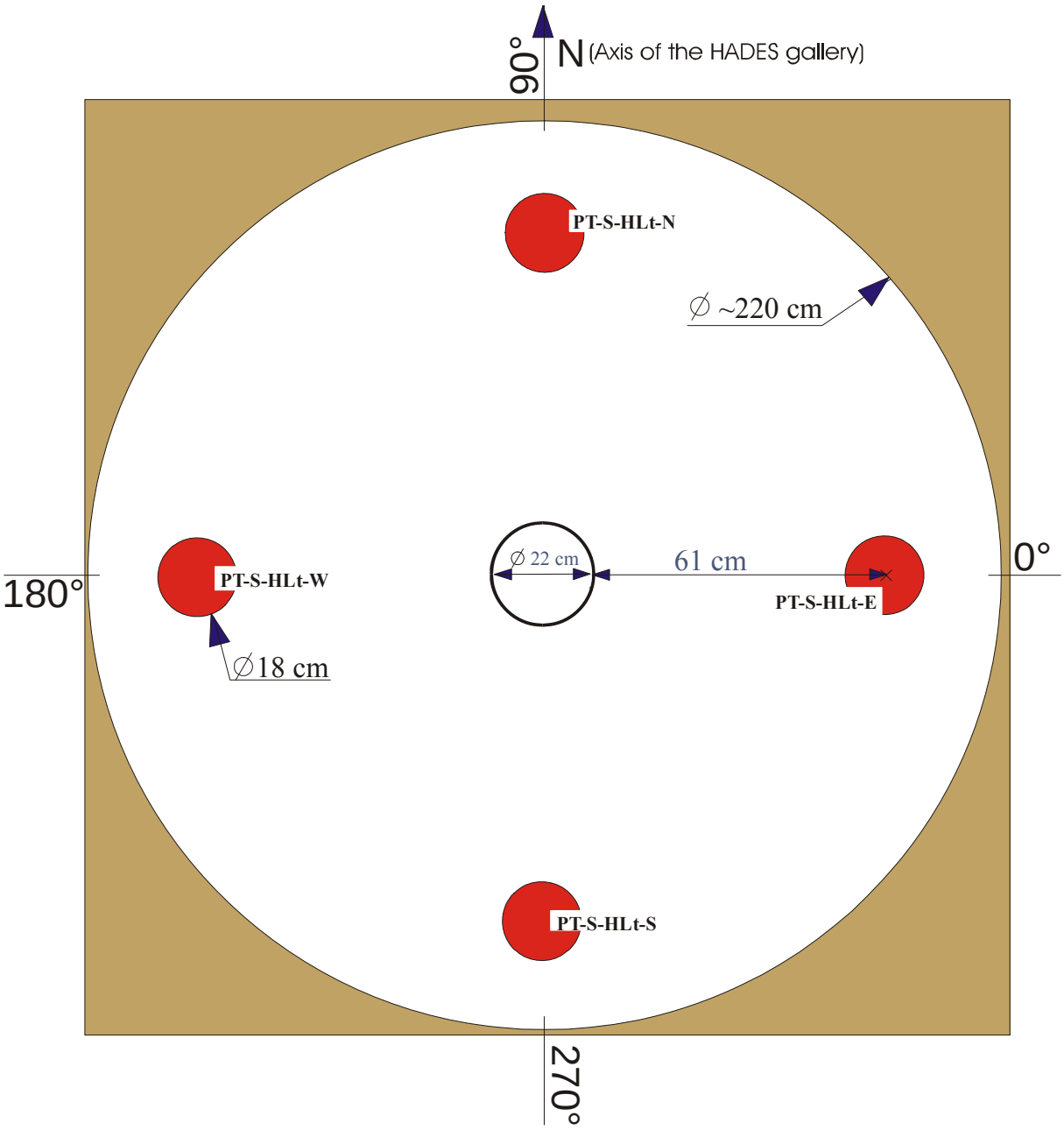

Location and identification of the sensors

Total stress			
Sensor code	Location		
PT-S-**HLt**	θ	*r [cm]*	*direction*
-N	90°	61	long.
-W	180°	61	long.
-S	270°	61	long.
-E	0°	61	long.

SECTION H - 240 cm

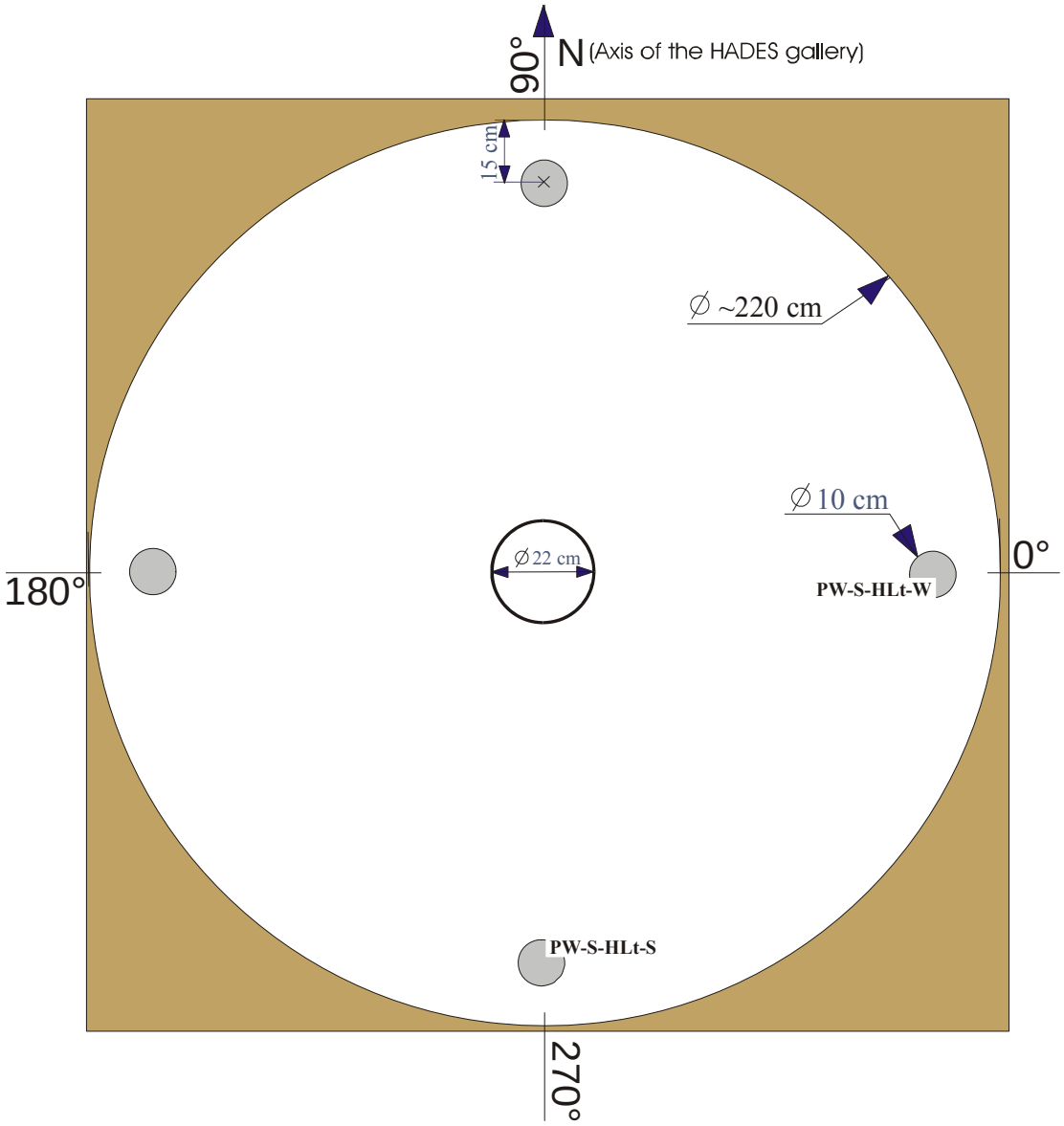

Location and identification of the sensors

Water pressure		
Sensor code	Location	
PW-SH-**HLt**	θ	*r [cm]*
-W	180°	85
-S	270°	85

VERTICAL PIEZOMETER

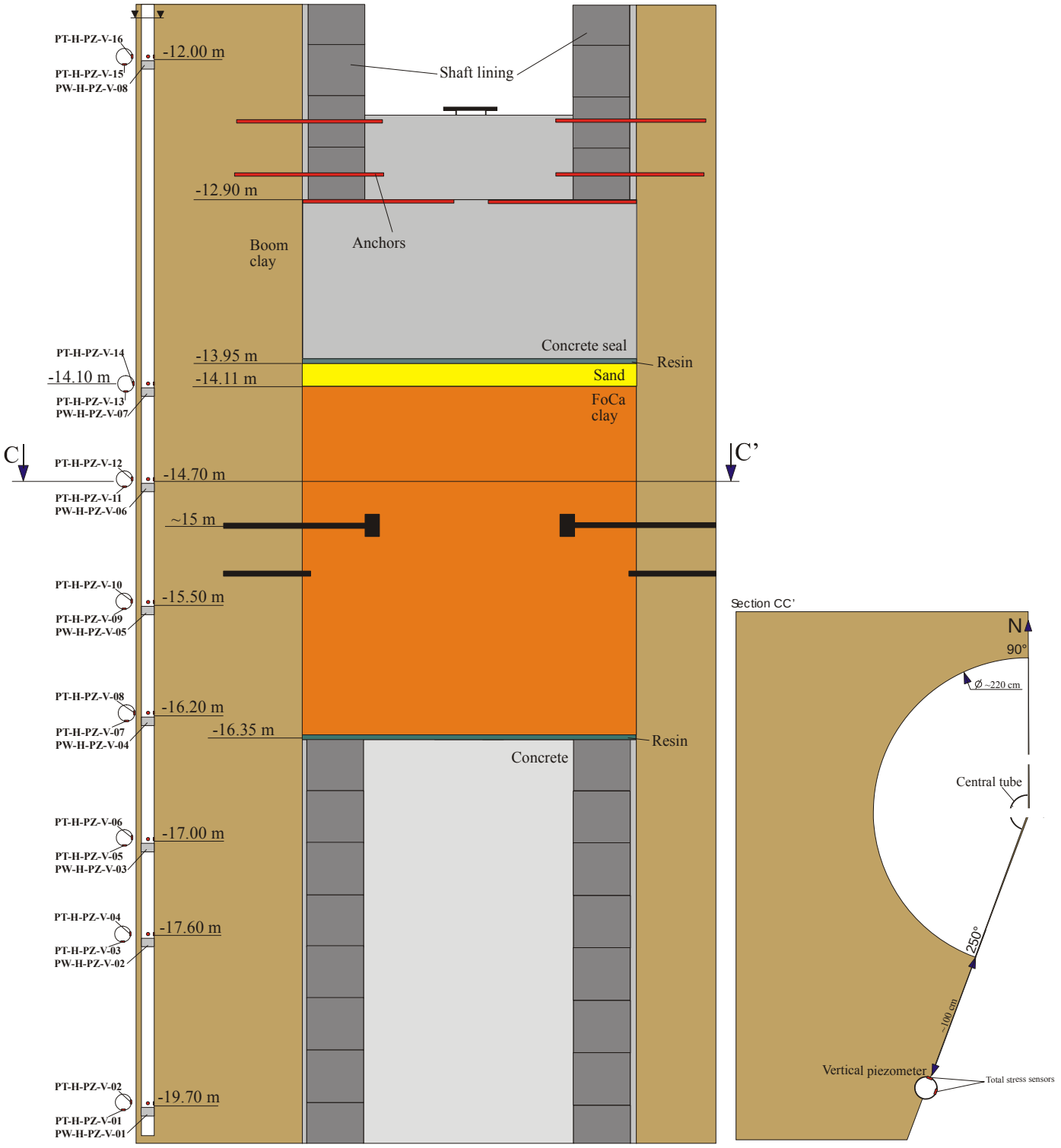

Location and identification of the sensors

Water pressure			
Sensor code	Location		
PW-H-**PZ**	θ	*R [cm]*	*H [m]*
-V-1	160°	100	-19.70
-V-2			-17.60
-V-3			-17.00
-V-4			-16.20
-V-5			-15.50
-V-6			-14.70
-V-7			-14.10
-V-8			-12.00

Total stress				
Sensor code	Location			
PT-H-**PZ**	θ	*R [cm]*	*D [m]*	*direction*
-V-1	160°	100	-19.70	tang.
-V-2			-19.70	radial
-V-3			-17.60	tang.
-V-4			-17.60	radial
-V-5			-17.00	tang.
-V-6			-17.00	radial
-V-7			-16.20	tang.
-V-8			-16.20	radial
-V-9			-15.50	tang.
-V-10			-15.50	radial
-V-11			-14.70	tang.
-V-12			-14.70	radial
-V-13			-14.10	tang.
-V-14			-14.10	radial
-V-15			-12.00	tang.
-V-16			-12.00	radial

Appendix 2 - Logbook shaft seal

Logbook shaft seal

Logbook sorted by date

CODE	START	STOP	ACTION
1	3 mai 2000		Start of artificial hydration. Pabs = atmospheric pressure + water column.
1	27 mai 2000		Hydration of sand layer was stopped.
4	5 juin 2000	9 juin 2000	Thermal pulse (70W)
1	7 nov 2000		Hydration of sand layer
1	13 nov 2000		Hydration of sand layer
1	14 nov 2000		Hydration of sand layer
4	20 nov 2000	24 nov 2000	Thermal pulse (70W)
1	23 janv 2001		Change hydration pressure. Pabs = 1.48 bar + water column.
1	26 févr 2001		Change hydration pressure. Pabs = 1.97 bar + water column.
5	9 août 2001		Disconnect INVAR-wire measuring displacement of the top of the seal
5	28 août 2001		Reconnect INVAR-wire
4	3 sept 2001	7 sept 2001	Thermal pulse (70W)
1	9 oct 2001		Hydration of sand layer
1	10 oct 2001		Hydration of sand layer
1	28 nov 2001		Hydration of sand layer
1	29 nov 2001		Hydration of sand layer
1	19 déc 2001		Remove gases from filters HLB1, HLB2, HLB5, HLM1, HLM2, HLM3, HLM5, HLM6, V1
1	14 mai 2002		Hydration of sand layer
1	15 mai 2002		Change hydration pressure. Pabs = 2.97 bar + water column.
1	17 mai 2002		Change hydration pressure. Pabs = 1.97 bar + water column.
1	29 mai 2002		Change hydration pressure. Pabs = 2.47 bar + water column.
1	11 juin 2002		Hydration of sand layer
1	23 août 2002		Hydration of sand layer
1	6 févr 2003		Change hydration pressure. Pabs = 2.68 bar + water column.
1	6 févr 2003		Hydration of sand layer
1	7 févr 2003		Hydration of sand layer
1	18 févr 2003		Remove gases from host filters V4, V5, V6, V7 and all filters on the 3 radial piezometers
5	19 févr 2003	ongoing	Add pressure of water column on graphs of radial host rock piezometers
1	4 avr 2003		Hydration of sand layer
1	12 mai 2003		Hydration of sand layer
1	11 juil 2003		Hydration of sand layer
1	26 sept 2003		Hydration of sand layer
1	5 nov 2003		Hydration of sand layer
1	13 nov 2003		Stop hydration through filters V1, HLB1 en HLB5.
1	20 nov 2003		Stop hydration through filters V5, HLB4, HLM1, HLM2, HLM5 and HLM6.
5	20 nov 2003		Repair pump, pressure rise in some filters
1	26 nov 2003		All hydration filters closed except: HLB2, HLM1, HLM2, HLM5 and HLM6.
1	2 déc 2003		Hydration system stopped.
1	2 déc 2003		Injection in sand layer
1	2 déc 2003		Hydration of sand layer
1	11 déc 2003		Hydration of sand layer

1	24 déc 2003		Restart of the hydration on all filters in the seal.
1	26 janv 2004		Hydration stopped.
1	26 janv 2004		Hydration of sand layer
2	9 févr 2004	23 févr 2004	Hydraulic conductivity testing on filter V1 (injection)
2	23 févr 2004	9 mars 2004	Hydraulic conductivity testing on filter V4 (injection)
2	9 mars 2004	23 avr 2004	Hydraulic conductivity testing on filter HLM4 (injection)
1	10 mars 2004		Connectivity tests on several seal filters
1	10 mars 2004		Remove gases from host filters E2, E4, E5 and N4
2	23 avr 2004	6 mai 2004	Hydraulic conductivity testing on filter HLM3 (injection)
1	10 mai 2004		Restart of hydration on filters V2, V3, V4, V6, HLM3 and HLM4.
1	9 juil 2004		Hydration stopped.
1	5 août 2004		Restart of hydration on filters V2, V3, V4, V6, HLM3 and HLM4.
1	12 janv 2005		Hydration of sand layer
1	2 juin 2005		Change hydration pressure. Pabs = 3.08 bar + water column.
1	2 juin 2005		Remove gases from host filters E4, E5, N4, N5 and V4
1	28 oct 2005		Stop hydration through V3, V4, HLM3 and HLM4 (only V2 and V6 remain).
2	3 nov 2005	22 nov 2005	Hydraulic conductivity testing on filter Host-West1 (extraction)
2	22 nov 2005	9 déc 2005	Hydraulic conductivity testing on filter Host-West3 (extraction)
2	23 nov 2005	25 nov 2005	Hydraulic conductivity testing on filter HLB1 (extraction)
2	25 nov 2005	30 nov 2005	Hydraulic conductivity testing on filter HLB1 (injection)
2	9 déc 2005	20 déc 2005	Hydraulic conductivity testing on filter Host-West5 (extraction)
2	9 déc 2005	20 déc 2005	Hydraulic conductivity testing on filter HLB1 (injection)
2	20 déc 2005	2 janv 2006	Hydraulic conductivity testing on filter Host-West2 (extraction)
2	20 déc 2005	2 janv 2006	Hydraulic conductivity testing on filter HLB3 (injection)
1	2 janv 2006		Injection (~0.5 litre) in filter HLB6
2	2 janv 2006	11 janv 2006	Hydraulic conductivity testing on filter Host-West4 (extraction)
2	11 janv 2006	23 janv 2006	Hydraulic conductivity testing on filter HLM3 (injection)
2	11 janv 2006	23 janv 2006	Hydraulic conductivity testing on filter Host-North3 (extraction)
2	23 janv 2006	3 févr 2006	Hydraulic conductivity testing on filter HLM4 (injection)
2	24 janv 2006	3 févr 2006	Hydraulic conductivity testing on filter Host-East2 (extraction)
2	3 févr 2006	20 févr 2006	Hydraulic conductivity testing on filter Host-V5 (injection)
3	20 févr 2006	5 avr 2006	Gasbreakthrough experiment1 on filter HLM3
3	28 mars 2006		Gasbreakthrough1
1	5 avr 2006		Hydration stopped.
3	28 avr 2006	15 mai 2006	Gasbreakthrough experiment 2 on filter HLM3
3	28 avr 2006		Gasbreakthrough2
2	15 mai 2006	1 juin 2006	Hydraulic conductivity testing on filter HLM3 (injection)
3	22 juin 2006		Hydraulic shock at HLB filters
5	21 sept 2006		Test injection pumps => pressure peak on filters V1 to V6
5	13 oct 2006		Tracer injection in host filters E2, N3 and W4
1	16 oct 2006	ongoing	Sampling (cf. tracer injection on 13okt06) on host filters E1, E3, N2, N4, W3 and W5

Logbook sorted by code

CODE	START	STOP	ACTION
1	3 mai 2000		Start of artificial hydration. Pabs = atmospheric pressure + water column.
1	27 mai 2000		Hydration of sand layer was stopped.
1	7 nov 2000		Hydration of sand layer
1	13 nov 2000		Hydration of sand layer
1	14 nov 2000		Hydration of sand layer
1	23 janv 2001		Change hydration pressure. Pabs = 1.48 bar + water column.
1	26 févr 2001		Change hydration pressure. Pabs = 1.97 bar + water column.
1	9 oct 2001		Hydration of sand layer
1	10 oct 2001		Hydration of sand layer
1	28 nov 2001		Hydration of sand layer
1	29 nov 2001		Hydration of sand layer
1	19 déc 2001		Remove gases from filters HLB1, HLB2, HLB5, HLM1, HLM2, HLM3, HLM5, HLM6, V1
1	14 mai 2002		Hydration of sand layer
1	15 mai 2002		Change hydration pressure. Pabs = 2.97 bar + water column.
1	17 mai 2002		Change hydration pressure. Pabs = 1.97 bar + water column.
1	29 mai 2002		Change hydration pressure. Pabs = 2.47 bar + water column.
1	11 juin 2002		Hydration of sand layer
1	23 août 2002		Hydration of sand layer
1	6 févr 2003		Change hydration pressure. Pabs = 2.68 bar + water column.
1	6 févr 2003		Hydration of sand layer
1	7 févr 2003		Hydration of sand layer
1	18 févr 2003		Remove gases from host filters V4, V5, V6, V7 and all filters on the 3 radial piezometers
1	4 avr 2003		Hydration of sand layer
1	12 mai 2003		Hydration of sand layer
1	11 juil 2003		Hydration of sand layer
1	26 sept 2003		Hydration of sand layer
1	5 nov 2003		Hydration of sand layer
1	13 nov 2003		Stop hydration through filters V1, HLB1 en HLB5.
1	20 nov 2003		Stop hydration through filters V5, HLB4, HLM1, HLM2, HLM5 and HLM6.
1	26 nov 2003		All hydration filters closed except: HLB2, HLM1, HLM2, HLM5 and HLM6.
1	2 déc 2003		Hydration system stopped.
1	2 déc 2003		Injection in sand layer
1	2 déc 2003		Hydration of sand layer
1	11 déc 2003		Hydration of sand layer
1	24 déc 2003		Restart of the hydration on all filters in the seal.
1	26 janv 2004		Hydration stopped.
1	26 janv 2004		Hydration of sand layer
1	10 mars 2004		Connectivity tests on several seal filters
1	10 mars 2004		Remove gases from host filters E2, E4, E5 and N4
1	10 mai 2004		Restart of hydration on filters V2, V3, V4, V6, HLM3 and HLM4.
1	9 juil 2004		Hydration stopped.
1	5 août 2004		Restart of hydration on filters V2, V3, V4, V6, HLM3 and HLM4.
1	12 janv 2005		Hydration of sand layer
1	2 juin 2005		Change hydration pressure. Pabs = 3.08 bar + water column.
1	2 juin 2005		Remove gases from host filters E4, E5, N4, N5 and V4
1	28 oct 2005		Stop hydration through V3, V4, HLM3 and HLM4 (only V2 and V6 remain).
1	2 janv 2006		Injection (~0.5 litre) in filter HLB6
1	5 avr 2006		Hydration stopped.
1	16 oct 2006	ongoing	Sampling (cf. tracer injection on 13okt06) on host filters E1, E3, N2, N4, W3 and W5

2	9 févr 2004	23 févr 2004	Hydraulic conductivity testing on filter V1 (injection)
2	23 févr 2004	9 mars 2004	Hydraulic conductivity testing on filter V4 (injection)
2	9 mars 2004	23 avr 2004	Hydraulic conductivity testing on filter HLM4 (injection)
2	23 avr 2004	6 mai 2004	Hydraulic conductivity testing on filter HLM3 (injection)
2	3 nov 2005	22 nov 2005	Hydraulic conductivity testing on filter Host-West1 (extraction)
2	22 nov 2005	9 déc 2005	Hydraulic conductivity testing on filter Host-West3 (extraction)
2	23 nov 2005	25 nov 2005	Hydraulic conductivity testing on filter HLB1 (extraction)
2	25 nov 2005	30 nov 2005	Hydraulic conductivity testing on filter HLB1 (injection)
2	9 déc 2005	20 déc 2005	Hydraulic conductivity testing on filter Host-West5 (extraction)
2	9 déc 2005	20 déc 2005	Hydraulic conductivity testing on filter HLB1 (injection)
2	20 déc 2005	2 janv 2006	Hydraulic conductivity testing on filter Host-West2 (extraction)
2	20 déc 2005	2 janv 2006	Hydraulic conductivity testing on filter HLB3 (injection)
2	2 janv 2006	11 janv 2006	Hydraulic conductivity testing on filter Host-West4 (extraction)
2	11 janv 2006	23 janv 2006	Hydraulic conductivity testing on filter HLM3 (injection)
2	11 janv 2006	23 janv 2006	Hydraulic conductivity testing on filter Host-North3 (extraction)
2	23 janv 2006	3 févr 2006	Hydraulic conductivity testing on filter HLM4 (injection)
2	24 janv 2006	3 févr 2006	Hydraulic conductivity testing on filter Host-East2 (extraction)
2	3 févr 2006	20 févr 2006	Hydraulic conductivity testing on filter Host-V5 (injection)
2	15 mai 2006	1 juin 2006	Hydraulic conductivity testing on filter HLM3 (injection)
3	20 févr 2006	5 avr 2006	Gasbreakthrough experiment1 on filter HLM3
3	28 mars 2006		Gasbreakthrough1
3	28 avr 2006	15 mai 2006	Gasbreakthrough experiment 2 on filter HLM3
3	28 avr 2006		Gasbreakthrough2
3	22 juin 2006		Hydraulic shock at HLB filters
4	5 juin 2000	9 juin 2000	Thermal pulse (70W)
4	20 nov 2000	24 nov 2000	Thermal pulse (70W)
4	3 sept 2001	7 sept 2001	Thermal pulse (70W)
5	9 août 2001		Disconnect INVAR-wire measuring displacement of the top of the seal
5	28 août 2001		Reconnect INVAR-wire
5	19 févr 2003	ongoing	Add pressure of water column on graphs of radial host rock piezometers
5	20 nov 2003		Repair pump, pressure rise in some filters
5	21 sept 2006		Test injection pumps => pressure peak on filters V1 to V6
5	13 oct 2006		Tracer injection in host filters E2, N3 and W4

Appendix 3 - Hydromechanical measurements shaft seal

Hydromechanical measurements shaft seal

Seal: total stress

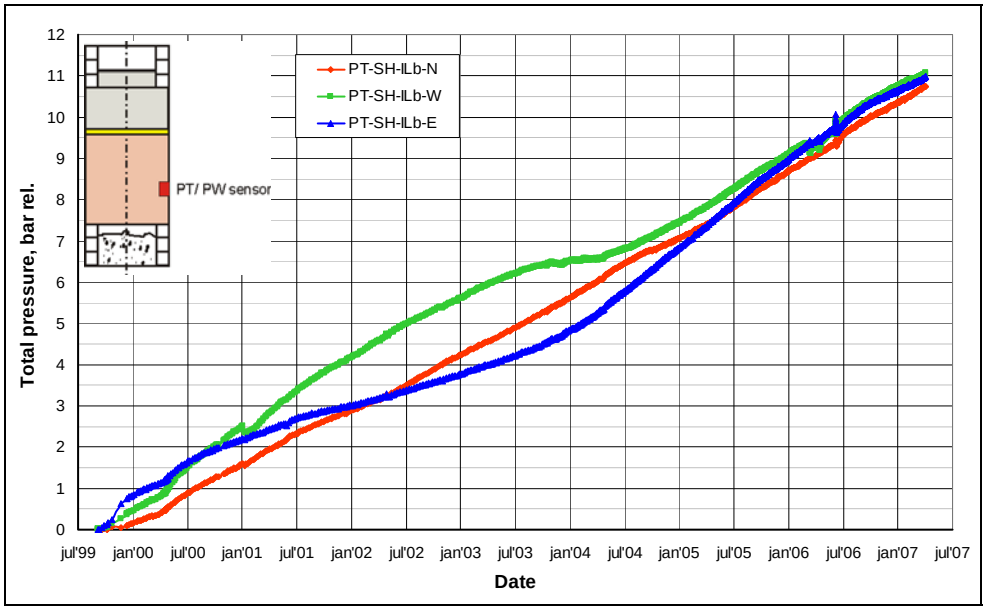

Figure 4: Total stress at the seal/host rock interface (at instrumentation level bottom).

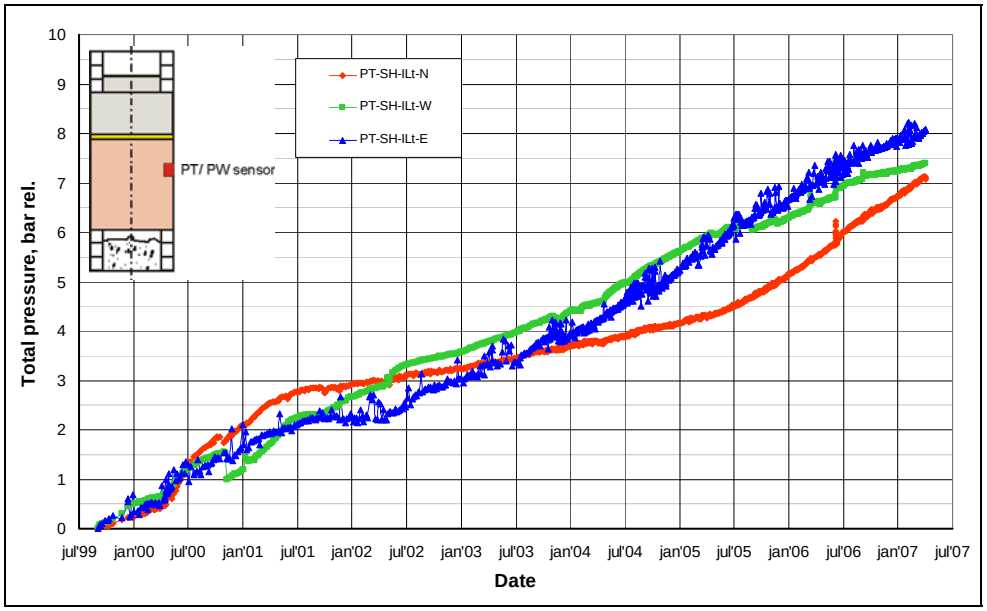

Figure 5: Total stress at the seal/host rock interface (at instrumentation level top).

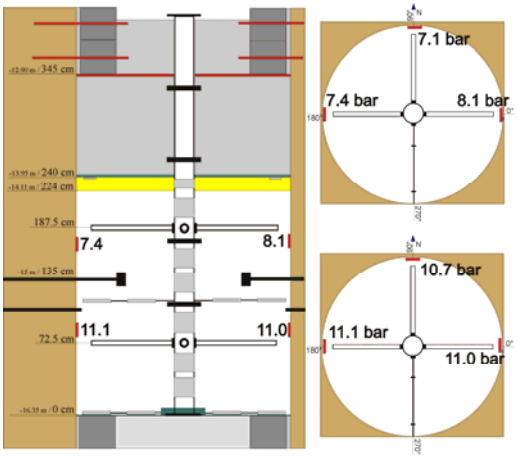

Figure 6: Total stress measurements at the seal/host rock interface on 18th April 2007. Results are shown in bar (relative).

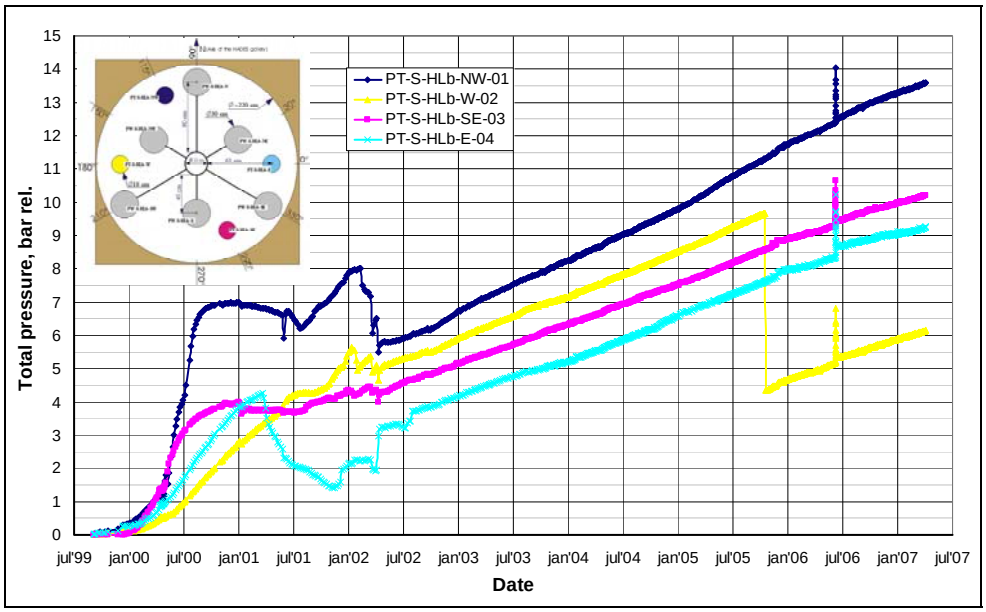

Figure 7: Total stress at the bottom of the seal (at hydration level bottom).

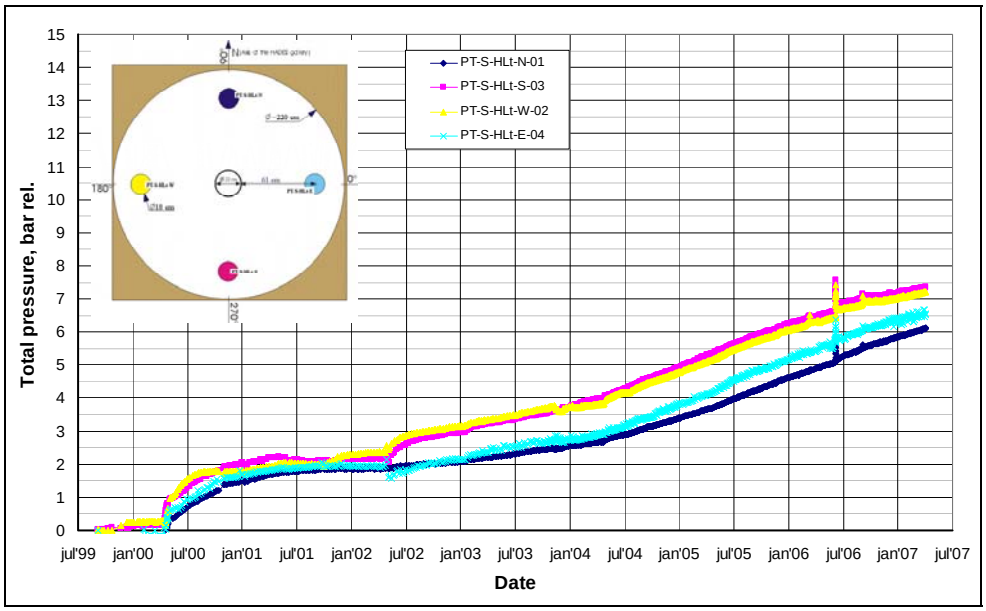

Figure 8: Total stress at the top of the seal (at hydration level top).

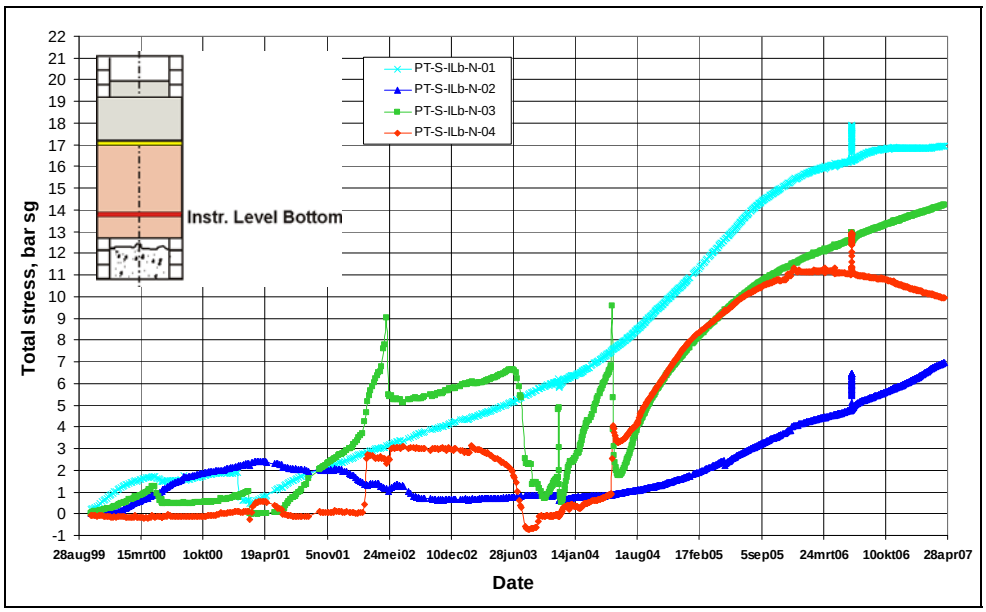

Figure 9: Total stress in the seal (at the northern rod of instrumented level bottom).

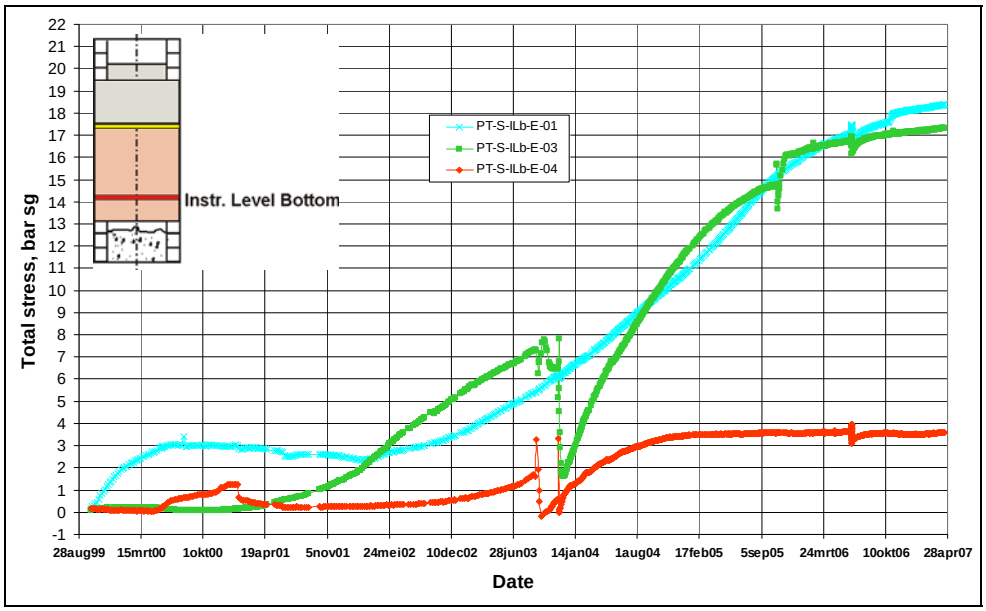

Figure 10: Total stress in the seal (at the eastern rod of instrumented level bottom).

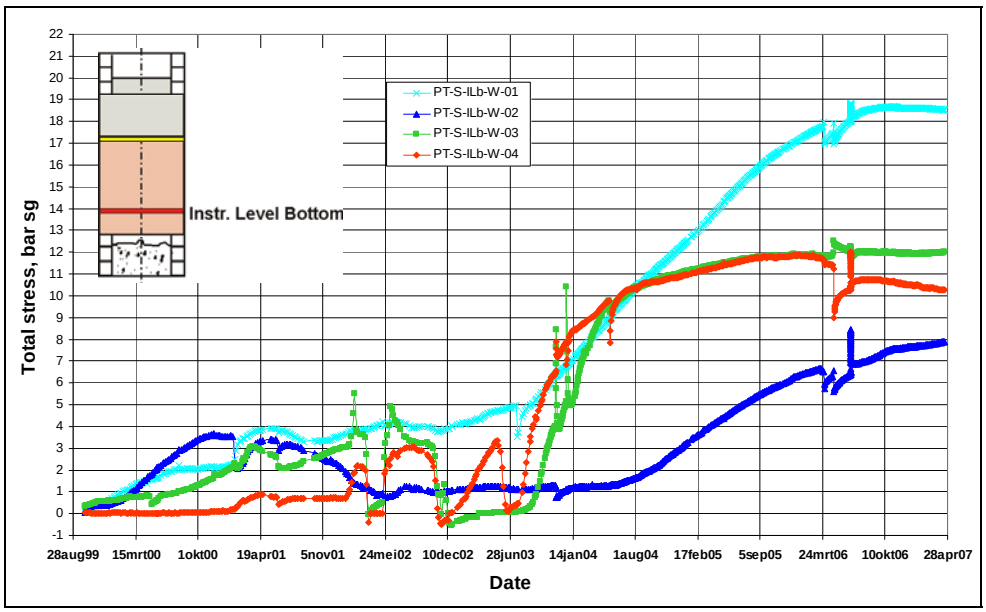

Figure 11: Total stress in the seal (at the western rod of instrumented level bottom).

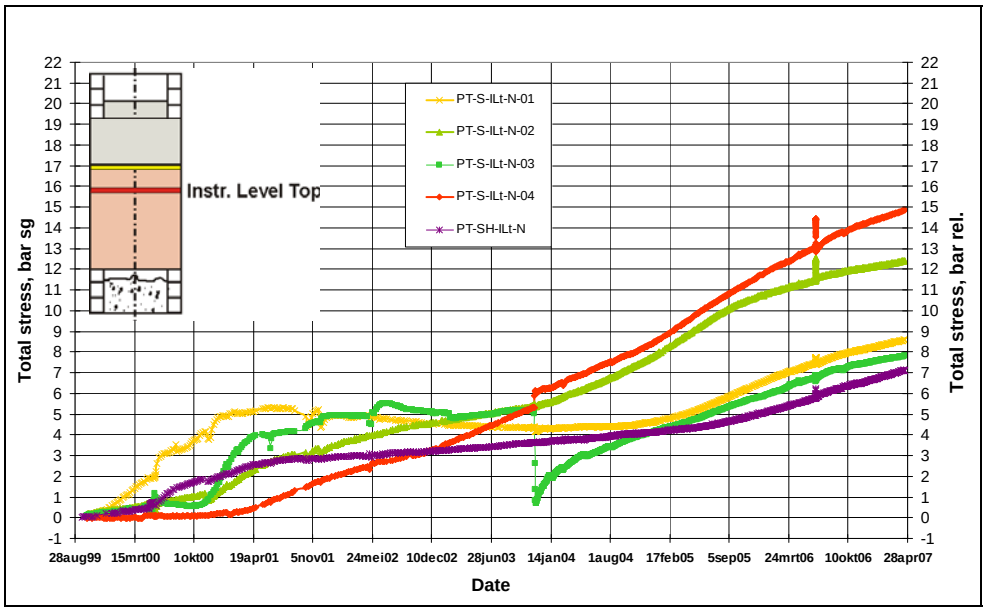

Figure 12: Total stress in the seal (at the northern rod of instrumented level top); one curve (purple) shows the total stress at PT-SH-ILt-N, at the seal/host rock interface near this rod.

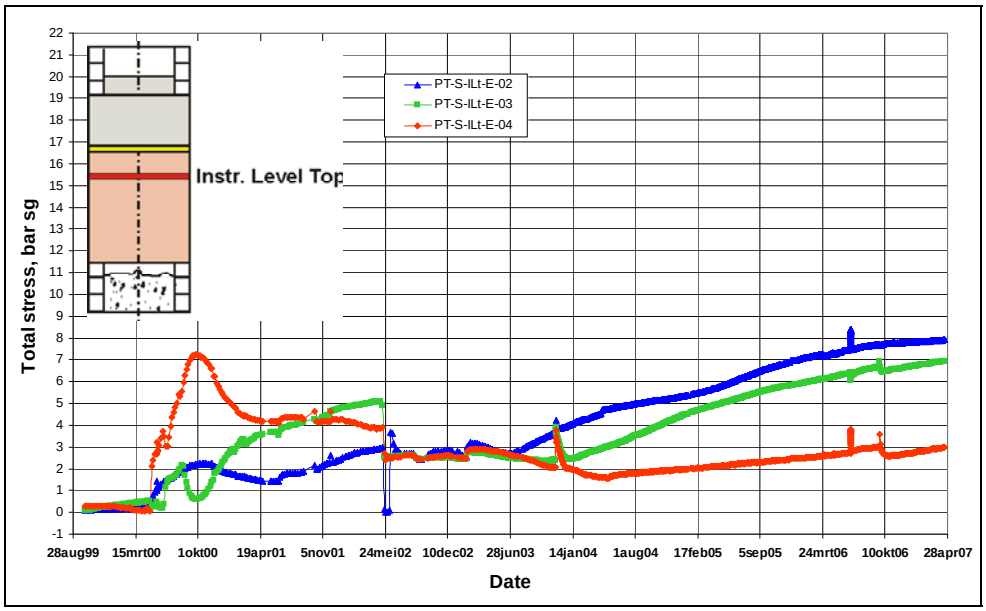

Figure 13: Total stress in the seal (at the eastern rod of instrumented level top).

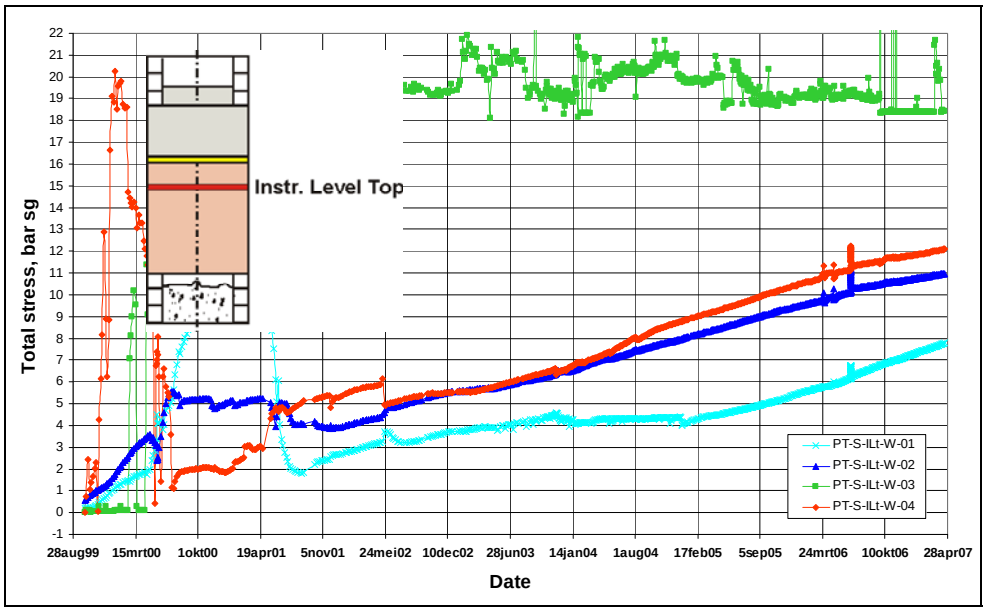

Figure 14: Total stress in the seal (at the western rod of instrumented level top).

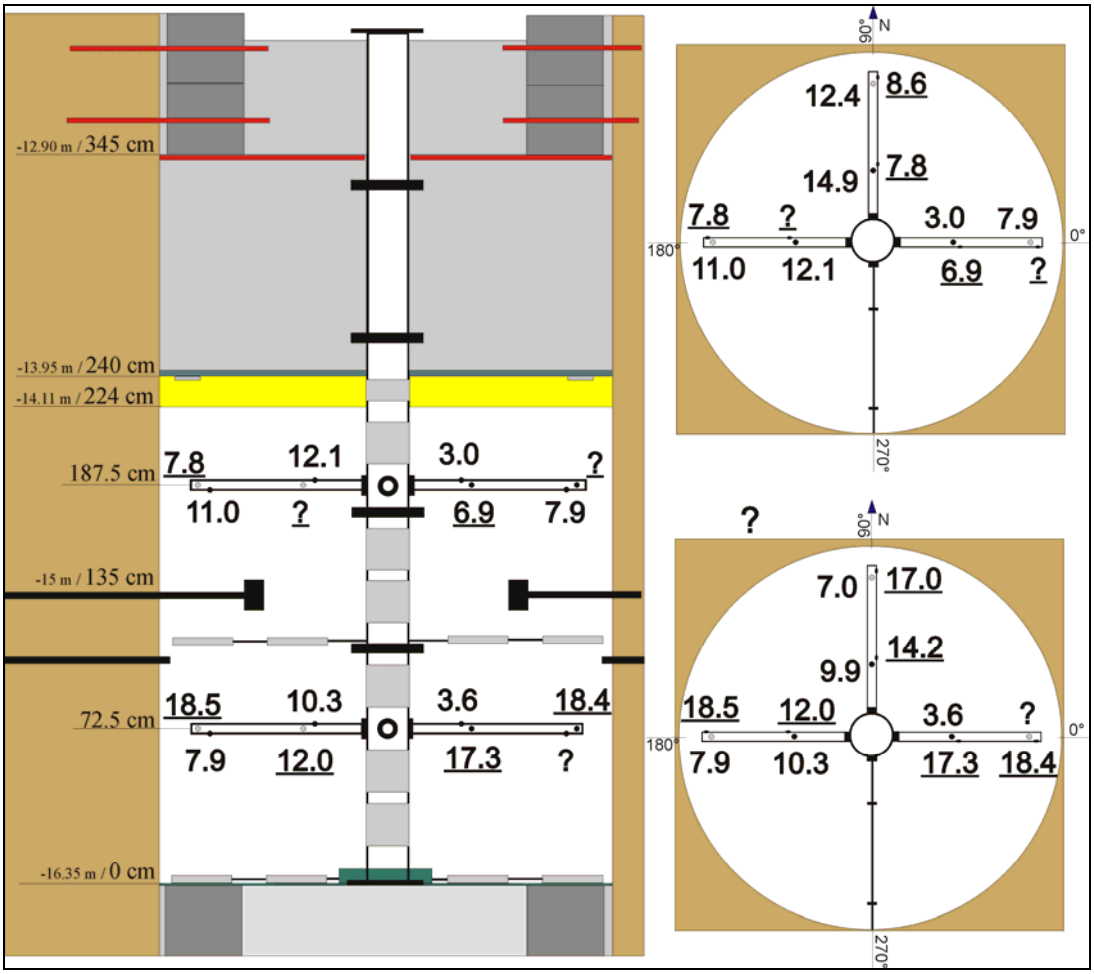

Figure 15: Total stress measurements at the instrumented levels on 18th April 2007. The values are given in bar sealed (gauge).

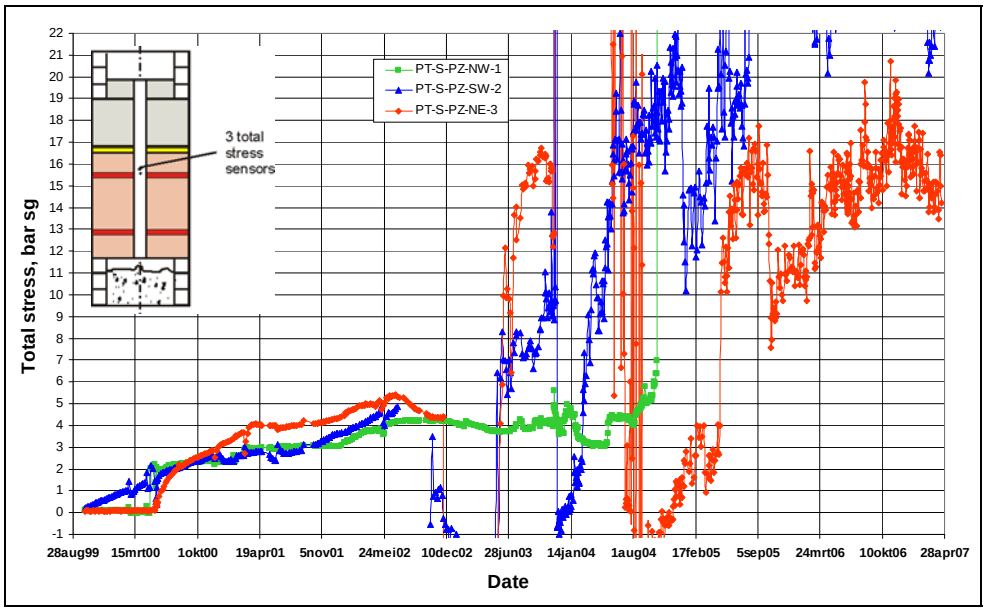

Figure 16: Total stress in the seal (near the top of the central tube).

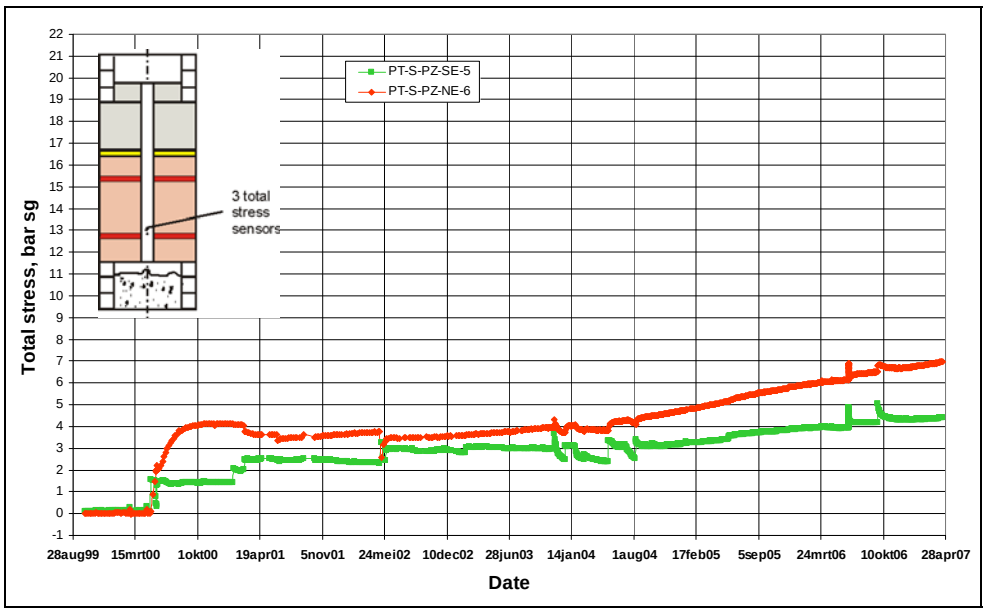

Figure 17: Total stress in the seal (near the bottom of the central tube).

Seal: water pressure & effective stress

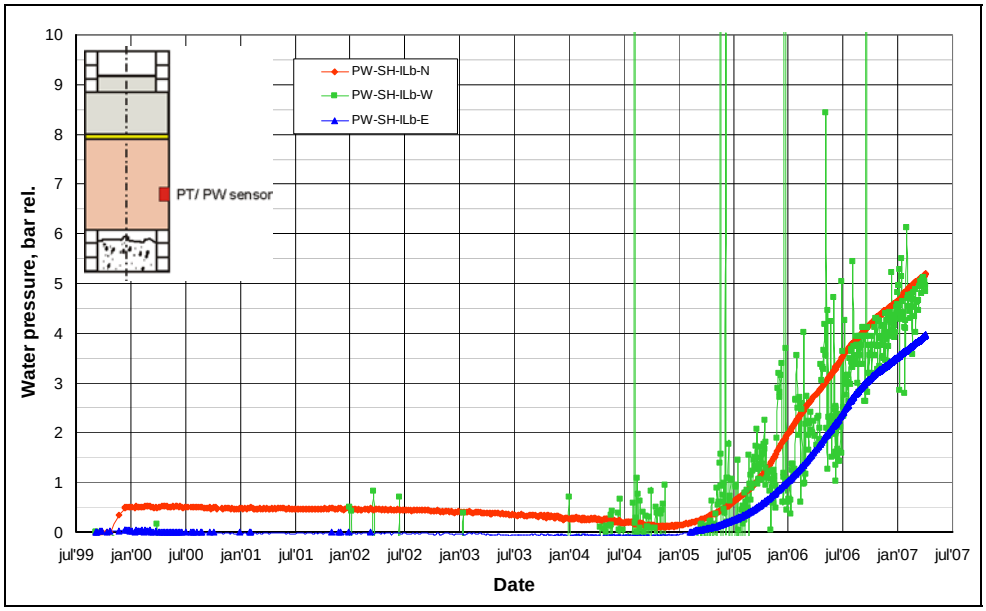

Figure 18: Pore pressure at the seal/host rock interface (at instrumentation level bottom).

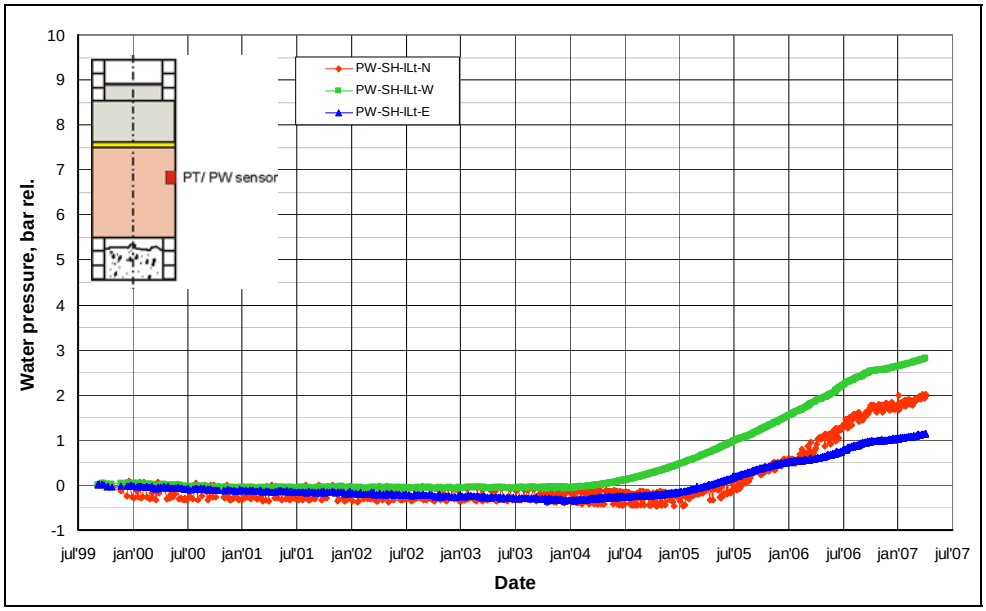

Figure 19: Pore pressure at the seal/host rock interface (at instrumentation level top).

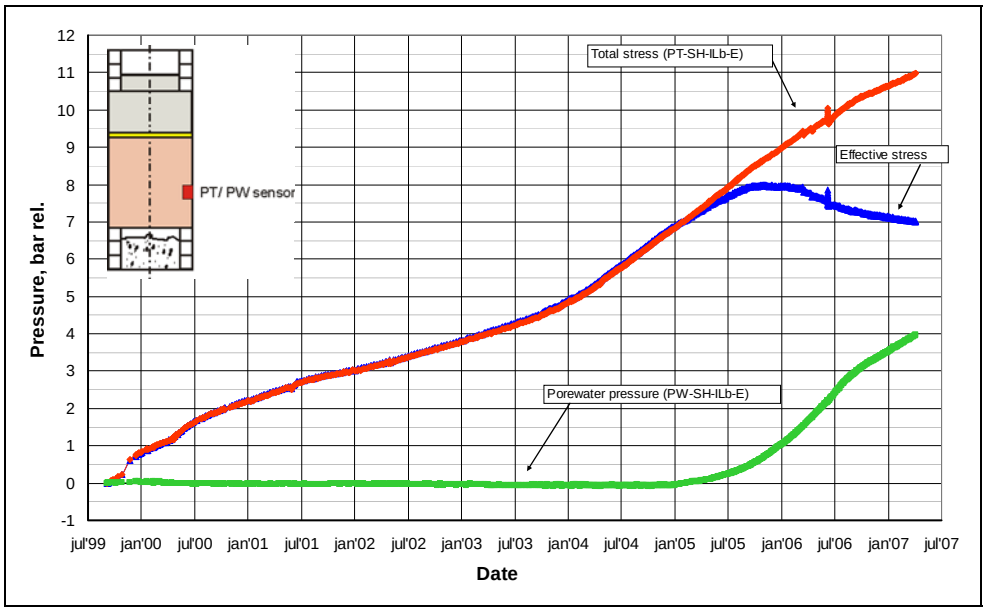

Figure 20: Total stress, pore pressure and effective stress at the seal/host rock interface (at the eastside of instrumented level bottom).

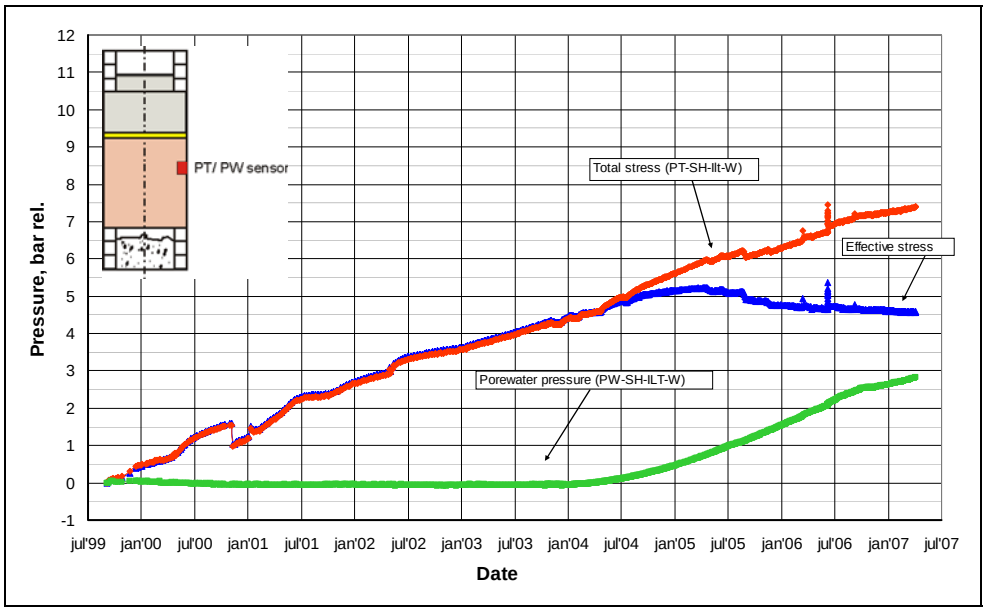

Figure 21: Total stress, pore pressure and effective stress at the seal/host rock interface (at the westside of instrumented level top).

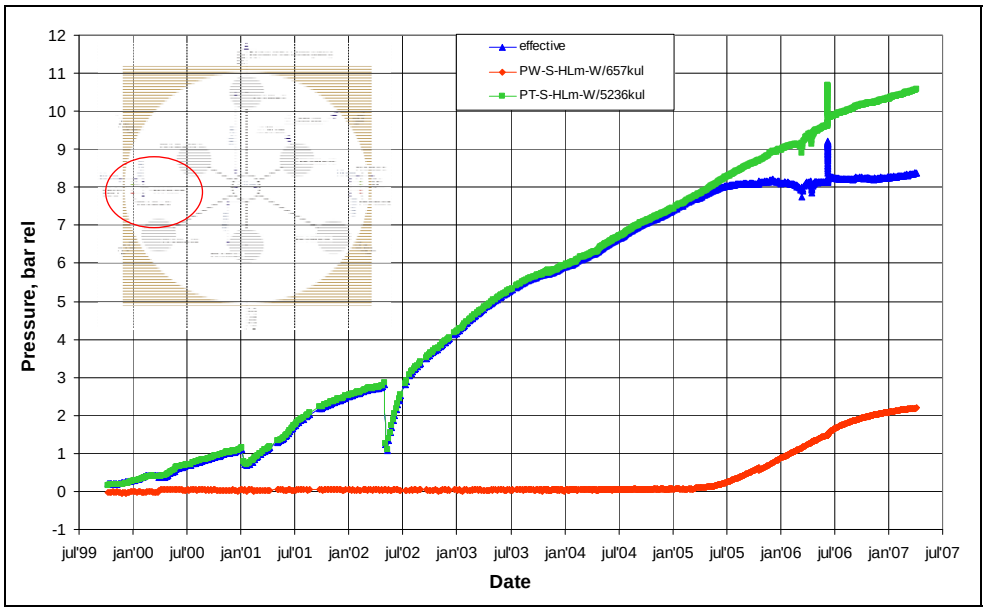

Figure 22: Total stress, pore pressure and effective stress near the seal/host rock interface (at the westside of hydration level middle).

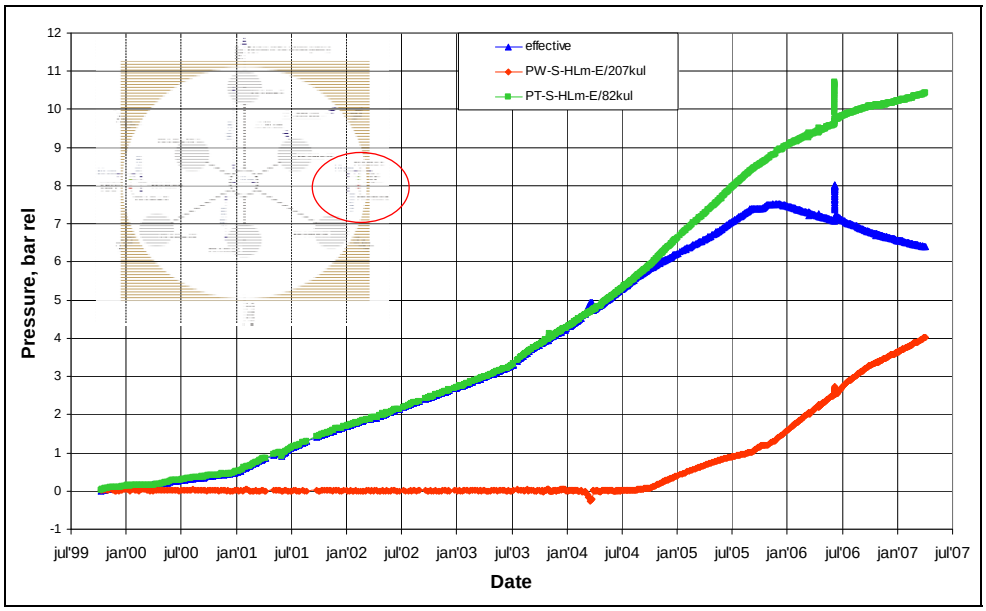

Figure 23: Total stress, pore pressure and effective stress near the seal/host rock interface (at the eastside of hydration level middle).

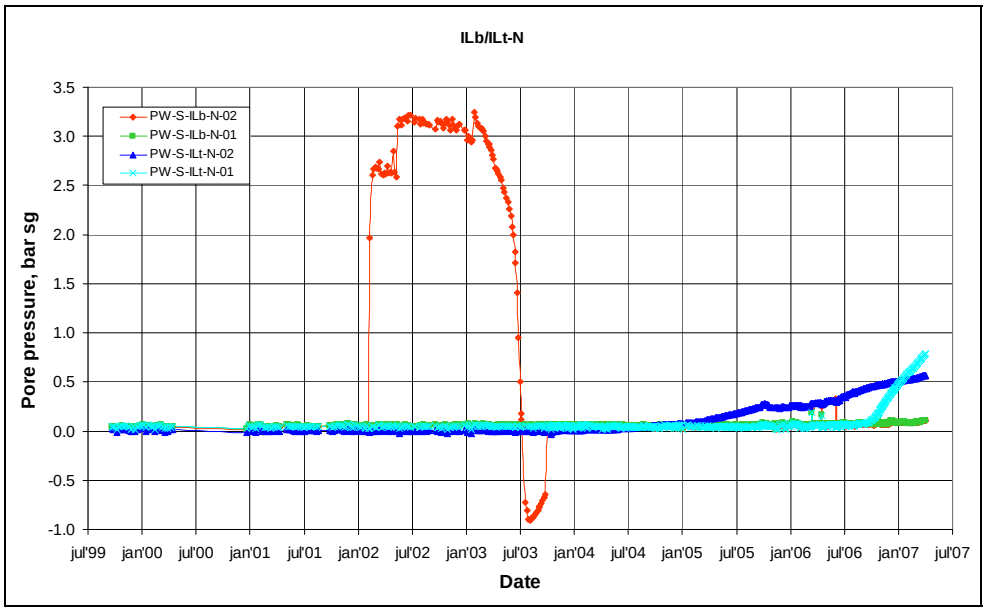

Figure 24: Pore pressure in the seal (at the northern rod of instrumented level bottom).

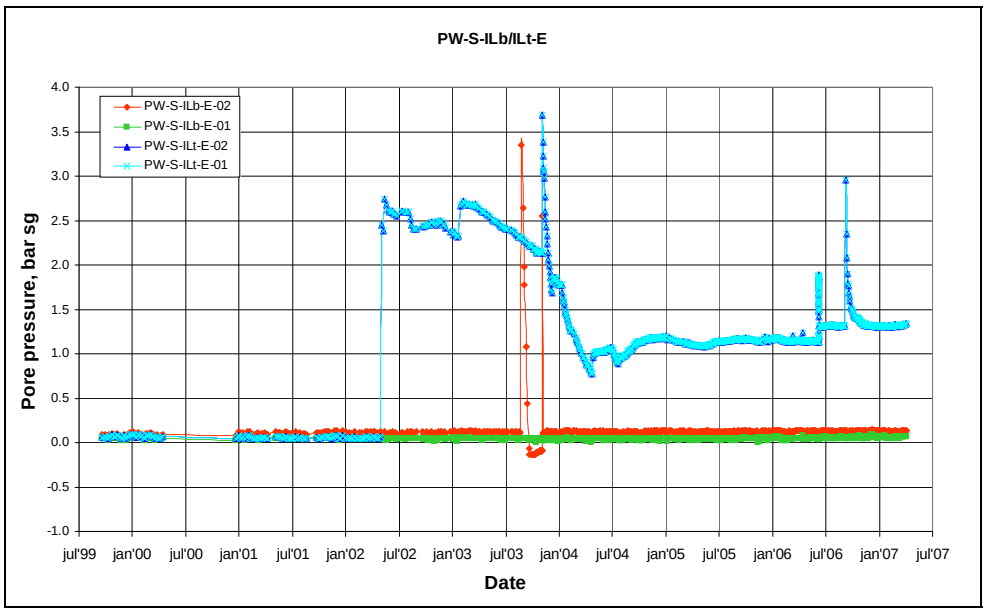

Figure 25: Pore pressure in the seal (at the eastern rod of instrumented level bottom).

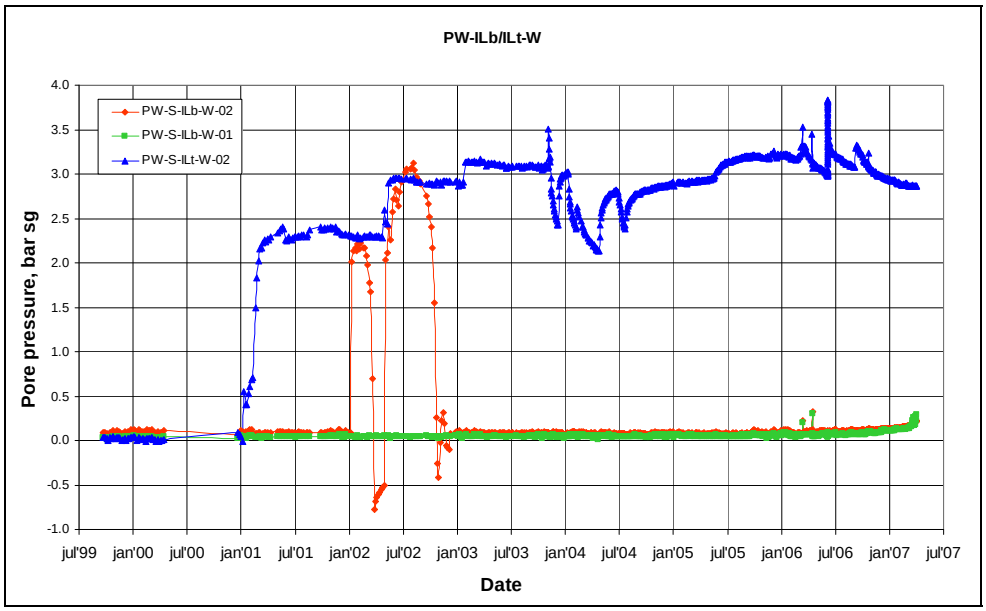

Figure 26: Pore pressure in the seal (at the western rod of instrumented level bottom).

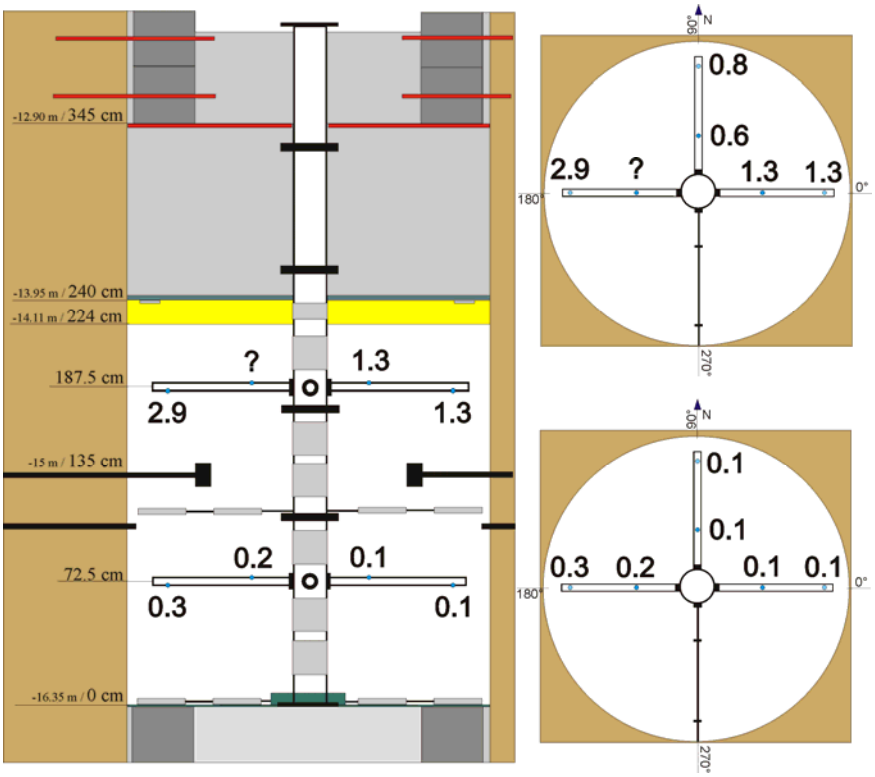

Figure 27: Pore water pressures measured on the instrumented levels (Kulite sensors with porous caps) on 18th April 2007. Pore pressure values are given in bar (sealed gauge).

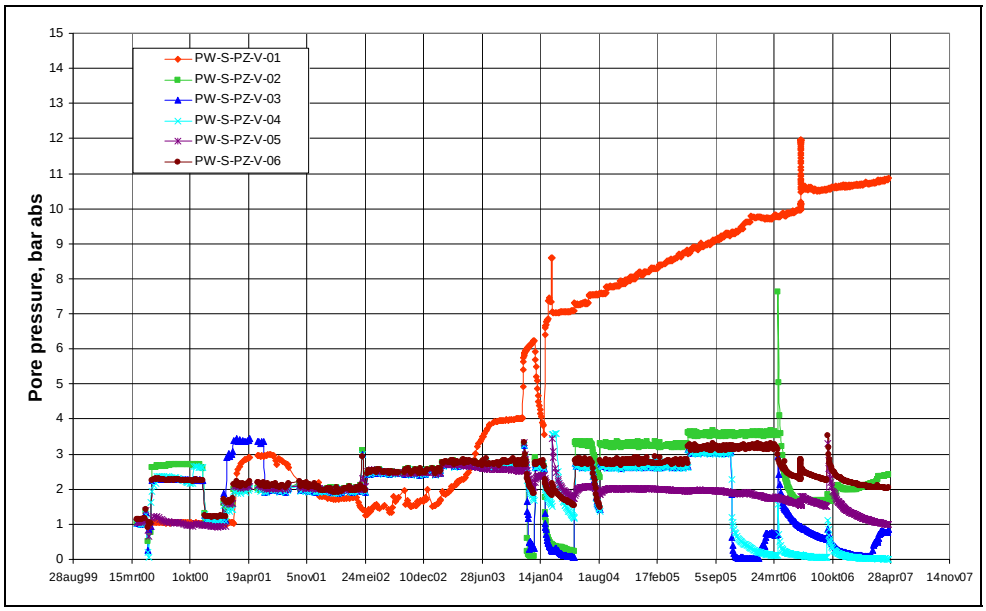

Figure 28: Pore pressure in the seal (at the central tube).

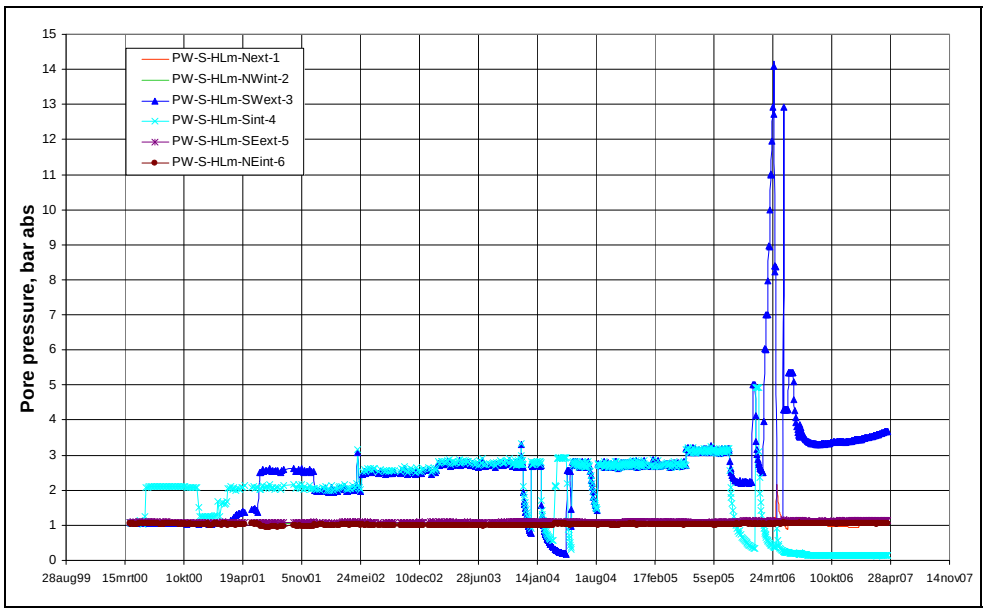

Figure 29: Pore pressure at hydration level middle. During artificial hydration these pressures correspond to the injection pressures, at other moments the sensors measure pore water pressure.

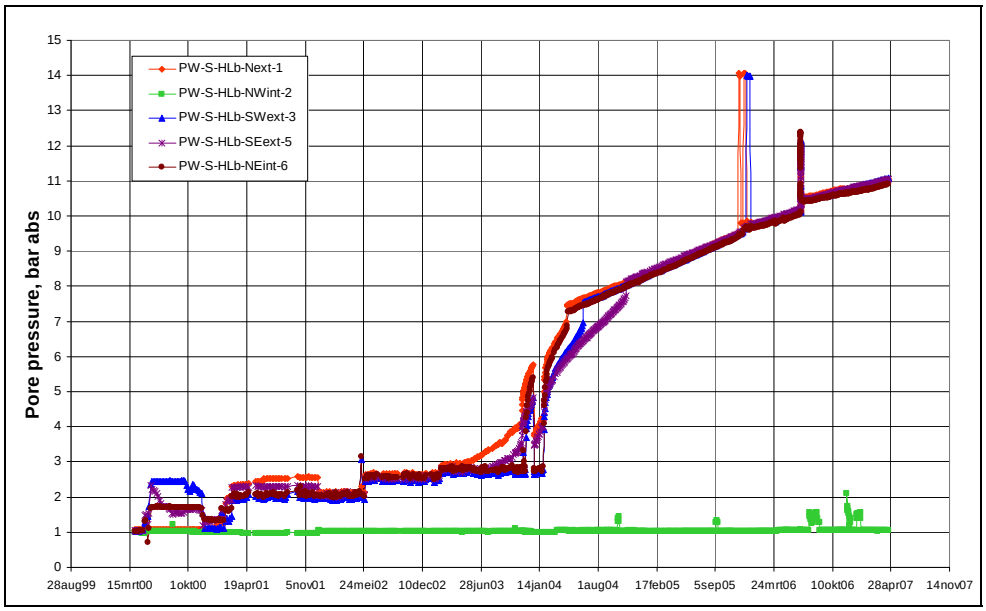

Figure 30: Pore pressure at hydration level bottom. During artificial hydration these pressures correspond to the injection pressures, at other moments the sensors measure pore water pressure.

Seal: displacements

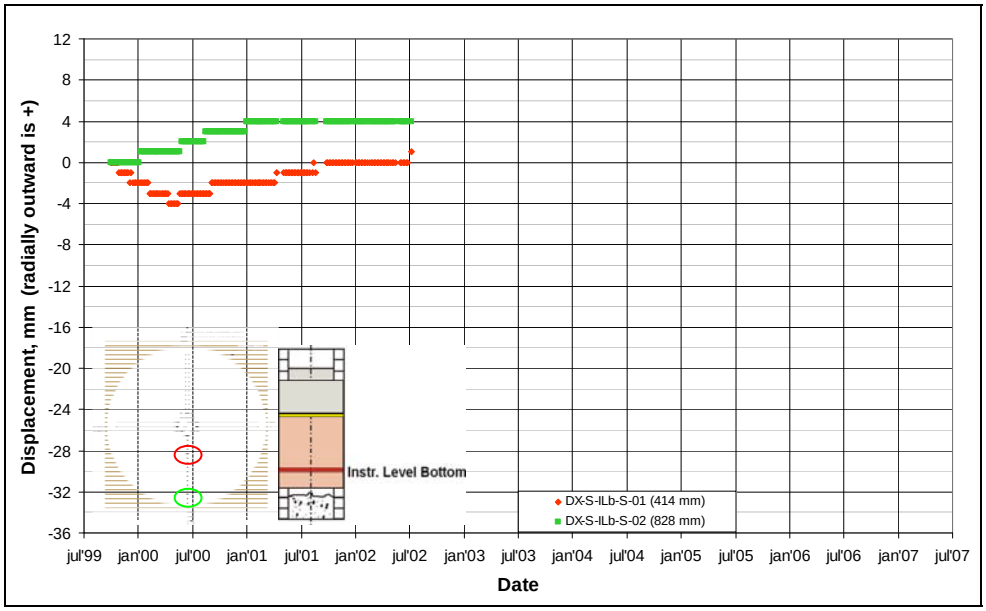

Figure 31: Displacements in the seal (at instrumented level bottom).

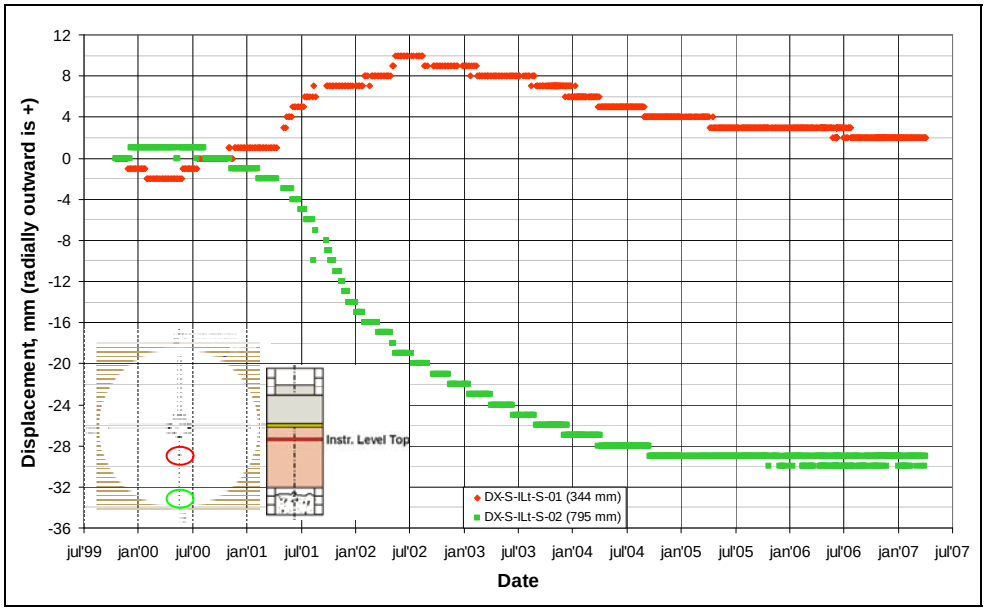

Figure 32: Displacements in the seal (at instrumented level top).

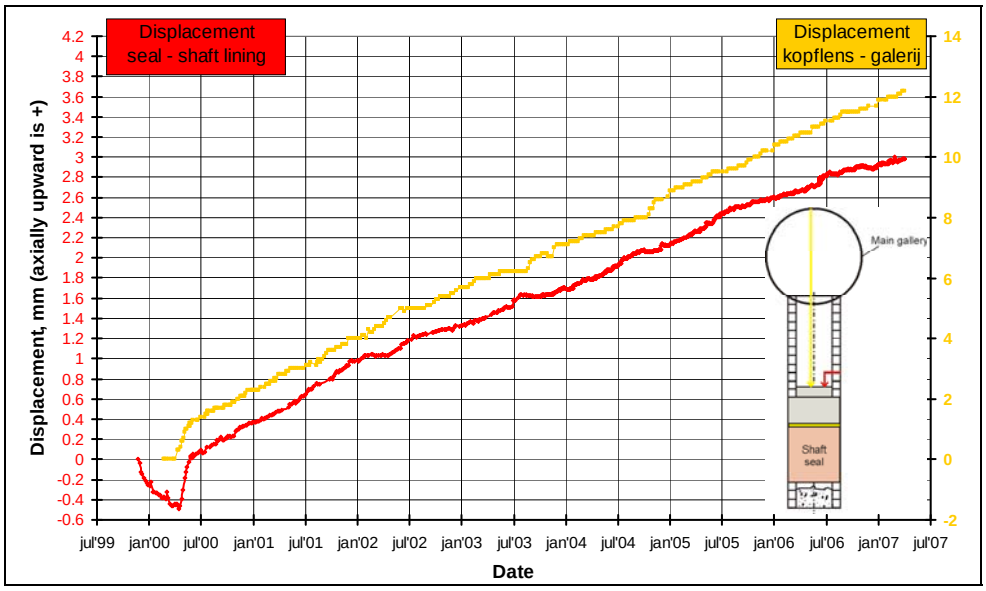

Figure 33: Displacements of the top of the seal. Two different reference points were used: inside the experimental shaft (red) and at the top of the main gallery (yellow).

Seal: relative humidity

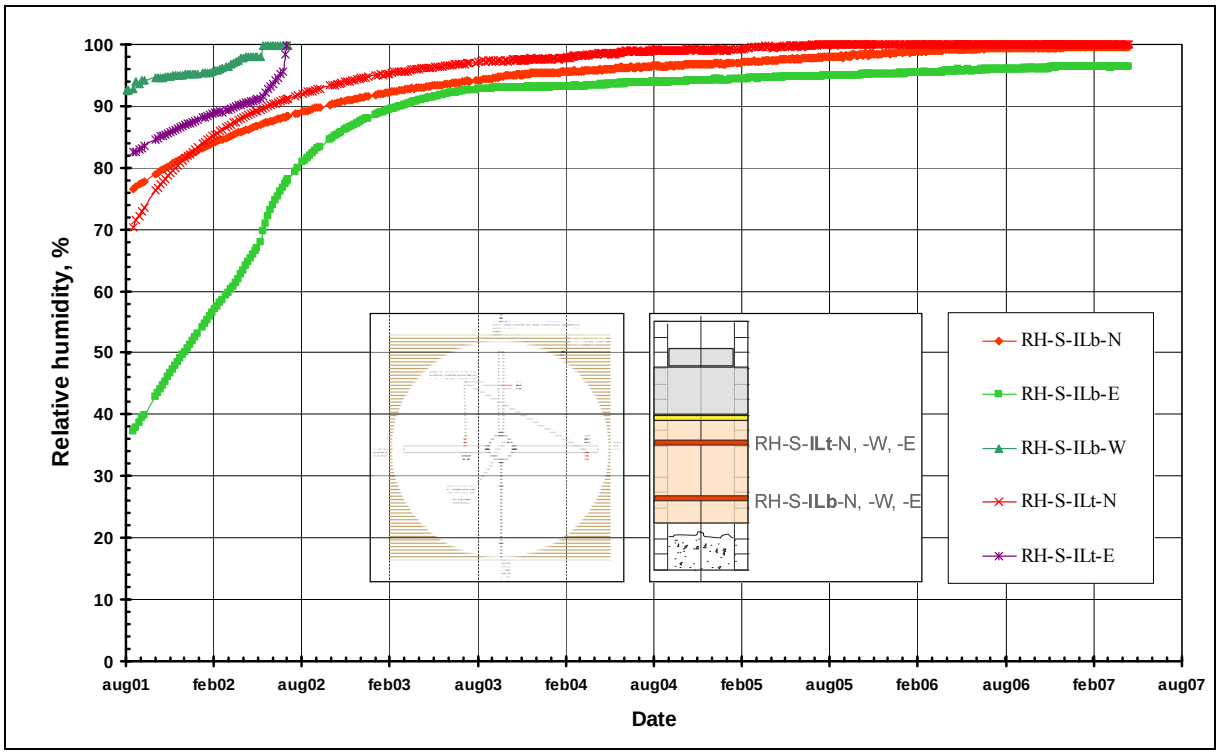

Figure 34: RH measurements in the seal at the instrumented levels (VAISALA sensors).

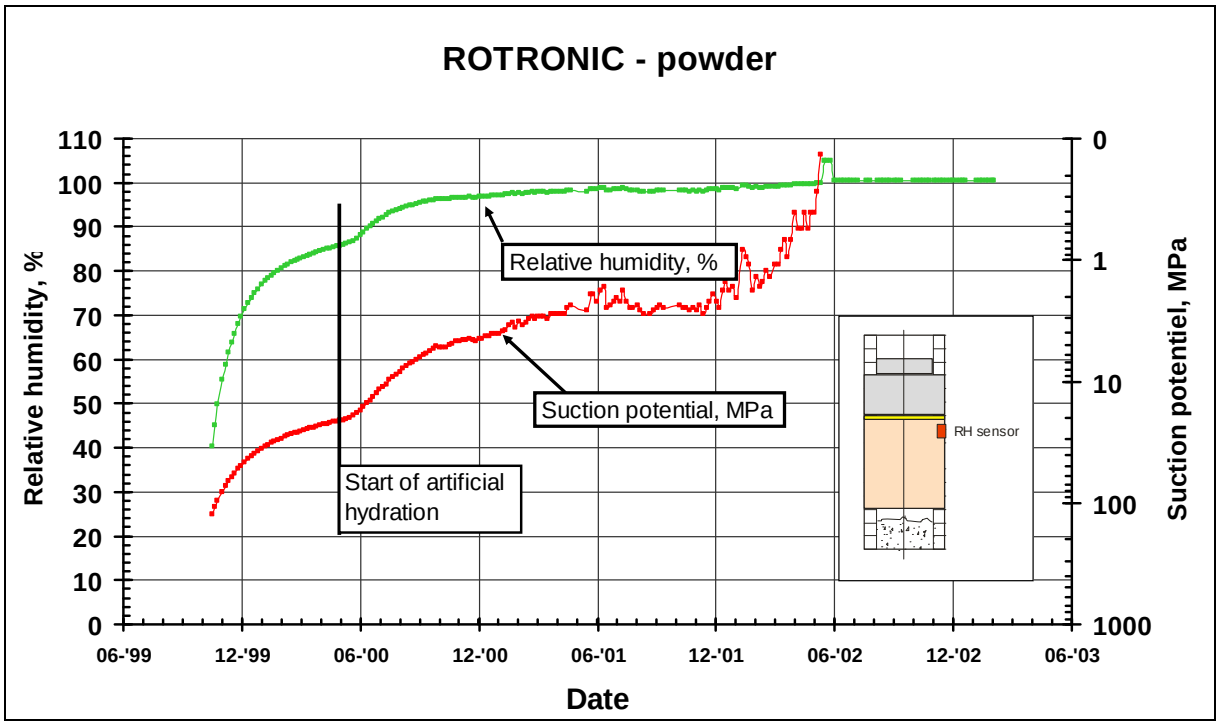

Figure 35: RH measurements at the seal/host rock interface (ROTRONIC sensor without clay cap).

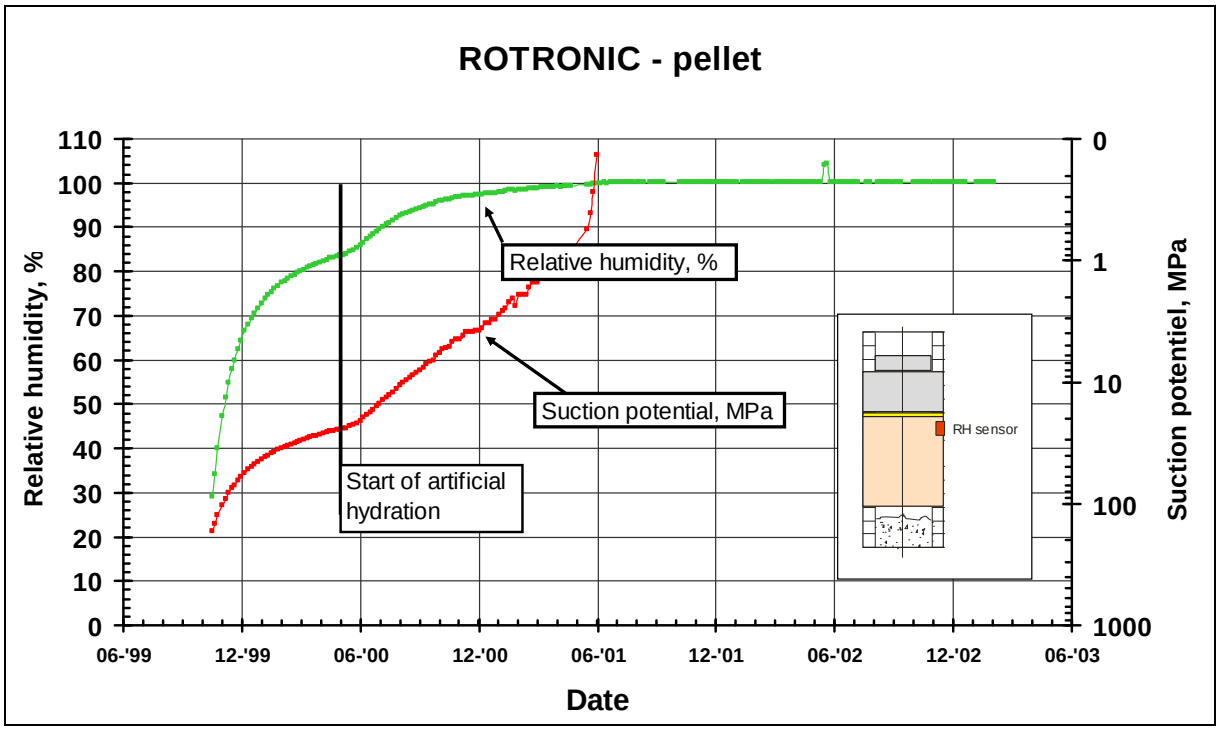

Figure 36: RH measurements at the seal/host rock interface (ROTRONIC sensor with clay cap).

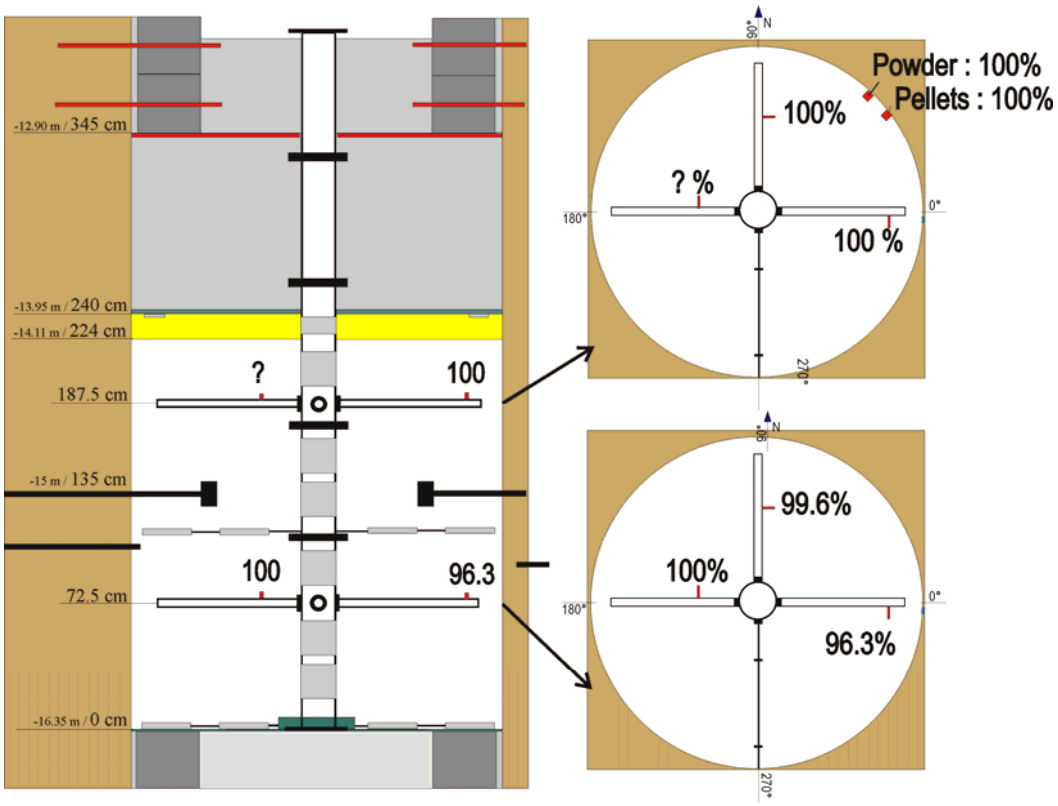

Figure 37: Overview of RH-measurements on 18th April '07.

Host rock: total stress

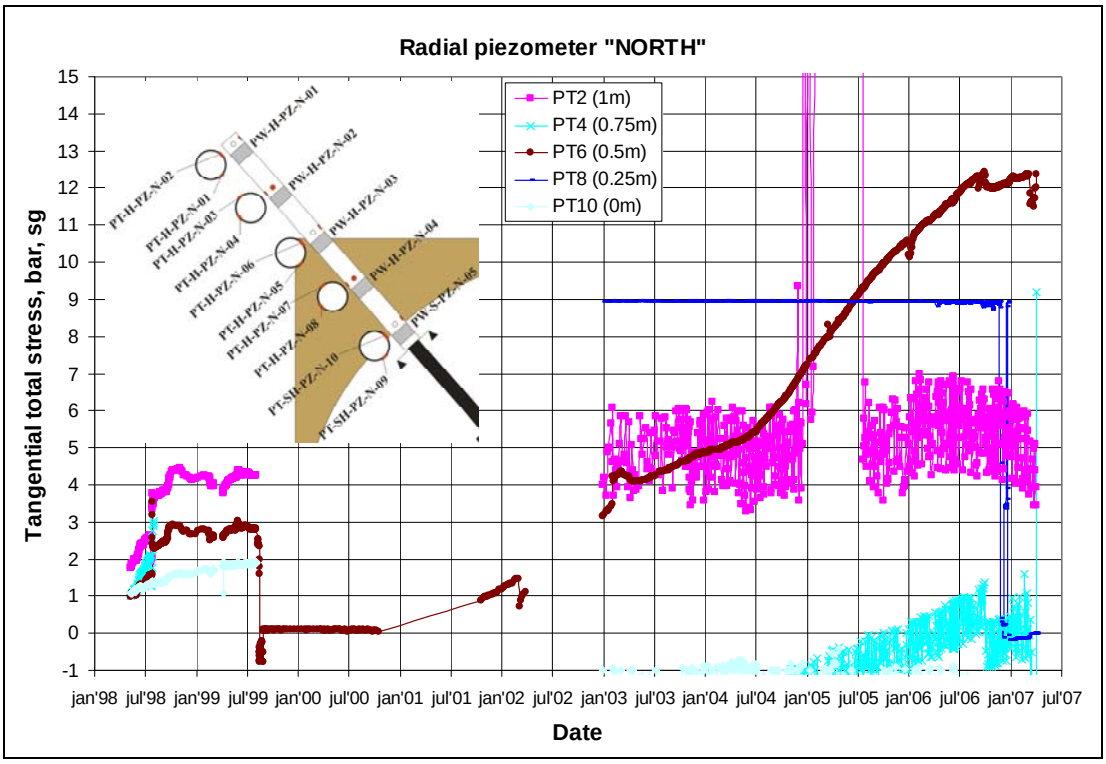

Figure 38: Tangential total stress in the host rock on the northern radial piezometer.

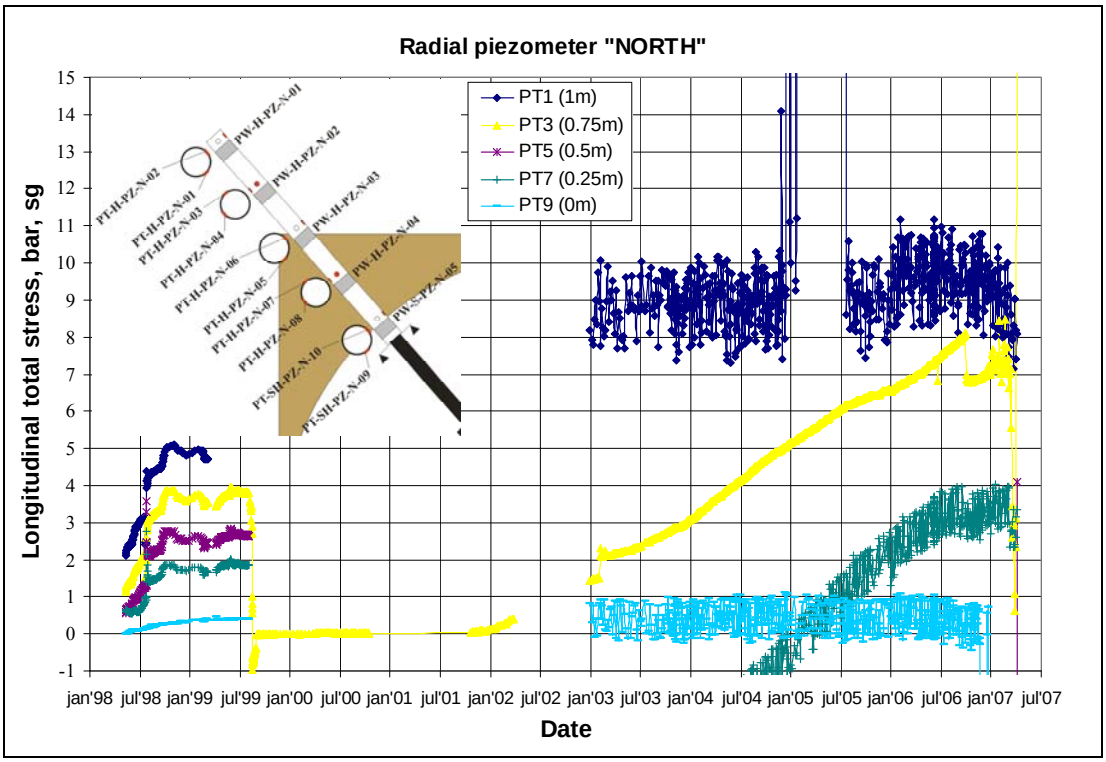

Figure 39: Longitudinal total stress in the host rock on the northern radial piezometer.

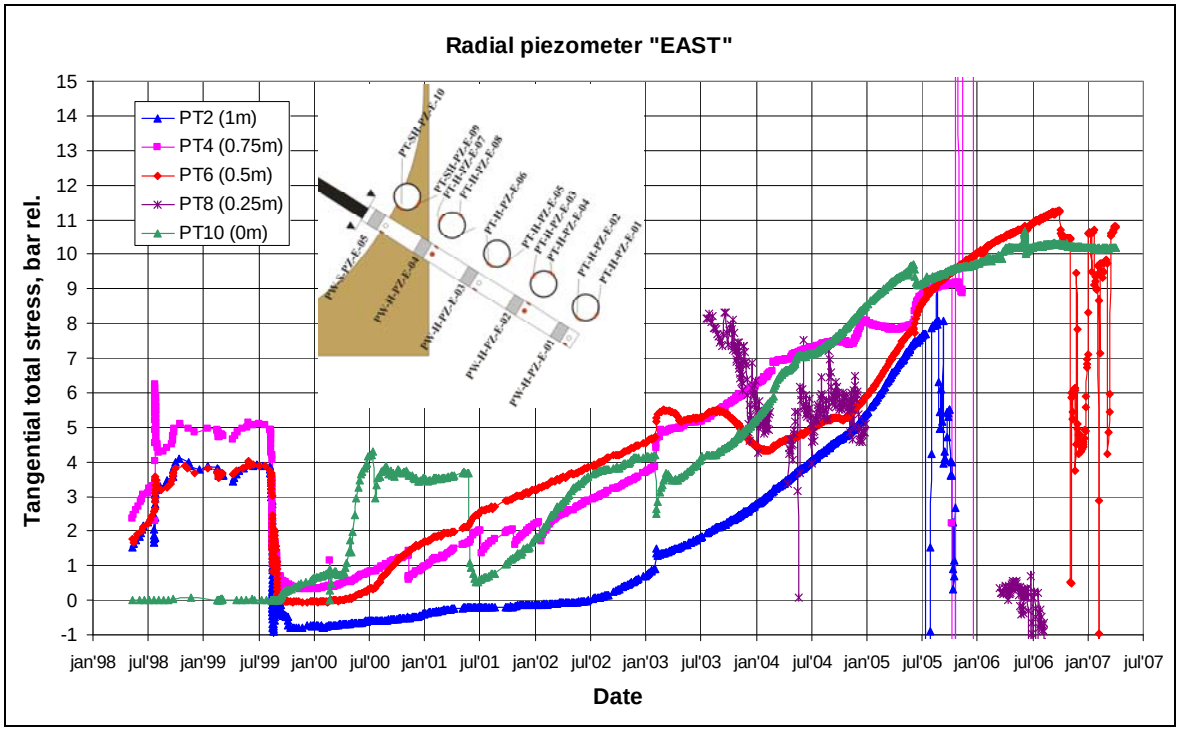

Figure 40: Tangential total stress in the host rock on the eastern radial piezometer.

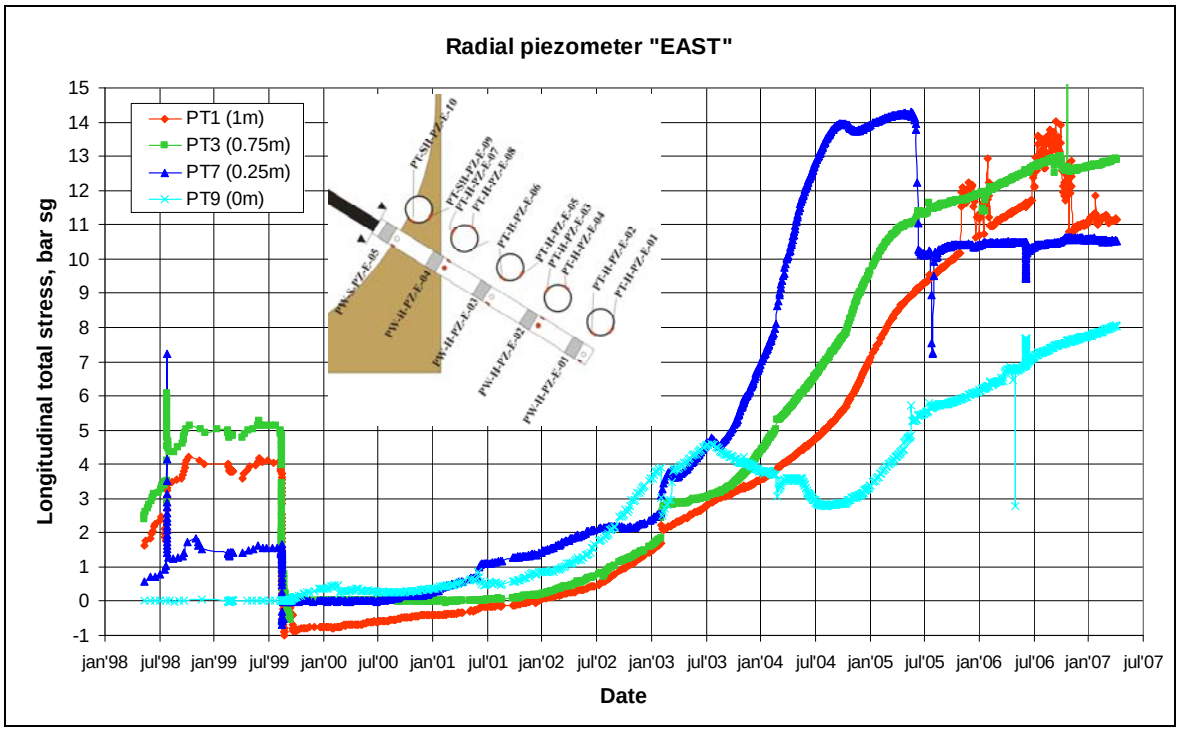

Figure 41:Longitudinal total stress in the host rock on the eastern radial piezometer.

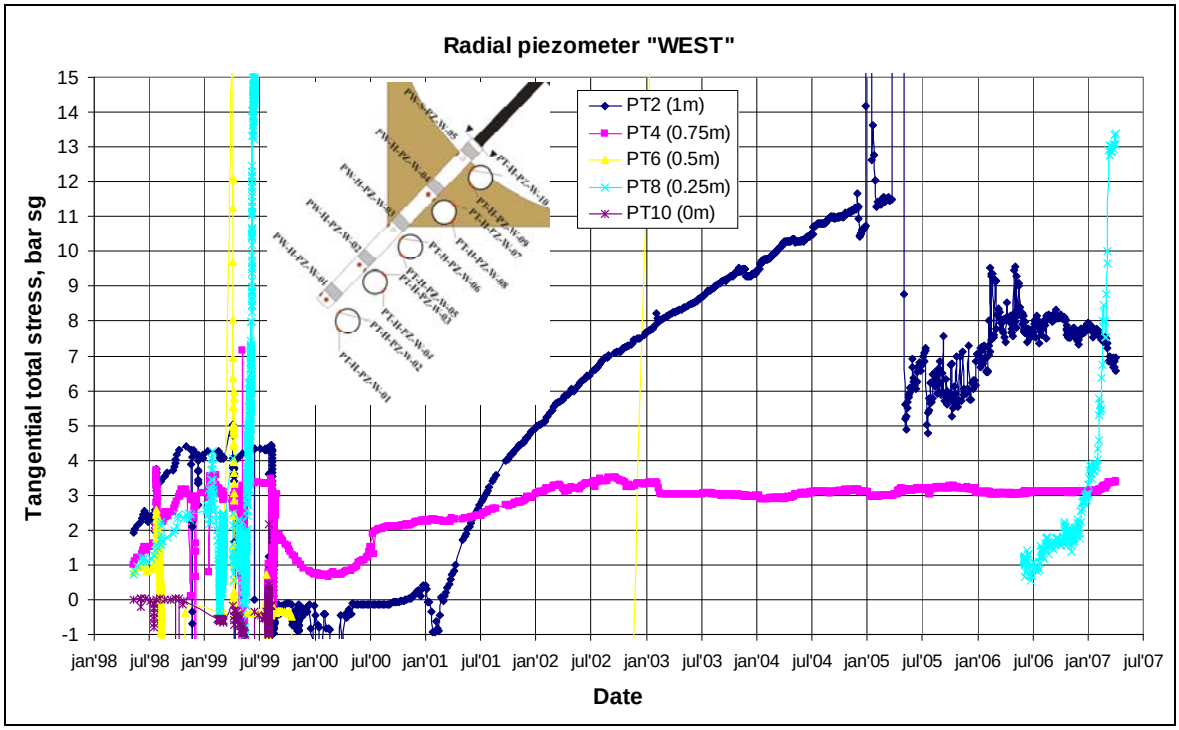

Figure 42: Tangential total stress in the host rock on the western radial piezometer.

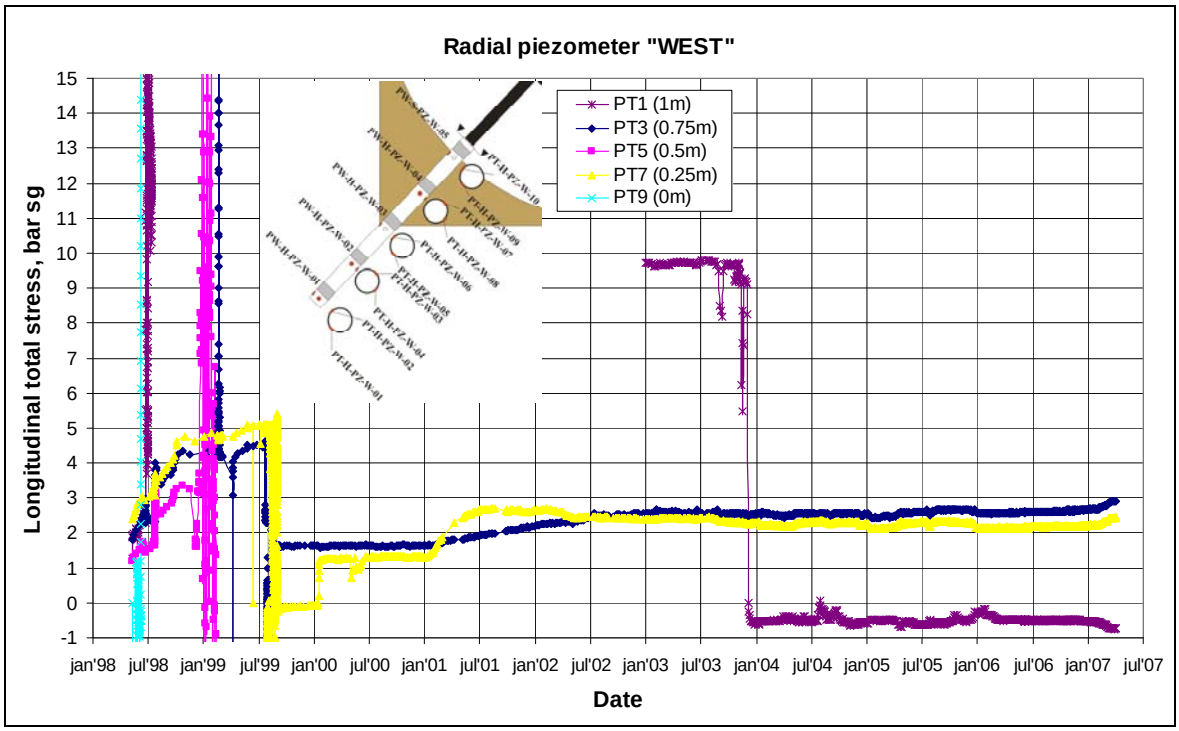

Figure 43: Longitudinal total stress in the host rock on the western radial piezometer.

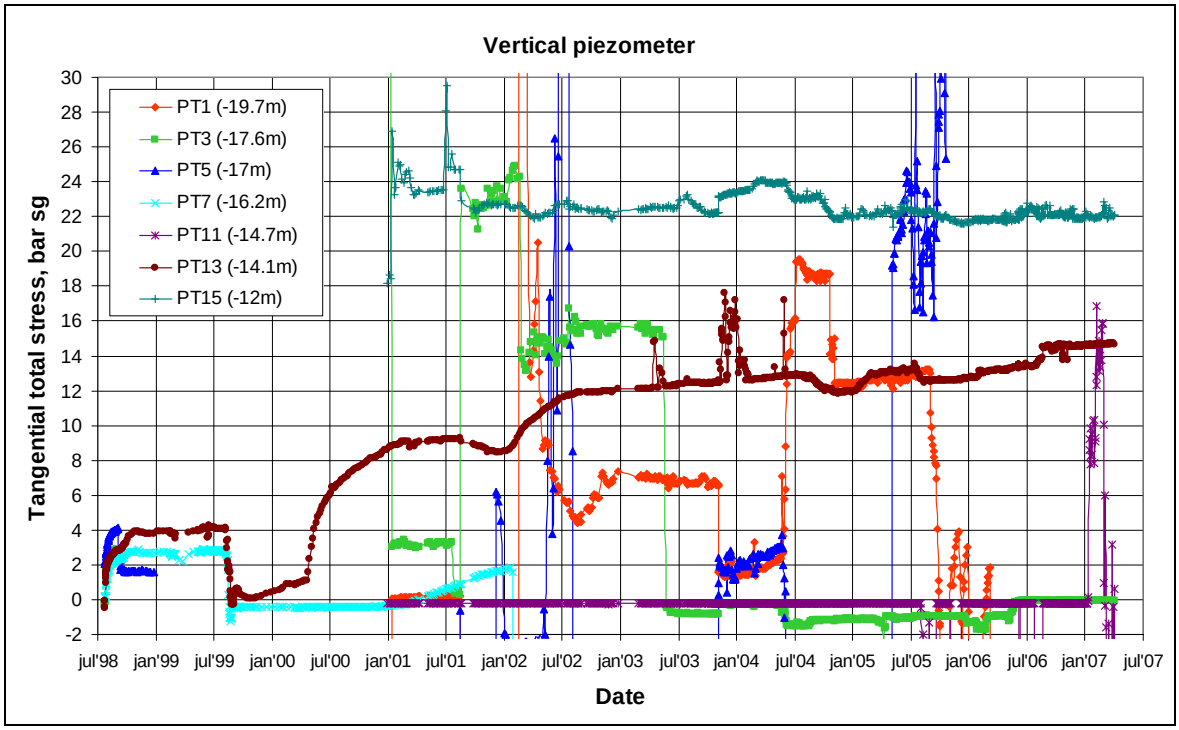

Figure 44: Tangential total stress in the host rock on the vertical piezometer.

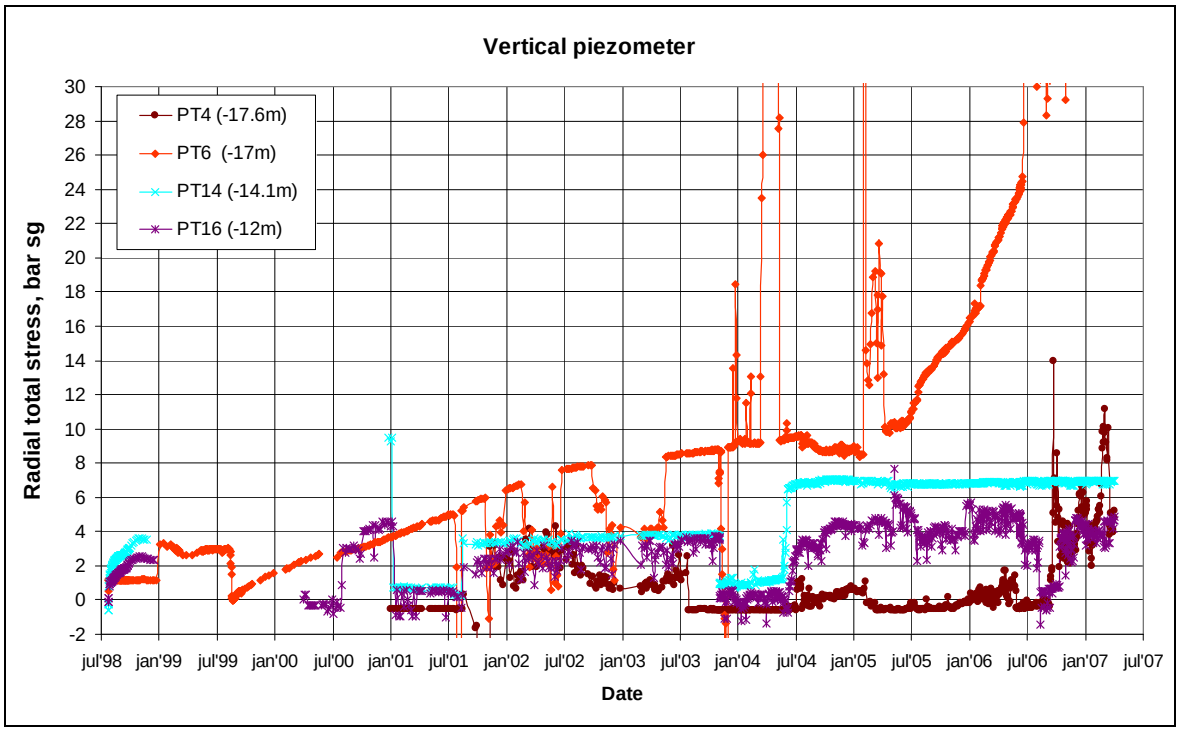

Figure 45: Radial total stress in the host rock on the vertical piezometer.

Host rock: pore pressure & effective stress

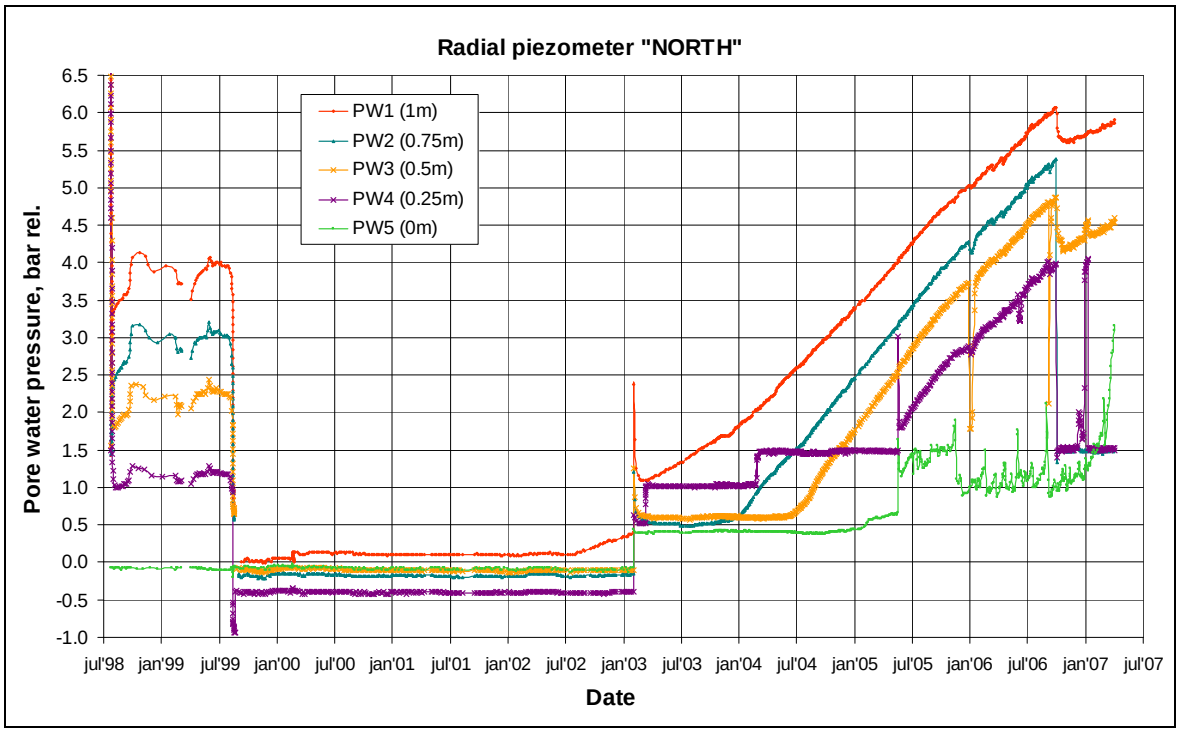

Figure 46: Pore pressure in the host rock at the northern radial piezometer.

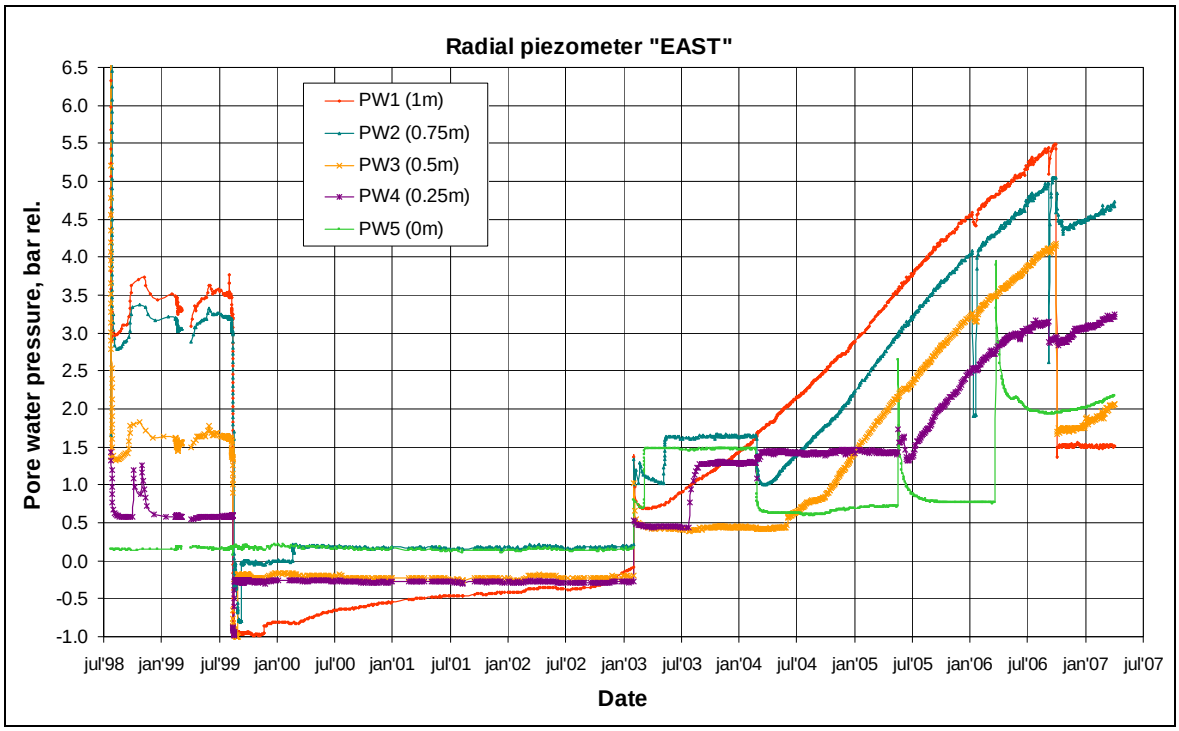

Figure 47: Pore pressure in the host rock at the eastern radial piezometer.

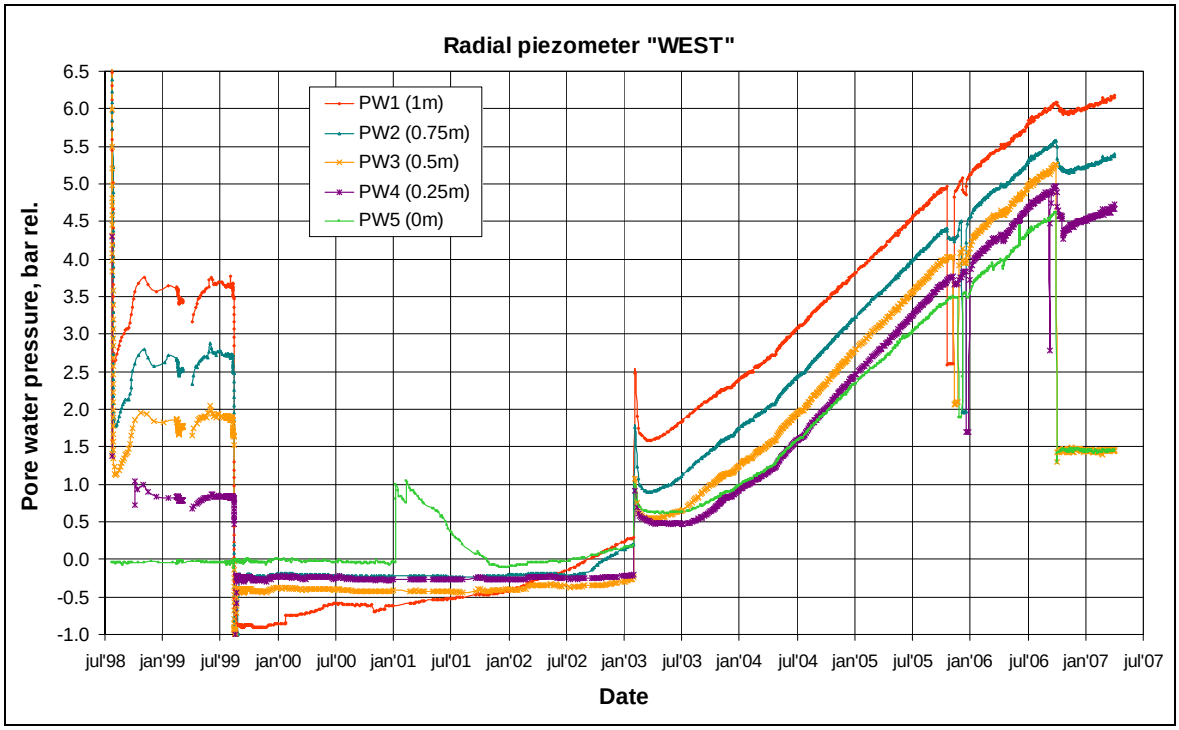

Figure 48: Pore pressure in the host rock at the western radial piezometer.

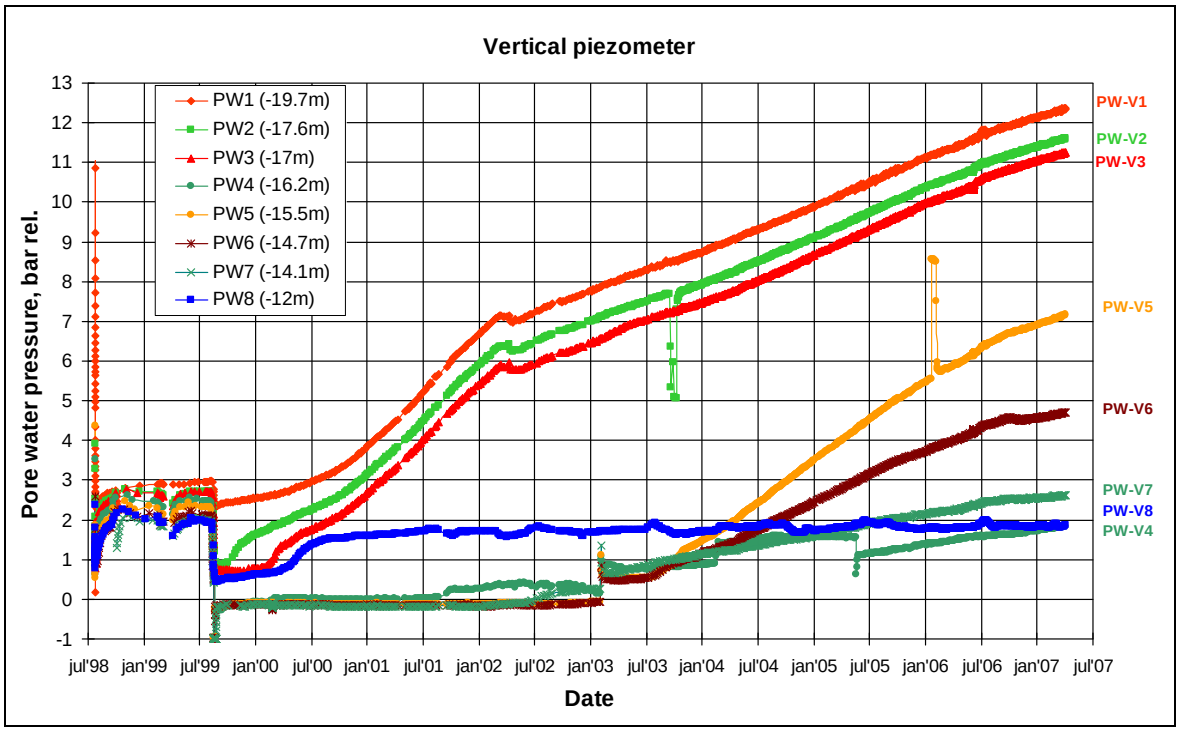

Figure 49: Pore pressure in the host rock at the vertical piezometer.

Host rock: displacements

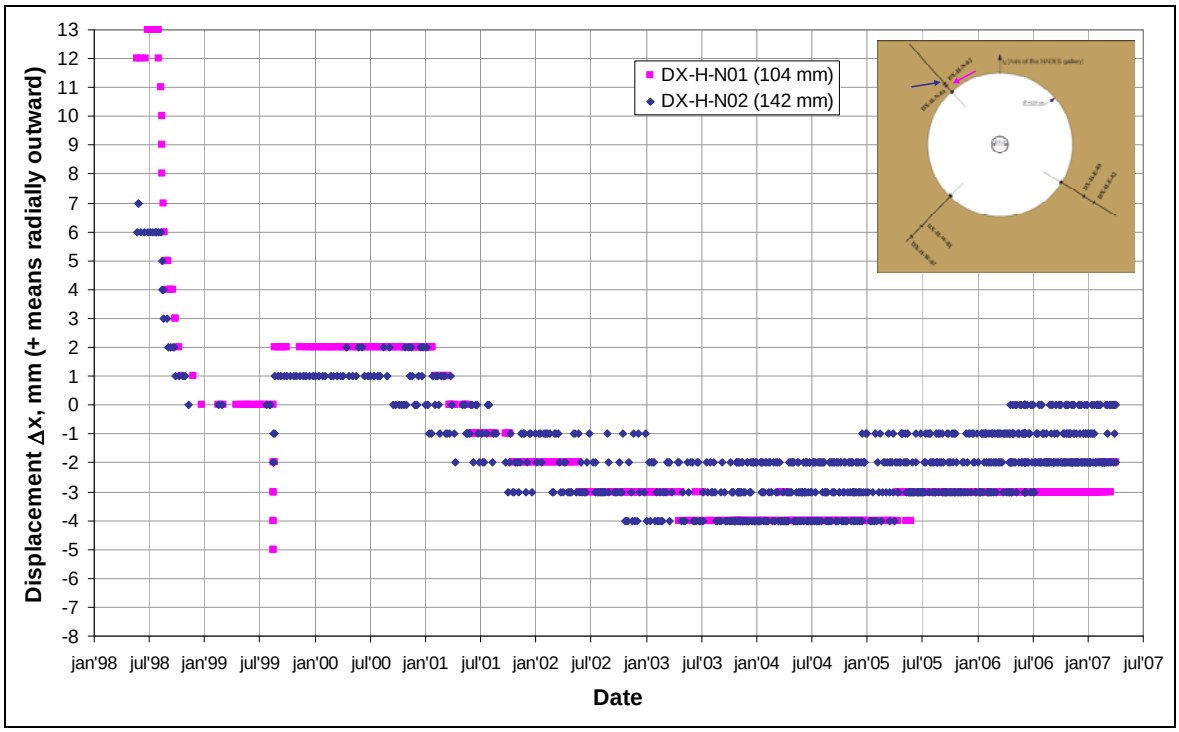

Figure 50: Displacements in the host rock at the north side of the seal (at hydration level middle).

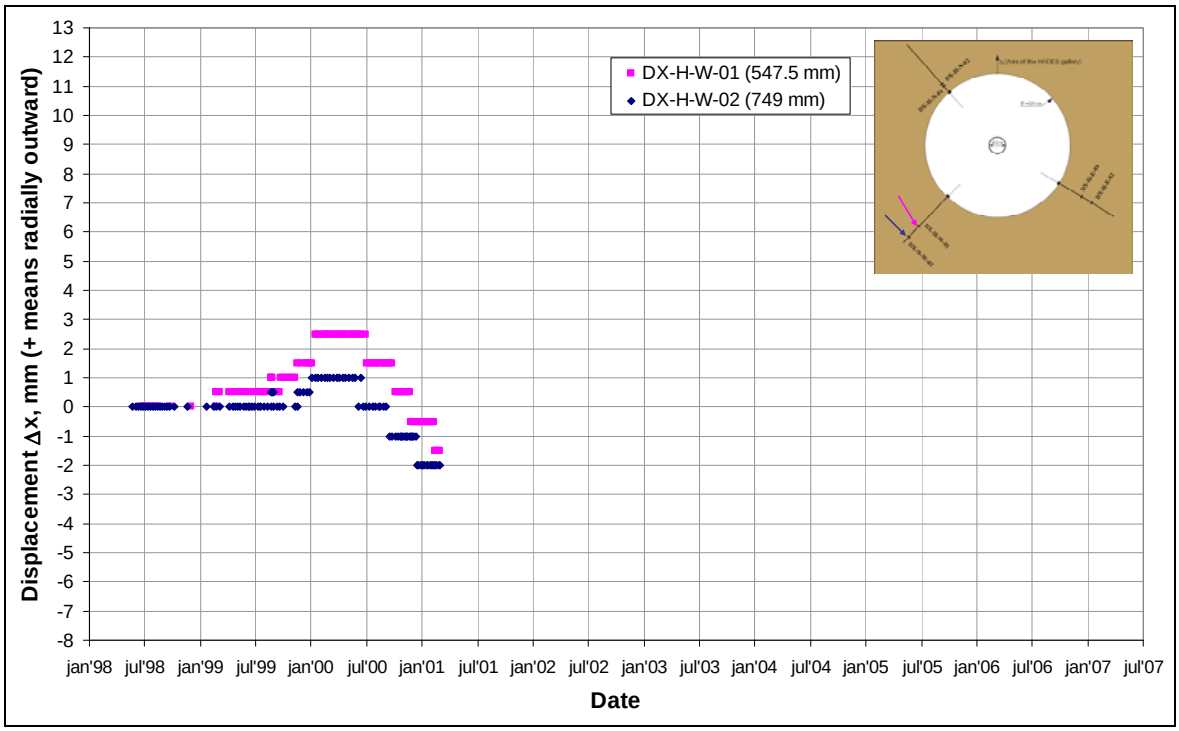

Figure 51: Displacements in the host rock at the west side of the seal (at hydration level middle).

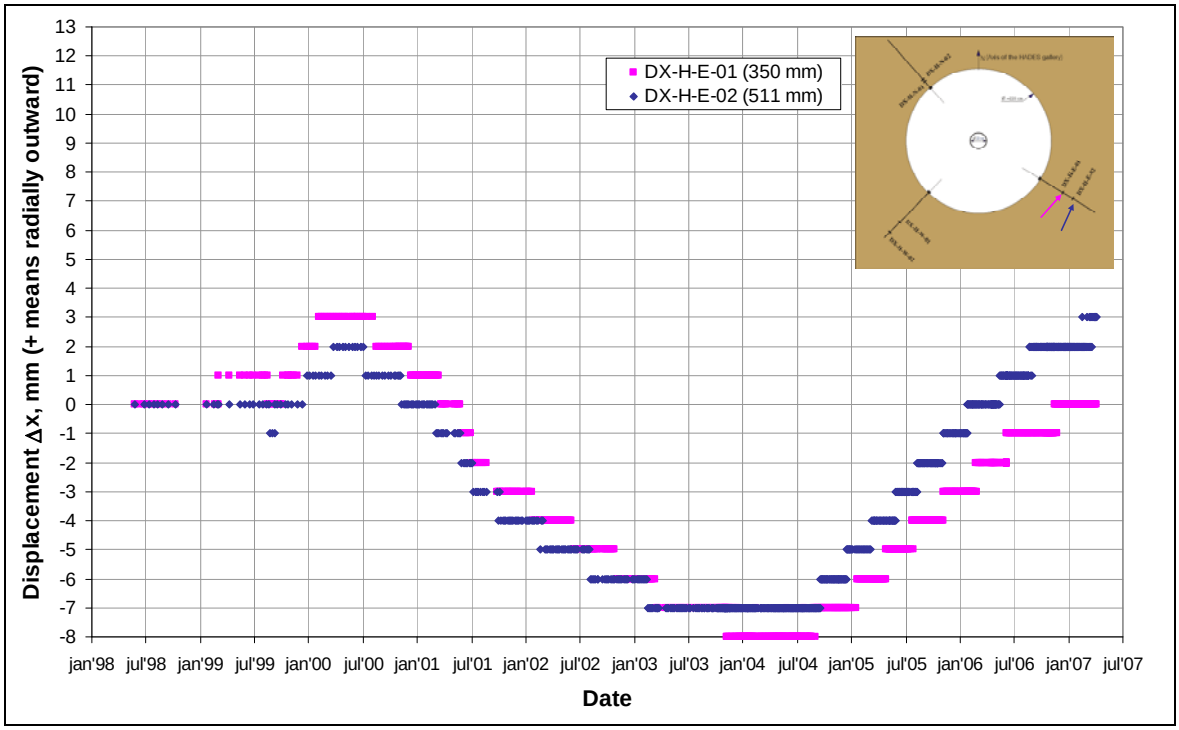

Figure 52: Displacements in the host rock at the east side of the seal (at hydration level middle).

Appendix 4 - Hydraulic conductivity testing

Hydraulic conductivity testing

Hydraulic conductivity is derived from constant head tests and in steady state flow regime. Darcy's law is applied. For 1D steady state water flow in porous media this law states that $Q = k \cdot A \cdot \frac{\Delta h}{l}$, where Q is the flow rate [m³/s], k the hydraulic conductivity [m/s], A the area [m²] and $\Delta h/l$: the gradient of the piezometric head [-].

Darcy's law can also be re-formulated for more complicated geometries. If, for example, a pressure change is applied at a sphere inside an infinite medium, the hydraulic conductivity of that medium can be calculated: $k = \frac{Q}{4 \cdot \pi \cdot \Delta h} \cdot \left(\frac{1}{r_0} - \frac{1}{r} \right)$, where Δh is the head difference between the applied pressure (at r_0) and the pressure at a distance "r" (see Figure 53). For $r \to \infty$, $k = \frac{Q}{4 \cdot \pi \cdot r_0 \cdot \Delta h}$.

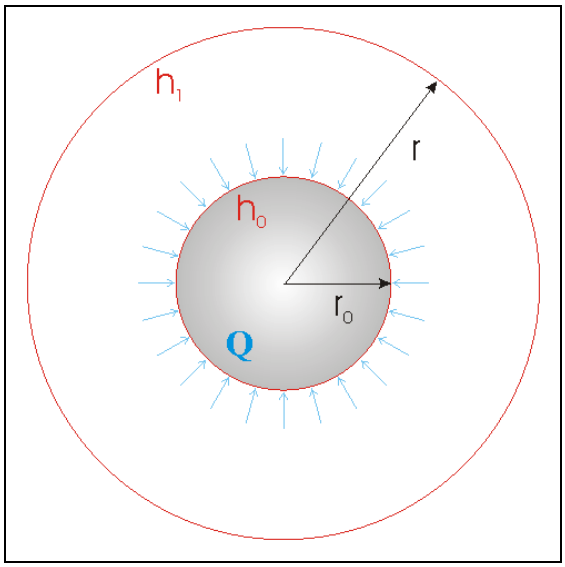

Figure 53: Sphere: a analytical solution is possible.

For other geometries, like a finite cylinder, there is no analytical solution. An approximation must thus be made. Figure 54 shows the applied approximation: a cylinder with spherical ends, for which an analytical solution can be found. $k = \frac{Q}{F \cdot \Delta h}$ (for $r \to \infty$) where $F = \frac{2 \cdot \pi \cdot D \cdot \left(\frac{L}{D} - 1 \right)}{\ln\left(\frac{L}{D} \right)}$ is a geometry factor. Numerical simulation of this problem revealed that

the accuracy of this approach is rather good and depends on the exact geometry of the cylinder. For the geometry of the filters used in RESEAL, a correction factor of 0.85 was determined.

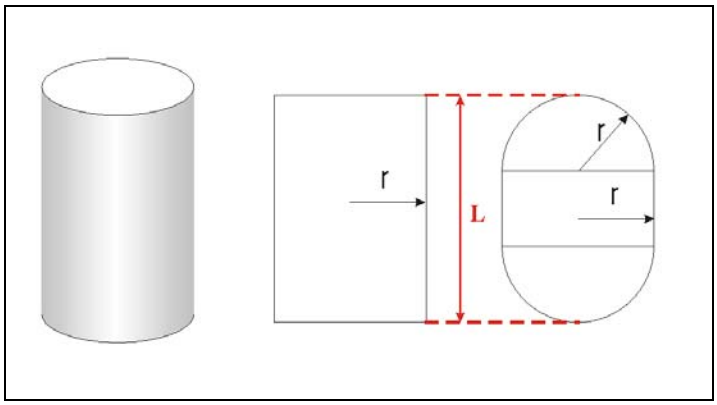

Figure 54: Approximation for cylindrical filters.

Another approximation was used for the disc-shaped filters (used at the horizontal hydration levels). The calculations are made assuming the injection is performed through a spherical filter with the same area as the disc (Figure 55). In this case, the geometry factor is $F = 4 \cdot \pi \cdot \frac{D}{2 \cdot \sqrt{2}}$. For the disc-shaped filters used in the seal, a correction factor of 0.87 was determined using numerical simulation.

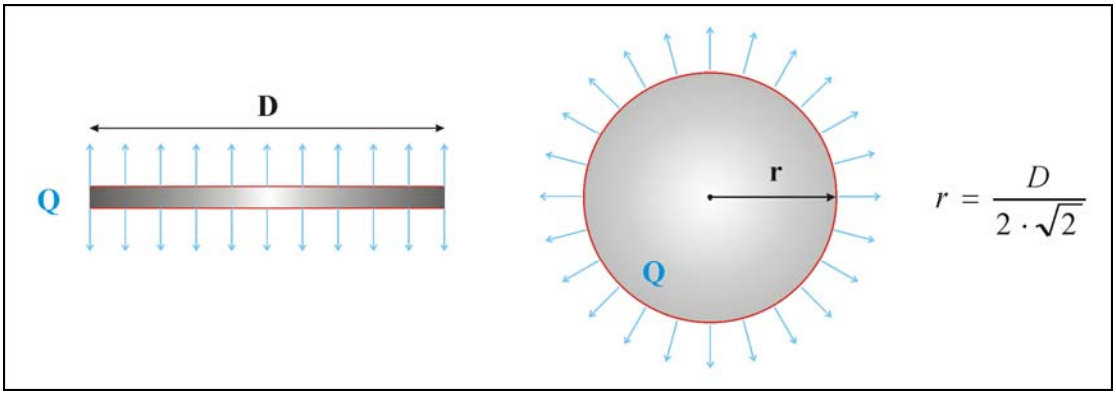

Figure 55: The disc-shaped filters are approximated by a sphere with the same area.

The actual test to determine the hydraulic conductivity of the seal is similar to tests performed to determine the in-situ hydraulic conductivity of Boom Clay around the URF. A conceptual lay-out of such a test is shown in Figure 56. A pressure controller imposes a constant pressure at a piezometric filter in the host rock. The flow rate Q is monitored using a precision balance, since Δh and F are known, k can be calculated. Each piezometric filter is connected to the gallery by a twin tube system (identical to that on Figure 56). One tube is used to measure water pressure, the other one to inject (or extract) water. Once the injection pressure is applied to one twin tube, the pressure transducer connected to the other twin tube should immediately measure the applied pressure: the tubes are both connected to the same filter and should therefore have the same hydraulic head.

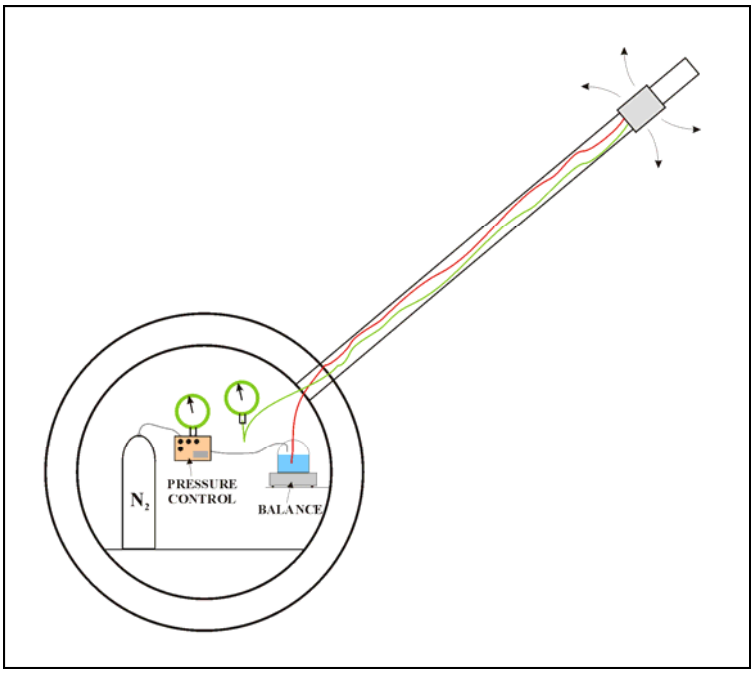

Figure 56: Lay-out of hydraulic conductivity measurements in Boom Clay.

Appendix 5 - Technical plans shaft seal

Technical plans shaft seal

Technical plans of the shaft seal are available on the CD-Rom included.

Appendix 6 - Sensor data shaft seal

Sensor data shaft seal

Sensor data of the shaft seal are available on the CD-Rom included.

European Commission

EUR 24161 – RESEAL II – A large-scale in situ demonstration test for repository sealing in an argillaceous host rock – Phase II

Luxembourg: Office for Official Publications of the European Communities

2009 — 288 pp. — format, e.g. 21.0 x 29.7 cm

ISBN 978-92-79-13626-9
doi 10.2777/54857

How to obtain EU publications

Publications for sale:

- via EU Bookshop (http://bookshop.europa.eu);
- from your bookseller by quoting the title, publisher and/or ISBN number;
- by contacting one of our sales agents directly. You can obtain their contact details on the Internet (http://bookshop.europa.eu) or by sending a fax to +352 2929-42758.

Free publications:

- via EU Bookshop (http://bookshop.europa.eu);
- at the European Commission's representations or delegations. You can obtain their contact details on the Internet (http://ec.europa.eu) or by sending a fax to +352 2929-427